U.S. DEPARTMENT OF COMMERCE
National Technical Information Service
AD-A023 923

INTERAGENCY SYMPOSIUM ON UNIVERSITY RESEARCH IN TRANSPORTATION NOISE (2ND) HELD AT NORTH CAROLINA STATE UNIVERSITY, RALEIGH ON JUNE 5-7, 1974.

BOOK OF PROCEEDINGS, VOLUME I

North Carolina State University

June 1974

AD A023923

128023

DEPARTMENT OF TRANSPORTATION
UNITED STATES OF AMERICA

SECOND INTERAGENCY SYMPOSIUM ON UNIVERSITY RESEARCH IN TRANSPORTATION NOISE

NORTH CAROLINA STATE UNIVERSITY
RALEIGH, NORTH CAROLINA

JUNE 5-7, 1974

PROCEEDINGS

VOLUME I

REPRODUCED BY
NATIONAL TECHNICAL
INFORMATION SERVICE
U. S. DEPARTMENT OF COMMERCE
SPRINGFIELD, VA. 22161

BIBLIOGRAPHIC DATA SHEET

1. Report No. DOT-TST-74-29

2.

3. Recipient's Accession No.

4. Title and Subtitle
Second Interagency Symposium on
University Research in Transportation Noise
VOLUME I

5. Report Date June 5-7, 1974

6.

7. Author(s)

8. Performing Organization Rept. No.

9. Performing Organization Name and Address
North Carolina State University
Raleigh, N.C

10. Project/Task/Work Unit No.

11. Contract/Grant No. DOT-OS-40040

12. Sponsoring Organization Name and Address
Department of Transportation
Office of Noise Abatement
2100 2nd St. S.W., Rm. 5222
Washington, D.C. 20590

13. Type of Report & Period Covered Final

14.

15. Supplementary Notes

16. Abstracts

The intent of the Second Interagency Symposium on University Research in Transportation Noise was to continue to focus attention on university research in basic and applied noise problems related to transportation. The purpose of these proceedings is to record and discuss current research studies, and objectives of research programs.

Volume I of the proceedings covers papers presented on Aerodynamic Noise, Noise from Flow Interaction with Solid Bodies, Rotor Noise, and Selected Problems I.

17. Key Words and Document Analysis. 17a. Descriptors

Transportation Noise

University Research Symposium

17b. Identifiers/Open-Ended Terms

PRICES SUBJECT TO CHANGE

17c. COSATI Field/Group

18. Availability Statement
Unlimited

19. Security Class (This Report) UNCLASSIFIED

20. Security Class (This Page UNCLASSIFIED

21. No. of Pages 469

22. Price # 12.00

BOOK OF PROCEEDINGS

Volume I

SECOND INTERAGENCY SYMPOSIUM ON UNIVERSITY RESEARCH IN TRANSPORTATION NOISE

North Carolina State University
Raleigh, North Carolina
June 5-7, 1974

Symposium Sponsor

U. S. Department of Transportation

Cooperating Agencies

National Aeronautics and Space Administration
National Science Foundation
Department of Defense:
Air Force Office of Scientific Research
Office of Naval Research
Army Research Office
Environmental Protection Agency

PREFACE

The contents of these Proceedings are papers contributed to the Symposium. Most of the papers are presented at the Symposium, while some are included only in the Proceedings. It is intended that these volumes will provide a broad current view of university research in basic and applied noise problems related to transportation that is being carried out under the support of the various Federal Agencies.

The contents of the volumes are arranged according to the subject topic as they appear in the program of presentations at the Symposium. For convenience, a complete author index is provided at the end in each of the volumes.

Our appreciation is extended to Ms. Anne Gregory for her patience and diligence in the preparation of these volumes.

Gordon Banerian William F. Reiter

North Carolina State University
Raleigh, North Carolina
June, 1974

TABLE OF CONTENTS

Page

VOLUME I

AERODYNAMIC NOISE. 1
NOISE FROM FLOW INTERACTION WITH SOLID BODIES. 185
ROTOR NOISE. 280
SELECTED PROBLEMS I. 401
ALPHABETICAL LISTING OF AUTHORS. 460a

VOLUME II

SELECTED PROBLEMS II 461
SOCIETAL PROBLEMS. 587
COMBUSTION NOISE 682
DUCT ACOUSTICS 755
ALPHABETICAL LISTING OF AUTHORS. 936
APPENDIX (LATE PAPERS) 938

BANQUET SPEAKER

Albert C. Trakowski
Deputy Assistant Administrator for Environmental Engineering
Environmental Protection Agency
401 M Street S.W.
Washington, D. C.

INVITED LECTURERS

Dr. M. Goldstein

"Recent Developments in Fan Noise Analysis"

Dr. J. E. Ffowcs-Williams

"Aircraft Noise and Prospects for Its Control"

Dr. R. John

"Surface Transportation Noise Abatement Programs in TSC"

Dr. A. Novick

"Nature's Sonar (Echo Location in Bats)"

Dr. H. E. von Gierke

"Noise Exposure Compatible with Public Health and Welfare"

Mr. H. Johnson

"The Price of Noise"

AERODYNAMIC NOISE

SUPPRESSION OF REFRACTION IN JET NOISE

T. Kelsall[1]

Institute for Aerospace Studies,University
of Toronto,Toronto,Canada.

ABSTRACT

The use of a jet of very cold gas to achieve refraction-free jet noise profiles is discussed and preliminary results given. They confirm the theoretical expectation that cancellation of refraction-elimination of the refraction 'valley' in the directivity-can be obtained by opposing temperature and velocity gradients (e.g., when $T = -35^\circ C$, $V = 0.074\ c_o$ at the jet nozzle). Although refraction is suppressed, effects of convection (small at this low Mach number) remain. This serves as a counter-example to the notion that convection and refraction are two inseparable aspects of the same physical process.

---

[1] Research Fellow. Institute for Aerospace Studies, U. of T. Toronto,Canada.

INTRODUCTION

The directivity of the noise from a jet can be simply explained in terms of the three processes demonstrated in figure 1 (following reference 1). The basic directivity of the jet is quasi-elliptical (figure 1a) but the sound profiles are bulged downstream by convection (figure 1b). Outward refraction due to velocity and temperature gradients causes the heart-shaped pattern characteristic of jets (figure 1c). The first two effects can be conveniently handled analytically, but the powerful third effect on the directivity; namely, refraction, cannot be so easily treated. This has prompted a new experimental approach which eliminates the refraction effect in selected circumstances.

To achieve refraction cancellation, a jet of air is used, cooled with liquid nitrogen, in which the temperature gradient opposes the velocity gradient in such a way that the inward refraction caused by the former effectively cancels the outward refraction imposed by the latter. The experimental set-up is similar to that of Grande[2], except that the air was pre-cooled by bubbling it through liquid nitrogen before it entered the jet. Narrow band (1/3 octave) jet noise profiles, and sound level profiles from a pure tone point source were obtained.

Representative results are shown in Fig. 2. All results are the average of two measurements, one on each side of the jet axis, plotted in polar coordinates with a scale of 5 db/inch, and normalized to zero at = 25°. The bottom curve shows the directivity of a normal room temperature jet, dominated by the outward bending from velocity gradient refraction, with its characteristic valley on the axis. The upper curve shows the directivity of a very cold jet (-70°C), whose pattern is dominated by the inward bending of the temperature gradient refraction, which causes an increase in intensity along the jet axis. The middle curve shows no pronounced refractive peak or valley at the axis and corresponds to the point where the refraction effects due to velocity and temperature gradients cancel each other. Figure 3 shows two sets of measurements for the non-refractive case, both those from the point source and those from the jet noise itself (within a 1/3 octave band) at 10,000 Hz. The error associated with these graphs is approximately ± 1 db. The jet was in all cases operating at $24.6 \pm .4$ m/sec. (M = .08), and refraction cancellation required a temperature of -35 ± 5°C. Room temperature was 28°C. These measurements were taken at 10,000 Hz. but similar work at 4,000 Hz. shows that the temperature for cancellation has little frequency dependence.

These preliminary results have indicated that refraction cancellation in a cold jet is feasible. This work is now being extended to higher jet velocities and correspondingly lower temperatures, and it is hoped that a direct comparison with theory, as well as a greater understanding of the refraction process in a jet, will be forthcoming.

ACKNOWLEDGEMENT

This research was sponsored by the National Research Council of Canada under N.R.C. Grant A-2003 and by the Air Force Office of Scientific Research, USAF, under Grant AF-AFOSR-70-1885A.

REFERENCES

1) H. S. Ribner, 1968. Canadian Aeronautical and Space Journal, 14, 281-298, Turnbull Lecture. Jets and Noise.

2) E. Grande. 1966. University of Toronto, Institute for Aerospace Studies, T.N. #110. (NASA CR-840 (1967)). Refraction of Sound by Jet Flow or Jet Temperature.

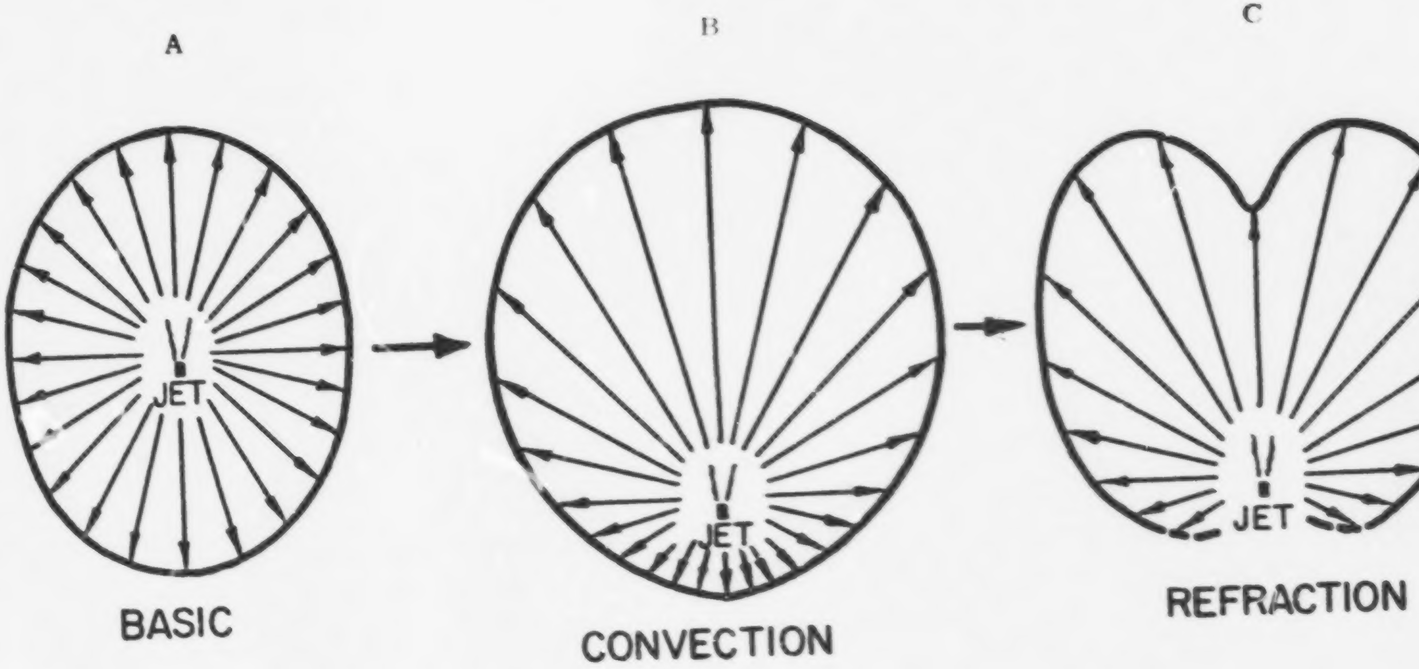
A
B
C
JET
JET
JET
BASIC
CONVECTION
REFRACTION

FIGURE 1 JET NOISE AS A BASIC PATTERN - NOT VERY DIRECTIONAL - WHICH IS POWERFULLY MODIFIED BY CONVECTION OF THE EDDY SOURCES AND REFRACTION OF THE SOUND WAVES BY THE MEAN FLOW.

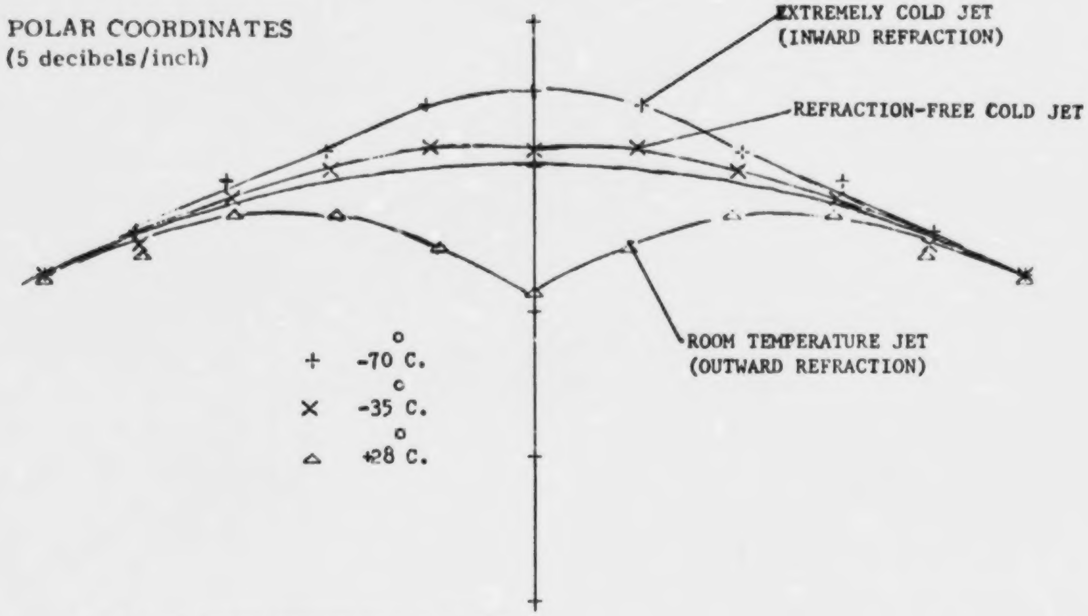

FIG. 2 JET NOISE DIRECTIONAL PATTERNS

Refraction has been completely suppressed in the middle case by balancing inward temperature-gradient refraction against outward velocity-gradient refraction.

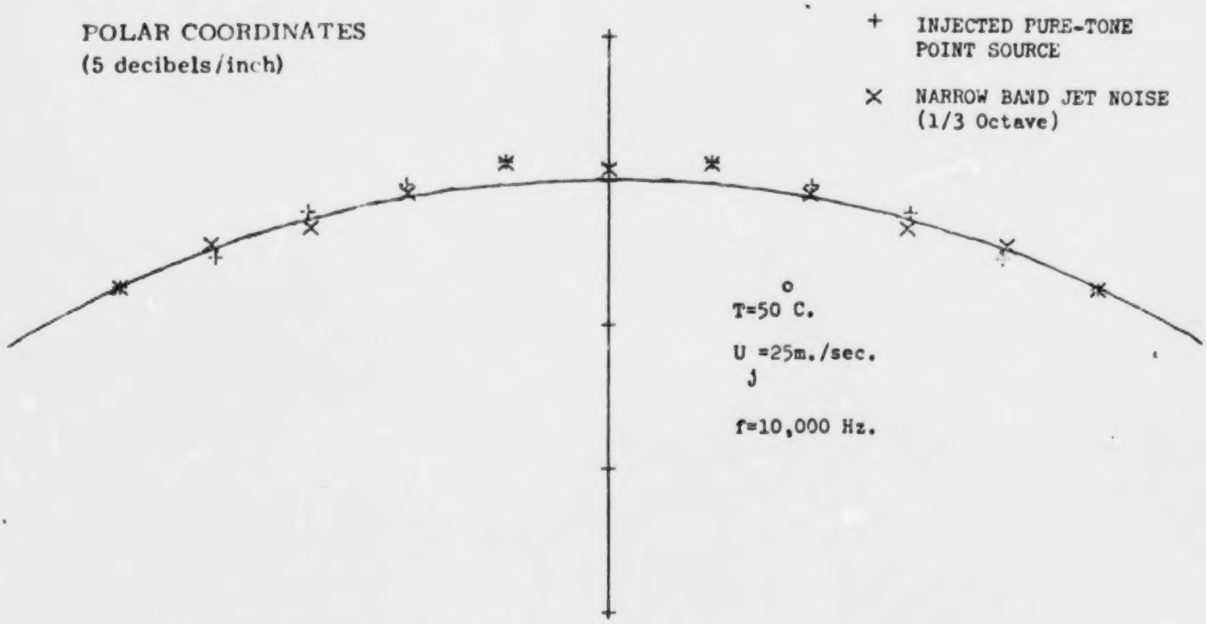

FIG.3 REFRACTION-FREE COLD JET

Match of directional patterns at small angles for injected pure-tone point source and narrow band filtered jet noise. Both show absence of refractive dip or peak centred on jet axis.

TURBULENT VELOCITY FIELD STRUCTURE IN A ROUND JET AND ITS RELATION TO FLUCTUATING PRESSURE FIELDS

by

D. P. Weber and B. G. Jones

Nuclear Engineering Program and Mechanical Engineering Department
University of Illinois at Urbana-Champaign, Urbana, Illinois 61801

In the classic works of Lighthill[1,2] on aerodynamic noise and turbulence as a noise producing phenomena, it was demonstrated that a fourth order velocity space-time correlation function plays the role of a quadrupole source in the classic wave equation. Kraichnan[3] has shown, by means of the general solution to the poisson equation, that the same type of term can be considered as the source of static pressure fluctuations in an incompressible flow. This term can be written as

$$T_{ijk\ell}(\vec{x},\vec{y},t,x) = \langle u_i(\vec{x},t)\ u_j(\vec{x},t)\ u_k(\vec{y},s)\ u_\ell(\vec{y},s)\rangle \qquad (1)$$

where $u_i(x,t)$ is the ith component of the turbulent velocity at spatial position x and time t, and the symbols $\langle\ \rangle$ indicate an ensemble average.

In order to develop analytical solutions for either the incompressible or compressible fluctuating pressure field, we must determine the structure of this fourth order tensor, containing 81 terms. The difficulty in examining experimentally so many terms with so many independent variables, and the lack of an adequate theory of turbulence, has prompted various assumptions to be made in an attempt to reduce this term to a small number of components which can possibly be experimentally determined.

The first of these assumptions is that the region over which the source term in (1) makes a contribution is relatively homogeneous and stationary. This allows us to write the two-point, two-time correlation function as being dependent only upon the spatial and temporal differences in their arguments. In the incompressible case, this leads to a closed form analytical solution for the pressure covariance with a modified Green's function for the bi-harmonic operator.[3] In the compressible case, the assumption is not so critical, but leads to considerable simplification in consideration of the third assumption below.

The second assumption deals with the fluctuating velocity field considered as a stochastic process. In particular, we are concerned with four random variables and the source term is a fourth order moment of the multivariate probability distribution. As difficult as it would be to determine these moments, it is much more difficult to determine the probability density function. Consequently, another hypothesis is introduced in which it is supposed that, from a rough use of the Central Limit Theorem, this velocity has an approximately normal, or Gaussian, probability distribution. This implies that all moments of the multi-variate distribution function can be written in terms of the second moments. Thus, we could write

$$\langle u_i(\vec{x},t)\, u_j(\vec{x},t)\, u_k(\vec{y},s)\, u_\ell(\vec{y},s)\rangle = \langle u_i(\vec{x},t)\, u_j(\vec{x},t)\rangle\langle u_k(\vec{y},s)\, u_\ell(\vec{y},s)\rangle$$

$$+ \langle u_i(\vec{x},t)\, u_k(\vec{y},s)\rangle\langle u_j(\vec{x},t)\, u_\ell(\vec{y},s)\rangle$$

$$+ \langle u_i(\vec{x},t)\, u_\ell(\vec{y},s)\rangle\langle u_j(\vec{x},t)\, u_k(\vec{y},s)\rangle \qquad (2)$$

Combining the first two assumptions, we have reduced the program to the determination of a second order tensor function of three spatial variables and one time variable.

The final assumption deals with the tensor structure itself. Robertson[4] has developed the invariant theory for isotropic tensors in turbulence, in which a single scalar function of a single spatial variable and a temporal variable will completely define the turbulent velocity covariance structure. Proudman[5] has used these forms to determine the noise from decaying isotropic turbulence. From Jones[6] measurements, it does not appear to be true that the turbulent structure in a jet fits the isotropic form and new structures are being investigated. Batchelor[7] and Chandrasekhar[8] have developed the invariant theory for axisymmetric tensor forms and Goldstein and Rosenbaum[9] have used these forms to predict noise patterns in round cold jets. With these tensor forms, it is only necessary to determine two scalar functions of two spatial variables and a temporal variable. It should be pointed out that the connection of this last assumption with the first assumption is that turbulent tensor invariant theory implies an assumption on homogeneity, in order that quantities of interest may remain invariant under reflection through points or planes.

An experimental examination of the turbulent velocity field structure in a 2.5 inch sub-sonic cold jet was performed. Primary emphasis was given to the description of the structure within the driven shear layer to five diameters downstream. Both single point and two-point correlation measurements were made with a special emphasis on the modeling of the two-point covariance function with axisymmetric tensor forms. A higher order stochastic analysis of the velocity field was performed using an extended version of the single variate gram-charlier expansion of the probability density function. Finally, a qualitative examination of the stochastic structure of the velocity field was performed using the Wiener-Hermite Expansion Theory for turbulence in an extended version to include the effect of mean velocity gradients.

The investigation was performed to provide fundamental information about the structure of the turbulent velocity field to be used in the prediction of aerodynamic noise in the Lighthill Formulation with an axisymmetric, joint-normal velocity covariance structure. The information provided, however, will serve an additional purpose. Ribner[10] has proposed a dilatation model of aerodynamic noise whose exploitation has not been made due to the difficulty in the experimental measurement of fluctuating pressure fields. The primary difficulty is the contamination of the sensor response with transverse velocity effects. Spencer and Jones[11] designed a bleed type pressure transducer and with a modification introduced by Planchon[12], it is believed that the spurious velocity effects have been significantly reduced. In order to verify this, an analysis of the pressure covariance in incompressible flow following Kraichnan[3] may be made. Similar to the compressible flow case, the velocity field covariance structure permits an analytic prediction of the true pressure field permitting a comparison with the measurements. If such a verification can be made, the dilatation model, being a scalar formulation, would be much simpler to implement at least for low mach number flows.

Measurements of both the mean velocity and Reynolds stress components were made and it was found that the mean velocity field exhibited a similarity development in the driven shear layer to five diameters downstream. That is, plots of mean velocity versus a similarity coordinate given by (r-R)/x were seen to collapse, where r is the radial position of the probe, x is the axial position, and R is the jet radius. Since turbulence production is related to the mean velocity gradient, we might imagine that the turbulent intensities would also develop similarity profiles. This was not found to be true to the extent exhibited by the mean velocity profiles, implying that the diffusion and viscous effects must be considered as well as production in the turbulent momentum transport. For application purposes, however, it was found that if the RMS velocity fluctuations were normalized with their maximum value across the shear layer, they collapsed very well when plotted against the similarity coordinate, (r-R)/x. Since this maximum value tends to lie at the point of maximum mean velocity gradient, the RMS velocity fluctuations can be easily modeled with a single axial measurement of variation with downstream position, and a single radial traverse giving the similarity development. These types of measurements were made for all three velocity components, with similar results.

The off diagonal elements of the Reynolds stress tensor, the shear stresses, were also measured. From these experimental results, several structure parameters, including the ratio of transverse to axial RMS velocities, a normalized shear stress, and the angle defining the direction of principal turbulent stress, were formed. In Figures 1 and 2, we have plotted these parameters, which show remarkable constancy in both the transverse and axial directions.

In addition to the single-point measurements, space-time correlations, both auto and cross, were made. The correlation is described by

$$R_{ij}(\vec{x},\vec{r},t,\tau) = \frac{\langle u_i(\vec{x},t)\; u_j(\vec{x}+\vec{r},t+\tau)\rangle}{\langle u_i^2(\vec{x},t)\rangle\langle u_j^2(\vec{x}+\vec{r},t+\tau)\rangle} \tag{3}$$

A typical plot of the correlation is given in Figure 3, where axial velocity components with axial spatial separations are given. Such correlations for both axial and transverse velocity components with axial and transverse separations without time delay were made, in addition to several space-time correlations. From the envelope of these latter curves, the integral time scale of the turbulence in the connected frame was determined. Several interesting facts were found including the linear trend of this time scale with the inverse of the mean velocity gradient. Most interesting, though, was the observed difference in this time scale for the two distinct velocity components. Since it is the variation of this time scale which accounts for the true source of noise from turbulence, use of this information will play a significant role in our noise predictions, as contrasted with the assumptions used by Goldstein and Rosenbaum.[9]

As mentioned earlier, the modeling of the velocity covariance structure would be considerably simplified if an assumption of local homogeneity could be employed. This was found to be moderately true and the velocity covariance was represented in the following manner:

$$<u_i(\vec{x})\, u_j(\vec{y})> = <u_i^2(\vec{x})>^{1/2} <u_j^2(\vec{y})>^{1/2} R_{ij}(\vec{z},\vec{r}) \tag{4}$$

where $$\vec{z} = \frac{\vec{x}+\vec{y}}{2} \quad \text{and} \quad \vec{r} = \vec{x}-\vec{y} \tag{5}$$

The inhomogeneity was factored out with the local RMS velocity fluctuations and the tensor structure function, R_{ij}, was found to be a slowly varying function of the absolute position, $\vec{z}$.

From the differences in the RMS velocity values, as well as the existence of significant shear stress components, it was felt that an isotropic description of the correlation function, R_{ij}, was inappropriate. The next more complicated form is the axisymmetric, which has invariance with respect to rotation about a line, rather than a point as in isotropic forms. When the mean velocity field has a uniform gradient, this axis of symmetry will be found to lie in the plane containing this gradient and the mean velocity and will not necessarily coincide with the axis of symmetry for the mean velocity profiles.[9,13] The axis that defines the rotational symmetry can be determined from single point x-probe measurements[14] and it coincides with the axes which define the principal stresses, which were defined by the angle β in Figure 1.

The importance of these considerations lies in the fact that the scalar functions which determine the covariance structure are functions of the separation distances along the axis of symmetry and transverse to it. Thus, if measurements are made in this rotated coordinate system, the modeling becomes considerably simplified. Figure 4 contains a schematic diagram of the fixed jet coordinate system and the rotated axisymmetric coordinate system. Both the velocities and the separation vectors must be rotated to this coordinate system, but in this lies the beauty of the x-probe. The simple transformations for velocity components are

$$\begin{aligned} \tilde{u} &= u \sin\beta + v \cos\beta \\ \tilde{v} &= -u \cos\beta + v \sin\beta \\ \tilde{w} &= w \end{aligned} \tag{6}$$

Since an x-probe output can be summed and differenced to give appropriate linear combinations of u and v, once β is determined, the axisymmetric components can be generated. Even more important for this analysis, however, is the experimental fact that β remained constant, implying a non-rotating axisymmetric structure.

The invariance of the forms was checked by comparing RMS levels and certain spatial correlations as shown, for example, in Figure 5. The curve labeled $\tilde{R}_{\tilde{v}\tilde{v}}(\tilde{\xi}_2)_{\text{corrected}}$ is simply $\tilde{R}_{\tilde{v}\tilde{v}}(0,\tilde{\xi}_2,\varepsilon)/\tilde{R}_{\tilde{v}\tilde{v}}(0,0,\varepsilon)$.

The defining scalar functions for axisymmetric forms are related to measurable correlations by the equations[9]

$$\tilde{\sigma}\,\tilde{R}_{\tilde{u}\tilde{u}}(\tilde{\xi}_1,\tilde{\sigma}) = -\frac{\partial}{\partial\tilde{\sigma}}\,\frac{\tilde{\sigma}^2 Q_1(\tilde{\xi}_1,\tilde{\sigma})}{\langle\tilde{u}_1{}^2\rangle} \tag{7}$$

$$\tilde{R}_{\tilde{v}\tilde{v}}(\tilde{\xi}_1,\tilde{\xi}_2,\tilde{\xi}_3) = -\frac{\partial}{\partial\tilde{\xi}_3}\,\frac{\tilde{\xi}_3 Q_2(\tilde{\xi}_1,\tilde{\sigma})}{\langle\tilde{u}^2{}_2\rangle} + \left[\tilde{\xi}_3^2\,\frac{\partial^2}{\partial\tilde{\xi}_1^2} - 2\,\frac{\partial^2}{\partial\tilde{\xi}_1\partial\tilde{\xi}_3}\,\tilde{\xi}_1\tilde{\xi}_3 + \tilde{\xi}_1^2\,\frac{\partial^2}{\partial\tilde{\xi}_3^2}\right]\frac{Q_1(\tilde{\xi}_1,\tilde{\sigma})}{\langle\tilde{u}_2^2\rangle} \tag{8}$$

where $\tilde{\sigma} = \sqrt{\tilde{\xi}_2^2 + \tilde{\xi}_3^2}$ and $\tilde{\xi}_1$ is the separation distance along the axis of symmetry.

Several models for Q_1 and Q_2 were examined and it was found that four parameters, the spatial integral scales along and transverse to the axis of symmetry for both axisymmetric velocity components, adequately model the entire velocity covariance structure. A matrix equation was also developed which relates commonly measured scales in the fixed jet coordinate system to these four defining parameters.[14] Since a simple inversion of equation (6) will give jet coordinate system velocities in terms of axisymmetric velocities, a general representation of these forms for integration purposes in the aerodynamic noise problem can be made.

Although we have adequately modeled the velocity covariance structure, we should recall that in calculating pressure fields from a velocity field structure, the source term is actually a fourth order moment of the multivariate distribution function. If the velocity field is broken into a mean component and a fluctuating component, the source term can be written in terms of the so-called turbulent-mean shear term and the turbulent-turbulent term. The first of these involves a second order covariance, the modeling of which we have just considered. The latter involves the fourth order moment which, under the joint normal hypothesis, can be reduced to products of second order covariances and modeled as before.

If the joint normal hypothesis is not true, the complexity of the fourth order moment precludes any hope of experimental measurement. Its utilization becomes an analytical necessity and a quantitative measure of its inadequacy becomes desirable. In an extension of our higher order moment temporal velocity covariances,[15] we have examined the convected frame higher order moments.

We recall that if a set of random variables is normally distributed, relatively few parameters are necessary to completely define the multi-variate probability density function. These include the means, the mean squares and the correlations defined by

$$\langle xy \rangle = \iint f(x,y)\ xy\ dxdy \tag{9}$$

where x and y are two random variables and f is their joint distribution function. When the random variables are stochastic processes such as a turbulent velocity field, these defining parameters become functions of the space-time differences in measurements. For our velocity field measurements, with zero means, the correlation that would define the density function for normally distributed random variables is:

$$R^{1,1}(\vec{r},\tau) = \frac{\langle u(\vec{x},t)\ u(\vec{x}+\vec{r},t+\tau) \rangle}{\sigma^2} \tag{10}$$

where $\sigma^2 = \langle u^2(\vec{x},t) \rangle = \langle u^2(\vec{x}+\vec{r},t+\tau) \rangle$ (11)

where we have restricted ourselves to the u-component of the fluctuating velocity field and consider only homogeneous, stationary fields. If the normal distribution holds, all higher order moments, defined by

$$R^{m,n}(\vec{r},\tau) = \frac{\langle u^m(\vec{x},t)\ u^n(\vec{x}+\vec{r},t+\tau) \rangle}{\sigma^{m+n}} \tag{12}$$

can be written in terms of $R^{1,1}$. A particular example considered here is

$$R^{2,2} = 1 + 2\left[R^{1,1}\right]^2 \tag{13}$$

Frenkiel and Klebanoff[16] have shown such relations to be quite well satisfied in grid generated isotropic turbulence. Our measurements, however, were conducted in a two stream mixing layer where the effect of the mean velocity gradient was significant. An example of the results is shown in Figures 6 and 7. In Figure 6 we have plotted the space-time correlation function and determined the converted frame covariance which was then used in equation (13) to predict a higher order moving frame correlation, the curve labeled Gaussian in Figure 7. The consistent discrepancy shows the limitations of the joint normal hypothesis by the turbulent-turbulent term, it is clear that some account must be given to this error introduced by the joint normal hypothesis.

An examination of the equations of motion using the Wiener-Hermite expansion technique has clearly indicated the source of the difficulty for the joint normal hypothesis.[14] The turbulent source function, consisting of the interaction of the mean velocity field with the turbulent shear stress, has clearly provided a mechanism for the direct creation of non-Gaussian turbulent energy. An examination of the flatness factor measurements in shear flow has also demonstrated the inapplicability of assuming a near to normal turbulent field, a requirement for validity of the joint normal hypothesis.

CONTINUING AND FUTURE RESEARCH

Having determined the relevant structural parameters to describe the homogeneous correlation structure with axisymmetric forms and adequately modeled the gross inhomogeneity through the mean square velocity fluctuations, we are now in a position to predict the incompressible and compressible flow pressure fluctuations. For the far field sound prediction, we will be using the four parameter model to perform the "Slice of Jet" integration[17] to compare with observed directionality patterns. Using the observed axial variation of the appropriate scales and the similarity development of the intensity profiles, we will then be able to predict total sound power output by integrating the source over the jet. Scaling arguments for these parameters will be developed so that comparison with large facility far field sound patterns can be made. Far field sound levels were not made on the 2.5 inch facility. Goldstein and Rosenbaum[9] have indicated that the turbulent-turbulent term may dominate the calculations and observed deviation from normality will be incorporated quantitatively in these latter calculations.

In pursuit of the pressure model and verification, an analytical effort is being made to reduce the incompressible, homogeneous mean square pressure field to a simple relation using the two axisymmetric defining scalars, similar in formulation to that of Batchelor[18] for isotropic forms. Using the jet measurements for evaluation of these functions, calculations will be made and comparison made with the measurements of Planchon.[12]

Future work will include a study of the effects on the field defining parameter by perturbations in temperature and in velocity of the jet exit.

ACKNOWLEDGEMENTS

This work was supported by grants from the National Aeronautics and Space Administration (NASA NGR 14-005-177 and NASA NGR 14-005-149) and by the University of Illinois.

REFERENCES

1. Lighthill, M.J., "On Sound Generated Aerodynamically: I. General Theory," Proc. Roy. Soc., A, 211, 1952.

2. Lighthill, M. J., "On Sound Generated Aerodynamically: II. Turbulence as a Source of Sound," Proc. Roy. Soc., A, 222, 1953.

3. Kraichnan, R., "Pressure Field Within Homogeneous Anisotropic Turbulence," J. Acous. Soc., 28, no. 1, 1956.

4. Robertson, H. P., "The Invariant Theory of Isotropic Turbulence," Proc. Camb. Phil. Soc., 36, 1940.

5. Proudman, I., "The Generation of Noise by Isotropic Turbulence," Proc. Roy. Soc., A, 214, 1952.

6. Jones, I. S. F., "Fluctuating Turbulent Stresses in the Noise Producing Region of a Jet," J. Fluid Mech., 36, Pt. 3, 1969.

7. Batchelor, G. K., "The Theory of Axisymmetric Turbulence," Proc. Roy. Soc., A, 186, 1946.

8. Chandrasekhar, S., "The Theory of Axisymmetric Turbulence," Phil. Trans. Roy. Soc., A, 242, 1950.

9. Goldstein, M. and B. Rosenbaum, "Aerodynamic Noise from Axisymmetric Turbulence," J. Acous. Soc., 54, No. 3, 1973.

10. Ribner, H. S., "Aerodynamic Sound from Fluid Dilatations," UTIA Report No. 86, 1962.

11. Spencer, B. W. and B. G. Jones, "A Bleed Type Pressure Transducer for In-Stream Measurement of Static Pressure Fluctuations," The Review of Scientific Instruments, 42, No. 4, 1971.

12. Planchon, H. P., "The Fluctuating Static Pressure Field in a Round Jet Turbulent Mixing Region," Ph.D. Thesis, Univ. of Illinois, 1974.

13. Hinze, J. O., Turbulence, McGraw-Hill Book Company, New York, 1959.

14. Weber, D. P., "Turbulent Velocity Field Structure in a Round Jet and Its Relation to Fluctuating Pressure Fields," Ph.D. Thesis, Univ. of Illinois, 1974.

15. Weber, D. P. and B. G. Jones, "Analytical Modeling of Aerodynamic Noise Sources with Experimental Verification of Hypotheses Introduced in the Modeling," Proceedings of the First Interagency Symposium on University Research in Transportation Noise held at Stanford University, Stanford, California, March 28-30, Vol. 1, 1973.

16. Frenkiel, F. N. and P. S. Klebanoff, "Space-Time Correlations in Turbulence," Dynamics of Fluids and Plasmas, Symposium Proceedings, Univ. of Maryland, 1965.

17. Ribner, H. S., "The Generation of Sound by Turbulent Jets," in Advances in Applied Mechanics, Vol. VIII, 1964.

18. Batchelor, G. K., "Pressure Fluctuations in Isotropic Turbulence," Proc. Camb. Phil. Soc., 47, 1951.

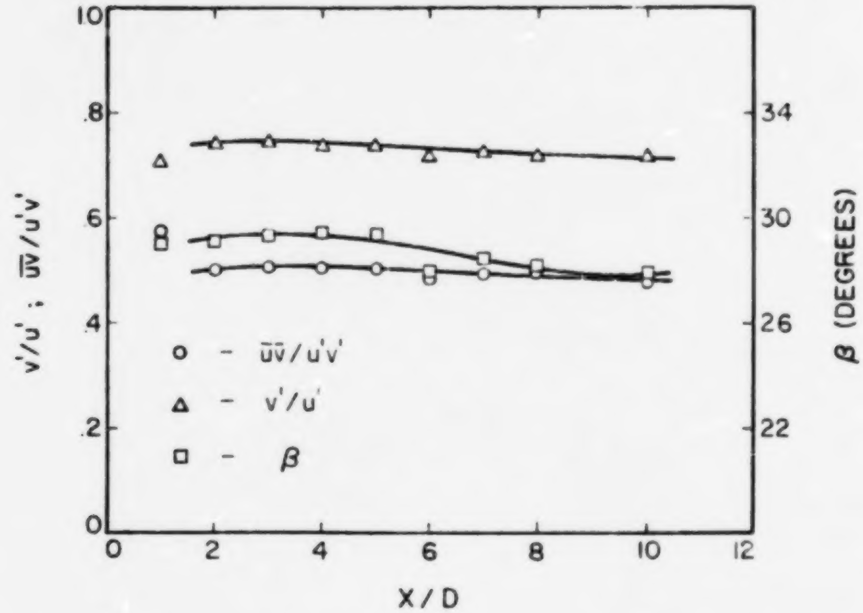

Fig. 1 Axial Variation of Turbulence Structure Parameters at r/R = 1.

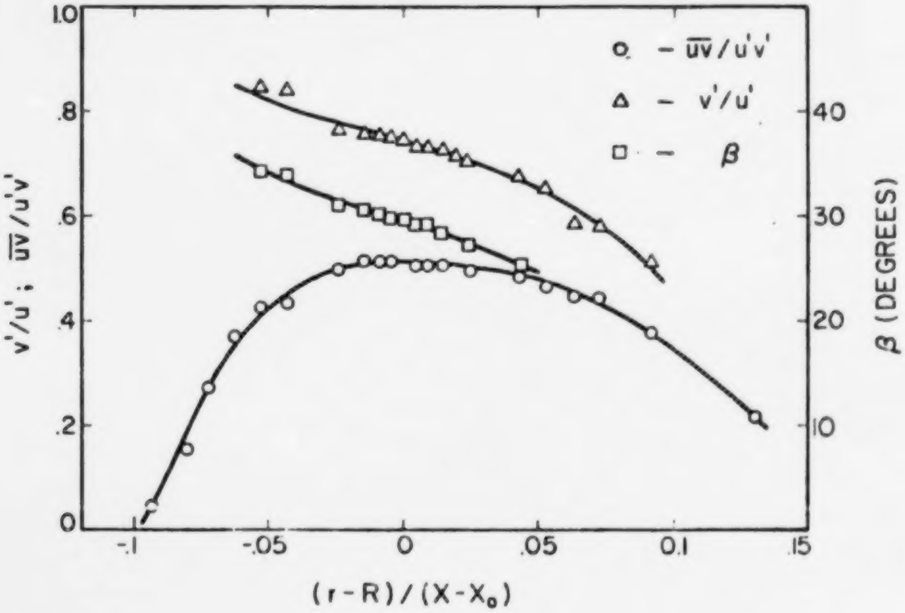

Fig. 2 Transverse Variation of Turbulence Structure Parameters at X/D = 4.

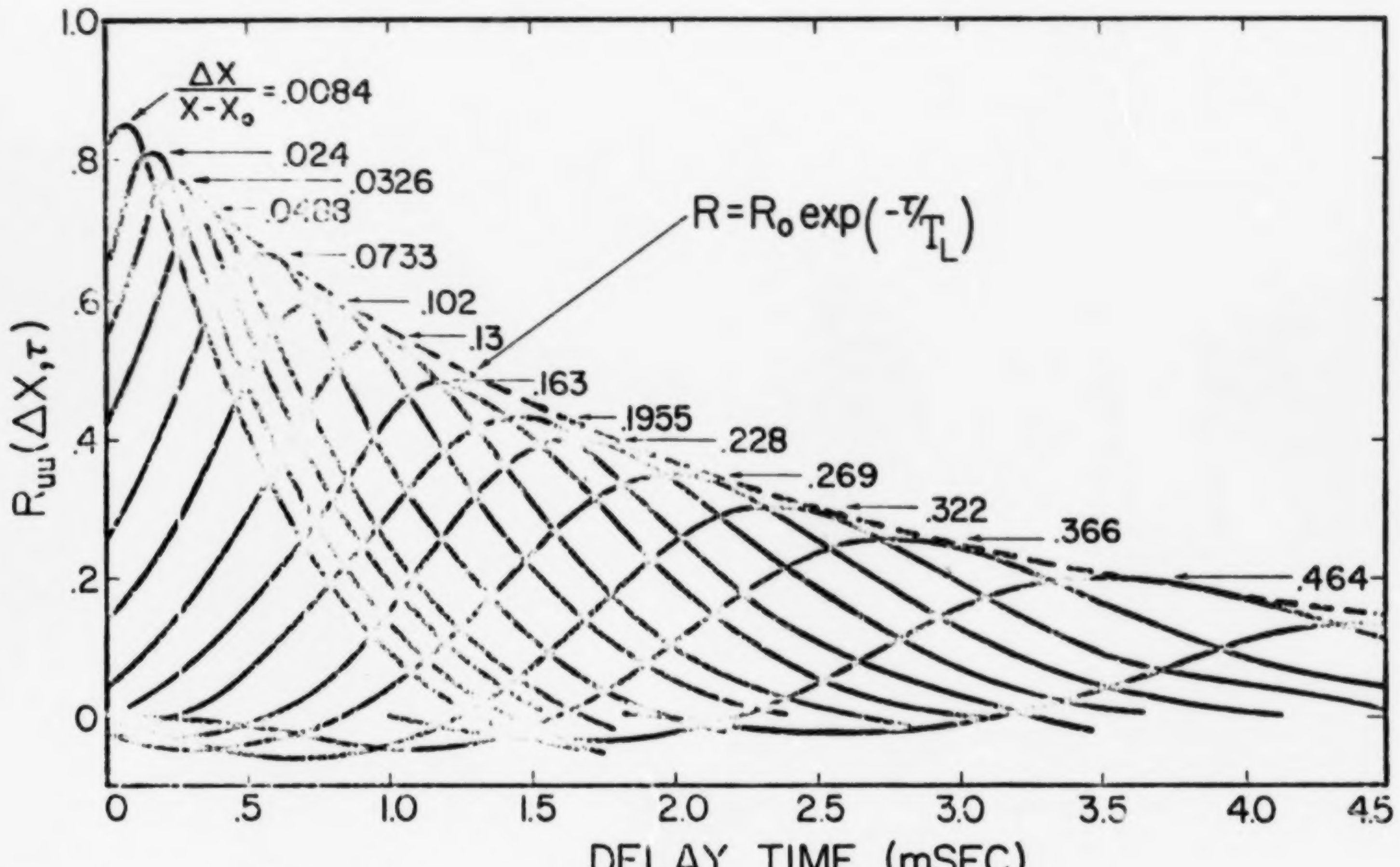

Fig. 3 Axial Velocity Component Space-Time Correlations at X/D = 6.

Reproduced from best available copy.

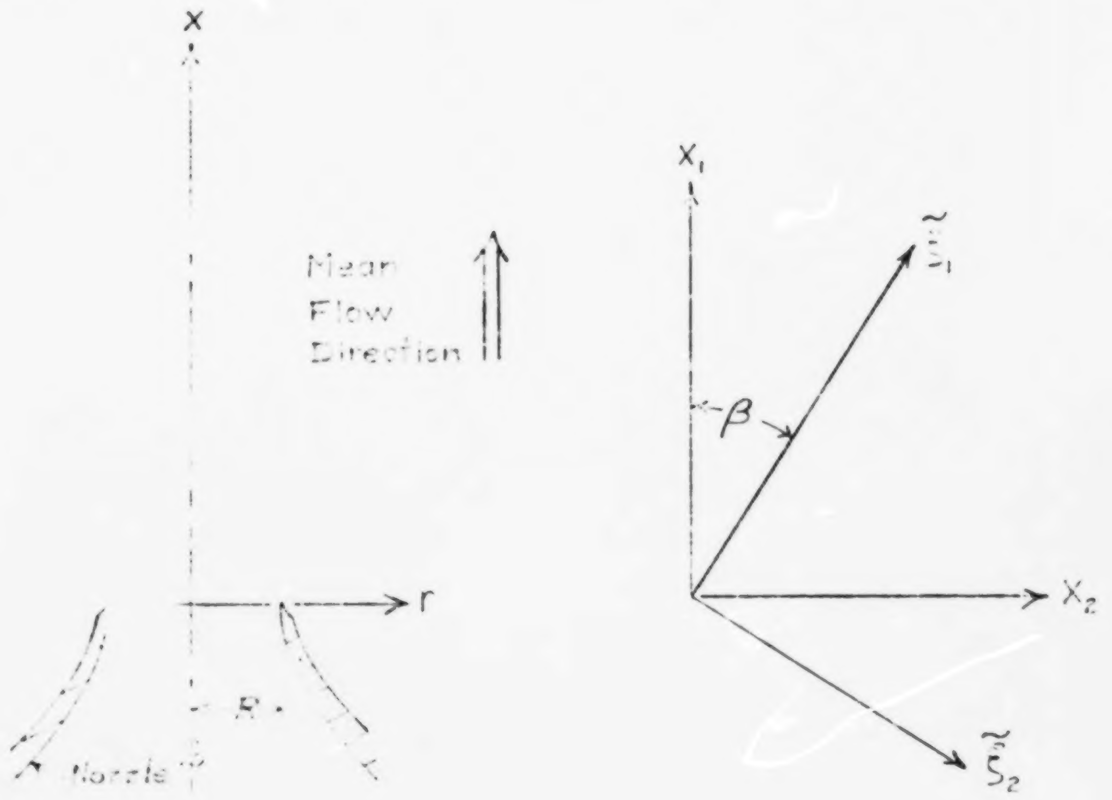
x
Mean
Flow
Direction
r
R
Nozzle
X_1
β
$\tilde{\xi}_1$
X_2
$\tilde{\xi}_2$

Fig. 4 Rotated Coordinate System for Axisymmetric Correlation Measurements.

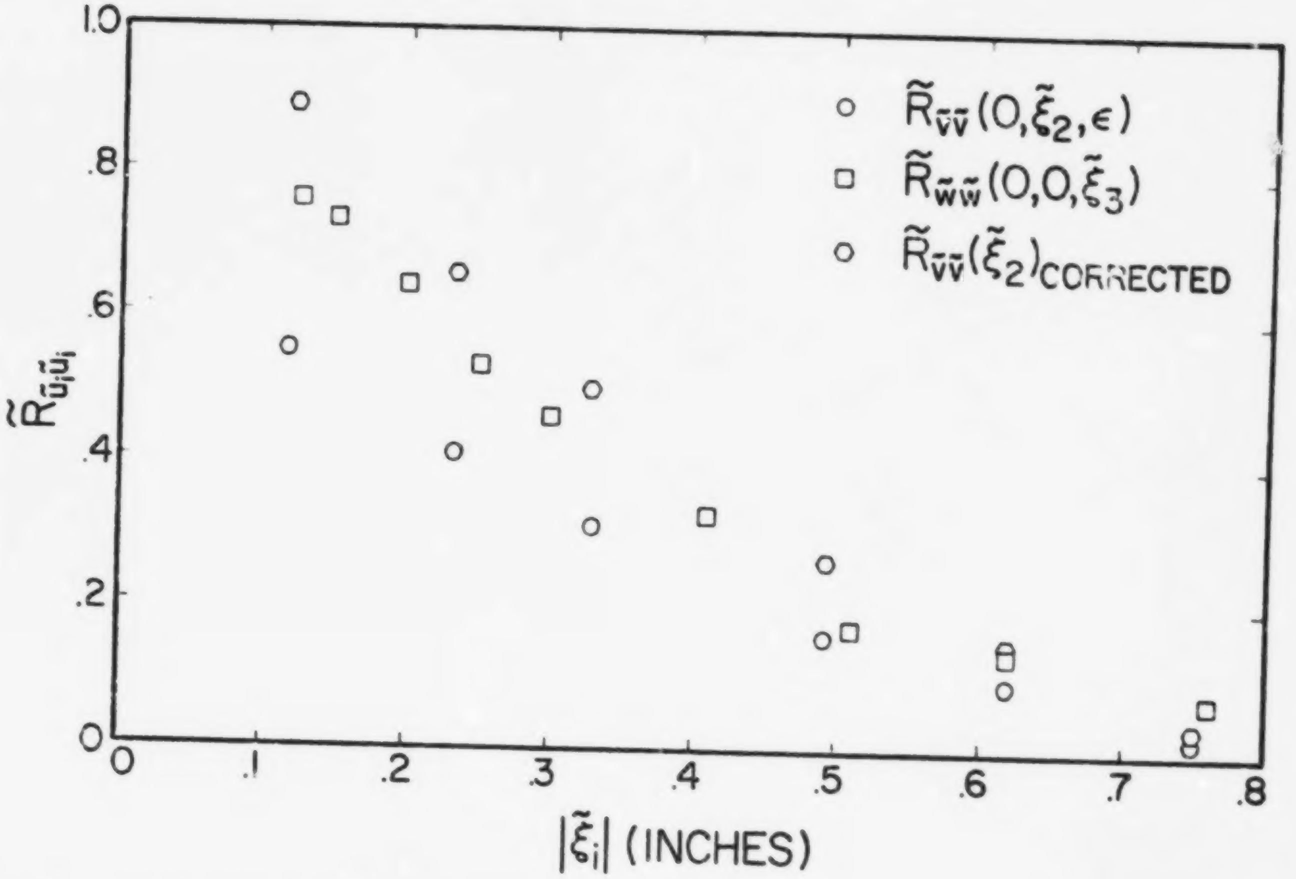

Fig. 5 Axisymmetric Correlations with Separations Along Direction of Fluctuating Velocity.

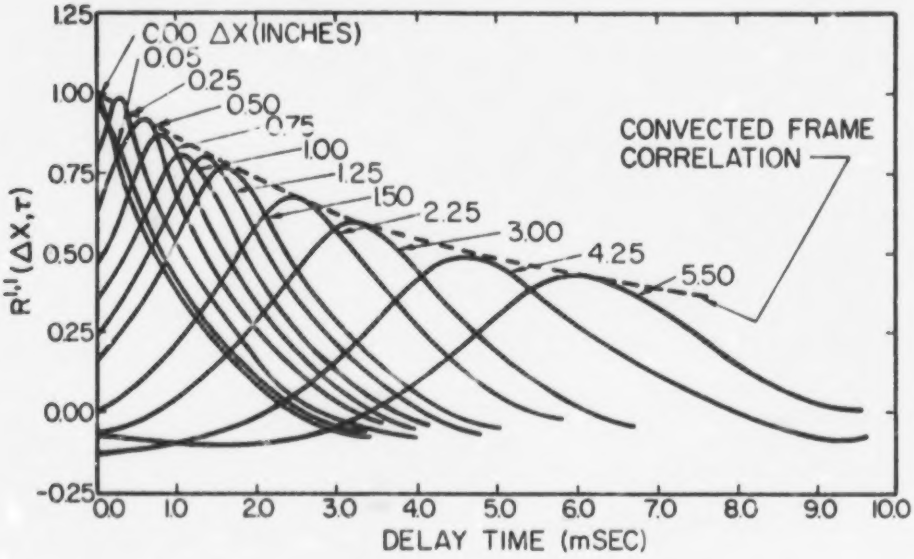

Fig. 6 Higher Order Moving Frame Correlations in Plane Mixing Layer - $R^{1,1}$.

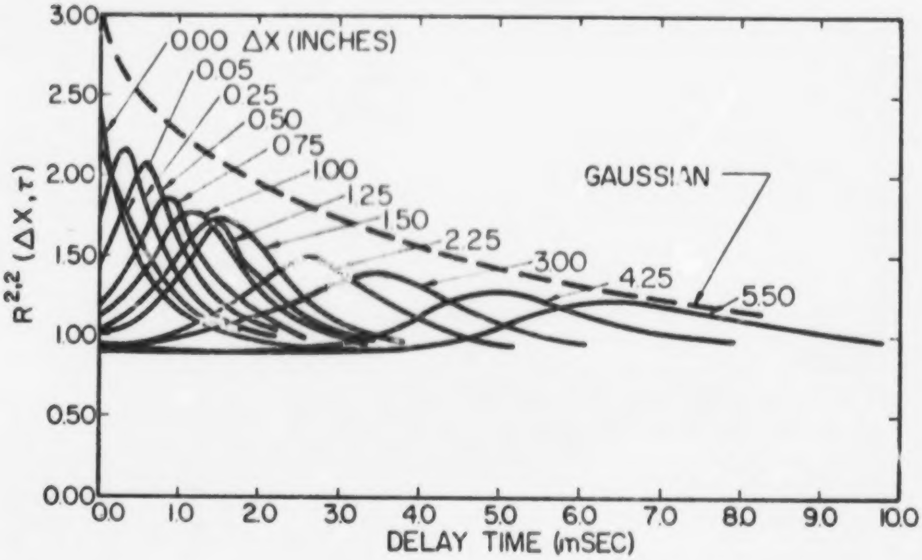

Fig. 7 Higher Order Moving Frame Correlations in Plane Mixing Layer - $R^{2,2}$.

A STUDY OF THE LOCAL PRESSURE FIELD IN TURBULENT SHEAR FLOW AND ITS RELATION TO AERODYNAMIC NOISE GENERATION - A STUDY OF THE MIXING REGION OF A ROUND JET

BY

H. P. Planchon, Jr. and B. G. Jones

Nuclear Engineering Program and Mechanical Engineering Department
University of Illinois at Urbana-Champaign, Urbana, Illinois 61801

INTRODUCTION

Ten years ago Ribner (1964) explained turbulent noise generation as a consequence of fluid inertial dilatations. His theory explicitly expressed the far field pressure in terms of the in-flow pressure space-time correlations. Until recently, direct applications of this theory were hampered by lack of adequate inflow pressure instrumentation. Planchon and Jones (1973) described a miniature transducer capable of measuring pressure correlations in a turbulent jet. Further, they outlined the theory and methods of a research program to measure the inflow pressure functions and directly relate them, with Ribner's theory, to far field sound distributions.

Planchon's thesis dissertation (1974) reported extensive measurements of pressure in the mixing region of a round jet. Supportive velocity field measurements and analysis to link in-flow velocity and pressure were also presented. The purpose of this paper is to summarize the portions of that investigation which are most important in describing aerodynamic noise generation.

EXPERIMENT DESCRIPTION

The turbulent region studied was provided by a 2-1/2 in. diameter, isothermal, incompressible, round jet. Extensive velocity field measurements demonstrated that the jet mixing layer was 'experimentally classic', that is, the results approached self similarity and compared closely with the jets described by Davies et. al. (1963), Lawrence (1965), and others. As shown in Fig. 1, the coordinates used are (x,y,z) in which z is an arc length. Directions along these coordinates are referred to as the axial, transverse and lateral directions, respectively. Pressure intensity was mapped throughout the mixing layer with single point measurements. Two point correlation measurements were made at several axial positions along the mixing centerline, $\frac{r-R}{x-x_o} = 0.0$, and at several transverse positions at $x/D = 4$.

PRESSURE INTENSITY RESULTS

The measured distributions of pressure intensity are shown in Fig. 2 and Fig. 3. These distributions are similar in shape; however, the peak values are observed to increase in the developing mixing region and to decay in the transition region. The peak intensity variation was explained by Planchon (1974) with a modified form of Kraichnan's (1956) theory and extensive velocity field measurements. The results showed that the turbulent mean shear pressure was given by

$$\frac{p'_{TM}}{\frac{1}{2}\rho U_j^2} = 2\sqrt{\frac{8}{15}}\left[\left|\frac{\partial(\overline{U}/U_j)}{\partial r}(x-x_o)\right|\right]\left[\frac{v'}{U_j}\right]\sqrt{J(s)\frac{2+s^2}{3}}\left[\frac{L_v}{x-x_o}\right] \tag{1}$$

where p' is the root mean square pressure, $\frac{\partial(\overline{U}/U_j)}{\partial r}(x-x_o)$ is a dimensionless mean velocity gradient, v'/U_j is a dimensionless root mean square velocity normal to the mean flow, and J(s) is Kraichnan's turbulent scale anisotropy function which is essentially constant. The s is the ratio of transverse velocity integral length scales in the flow and mean velocity gradient directions. Fig. 4 shows the variations in Eq. 1 compared to measured pressure intensities on the mixing centerline. The increase of p' in the driven mixing region ($x/D<4$) is a result of increasing v'. In the transition region ($4<x/D\leq 10$), the decrease is due primarily to the decrease of the gradient and scale factors. The predicted value of intensity was 17% higher than measured at $x/D=4$. This is probably due to a theoretical assumption of slowly varying mean velocity gradient and turbulent intensity.

SPACE TIME CORRELATION RESULTS

Pressure two point correlations describe the spatial extent, shape, and time evolution of coherent pressure volumes. They form the foundation for a model which can be utilized in Ribner's (1964) theory.

The general pressure space time correlation is defined as

$$R_{pp}(x,r,z,\Delta x,\Delta r,\Delta z,\tau) = \frac{\overline{p(x,r,z)\;p(x+\Delta x,\; r+\Delta r,\; z+\Delta z,\tau)}}{\left[\overline{p^2(x,r,z)}\;\;\overline{p^2(x+\Delta x,\; r+\Delta r,\; z+\Delta z)}\right]^{1/2}} \tag{2}$$

For conciseness, position arguments (x,r,z) and spatial and temporal separation arguments ($\Delta x,\Delta r,\Delta z,\tau$) for zero separations are suppressed. The space correlations for zero time delay are denoted as $R_{pp}(\Delta x)$, $R_{pp}(\Delta y)$, and $R_{pp}(\Delta z)$. The convected frame, following Wills (1964), is that frame for which the time scale is largest and its autocorrelation R^L_{pp}, is identified as the envelope of the measured family $R_{pp}(\Delta x,\tau)$. The associated convection velocity, U^p_c, is determined as the limiting quotient of the envelope's ($\Delta x,\tau$) coordinates.

The space correlations for lateral and radial separations are shown in Fig. 5 and Fig. 6, respectively. The measurements were made with a fixed sensor at the mixing center and the second sensor at varying separations. Both correlations are exponential at small to moderate separations, viz:

$$R_{pp}(\Delta z) = \exp(-z/L^p_2) \tag{3}$$

$$R_{pp}(\Delta z) = \exp(-z/L^p_r) \tag{4}$$

where L_z^p and L_r^p are the spatial lengths associated with the decay of correlation in the lateral and transverse directions, respectively. The size of the exponential region increases with axial position and corresponds to the transverse velocity scale length and the region of appreciable mean velocity gradient. At larger separations, the azimuthal and radial correlations vary according to an inverse power law, viz:

$$R_{pp}\ (\Delta z) = 1/(\Delta z)^m \tag{5}$$

$$R_{pp}\ (\Delta r) = 1/(\Delta r)^n \tag{6}$$

For the larger radial separations the movable sensor is outside the highly sheared turbulent flow. It is therefore clear that the power law is characteristic of correlation between centerline pressure and the coupled near field.

The axial space correlations shown in Fig. 7 are characterized as a damped periodic function

$$R_{pp}\ (\Delta x) = \exp(-\Delta x/L_x^p)\ \cos\left(\frac{2\pi\ \Delta x}{\lambda_c(x-x_o)}\right) \tag{7}$$

Two length scales are evident in the results and, with the aid of Eq. 7, are identified as a wavelength of periodicity, $\lambda = \lambda_c(x-x_o)$, and a damping length, L_x^p. The wavelength increases linearly with axial position so the wavelength scale constant, λ_c, is 0.3 throughout the mixing layer. Although not shown, the one dimensional spectra of both pressure and transverse fluctuating velocity, measured with a single pressure or velocity sensor, exhibit this same periodicity and scaling. The damping of the axial correlation described by L_x^p varies only with separation and is not a function of position.

A representative space-time correlation is shown in Fig. 8. This family of curves is traditionally described by its envelope's convection velocity and integral time scale. As shown in Fig. 9 and Fig. 10, the convection velocity is nearly constant throughout the mixing layer. This constancy was verified for a range of jet velocities and is consistent with the idea that pressure is correlated over large transverse volumes.

The variation of the convected frame time scale is shown in Fig. 11 and Fig. 12. Except for small separations $R_{pp}^L(\tau)$ was exponential, thus its integral time scale in the convected frame, T_L^p, was inferred from an exponential fit. Fig. 11 shows neither T_L^p nor transverse velocity convected frame time scale, T_L^v, vary linearly with axial position. This contrasts with our measurements as well as those of others which show the axial velocity component convected frame time scale, T_L^u, increases linearly with axial position. Another important feature shown in Fig. 11 is that the pressure time scale is almost twice as large as the velocity scale T_L^v.

CORRELATION SEPARABILITY

For direct use as a source function in Ribner's (1964) theory a model of the three dimensional space-time correlation was constructed. A simple separability model,

$$R_{pp}(\Delta x,\Delta r,\Delta z,\tau) = R_{pp}^{(1)}(\Delta x)\ R_{pp}^{(2)}(\Delta r)\ R_{pp}^{(3)}(\Delta z)\ F(\Delta x - U_c\tau) \qquad (7)$$

was found to accurately express most of the important features of the data. Spatial separability as shown in Fig. 13 is almost exact. The open circles are from measurements with simultaneous radial and axial separations along a line 30 degrees from the flow direction. The solid points result from combining two independent axial and radial correlations. The sensors in both cases were offset in the lateral direction by ε_z(= small Δz) to avoid probe interference.

Considering both space and time separability, Planchon (1974) has shown the separability model is a generalization of Taylor's frozen pattern hypothesis. That is, the space-time correlations are converted single point autocorrelations with a decaying amplitude fixed by the convected frame autocorrelation. Fig. 14 shows, when time separability is included, that the model does not account for a dispersive effect that broadens and skews the space-time correlation. However, as is shown, it does properly predict the space-time peak amplitudes. Further, Fig. 15 shows that the model correctly constructs the 3-dimensional convected frame autocorrelation from independent measurements in the three orthogonal directions.

CONCLUSIONS

The radial variation of the measured pressure intensities were found to be similar in shape, but to vary in amplitude with down stream position. This axial variation is consistent with theory and velocity field measurements. The pressure correlation measurements indicate large, slowly varying, correlated regions of pressure that are uniformly convected down stream. These correlations are shown to be spatially separable. However, space-time separability was determined not to be exact but a useful model.

ACKNOWLEDGEMENTS

This work was sponsored by a grant from the National Aeronautics and Space Administration (NASA NGR 14-005-149) and by the University of Illinois at Urbana-Champaign.

REFERENCES

P. O. A. L. Davies, M. J. Fisher, and M. J. Barratt, "The Characteristics of the Turbulence in the Mixing Region of a Round Jet," J. Fluid Mech. 15, pp. 337-367 (1963).

R. H. Kraichnan, "Pressure Field Within Homogeneous Anisotropic Turbulence," Jour. Acoustic Soc. Am. 28, pp. 64-72 (1956).

J. C. Lawrence, "Intensity, Scale, and Spectra of Turbulence in the Mixing Region of a Free Subsonic Jet," NACA TR 1292, pp. 891-917 (1956).

H. P. Planchon and B. G. Jones, "A Study of the Local Pressure Field in Turbulent Shear Flow and Its Relation to Aerodynamic Noise Generation," Proceedings of the First Interagency Symposium on University Research in Transportation Noise held at Stanford University, Stanford, California, March 28-30, 1, pp. 128-143 (1973).

H. P. Planchon, "The Fluctuating Static Pressure Field in a Round Jet Turbulent Mixing Region," Ph.D. Thesis, University of Illinois (1974).

H. S. Ribner, "The Generation of Sound by Turbulent Jets," Advances in Appl. Mech. 8, pp. 103-187, Ed: H. L. Dryden, Th. Von Karman, G. Kuerti, Academic Press, New York, New York (1964).

J.A.B. Wills, "On Convection Velocities in Turbulent Shear Flows," J. Fluid Mech. 20, pp. 417-432 (1964).

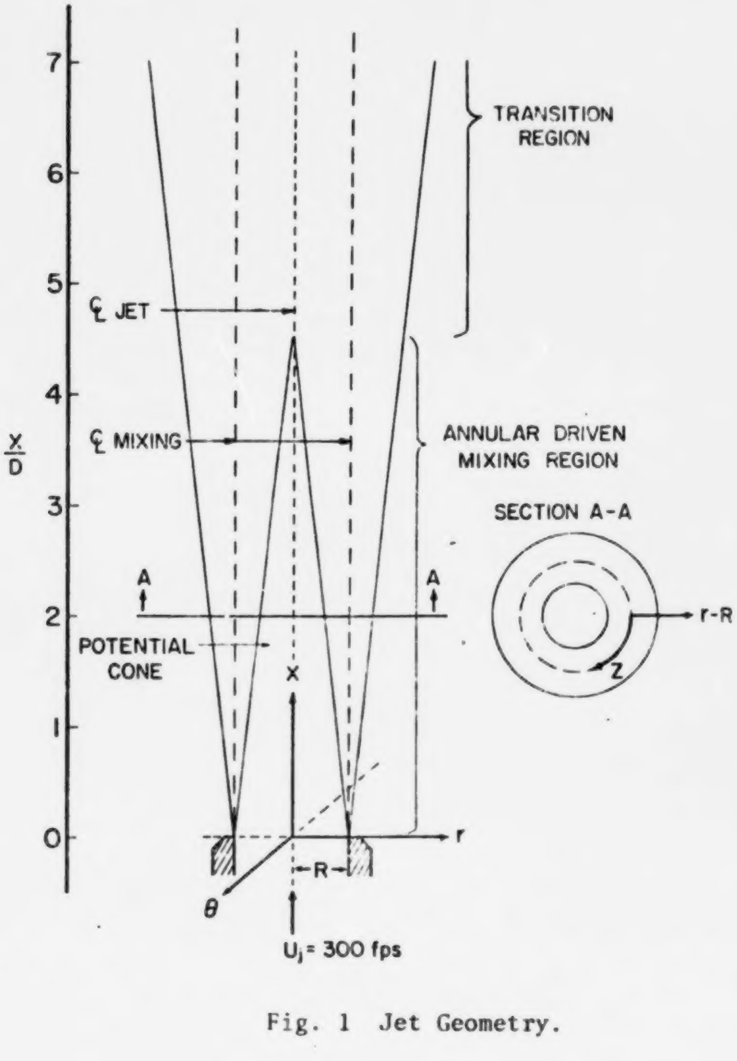
7
6
5
4
3
2
1
0
X/D
TRANSITION REGION
℄ JET
℄ MIXING
ANNULAR DRIVEN MIXING REGION
SECTION A-A
A
A
r-R
z
POTENTIAL CONE
x
r
R
θ
U_j = 300 fps

Fig. 1 Jet Geometry.

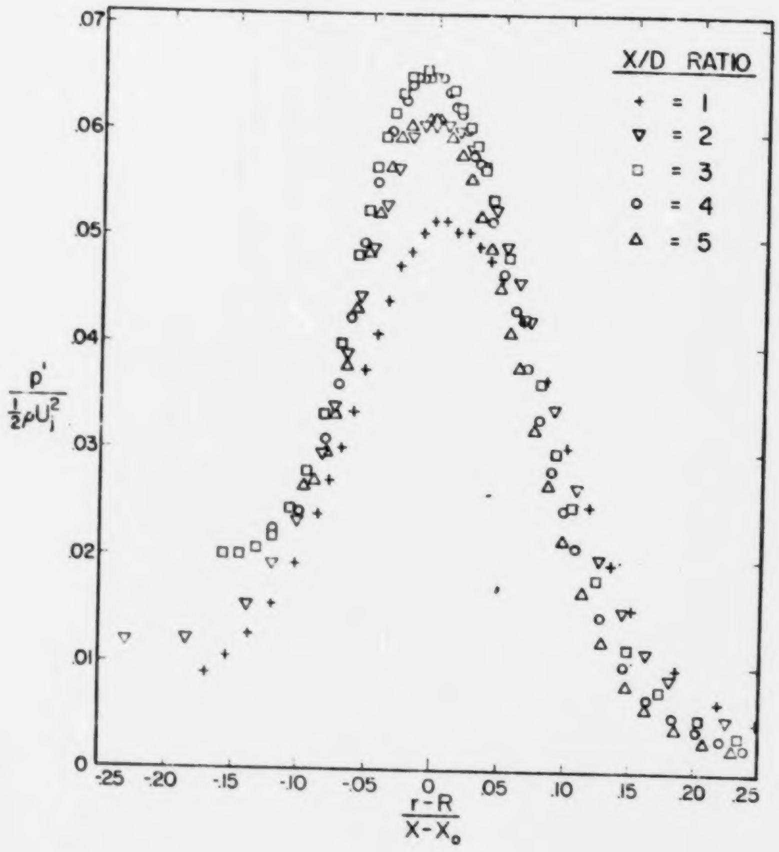

Fig. 2 Pressure Intensity, Driven Mixing Region. U_j = 300 ft/sec, R = 1.25 in., x_o = -0.4 in.

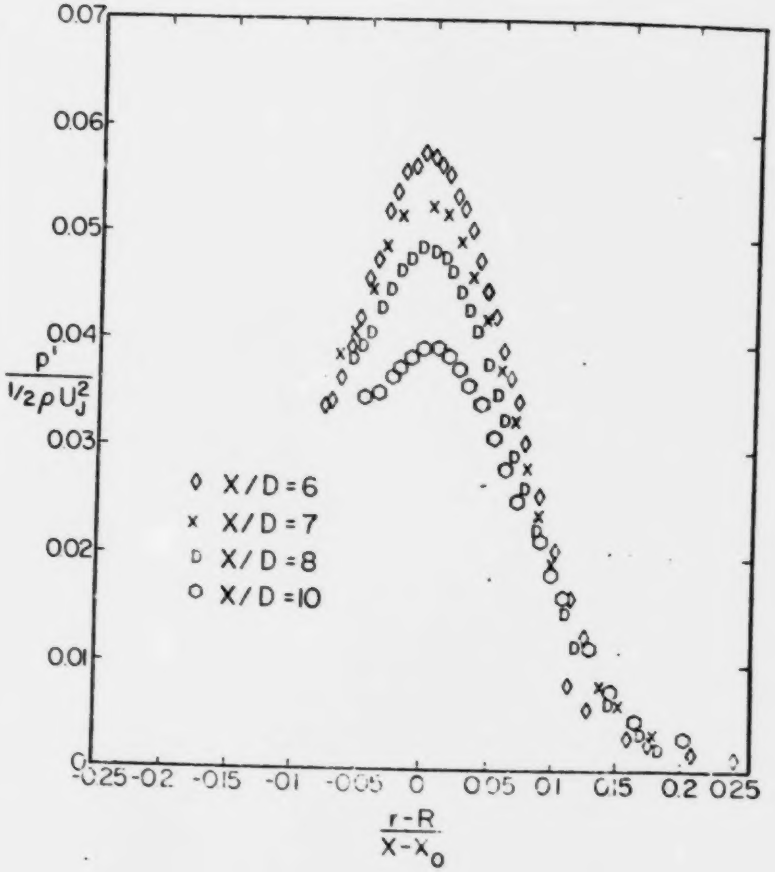

Fig. 3 Pressure Intensity, Transition Region. U_j = 300 ft/sec, R = 1.25 in., x_o = -0.4 in.

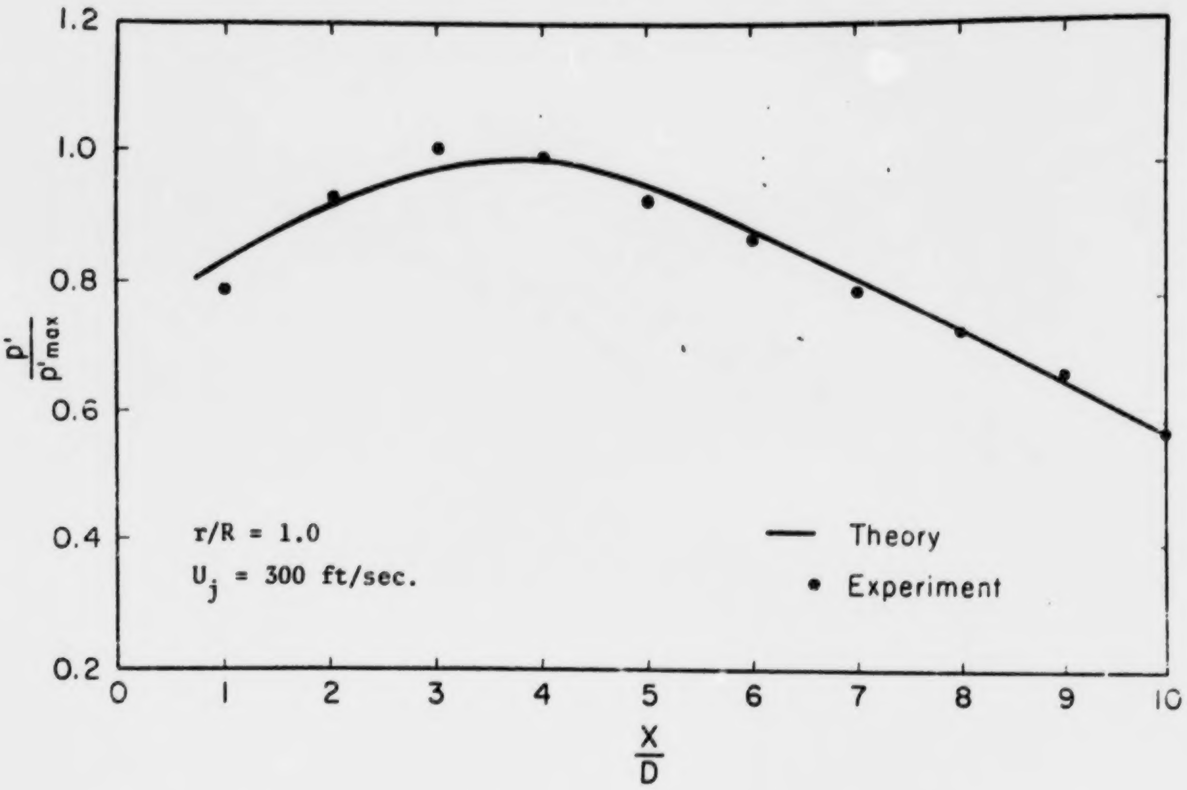

Fig. 4 Comparison of Theoretical and Experimental Pressure Intensities.

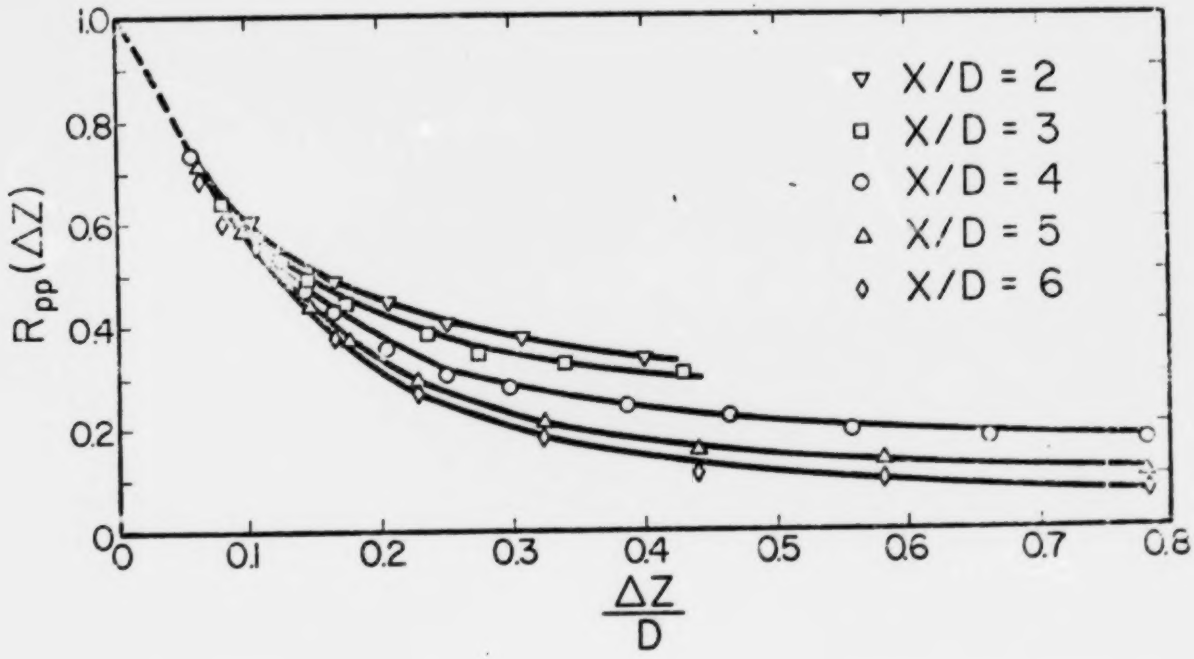

Fig. 5 Pressure Lateral Space Correlations. $r/R = 1.0$, $D = 2.5$ in., $U_j = 300$ ft/sec.

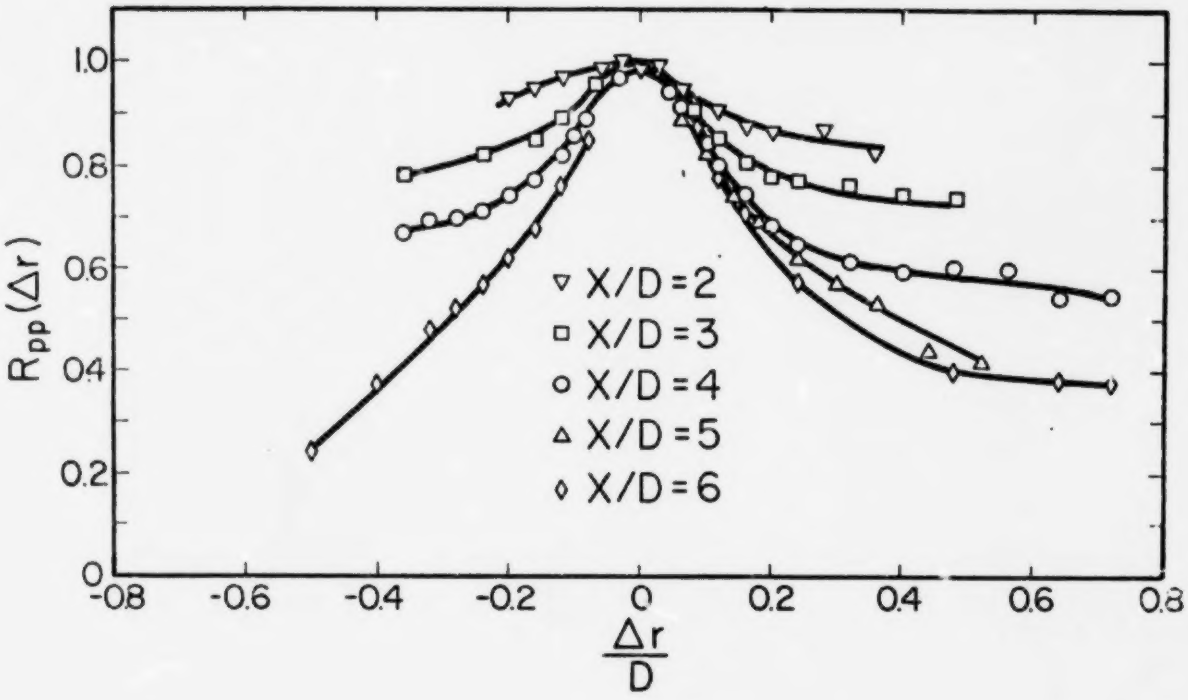

Fig. 6 Pressure Transverse Space Correlations. D = 2.5 in., U_j = 300 ft/sec. Stationary Probe at r/R = 1.0.

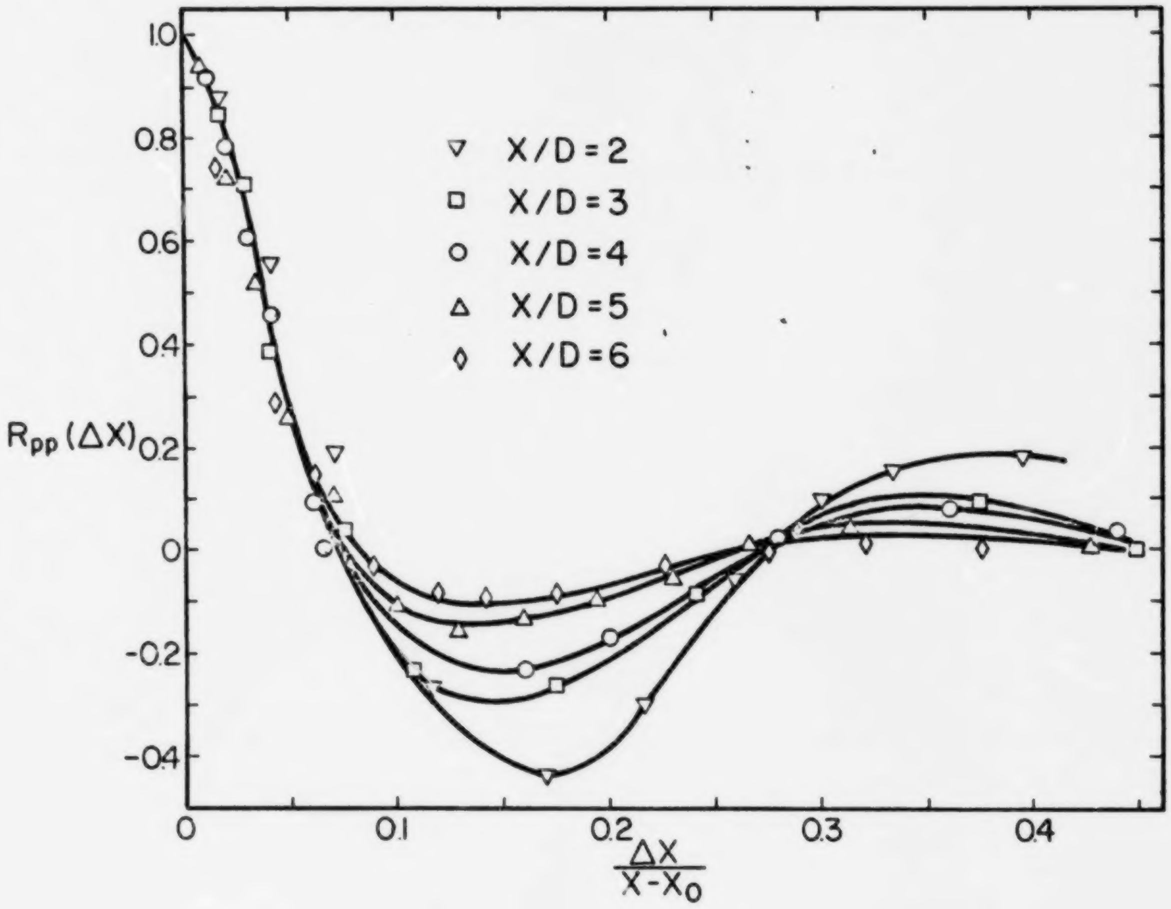

Fig. 7 Pressure Axial Space Correlations. $r/R = 1.0$, $D = 2.5$ in., $U_j = 300$ ft/sec.

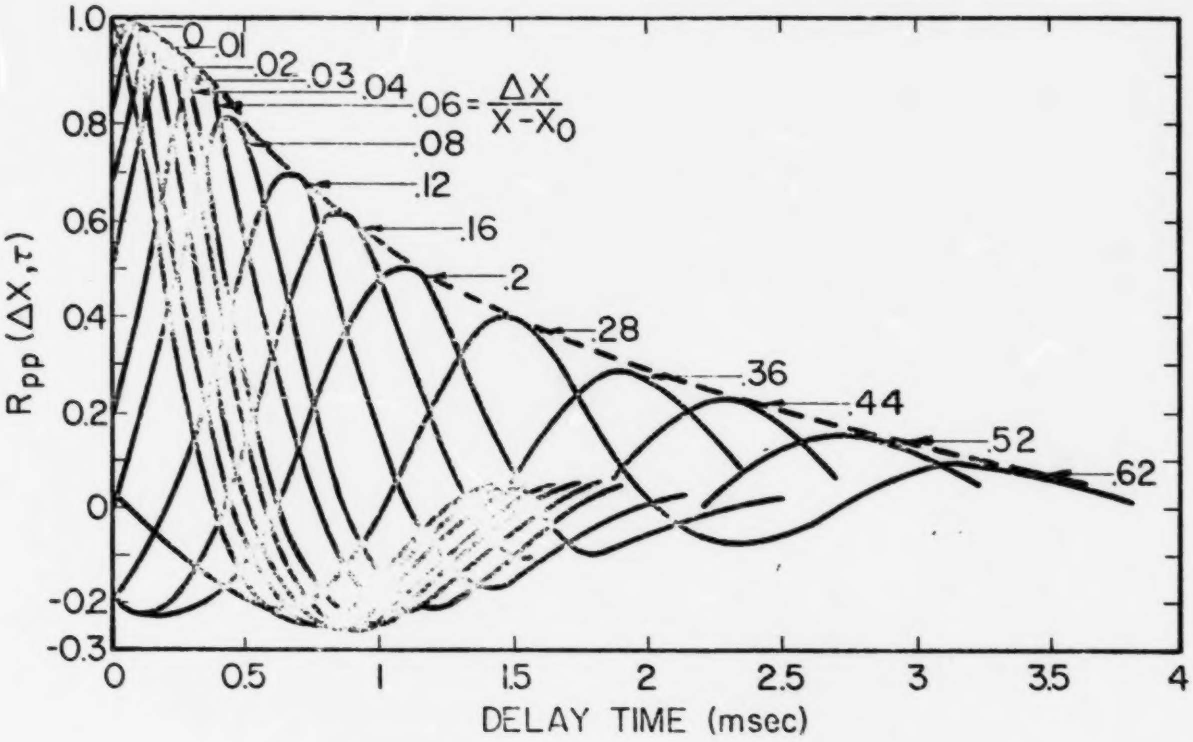

Fig. 8 Pressure Space-Time Correlations. $r/R = 1.0$, $U_j = 300$ ft/sec, $x_o = -0.4$ in., $x/D = 4$.

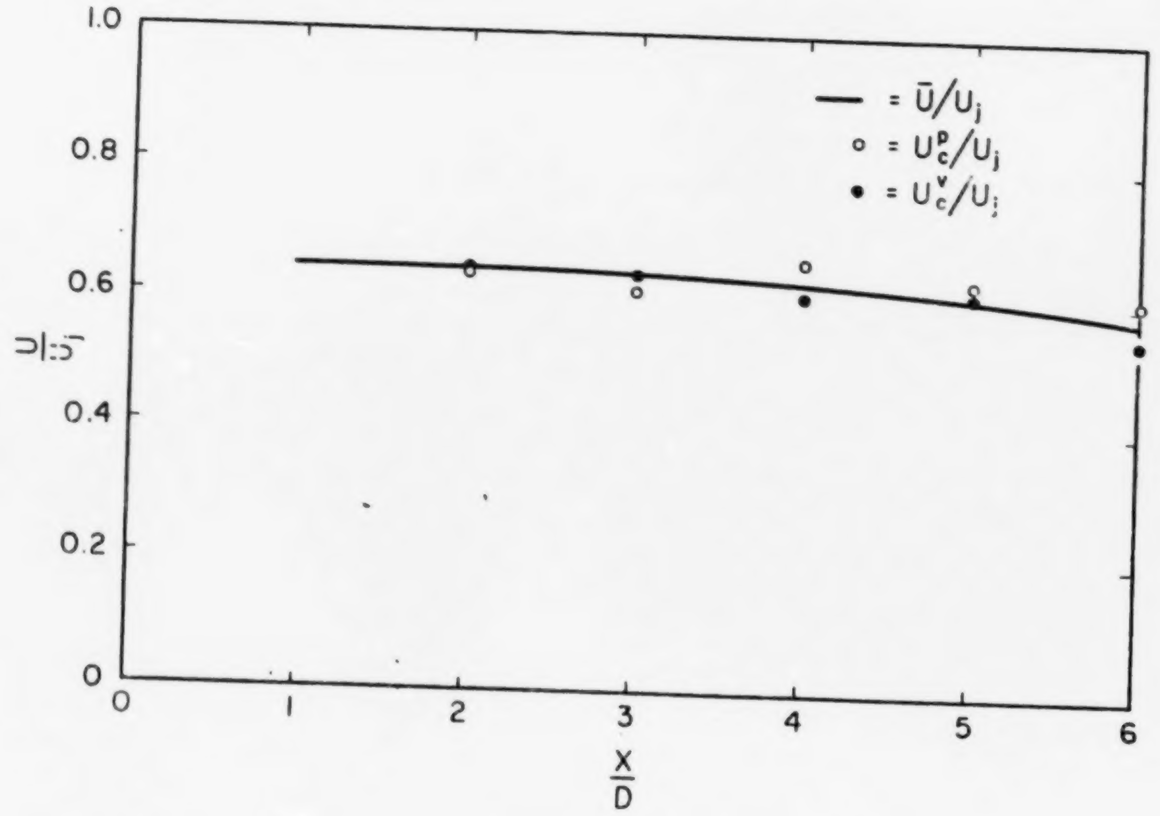

Fig. 9 Pressure Convection Velocity. $r/R = 1.0$, $U_j = 300$ ft/sec, $D = 2.5$ in.

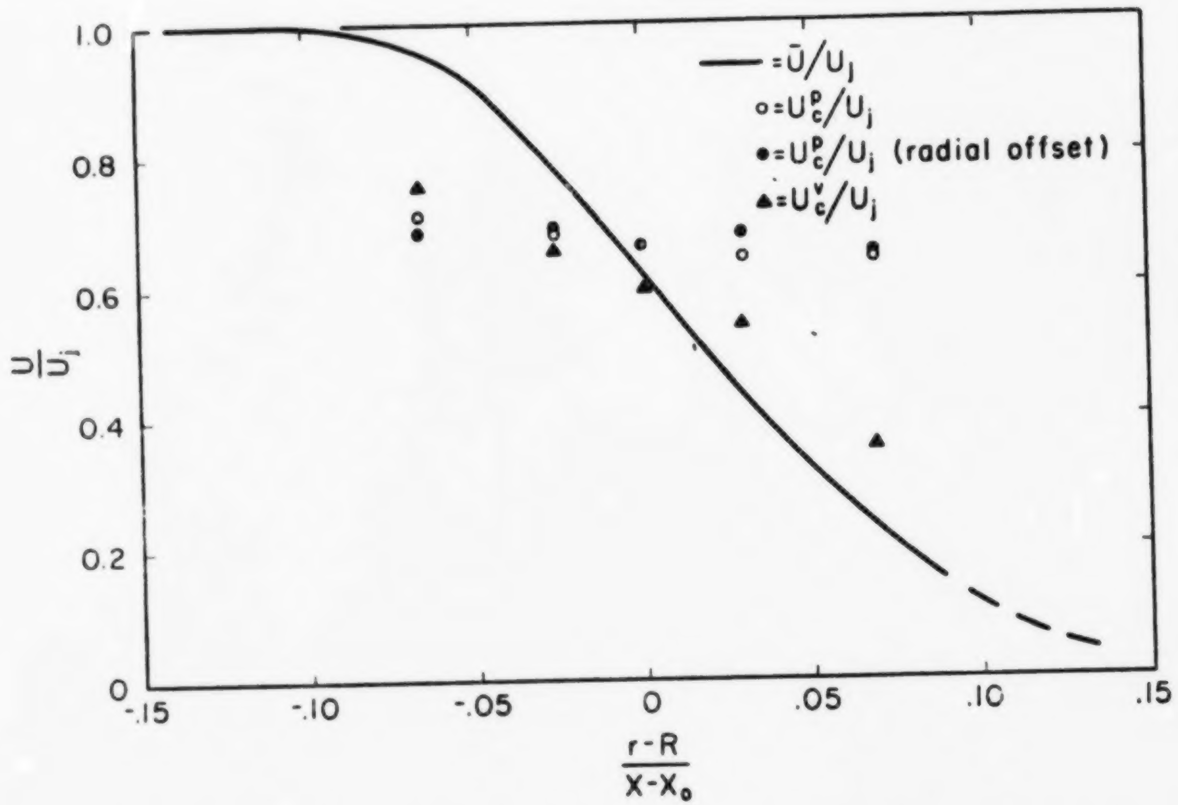

Fig. 10 Pressure Convection Velocity x/D = 4. U_j = 300 ft/sec, R = 1.25 in.

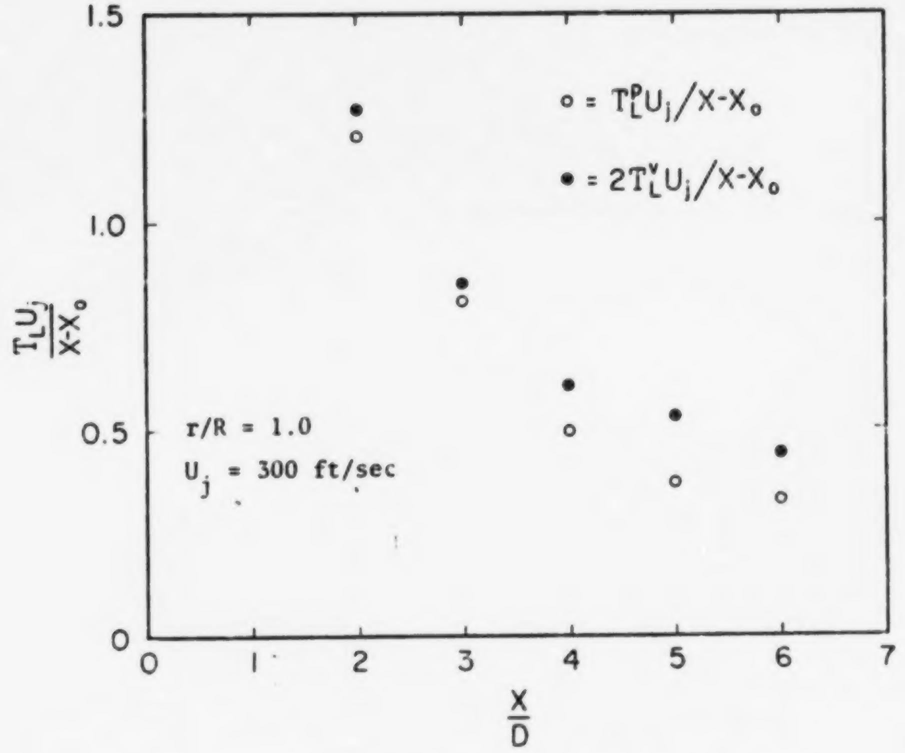

Fig. 11 Pressure Convected Frame Time Scale.

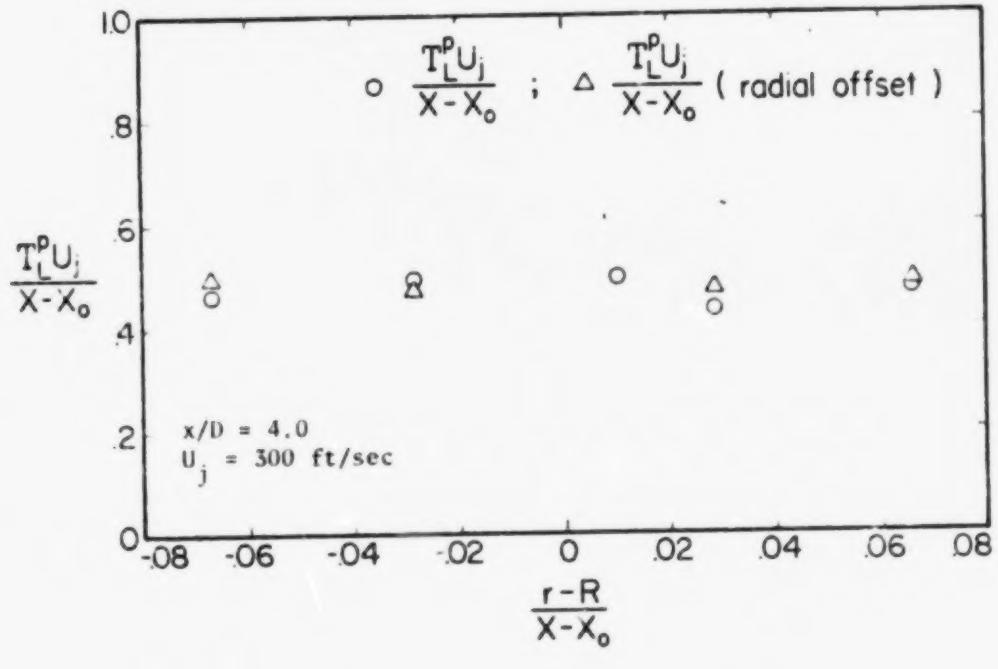

Fig. 12 Pressure Convected Frame Time Scale.

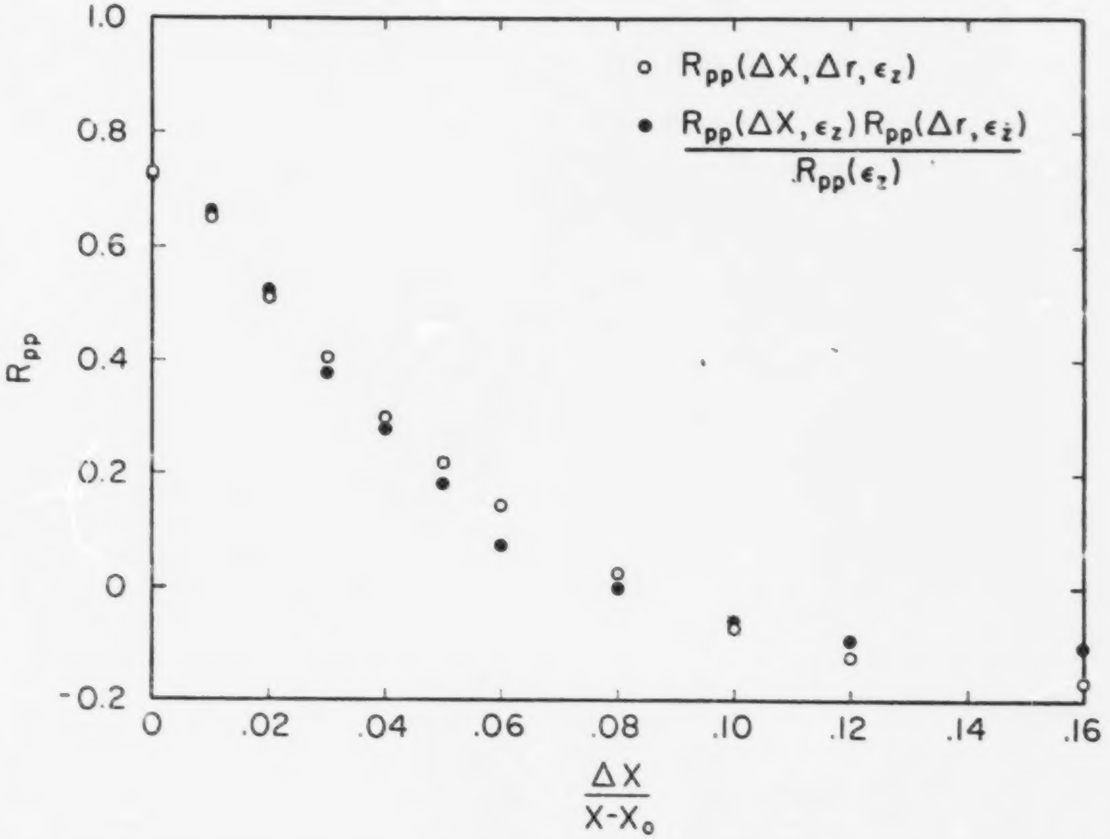

Fig. 13 Pressure Space Correlation Separability. $x/D = 4$, $U_j = 300$ ft/sec, $x_o = -2.5$ in., Stationary Probe at $r/R = 1$.

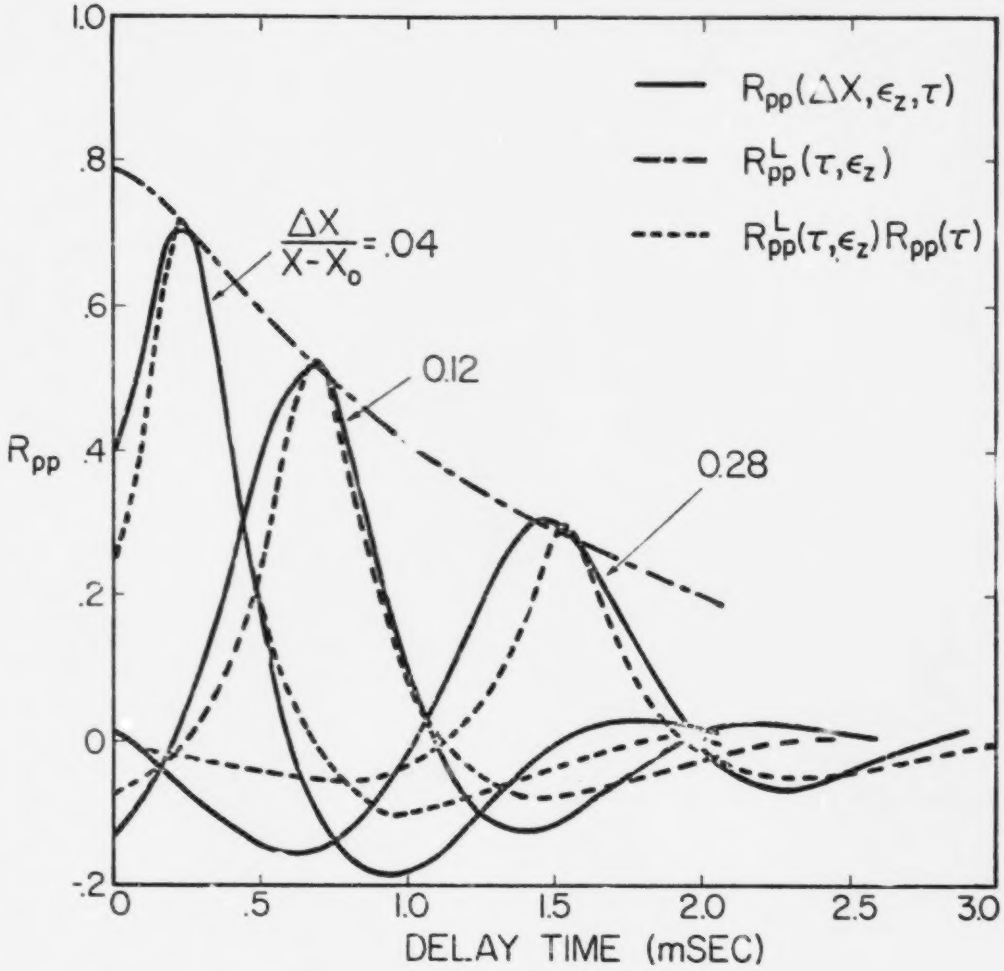

Fig. 14 Pressure Space-Time Correlation Separability. $x/D = 4$, $r/R = 1.0$, $U_j = 300$ ft/sec.

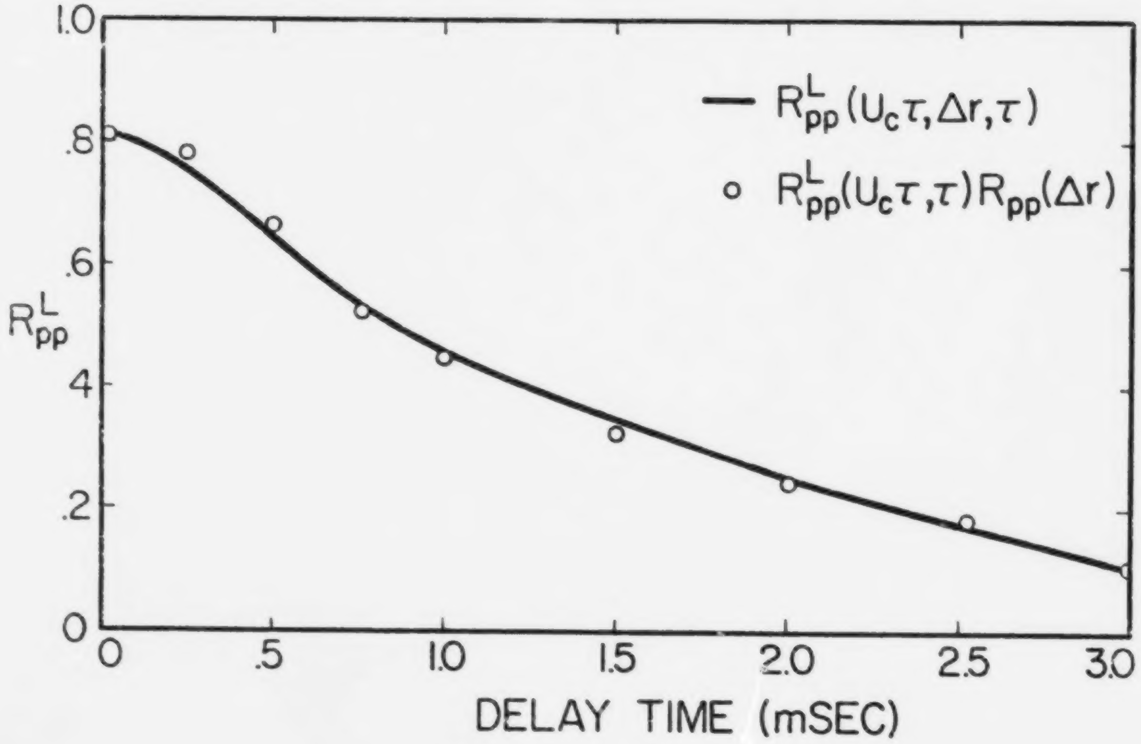

Fig. 15 Pressure Space-Time Envelope Separability. U_j = 300 ft/sec; Stationary Probe at x/D = 4, r/R = 1.

AN EXPERIMENTAL INVESTIGATION OF THE TURBULENT CHARACTERISTICS OF CO-ANNULAR JET FLOWS AND THEIR ROLE IN AERODYNAMIC NOISE GENERATION

by

R. J. Hammersley and B. G. Jones

Nuclear Engineering Program and Mechanical Engineering Department
University of Illinois at Urbana-Champaign, Urbana, Illinois 61801

INTRODUCTION

Current models for predicting aerodynamic noise generation by jet flows require knowledge of the detailed turbulence characteristics of the jet flow field. Typical characteristics included in models are turbulent intensities, scales and convection velocity. These quantities have been documented in sufficient detail for simple jet flows, but not for co-annular (by-pass) jets flows, which are currently being used in high by-pass ratio, low noise jet engine designs.

In this experimental study the turbulent characteristics of both the velocity and static pressure fields of a co-annular nozzle configuration are measured. These data are obtained through the use of standard constant temperature anemometry techniques using multisensor hot wire probes and our bleed type pressure transducer sensor. The experimental results supply the information required for use in existing noise source models and for development of new and modification of existing models. Of primary importance is the development of an appropriate model for the two-point pressure correlation structure in the driven shear layers of the coannular jet flow. This model will be used in the Ribner dilatational formulation of the noise source to predict the far field noise. The predictions will be compared directly with far field noise data taken from the same experimental facility.

In this paper we describe the experimental facility and equipment, present preliminary results of the turbulent flow field structure and outline the continuing research work.

EXPERIMENTAL FACILITY AND EQUIPMENT

Air Supply System

A large co-annular nozzle flow facility at the NASA-Lewis Research Center was used for the experimental study; see Olsen and Friedman (1974) for flow system details. The facility is located outdoors and a large tent canopy was placed over the measurement area to help eliminate atmospheric and wind influences. Compressed air from a 140 psia source was supplied at near ambient temperatures (≤4 F difference). Two separate, but similar, flow paths were used to supply air to the two nozzles. Each flow path consisted of the following elements (proceeding downstream from the air supply): pneumatically operated flow control valve, valve noise quieting section, inlet piping, and the test nozzle. For each flow path the valve noise quieting section consisted of a perforated plate and an acoustically lined baffled muffler. The inner or core nozzle inlet piping was a straight run of 8 inch diameter pipe with two sets of screening. The outer or by-pass nozzle inlet piping was a 16 inch diameter pipe which split into two 12 inch diameter lines which terminated in a plenum. The plenum had two sets of screening which were just upstream of the outer nozzle inlet. Figure 1 illustrates the air supply system.

Nozzles

A 3.0 inch diameter nozzle was used in all cases for the inner nozzle. Two outer nozzles were used and had diameters of 5.35 inches and 8.7 inches which correspond to area ratios of 2.2 and 7.4, respectively. The nozzle profiles were determined from a potential flow solution of a uniform incompressible flow between two co-axial, parallel surfaces of different cross-sectional areas as was done by Spencer (1970). The inner nozzle was designed so that both its outer and inner surfaces had the proper profile whereas only the inner surface of the outer nozzles was so constructed. The attention given to the nozzle profiles assured that at the exit plane of the co-annular nozzles the mean velocity profiles were flat, the turbulence intensities in each were low and the two streams were parallel. Figure 2 demonstrates the success of these nozzle configuration designs. Further, a symmetry check at several axial positions indicates proper alignment of the nozzles and that the flow from each is parallel and parallel to the geometric axis of the nozzles centerlines.

Sensors and Instrumentation

The mean velocity profiles were measured with anemometry equipment and pitot tube rakes. The rakes (one for each nozzle configuration) were made of five impact tubes (0.062 inch diameter tubes) spaced to correspond to the nozzle lips. The rakes were connected to 0-5 psi pressure transducers which were monitored and recorded via a data collection system.

The hot wire probes were also built at NASA-Lewis. Several single sensor probes and two end-flow x-probes were also made. The wire sensors were all made of 0.00019 inch diameter tungsten wire. The total wire lengths were 0.0625 inches and the active length was 0.050 inches. Hence, the length to diameter ratio was 300 which is high enough to assure that no probe support interference should occur and end losses can be ignored. Constant temperature DISA anemometry was used and the bridge output was recorded directly. The velocity signals were linearized via a small analog computer and re-recorded.

The fluctuating static pressure was measured by a miniature pressure transducer. The details of operation and an error analysis of the pressure transducer have been presented by Planchon (1974).

PRELIMINARY EXPERIMENTAL RESULTS

The measurement program consisted of single and two point measurements of the velocity and fluctuating pressure fields. In all cases a cold, subsonic jet was studied with an inner core velocity of 450 fps. A range of velocity ratios (defined as velocity of by-pass flow divided by velocity of inner core flow) from zero to one was investigated. Only round coplanar and no extended or plug nozzles were used in this work.

Mean Velocity Measurements

The mean velocity measurements of the single probe hot wire and rakes were combined for each nozzle configuration into a spread diagram. These diagrams (see Figure 3) show the extent of the potential cores and hence the length of the mixing regions formed. The various regions are defined by constant "phi" lines of 0.05 and 0.95. The parameter phi is defined as

$$\phi = \frac{\overline{U}_{local} - U_b}{U_a - U_b}$$

where: U_a is the velocity of the high velocity side of the driven mixing region and U_b is the velocity of the low velocity side of the driven mixing region. The same core velocity and velocity ratio were used in both cases and only the area ratio is different. The larger area ratio configuration has the largest outer potential core--5 core diameters compared to 2.5 core diameters for the smaller area ratio configuration. This effect is believed to have significant implications in terms of the far-field sound since it is observed that the far-field sound decreases as the area ratio increases; all other parameters remaining constant. The measurements also show that the inner potential core is longer than for a simple jet. Further, the inner potential core was found to be 7 core diameters for both area ratios. Champagne and Wygnanski (1971) also observed the longer inner potential core for velocity ratios less than one and suggest this effect is primarily from the decreased shear between the inner jet and its surroundings.

For both area ratios, the outer potential core was shorter than the inner potential core. Hence, the flow field is quite complex since it proceeds through the following situations starting from the exit plane and proceeding downstream:

a) Two driven shear layers (both inner and outer potential cores still exist)

b) A driven shear layer and transition region superimposed on each other (inner potential core only)

c) A transition region only (in which both potential cores have completely dissipated)

This complexity must be considered when one estimates the sound sources in the co-annular jet and how to combine them to get the total source in the jet.

Single Point Velocity and Pressure Measurements

The radial variations of the rms fluctuations in the axial (u') and radial (v') velocity components and pressure (p') were measured for a series of axial positions for each nozzle configuration. The respective profiles for the 5.35 inch outer nozzle case are shown in Figures 4, 5, and 6. All three figures show the above mentioned evolution of the flow as one moves downstream. When the profiles are presented in similarity coordinates ([r-R]/x where: r=radial position, R=jet radius and x=axial position), they become self-similar from one core diameter to the end of the outer potential core. At this point, the transitional effects of the outer mixing layer appear but self-similarity is roughly approached again by the end of the inner potential core. These trends are also indicated in the non-dimensionalized spectra for the axial velocity component.

The single point pressure spectra for the 5.35 inch diameter nozzle configuration are shown in Figures 7 and 8. Figure 7 is for the outer, zero velocity ratio, mixing region while figure 8 is the inner, velocity ratio of 0.4, mixing region. The spectra are non-dimensionalized on the common basis of Taylor's frozen pattern hypothesis. This technique should collapse structurally similar spectral distributions as long as the velocity and scale used are proportional to the local convection speed and scale size. The spectra presented were all measured on the center line of mixing in the respective shear layers. The spectra were measured by an analog 1/3-octave band pass filtering network. The resulting spectral distribution was normalized and each band-passed frequency region was divided by its respective filter width. Thus, the final spectral distribution is on a per unit frequency basis. The local mean velocity (U_{local}) and mixing layer widths (b) were used to non-dimensionalize the spectral curves. The figures show good collapse of the data. This suggests that for both the zero and non-zero velocity ratio mixing regions the pressure field has a nearly frozen pattern with structural similarity, constant convection velocity and linearly growing scales. Planchon (1974) has found similar results for both the pressure and velocity fields of a simple round jet.

The axial distribution of velocity and pressure is of interest in describing the sound source in the shear layer. The effect of velocity ratio on this axial variation was studied near the center of the inner mixing layer. The results are presented in figure 9. The pressure intensity is non-dimensionalized by the inner core exit plane head and axial position is plotted in terms of core diameters. The figure illustrates the effect of the reduced shear between the inner jet and its surrounding flow field as the velocity ratio is increased. At distances greater than x/D_c of 7, both potential cores have completely dissipated and the axial distributions for all the velocity ratios appear to approach the same value. This seems to imply that the jet flow is rapidly developing into a self-preserving flow--identical to a simple axisymmetrical free jet.

CONTINUING WORK

The current research effort shall continue into the analysis of the two point measurements to ascertain the effect of velocity ratio on scales and convection velocities. A narrow band frequency model for the two point pressure cross correlation function will be developed and employed in the Ribner dilatation formulation of the jet noise problem. The predicted trends in the far-field noise will be compared to measured far-field sound power levels.

ACKNOWLEDGEMENTS

This work was supported by a grant from the National Aeronautics and Space Administration (NASA NGR 14-005-177) and by the Nuclear Engineering Program and Mechanical Engineering Department at the University of Illinois at Urbana-Champaign.

REFERENCES

F. H. Champagne and I. J. Wygnanski, "An Experimental Investigation of Coaxial Turbulent Jets," International Journal of Heat and Mass Transfer, Vol. 14 (1971).

W. Olsen and R. Friedman, "Jet Noise from Co-Axial Nozzles Over a Wide Range of Geometric and Flow Parameters," NASA TMX-71503 (1974).

H. P. Planchon, "The Fluctuating Static Pressure Field in a Round Jet Turbulent Mixing Region," Ph.D. Thesis, Nuclear Engineering Program, University of Illinois at Urbana-Champaign (1974).

B. W. Spencer, "Statistical Investigation of Turbulent Velocity and Pressure Fields in a Two Stream Mixing Layer," Ph.D. Thesis, Nuclear Engineering Program, University of Illinois at Urbana-Champaign (1970).

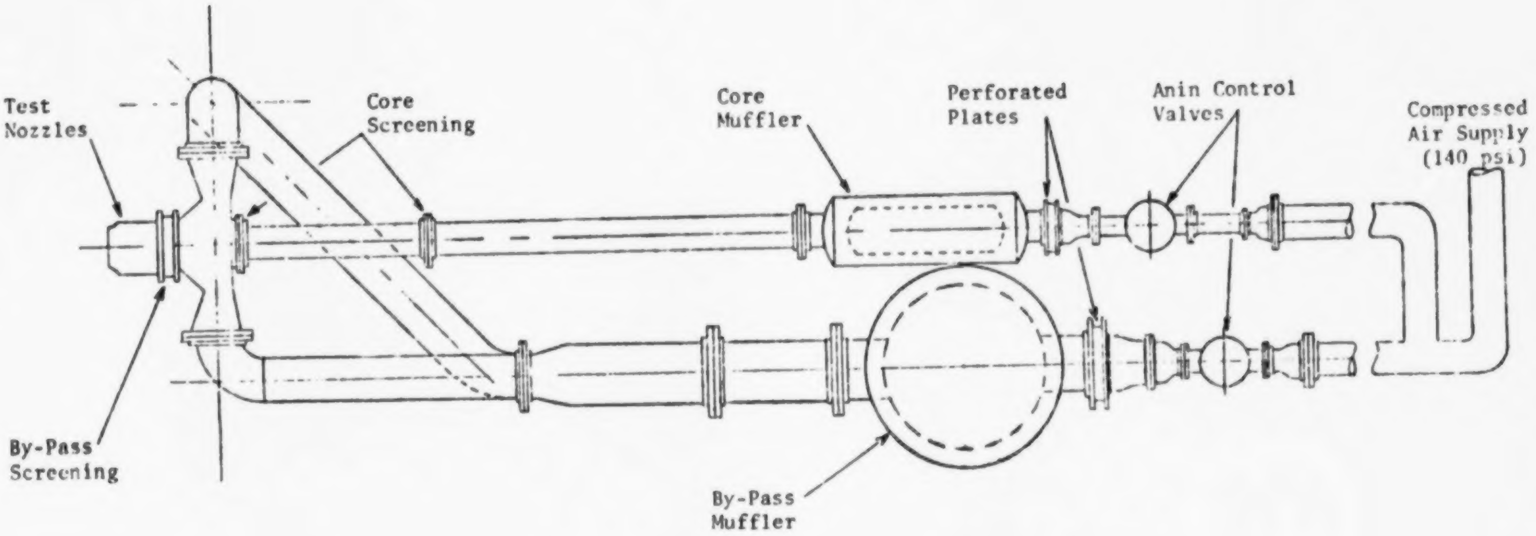
Test Nozzles
Core Screening
Core Muffler
Perforated Plates
Anin Control Valves
Compressed Air Supply (140 psi)
By-Pass Screening
By-Pass Muffler

Figure 1 Co-Annular Nozzle Test Facility

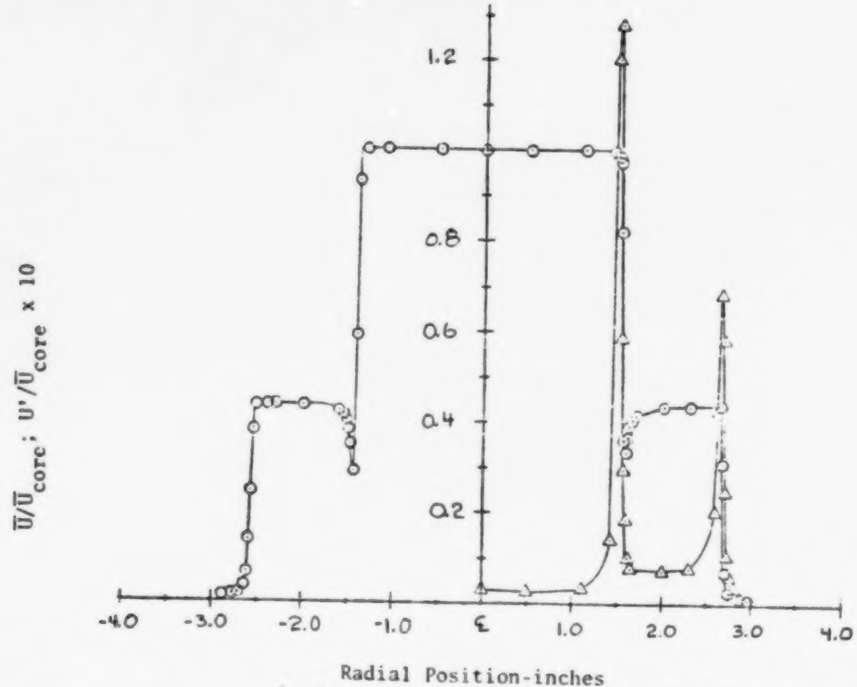

a) $D_{BY\text{-}PASS}$=5.35 in. Area ratio = 2.2.

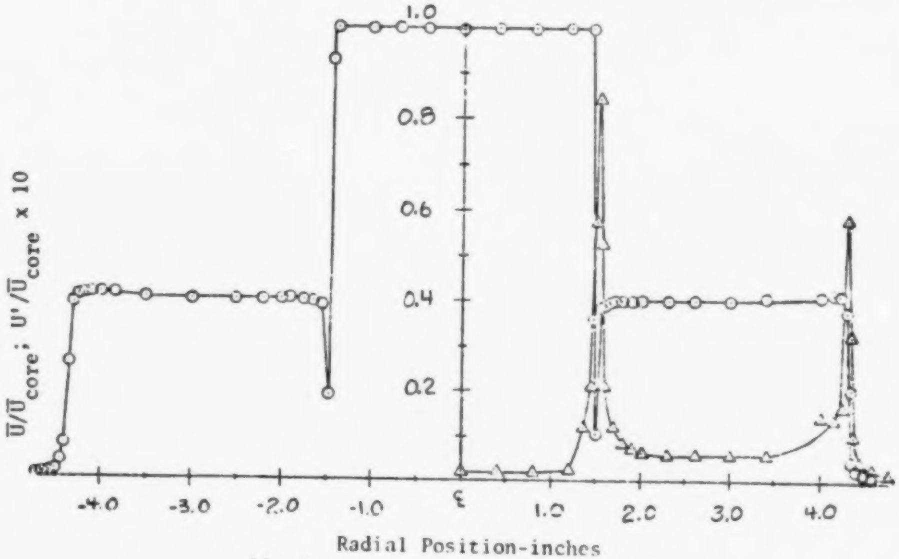

b) $D_{BY\text{-}PASS}$=8.7 in. Area ratio = 7.4.

Figure 2. Nozzle Exit Conditions and Symmetry Check. X = 1/8 in., U_c = 450 fps, $U_{BY\text{-}PASS}$ = 180 fps, D_{CORE}=3.0 in., O = mean velocity profile, Δ = u' turbulent intensity (x 10) profile.

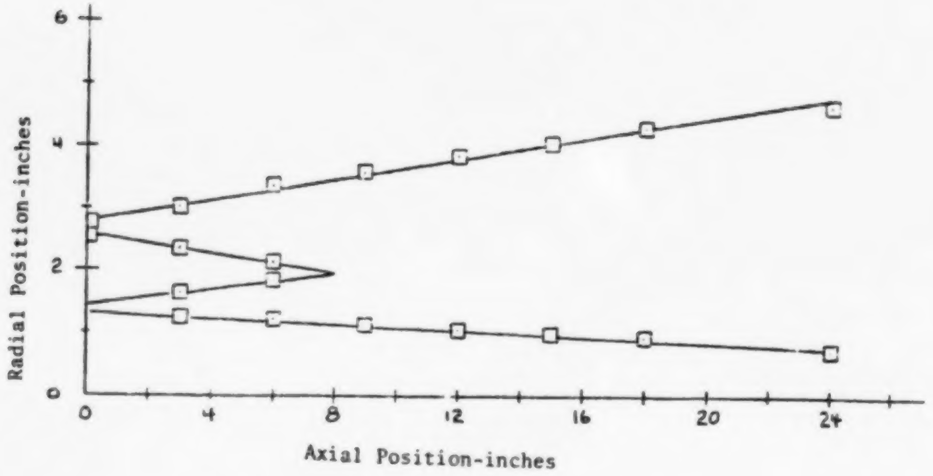

a) $D_{BY-PASS}$ = 5.35 in. Area ratio = 2.2.

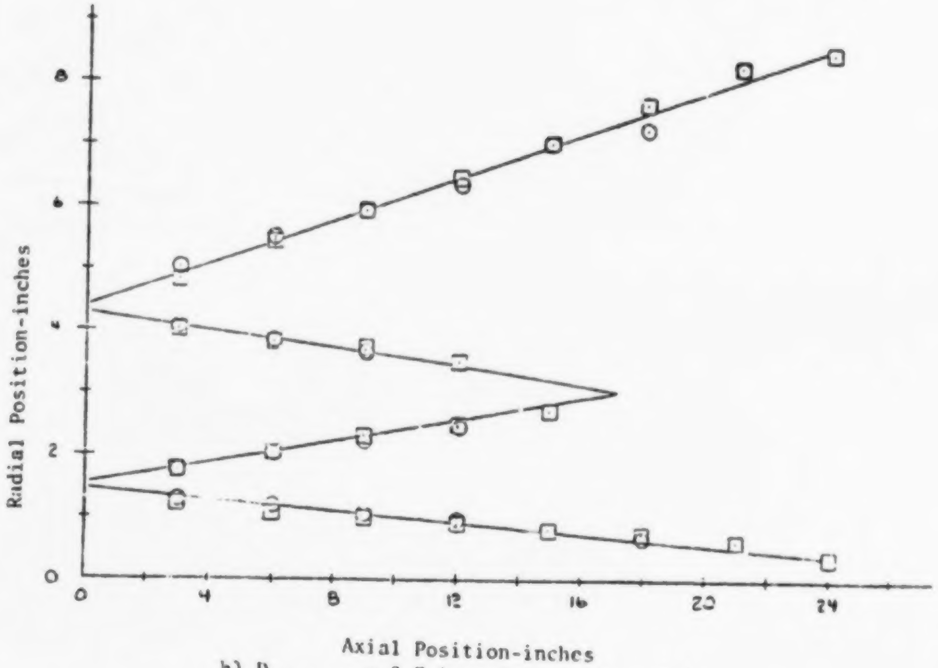

b) $D_{BY-PASS}$ = 8.7 in. Area ratio = 7.4.

Figure 3 Spread Diagrams. U_{core} = 450 fps, $U_{BY-PASS}$ = 180 fps, D_{core} = 3.0 in., O = Hot wire data, = Rake data.

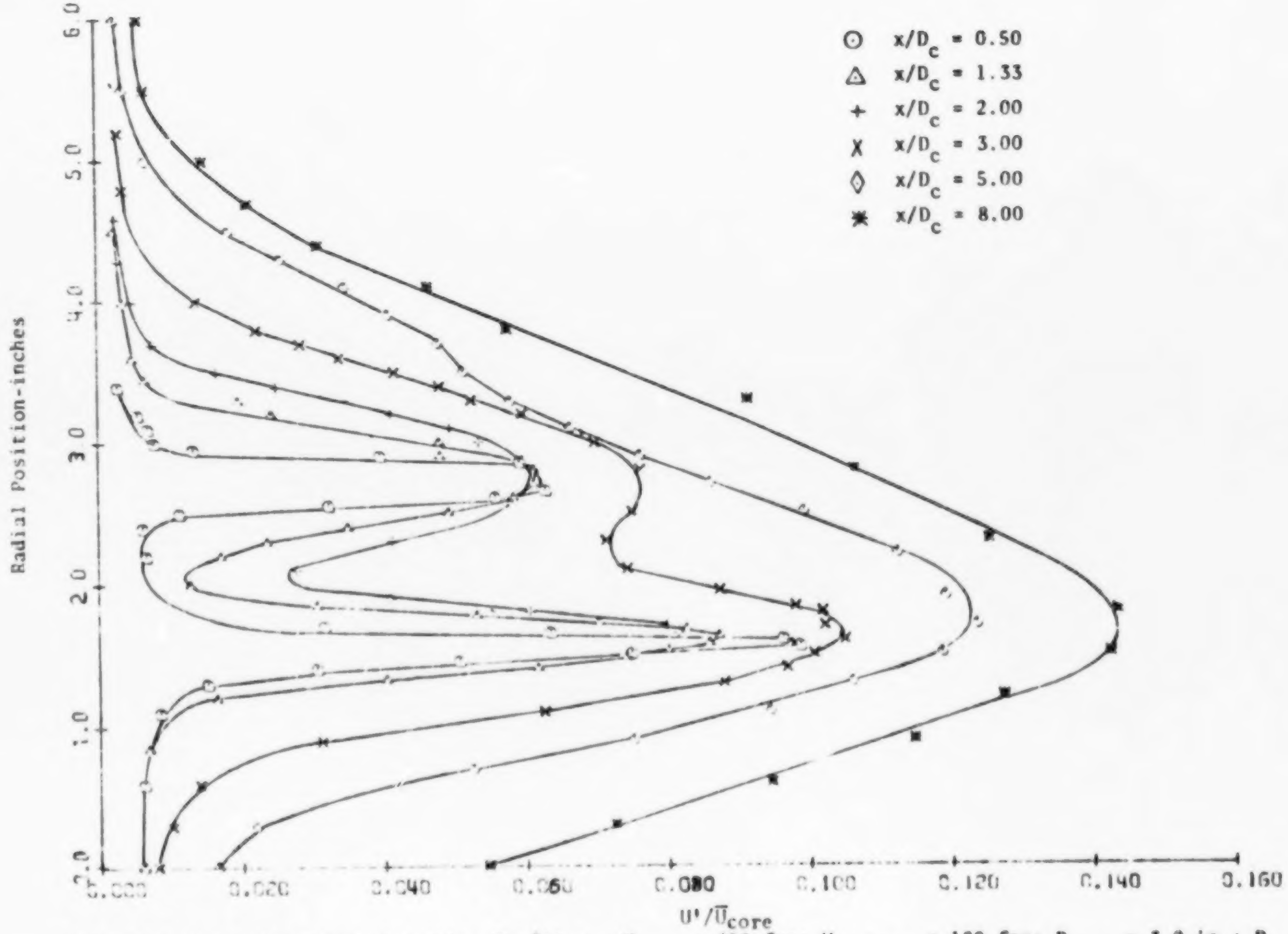

Figure 4 Axial Turbulent Intensity Profiles. U_{core} = 450 fps; $U_{BY-PASS}$ = 180 fps; D_{core} = 3.0 in.; $D_{BY-PASS}$=5.35 in.

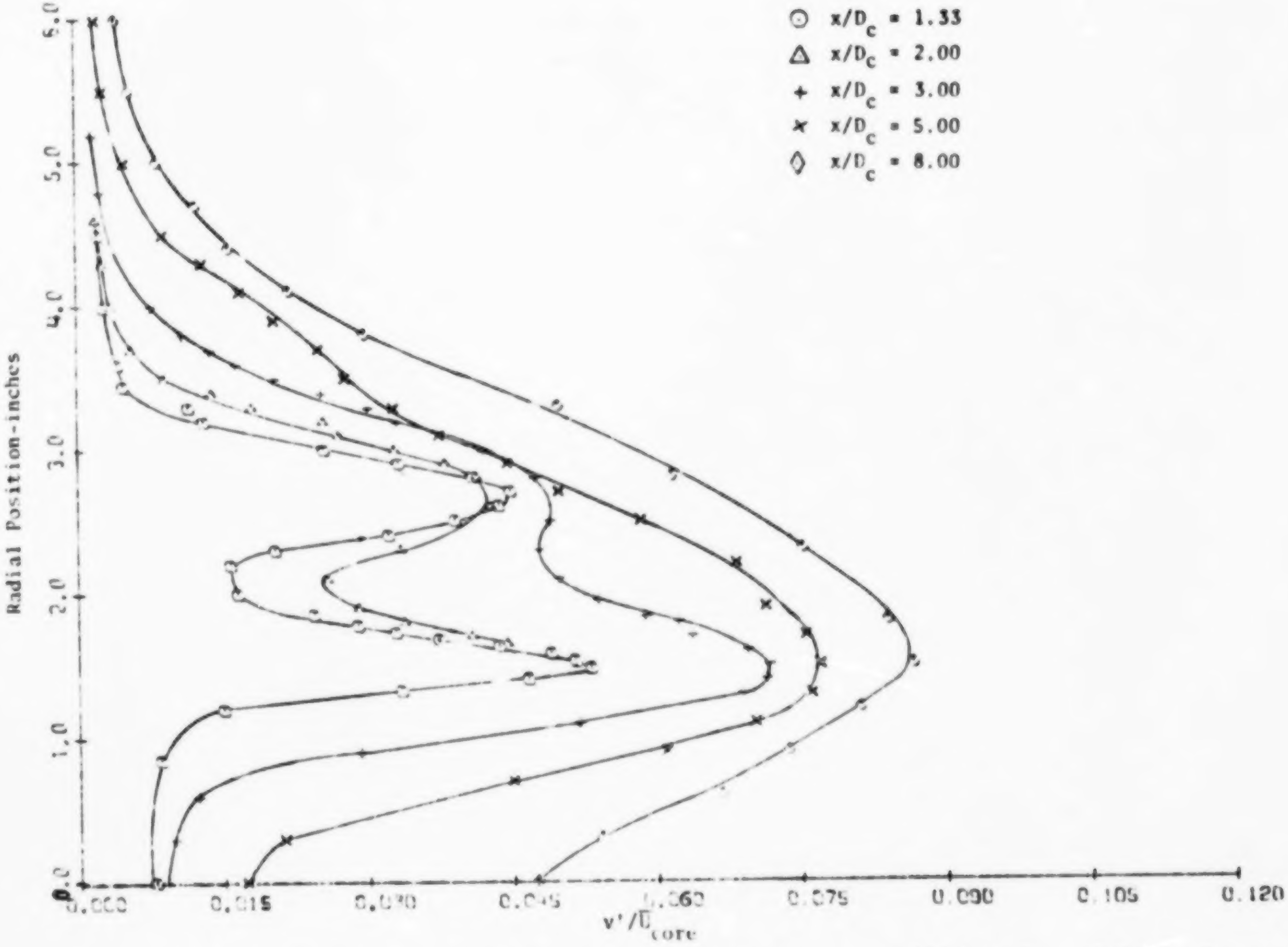

Figure 5 Radial Turbulent Intensity Profiles. U_{core} = 450 fps; $U_{BY\text{-}PASS}$ = 180 fps; D_{core}=3.0 in.; $D_{BY\text{-}PASS}$=5.35 in.

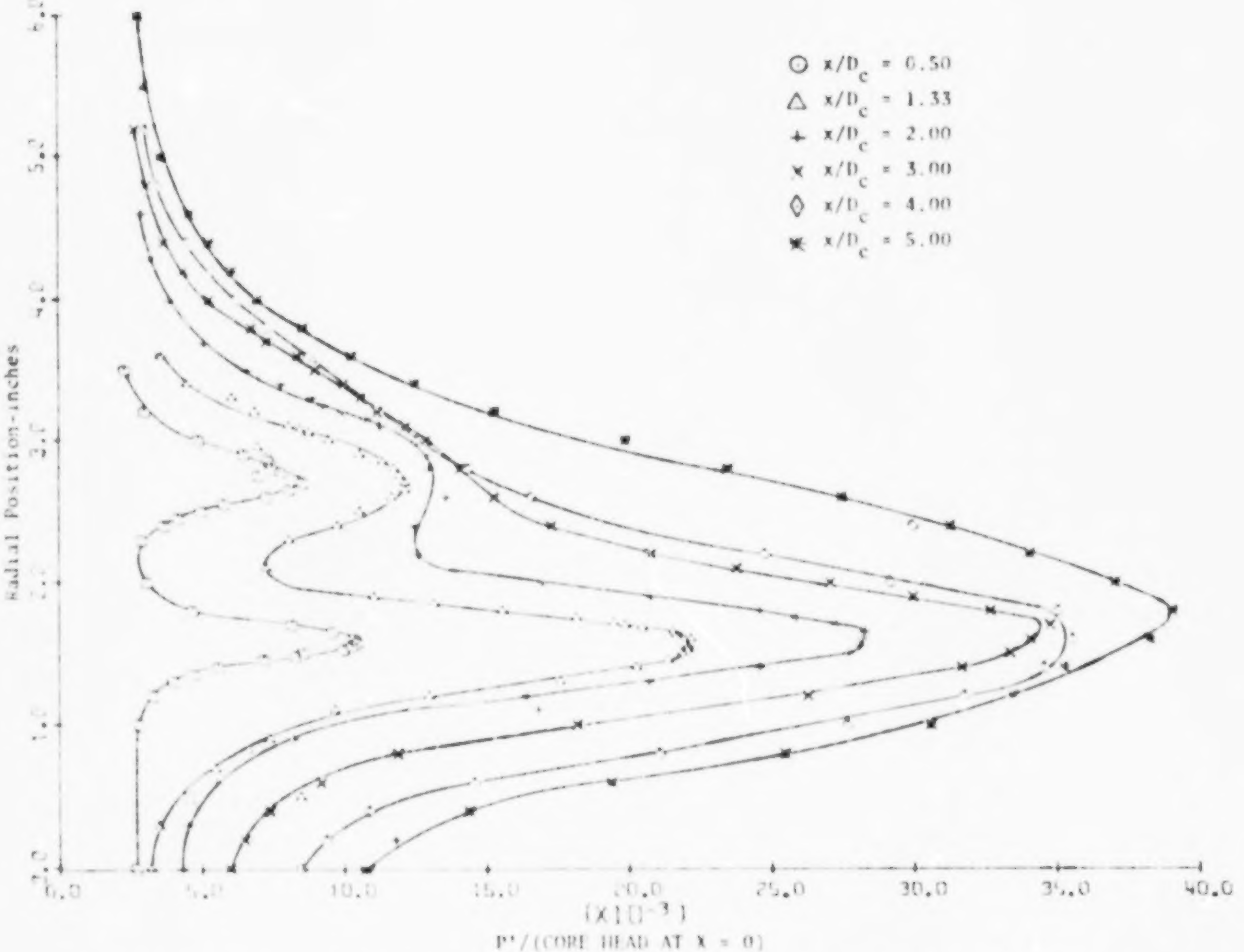

Figure 6 Pressure Intensity Profiles. U_c=450 fps; $U_{BY\text{-}PASS}$=180 fps; D_{core}=3.0 in.; $D_{BY\text{-}PASS}$=5.35 in.

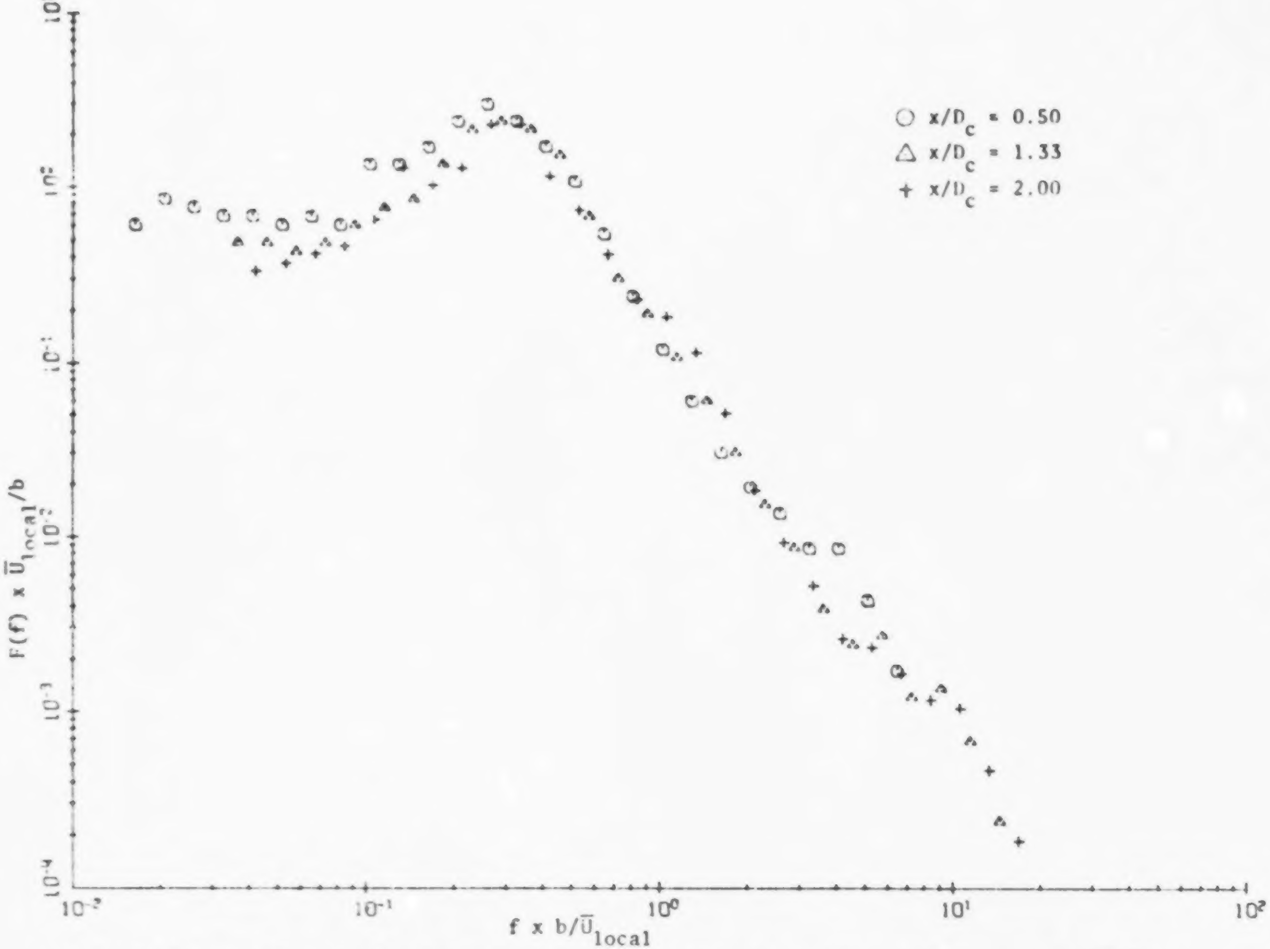

Figure 7 Pressure Spectra for Outer Mixing Region. Velocity ratio = 0.0; $U_{BY\text{-}PASS}$ = 180 fps; $D_{BY\text{-}PASS}$ = 5.35 in.; $r/R_{BY\text{-}PASS}$ = 1.0.

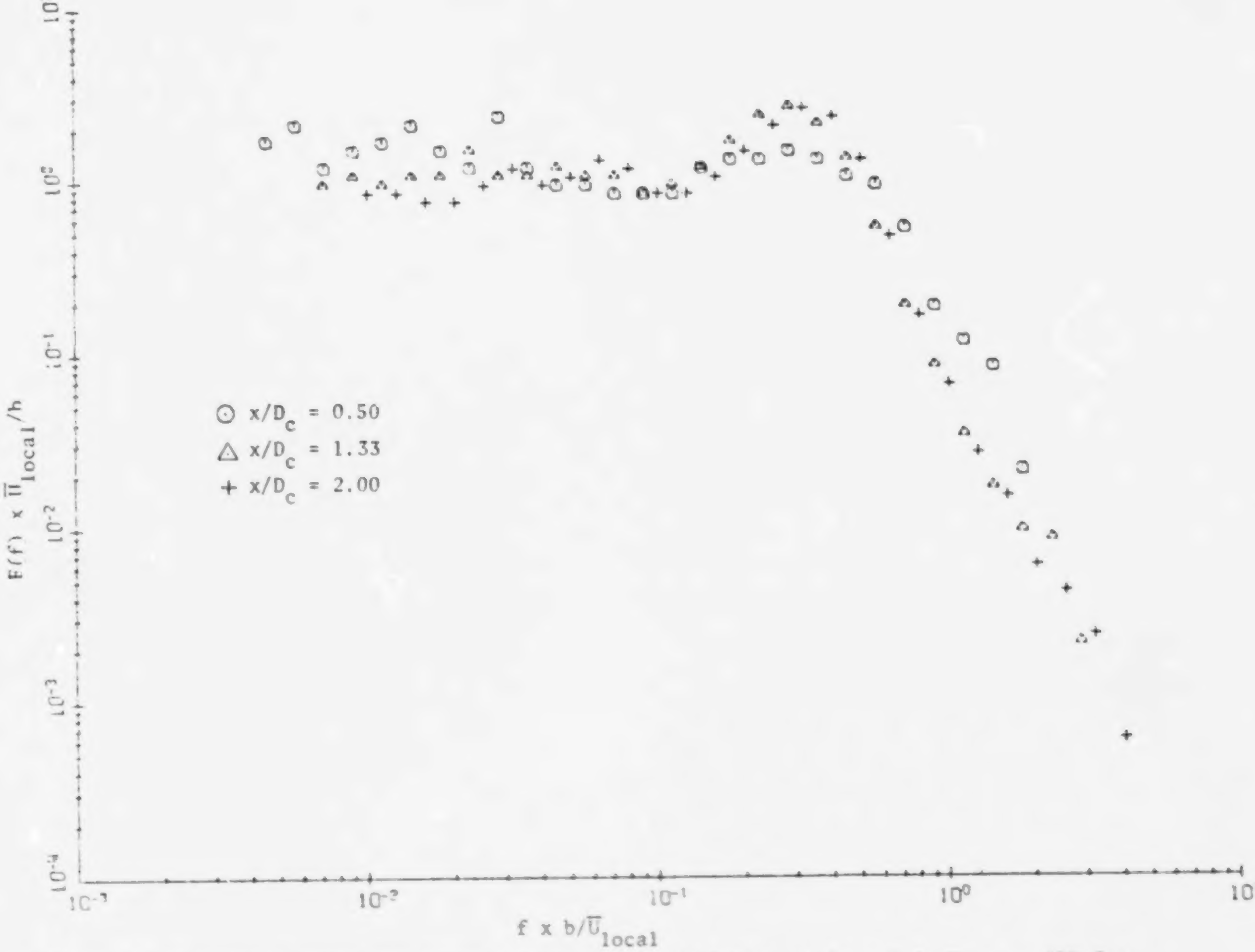

Figure 8 Pressure Spectra for Inner Mixing Region. Velocity ratio = 0.4; U_{core} = 450 fps; $U_{BY\text{-}PASS}$=180 fps; D_c=3.0 in.; $D_{BY\text{-}PASS}$=5.35 in.; r/R_{core}=1.0.

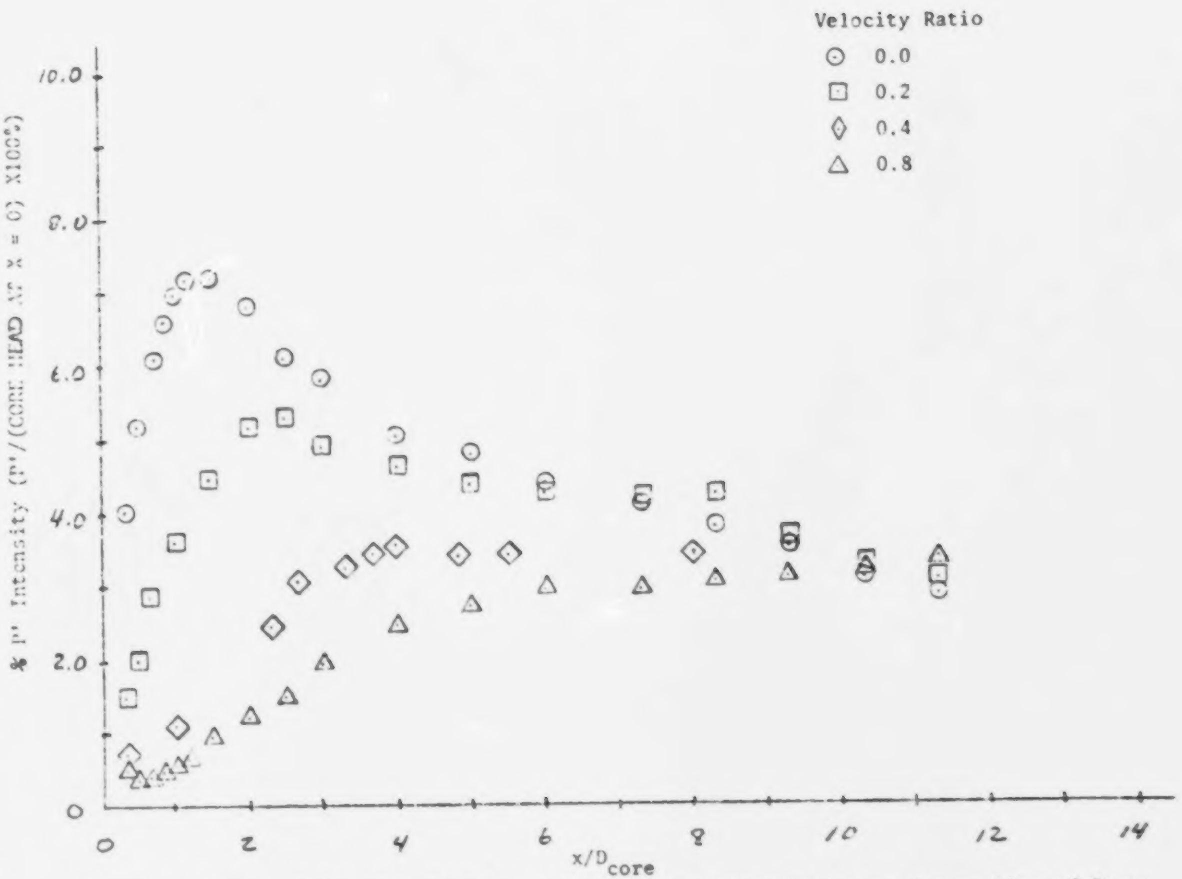

Figure 9 Effect of Velocity Ratio on Axial Pressure Distribution on Center Line of Inner Mixing Layer U_c=450 fps; d_{core}=3.0 in.; $d_{BY\text{-}PASS}$=5.35.

ON NOISE PRODUCED BY SUBSONIC JETS

by

John Laufer, Richard E. Kaplan and Wing T. Chu

University of Southern California
Department of Aerospace Engineering
Los Angeles, California 90007

At the 1973 Interagency Symposium the development of a directional microphone system was described and some preliminary results were presented (Ref. 1). In view of the very promising aspect of this method for the location of noise sources along a jet exhaust, additional effort has been spent to improve the technique and to obtain more accurate results. This involves developing more effective statistical methods to improve the spatial resolution of the directional microphone system and second, to use some specially designed filter amplifiers to counteract the frequency discrimination of the reflector type directional microphone system. These filters improve the accuracy of the measurement in the low frequency regime of the system.

Since most of the features of the experiment have been previously discussed (Ref. 1, 2, 3), we shall dispense with their repetition at this time, and concentrate only on the differences in experimental and analytical techniques as well as a presentation of our latest results.

Analytical Techniques

As explained in Ref. 1, the gain of the reflector microphone system initially increases with frequency like f^2. Since the high frequency portion of jet noise only decreases as f^{-2}, the total measured signal will be heavily weighted by the relatively unimportant high frequency portion of the noise spectrum. To counteract this frequency discrimination of the reflector microphone system, a specially designed filter amplifier has been used in obtaining our final results. Figure 1 shows the configuration of this special amplifier and its frequency response.

If we model the jet by a line distribution of compact acoustic sources of strength W per unit length, each having a spectrum and a directionality, the measured response, W_m, of a directional microphone located in the far field (X, r) and aiming at the point x (Figure 2) is given by

$$W_m(x\, , f) = \int_0^\infty \frac{G(f)}{4\pi R^2} H(\eta)\, W(\xi\, , f\, , \phi)\, d\xi \qquad (1)$$

where H is the "window function" of the directional microphone system and

$\eta = \pi D \sin\theta/\lambda$, D being the diameter of the reflector, and λ is the acoustic wave length. G is the gain of the microphone system and is a function of frequency f. There are at least three possible ways to solve Equation 1 to recover W depending on the assumptions used. The first is the integral transform technique which was originally used in Ref. 2. The second is the matrix inversion technique used in Ref. 1. The third one is the relaxation technique which involves an iterative procedure. A systematic study of these three methods has been carried out and reported in Ref. 3. It has been found that the last technique is superior as demonstrated by Figures 3 and 4. Figure 3 is a reproduction of Figure 8 of Ref. 1 and Figure 4 shows distribution obtained by the relaxation technique. It is seen that the spatial resolution (the spread of each curve) has been considerably improved although the qualitative results are essentially the same. The same data replotted as contours of constant intensity are shown in Figure 5a, while 5b gives a similar plot for a two inch jet showing that the conventional scaling laws are essentiall, satisfied. This technique is currently being used to analyze data recorded for other exhaust velocities and with reflector located at positions other than the 90° case.

The good spectral scaling for both overall noise and the present directional microphone results in terms of the Strouhal number (fD/U) strongly suggest that the large scale turbulent motion may play a very important role in the noise production of turbulent jets. Studies of these large scale structures have been started under an additional contract from NASA Lewis Research Center. In addition, simple experiments involving far field acoustic measurements are being carried out to substantiate our current thinking on the generation mechanism of jet noise.

The results cited above were analyzed by numerical Fourier Transform methods, using a 500 hz "ideal" bandwidth on the Hanned spectra. The high cost of digital spectral analysis caused us to use an analog, narrow band filter for the initial Fourier Analysis of the data. The bandwidth characteristic of the analog filter is shown in Figure 6 as an amplitude a(f).

Whereas the previously cited results used an experimentally measured window function, derived from a "point" acoustic source, an analytic window function was computed by convolving the filter characteristic shown in Figure 6 with the theoretical diffraction distribution expected in an axisymmetric coordinate system $(2J_1(\eta)/\eta)^2$.

$$H(\eta) = \frac{\int_{-\infty}^{\infty} (2J_1(\eta)/\eta)^2 \, a(f)df}{\int_{\infty}^{\infty} a(f)df} \qquad (2)$$

and η now is expressed in terms of frequency f and the sound speed C

$$\eta = \pi Df \sin\theta/C$$

This integration was performed for all center frequencies and all aiming locations for each virtual source (yielding the θ as shown in Figure 2).

It was noted that at very low frequencies, the gain of the reflector is so small that the microphone responds appreciably to sound that has not been reflected. Hence, the kernal $H(\eta_\ell)$ in (1) was replaced by

$$H(\eta_\ell) + \frac{D(x)R^2}{a(f)R_1^{\,2}} \qquad (3)$$

where the second term accounts for the direct response with a shielding term $D(x)$ which included the directional characteristics of the focal point microphone converted into our coordinate system.

The source distribution $W(x,f)$ is recovered by an iterative technique wherein $W_1(x,f)$ is chosen as the measured $W_m(x,f)$ distribution and $D(x) = 1$.

The $W_{m_1}(x,f)$ generated by (1) is compared to the measured $W_m(x,f)$ and the error is used to generate the next $W_2(x,f)$. After proceeding through four iterations, the error is used to generate a new $D(x)$ distribution

$$D_5(x) = D(x) - .5 \quad \text{ERROR}/W_m(x,f) \qquad (4)$$

Beyond this alternate iteration, errors are corrected for in either the $W_j(x,f)$ distribution or the $D_j(x)$ distributions until

$$\frac{\displaystyle\int_{-\infty}^{\infty} \left| W_m - W_{m_j}(\xi, f) \right|^2 d\xi}{\displaystyle\int_{-\infty}^{\infty} \left| W_m(\xi, f) \right|^2 d\xi} < .0001 \qquad (5)$$

Experimental Results

In Figure 7 a sample of the raw experimental data representative of an oblique observation angle for a sonic jet is presented at a representative frequency. Observe in Figure 7 the "raggedness" of the amplitude distribution as a function of aiming position along the jet axis. The variation of intensity from a nominal smooth curve is the spatial noise of the measurement, and is indicative of minor variations of jet exit condition in time, translated to an apparent spatial noise since the reflector was stepped in x.

When this spatial noise was "smoothed" (Figure 8), the observed distributions in frequency (spectra at fixed x) were subject to increasing scatter, so that an initial smoothing in both space and frequency was desirable to yield data which could be enhanced.

This process is necessary since the enhancement essentially restores high spatial frequencies lost by the diffraction of the reflector, which serves as a spatial low pass filter.

The enhanced results (Figure 9) often suggest spurious structures associated with the limits of the measured data (i.e., far upstream and downstream). These spurious responses result from the truncation of the incident data in x whereas the measurements should have been taken for a larger range of included viewing angles. Generally, these structures are sufficiently far removed from the primary peaks that they may be easily separated from the main structure except at the lowest frequencies investigated.

Conclusions

As with previous results, the existence of Strouhal scaling and the source location is in accord with known features of jet noise structure. While care must be taken to minimize the spatial noise, and much of the fine structure measured needs further clarification to determine its physical significance, the technique is now sufficiently advanced to warrant its use for both supersonic and muffled jet configurations.

This work was supported by a research grant from the Department of Transportation DOT-OS-00002. The authors acknowledge the assistance of Robert H. Schlinker who performed the data reduction and numerical calculations.

References

1. Laufer, J., Kaplan, R. E., and Chu, W. T. "Acoustic Modelling of the Jet Noise Abatement Problem," Proceedings Interagency Symposium in Transportation Noise, Stanford University, March 28 - 30, 1973.

2. Chu, W. T., Laufer, J., and Kao, K. "Noise Source Distribution in Subsonic Jets," Proceedings of the 1972 International Conference on Noise Control Engineering, Washington, D. C., October 4 - 6, 1972, pp. 472-476.

3. Schlinker, R. H., Petersen, R. A., and Kaplan, R. E. "Enhancement of Directional Microphone Measurements," AIAA Reprint No. 73-1040, presented at the AIAA Aero-Acoustics Specialists Conference, Seattle, Washington, November 1973.

Figures 6, 7, and 8 not available at submission time, but will be available for the Symposium.

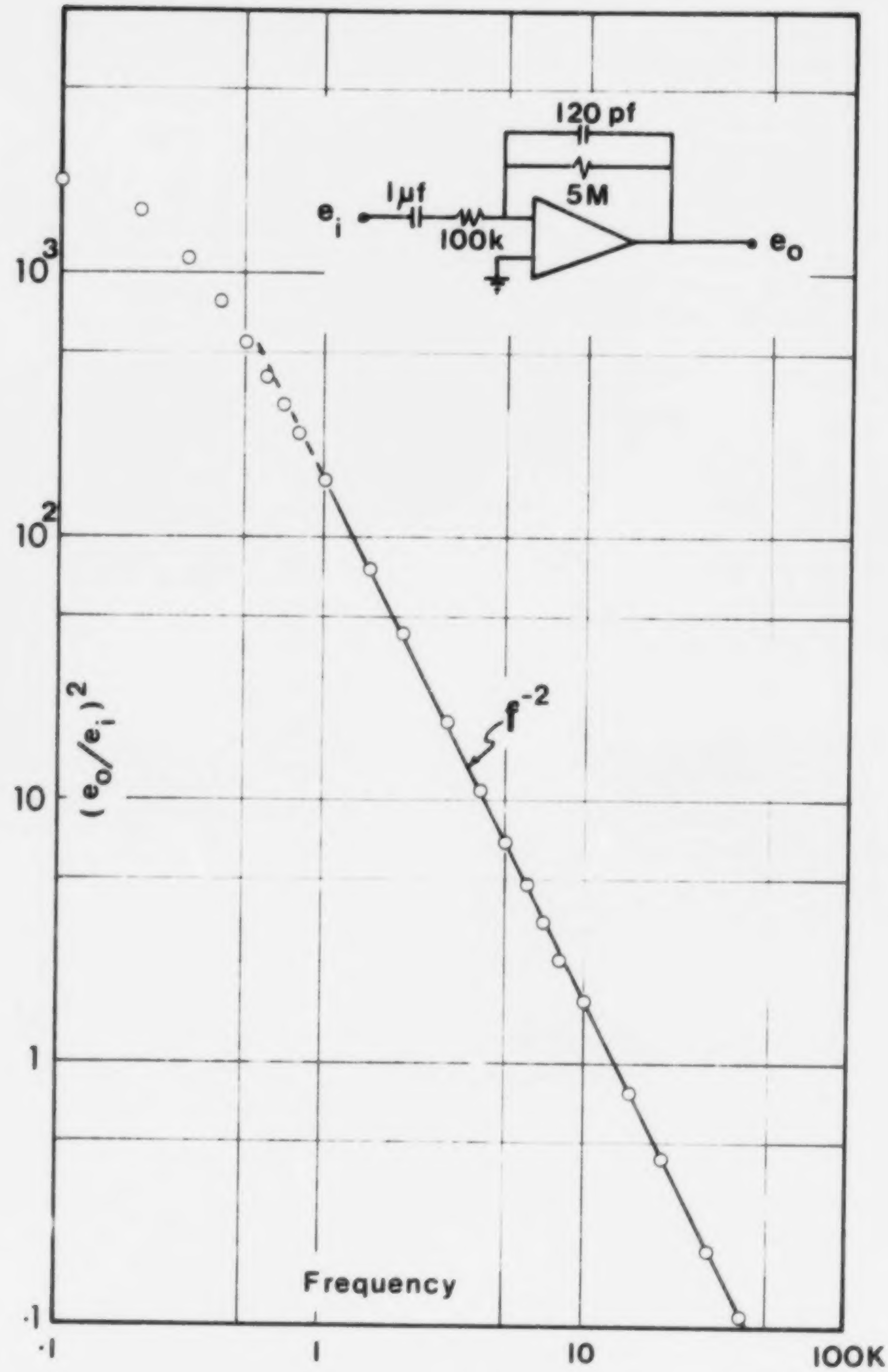

FIG. 1. FREQUENCY RESPONSE OF FILTER AMPLIFIER

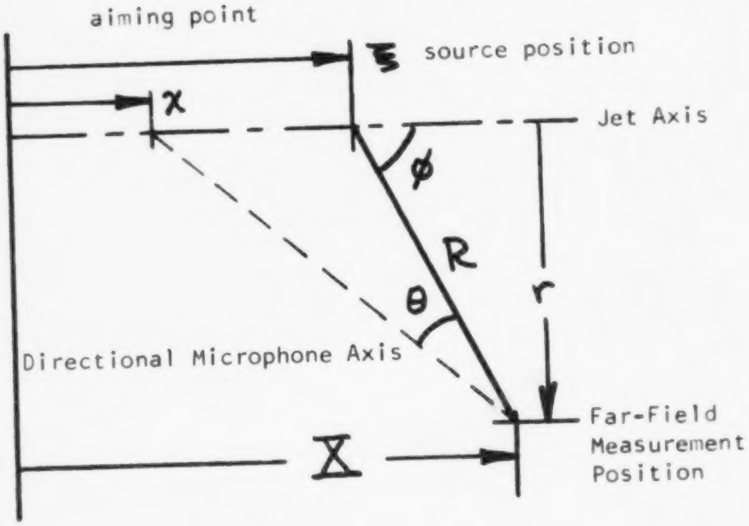
aiming point
ξ source position
x
Jet Axis
φ
R
θ
r
Directional Microphone Axis
Far-Field Measurement Position
X

FIG 2 COORDINATES FOR DIRECTIONAL MICROPHONE MEASUREMENTS

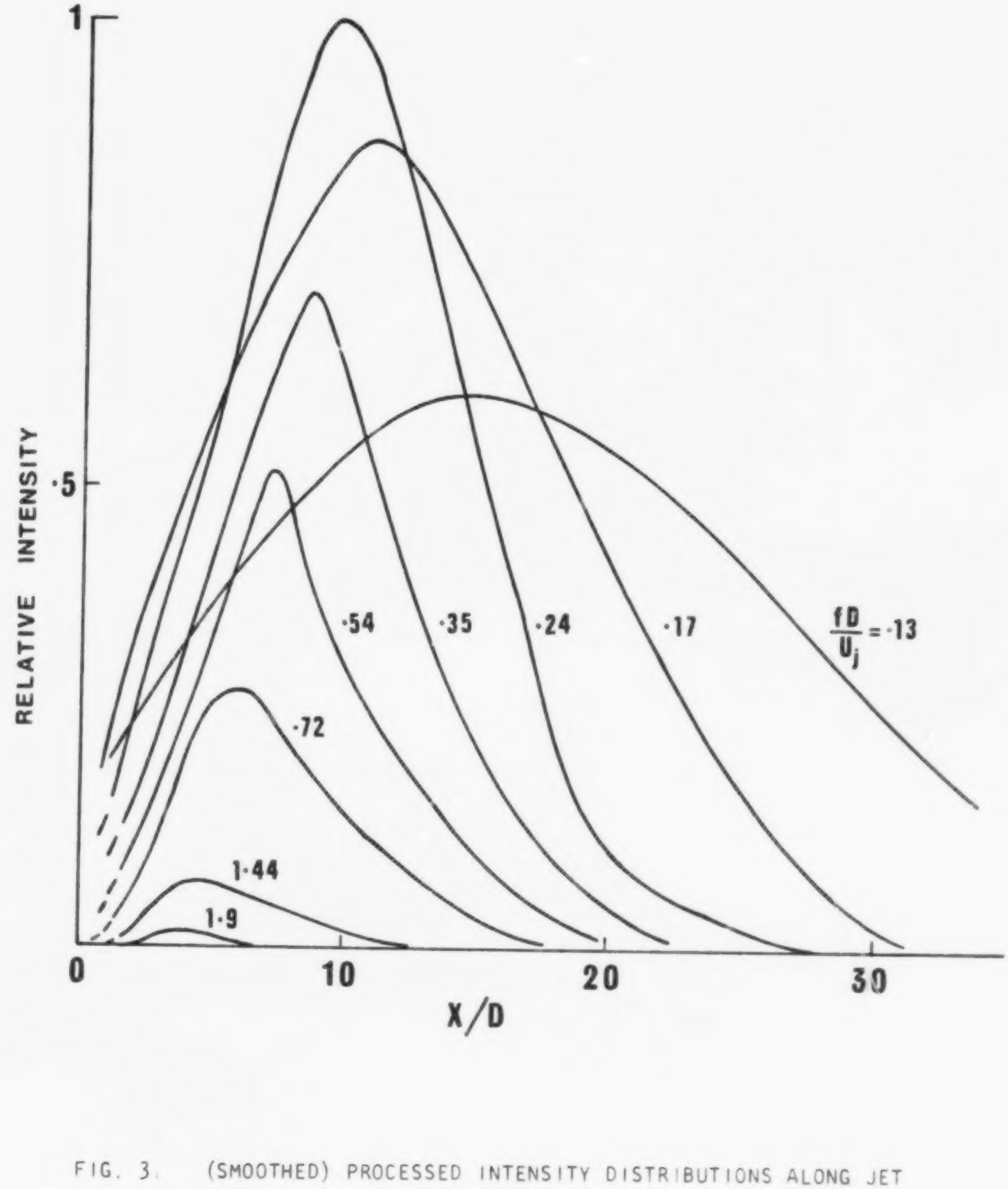

FIG. 3. (SMOOTHED) PROCESSED INTENSITY DISTRIBUTIONS ALONG JET

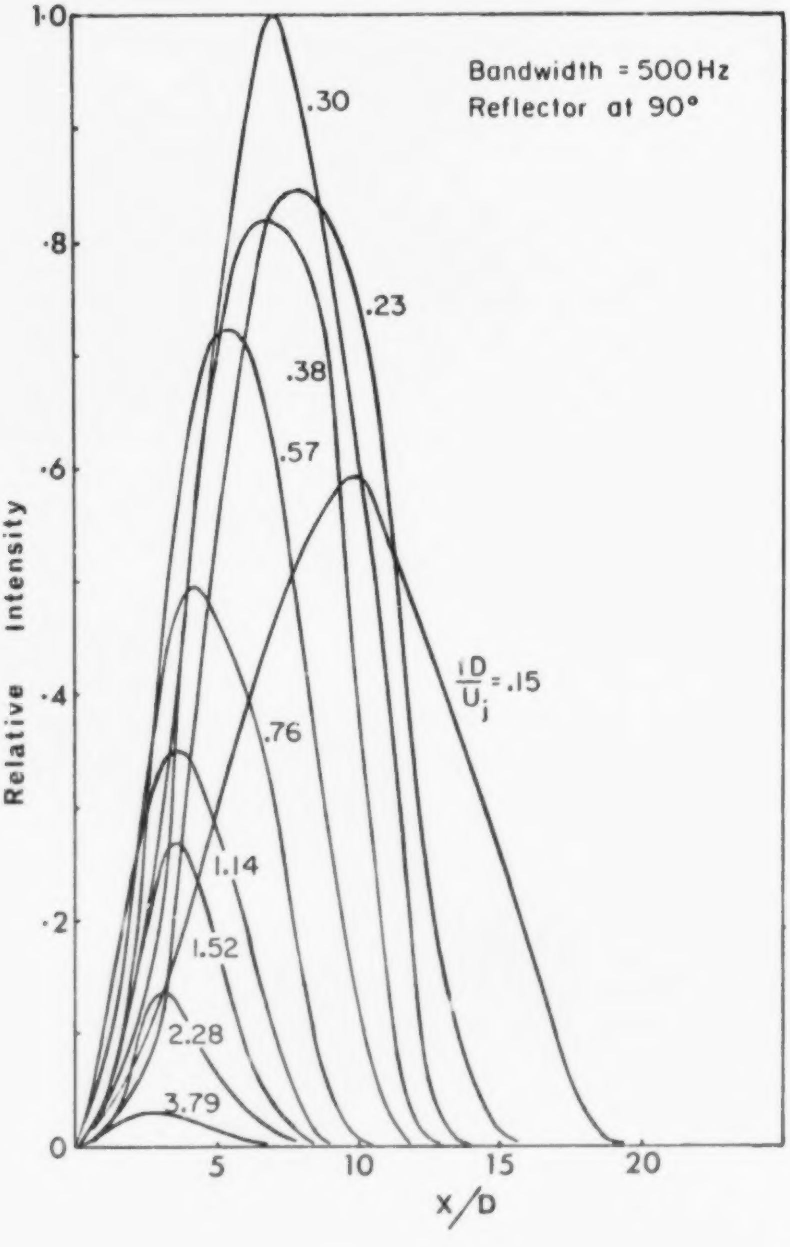

FIG. 4. PROCESSED INTENSITY DISTRIBUTIONS ALONG A 1'', M=.97, JET

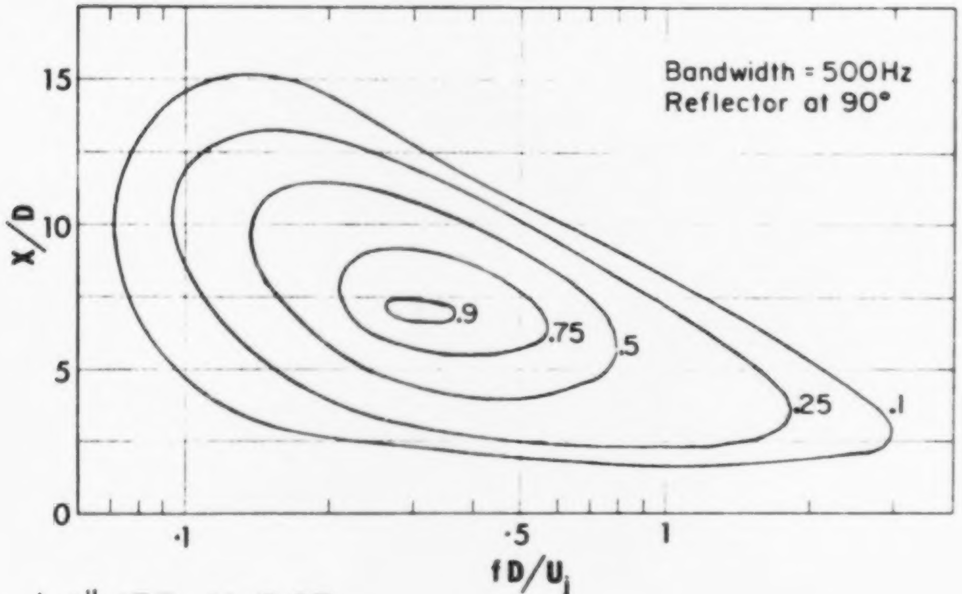

a) 1" JET M=0.97

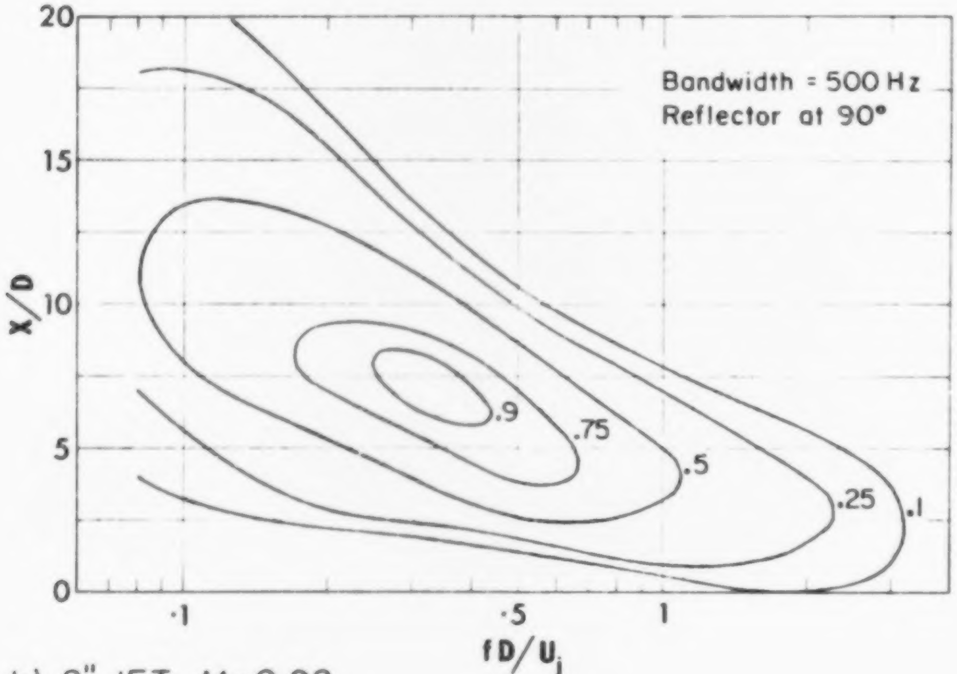

b) 2" JET M=0.98

FIG. 5. CONTOUR PLOT OF INTENSITY DISTRIBUTION

SUPERSONIC JET NOISE INVESTIGATIONS

by

John Laufer, W. T. Chu, R. H. Schlinker,
and R. E. Kaplan

University of Southern California
Department of Aerospace Engineering
Los Angeles, California 90007

ABSTRACT

The acoustic source strength distributions along a jet axis at Mach numbers 1.5, 2.0, 2.5 are presented. Certain measurements were made in narrow frequency bands using a directional microphone system aligned at both 90° and approximately 40° to the jet axis. Equal intensity contours illustrate the Strouhal number of maximum intensity and the spatial extent of the acoustic sources at each viewing angle.

Recent measurements of the jet far field and near field pressure signals exhibit wave shapes characteristic of Mach wave radiation. Various statistical information regarding these signatures as well as conjectures about their generation are given.

Narrow band directivity measurements obtained with an omnidirectional microphone are included.

I. INTRODUCTION

Before the next generation of supersonic jet noise suppressor devices can be designed the location and nature of the important noise sources must be understood. Previous approaches to this problem include: (1) Theoretical prediction based on various models of generation mechanisms and dimensional arguments (Ref. 1, 2, 3, 4, 5, 6, 7); (2) Intensity surveys along the jet boundary (Ref. 8, 9); (3) Optical visualizations of the flow and acoustic near field (Ref. 10, 11, 12, 13, 14, 15); (4) Extrapolation from the far field intensity contours (Ref. 16, 9); (5) Wall isolation techniques (Ref. 17, 18, 19); and (6) Imaging techniques (Ref. 20).

Results are now available on the location of the sources from measurements made at the University of Southern California using an imaging type directional microphone system. The unit, consisting of spherical reflector with a microphone at the focal point, rotates to scan along the jet axis. The details of the system are discussed in Ref. 21.

The measured far field response $W_m(x,f)$ for the directional microphone located at X, r and aimed at point x, is related to the assumed incoherent source strength distribution $W(x,f,\phi)$ by the time averaged integral equation:

$$W_m(x,f) = \int_0^\infty \frac{G(f)}{4\pi R^2}\left[H(\eta) + \frac{D(x)\ R^2}{G(f)\ R_1^2}\right] W(\xi, f, 0)\, d\xi \qquad (1)$$

(For a discussion of the variables involved and the relaxation technique used to recover the source distribution $W(x,f)$ see "On Noise Produced by Subsonic Jets by Laufer, Kaplan, and Chu, also presented at this symposium.) If the frequency dependent gain is not considered, the peak Strouhal number is shifted to higher frequencies (Ref. 20).

The recovered narrow band $W(x,f,0)$ distributions have been combined to provide constant acoustic source strength contours plotted against x/D and fD/U_j. These show the spatial extent and the peak Strouhal number of the source distribution.

Measurements made with an omnidirectional microphone in the near field and at oblique far field positions show a randomly occurring skewed pressure signal. Detailed cross-correlation and conditional sampling measurements of the signals are presented. Conjectures on their generation are made. Finally, narrow band spectra obtained with an omnidirectional microphone are given.

II. FACILITY AND PROCEDURE

Three converging diverging nozzles were designed for shock free flow at Mach numbers $M = 1.5, 2.0, 2.5$. A standard NASA program based on three dimensional methods of characteristics was used. The exit diameters are one inch and boundary layer corrections were made. A similar set of two inch exit diameter nozzles was also fabricated but has not yet been used. Fabrication of the nozzles was done on a numerically controlled lathe to insure contour accuracy of .0001 inch.

The nozzles are coupled to the existing settling chamber by a contraction section. Mismatch tolerances on the radii at the joining point between the nozzle and contraction section were held to .002 inch. This is less than the estimated boundary layer displacement thickness originating upstream. With $M = .2$ at the joining point the high accelerations downstream tend to suppress any boundary layer disturbances which develop. The first derivative of the contour was required to be continuous at all joining points. Generally, care was taken to keep the upstream turbulence level low.

Shadowgraphs were taken at increments of 1 psi near the design stagnation pressure to determine the optimum shock free operating pressure. The deflection angles of the weak intersecting compression waves emanating from the nozzle lip were minimal at absolute pressures corresponding to $M =$ 1.47, 1.97, 2.47. Consequently, these were selected as the operating Mach numbers. In all cases the bounding shear layers of the flow were straight and no shock cells were visible.

During the blowdown operation settling chamber pressures are maintained within ± .5% of the operating pressure. The stagnation temperatures were slightly lower than ambient because of the work done by the expansion of the gas from the reservoir. Studies will be made for heated jets at a future date.

All acoustic measurements are made in an anechoic chamber with 1/8" B & K condenser microphones. Free field corrections are applied to all microphones. The frequency response characteristics of the remaining electronic equipment is calibrated and corrected following standard procedures. A 100 Hz bandwidth is used for all narrow band spectra.

III. EXPERIMENTAL RESULTS AND DISCUSSION

1. Source Strength Distributions

Measurements have been made and the data analyzed for the Mach numbers and angles shown in Figure 1. Space limitations allow us to present only a few typical results in this paper. Figure 2 shows a measured source strength distribution for a representative center frequency. As mentioned in Ref. 22, the window function acts to smooth the source distribution. Conversely, noise present in the measured distribution induces large oscillations. Thus, it is necessary to pre-smooth $W_m(x,f)$ prior to enhancement. The result (using the method of Ref. 22) is shown in Figure 2 along with the corresponding enhanced distribution $W(x,f)$ obtained by relaxation. Notice that the spatial extent of the recovered distribution is narrower indicating that the resolution of the system can be enhanced by numerical analysis of the data.

To test if the originally measured source strength $W_m(x,f)$ could be recovered, the integral equation was evaluated using the enhanced distribution $W(x,f)$. The resulting $W_{m_1}(x,f)$ distribution obtained in this way agrees with $W_m(x,f)$ as shown in Figure 2.

Figure 3 shows a constant intensity contour plot obtained by combining 33 measured (and smoothed) narrow band source distributions for the case $M = 2.0$, $\theta = 37.5^\circ$. The corresponding contour plot for the source strength after enhancement is also shown.

Figure 4 shows a set of constant intensity and source strength contour plots for the case $M = 2.0$, $\theta = 37.5^\circ$.

Additional results obtained during the course of the supersonic jet noise investigation not shown here include: (1) Total power per unit length as a function of x/D; (2) Location of maximum intensity as a function of St number; and (3) Comparison of the power spectral density $I(0,f)$ obtained by the directional microphone and a single omnidirectional microphone.

2. Near Field Far Field Pressure Signals

The $M = 2.5$, 45° directional microphone pressure signals exhibited rather characteristic shapes as shown in Figure 5. Since the reflector accentuates the high frequency content of any signal an omnidirectional microphone is needed to check the exact waveform. As Figure 6 shows, randomly occurring high amplitude positive peaks followed by less intense negative ones were again observed. By comparison, the 90° omnidirectional microphone showed no such skewness (Figure 7). Similar results were obtained for the $M = 2.0$, 37.5° directional and omnidirectional microphone measurements. In both the $M = 2.5$, 45° and $M = 2.0$, 37.5° case the skewed signals were confined to a region $0 < \frac{x}{D} < 15$. No skewness was observed for the $M = 1.5$ jet.

It was conjectured that these skewed pressure signals are produced by the so-called Mach wave radiation of the jet. The existence of such Mach waves in the jet near field was observed on the previously mentioned shadowgraphs and is well-documented (Ref. 10, 11, 12, 13, 14). It should be noted that the oblique angle positions used for the $M = 2.0$, 2.5 directional and omnidirectional measurements were selected to coincide with the propagation angle of the shadowgraph Mach waves. (The $M = 1.5$ oblique angle was chosen from the peak intensity on polar plots). These preliminary results suggested that since the Mach waves might be reaching the far field, a more detailed study was in order.

First, the probability distributions were analyzed. Figure 8 shows a typical probability density $B(p)$ for $M = 2.5$, $\theta = 45^\circ, 90^\circ$. The skewness is evident. Table I lists the skewness values S for the cases shown in Figure 1. Here,

$$S = \frac{\int_{-\infty}^{\infty} p^3 \, B(p) \, dp}{\sigma^3} \qquad (2)$$

where σ represents the r.m.s. pressure level.

To check if some of the acoustic signals are propaged in a preferred direction corresponding to the Mach wave propagation angle near field--far field cross correlations were made for the $M = 2.0$ jet. Figure 9 shows two microphones aligned with a source point at $x/D = 7.5$. The measured cross correlation coefficient for the source at $x/D = 7.5$ radiating in the preferred direction $\theta = 39.4^\circ$ (close to the shadowgraph Mach wave propagation angle of 37.5°) was $C = .54$. Here C is defined as

$$C = \frac{\overline{P_1(t)\, P_2(t)}}{\left(\overline{P_1^{\,2}(t)}\ \overline{P_2^{\,2}(t)}\right)^{\frac{1}{2}}} \qquad (3)$$

(See Figure 10 for the cross correlation curve.) The propagation speed was determined as 1129 ft/sec--equivalent to the ambient speed of sound in the room.

Inspired by the large cross correlation coefficient conditional sampling was initiated to determine the details of the pressure signals. Using the line array (Figure 9), a trigger signal was obtained from the first microphone (m_1) from the conditions (a) $P(t) \geq .75\ P(t)_{max}$ and (b) slope positive. The trigger signal was delayed until the acoustic signal travelling at the experimentally determined propagation speed reached m_2. Figure 11 shows the educted pressure signal obtained at m_2.

A similar cross correlation and conditional sampling study was made in the near field (Figure 12). Both m_1 and m_2 are now located in the vicinity of the previously studied acoustic source point at $x/D = 7.5$. To avoid possible interference with the jet boundary, the microphones were located on a 7^o conical slope starting at 1.2 diameters. The cross correlation result is shown in Figure 13 with $C = .62\ U_j$. The travelling speed corresponds to 992 ft/sec. The educted waveform obtained at m_2 is shown in Figure 14.

IV. DIRECTIVITY PATTERNS

Directional distributions were measured for narrow band spectra at each of the angles listed in Figure 1. Figure 15 shows the measured directivities for the 90^o incidence, while Figure 16 is the corresponding result for oblique incidence.

V. CONCLUSIONS

Until a more complete parametric study of the supersonic results is completed, it is impossible to distinguish the separate influences of the Mach wave radiation and temperature distribution in the acoustic source distribution. Supersonic jets exhibit peak acoustic source intensities farther from the jet exit plane, and for a significantly larger spatial extent when measured in exit diameters. The results need to be further interpreted as to the best reference velocity (and Mach number) to characterize the far field acoustics.

The measurements of the Mach wave radiation are anomalous in that the component of their near field convection speed parallel to the jet axis occurs at subsonic velocities. Hence, the radial velocities associated with the generation of this field must be of the same order as the axial velocities of proto-shock waves are to be generated. Until the complete history of these waves can be traced out, it is difficult to determine how much of the far field acoustic energy is directly associated by this radiation source.

This work was supported by a research grant from the Department of Transportation DOT-OS-00002.

REFERENCES

1. Phillips, O. M. "On the Generation of Sound by Supersonic Turbulent Shear Layers," J. Fluid Mech., Vol. 9, Part 1, pp. 1-28 (1960).

2. Williams, F. J. E. "The Noise from Turbulence Convected at High Speed," Phil. Trans. Roy. Soc. London, Ser. A, Vol. 255, pp. 479-503 (1963).

3. Ribner, H. S. "Aerodynamic Sound from Fluid Dilatations. A Theory of the Sound from Jets and Other Flows," UTIA Rept. 86, Inst. Aerospace Studies, Univ. of Toronto (1962).

4. Ribner, H. S. "Eddy-Mach Wave Noise from a Simplified Model of a Supersonic Mixing Layer," NASA SP-207, pp. 53-61 (July 1969).

5. Nagamatsu, H. T., Horvay, G. "Supersonic Jet Noise," AIAA Paper No. 70-237.

6. Tam, C. K. "Supersonic Jet Noise Generated by Large Scale Disturbances," AIAA Paper No. 73-992.

7. Doak, P. E. "Analysis of Internally Generated Sound in Continuous Materials: Part 2," J. Sound and Vibration, Vol. 25, Part 2, pp. 263-335 (1972).

8. Nagamatsu, H. T., Sheer, R. E., Jr., Gill, M. S. "Flow and Acoustic Characteristics of Subsonic and Supersonic Jets from Convergent Nozzle," AIAA Paper, No. 70-802.

9. Yu, J. C., Dosanjth, D. S. "Noise Field of Coaxial Interacting Supersonic Jet Flows," AIAA Paper No. 71-152.

10. Lowson, M. V., Ollerhead, J. B. "Visualization of Noise from Cold Supersonic Jets," J. Acoust. Soc. Amer., Vol. 44, No. 2, pp. 624-630 (1968).

11. Jones, I. S. F. "Finite Amplitude Waves from a Supersonic Jet," AIAA Paper No. 71-151.

12. Dosanjh, D. S., Montegani, F. J. "Underexpanded Jet Noise Reduction Using Radial Flow Impingement," AIAA Journal, Vol. 7, No. 3. pp. 458-464 (1969).

13. Salant, R. F., Zaic, G. F., Kolesar, R. R. "Holographic Study of the Mach Wave Field Generated by a Supersonic Turbulent Jet," Proceedings Purdue Noise Control Conference, Lafayette, Indiana (July 14-16, 1971).

14. Chan, Y. Y., Westley, R. "Directional Acoustic Radiation Generated by Spatial Jet Instability," C.A.S.I. Transactions, Vol. 6, No. 1, (March 1973).

15. Ozkul, A. "Investigation of Acoustic Radiation from Supersonic Turbulent Jets," Proceedings Eighty-Seventh Meeting Acoust. Soc. Amer., New York, New York (April 23-26, 1974).

16. Mayes, W. H., Lanford, W. E., Hubbard, H. H. "Near-Field and Far-Field Noise Surveys of Solid Fuel Rocket Engines for a Range of Nozzle Exist Pressures," NASA Tech. Note, D-21.

17. Potter, R. C. "An Investigation to Locate the Acoustic Sources in a High Speed Jet Exhaust Stream," Wyle Laboratories Tech. Report WR68-4 (1968).

18. Bishop, K. A., Williams, J. E. F., Smith, W. "On the Noise Sources of the Unsuppressed High Speed Jet," J. Fluid Mech., Vol. 50, Part 1, pp. 21-31 (1971).

19. MacGregor, G. R., Simcox, C. D. "The Location of Acoustic Sources in Jet Flows by Means of the Wall Isolation Techniques," AIAA Paper No. 73-1041.

20. Grosche, F. R., Jones, J. H., Wilhold, G. A. "Measurements of the Distribution of Sound Source Intensities in Turbulent Jets," AIAA Paper No. 73-989.

21. Laufer, J., Kaplan, R. E., Chu, W. T. "Acoustic Modelling of the Jet Noise Abatement Problem," Proceedings Interagency Symposium on Univ. Research in Transportation Noise, Vol. 1, Stanford Univ., Stanford, California (March 28-30, 1973).

22. Schlinker, R. H., Petersen, R. A., Kaplan, R. E. "Enhancement of Directional Microphone Measurements," AIAA Paper No. 73-1040.

Figures 2, 3, and 4 not available at submission time, but will be available for the Symposium.

M	$S_{32°}$	$S_{90°}$
1.5	.045	.026

M	$S_{37.5°}$	$S_{90°}$
2.0	.25	.073

M	$S_{45°}$	$S_{90°}$
2.5	.32	.090

TABLE 1 - OMNIDIRECTIONAL MICROPHONE SKEWNESS VALUES

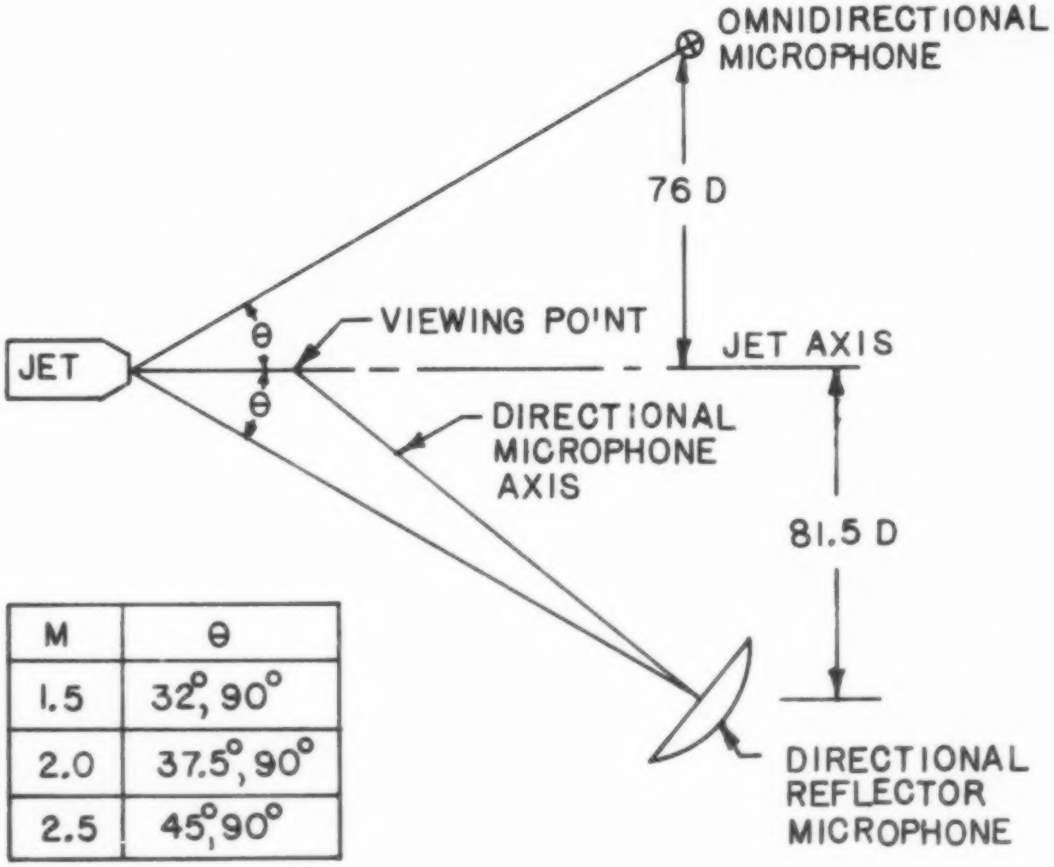
OMNIDIRECTIONAL MICROPHONE
76 D
VIEWING POINT
JET AXIS
JET
θ
θ
DIRECTIONAL MICROPHONE AXIS
81.5 D
M | θ
1.5 | 32°, 90°
2.0 | 37.5°, 90°
2.5 | 45°, 90°
DIRECTIONAL REFLECTOR MICROPHONE

FIG. 1: FAR-FIELD COORDINATES

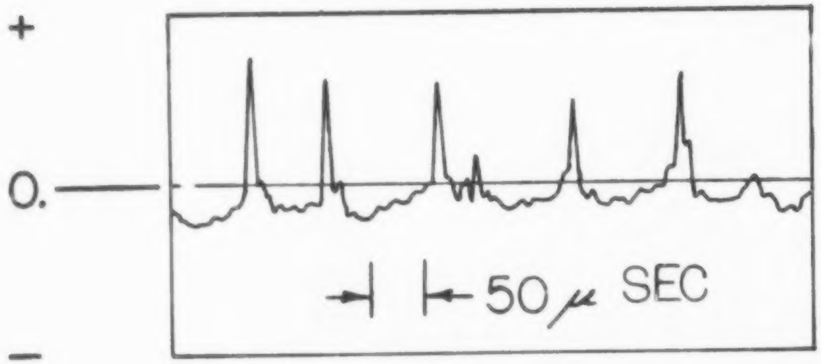

Fig. 5: TYPICAL SIGNALS DIRECTIONAL REFLECTOR MICROPHONE, M = 2.5, $\theta = 45^\circ$

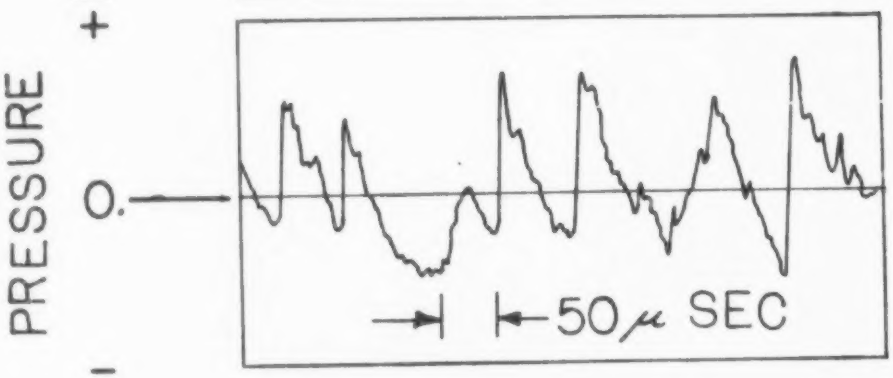

Fig. 6: TYPICAL SIGNALS OMNIDIRECTIONAL MICROPHONE, M = 2.5, $\theta = 45^\circ$

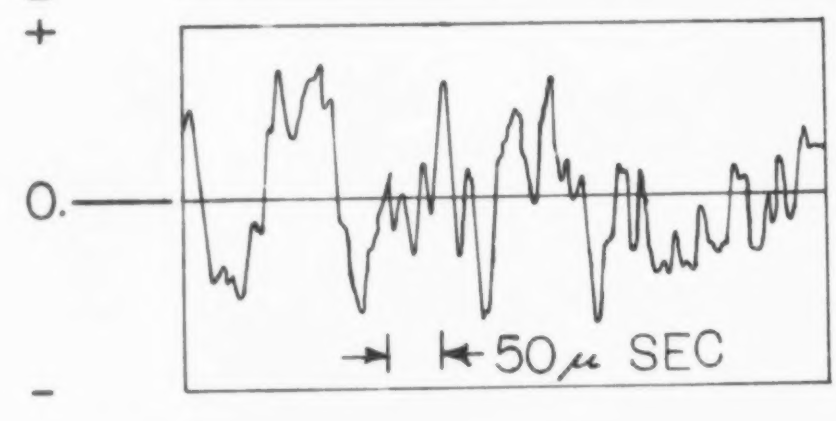

Fig. 7: TYPICAL SIGNALS OMNIDIRECTIONAL MICROPHONE, M = 2.5, $\theta = 90^\circ$

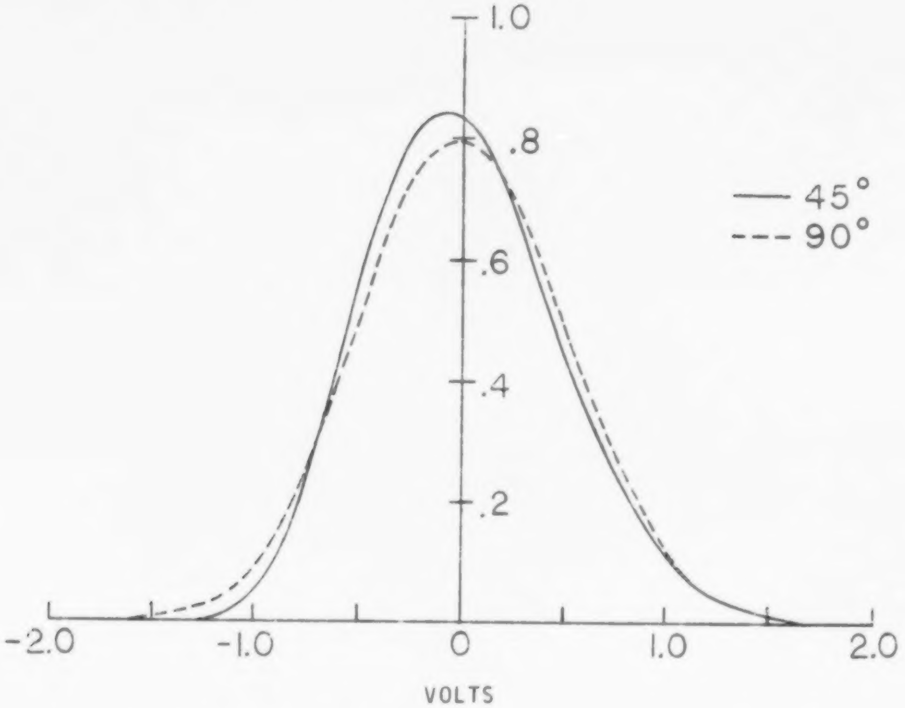

FIG. 8: PROBABILITY DENSITY, M = 2.5; θ = 45°, 90°

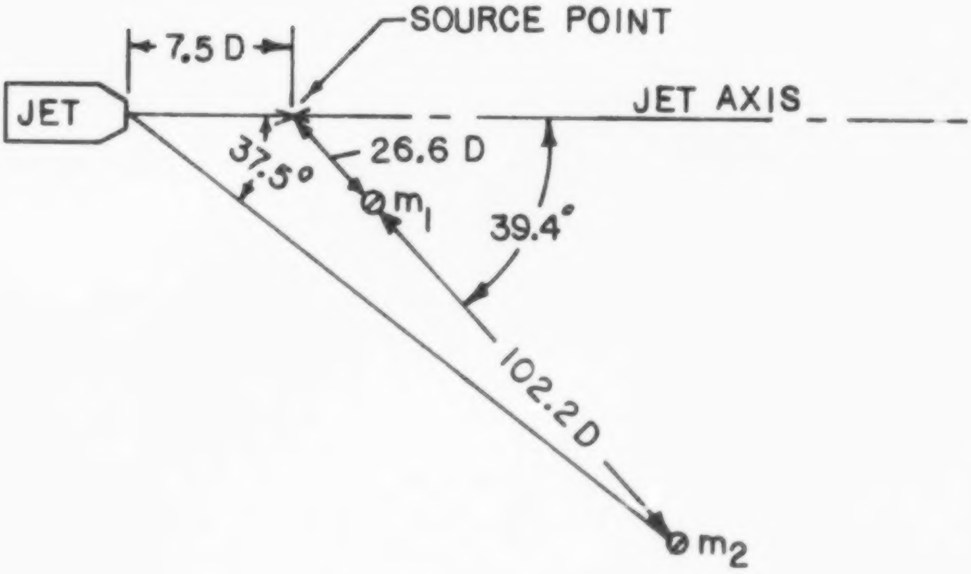
SOURCE POINT
7.5 D
JET
JET AXIS
37.5°
26.6 D
m1
39.4°
102.2 D
m2

FIG. 9: NEAR-FIELD FAR-FIELD COORDINATES

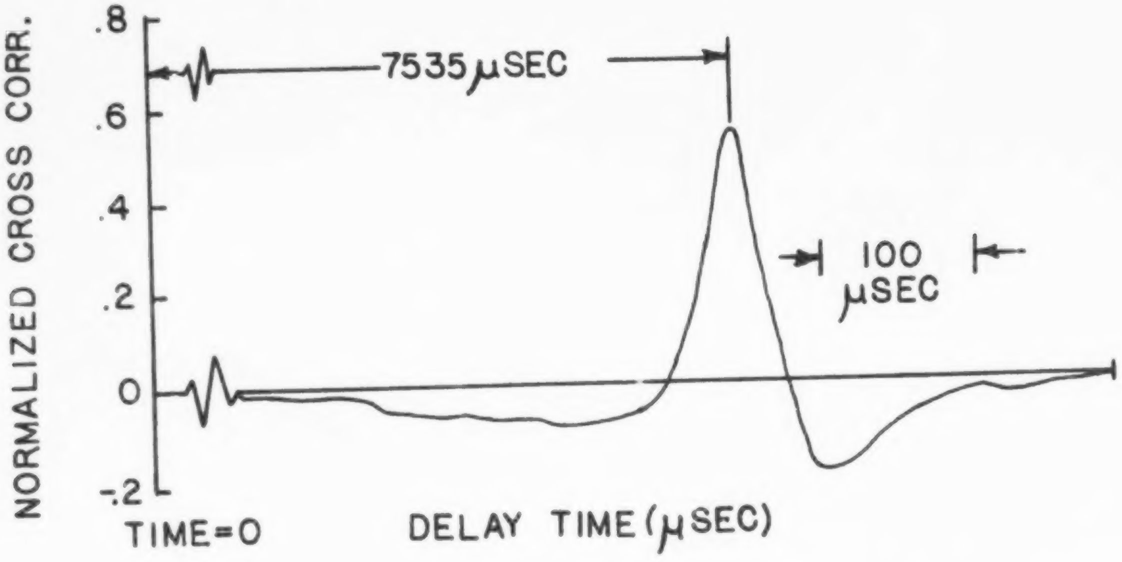

FIG. 10: NEAR-FIELD FAR-FIELD NORMALIZED CROSS CORRELATION COEFFICIENT

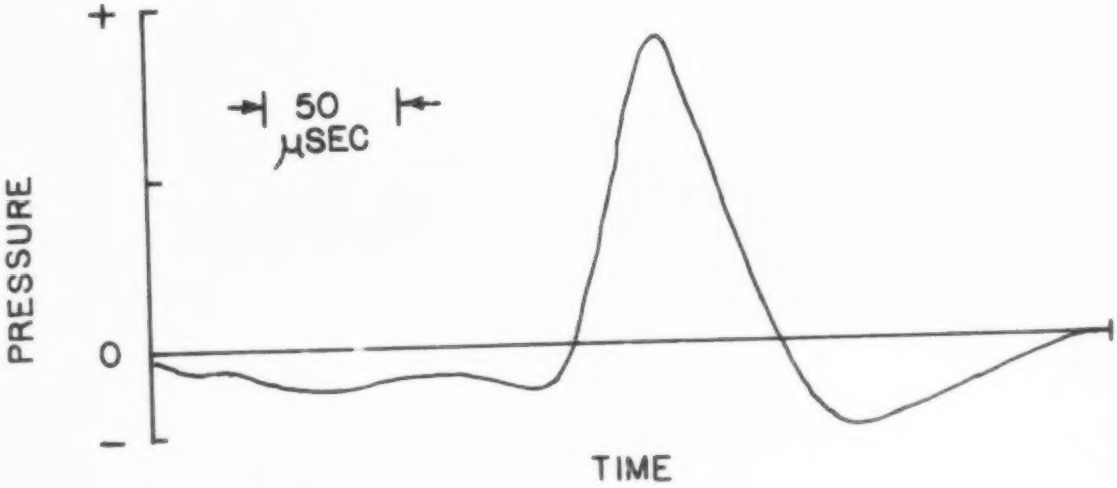

FIG. 11: CONDITIONALLY SAMPLED FAR-FIELD PRESSURE SIGNAL

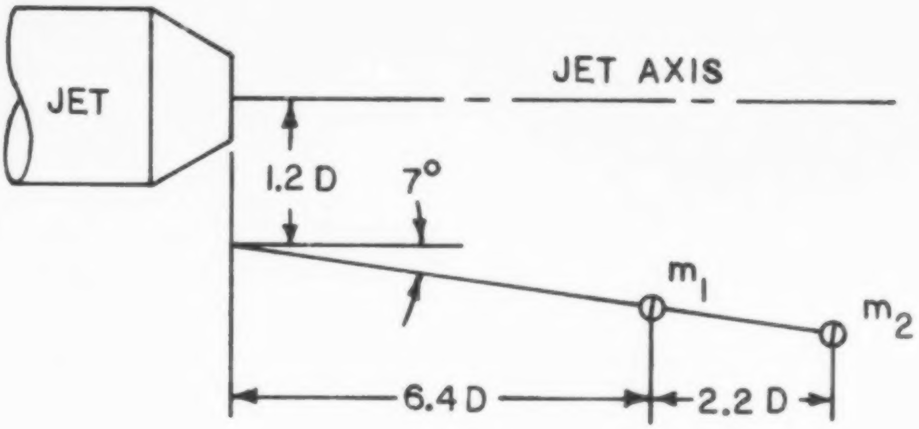
JET
JET AXIS
1.2 D
7°
m_1
m_2
6.4 D
2.2 D

FIG. 12: NEAR-FIELD COORDINATES

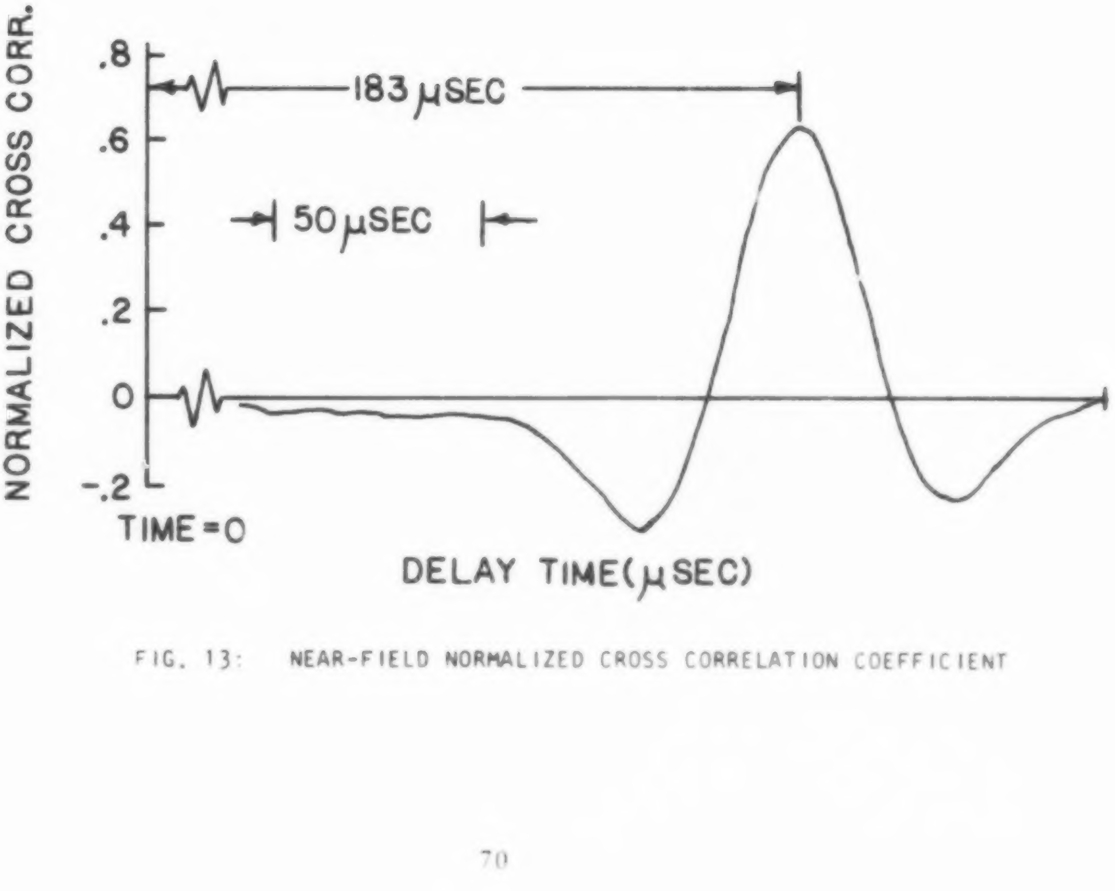

FIG. 13: NEAR-FIELD NORMALIZED CROSS CORRELATION COEFFICIENT

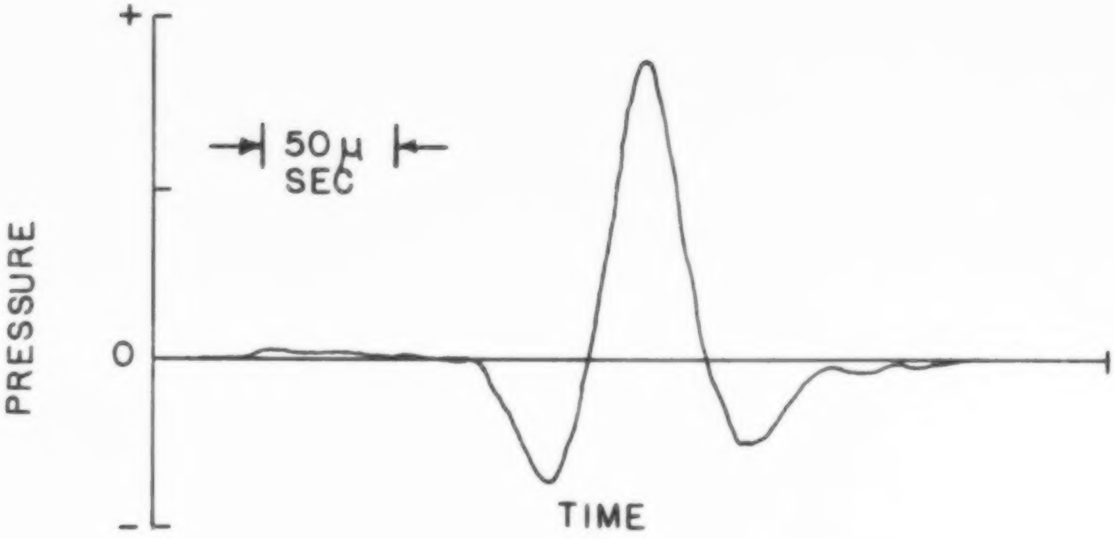

FIG. 14: CONDITIONALLY SAMPLED NEAR-FIELD PRESSURE SIGNAL

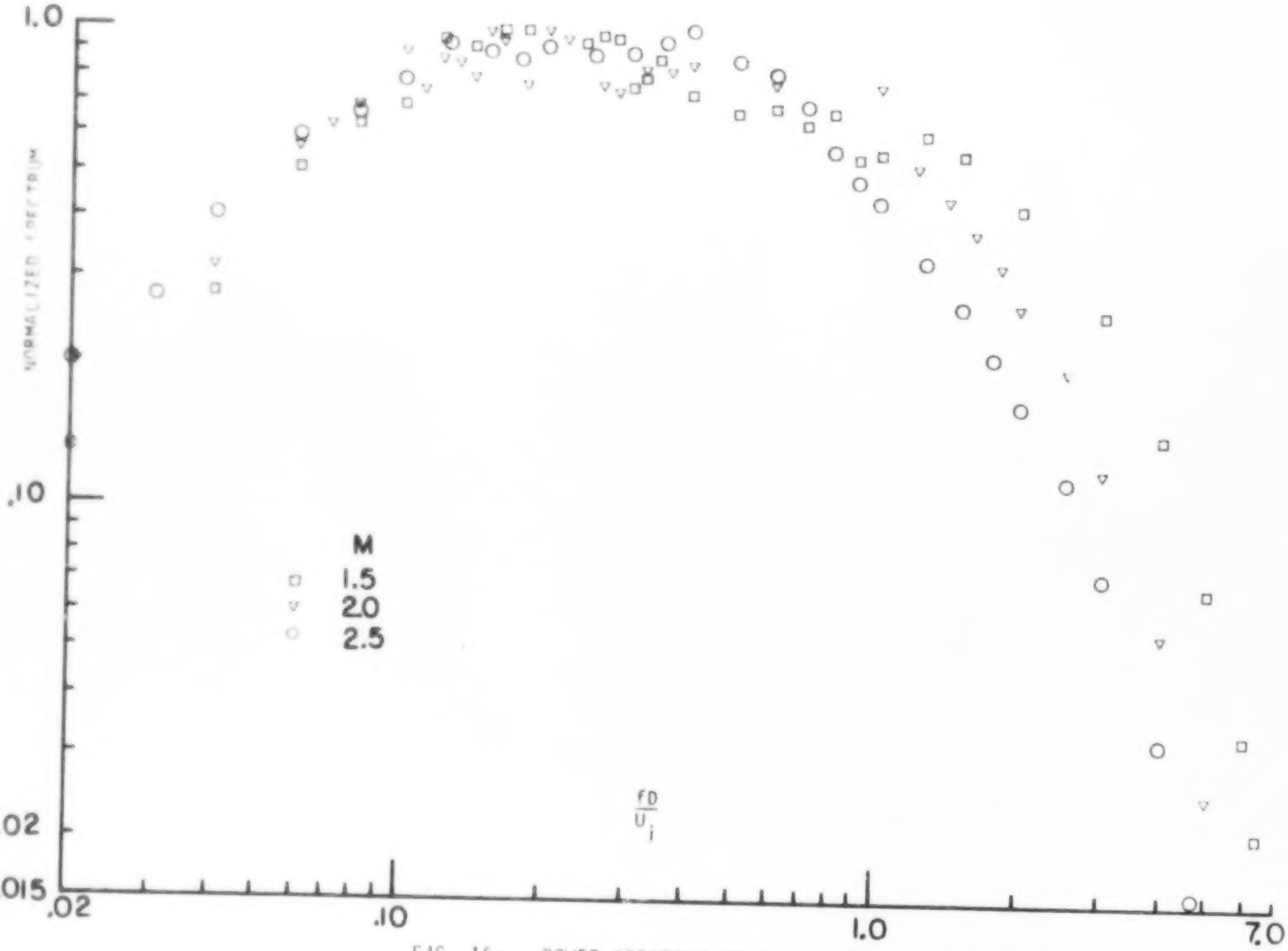

FIG. 15: POWER SPECTRUM OF A 1" SUPERSONIC JET AT 90°

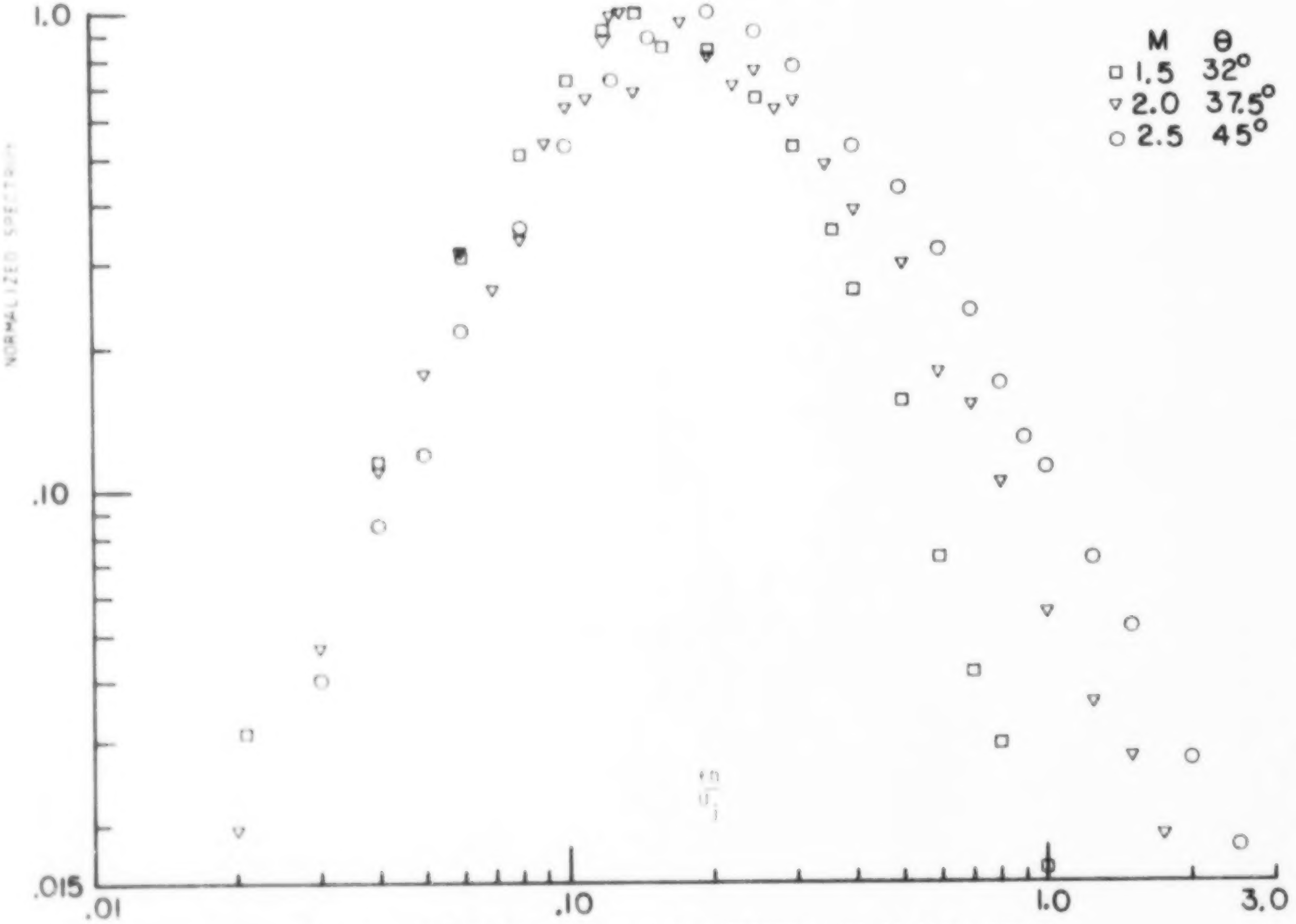

FIG. 16. POWER SPECTRUM OF A 1" SUPERSONIC JET AT ACUTE ANGLES

SOME OBSERVATIONS ON SOURCE DETECTION METHODS
WITH APPLICATION TO JET NOISE

by

Thomas E. Siddon

Associate Professor
Department of Mechanical Engineering
The University of British Columbia

ABSTRACT

A principal objective of this paper is to contrast several of the current "popular" methods of noise source detection, giving special emphasis to the author's experiences with causality correlation techniques. Some legitimate deficiencies of these methods, and a number of mis-construed criticisms, will be discussed. At the conclusion we briefly describe our plans for future investigations of basic noise suppression principles, using appropriate source detection methods.

1. INTRODUCTION

Research into the physical mechanisms of aerodynamic noise has, for more than two decades, focussed heavily on the fundamental behavior of isolated turbulent gas jets. Paradoxically, even after some twenty years of effort we do not understand the noise generating features of high velocity jets sufficiently well enough to effect a substantial change in the process. Recently our discussions have centered on three principal issues:

First, we have been concerned that *Lighthill's original theoretical model* for aerodynamic noise, posed in terms of equivalent stationary acoustic sources imbedded in a quiescent compressible medium is not adequate to predict the propagation properties associated with high velocity and/or high temperature jets. This has lead to a class of extended non-linear solutions to the wave equation such as those proposed by Lilley[1]. and Doak[2]., and to alternative means of linearly separating the effects of convection and refraction from the basic radiation process, as described by Ribner[3]. and Mani[4]..

Second, we have been encouraged to consider the possibility that the *process of turbulence* evolution (not just its "decay") plays an important role in the generation of aerodynamic noise. From the work of Crow and Champagne[5]., Michalke[6]., Laufer[7]., and Karamcheti[8]., we have seen how the amplification of coherent disturbances in the early shear layer may contribute to the generation of sound either directly, or perhaps indirectly through an almost catastrophic collapse of organized vorticity which appears to occur near the end of the potential core (in analogy to the "breaking" of waves on the seashore). Whether or not the organized structure itself is of major consequence to the noise of typical full-scale jets, at high Reynolds number and with "dirty" core flows, is yet to be demonstrated. Nevertheless we are being forced to reconsider our concept of what these "eddies" really look like, which have for so many years been described rather loosely as "roughly ellipsoidal volumes of coherent motion".

Third, there have been growing efforts, both on this continent and overseas to develop practical experimental methods for noise source localization and quantification. These methods have generally taken a physical, rather than a theoretical point of view; that all of the noise being generated by the turbulent jet is coming from somewhere and it should therefore be possible to measure by suitable means, the fractions of time average acoustic power (or intensity) which are "apparently" emitting from each unit volume of the turbulent region. A detailed account of progress along these lines is to be found in the Proceedings to two recent Specialists' Conferences on Aerodynamic Noise*.

Unfortunately, as in theoretical work the experimentalist must learn to walk, before he tries to run; our experiments must often be based on simplified approximate versions of the aerodynamic noise theory, expressed in terms of quantities which are readily measureable. If we are lucky these simplistic linear models, employing quasi-incompressible, inviscid and/or isentropic approximations, will lead to better results than we might have felt possible. Such has been the historical experience in regard to theoretical modeling in fluid mechanics (e.g., thin airfoil theory).

It is a thesis of this paper that the aforementioned areas of activity contribute to a triune of effort which is essential to our continued assault on the physical origins of jet noise. If the three schools can "cross-correlate" in a cooperative spirit, each will offer important benefits to the other two.

2. CRITERIA FOR SOURCE LOCATION METHODS

With the increased complexity of modern aircraft powerplants the traditional experimental method of "stand back and listen" is inadequate. We must develope means of locating and measuring the individual contributions which emanate naturally from each unit of volume or surface area associated with the source region. Otherwise, where several uncorrelated phenomena make roughly equal contributions to the total noise, we have no reliable means of determining whether we have suppressed or aggravated a given source contribution, in response to a local configuration change. Thus an ideal source detection method should possess the following characteristics:

i) Ability to measure the "apparent" acoustic emission, expressed as contribution to total acoustic power from unit volume (dW/dV) or contribution to radiated intensity per unit volume (dp^2/dV) in a given direction.

ii) Distributions of local source strength should stand the test of integral closure; that is, the distributions should integrate out to the correct total W or $\overline{p^2}$ for the entire source region.

---

* AGARD Noise Mechanisms Conference, Brussels, Belgium/ September 19-21, 1973.

AIAA Aero-Acoustics Conference, Seattle, Washington/ October 15-17, 1973.

iii) The measurement of local source strength should be effected with a high degree of spatial resolution. For example in studying the emission from a multi element suppressor nozzle where the streamwise extent of the source strength is not large compared with the cross sectional dimension, a method which can only estimate the streamwise source distribution will be of very limited value. For such a case, we will wish to obtain information about the relative emission from "shielding" and "shielded" flows, and the intervening regions of coalescence, as a function of entrainment velocity and nozzle spacing. Clearly we need a method which is suited to resolving source distributions over surfaces perpendicular to the mean motion, not just along its axis.

iv) The device or devices employed for source strength detection should not substantially disturb the source region, nor generate any additional noise.

v) It should be possible to modify the distributions of "apparent" emission strength to determine the "true" emission strength. The distinction here is subtle, resulting from the combined effects of source convection and refraction. Although the degree of this potential difficulty is so far unknown, it may not be a negligible effect for high velocity and/or high temperature flows.

The foregoing criteria have been implicit in most experimental attempts to decompose the source region into its constituent "parts". However at the present point in time, none of the known methods of source strength diagnosis satisfy the criteria adequately.

3. POPULAR METHODS OF SOURCE ANALYSIS

Of the various techniques of source location which have been tried, several are still under active consideration. These are outlined below:

3.1 Two-Point In-Flow Cross-Correlations

In theory, two point in-flow cross-correlations, with time delay τ and with probe separations $\underline{\xi}$ in all possible directions can be employed to predict, indirectly, the elementary source strength dp^2/dV [9]. Detectors can be either in-flow probes (hot wire or pressure probes) or non intrusive sensors which monitor velocity, pressure, density, and/or temperature fluctuations remotely. Currently such experiments are being attempted using laser velocimeters (General Electric and Lockheed Companies), a crossed beam densitometer (Damkevala, et al[10].) and focussed infra-red detectors (Belleval and Perulli[11].); in each case to monitor the source fluctuations at two points simultaneously. Each of these "remote" detection schemes suffers from growing pains relative to uncertainty about the quantitative nature of its response. For example, the crossed beam infra-red absorption technique of Damkevala, et al, measures coherence between two elongated (beam-wise) regions of volume, which is only an approximation of the desired two-point space time correlation. The infra-red emission detectors of Belleval and

Perulli give a signal which contain both temperature and density information, but in an uncertain mixture.

In practise, the two-point in-flow correlation methods entail an enormous number of measurements to yield each local value of dp^2/dV (e.g., see Chu[9] or Damkevala et al[10]). A further difficulty results from the necessity of determining a fourth order derivative $\partial^4/\partial\tau^4$ of the moving frame space-time correlation function, a complication which introduces considerable uncertainty into the end result. To this author's knowledge, integral closure has not been documented for the two-point in-flow method.

3.2 Physical Shielding of Source

Several experiments have been attempted where a rigid physical shield is used to block off portions of the source region from the far-field listening point. Perhaps the most publicized of these have been the hole-in-the-wall experiments first reported by Potter and Jones[12] and more recently by MacGregor and Simcox[13]. The technique features experimental simplicity, but is only capable of yielding a stream-wise estimate of the "slice-wise" source strength ($d\overline{p^2}/dy$ or dW/dy, depending on whether the measuring environment is anechoic, or reverberant). Information on transverse plane source distributions is lost. Furthermore there are still serious, unresolved questions about acoustic and aerodynamic interference between the edge of the hole and the developing jet; and on the importance of acoustic flanking through the hole at frequencies where λ is not small compared with the hole diameter.

3.3 Directional Detectors

These currently popular schemes, employing various forms of spherical and ellipsoidal collectors or equivalent summing microphone arrays, have been successessully demonstrated by Chu and Laufer[14], Grosche[15] and others. Such space filters are potentially quite powerful, and to date have been able to resolve the stream-wise source distribution ($d\overline{p^2}/dy$) in a sonic jet and to successfully achieve integral closure for that quantity. However, two notes of caution are in order:

First, these devices are essentially pressure summers; they will only achieve meaningful estimates of dp^2/dy if the beamwidth $\Delta\theta$ is small and if the collecting dish or array is several wavelengths and source dimensions removed from the source. If the collector is too close to the source so as to sum the pressure being radiated in many different angles, the output will be related to the emission from a finite focal volume, but this output will represent neither the characteristic power, nor the acoustic intensity from that volume. The reason is related to the fact that the sum of the squares p^2_i for many different ray paths does not equal the square of the sum $(\Sigma p_i)^2$. Furthermore there are some types of directional sources, for example a streamwise oriented dipole, which will give a summed output of zero, even though we know that a net acoustic power is being emitted.

Secondly, when the beamwidth of such devices is narrow, the depth of resolution is very large. The cross-sectional resolving dimension (often called a window function) is subject to a diffraction limit, on the order of one or more wavelengths. Thus since the characteristic wavelengths emitted by sonic and subsonic jets generally exceed one jet diameter, the streamwise resolution is rather smeared out, and radial resolution is not achievable.

3.4 Near Field Monitoring

Several methods of near field monitoring have been tried in the past. These usually employ measurements of p^2 in various octave bands as approximations to the true acoustic intensity flux $\overline{pu}$. Thus contours of apparent intensity flux are obtained for different frequency components of the near field pressure. Since a genuine acoustic wattmeter has not been used, such results are open to considerable debate.

Another class of near field experiments utilizes a rigid imaging plane, as described by Maestrello[16] or Rackl and Siddon[17]. By forming two-point pressure correlations on the rigid plane[16] or causality correlations with the far field sound[17] a footprint of apparent acoustic flux is produced, to be associated with the image jet behind the plane. Integral closure has been demonstrated for the total noise from the image jet[20]. These latter techniques suggest a compromise which may be quite useful when jets must be tested in close proximity to rigid ground planes.

Needless to say, the near field methods offer little potential for spatial resolution beyond the simple stream wise distribution of source strength and frequency.

4. CAUSALITY CORRELATION METHOD

The technique of "causality correlation" has been found extremely convenient for determining acoustic source distributions in noise generating flows and on adjacent surfaces[18-21]. The method bears a theoretical similarity with the classical two-point in flow correlation method of Sec. 3.1, but for one distinct difference. Instead of cross-correlating two points within the flow, only one point is required. The signal from this (cause) is cross correlated with the resulting far-field acoustic signal (effect). The answers come out in the form of source strength estimates $d\overline{p^2}/dV$ or $d\overline{p^2}/dS$ characteristic of each source detection point. Only one measurement is required to characterize each source point, as compared with perhaps one hundred or more by the classical two-point method. Also the data reduction is much more straightforward, since τ derivatives of lower order are involved (only $\partial/\partial\tau$ or $\partial^2/\partial\tau^2$).

4.1 The Basic "Causal" Relationships

The theoretical basis for the causal approach is now well documented. A solution integral for the far field radiated sound p(t) is multiplied on both sides by the same far field pressure signal p' evaluated at a slightly different time t'. Upon time averaging, we find the autocorrelation function for the net far field sound $\overline{pp'}(\tau)$ depending on integral distributions of several contributing causality functions:[19,21]

$$\overline{pp'}(\tau) = -\int_S \left[\frac{\partial}{\partial\tau}\left(\overline{\rho u_n p}c + \overline{p_s p}\mathrm{Cos}\,\theta\right)\right]_{\tau-\frac{x}{c}} \cdot \frac{dS(y)}{4\pi xc} + \int_V \left[\frac{\partial^2}{\partial\tau^2}\left(\overline{\rho u_x^2 p}\right)\right]_{\tau-\frac{x}{c}} \cdot \frac{dV(y)}{4\pi xc^2} \qquad (1)$$

Here, $\tau = t - t'$. The causality functions are, in fact, time delay correlations between local "effective sources" and the net far field sound. Typical functions appear as sketched below:

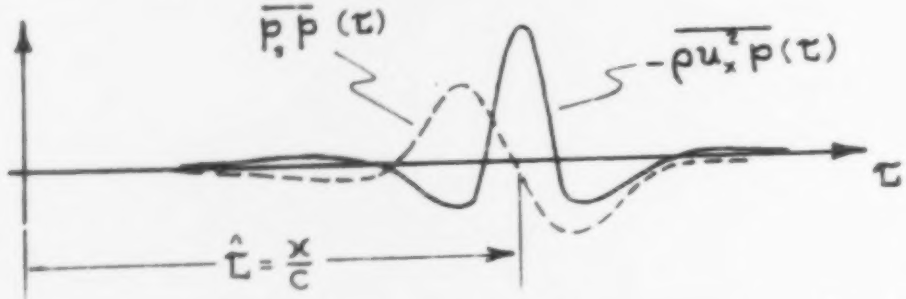

Note that these functions will have their largest magnitude (or slope, for certain choices of source variable) at or near the correct retarded time delay value for acoustic propagation from source to receiver. The acoustic contributions from each unit of source surface area or volume are determined explicitly by setting $t = t'$ ($\tau = 0$), giving the following "causality" relations:

$$\frac{d\overline{p^2}}{dS} = \frac{1}{4\pi xc}\left[\frac{\partial}{\partial\tau}\left(\overline{\rho u_n pc} + \overline{p_s p}\cos\theta\right)\right]_{\tau=x/c} \tag{2}$$

and

$$\frac{d\overline{p^2}}{dV} = \frac{1}{4\pi xc^2}\left[\frac{\partial^2}{\partial\tau^2}\left(\overline{\rho u_x{}^2 p}\right)\right]_{\tau=x/c} \tag{3}$$

A completely equivalent alternative form of (3) is obtained if one replaces ρu_x^2 with the source dilatation pressure $p^{(o)}$, following the approach of Ribner or Meecham and Ford[22,23] :

$$\frac{d\overline{p^2}}{dV} = \frac{-1}{4\pi xc^2}\left[\frac{\partial^2}{\partial\tau^2}\left(\overline{p^{(o)}p}\right)\right]_{\tau=x/c} \tag{4}$$

This alternative formulation, while experimentally more convenient, has come in for a good deal of undeserved criticism, an aspect to be considered more fully on later pages.

Other useful information may be extracted from the "shape" of the causality functions (1), including the local scales of coherence and spectra of the sound contribution from each point of source detection[18,19,20].

The success of the causality methods is directly dependent on the accuracy and confidence which can be assigned to our measurements of the various source fluctuations. In-flow detection of turbulence generated fluctuations such as $p^{(o)}$ or ρu_x^2 is fraught with difficulty. Nevertheless, it has been possible to produce approximate facsimiles of the source strength distribution in turbulent jets, on rigid airfoils and rotating fan blades[24]. For example, see the results of Rackl[20], depicted in Figure (1).

4.2 To Normalize or Not?

There is frequent confusion as to the significance of correlations between two points widely separated in space, one of which is purported to be a source. This confusion results partly from the widespread practise of normalizing the coherence, i.e., dividing by the individual root-mean-square values of the partner variables. Whereas the concept of normalized coherence may be of considerable value in establishing the direction and strength of energy flows in multi-path (reverberant) systems, its use can be seriously mis-leading in analyzing single path (source → receiver) situations.

For example as depicted in Figure 2 it is possible to get one-hundred percent correlation between two microphones, both of which are located in the acoustic far field of a small loudspeaker. This will result if the normalized cross-correlation is evaluated at the correct time delay for wave propagation from A to B. Of course neither microphone need be close to the source, so the process of normalization has produced a meaningless result. However if the surface motion of the loudspeaker, or the adjacent baffle, were correlated against microphone B with an appropriate time delay and if the correlation was evaluated without normalization as shown lowermost on Figure 2, a correct localization of the source would occur. In accordance with equations (1) and (2), integration of the cross-correlation value $[\overline{\rho \dot{u}_n p_B}]_{\hat{\tau}} = [-\partial/\partial\tau\,(\overline{\rho u_n p_B})]_{\hat{\tau}}$ will yield the total radiation $p^2{}_B$ from the speaker. For radiation directions not in the plane of the baffle a further contribution would be found by forming the correlations $\overline{p_s p}\mathrm{Cos}\theta$, according to Equation (2).

Similarily, in the more complex case of a turbulent jet, the correct distribution of source strength will only result if the raw (unnormalized) correlation is used. As in Figure 3, we consider a fixed microphone measuring p_B and a moving probe which measures p_A. As the probe begins to penetrate the intense, inertia-dominated pressure field of the turbulence, the maximum correlation $\overline{p_A p_B}_{\hat{\tau}}$ will rise sharply while the normalized correlation will correspondingly drop. Integration of source distribution profiles as shown in the lower part of the figure should lead to closure, and recovery of the total $p^2{}_B$ radiated by the entire complex array of turbulence sources. The use of normalized correlation as in the uppermost curve leads only to the mistaken conclusion that the jet noise sources are coherent over a substantially larger volume than the correlation lengths for the turbulence itself. We must remember that normalization may indeed demonstrate the extent of coherence in the pressure field, but it does not reveal the source of that coherent field.

For a fixed far field point it seems natural to conclude that the largest causality correlation, at correct time delay, will locate the region of greatest source strength. If a "source" probe is only near to this region of strong sources (say outside the turbulence interface, or the the potential core) the probe signal will be much weaker and the correlation may not "peak" at the correct time delay. Likewise the apparent source strength will be small, even though the normalized coherence may seem higher than it was in the active part of the flow.

4.3 The Numbers Game

Assuming an array of discrete, well separated, and uncorrelated sources, it has been an established practise to estimate the number of such uncorrelated sources from the inverse of the maximum coefficient of causality correlation, squared[22]. The appropriate relationships are given on Figure 4, for either surface or volume distributed sources (or both). However, recalling our findings of the previous section it should be apparent that a large value of normalized correlation is neither necessary, nor sufficient to identify a noise source, nor to draw conclusions about the number of such sources. Furthermore, the turbulent jet is not a distribution of spatially separated, uncorrelated sources. Several factors can lead to either an exaggeration of the number estimate (e.g., resulting from spurious, non-correlating noise on either channel) or a deficient estimate (resulting from band pass filtering of the signals or a correlatable contaminant in both signals)[21]. Such constraints apparently lead to wide variations in number estimates, as indicated by the data of Figure 7.

4.4 Negative Source Strength?

Occasionally, especially where periodic sources are dominant or some form of spatial symmetry exists, evaluation of the causality functions (2) or (3) leads to an apparent "negative source strength" for certain source point locations. This observation was initially puzzling since it had been felt that all contributions to dp^2/dV or dp^2/dS should be positive. In fact it has now been demonstrated that unequal, anti-phased motions of two adjacent sources emitting the same frequency will give an apparent negative source strength, when the weaker source disturbance is correlated with the far field sound[24]. This is because the stronger of the two sources controls the phase of the far-field radiation; the weaker tends to cancel some of the far field pressure, being anti-phase with the dominant disturbance. This effect has been clearly demonstrated with the aid of a simple dual loudspeaker apparatus having provision for driving the two speakers unevenly, and counterphase.

Our causality experiments with single round jets have shown no tendency for negative source strength, supporting the notion of a spatially random source distribution. At this point it is useful to stress the special virtue of the causality approach; the method singles out only that portion of the source fluctuation field responsible for some net contribution to the far field sound. Certain types of large scale source fields, for example arising from a "coherent vortex-like structure", may be internally self cancelling, so that no significant contribution is made to the far-field sound.

5. PRESSURE SOURCE MODEL FOR JET NOISE

The so-called dilatation model for jet noise, which has been variously ascribed to Ribner[22] and/or Meecham and Ford[23], separates the total pressure fluctuation into two parts $p = p^{(o)} + p^{(1)}$. In the source region the pseudosound $p^{(o)}$ (inertial in origin) is said to dominate over the acoustic fraction; the converse is true in the acoustic far field. This separation enables one to write the solution integral for the far-field acoustic pressure in terms of a distribution of equivalent dilatory sources confined to the noise generating region:

$$p^{(1)}_{(\underline{r},t)} = \frac{-1}{4\pi r c}\int_V \left[\frac{\partial^2 p^{(o)}}{\partial t^2}\right]_{\hat{t}} \cdot dV(y) \qquad (5)$$

Although this is now a widely accepted equivalent form to Lighthill's quadrupole model (both being restricted to "relatively" incompressible turbulence), there are persistent criticisms of its validity. Nonetheless, the work of Batchelor shows us that Ribner's key assumption:

$$\nabla^2 p^{(o)} = - \frac{\partial^2 (\rho u_i u_j)}{\partial x_i \partial x_j}$$

becomes exact in the incompressible limit.

If the inertial pressure $p^{(o)}$ can be shown to dominate in the source region, equation (5) leads directly to the convenient causality source strength relation (4). The dominance of $p^{(o)}$ can be confirmed by a simple experiment. If one plots the radial distribution of fluctuating pressure from the jet centerline outwards to large distance, one gets a picture as shown in Figure 5. If we assume for the moment that all of the acoustic power of the jet is radiated by one equivalent point source, then by extrapolation of the free-field line into the source region (dashed) we must conclude that the net acoustic pressure level of that one source will fall well below the overall jet pressure level, by 20 decibels or more, for most points within the turbulent region. Indeed if the total jet acoustic power is viewed as coming from a large number of uncorrelated sources, their individual acoustic fields will be even less significant with respect to the total jet pressure fluctuations. Thus the inertially induced pseudosound pressures may be viewed as a causative mechanism for a major portion of the far field sound.

All theoretical arguments aside, one could argue that the turbulent pressure fluctuation is a "natural" quantity to cross correlate against the far field sound. Where the unnormalized causality correlation is largest, it seems logical that we might expect the strongest sources. This should be a useful technique, at least to within engineering accuracy, but we must pay careful attention to two contaminating influences; First, the source detection probe may not register the true correct value of $p^{(o)}$, because of its interference with the turbulent flow. Secondly, the source probe may generate dipole sound due to the force fluctuations imposed by the interacting flow. These will be at the frequencies of the approaching turbulence and may radiate an additional correlatable sound to the far-field point.

As a consequence of these potential contaminants the causality correlation may contain two or more error terms:

$$\left[\overline{p_{ff}\, p^{(o)}}\right]_{\text{meas}} = \left[\overline{p_{ff}\, p^{(o)}}\right]_{\text{true}} + \left[\overline{p_{ff}\, p^{(o)}_{\text{error}}}\right]_{\text{probe error}} + \left[\overline{p_{ff_{\text{error}}}\, p^{(o)}_{\text{true}}}\right]_{\text{probe noise}} + \text{Cross term} \qquad (6)$$

The error terms must be adequately suppressed.

6. CONTAMINATION OF PRESSURE PROBE SIGNAL

It was once felt, by some, that reliable measurements of the fluctuating static pressure field of a turbulent jet would be virtually impossible, because of an inevitable error arising from interaction between the probe and the flow. However, recent research by the present author and others has shown that in certain cases the probe/flow interaction error can be suppressed considerably, using specially shaped probes which minimize sensitivity to incidence changes in the approaching flow, or probes which actively compensate for the interaction error in real time[20,25,26].

Of course one must ensure that the probe or measuring device is small compared with the smallest wavelengths of turbulence (corresponding to highest frequencies), if meaningful "point" measurements are to result. On the foregoing assumption, the flow past the probe can be regarded as locally quasi-steady; an empirical approximation yields estimates of the pressure errors arising from incidence and velocity changes in each of the three coordinate directions:[25]

$$p^{(o)}_{meas} - p^{(o)}_{true} = A\rho(2u\bar{U} + u^2) + B\rho(2u_r\bar{U}_r + u_r^2) + C\rho(2u_\theta\bar{U}_\theta + u_\theta^2) + D \qquad (7)$$

The fluctuating velocity components u, u_r, u_θ are in the streamwise, radial and tangential directions, respectively; likewise for the steady components $\bar{U}$, $\bar{U}_r$ and $\bar{U}_\theta$. This equation is reasonably valid in low speed flows, but corrections may be required where compressibility effects are strong.

The constants A, B, C, and D of equation 6 can be estimated from steady flow incidence calibrations. By careful control over the shape of the probe it is possible to reduce these constants to a point where the error makes a minimal contribution to the pressure reading. For example, given a cylindrical static pressure probe aligned with the jet axis, and assuming the coefficient A has been made very small, with B and C taking values of about -1/3, we can write:[25]

$$p^{(o)}_m - p^{(o)}_t = -1/3\rho\,(u_r^2 + u_\theta^2 - \overline{u_r^2} - \overline{u_\theta^2}) \qquad (8)$$

While it is true that errors of the above order may approach the theoretical "true" pressure fluctuations in isotropic turbulence ($p' = \frac{1}{2}\rho u'^2$), the pressure fluctuations characterizing the shear layers of turbulent jets are now known to be much larger, and seem to vary like $\rho u\bar{U}$. Thus, as depicted in Figure 6, the rms pressure error is expected to be on the order of 25% of the total observed pressure, or less, everywhere in the shear layer. Specially shaped probes, such as the tongue-shaped configuration of Rackl[20], appear to do even better.

Of further significance to causality correlation experiments is the observation that certain of the error terms on the right hand side of (6) will not correlate with the radiated sound, if one introduces arguments based on symmetry and normality of probability functions. Thus if the field microphone is in the plane of r, the u_θ term will not correlate. This sort of consideration deserves further investigation.

7. CONTAMINANT TO FAR FIELD SOUND

As illustrated in Figure 6, Rackl's tongue-shaped pressure probe substantially reduced the errors in $p^{(o)}$ caused by quasi-steady incidence variations and velocity modulations in the plane of the foil $(M_o=0.3)^{20}$. Also the broad multi-crested causality correlation which had been observed with a conventional cylindrical probe was replaced by a relatively smooth bell-shaped curve (Fig. 1.). The broadening was found to arise from spurious dipole radiation due to unsteady flow interactions with the nose and stem of the probe[21] (see Fig. 7). Note that the interactions occur with all characteristic frequencies of the turbulence spectrum, not merely the vortex shedding frequencies for the probe. Thus they contribute a correlatable contaminant to the far field pressure which is difficult to separate from the authentic sound generated by the adjacent turbulence. It was expected that a foil shaped probe which offered minimium surface area in the direction of far-field radiation would reduce the dipole contaminant substantially. However, on integrating his source distribution function dp^2/dV over the entire jet (Fig. 1), Rackl obtained a value for total p^2 which was about 8 times larger than the direct measured sound level at 45 degrees to the jet axis. This lead to the conclusion that the causality correlations $p^{(o)}p(\ )$ were much too large, probably because of an unsteady "drag" dipole radiation arising from streamwise buffeting of the probe supporting stem, by the approaching turbulent flow.

The noise coming from a lift, side force, or drag-producing surface imbedded in the flow can be estimated by a compact dipole model giving:

$$\overline{p^2}_{\text{drag dipole}} = \frac{\cos^2\theta}{(4\pi x c)^2}\overline{\left[\frac{dF}{dt}\right]^2} = \left[\frac{\rho\omega S_c \cos\theta}{4\pi x}\right]^2 M^2 C_D^2 \overline{u^2} \qquad (9)$$

Here M is the local Mach no., ω is a characteristic frequency, C_D is the quasi-steady drag coefficient, and S_c is the effective coherence area of the force distribution. A similar equation for lift or side force noise will result if C_D is replaced by $C_L/4$, and u^2 by v^2. The noise coming from an adjacent correlated volume element of the turbulence (V_c) is:

$$\overline{p^2_{V_c}} = \frac{V_c^2}{(4\pi x c^2)^2}\overline{\left[\frac{d^2(\rho u_x^2)}{dt^2}\right]^2} = \left[\frac{\rho\omega^2 V_c}{4\pi x}\right]^2 \cdot M^4 \cdot \left(\frac{\overline{u_x^2}}{U^2}\right)^2 \qquad (10)$$

The contamination effect is conveniently described by a probe contamination ratio PCR. For a drag fluctuation:

$$PCR = \frac{\overline{p^2}_{\text{dipole}}}{\overline{p^2_{V_c}}} = \left[\frac{C_D U S_c \cos\theta}{\omega V_c M}\right]^2 \cdot \left(\frac{\overline{u^2}}{U^2}\right)^{-1} \qquad (11)$$

Thus for a probe of diameter d in a round turbulent jet of diameter D, equation (11) yields, at x/D ≈ 4:

$$PCR_{\text{drag}} \approx 40\left(\frac{d}{D}\right)^2 \cdot \frac{1}{M^2_{\text{loc}}} \quad \text{also,} \quad PCR_{\text{sideforce}} \approx 80\left(\frac{d}{D}\right)^2 \cdot \frac{1}{M^2_{\text{loc}}} \qquad (12)$$

A 1/8 inch diameter probe stem in a jet of 1½ inch nozzle diameter operating at $M_o=.3$ will have a $PCR_{\text{drag}} \approx 8.5$, but at $M_o=1$ the PCR will reduce to only about 0.8. The dipole nature of the contaminant noise obviously works to advantage at higher Mach numbers. For accurate measurement of causality correlations it is essential that the probe radiation be much weaker then the inherent self-radiation from an adjacent correlation volume V . Since evidence seems to suggest a highly uncorrelated structure for the basic noise generators in subsonic jets, it is insufficient to disregard probe interference noise merely on the basis of little observed change in the far field level, when the probe is inserted.

8. CONCLUSIONS AND OUTLINE OF FUTURE WORK

Our ultimate objective is to contribute to the resolution of fundamental jet noise suppression mechanisms, and their inherent limitations, for multi-element suppressor nozzles. Unlike some experimental methods which measure only the integrated streamwise source distribution, causality correlation techniques are also suited to determining the source strength profiles in directions transverse to the mean motion. While these methods appear to produce results to an adequate degree of engineering approximation, there are a number of unresolved features which demand further exploration. For example we can perhaps reduce the drag dipole contamination by going to an air foil-shaped probe stem, with much lower C_D. We will further investigate the possibility of designing a truly error-free pressure probe, by finding ways to "zero" the coefficients of equation (7) in the sense that they are more independent of Mach number and turbulence spectrum. We plan to make measurements of the sensitivity of causality correlations to probe generated noise by testing identical probes of various sizes in a single jet. We are looking more fully into questions of source convection, and refraction, as they effect the time of arrival of the causality "signature". Consequences of multiple path propagation between source and receiver (especially as applies to shielded or enclosed sources) are also under study.

In parallel with the above work we are preparing to experiment with a laser-shadograph source detection scheme, as a substitute for a physical pressure probe in the flow. We expect also to employ a far-field ellipsoidal microphone system as an independent check on probe generated noise, and to test for integral closure of the measured source distributions.

These studies are all essential prerequisites to our main task, which is to experimentally distinguish between relative emission strength of "shielding" and "shielded" jets, and the intervening regions of coalescense, for multi element suppressor nozzles. In this way we should learn more about the influence of entrainment velocity and nozzle spacing on overall noise suppression. In a companion experiment the role of edge noise generated at the nozzle lips is being assessed by causality correlation, using the surface pressure p_s as the "source" fluctuation. Thus we intend to examine the possibility that lip generated noise imposes a lower limit on the noise reduction capability of highly segmented nozzles.

ACKNOWLEDGEMENT

The completed work described herein has been funded largely by the National Research Council of Canada, under Grant No. A-7106 and the Defense Research Board of Canada, under Grant No. 9611-03. Major portions of the ongoing work, concerning the validation of source location techniques and their application to suppressor nozzle studies are conducted under sub-contract to GE/DOT-OS-30034. The assistance of the United States DOT is gratefully appreciated.

REFERENCES

1. LILLEY, G.M. - On the Noise From Jets, Proceedings of AGARD Conference on "Noise Mechanisms", September 1973, AGARD-CPP131, pp. 13-1 - 13-11.
2. DOAK, P.E. - The Momentum Potential Field Description of Fluctuating Fluid Motion as a Basis of Unified Theory of Internally Generated Sound, AIAA Aero-Acoustics Specialists Conference, October 1973.
3. RIBNER, H.S. - Convection and Refraction in Jet Noise, presented at 86 Meeting of Acoust. Soc. of Amer., Los Angeles, Oct. 1973.
4. MANI, R. - The Issue of Convective Amplification in Jet Noise, Proceedings of AGARD Conf. on "Noise Mechanisms", Sept. 1973, AGARD-CPP131, pp. 10-1 - 12.
5. CROW, S.C. and CHAMPAGNE, F.H. - Orderly Structure in Jet Turbulence, J. Fluid Mech. V. 48, p. 547, 1971.
6. MICHALKE, A. - A Wave Model For Sound Generation in Circular Jets, 1970, Deutsche Luft-und Raumfahrt, FB 70-57.
7. LAUFER, J., et al - On the Generation of Jet Noise, Proceedings of AGARD Conf. on "Noise Mechanisms", Sept. 1973, AGARD-CPP131, pp. 21-1 - 21-6.
8. KARAMCHETI, K. - On the Amplification of Disturbances in Developing Shear Layers, Unscheduled presentation at AGARD Conference on "Noise Mechanisms".
9. CHU, W.T. - Turbulence Measurements Relevant to Jet Noise, UTIAS Report 119, 1966.
10. DAMKEVALA, R.J. et al - Sound Source Measurement in Air Jets Using The Crossed Beam Correlation Technique, AGARD Conf., Sept 1973, AGARD-CPP131.
11. DE BELLEVAL, J.F. et al - Representation de la Turbulence d'un Jet Chaud a Partir de Son Emission Infrarouge, AGARD Conf., Sept 1973, AGARD-CPP131.
12. POTTER, R.C., JONES, J.H. - An Experiment to Locate the Acoustic Sources in a High Speed Jet Exhaust Stream, Abstract, 74th Meeting of the Acoust. Soc. Am., [illegible], 1967.
13. MACGREGOR, [illegible] E. - The Location of Acoustic Sources in Jet Flows by Means of the "Wall Isolation" Technique, AIAA Conference, Seattle, October, 1973.
14. CHU, W.T. et al - Noise Source Distribution in Subsonic Jets, Inter-Noise 72 Proceedings, Washington D.C., Oct. 4 - 6, 1972.
15. GROSCHE, F.R. - Distributions of Sound Source Intensities in Subsonic and Supersonic Jets, AGARD Conf., Sept. 1973, AGARD-CPP131, pp. 4-1 - 4-10
16. MAESTRELLO, L. & McDAID, E. - Acoustic Characteristics of a High Subsonic Jet, AIAA Paper No. 70-234, Jan. 1970.
17. RACKL, R. & SIDDON, T.E. - Jet Noise Study Using Image Technique, CANCAM 1971, Calgary, Proceedings p. 473.
18. SIDDON, T.E. - New Correlation Method for Study of Flow Noise, Proc. of 7th Int'l Congress of Acoustics, Budapest, August 1971, pp. 533-536.
19. SIDDON, T.E. - Surface Dipole Strength by Cross Correlation Method, JASA Vol. 53 No. 2 pp. 619-633, Feb. 1973, also abstracted JASA July 1970.
20. RACKL, R. - Two Causality Correlation Techniques Applied to Jet Noise, Ph. D. Thesis, Univ. of British Columbia, Canada, April, 1973.
21. SIDDON, T.E. - Noise Source Diagnostics Using Causality Correlations, Proc. AGARD Conf. on "Noise Mechanisms", Sept 1973, AGARD-CPP131, pp. 7-1 - 7-12.
22. RIBNER, H.S. - Aerodynamic Sound From Fluid Dilatations, Univ. of Toronto, Inst. of Aerophysics Rep. No. 86, July 1962. Also AFOSR TN 3430.
23. MEECHAM, W.C. & FORD, G.W. - Acoustic Radiation from Isotropic Turbulence, J. Acoust. Soc. Am. 30(4), pp. 318-322, April 1958.
24. LEGGAT, L.J. - Measurement of Dipole Source Distributions on Components of an Axial Flow Fan, presented Acoust. Soc. Am. Mtg, Los Angeles, 1973.
25. SIDDON, T.E. - On the Response of Pressure Measuring Instrumentation in Unsteady Flow, University of Toronto, UTIAS Report 136 (Jan. 1969).
26. WILLMARTH, W.W. - Unsteady Force and Pressure Measurements, Annual Review of Fluid Mechanics 1971, pp. 147-170.

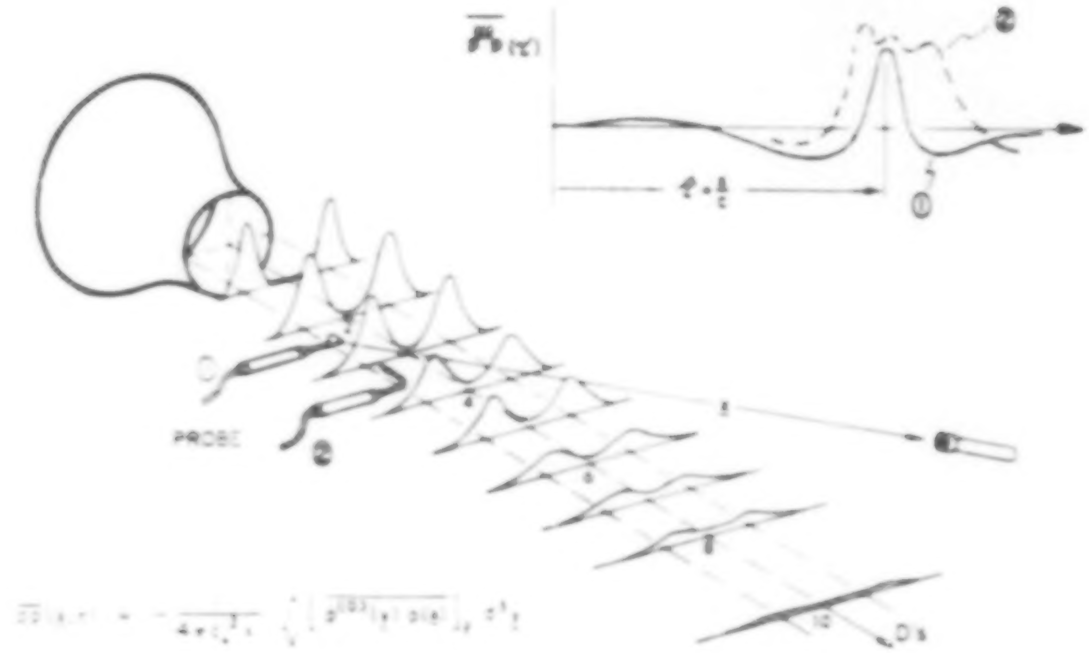

FIGURE 1 - METHOD OF NOISE SOURCE ANALYSIS BY CAUSALITY CORRELATION (After Rackl[20])

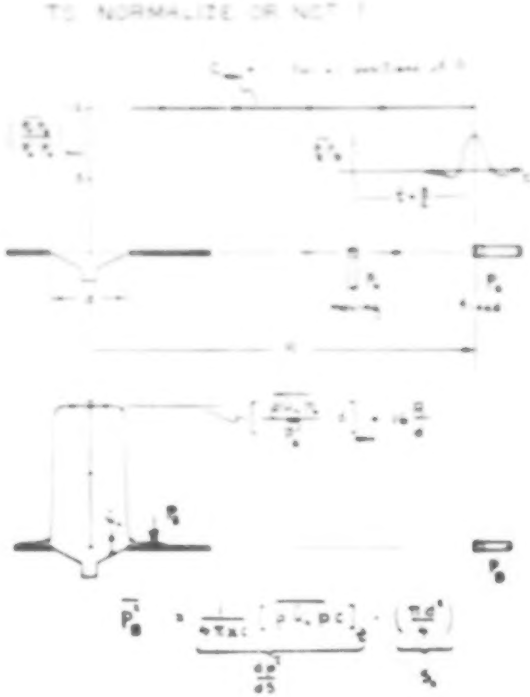
TO NORMALIZE OR NOT ?

FIGURE 2 - PROFILES FOR SINGLE LOUDSPEAKER (Broad Band Input)

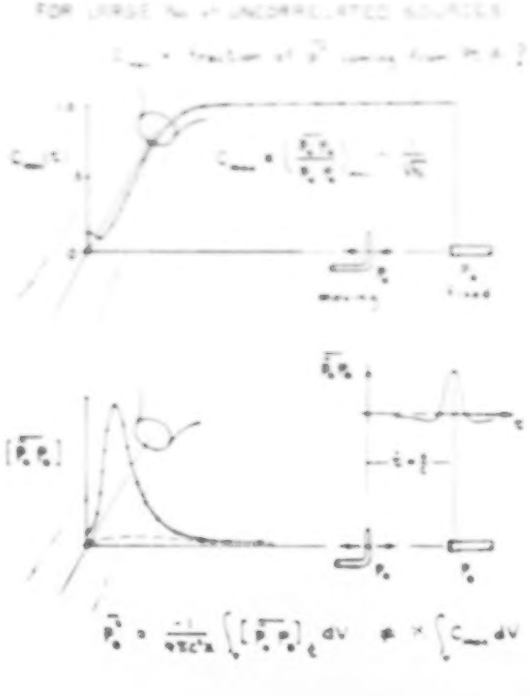
FOR LARGE N → UNCORRELATED SOURCES

FIGURE 3 - PROFILES FOR TURBULENT JET

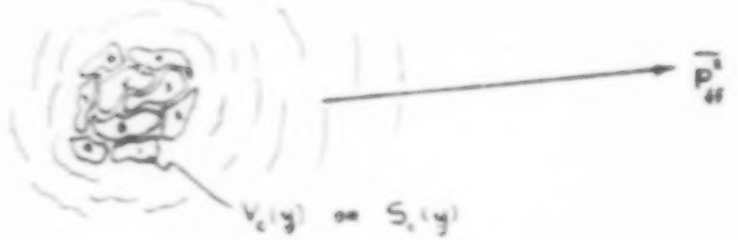

$$\overline{p^2_{ff}} = \sum_{m=1}^{M}\left(\frac{d\overline{p^2}}{dS}\cdot S_i\right)_m + \sum_{n=1}^{N}\left(\frac{d\overline{p^2}}{dV}\cdot V_i\right)_n$$

CAN SHOW THAT

$$\frac{\left(\frac{d\overline{p^2}}{dV}\cdot V_i\right)_n}{\overline{p^2_{ff}}} = \frac{\left[\overline{p^{i*}\, p_{ff}}\right]^2_t}{\overline{p^2_{ff}}\ \overline{p^{i2}}} = C^2_{max}(t)$$

IF ALL N OR M SOURCES HAVE EQUAL STRENGTH

$$C^2_{max} = \frac{V_i}{V_{total}} = \frac{1}{N} \text{ or } \frac{1}{M}$$

FIGURE 4 - ARRAYS OF DISCRETE SOURCES

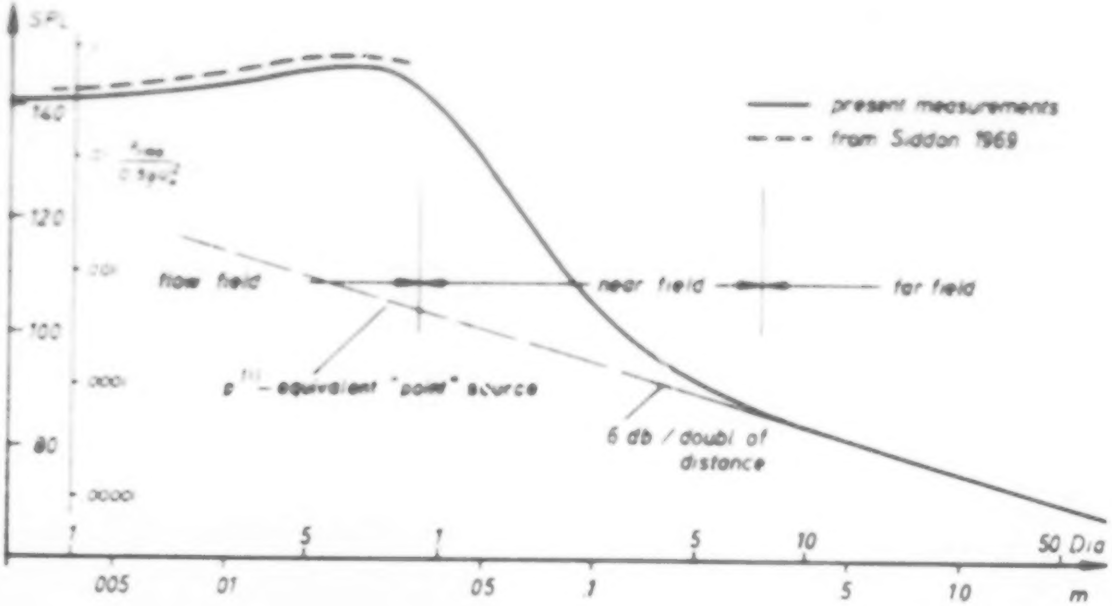

FIGURE 5 - VARIATION OF PRESSURE FLUCTUATION WITH DISTANCE FROM A 38 MM JET, STARTING AT 4 DIAMETERS DOWNSTREAM IN THE JET AND PROCEEDING AT RIGHT ANGLES TO THE JET AXIS

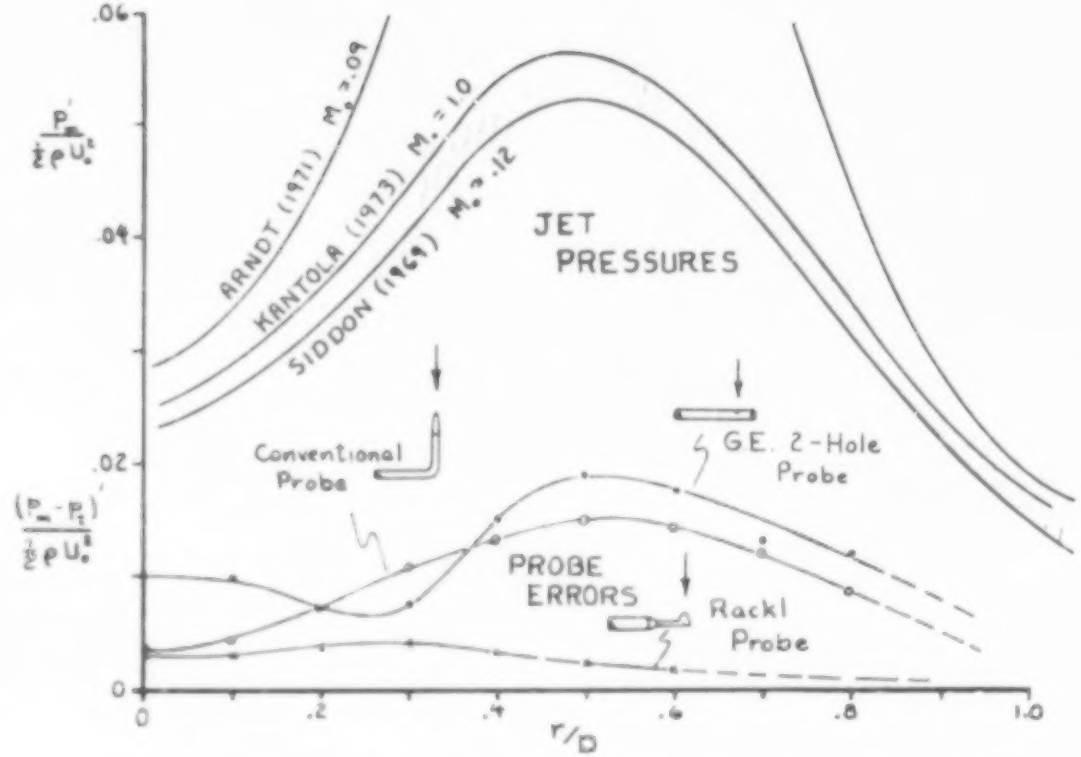

FIGURE 6 - PROFILES OF RMS PRESSURE FLUCTUATION AND ESTIMATED PROBE ERRORS IN ROUND TURBULENT JETS x/D = 4.5

PROBE CONTAMINATION RATIO

$$\mathrm{PCR}_{\mathrm{drag}} \equiv \frac{\overline{p^2_{sp}}}{\overline{p^2_{v_c}}} \simeq \frac{40}{M^2_{\mathrm{loc}}}\left(\frac{d}{D}\right)^2$$

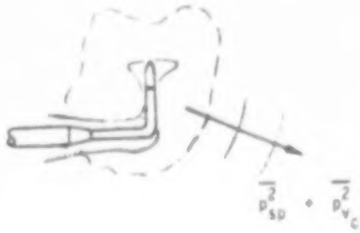

COHERENCE OF FUNDAMENTAL RADIATORS (Jet Noise)

$$N \cong \left(\frac{V}{V_c}\right) \cong \frac{1}{C^2_{\mathrm{max}}} = \left(\frac{\overline{\ddot{p}^{(0)\prime}\,p'}}{\overline{\ddot{p}^{(0)}\,p}}\right)^2$$

	Mach. No.	Source fluct'n	N	PCR
Lee-Ribner (1971)	0.3	turb. velocity	~ 2500	unknown
Rackl-Siddon (1972)	0.3	jet pressure	> 150	~ 8 (drag dipole?)
Scharton-White (1972)	~ 1	jet pressure	~ 3 (filtered)	~ 4
Meecham-Hurdle (1973)	~ 1	near field press.	40 → 60,000 ?	unknown

FIGURE 7 - PROBE RADIATED NOISE CONTAMINATES CROSS CORRELATION FUNCTIONS

MEASUREMENT OF THE AXIAL VARIATION OF THE SOURCE STRENGTH INTENSITY IN AN AXISYMMETRIC SUBSONIC JET

by

Gerhard Reethof and John M. Seiner

Noise Control Laboratory
The Pennsylvania State University
University Park, Pennsylvania

Abstract

This research deals with the experimental evaluation of the jet source strength intensity per unit length of jet. The direct correlation technique of Lee and Ribner(1) was employed to produce the desired evaluation. The radiated acoustic intensity is expressed in terms of an integral over the source region of a far field pressure-source field velocity coherence function. Substantial improvement in the implementation of this technique was achieved by use of a polarity-coincidence detector and two phase matched bandpass 4-pole Butterworth filters. The results are given in terms of shear and self-noise components for six reduced filter center frequencies $0.1 \leq f_o^* = f_o D/U_j \leq 3.2$ For the emission angle of $\psi = 30°$, peak acoustic emission for the 2 in. diameter nozzle was found to occur at $f_o^* = 0.36$ at an exit Mach number of 0.33. The results indicate that peak acoustic emission can be associated with the transition region of the jet flow. The radial distribution of the shear noise component suggests that advection of turbulent v' kinetic energy from the fully turbulent region of the shear layer produces maximum coherence along the axis of symmetry. It is proposed that the centerline value of the shear noise component serves as an adequate estimate for acoustic emission per unit slice of shear layer.

Introduction

The objective of this work has been the experimental evaluation of the source strength intensity per unit axial length of subsonic jet. A direct correlation technique, which simultaneously relates the flow and acoustic far field time domains, has been employed for this purpose. Within the general framework of our effort in the jet noise field, this information was needed to assist in estimating the effectiveness of converting turbulent kinetic energy to magnetic field fluctuations.

Since the time this investigation was undertaken, a number of fine research works relating to estimating the sound power distribution in subsonic jets have appeared in the literature. See for example the works of Lee and Ribner(1), Maestrello(2), and Rackl(3). Except for the work of Lee and Ribner, the methods used by Maestrello and Rackl to estimate the sound power distribution differs considerably from the method adopted in this investigation. The technique employed by Maestrello consists essentially of measuring the acoustic energy density flux along the boundary of a jet, and then solving the Newmann problem for the far field acoustic intensity using the measured distribution of the pressure gradient. The method used by Rackl consists of correlating the far field acoustic pressure with the surface pressure of a rigid plate located along the jet boundary. Source location is then obtained using the ray acoustics reflection principle. The results of Maestrello and Rackl concerning the sound power distribution per unit jet length are essentially in agreement with the results of this investigation.

The experimental technique used in the present investigation differs from that used by Lee and Ribner in two important respects. First, the required correlation computations are made using a polarity-coincidence detector, rather than an ordinary correlator. Wolff, Thomas, and Williams(4) have shown that such a detector is superior to an ordinary correlator when subjected to non-Gaussian inputs. For fixed input distributions, the probability of detection with this device is a nondecreasing function of the signal to noise ratio. This is a particularly important feature, for in subsonic jet flow measurements the direct correlation technique rarely admits covariance amplitudes exceeding a value of 0.1. Such small covariance amplitudes require filtering the input signals to again improve on the dynamic range of the measured covariance.

The selection of the filter bandwidth enters as an important parameter, since the bandwidth serves to determine the required averaging time for measurement within a certain desired accuracy. For example, if the random functions are normally distributed and covariance stationary, then detection of a covariance amplitude of 0.01 requires an averaging time of

$$T = 2\pi\ (\sqrt{2}B\rho^2\varepsilon^2)^{-1} = (\pi\sqrt{2}/B) \times 10^6$$

seconds to achieve a relative accuracy of ten percent. Here B, ρ, and ε respectively represent the filter bandwidth, covariance amplitude, and relative error.

In the present investigation two phase matched bandpass 4-pole Butterworth filters are used with octave wide bandwidth settings. Since the normalized bandwidth of such a filter is 0.707, the required averaging time is tempered by a factor of order 10 over that of a narrow band filter with a normalized bandwidth of 0.06. In addition to this feature, it is easily shown that when the normalized bandwidth exceeds 0.3 the first zero crossing of the envelope becomes comparable to that of the high frequency carrier, and a well defined (sin x)/x distribution is obtained for the covariance function.

Lee and Ribner confined their measurements to the first seven jet diameters, and performed measurements around the periphery of the jet in the central turbulent zone at one nozzle radius. At this nozzle radius the coherence amplitude is typically 0.01. The results of this investigation show that the coherence amplitude increases exponentially as the jet centerline is approached radially from the central turbulent zone. Along the jet centerline and in the potential core turbulence production is negligible, and one can additionally assume that the sound production in these regions of the flow is also small. Since maximum coherence is obtained along the axis of symmetry, axisymmetric advection of turbulent kinetic energy from the fully turbulent regions of the flow, where turbulence production is maximum, appears as a probable source for this observation. In this sense the measurements, which are presented at this time, are only of a preliminary nature. Nevertheless, the current measurements do indicate that the measured value of the coherence at a single point do not necessarily reproduce the source strength intensity for that point alone.

Along the centerline of the flow the coherence amplitude is typically 2π times larger than those values measured at $r/r_o = 1.0$. Thus for a fixed averaging time, the relative error obtained along the centerline is $(2\pi)^2$ times smaller than that obtained at $r/r_o = 1$. Therefore, an effort to qualify the meaning to be attached to the centerline values of coherence is important from the standpoint of improved relative accuracy in measurement of the source strength intensity.

The Direct Correlation Method

The mathematical development used to implement the direct correlation technique can be found either in Seiner and Reethof(5) or Lee and Ribner(1). Basically the approach functions well under the limiting assumptions of high Reynolds', low Mach number isothermal free jet flows. In this way the effects of thermal conductivity and viscosity are considered negligible. The radiated acoustic pressure can then be expressed in Proudman form, after contraction of the resulting stress tensor T_{ij}. Assuming to the first order that the gas flow dynamics are incompressible, the radiated acoustic intensity can be expressed using Lighthill's(6) integral equation as,

$$I(\underline{x}) = (\rho_o a_o)^{-1} \langle [P_s(\underline{x},t)]^2 \rangle$$

$$= (4\pi\rho_o a_o{}^3)^{-1} \int_{v^1} \partial^2/\partial\tau^2 \left[R_{P_s T_{rr}}(\underline{x}, \underline{x}';\tau)\right] \Big|_{\tau = r/a_o} d\underline{x}' \qquad (1)$$

where $R_{P_s T_{rr}} = \langle P_s(\underline{x},t)\ \partial^2\ T^0{}_{rr}(\underline{x}',t + \tau)/\partial(t + \tau)^2 \rangle \qquad (2)$

Figure 1 details the coordinate system used to define the variables used in equations 1 and 2. Ribner(7) Reynolds' decomposed the stress tensor $T_{r^0 r}$ to obtain the following components with intrinsic time variations,

$$T^0{}_{rr} = \rho_o v_r{}^2 = \rho_o\ [U_r + u_r]^2 = \rho_o\ [2U_r u_r + u_r{}^2] \qquad (3)$$

He denoted the first term of equation 3 as the shear noise component, and the second as the self noise component. Due to the self-noise component's quadratic dependence upon the turbulent velocity component, the self-noise component is composed of turbulent frequencies that are an octave lower than those turbulent frequencies which produce the shear-noise component.

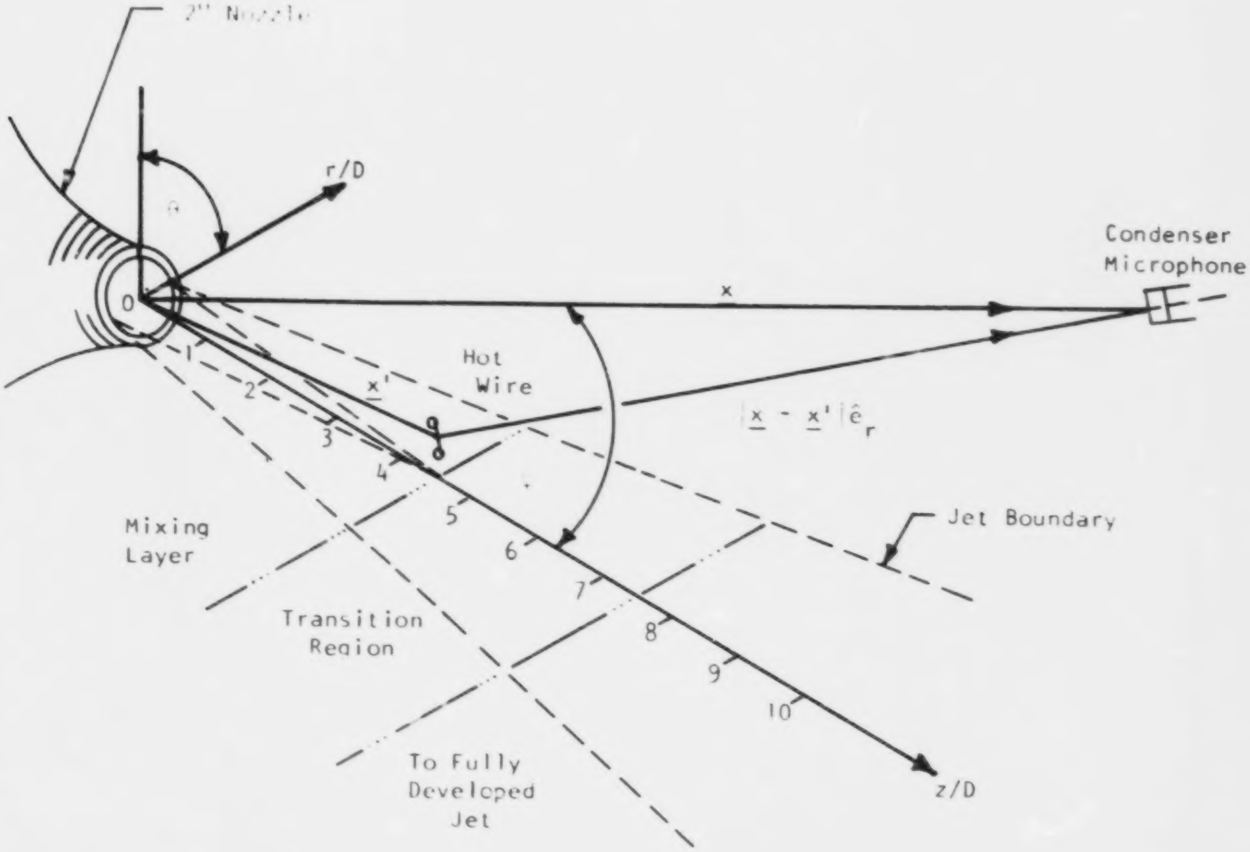
2" Nozzle
θ
r/D
0
x
Condenser
Microphone
Hot
Wire
x'
|x - x'|ê_r
Jet Boundary
1
2
3
4
5
6
7
8
9
10
z/D
Mixing
Layer
Transition
Region
To Fully
Developed
Jet

Figure 1 Coordinate System

To relieve the problem of estimating the second derivative on the required cross-correlation $R_{P_s T_{rr}}$, and at the same time improve on the signal to noise ratio in the detection of $R_{P_s T_{rr}}$, the derivative property of a real linear filter system can be utilized. Seiner and Reethof$^{(5)}$ have calculated the following filter relation for a pair of phase matched bandpass 4-pole Butterworth filters,

$$\partial^2 R_{P_s T_{rr}}(\underline{x},\underline{x}';\tau)/\partial\tau^2 = -\frac{2}{A}\int_0^{+\infty} \omega_o R_{P_s T_{rr}}(\underline{x},\underline{x}';\tau,\omega_o)\,d\omega_o \qquad (4)$$

where ω_o represents the filter radian center frequency and $A = 3\pi B/4$. The normalized bandwidth B has a value of $\sqrt{2}/2$ for octave bandwidth selections.

Nondimensionalizing equation 1 by the Lighthill parameter for acoustic intensity $L = \rho_o U_j{}^8 D^2/a_o{}^5 R^2$, and substitution of relations 3 and 4 into equation 1 produces the following useful definitions,

$$I(\underline{x})/L = \int_{V'}\int_0^{+\infty} (\eta_{shear} + \eta_{self})\, d\omega_o{}^* \, d\underline{x}' \qquad (5)$$

$$\text{where } \eta_{shear} = 2K\, U_r\, \tilde{P}_s\, \tilde{u}_r \left[-\rho_{P_s u_r}(\underline{x}^*,\underline{x}'^*;\ \tau,\ \omega_o{}^*)\right]\Big|_{\tau = r/a_o} \qquad (6)$$

$$\eta_{self} = K\, \tilde{P}_s \tilde{u}_r{}^2 \left[-\rho_{P_s u_r{}^2}(\underline{x}^*,\underline{x}'^*;\ \tau,\ \omega_o{}^*)\right]\Big|_{\tau = r/a_o} \qquad (7)$$

$$K = \frac{DR^{*2}}{2\pi AB\rho_o a_o{}^5 M_j{}^7 r^*} \qquad (8)$$

In the above relations ρ_{xy} represents the filtered cross covariance function and $\tilde{f}$ denotes the RMS value. It is of importance to note that the integrand of equation 5 does not depend upon the local value of the coherence, but rather it represents a percentage of the total contribution to the radiated acoustic intensity. This is necessary for one encounters regions of the flow with a high coherence and low fluctuation level. The covariance functions $\rho_{P_s u_r}, \rho_{P_s u_r{}^2}$ appearing in relations 6 and 7 are experimentally evaluated. The $\omega_o{}^*$ integral is graphically evaluated, and the resulting spatial distribution of the source strength intensity is presented in terms of its axial variation per unit length of jet.

Experimental Apparatus

A comprehensive description of the experimental apparatus, electronic instrumentation, and the measured turbulent flow and acoustic field characteristics is given by Seiner(8). The flow field is generated by an axisymmetric contraction cone with a 60:1 area contraction ratio producing an initially laminar top-hat exit plane velocity profile with a displacement thickness of $\delta^*/D = 0.0065$ and a shape factor of $H = 1.8$. At a jet exit Mach number of 0.33 the turbulence level is found to be 0.25%.

The jet apparatus was located in an anechoic chamber with a 125 Hz cut-off frequency. The microphone used was a B&K 1/2-inch condenser microphone, and it was positioned 60 nozzle diameters distant at an angle of 30° to the jet axis. The hot-wires used were 0.003 mm diameter platinum plated tungsten wire etched to an active length of 0.75 mm, and operated in the constant temperature mode at an over-heat ratio of 0.8. The aspect ratio ℓ/d of these wires was 380. Since measurements were conducted across the shear layer, the hot-wires output was linearized to provide constant resolution over the mean flow velocity range encountered.

The cross covariance functions were computed using a Saicor 42 correlator operating in the clip mode. The hot-wire and microphone signals were pre-filtered before correlation by two phase matched bandpass 4-pole Butterworth filters. To permit use of the incompressible approximation to Lighthill's applied stress tensor, a jet exit Mach number of 0.33 was selected for all tests concerned with application of the direct correlation technique. At this Mach number the jet Reynolds' number for the 2 inch diameter orifice was 3.7×10^5. Therefore, beyond the first jet diameter, the mean velocity profiles were found to be self-similar in the mixing layer as is shown by Figure 1. Beyond the mixing layer good agreement was achieved between measured and calculated mean velocity profiles as is shown by Figure 2. From measurements of the centerline value of mean velocity, the jet's transition cross section occurred between $z/D = 7.5 \rightarrow 8.0$. Tollmien's solution for the axially symmetric source was used for the calculated profile in Figure 2.

Using the mean velocity similarity profile of Figure 1, Prandtl's momentum transport theory is applied to calculate the u' - component turbulent intensity. This result is presented in Figure 3, where it can be observed that good agreement with measured values was achieved. This of course indicates that the jet spreads linearly in the mixing region, or equivalently, a single length scale governs the flow in that region. From space-time cross-correlation measurements the longitudinal integral length scale is found to grow linearly with increasing downstream distance according to the relation $L_z = 0.095\ (z-z_o)$. Here z_o refers to the jets virtual origin, and is located inside the nozzle at $z_o = 1.5D$.

The measured sound power slope with jet exit Mach number for the emission angle of 30° is shown in Figure 5. There it can be observed that in the low subsonic range the sound power slope varies with a 6.5 exponent, and in the high subsonic range varies with an 8.1 exponent. At emission angles near

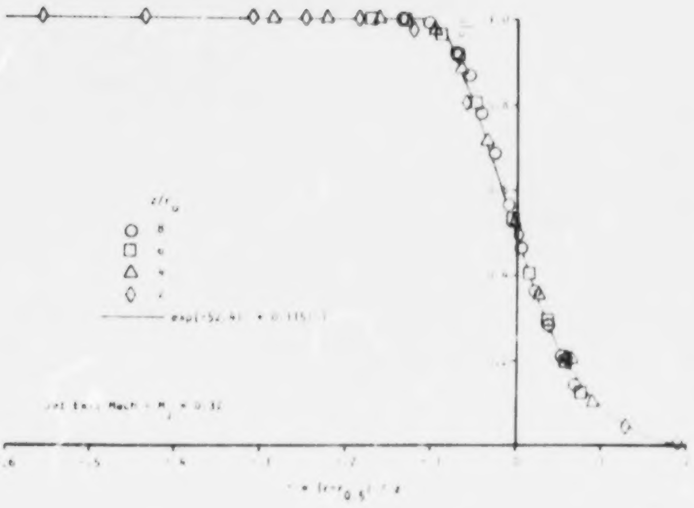

Figure 2 Mean Velocity Similarity in the Jet's Mixing Layer

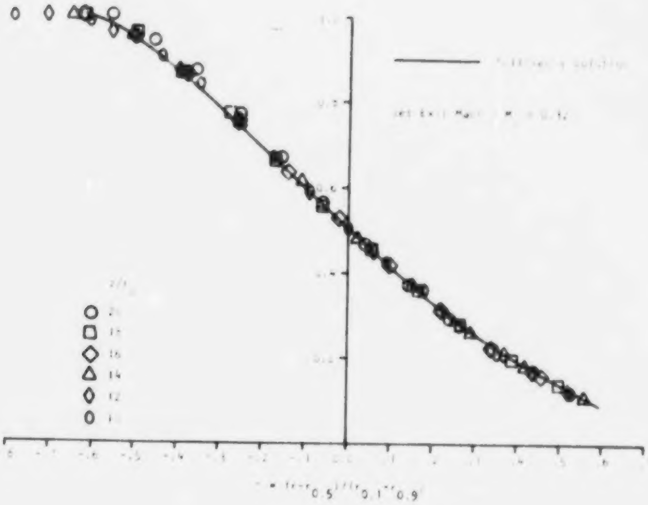

Figure 3 Mean Velocity Similarity in the Jet's Transition and Fully Developed Regions

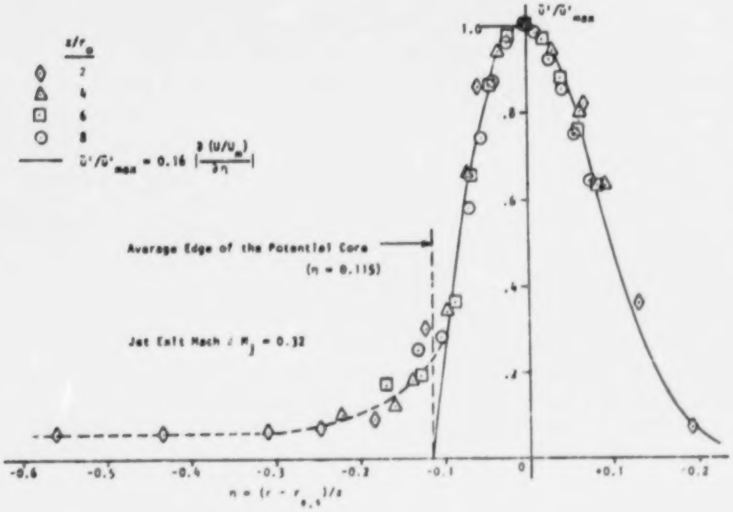

Figure 4 Similarity of the Turbulent Longitudinal Component in the Mixing Layer

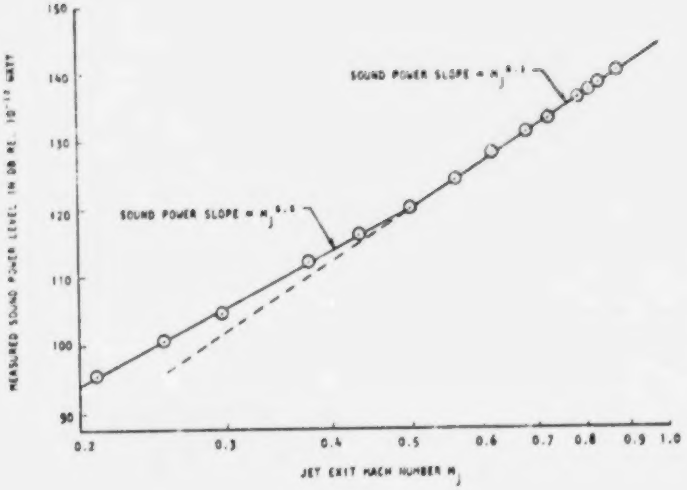

Figure 5 Sound Power Level Vs. Jet Exit Mach Number at $\psi = 30^{\circ}$

normal to the jet axis, the sound power slope is nearer the sixth power of jet exit Mach number across the entire subsonic range. This result is in general agreement with the measurements conducted by Gerrard(9). Lighthill(10) explains this observation as being due to the reduction of turbulence intensity with increase in jet exit Mach number. This produces a basic $U_j{}^6$ variation for the sound power, but the effects of convection produces a directivity that steepens this slope to $U_j{}^9$ at high subsonic Mach numbers for small emission angles to the jet axis.

Measured Sound Power Distribution

In Figure 6 typical hot-wire microphone measured cross covariance functions are shown for the reduced filter center frequency of $f_o{}^*$ equal to $f_oD/U_j = 0.20$. Peak acoustic power emission occurs at $f_o{}^* = 0.36$, and six octave center frequencies were selected around this peak at $f_o{}^* = 0.1$, 0.2, 0.4, 0.8, 1.6, and 3.2. As can be observed from Figure 6, two distinct types of covariance functions are obtained. The upper trace is typical of measurements obtained in the potential core where a concentration of turbuelnt kinetic energy density is observed centered around the reduced filter center frequency $f_o{}^* = 0.40$. A strong filter ringing can be observed from this trace. In the more fully turbulent regions of the flow the output cross covariance takes on the familar $\sin (B\tau/2)/(B\tau/2) \cos \omega_o\tau$ functional appearance, since the turbulent spectrum is essentially flat across each octave bandwidth.

For a Gaussian process with an exponential autocorrelation function, Lumley and Panofsky(11) show that an autocorrelation function estimate at lag τ has a relative fluctuation level of $\sqrt{1 + \rho^2}/\rho$, and an integral scale of $I_\tau/(1 + \rho^2)$. They then show that the averaging time required to produce an estimate with a variance no larger than ε is given by

$$T = 2I_\tau/\rho^2\varepsilon^2 \tag{9}$$

For band limited cross covariance functions the filter's center frequency can be used to approximate the integral time scale in 9, since for an octave filter the bandwidth $B = \sqrt{2}\,\omega_o/2$. Thus 9 can also be written as

$$T = \frac{2\pi}{\sqrt{2}\ B\ \rho^2\varepsilon^2} = \frac{1}{2f_o\ \rho^2\varepsilon^2} \tag{10}$$

Equation 10 was used as a guideline for selection of a suitable averaging time, such that for all values of the measured coherence amplitude $\rho \geq 0.01$, the relative error would be $\varepsilon \leq 0.15$. For values of $\rho \geq 0.03$ the relative error was typically less than 0.1.

Figure 6 shows that a positive spike occurs near the expected time delay $\tau = r/a_o$ rather than a negative going spike as prescribed by equation 4. This occurs since a condenser microphone is normally inverting (i.e. a positive pressure exerted on the microphone's diaphragm requires a decrease in voltage to maintain a constant electrostatic charge). Thus the positive peaks like those shown in Figure 6 are selected as the value for $[-\rho_{p_s u_r}] \| \tau = r/a_o$ appearing in equation 6. Figure 7 shows the resulting spatial distribution from similar measurements within the first ten jet diameters. In this case the distribution is for the shear noise coherency function for the reduced filter center frequency of $f_o^* = 0.40$. The measurements were limited to the first ten jet diameters, for beyond this point insufficient distance would exist between the source and observervation point.

From Figure 7 we note that the shear noise coherency function attains a maximum value along the axis of symmetry, having an ampliutde value 2[illegible] times greater than those which occur at $r/D = 0.5$ for the same axial location. Fuchs(12) demonstrates that the power spectral density for the hydrodynamic pressure in the potential core can be synthesized by the Fourier transform of the azimuthal pressure components that result from a synthesis of a circumferential space correlation in the mixing layer. He further shows that maximum coherence results when the sum of two diametrically opposed pressure components in the mixing layer are correlated with the pressure component along the jet centerline. This observation indicates that the dominant pressure component is the axisymmetric mode, that may have its parallel with the large scale coherent ring-like vortex structure observed by Crow and Champagne(13).

The results of Fuchs fit into our context in the sense that contributions from the entire periphery of the mixing layer simultaneously contribute to the fluctuations along the axis of symmetry. Thus the resulting cross covariance measurement between the centerline velocity fluctuations and the far field acoustic pressure is essentially an integrated measure of the entire contribution from around the periphery of the fully turbulent flow. However, it is to be expected that the measured value at a particular axial location along the jet centerline may well be associated with turbulent motion advected to that point from farther upstream.

Figure 8 displays the spatial distribution for the shear-noise component η_{shear} at $f_o^* = 0.40$. As can be observed, except for measurements within the potential core, the maximum acoustic contribution is evidently again funneled into the centerline value from the fully turbulent zone. Also evident from Figure 8, is the result that the amplitude level of η_{shear} at the peak acoustic frequency of $f_o^* = 0.36$, is relatively constant through the entire transition region. Figure 9 shows that a definite peak frequency can be associated with any particular axial location, and that this peak frequency is constant across the entire shear layer.

The variation of the reduced frequency parameter f_o^* with axial location where the peak frequency dominates like that shown in Figure 9, produces the Strouhal number dependence like that shown in Figure 10. There it is evident that in the mixing layer, both the shear and self noise components vary inversely with f_o^* with increasing downstream distance. In the transition layer the peak frequency remains constant, and then falls off like $(f_o^*)^{-2}$ downstream of the jet's transition cross section. The behavior of

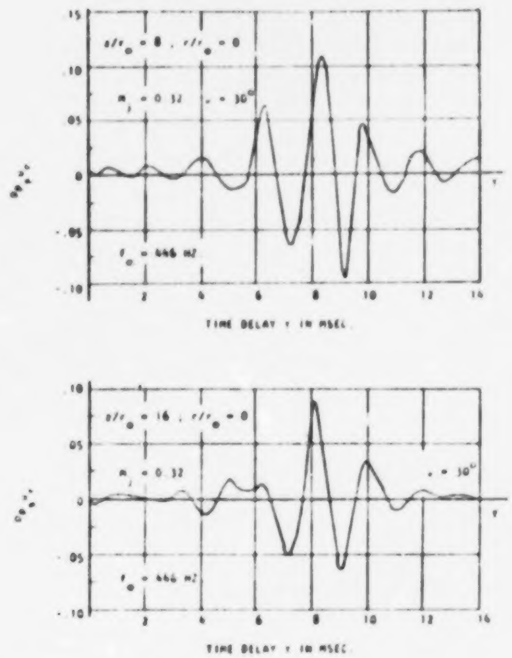

Figure 6 Typical Hot-Wire-Microphone Cross Correlation for $f_o^* = 0.20$

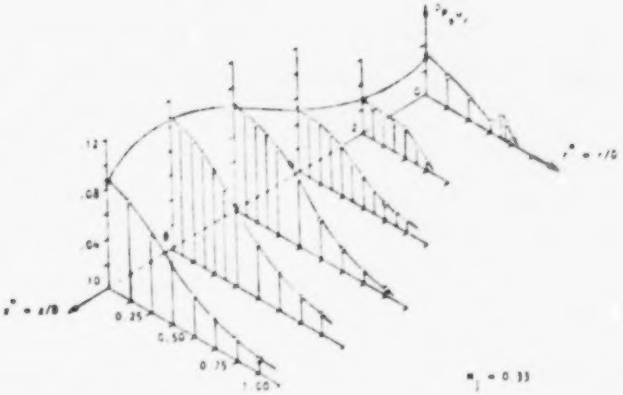

Figure 7 Spatial Distribution of $\rho_{P_s u_r}$ at $\psi = 30^o$ for $f_o^* = 0.20$

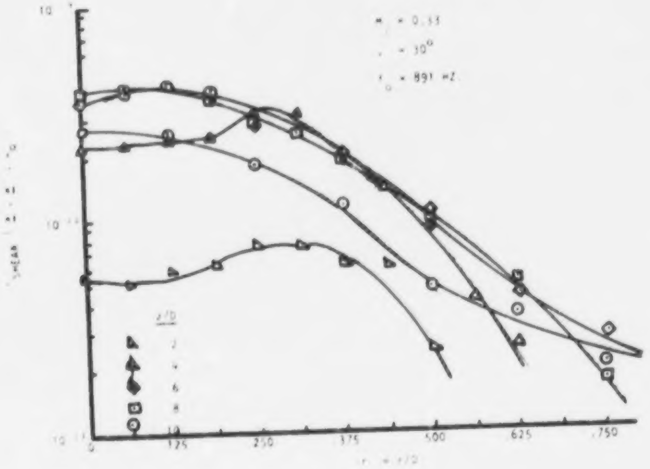

Figure 8 Radial Distribution of η_{shear} Per Unit Slice of Jet for $f_o^* = 0.40$

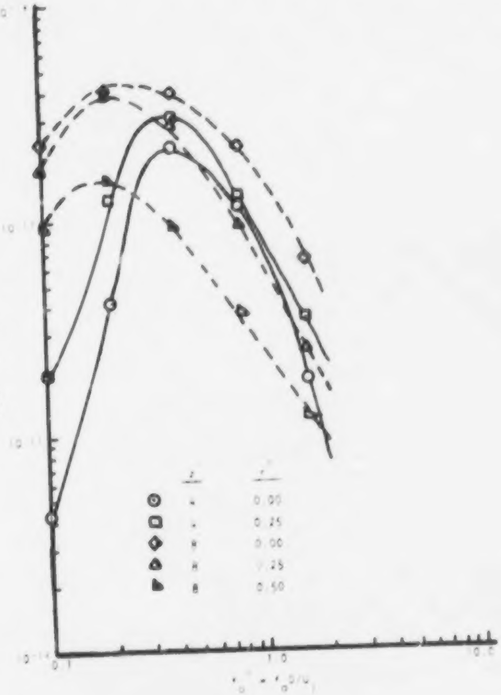

Figure 9 Power Spectrum for η_{shear} in the Mixing Layer and Fully Developed Jet

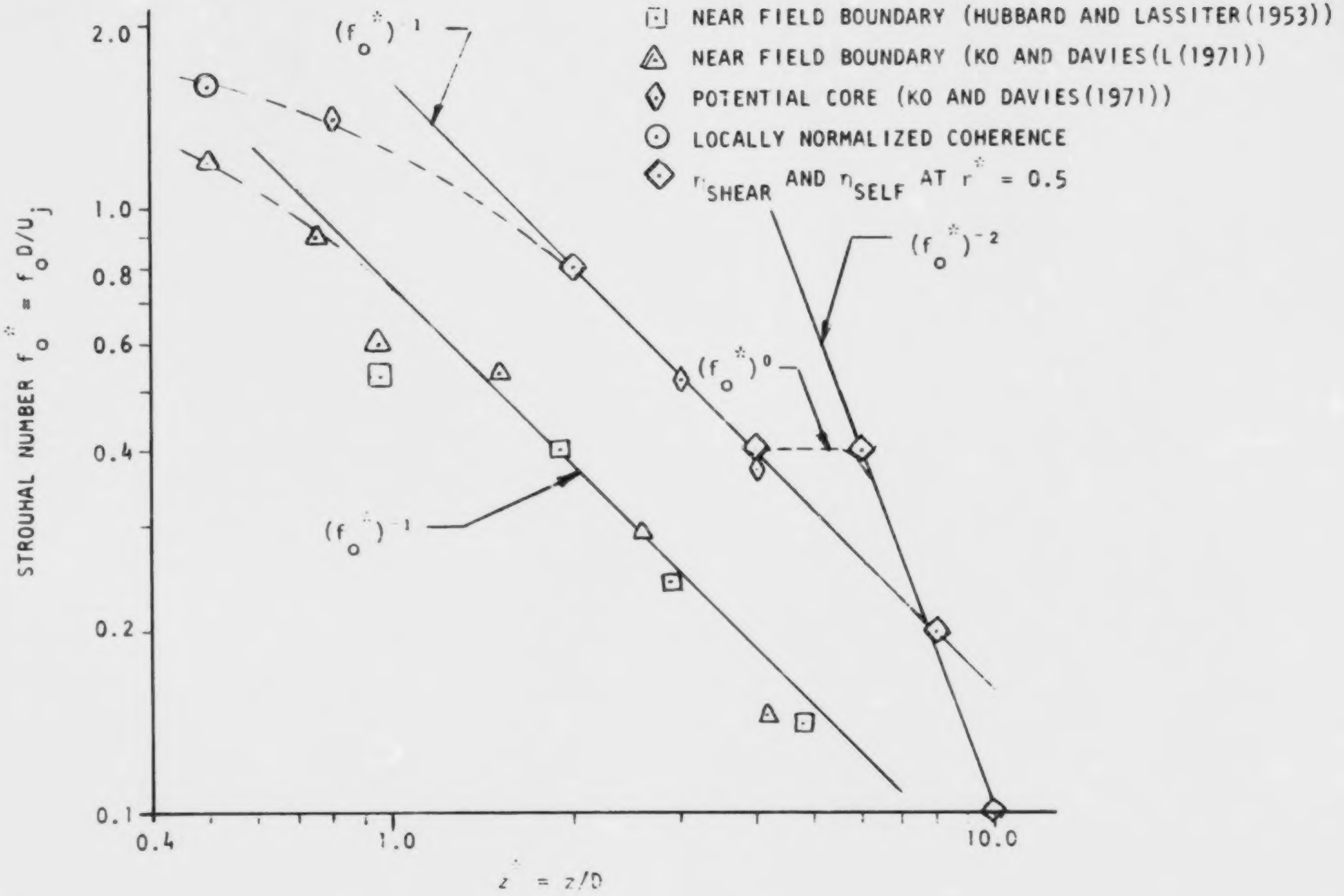

Figure 10 Inverse Variation of the Strouhal Number with Increasing Downstream Distance

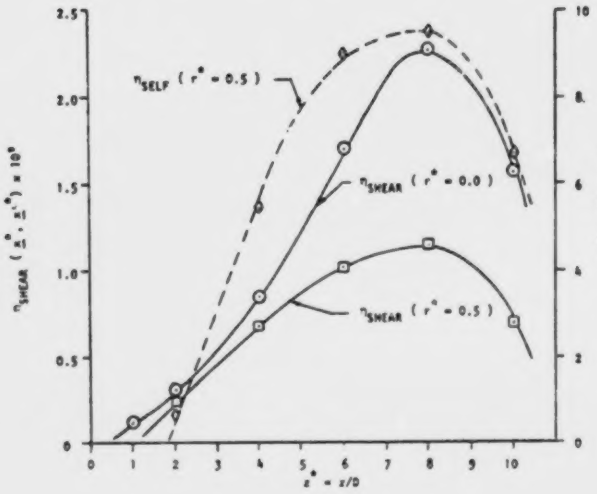

Figure 11 Axial Variation of Shear and Self Nondimensionalized Source Strength Intensity Per Unit Volume

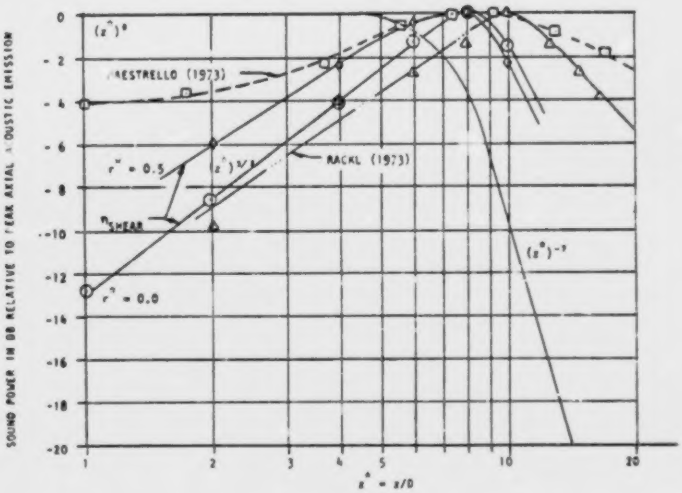

Figure 12 Axial Distribution of η_{shear} and Comparison with the z^0 and z^{-7} Laws and Other Results

f_o^* in the mixing layer and fully developed jet is expected from the similarity laws of Powell(13). The invariancy of peak frequency in the transition region is an unexpected result, and deserves further attention.

To obtain the broadband source strength intensity distribution in the jet, the ω_o^* integral of equation 5 must be evaluated. An estimate for this integral was obtained by replotting single point spectra, like those shown in Figure 9, in semi-logarithmic form and evaluating the area under the integral of the $\omega_o^* \eta (\underline{x}^*, \underline{x}'^* ; \omega_o^*)$ integrand with a polar planimeter.

Figure 11 displays the results of doing this for both the shear and self noise components. For both components peak acoustic emission occurs eight jet diameters downstream, but the actual maximum peak emission may occur farther upstream due to turbulent kinetic energy advection. Apparently for the jet emission angle of 30°, the shear noise component dominates the self-noise component by a factor of 13 dB.

In Figure 12 a comparison of the results for the axial distribution of the integrated shear-noise component relative to the location of peak emission is made with the results obtained by Maestrello and Rackl. In general, the agreement is good, especially when one considers that all three methods that appear in Figure 12 were remarkably different. In Maestrello's measurements a fully turbulent exit plane profile was used, possibly accounting for the relatively smoother variation in sound power emission from the peak emission point of 9 jet diameters. Rackl used an initially laminar exit plane profile, and obtained peak acoustic emission at 10 jet exit diameters. It should be noted that for all three of the measurement techniques appearing in Figure 12, peak emission probably occurs farther upstream leading to the conclusion that peak emission can be associated with the transition region in low subsonic jet flows.

Conclusions

A direct correlation between the signals from a hot-wire probe and a far field microphone has been used to produce an estimate for the sound power distribution in a laboratory scale model low subsonic jet. The tests were conducted at a jet exit Mach number of 0.33, and at an emission angle of 30° to the jet axis where the jet has its directional peak. The shear noise component was found to dominate the self-noise component by a factor in the order of 13 dB. The shear component peaks along the axis of symmetry, while the self-noise component peaks close to the center of the shear layer. The analysis of Fuchs(12) appears relevant for the observed spatial distribution of the shear noise component. Apparently the integrated axisymmetric contribution from around the periphery of the fully turbulent flow funnel their contribution to the observed centerline value of coherence amplitude.

The results indicate that peak acoustic emission occurs eight jet exit diameters downstream of the orifice. From that point the sound power slope falls away like $(z^*)^{\pm 1.5}$. Examination of the local value for the shear noise coherence function, indicates from the centerline coherence amplitude that advection of turbulent kinetic energy from the fully turbulent region of flow upstream of that point would place peak acoustic emission closer to the nozzle exit. Single point power spectra have shown that a dominant frequency component exists across the entire shear layer for a particular axial location. Definition of a Strouhal number $f_o^* = f_oD/U_j$ leads to a $(f_o^*)^{-1}$, f_o^*, $(f_o^*)^{-2}$ variation with axial downstream for the respective mixing, transition, and fully developed jet regions.

Acknowledgement

The work reported here was supported by a research grant from the NASA Langley Research Center under Grant Number NGL 39-009-021.

Nomenclature

a_o	ambient speed of sound
B	normalized bandwidth $(\omega_{o\ell} - \omega_{oh})/\omega_o$
D	jet exit diameter
f_o	filter center frequency
f_o^*	reduced filter center frequency f_oD/U_j
$P_s(\underline{x},t)$	radiated sound pressure
r	radial coordinate for jet flow field
r_o	jet exit radius
R	microphone distance from jet nozzle
u_r	turbulent component in direction of observation
U_r	mean flow component in direction of observation
U_j	jet exit flow mean velocity
z	axial coordinate for jet flow field
δ^*	displacement thickness
ε	relative error in correlation measurement
ρ	cross covariance function
ρ_o	ambient density
τ	time delay
ψ	angle of acoustic emission to jet axis
ω_o	radian filter center frequency

References

1. Lee, H.K., and Ribner, H.S., "Direct Correlation of Noise and Flow of a Jet", J. Acoust. Soc. Amer., Vol. 52, Number 5, pp. 1280-1290 (1972).

2. Maestrello, L., "On the Relationship Between Acoustic Energy Density Flux Near the Jet and Far Field Acoustic Intensity", AIAA Paper No. 73-988 (1973).

3. Rackl, R., "Two Causality Correlation Techniques Applied to Jet Noise", Ph'D Thesis, Dept. of Mech. Eng., Univ. of British Columbia (1973).

4. Wolff, S.S., Thomas, J.B., and Williams, T.R., "The Polarity Coincidence Correlator : A Nonparametric Detection Device", IRE Trans. on Information Theory, IE-8, pp. 5-9 (1962).

5. Seiner, J.M., and Reethof, G., "On the Distribution of Source Coherency in Subsonic Jets", AIAA Paper No. 74-4 (1974).

6. Lighthill, M.J., "On Sound Generated Aerodynamically, I. General Theory", Proc. Roy. Soc., A211, pp. 564-587 (1952).

7. Ribner, H.S., "The Generation of Sound by Turbulent Jets", Advances in Applied Mech., Vol. 8, Academic Press, New York, pp. 103-189 (1964).

8. Seiner, J.M., "The Distribution of Jet Source Strength Intensity by Means of a Direct Correlation Technique", Ph'D Thesis, Dept. Aersp. Eng., Pennsylvania State University (1974).

9. Gerrard, J.H., "An Investigation of the Noise Produced by a Subsonic Air Jet", J. of Aero. Sci., Vol. 23, pp. 855-866 (1956).

10. Lighthill, M.J., 'The Bakerian Lecture 1961, Sound Generated Aerodynamically", Proc. Roy. Soc. (London), A267, pp. 147-182 (1962).

11. Lumley, J.L., and Panofsky, H.A., "The Structure of Atmospheric Turbulence", John Wiley and Sons, New York, (1964).

12. Fuchs, H.V., "Resolution of Turbulent Jet Pressure Into Azimuthal Components", Institute for Turbulent Flow, Berlin, Internal Report Number IB357-73/4 (1973).

13. Crow, S.C. and Champagne, F.H., "Orderly Structure in Jet Turbulence", J. Fluid Mechanics, Vol. 48, pp. 547-591 (1971).

14. Powell, A., "Similarity and Turbulent Jet Noise", J. Acoust. Soc. Amer., Vol. 31, Number 6, pp. 812-813 (1959).

FLOW INSTABILITIES AND SUPERSONIC JET NOISE

by

Christopher K. W. Tam

Department of Mathematics
Florida State University
Tallahassee, Florida 32306

ABSTRACT

The principal aim of the present research is to develop a mathematical model of supersonic jet noise based on the concept that "large scale flow disturbances" is the dominant noise generation mechanism. To achieve this goal a quasi-linear integral method is used to calculate the amplitude of the large scale disturbances in the flow of a supersonic jet. The result of this calculation is used to determine the unsteady entrainment velocities and lateral vibrations of the jet. The noise emitted by these unsteady processes are subsequently computed by the method of Fourier Transform. On applying the present method to a 2.2 Mach number cold jet the predicted directivity is found to compare favorably with experimental measurements. Future plan involves the extension of the present work to include the prediction of near field jet noise.

I. INTRODUCTION

It has long been noticed, Rayleigh (1896) that sound waves can trigger flow instabilities in a jet. Relatively recently, a body of evidence becomes available which seems to indicate that the converse is also true i.e. "flow instabilities" is an important noise generation mechanism especially in supersonic jets. This basic idea has been expressed by various authors at times e. g. Mollo-Christensen (1967), Sedel'nikov (1969) and others even though fruitful results were not obtained immediately. Our earlier work (Tam, 1971) on this subject involved the study of high frequency noise generated by shear layer instabilities of supersonic jets. Although this high frequency noise is not the most important supersonic jet noise component yet the problem has the advantage that it can by analysed mathematically in a simple but vigorous way. The comparison of these mathematical results and experimental measurements, therefore, offer a reasonable but unambiguous test on the fundamental concept of noise generation by flow instabilities. Following this line of thought, we (Tam, 1971) found good agreement between predicted directional pattern of sound waves generated in this way and shadowgraphic observations. Further work in this direction has since been carried out by Chan and Westley (1973). By carefully choosing the optimal experimental parameters not only they were able to find good agreement between theory and experiment on the relationship among frequency, wave length and wave directional pattern but also they were able to confirm the rater remarkable prediction that under certain flow conditions some of the directional waves actually propagate at velocities less than the ambient speed of sound in the near field. The very favorable agreement between predictions and observations obtained by Chan and Westley seems at this time to leave little room for doubt that "flow instabilities" is a mechanism of noise generation.

In subsonic jet noise theory Crow and Champagne (1971) appeared to be the first to conceive the idea that perhaps the dominant part of jet noise is generated by large scale orderly disturbances rather than random turbulence as had been generally believed. Their pioneering investigation has subsequently motivated the work of Hardin (1973) and Morris (1974). Parallel to the subsonic work of Crow and Champagne but somewhat later results of a number of earlier experiments strongly suggested to us (Tam, 1972) that the dominant part of supersonic jet noise could also be generated by large scale flow disturbances. Shadowgraphic observations (Tam, 1972; Lowson and Ollerhead, 1968; Porter, 1968) clearly identified the existence of large scale helical disturbances in supersonic jets. If one assumes that these disturbances are hydrodynamic instability waves one can calculate the frequency-wave length relationship very easily by using relatively simple but reasonable mean velocity profiles. Further, if one accepts the assumption that these waves are the result of selective amplification of flow disturbances by the periodic shock cell structure downstream of the nozzle exit of a supersonic jet it is then possible to predict the wave length and frequency of these large scale disturbances from first principle. On comparing the predicted wave length with shadowgraphic measurements very reasonable agreements were found. The presence of the large scale disturbances causes the jet to oscillate which leads to rapid broadening and decay of the jet due to strong interaction between jet and ambient fluid at a location where the amplitude of oscillation is sufficiently large. This violent interaction between jet and ambient fluids naturally generates unsteady pressure fluctuations and hence noise radiation. If the dominant part of supersonic jet noise is generated by this process then one would expect that the dominant frequency of the radiated noise must be the same as the frequency of the large scale disturbances and that most of the noise must be generated in the proximity where the jet broadens abruptly. On comparing the calculated wave frequency and the dominant frequency of the power spectrum of the far field noise data of Dosanjh and Yu (1968), Porter (1968) and Yu and Dosanjh (1972) very favorable agreement were obtained. Moreover, the interpretation of noise source location was found to be consisted with the direct measurement of Porter (1968) and near field noise measurement of Mull and Erickson (1957) and Yu and Desanjh (1972). These results although are fragmentary yet are definitely encouraging. This is especially so when similar ideas about the role of large scale disturbances in relation to supersonic jet noise generation were expressed by Bishop, Ffowcs-Williams and Smith (1971) who were motivated by different types of experimental observations.

Most recently, McLaughlin and McColgan (1973) and McLaughlin, Morrison and Troutt (1974) studied the noise generated by supersonic jets at low Reynolds numbers. They found that discrete frequency large scale distrubances were indeed present. Their microphone measurements of near field noise yielded discrete spectral peaks at corresponding frequencies. These peaks dominated the noise power spectrum. By forcing the jet slightly near the jet exit using a glow discharge they were even able to perform phase lock measurements of the near field noise. These experiments are extremely important for they settle once and for all the question whether large scale instabilities in a supersonic jet can produce noise. Further they show that these instabilities are dominant noise sources at least for low Reynolds number jets. What remains to be seen experimentally at this time is whether the same holds true for a real high Reynolds jet number!

II. A SIMPLE MATHEMATICAL MODEL OF SUPERSONIC JET NOISE GENERATED BY LARGE SCALE DISTURBANCES.

Without the benefit of knowing the results of McLaughlin and his co-workers, we (Tam, 1973) attempted to formulate a simple mathematical model of supersonic jet noise generated by large scale disturbances. Our model is only an approximate one and because of our inability to understand fully the mechanics of turbulence and turbulence-wave interaction our conclusion must be regarded as tentative. We divide our model into two parts. The first part involves the modelling of the noise sources, namely, the large scale disturbances and the second part involves the modelling of the acoustic field outside the jet. That this can be done is based on the recognition that the total acoustic power radiated is small which is usually less than one half of one per cent of the power of the jet. The back reaction of the noise on the mean flow in the absence of jet screech is, therefore, expected to be negligible.

Physically a supersonic jet is highly unstable. Because of selective amplification by the periodic shock cell structure downstream of the nozzle exit a certain large scale unstable wave is often amplified. The amplitude of this large scale disturbance depends on the amplitude of turbulent excitation at the nozzle exit which fluctuates in time. As a result the large scale wave motion is not a permanent structure of the jet flow. Rather ir forms and breaks up, forms again and breaks up again. The whole process goes on continually and randomly. Although the large scale wave has a preferred frequency yet the process of random formation and decomposition causes the noise emitted to be broadband. This tendency of radiating broadband noise is further enhanced by turbulent mixing at the noise generating regions. To model the above described process fully is beyond the scope of our present work. As an approximation we neglect the processes of random formation and decomposition so that the mean flow oscillates with a fixed frequency with a definite initial amplitude at the nozzle exit. Our simplified model (Tam, 1973) therefore, has one single frequency and naturally is incapable of predicting the noise power spectrum. However, it is useful in that it offers a simple way of estimating the total noise power emitted together with its directivity.

The amplitude of large scale disturbance is determined by a set of quasi-linear equations first used by Ko, Kubota and Lees (1970) and Ko (1971). Some slight modifications are made to account for the potential energy density of the flow and an empirical eddy viscosity is used to simulate the effect of fine scale turbulence. The solution of the quasi-linear equations gives the variation of the amplitude of large scale disturbance and the mean flow parameters as functions of the axial distance downstream of the nozzle exit.

The jet broadens out as more and more fluid is entrained into the jet. The presence of large scale disturbances in the jet flow further enhances the entrainment process. An estimate of the amount of unsteady entrainment due to the large scale disturbances is made by accounting for the broadening out of the jet (Tam, 1973). A precise calculation is; of course, impossible but a reasonable estimate can be obtained by integrating the continuity equation. Unsteady entrainment invariably leads to noise radiation. The unsteady entrainment velocity obtained at this stage thus provides the noise source strength. Because of entrainment the radial and tangential momuntum of the jet fluid associated with the large scale disturbances are not precisely balanced. In other words the jet vibrates laterally which is another process by which noise is generated. In our work (Tam, 1973) a very simple model was used to estimate the amplitude of vibration from which, the boundary condition for the acoustic field outside the jet was determined.

Outside the jet if the effect of refraction is neglected then the propagation of acoustic disturbance is described adequately by the use of the simple acoustic wave equation. This equation together with the boundary condition on the surface of the jet provided by the entrainment and jet vibration velocities can be solved easily by the method of Fourier Transform. In this way the directivity and total noise power generated by large scale disturbances are found. It is to be noted that according to this model the acoustic disturbances outside the jet propagate with the speed of sound. Since the source of this noise consists of a helical large scale wave the noise produced would be in the form of mach waves. If the more realistic model that the large scale disturbances form and decay randomly is used then the radiated noised would be in the form of patches of mach waves somewhat different from that of our present simple model.

Numerical calculations on a 2.2. mach number cold jet have been carried out (Tam, 1973). On comparing the calculated noise directivity with experimental measurements of Dosanjh and Yu (1969) very favorable agreement was found. Of course, further comparisons with experiments are needed before any definite conclusion can be drawn. Yet the good agreement in the case of the 2.2 mach number jet seems to indicate that further study of large scale disturbances as the dominant source of supersonic jet noise both experimentally and theoretically may be worthwhile.

III. DISCUSSION

One of the most difficult problem in jet noise research is to find exactly how noise is generated physically. By noise here we mean pressure disturbances which propagate with local speed of sound (pseudo-sound is not the subject of this discussion). In most existing work on turbulence generated sound it is generally assumed that each small volume of turbulent fluid produces sound. Ribner (1964) conceived that turbulent fluid elements collided with each other constantly in a turbulent flow. Because of compressibility the colliding fluids compressed and then rebound emitting an acoustic pressure wave in this process. According to this physical picture one sees that compressiblity is crucial to the production of sound waves. Without compressibility, turbulence will generate pressure fluctuations. However, these pressure fluctuations are not sound waves which can propagate to great distances. Now consider a water jet issuing into free air. Clearly noise is generated. But for all intents and purposes water is incompressible. So sound waves are not actually produced inside the jet! They are generated at the air water interface or broadly speaking a mixing zone on the surface of the jet. To calculate the noise produced by the water jet it would therefore be more natural to estimate first the pressure or velocity fluctuations at the water air interface and then determine the sound and pressure fluctuations outside. In our model (Tam, 1973) this procedure is adopted. For an air jet sound waves are, of course, generated inside the jet as well. In the case of noise generated by large scale disturbances volume sources are, however, believed to be less important. The dominant part of the noise is produced by violent intense interaction between jet and ambient fluids brought about by the large scale oscillatory motion of the jet.

IV. FUTURE PLAN

Future work includes possible refinement of the present model to account for the formation and decay processes of the large scale disturbances. Extension of the present calculation to include prediction of near field supersonic jet noise is comtemplated.

V. ACKNOWLEDGMENT

The work reported here was supported by NSF under Grant GK-35790.

VI. REFERENCES

Bishop, K. A., Ffowcs-Williams, J. E. & Smith, W., 1971 On the noise sources of the unsuppressed high-speed jet. J. Fluid Mech., 50, 21.

Chan, Y.Y. and Westley, R. 1973 Directional acoustic radiation generated by spatial instability. CASI Trans., 6, 36.

Crow, S. C. and Champagne, F. H. 1971 Orderly structures in jet turbulence. J. Fluid Mech., 48, 547.

Dosanjh, D. S. and Yu, J. C. 1968 Noise from underexpanded axisymmetric jet flow using radial jet impingement. Proc. of AFOSR-UTIAS Symposium on Aerodynamic Noise, Toronto, Canada.

Hardin, J. C. 1973 Analysis of noise produced by an orderly structure of turbulent jets. NASA TN D-7242.

Ko, D.R.S., Kubota, T. & Lees, L. 1970 Finite disturbance effect on the stability of a laminar incompressible wake behind a flat plate. J. of Fluid Mech., 40, 315.

Ko, D. R. S. 1971 Integral theory for the instability of laminar compressible wake behind slender bodies. AIAA J., 9, 1777.

Lowson, M. V. and Ollerhead, J. B. 1968 Visualization of noise from cold supersonic jets. J. Acoust. Soc. Amer., 44, 624.

McLaughlin, D. K. and McColgan, C. J. 1973 Hot wire measurements in a supersonic jet at low Reynolds numbers. School of Mechanical and Aerospace Engineering, Oklahoma State University Report ER-74-ME-3.

McLaughlin, D. K., Morrison, G. L. & Troutt, T. R. 1974 Experiments on the instability waves in a supersonic jet and their acoustic radiation. School of Mechanical and Aerospace Engineering, Oklahoma State University Report ER-74-ME-5. (see also this Proceeding)

Morris, P. J. 1974 A model for the structure of jet turbulence as a source of noise. AIAA paper no. 74-1.

Mollo-Christensen, E. 1967 Jet noise and shear flow instability seen from an experimenter's viewpoint. J. of Appl. Mech., 34, 1.

Mull, H. R. and Erickson, J. C. Jr. 1957 Survey of the acoustic near field of three nozzles at a pressure ratio of 30. NACA TN-2978.

Potter, R. C. 1968 An investigation to locate the acoustic sources in a high speed jet exhaust stream. Wyle Lab. Tech. Report. WR 68-4.

Rayleigh, Lord 1896 The Theory of Sound Dover.

Ribner, H. S. 1964 "The generation of sound by turbulent jets" in Advances in Applied Mechanics. vol. 8. Academic Press, New York.

Sedel'nikov, T. Kh. 1969 "The frequency spectrum of the noise of a supersonic jet" in Physics of Aerodynamic Noise ed. by A. V. Rimsky-Korsakov. (Nauka Press, Moscow, 1967). Translated as NASA TT F538 (1969).

Tam, C. K. W. 1971 Directional acoustic radiation from a supersonic jet generated by shear layer instability. J. Fluid Mech., 46, 757.

Tam, C. K. W. 1972 On the noise of a nearly ideally expanded supersonic jet. J. of Fluid Mech., 51, 69.

Tam, C. K. W. 1973 Supersonic jet noise generated by large scale disturbances. AIAA paper no. 73-992.

Yu, J. C. and Dosanjh, D. S. 1972 Noise field of a supersonic mach 1.5 cold model jet. J. Acoust. Soc. Amer., 51, 1400.

EXPERIMENTS ON THE INSTABILITY WAVES IN A SUPERSONIC JET AND THEIR ACOUSTIC RADIATION

by

D. K. McLaughlin, G. L. Morrison, and T. R. Troutt

Oklahoma Stare University
Stillwater, Oklahoma

An experimental investigation of the instabilities and the acoustic radiation of the low Reynolds number axisymmetric supersonic jet is being performed. This study was prompted by the recent theoretical interest in the instability process which leads to large scale organized wave motion in the supersonic jet. Tam has had surprising success in predicting noise radiation properties using an instability theory.

Hot-wire measurements in the flowfield and microphone measurements in the acoustic field of supersonic jets ($M \approx 2$) have been made in this study. The instability process in the perfectly expanded jet consists of numerous discrete frequency modes. Measurements of frequency, wavelength and wavespeed of the 'dominant' oscillation agree closely with Tam's predictions.

Microphone measurements have shown that the wavelength, wave orientation, and frequency of the acoustic radiation generated by the dominant instability agree with the Mach wave concept. Amplitude measurements indicate that the major noise generation mechanism is the large scale instabilities.

INTRODUCTION

There are several groups of researchers (1-3) who believe that the turbulence properties in unbounded flows retain some of the characteristic structure of the initial instability in the process of transition. Presently there are a few authors (4-6) who have applied this idea to the analysis of supersonic jet noise. It is the goal of the present research to provide the experimental foundation that is necessary for a complete development of the instability approach in supersonic jet noise analysis.

Of the supersonic jet noise stability theories, the work of Tam (4,7) is the most extensive. Tam's model is unique in that an amplified frequency selection mechanism governed by the wave cell structure of the jet is proposed. Figure 1 shows a schematic of some of the major features of Tam's model. Since Tam uses a linearized theory, many of the physical processes in the jet flow are unaccounted for. In our view there are two reasons which justify applying the simplified theory to the more complex physical situation. First, there is some evidence that the dominant noise production mechanism is the large scale instability of the jet (8) which may be calculated with stability theory. Second, if one hypothesizes a more complete calculation scheme with a hierarchy of analyses, each becoming more complicated, the linear stability theory is the logical starting point for the complete calculation.

Rather than measure the flow disturbances and acoustic properties of the high Reynolds number, fully turbulent jet for comparison with the instability theories, we have taken the approach of experimentally working hand in hand with the developing theories. In this spirit we have begun a program of measuring the fluctuations with a hot-wire anemometer in a low Reynolds number jet where the transition from laminar to turbulent flow is stretched out over several diameters. We obtain this low Reynolds number situation by exhausting the jet into a vacuum chamber whose pressure is maintained at a small fraction of the atmospheric pressure. Hot-wire spectra and wavelength and growth of dominant spectral components are measured in the flowfield of a supersonic axisymmetric jet. Microphone measurements are made in the acoustic field of the same jet. Sound pressure levels, spectra and wavefront orientation of a single dominant spectral component are measured and related to the disturbances in the jet.

DESCRIPTION OF THE EXPERIMENT

A schematic of the test facility is shown in Fig. 2. An axisymmetric supersonic de Laval nozzle is located on the inside wall of the vacuum chamber whose pressure, P_{CH}, is controlled by a variable exit diffuser. The vacuum chamber is lined with 1.5 cm acoustic tile to reduce the reflected sound waves. Two nozzles with exit diameters, D, of 6.35 mm and 9.52 mm were used in this study. The jets are supplied by atmospheric air through a 15 cm diameter stilling section. The stagnation temperature, T_o, for all measurements is atmospheric temperature (530°R). A two degree of freedom probe drive is located inside the vacuum chamber to support either a pressure, hot-wire, or microphone probe.

Spectral analysis data is obtained with a Hewlett Packard Model 302 A Wave Analyzer with a bandwidth of 6Hz and a sweep rate of 1000 Hz/min. Wavelengths of both the flow instability waves and acoustic waves outside the jet are obtained by artificially exciting the jet using a glow discharge excitation technique similar to that used by Kendall (9). The exciter signal provides the phase reference from which to make relative phase measurements with either the hot-wire or the microphone.

EXPERIMENTAL RESULTS

Pitot pressure and static pressure probe measurements were made on the centerline of the jets. Local jet Mach numbers were evaluated from these measurements. These measurements showed some degree of wave cell structure when the jet was perfectly expanded (ratio of nozzle exit pressure, P_N, to chamber pressure, P_{CH}, was held between 1.00 and 1.01). The average Mach numbers (on the centerline between the exit and two diameters downstream) were as follows: M=2.2 for the 6.35 mm jet and M=2.3 for the 9.52 mm jet.

Microphone and Hot-wire Spectra

Figure 3 presents representative microphone spectra measured in the acoustic field of the two supersonic jets. The data is presented in terms of the non-dimensional frequency $St = \frac{fd}{U}$ where U is the mean centerline jet velocity and d is the effective jet diameter (the exit diameter of the nozzle D, minus twice the displacement thickness of the boundary layer at the nozzle exit). The purpose of presenting data from the two size jets is to demonstrate that the dominant spectral components, being at similar Strouhal numbers, are phenomena characteristic of the jet and not the flow facility. Notice, however, in both spectra, there is a large low frequency content at St=0.02 or less. This low frequency noise is mostly due to vacuum chamber resonance and is, therefore, filtered out of amplitude measurements presented later in this paper.

There are two comparisons which are appropriate to make with the frequency spectra data. First, the largest frequency peak in both jets occurs at a nondimensional frequency of approximately St=0.18 which is very close to the value predicted by Tam (4) for the most dominant instability mode. However, there is a discrepancy here in that our measurements show in many cases three or more major spectral components whereas Tam predicts a single frequency dominant mode. (He disregards a second predicted mode with a much shorter wavelength as being unimportant. This second mode is none of the major modes measured in the present study.) The second important comparison to make with the spectral data of Fig. 3 is with spectra measured by many investigators, for example Dosanjh and Yu (10), of the noise radiation from high Reynolds number supersonic jets. The modes depicted in Fig. 3 are grouped around a Strouhal number of 0.18 which coincides with the maximum amplitude frequency of the rather broad spectra measured in high Reynolds number jets. Tam's thesis is that the major noise generation mechanism of the high Reynolds number jet is the large scale instability, and the small scale turbulence is responsible for broadening of the spectrum around the peak caused by the dominant oscillation. With this latest experimental evidence demonstrating several dominant modes, the hypothesis of the small scale turbulence broadening the spectrum around the instability waves, seems more plausible than ever.

A spectrum of the hot-wire voltage fluctuation signal measured in the smaller jet is presented in Fig. 4a) for comparison with the microphone spectra. Some of the peak amplitude frequencies occur at the same Strouhal number as those in the microphone spectra, however, in general there are more peaks in the hot-wire data and the relative amplitudes of the spectral components are not the same. Unfortunately, the picture is further confused when we consider another hot-wire spectrum, shown in Fig. 4b) which has been recorded with almost identical mean flow conditions as the data of Fig. 4a). What we are seeing is a tendency for the instability process to assume different dominant modes of oscillation depending upon very small changes in the mean flow conditions.

After recording over 50 spectra at various locations in the jet for various mean flow conditions, we have determined that very few are exactly identical. However, virtually all of the spectra of the 6.35 mm jet have recurring dominant modes at St=0.148, 0.176, and 0.185. In numerous cases (but not all) the 9.52 mm jet has only one dominant mode at St=0.18 provided the probe is upstream of x/D=5. As explained in Ref. 11, we believe this is due to the wider divergence angle of the conical contour of the larger nozzle. We have also observed that the exact characteristics of a frequency spectrum depend upon the pressure balance condition and on the humidity of the air.

Microphone Amplitude Measurements

Microphone measurements were made in the acoustic field of the perfectly expanded 6.35 mm jet at a Reynolds number of 12,600. Fig. 5 presents sound pressure level contours determined from this data. The general shape of the contours is in good agreement with the measurements of Mayes et al (12), Yu and Dosanjh(13) and Louis et al (14) in high Reynolds number jets in the Mach number range $1.5 < M < 2.75$.

In addition to the shape of the contours a comparison can be made of the magnitudes of the sound pressure levels in the low and high Reynolds number jets (at the same non-dimensional locations). To make a meaningful comparison 34db must be added to the present measurements to scale the ambient pressure (P_{CH} = 0.02 atmospheres) up to the exhaust pressure of atmosphere used in the high Reynolds number tests. The values of the sound pressure levels adjusted in this manner are given in parenthesis in Fig. 5. These values approach the levels measured by other researchers in high Reynolds number jets at similar non-dimensional locations. These comparisons seem to indicate that the dominant noise producing mechanisms of the low and high Reynolds number jets are equivalent.

Hot-Wire Fluctuation Amplitude Measurements

Typical profiles of hot-wire voltage fluctuations are shown in Fig. 6 for the 9.52 mm jet at Re=14,700. The shape and development of these profiles is similar to that found in many wake transition flows (for example Behrens (15)). Similar measurements were made in the 6.35 mm jet, along with extensive mean flow hot-wire measurements. The mean flow measurements were needed to establish the hot-wire sensitivity coefficients A_m and A_T in the modal decomposition of the hot-wire voltage fluctuations. Following Kovasznay(16) the hot-wire voltage fluctuation can be decomposed into mass flux and stagnation temperature fluctuations as follows:

$$\frac{e'}{E} = A_m \frac{(\rho u)'}{\bar{\rho}\bar{u}} - A_T \frac{(T_o)'}{\bar{T}_o}$$

The mass flux fluctuation sensitivity A_m was calibrated directly in the mean flowfield using the technique of Rose (17). In order to properly account for end loss effects an extension of Rose's approach was used to determine the total temperature fluctuation sensitivity, A_T.

The modal decomposition was performed at a few selected positions in the flowfield. At these locations it was established that the mass flux fluctuations were much greater than the stagnation temperature fluctuations. This led us to the approximation used by several experimenters, such as Behrens (15), that $\frac{e'}{E} \approx A_m \frac{(\rho u)'}{\bar{\rho}\bar{u}}$. It is estimated that this approximation introduces about 20% error in the present flow situation. However, the saving in experimental time is enormous.

In order to obtain the growth rates of some of the dominant spectral components, the amplitude of a bandpassed hot-wire signal was recorded at several downstream locations. A 100 hertz bandpass was used for the spectral components at 15.4, 18.2, and 19.4 kilohertz (St=.148, .176, and .185) which corresponds to major peaks in the naturally occurring spectra of the 6.35 mm jet. These measurements were made only at the radial location in the jet of maximum fluctuation of the entire spectrum. This point may not coincide with the point of maximum fluctuation for a given spectral component. Therefore, the growth rates determined here must be treated as preliminary.

The hot-wire fluctuation amplitudes were converted to mass flux fluctuations using local values of A_m. These are plotted on semi-log paper in Fig. 7. This data is consistent with the type of data found in numerous laminar instability investigations (15,18). The growth of the fluctuations is clearly exponential for several diameters. As the amplitude of the dominant spectral component reaches about 5% of the local mean, non-linear effects begin to exert a controlling influence.

The mass flux fluctuation data plotted in Fig. 7 are for the 6.35 mm jet at a Reynolds number of 28,900. Similar measurements were made at Re = 9,600 and Re = 19,300, and the growth rates were all within 30% of each other with no systematic Reynolds number dependence evidenced.

Comparison of numerical values of growth rates at Re = 28,900 with theoretical predictions are shown in Table I. Recalling from Fig. 7 that the St = 0.148 mode has the largest amplitude, it is encouraging that Tam's theory(4) does a good job of predicting its growth rate. More measurements are needed to better explain the behavior of the other modes.

St	Growth Rate $-k_I d$	
	Measured	Tam Prediction
0.148	0.58	0.64
0.176	0.44	0.76
0.185	0.44	0.82

Table 1. Comparison of measured to predicted growth rates for the 6.35 mm jet, M = 2.2.

Instability Excitation and Phase Measurements

Phase measurements were made by artificially exciting one of the dominant modes of the instability and measuring the distribution of phases either within the jet with the hot-wire or in the acoustic field with the microphone. In both cases, the phase difference between the excitation signal and the spectral component of the sensor signal provides the distribution of relative phases in the region of measurement.

The excitation is of very low amplitude and is intended only as a triggering device. In many cases the exciter produced no major influence on the microphone or hot-wire spectra. However, in the 6.35 mm jet in some instances, the excitation enhanced the mode being excited and reduced the other major modes. Fig. 8 presents the results of phase measurements for the 9.52 mm jet excited at 0.17 in which the hot-wire probe was located on the bottom shear layer of the jet at the radial location of maximum fluctuation. The probe was then moved to various downstream locations where phase differences between the exciter signal and the hot-wire signal were determined visually using a dual-beam oscilloscope. A least squares linear regression analysis gave an instability wavelength of $\lambda i/D = 3.36 \pm 0.15$ where the uncertainty limits are the 95% confidence interval for the random error of the measurement.

Besides the random error, there was a small degree of systematic error from day to day due to changes in humidity and/or the pressure balance condition. To help evaluate the systematic error, the instability wavelength was determined from measurements on several different days. This systematic error was on the order of 10% of the measured wavelength.

The 6.35 mm jet was excited at three frequencies : St = 0.15, 0.18, and 0.21. The best estimate of the instability wavelength measurements made are presented in Table II. For the indicated Strouhal numbers, wavelengths were calculated from Tam (4) and included in Table II.

		Measured		Tam Prediction
D	St	λ_i/d	C/U	λ_i/d
6.35	0.148	4.7	0.70	5.71
6.35	0.185	3.9	0.72	4.42
6.35	0.213	3.1	0.66	3.78
9.52	0.170	3.8	0.65	4.91

Table II. Comparisons of measured wavelengths with predictions of Tam (4); D = 6.35 mm, M = 2.2, U/d = 104,500/sec; D = 9.52 mm, M = 2.3, U/d = 67,800/sec.

This comparison shows reasonably good agreement between the measurements and Tam's theoretical predictions. It appears that the only major discrepency between his predictions and the measurements is in the phenomenon of mode selection. His analysis does not accurately predict the multimodal selection process. However, his single predicted amplified frequency is within the range of the measured modes.

Wave speeds, C/U, of the dominant spectral components calculated from measured wavelengths and frequencies are also included in Table II. The wavespeeds of the spectral components (in the x direction) are equal within the uncertainty of the measurements. Tam's predictions show a very weak dependence of wavespeed on the frequency of the spectral component.

Acoustic Phase Measurements

Acoustic wavelength measurements of the St = 0.18 mode were obtained with the microphone in the same manner as the hot-wire measurements. In this case, however, wavelengths were measured in both the axial and radial directions as depicted schematically in Fig. 9. The axial wavelength was determined by moving the probe along the x axis at a constant radial probe position of $r/D = 4$. The radial wavelength measurements were made at an axial location of $x/D = 11$, traversing the probe in the radial direction. The total range of measurements was $8 < x/D < 16$ and $3 < r/D < 7$.

Numerous acoustic phase measurements were made on several days using the 6.35 mm jet. From these measurements the best estimates of the wavelengths in the axial and radial direction are $\lambda x/d=4.0 \pm .4$ and $\lambda r/d=6.3 \pm .8$. The wavelength perpendicular to the acoustic wave fronts (in the zero azimuth plane) and the angle which the wavefronts make with the x axis can now be determined. These are $\lambda a/d=3.45 \pm .3$ and $\theta=57.5^{\circ} \pm 4^{\circ}$ respectively. (See Fig. 9.) A calculation of the acoustic wave speed from the frequency and measured wavelength gives a value of 332 meters/sec which agrees with the ambient speed of sound $a_o=342$ m/sec within the uncertainty of the measurements.

Another confirmation of the reliability of our results is to calculate the Mach angle associated with the convection velocity of the St=0.18 instability wave in the jet (C = 392 meters/sec). This calculation yields $\mu = \sin^{-1} \frac{a_o}{C} = 60.2 \pm 2^{\circ}$ which is within the uncertainty of the measured acoustic wave angle. These measurements indicate that the noise radiated from the jet disturbances propagates like Mach waves.

CONCLUSIONS

Hot-wire measurements in the low Reynolds number supersonic jet demonstrate that the initial disturbances, moving at a velocity greater than the ambient speed of sound, propagate and grow like instability waves. In fact the measured wave properties of the St=0.18 instability are in close agreement with the prediction of Tam (4).

There are numerous major modes in the instability process of a perfectly expanded supersonic jet which contradicts the theory of Tam (4). These instability modes were identified as the dominant noise generators of the low Reynolds number supersonic jet. Comparison of the present frequency spectra with the results from high Reynolds number jets suggests that the multimodal instability phenomenon plays an important role in the development of the turbulence in the high Reynolds number jets. This we believe is an area of analysis where both experimental and theoretical efforts need to be extended.

Microphone measurements have shown that the wavelength, wave orientation, and frequency of the acoustic radiation generated by the dominant instability agree with the Mach wave concept. The sound pressure levels measured in the low Reynolds number jet extrapolate to values approaching the noise levels measured by other experimenters with high Reynolds number jets. These measurements provide more evidence to suggest that the dominant noise generation mechanism in high Reynolds number jets is the large scale instability.

ACKNOWLEDGMENTS

This research was supported by the National Science Foundation under Grant Number GK-32686. The authors would like to acknowledge the helpful suggestions of Professor C.K.W. Tam of Florida State University and Professor W. G. Tiederman of Oklahoma State University.

REFERENCES

1. Crow, S. C. and Champagne, F. H., 1971, Orderly Structure in Jet Turbulence, J. Fluid Mech., 48, 547-591.

2. Brown, G. and Roshko, A., 1971, The Effect of Density Difference on the Turbulent Mixing Layer. AGARD Conference on Turbulent Shear Flows, Conf. Proc. No. 93, 23.

3. Winant, C. D. and Browand, F. K. 1974, Vortex Pairing, the Mechanism of Turbulent Mixing Layer Growth at Moderate Reynolds Number, to be published in the J. Fluid Mech.

4. Tam, C.K.W., 1972, On the Noise of a Nearly Ideally Expanded Supersonic Jet. J. Fluid Mech., 51, 69-95.

5. Chan, Y. Y., and Westley, R., 1973, Directional Acoustic Radiation Generated by Spatial Jet Instability. CASI Trans., 6, 36-41.

6. Sedel'nikov, T. Kh., 1967, The Frequency Spectrum of the Noise of a Supersonic Jet. Phy. of Aero. Noise, Nauka Press, Moscow (Translated NASA TTF-538, 1969, 71-75).

7. Tam, C.K.W., 1973, Supersonic Jet Noise Generated by Large Scale Disturbances. AIAA Paper 73-992.

8. Bishop, K. A., Ffowcs Williams, J. E., and Smith, W., 1971, On the Noise Sources of the Unsuppressed High-Speed Jet. J. Fluid Mech., 50, 21-31.

9. Kendall, J. M., Jr., 1967, Supersonic Boundary Layer Stability Experiments. Proc. of the Boundary Layer Trans. Study Group, Meeting II, Aerospace Rept. TR-0158, (S3816-63)-1.

10. Dosanjh, D. S. and Yu, J. C., 1968, Noise From Underexpanded Axisymmetric Jet Flow Using Radial Jet Impingement. Proc. of AFOSR-UTIAS Symposium on Aerodynamic Noise, Toronto, Canada.

11. McLaughlin, D. K., Morrison, G. L., and Troutt, T. R., 1974, Experiments on the Instability Waves in a Supersonic Jet and Their Acoustic Radiation. Oklahoma State University MAE Report ER-74-ME-5.

12. Mayes, W. H., Lanford, W. D. and Hubbard, H. H., 1959, Near Field and Far Field Noise Surveys of Solid Fuel Rocket Engines for a Range of Nozzle Exit Pressures. NASA TN D-21.

13. Yu, J. C. and Dosanjh, D. S., 1972, Noise Field of a Supersonic Mach 1.5 Cold Model Jet. J. Acous. Soc. Amer., 51, 1400.

14. Louis, J. F., Letty, R. P. and Patel, J. R., 1972, A Systematic Study of Supersonic Jet Noise, AIAA Paper 72-641.

15. Behrens, W., 1968, Far Wake Behind Cylinders at Hypersonic Speeds: II Stability. AIAA J., 6, 225-232.

16. Kovasznay. L. S. G., 1953, Turbulence in Supersonic Flow. J. Aero. Sci., 20 No. 10, 657-675.

17. Rose, W. C., 1973, The Behavior of a Compressible Turbulent Boundary Layer in a Shock-Wave-Induced Adverse Pressure Gradient. NASA TN D-7092.

18. McLaughlin, D. K., 1971, Experimental Investigation of the Stability of the Laminar Supersonic Cone Wake. AIAA J., 9, 696-702.

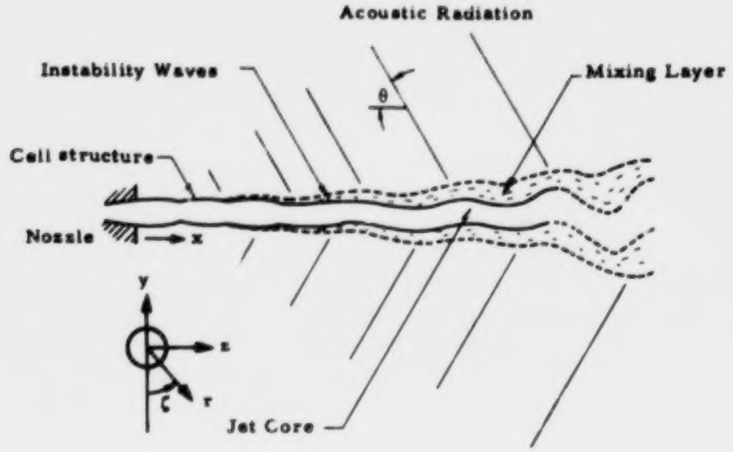
Acoustic Radiation
Instability Waves
Mixing Layer
θ
Cell structure
Nozzle
x
y
z
r
ζ
Jet Core

Figure 1. General features of the supersonic jet and its acoustic radiation.

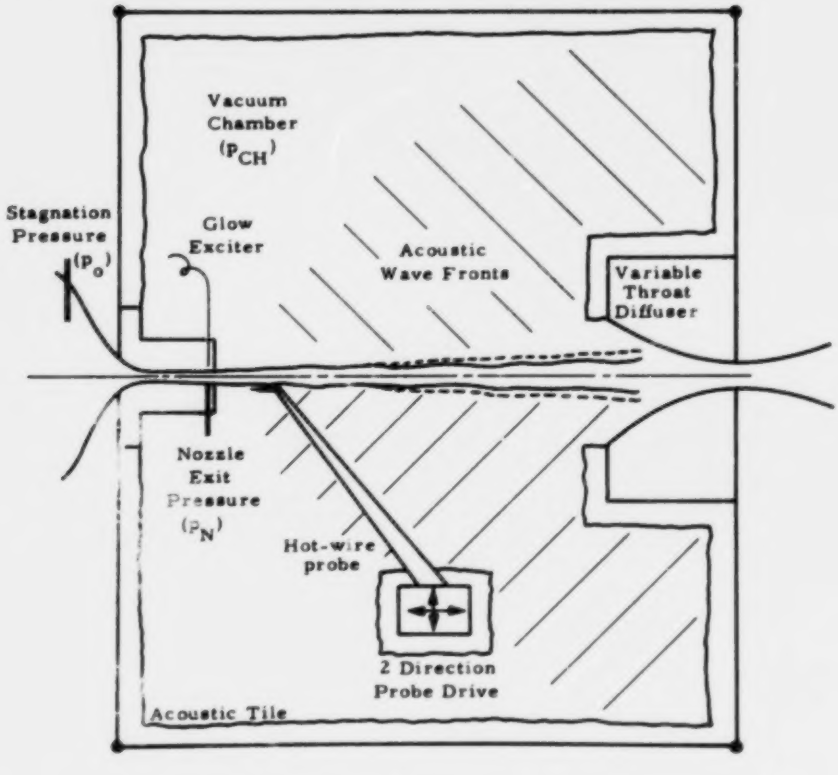
Vacuum Chamber (P_{CH})
Stagnation Pressure (P_o)
Glow Exciter
Acoustic Wave Fronts
Variable Throat Diffuser
Nozzle Exit Pressure (P_N)
Hot-wire probe
2 Direction Probe Drive
Acoustic Tile

Figure 2. Schematic of the supersonic jet test facility.

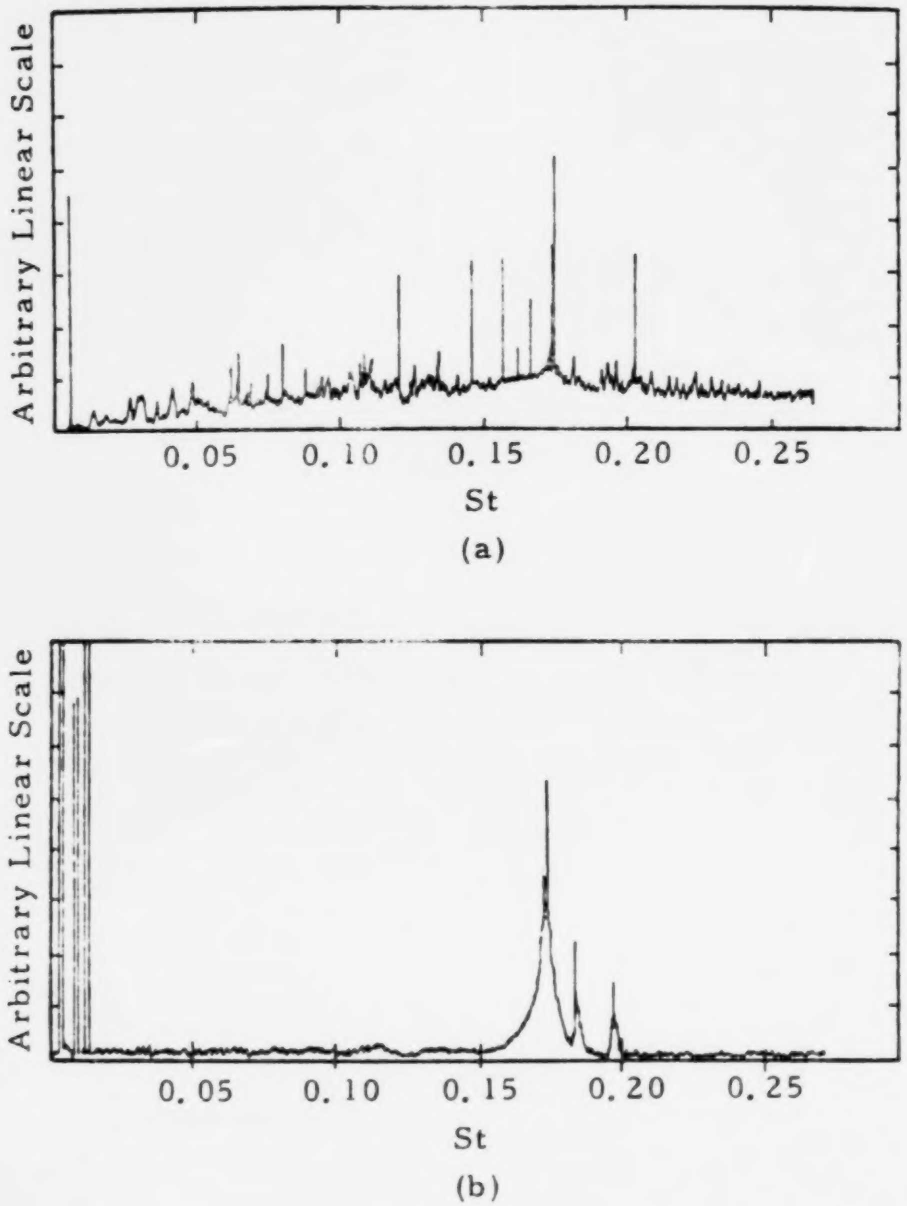

(a)

(b)

Figure 3. Microphone spectra in the near radiation field of the supersonic jet. The band pass is 6 hz and the sweep rate is 1000 hz/min. (a) D = 6.35 mm, Re = 14,400, (b) D = 9.52 mm, Re = 11,000.

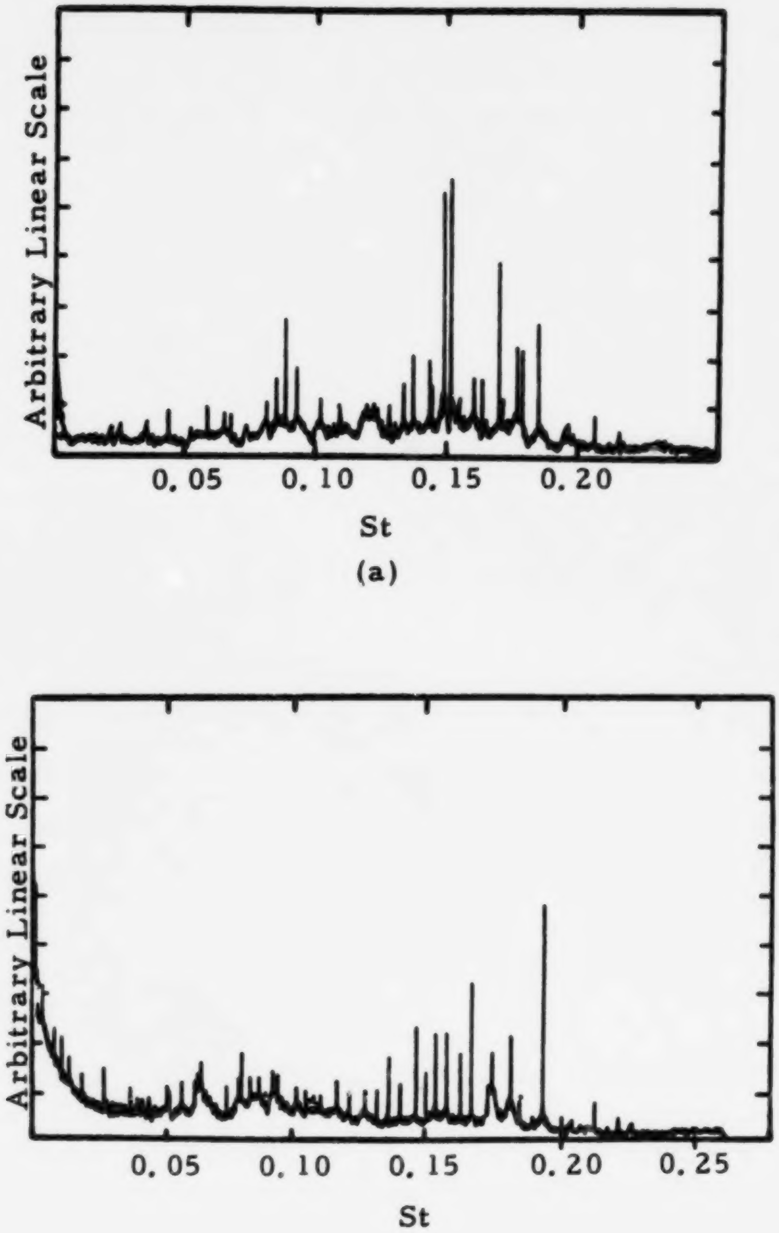

(a)

(b)

Figure 4. Spectra of hot-wire voltage fluctuations at Re = 14, 600 recorded on different days. (D = 6.35 mm, $(x/D)_{probe}$ = 5).

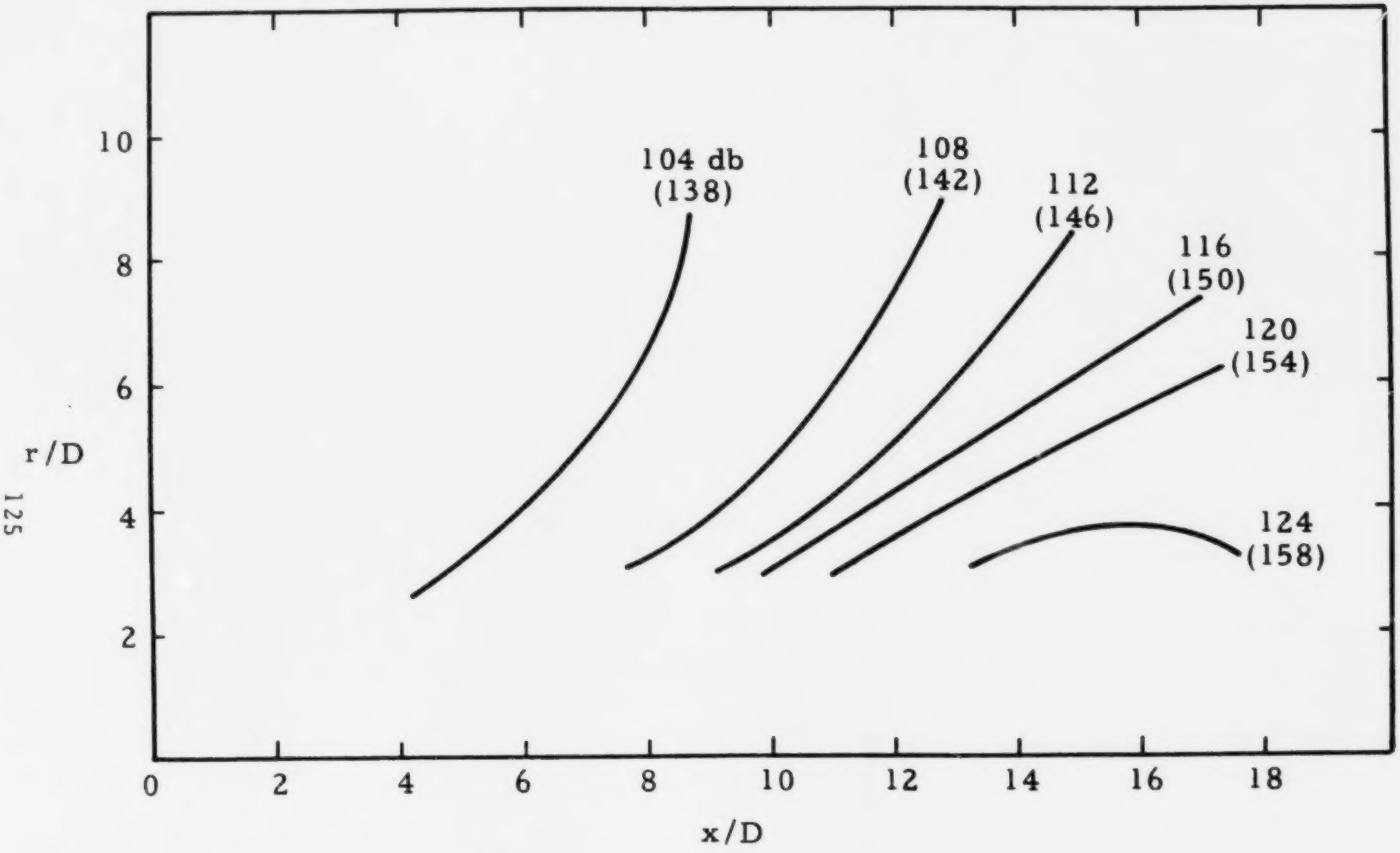

Figure 5. Microphone constant amplitude noise contours. Amplitudes scaled to atmospheric exhaust pressure in parentheses. Re = 12,600, D = 6.35 mm, $p_N/p_{CH} = 1.01$.

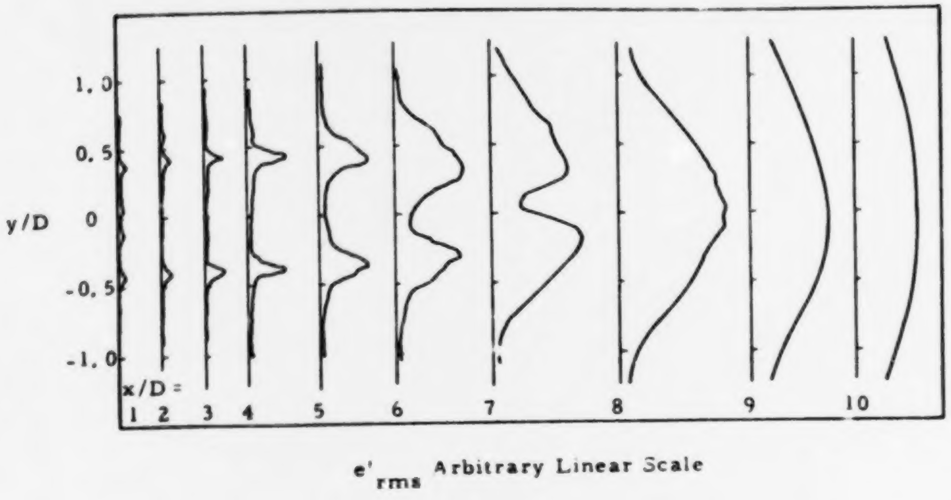

Figure 6. Profiles of root mean square hot-wire voltage fluctuations at various downstream locations in the jet. D = 9.52 mm, Re = 14,700.

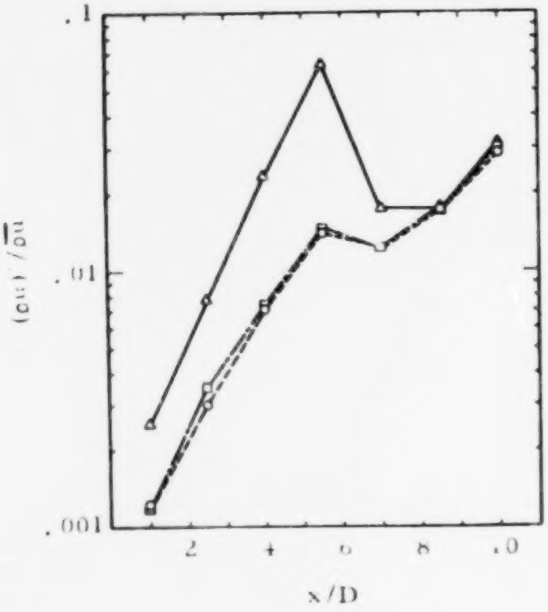

Figure 7. Axial distribution of peak hot-wire voltage fluctuations for a 100 Hz wide band centered about △ St = 0.148, □ St = 0.176, ○ St = 0.185.

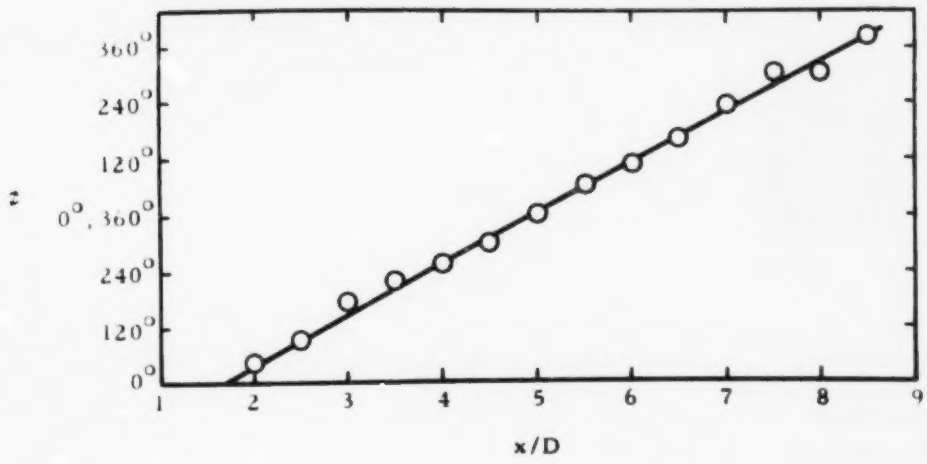

Figure 8. Axial distribution of hot-wire relative phase (ϕ). D = 9.52 mm, Re = 14,700 and St = 0.17.

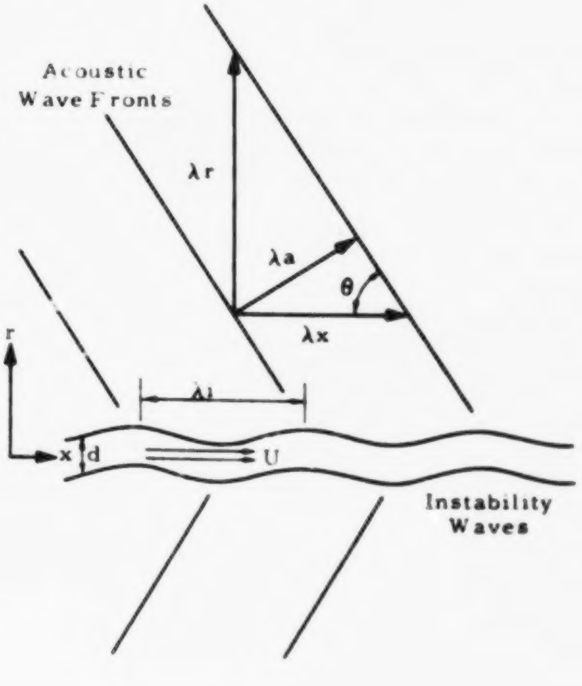

Acoustic Wave Fronts
λr
λa
θ
λx
r
λi
x
d
U
Instability Waves

Figure 9. Orientation of acoustic and instability waves.

ACOUSTICAL THEORY OF TURBULENCE

by

Czeslaw P. Kentzer

School of Aeronautics and Astronautics
Purdue University, Lafayette, Indiana

I. INTRODUCTION

The internally generated sound in turbulent flows represents one of the most difficult problems of analysis for the following reasons: (1) the distinction between sound and the so-called "pseudo-sound" in turbulence is not clear; (2) generation, absorption, and propagation of sound is strongly coupled to the dynamics of the mean and fluctuating components of turbulent flows; (3) turbulence itself is a phenomenon not yet well understood.

The objectives of the research reported here are: (1) to provide for a common theory of sound and turbulence, a theory derived from the Navier-Stokes equations of fluid mechanics, and based on a mathematical formalism common to acoustics and turbulence, (2) to separate the turbulent velocity field into solenoidal and irrotational parts, (3) to separate turbulent fluctuations into those which do, and do not, propagate relative to the fluid thus allowing us to define sound as those fluctuations which propagate relative to the fluid as a convected sound radiation field.

A convenient mathematical formalism, common to acoustics and fluid mechanics of turbulence, is the normal mode (characteristic wave) analysis. While there have been in the past several attempts to represent turbulence as a random superposition of characteristics waves, see, e.g., Lumley (1967) and Landahl (1967), the progress was seriously affected by the fact that no satisfactory closed system for Lumley's "characteristic eddies" or Landahl's characteristic waves (eigensolutions of the Orr-Sommerfeld equation) has yet been found. In contrast, in the work of Chu and Kovásznáy (1958), and Kentzer (1973), the Fourier modes, as characteristic solutions, play a prominent role in the decomposition of turbulent fields into vortical, entropy, and sound modes. The Fourier modes of the locally linearized compressible Navier-Stokes equations offer the most useful representation because, (1) - explicit expressions for the Fourier modes are known, and, (2) - the Fourier modes form a complete orthogonal set of eigenfunctions suitable for use as vector basis in the expansion of the nonlinear fluctuating turbulent field. In the sequel we shall make use of the characteristic waves (Fourier modes) to form an expansion of the nonlinear solution for the turbulent fluctuations. We shall then interpret the squares of the absolute values of the wave amplitudes as the energy density or the probability density distribution function. We shall indicate how the use of distribution functions suffices to describe turbulence statistically, and how to separate the effects of the acoustic mode from other turbulent fluctuations. In lieu of the method of solution of the set of integro-differential equations for the distribution functions, we shall discuss possible forms of the distribution functions which may be useful as approximations to be used in modeling of turbulence and of sound generated by it.

II. CHARACTERISTIC WAVES AS NORMAL MODES

We are concerned here with solutions u_i, $i = 1,\dots,5$, of a system of equations governing viscous, heat conducting, compressible gas, the Navier-Stokes system of fluid mechanics. As it is customary, we shall separate the vector field u_i into the slowly varying part $\overline{u}_i$ and the turbulent fluctuations u_i', where the overbar indicates the result of averaging, and $\overline{u_i'} = 0$. Substituting $u_i = \overline{u}_i + u_i'$ into the Navier-Stokes equations and averaging, results in the so-called Reynolds system for the average or mean turbulent properties. To determine the fluctuations u_i', we subtract the averaged equations from the full equations and obtain, modulo terms quadratic in perturbations,

$$\frac{\partial u_i'}{\partial t} + L(u_i') + B(u_i',u_i') = 0 \tag{1}$$

where

$$L(u_i') = \begin{bmatrix} \vec{q}\cdot\nabla, & c\,\frac{\partial}{\partial x}, & c\,\frac{\partial}{\partial y}, & c\,\frac{\partial}{\partial z}, & 0 \\ c\frac{\partial}{\partial x}, & \vec{q}\cdot\nabla-\nu\nabla^2-\frac{\nu\partial^2}{3\partial x^2}, & -\frac{\nu}{3}\frac{\partial^2}{\partial x\partial y}, & -\frac{\nu}{3}\frac{\partial^2}{\partial x\partial z}, & c\sqrt{\gamma-1}\,\frac{\partial}{\partial x} \\ c\frac{\partial}{\partial y}, & -\frac{\nu}{3}\frac{\partial^2}{\partial x\partial y}, & \vec{q}\cdot\nabla-\nu\nabla^2-\frac{\nu\partial^2}{3\partial y^2}, & -\frac{\nu}{3}\frac{\partial^2}{\partial y\partial z}, & c\sqrt{\gamma-1}\,\frac{\partial}{\partial y} \\ c\frac{\partial}{\partial z}, & -\frac{\nu}{3}\frac{\partial^2}{\partial x\partial z}, & -\frac{\nu}{3}\frac{\partial^2}{\partial y\partial x}, & \vec{q}\cdot\nabla-\nu\nabla^2-\frac{\nu\partial^2}{3\partial z^2}, & c\sqrt{\gamma-1}\,\frac{\partial}{\partial z} \\ 0, & c\sqrt{\gamma-1}\,\frac{\partial}{\partial x}, & c\sqrt{\gamma-1}\,\frac{\partial}{\partial y}, & c\sqrt{\gamma-1}\,\frac{\partial}{\partial z}, & \vec{q}\cdot\nabla-\frac{\gamma\nu}{Pr}\nabla^2 \end{bmatrix} \begin{Bmatrix} \rho \\ u \\ v \\ w \\ T \end{Bmatrix}$$

$$B(u_i',u_i') = \begin{Bmatrix} c[u\rho_x+v\rho_y+w\rho_z+\rho(u_x+v_y+w_z)] \\ c[uu_x+vu_y+wu_z+\sqrt{\gamma-1}T\rho_x]+\nu\rho[\nabla^2u+\frac{1}{3}(u_{xx}+v_{xy}+w_{xz})] \\ c[uv_x+vv_y+wv_z+\sqrt{\gamma-1}T\rho_y]+\nu\rho[\nabla^2v+\frac{1}{3}(u_{xy}+v_{yy}+w_{yz})] \\ c[uw_x+vw_y+ww_z+\sqrt{\gamma-1}T\rho_z]+\nu\rho[\nabla^2w+\frac{1}{3}(u_{xz}+v_{yz}+w_{zz})] \\ \frac{\gamma\nu}{Pr}\rho\nabla^2T-\nu\sqrt{\gamma-1}[2(u_x^2+v_y^2+w_z^2)+(v_x+u_y)^2+(w_y+v_z)^2+(u_z+w_x)^2-\frac{2}{3}(u_x+v_y+w_z)^2] \end{Bmatrix}$$

Here L and B are a linear and bilinear differential operators with respect to the position variable $\vec{x}$, $\overline{T}$ = mean temperature, c = mean isothermal speed of sound = $(R\overline{T})^{1/2}$, $\vec{q}$ = mean velocity vector, ∇ = vector differential operator, ∇^2 = Laplace's operator, $\nu = \overline{\mu}/\overline{\rho}$ = kinematic viscosity, γ = ratio of specific heats, Pr = Prandtl number, and where primes have been dropped from the nondimensionalized fluctuations,

$$u_i' = \left[\frac{\rho'}{\bar{\rho}}, \frac{u'}{c}, \frac{v'}{c}, \frac{w'}{c}, \frac{T'}{\bar{T}\sqrt{\gamma-1}}\right] = (\rho, u, v, w, T), \quad i = 1,\ldots,5 .$$

Thus ρ, u, v, w, T are the nondimensional fluctuations in density, velocity, and temperature, respectively.

Since an exact solution of Equ. (1) is out of question, retaining only the linear and quadratic terms in the fluctuations will suffice for the purpose of discussion. The vector B may be interpreted as $B = -[\dot{m}, F_x, F_y, F_z, \dot{Q}]$, a negative of a source term vector representing mass-like, force-like, and heat-like effects of the wave interactions.

A standard method of solution of nonlinear dynamical systems such as Equ. (1) is the Kryloff-Bogoliuboff procedure of expansion of the solution u_i' in terms of eigensolutions of the linear part of Equ. (1). We shall investigate next the solutions of the linear part

$$\frac{\partial u_i'}{\partial t} + L(u_i') = 0 \quad , \quad B(u_i', u_i') = 0 \quad ,$$

which may be assumed in the form

$$u_j' = \sum_{\alpha} \sum_{\vec{k}} C_\alpha(\vec{k})\ \phi_{\alpha j}(\vec{k})\ \exp\left[\Gamma_\alpha t + i(\vec{x} \cdot \vec{k} - \omega_\alpha t)\right] \tag{2}$$

where, in case of a continuous spectrum, the summation over the wavenumber $\vec{k}$ is to be replaced by integration. The subscript α allows for separate contributions to the variable u_j' to be made by five different modes of propagation, $\alpha = 1,\ldots,5$. Equation (2) is a "local" Fourier representation in which the quantities C_α, $\phi_{\alpha j}$, Γ_α, ω_α are considered to be slowly varying functions of space and time. Substitution of the expansion (2) into the linear part of (1) leads to a matrix equation, $||A_{ij}||\ C_\alpha \phi_{\alpha j} = 0$. The matrix A_{ij} is symmetric but not Hermitian. The condition for the existence of nontrivial solutions of the matrix equation is the vanishing of the determinant of the matrix A_{ij}. Under the assumption that $V \cdot Pr = 1$, where $V = 2 + \mu_2/\mu_1$, μ_1, μ_2 are the first and second coefficients of dynamic viscosity (bulk viscosity $= \frac{2}{3}\mu_1 + \mu_2 = \mu_1 (V - 4/3) \overset{>}{=} 0$ if $V \overset{>}{=} 4/3$, thus $V = 4/3$ corresponds to a Stokesian fluid), we may factor out the determinant as follows:

$$\det A_{ij} = (\lambda + \nu k^2)^2 (\lambda + \nu k^2/Pr)[\lambda(\lambda + \gamma\nu k^2/Pr) + a^2 k^2] = 0 \tag{3}$$

where $\lambda = \Gamma + i(u_m k_m - \omega)$, $m = 1,2,3$, $a^2 = \gamma R\bar{T}$ = square of the mean adiabatic speed of sound. Equation (3) is formally equivalent to a characteristic determinant of the theory of characteristics in the gasdynamic case, $\nu = 0$. In analogy to gasdynamics we shall refer to the waves corresponding to the vanishing of the first (double) factor as the vorticity waves, the waves corresponding to the second (linear) factor will be referred to as entropy waves, and the quadratic factor gives rise to pressure or acoustic waves. The five roots of the determinant (3) will be distinguished by subscript α, $\alpha = 1,\ldots,5$. The roots are:

$$\begin{array}{llll} \alpha = 1,2: & \Gamma_\alpha = -\nu k^2, & \omega_\alpha = u_m k_m, & \text{vorticity modes} \\ \alpha = 3: & \Gamma_\alpha = -\nu k^2/Pr, & \omega_\alpha = u_m k_m, & \text{entropy mode} \\ \alpha = 4,5: & \Gamma_\alpha = -\gamma\nu k^2/2Pr, & \omega_\alpha = u_m k_m \pm ak(1-K^2)^{1/2}, & \text{acoustic modes} \end{array} \qquad (4)$$

where $K = \gamma\nu k/2aPr$ = Knudsen number based on the mean wavelength, $2\pi/k$, or the ratio of the molecular mean free path to the mean wavelength. With five sets of Γ_α and ω_α uniquely determined from Equ. (4), one may return to the matrix equation and determine a set of eigenvectors $\phi_{\alpha j}$. Since the matrix equation is homogeneous, the components of such a vector may be determined only up to a common factor. We may, therefore, leave C_α, a wave amplitude, arbitrary and choose the eigenvectors $\phi_{\alpha j}$ so that

$$\sum_j \phi_{\alpha j}\, \phi^*_{\alpha j} = |\phi_{\alpha j}|^2 = 1 \qquad \text{(normalization conditions)} \qquad (5)$$

where the asterisk denotes complex conjugate. With each vector $\phi_{\alpha j}$ corresponding to a different root of the determinant (3), the five eigenvectors may further be chosen so that they are mutually orthogonal, i.e.,

$$\sum_j \phi_{\alpha j}\, \phi_{\beta j} = 0 \quad , \alpha \neq \beta \qquad \text{(orthogonality conditions)} \qquad (6)$$

Further, because of the choice of the manner of nondimensionalization of the fluctuations, the matrix A_{ij} is symmetric, and $\phi^*_{\alpha j}$ serves as a solution of the adjoint equation. The set of the five eigenvectors $\phi_{\alpha\beta}$ represents a matrix of participation coefficients, giving the β-component of the normalized amplitude of the fluctuation vector $u'_j = (\rho,u,v,w,T)$ in the α-mode of propagation. The complete set of eigenvectors is

$$\left.\begin{aligned}
\phi_{1\beta} &= [0,\ k_2k_3,\ -k_1k_3,\ 0,\ 0]/[k_3^2(k_1^2 + k_2^2)]^{1/2} \\
\phi_{2\beta} &= [0,\ -k_1k_3,\ -k_2k_3,\ k_1^2+k_2^2,\ 0]/[k^2(k_1^2 + k_2^2)]^{1/2} \\
\phi_{3\beta} &= [1,\ -2ik_mK/k\sqrt{\gamma},\ -1/\sqrt{\gamma-1}]/[\frac{\gamma}{\gamma-1} + \frac{4K^2}{\gamma}]^{1/2} \\
\phi_{4\beta} &= [-g,\ -ik_m\gamma c,\ g^{*}\sqrt{\gamma-1}]/[2\gamma a^2k^2]^{1/2} \\
\phi_{5\beta} &= [-g^{*},\ -ik_m\gamma c,\ g\sqrt{\gamma-1}]/[2\gamma a^2k^2]^{1/2}
\end{aligned}\right\} \quad (7)$$

where $m = 1,2,3$, and $g = -ak[K+i(1-K^2)^{1/2}]$, $k = |\vec{k}|$.

The vectors $\phi_{\alpha\beta}$ satisfy the normalization and orthogonality conditions, Equs. (5) and (6). In addition, we observe that

$$\phi_{\alpha\beta}(k_m) = \phi^{*}_{\alpha\beta}(-k_m) \quad \text{for} \quad \alpha = 1,2,3,$$

$$\phi_{4\beta}(k_m) = \phi^{*}_{5\beta}(-k_m)\ ,\ \phi_{5\beta}(k_m) = \phi^{*}_{4\beta}(-k_m)$$

while from Equ. (4) we have

$$\Gamma_\alpha(k_m) = \Gamma_\alpha(-k_m) \quad \text{for} \quad \alpha = 1,\ldots,5$$

$$\omega_\alpha(k_m) = -\ \omega_\alpha(-k_m) \quad \text{for} \quad \alpha = 1,2,3$$

$$\omega_4(k_m) = -\ \omega_5(-k_m),\ \omega_5(k_m) = -\ \omega_4(-k_m) \quad .$$

Thus, to assure reality of solutions u_i' of Equ. (1) it suffices to impose the condition that

$$C_\alpha(k_m) = C^{*}_\alpha(-k_m) \text{ for } \alpha = 1,2,3, \text{ and } C_4(k_m) = C^{*}_5(-k_m),\ C_5(k_m) = C^{*}_4(-k_m)\ .$$

The associated state vectors, $\phi_{\alpha j}(k_m)\exp[\Gamma_\alpha t + i(x_mk_m - \omega_\alpha t)]$ represent wave motions of α-mode of propagation carrying perturbations ρ,u,v,w,T consistent with the constraints of the conservation laws of fluid mechanics, that is, the state vectors are solutions of the linearized equations, and they satisfy the exact nonlinear equations if their amplitudes are infinitesimal. Thus one may interpret the wave amplitudes C_α as the number of such infinitesimal waves in the differential neighborhood dx_mdk_mdt of the point in question.

As observed by Chu and Kovásznáy (1958), the vortical modes correspond to an incompressible flow. This is reflected by the fact that fluctuations in density and temperature are absent from the first two modes, $\alpha = 1,2$. Observe that the participation coefficients ϕ_{11}, ϕ_{15}, ϕ_{21}, and ϕ_{25} are equal to zero. We observe further that the velocity field induced by the vorticity modes is orthogonal to the wavenumber vector, or that the velocity represents a transverse motion in the plane of the wave. The remaining modes, $\alpha = 3,4,5$ give rise to a velocity field directed along wavenormals. Velocity induced by the entropy mode, $\alpha = 3$, is of order K and hence is negligible except at the shortest wavelength on the order of the molecular mean free path. Taking the divergence and curl of the state vector, it is easy to show that the velocity field induced by the vortical modes, $\alpha = 1,2$, is solenoidal (nondivergent), while the fields induced by the entropy, $\alpha = 3$, and acoustic modes, $\alpha = 4,5$, are irrotational (potential fields). Thus we have a simple procedure for a formal separation of velocity into solenoidal and irrotational fields - it suffices to separate the vortical modes ($\alpha = 1,2$) from the remaining modes ($\alpha = 3,4,5$).

If $\vec{u}_\alpha$ represents the velocity induced by the α-mode, then, taking a curl of $\vec{u}_\alpha$ we have

$$\mathrm{curl}\ \vec{u}_1 = -ik\vec{u}_2, \quad \mathrm{curl}\ \vec{u}_2 = ik\vec{u}_1, \quad \mathrm{curl}\ \vec{u}_3 = \mathrm{curl}\ \vec{u}_4 = \mathrm{curl}\ \vec{u}_5 = 0 .$$

Now we may introduce the concept of helicity, defined as a scalar product of velocity with its curl. Thus

$$\vec{u}_1 \cdot \mathrm{curl}\ \vec{u}_1 = -ik\vec{u}_1 \cdot \vec{u}_2 = 0, \quad \vec{u}_2 \cdot \mathrm{curl}\ \vec{u}_2 = ik\vec{u}_2 \cdot \vec{u}_1 = 0$$

since the vectors $\vec{u}_1$ and $\vec{u}_2$ are orthogonal, and the helicity of any single and separate mode, $\alpha = 1,\dots,5$, is identically zero. However, the helicity of a sum of two waves of different wavenumbers or belonging to different modes does not vanish in general. Consequently, nonzero helicity may be obtained simply by a linear superposition of plane waves, a fact of importance in representing turbulence by plane waves. As shown by Moffatt (1969), the volume integral of helicity is a constant of motion of inviscid flows, and it serves as a convenient measure of the degree of linkage or knottedness of vortex lines in turbulence.

We return now to the problem of determination of mode amplitudes C_α. Since C_α cannot be determined from the linear homogeneous equation, we allow C_α to depend on space and time, and we substitute expression (2) into Equ. (1) making use of the fact that u_j' satisfies the linear part of (1). The result is

$$\sum_\alpha \sum_{\vec{k}} \frac{\partial C_\alpha}{\partial t} \phi_{\alpha j} \exp[\Gamma_\alpha t + i(x_m k_m - \omega_\alpha t)] + B(u_i', u_i') - \overline{B(u_i', u_i')} = 0 .$$

We may make use now of the orthogonality of the complex exponentials and of the vectors $\phi_{\alpha j}$ to arrive at an expression for $f_\alpha = C_\alpha C_\alpha^* = |C_\alpha|^2$:

$$\frac{\partial_e f_\alpha}{\partial t} = \sum_\beta \sum_\delta \iint d\vec{k}_2 d\vec{k}_3 \delta(\vec{k}_1-\vec{k}_2-\vec{k}_3)\delta[\omega_\alpha(\vec{k}_1) - \omega_\beta(\vec{k}_2) - \omega_\delta(\vec{k}_3)]$$

$$\times K(\vec{k}_1,\vec{k}_2,\vec{k}_3)[f_\beta(\vec{k}_2)f_\delta(\vec{k}_3) - f_\alpha(\vec{k}_1)f_\beta(\vec{k}_2) - f_\alpha(\vec{k}_1)f_\delta(\vec{k}_3)] \qquad (8)$$

where the kernel K depends on the vector B. The properties of the derivative $\partial_e f_\alpha/\partial t$ and of the other possible correlation functions are discussed, e.g., by Davidson (1967). Since C_α and f_α remain rigorously constant in the linear case (i.e., when the amplitudes C_α are negligibly small), and $\partial_e f_\alpha/\partial t$ depends only on the bilinear terms B, we shall interpret Equ. (8) as giving the time rate of change of the square of the wave amplitudes solely due to wave interactions (wave encounters, in analogy to molecular encounters in the kinetic theory of gases). Thus the mechanism of wave interactions is specified completely by the Navier-Stokes system through the vector B. When higher order terms are retained, e.g. trilinear terms, then additional interaction terms appear which are trilinear in f_α.

For the sake of brevity, the expression for $\partial_e f_\alpha/\partial t$ is not given here in full. It suffices to say that it takes the form of integrals which are bilinear in f_α, and represents three-wave resonance interactions. It appears that a sufficient condition for vanishing of the interaction integral (8) is that f_α be of the Rayleigh-Jeans form, that is, that f_α be equal to the inverse of a most general linear combination of interaction invariants. Two such invariants are known, namely $\vec{k}_1 - (\vec{k}_2+\vec{k}_3) = 0$ and $\omega_1-(\omega_2+\omega_3) = 0$. These are the three-wave resonance conditions representing conservation of momentum and energy.

III. WAVE-PARTICLE DUALITY

Plane wave representation of local disturbances is inconvenient in as much as a train of plane waves fills the entire space. In other words, when the wavenumber vector k_m is specified exactly, then the position of the disturbance, the vector x_m, is left indeterminate because the vectors x_m and k_m are canonically conjugate. This difficulty is simply a consequence of the Fourier representation. To circumvent this difficulty we shall assume the continuity of the distribution of waves so as to allow for differentiation of the phase function $(x_m k_m - \omega t)$ with respect to x_m and k_m. Then we may invoke the theory of group velocity and introduce wave packets (pseudo- or quasi-particles) whose motion is given by Hamiltonian canonical equations:

$$U_{\alpha j} = \frac{dx_j}{dt} = \frac{\partial\omega_\alpha}{\partial k_j} \quad , \quad F_{\alpha j} = \frac{dk_j}{dt} = -\frac{\partial\omega_\alpha}{\partial x_j}$$

where $U_{\alpha j}$ is the group velocity and $F_{\alpha j}$ is the pseudo-force acting on a quasi-particle associated with the α-mode of propagation. Using Equs. (4) we evaluate the derivatives of the frequency and obtain

$$U_{\alpha j} = \bar{u}_j + c_\alpha a(k_j/k)(1-2K^2)(1-K^2)^{-1/2} \tag{9}$$

$$F_{\alpha j} = -\left[k_m \frac{\partial \bar{u}_m}{\partial x_j} + c_\alpha k(1-K^2)^{-1/2} \frac{\partial a}{\partial x_j}\right], \quad j = 1,2,3 \tag{10}$$

where $c_\alpha = 0$ for $\alpha = 1,2,3$, and $c_4 = 1$, $c_5 = -1$.

We observe that only the quasi-particles associated with the acoustic modes, $\alpha = 4,5$, have non-zero group velocity relative to the fluid. Consequently, any property of the wave motion, e.g. energy or pressure fluctuation, will be transported relative to the fluid only by wave motion in the acoustic mode. Thus the acoustic modes represent radiation sound field propagating relative to the fluid, while the remaining modes, $\alpha = 1,2,3$, represent pseudo sound (fluctuations which remain stationary relative to the fluid and are convected by the fluid motion). Examination of the participation coefficients $\Phi_{\alpha j}$, Equ. (7), reveals that the acoustic modes carry perturbations in all the primitive variables (density, velocity, and temperature, therefore also in pressure). The pseudo-sound also involves fluctuations in all primitive variables, viz., velocity fluctuations are associated with both the vorticity and entropy modes, while density and temperature fluctuations are associated with the entropy mode.

Borrowing the idea from quantum mechanics, we shall set the energy of a quasi-particle, ε, as equal to a multiple of $h\omega/2\pi$, say $mh\omega/2\pi$, where h = Planck's constant, and nondimensionalize ε by dividing it by the fundamental quantum of energy, $h\omega/2\pi$. Thus $\varepsilon = m$. Since energy must be proportional to the amplitude squared and $|c_\alpha|^2 = f_\alpha$ is nondimensional, we could normalize f_α so that $f_\alpha(\omega) = m_\alpha(\omega)$. Then f_α may be interpreted as either a nondimensional energy density in a normal mode of frequency ω per unit range of ω (in units of fundamental quantum of energy) or a nondimensional particle number density if all "particles" have the same ground level energy. The latter interpretation was used by Kentzer (1973). However, the former choice seems less artificial, and we shall set

$$|c_\alpha|^2 = f_\alpha(x_m,k_m,t) = \text{energy probability density.}$$

The integral,

$$e_\alpha(x_m,t) = \int f_\alpha(x_m,k_m,t)\,dk_m = e_\alpha \int f'_\alpha\,dk_m, \quad \int f'_\alpha\,dk_m = 1,$$

will be referred to as the energy probability density of the α-mode in the physical space or, simply, the energy density. The energy spectrum f_α must satisfy obvious requirements, namely

$$\text{(a)}\quad \lim_{k_m \to 0} \omega_\alpha f_\alpha = 0 \qquad\qquad \text{(b)}\quad \lim_{\substack{k_m \to k_{max} \\ k_{max} \to \infty}} \omega_\alpha f_\alpha = 0$$

$$\text{(c)}\quad \int \omega_\alpha f_\alpha \, dk_m < \infty \qquad (11)$$

The maximum magnitude of wavenumber, k_{max}, is determined from the condition that all group velocities are equal at $K^2 = 1/2$ (observe that at $K = 1$ group velocities of acoustic modes become infinite). Thus $k_{max} = \frac{2\sqrt{2}aPr}{\gamma\nu}$. The requirement (b) represents the condition that, at very high frequencies, the energy in a collective wave motion becomes indistinguishable from (or is dissipated or converted into) the random thermal motion of the gas molecules.

Since the energy density f_α is a function carried by the quasi-particles in the phase-space, we have upon differentiation

$$\frac{\partial f_\alpha}{\partial t} + \frac{\partial f_\alpha}{\partial x_j}\frac{dx_j}{dt} + \frac{\partial f_\alpha}{\partial k_j}\frac{dk_j}{dt} = 0$$

in absence of wave interactions along the trajectories of quasi-particles. Here dx_j/dt and dk_j/dt are given by Equs. (9) and (10). To account for wave interactions, we equate the above derivative to the interaction terms given by Equ. (8), that is,

$$\frac{\partial f_\alpha}{\partial t} + \frac{\partial f_\alpha}{\partial x_j}\frac{\partial \omega_\alpha}{\partial k_j} - \frac{\partial f_\alpha}{\partial k_j}\frac{\partial \omega_\alpha}{\partial x_j} = \frac{\partial_e f_\alpha}{\partial t} \qquad (12)$$

This is the integro-differential equation of Maxwell-Boltzmann type for the energy probability distribution functions $f_\alpha(x_m, k_m, t)$. While there is no hope ever to find a set of functions f_α, $\alpha = 1, \ldots, 5$, as solutions of Equ. (12) except in exceptionally simple cases, the form of the interaction integral $\partial_e f_\alpha/\partial t$, as indicated in Equ. (8), is of importance to the theory of turbulence. For, in the case of turbulence governed by the Navier-Stokes theory, the nonlinear interaction terms are derivable in terms of one-point distribution functions and joint probabilities are expressible as products of probabilities of single events. Thus multi-point distribution functions, satisfying a hierarchy of coupled equations of the Bogoliuboff-Born-Green-Kirkwood-Yvon (BBGKY hierarchy) and introduced by Lundgren (1967), describe evidently a turbulence model of order higher than that admitted by the Navier-Stokes theory. This observation partially justifies the use of one-point distribution functions in modeling of turbulence.

Equation (12), which forms the basis of a kinetic theory of a random motion of quasi-particles (turbulent wave packets), describes a theory of approximate constitutive equations for a turbulent medium. In particular, the wave interaction terms, $\partial_e f_\alpha/\partial t$ in Equ. (8), express a special kind of fading memory which makes triplets of resonating waves, which otherwise have well determined histories, instantly loose the correlations their encounters give them. The frequency with which such three-wave resonances occur governs the rate of fading of the memory or the rate at which turbulent correlations decrease with time. The theory of constitutive equations based on the distribution functions f_α has two aspects. First, if the form of f_α is assumed known, than, in principle, any average turbulent property may be calculated, e.g., Reynolds stresses $\rho\overline{u_i'u_j'}$ or the turbulent energy $(\overline{u_i'^2})$. Secondly, taking moments of Equ. (12) will generate convective transport equations for arbitrary average turbulent property consistent with the assumed form of the distribution function f_α. If the form of f_α is postulated in terms of the various moments of f_α, then the space and time development of f_α could be calculated by solving the appropriate convective transport equation for the needed moments.

IV. AVERAGES AND THE CONVECTIVE TRANSPORT EQUATION

Defining averages of any property ψ, a function of the wavenumber k_m, as

$$\overline{\psi} = \int \psi(k_m) f_\alpha \, dk_m \Big/ \int f_\alpha \, dk_m = \frac{1}{e_\alpha} \int \psi(k_m) f_\alpha \, dk_m ,$$

multiplying Equ. (12) by $\psi(k_m)$ and integrating with respect to k_m gives

$$\frac{\partial}{\partial t}[e_\alpha \overline{\psi}] + \frac{\partial}{\partial x_m}\left[e_\alpha \left(\overline{\frac{\partial \omega_\alpha}{\partial k_m}}\right)\right] - e_\alpha \left[\left(\overline{\frac{\partial \psi}{\partial t}}\right) + \left(\overline{\frac{\partial \psi}{\partial x_m}\frac{\partial \omega_\alpha}{\partial k_m}}\right) - \left(\overline{\frac{\partial \psi}{\partial k_m}\frac{\partial \omega_\alpha}{\partial x_m}}\right)\right] = \Delta_\alpha(\psi)$$

where

$$\Delta_\alpha(\psi) = \int \psi(k_m) \frac{\partial_e f_\alpha}{\partial t} dk_m \quad .$$

This is the turbulent convective transport equation for the arbitrary function $\psi(k_m)$. In particular, if $\psi = 1$, we have

$$\frac{\partial e_\alpha}{\partial t} + \frac{\partial}{\partial x_m}[e_\alpha \overline{U}_{\alpha m}] = \int \frac{\partial_e f_\alpha}{\partial t} dk_m = \Delta_o(1)$$

where $e_\alpha \overline{U}_{\alpha m} = e_\alpha(\overline{u}_m + d_{\alpha m})$, and where the acoustic diffusion vector

$$d_{\alpha m} = c_\alpha a \int \frac{k_m}{k} (1-2K^2)(1-K^2)^{-1/2} f'_\alpha \, dk_m \quad , \quad \alpha = 4,5 \; .$$

With e_α known as a solution of the transport equation, the distribution function may be normalized as $f_\alpha = e_\alpha f'_\alpha$, $\int f'_\alpha \, dk_m = 1$. Then one may form averages of any function of the turbulent fluctuations of the primitive variables making use of the expansions (2) and the participation coefficients $\phi_{\alpha j}$, Equ. (7), e.g., for the turbulent energy tensor $\overline{u'_i u'_j}$ we have

$$\overline{u'_i u'_j} = c^2 \sum_\alpha \sum_\beta \iint C_\alpha(k_m) C_\beta(k_n) \; \phi_{\alpha,i+1}(k_m) \; \phi_{\beta,j+1}(k_n)$$

$$\times \exp \{(\Gamma_\alpha + \Gamma_\beta)t + i[x_m k_m + x_n k_n - i(\omega_\alpha + \omega_\beta)t]\} \, dk_m \, dk_n \; .$$

In evaluating this integral one must average over the random phases of the complex amplitudes C_α and C_β. Further, one should observe that nontrivial contributions are possible only if $k_m + k_n = 0$, and $\omega_\alpha(k_m)+\omega_\beta(k_n)=0$. These conditions will be satisfied by the acoustic modes only if $\alpha = 4$, $\beta = 5$ or $\alpha = 5$, $\beta = 4$.

We observe at this point that evaluation of averages of fluctuations is possible if one knows (or postulates) the forms of the expressions for $|C_\alpha| = f_\alpha^{1/2}$. Thus modeling of turbulence and prediction of sound generated by it reduces to finding suitable approximations to the distribution functions f_α. A given approximation to f_α will then generate a consistent model of turbulence, that is, to a given f_α there corresponds a set of expressions for all desired averages or correlations of the turbulent quantities. With expressions for the needed averages available, one may then proceed to solve the averaged conservation equations for the mean turbulent quantities.

V. THERMODYNAMICS OF ACOUSTIC ENERGY SPECTRUM

In lieu of formal solutions of the Maxwell-Boltzmann equation (12), we propose to investigate distribution functions f_α by methods used in the thermodynamics of black body radiation.

Lord Rayleigh (1900) has shown that the number of normal modes of vibration in a volume V, having frequencies between ω and $\omega + d\omega$, is $(\omega^2 V/\pi^2 c^3)d\omega$, where c = velocity of wave propagation. If T denotes the temperature of oscillators which are in termal equilibrium with radiation, then the space density of radiant energy, per unit range of frequency, is given by

$$e_{\omega}(\omega,T) = \frac{\omega^2}{\pi^2 c^3}\, kT$$

where k = Boltzmann constant, and where Rayleigh-Jeans distribution, $f = kT/h\omega$ was used. This classical result implies that most of the energy resides at high frequencies, and energy becomes infinite when $\omega \to \infty$, the so called "ultraviolet catastrophe" so named by Paul Ehrenfest. Recently, Millsaps (1974) proposed to invoke the 1st and 2nd Laws of Thermodynamics and conditions (11) of this paper to restate, for the case of hydrodynamic turbulence, Poincare's (1912) proof of the necessity of the energy spectrum to be governed by a discrete energy exchange process (the necessity of Planck's quantum hypothesis). Poincare's proof gives also the most general distribution of energy attainable after sufficient time. Poincare's distribution includes that of Planck's as a special case. Here we shall propose to use Planck's distribution law in the form $f_{\alpha} = 1/[\exp(h\omega/2\pi kT) - 1]$ which gives $(h\omega/2\pi)/[\exp(h\omega/2\pi kT) - 1]$ as the average energy of an oscillator whose energy is restricted to integral multiples of $h\omega/2\pi$. This distribution satisfies conditions (11) and yields the following expression for the energy density per unit frequency range

$$e_{\omega}(\omega,T) = \frac{h\omega^3}{2\pi^3 c^3}\,\frac{1}{\exp(h\omega/2\pi kT) - 1}$$

Applying this result to the two acoustic modes, $f_4(k_m) = f_5(-k_m)$, using only the absolute values of ω, and integrating over the frequency we obtain for the acoustic energy per unit volume

$$e(T) = \frac{h}{\pi^3 c^3}\int_0^{\infty}\frac{\omega^3\, d\omega}{\exp(h\omega/2\pi kT) - 1} = \frac{(2\pi kT)^4}{\pi^3 c^3 h^3}\int_0^{\infty}[e^{-x} + e^{-2x} + \ldots]x^3 dx$$

$$= \frac{16\pi h}{c^3}\left[\frac{kT}{h}\right]^4 \times (1.0823) \qquad \text{(Stefan-Boltzmann Law)}$$

In order to bring the Stefan-Boltzmann Law into conformity with the Lighthill's "8th power of Mach number law" in the case of the acoustic radiation, we should identify the propagation speed c with the adiabatic speed of sound and kT with the average energy of oscillators in thermal equilibrium with the acoustic radiation, that is, with the turbulent energy $\frac{1}{2}\frac{(\overline{u'^2})}{U^2} \cdot U^2$ where U = mean flow velocity.

The attractive possibility of deriving the Lighthill's Law as the equilibrium law of acoustic radiation gives credence to the idea that turbulence is quantized or that it should be looked upon as such. However, neither the Poincare's proof of necessity nor Ehrenfest's (1911) elegant normal mode arguments predict the value of the quantum of action, h. In atomic physics h is an experimentally determined universal constant. In the physics of normal mode vibrations of continuous media the numerical value of h is not known. It is of interest to note, however, that the units of dynamic viscosity μ are those of action per unit volume. Likewise, the product ρUL (the numerator of the Reynolds number) has units of action per unit volume. Thus Reynolds number represents a ratio of magnitudes of actions characteristic of maroscopic (continuum) and microscopic (molecular) phenomena. It is expected that acoustic energy density measurements will permit eventual determination of the "turbulent quantum of action" which should appear in the acoustic form of the Stefan-Boltzmann Law.

Other forms of distribution functions may be tried provided that the conditions of finite energy and of proper behavior at the limits, Equs. (11), are satisfied. Among possible distribution functions presently investigated are the Wien's (or Gaussian) and Wiener-Hermite distributions (Gram-Charlier expansions). Using various approximations to the distribution functions it is planned to evaluate mean turbulent properties, integrate numerically the averaged Reynolds differential equations, together with appropriate convective transport equations, for some simple turbulent flow cases, and to arrive at sound source terms consistent with the assumed model of turbulence. Comparison with experimental data, consisting of simultaneous measurements of acoustic intensities and mean turbulent flow properties, would permit assessing the usefulness of the various approximations to the distribution functions.

[Research supported by NASA Grant NGR 15-005-174]

References

Chu, Boa-Teh, and Kovásznáy, L. S. G., "Non-linear Interactions in a Viscous Heat-Conducting Compressible Gas," J. Fluid Mech., Vol. 3, Part 5, p. 494 (1958).

Davidson, R. C., "The Evolution of Wave Correlations in Uniform Turbulent, Weakly Non-linear Systems," J. Plasma Phys., Vol. 1, Part 3, p. 341 (1967).

Ehrenfest, P., "Welche Züge der Lichtquantenhypothese spielen in der Theorie der Wärmestrahlung eine wesentliche Rolle?," Ann. Physik, Vol. 36, p. 91, (1911).

Kentzer, C. P., "Acoustical Theory of Turbulence," XI-th Biennial Fluid Dynamics Symposium on Advanced Problems and Methods in Fluid Mechanics, Sopot-Kamienny Potok, Poland, Sept. 3-8, (1973). To appear in Archives of Mechanics (Archiwum Mechaniki Stosowanej).

Landahl, M. T., "A Wave-Guide Model for Turbulent Shear Flow," J. Fluid Mech., Vol. 29, Part 3, p. 441 (1967).

Lumley, J. L., in Proceedings of the International Colloquium on the Fine Scale Structure of the Atmosphere and Its Influence on Radio Wave Propagation, Doklady A. N. SSSR, Moscow, p. 166 (1967).

Lundgren, T. S., "Distribution Functions in the Statistical Theory of Turbulence," Phys. Fluids, Vol. 10, No. 5, p. 969 (1967).

Millsaps, K., "A Thermodynamic Constraint on the Equilibrium Spectrum of Homogeneous Isotropic Turbulence," to appear in Mechanics Research Communications.

Moffatt, H. K., "The Degree of Knottedness of Tangled Vortex Lines," J. Fluid Mech., Vol. 35, Part 1, p. 117 (1969).

Poincaré, H., "Sur la théorie des quanta," Journal de Physique, Vol. 2, p. 5 (1912).

Rayleigh, Lord J. W. S., "Remarks upon the Law of Complete Radiation," Phil. Mag., Vol. 49, p. 539 (1900).

INVESTIGATION OF THE LARGE-SCALE COHERENT STRUCTURE IN A JET AND ITS RELEVANCE TO JET NOISE

by

Roger E. A. Arndt and W. K. George*

The Pennsylvania State University
University Park, Pa. 16802

INTRODUCTION

Reason for Study

Significant strides have been made during the last 15 years in the reduction of aircraft noise. The flyover OASPL at 1000 ft. is more than 20 dB lower for the new higher powered L1011 aircraft than for the early turbojet versions of the 707 and DC-8. On the basis of acoustic efficiency (noise power/thrust power ratio) the advances in technology are even more impressive amounting to a reduction by a factor of about 1000 (1% vs. 0.001%). Comparison in terms of the noise footprint is also enlightening. The 110 dB contour extended more than 2000 ft. from a typical engine (J-57) in 1956 whereas the 110 dB contour for the new CF6-6 engine extends less than 200 ft.

Basically, there have been two important theoretical concepts which have led to these advances: first, an understanding that jet noise varies strongly with velocity and, second, an understanding of the significance of pure tones generated by rotor-stator interaction. Lighthill (1952, 1954), in a pioneering study of jet noise, pointed out that acoustic power from jets varied like $\rho U^8 d^2$ whereas thrust power varies like $\rho U^3 d^2$. This observation led to the evolution of the high bypass engine which relies on a high mass rate of flow at low velocity to achieve the required thrust.

Currently, the state of the art in fan and compressor noise technology is at the point where jet noise and rotor noise are of equal significance. Unfortunately, current suppressor technology is ineffective at the lower jet velocities that are characteristic of current high bypass ratio engines. It appears at this point that further jet noise suppression will require an even more basic understanding of the mechanism of jet noise.

Over the past 20 years, numerous investigators have attempted to determine the dominant noise producing structure of a jet by a variety of measurements of the velocity and pressure fluctuations in the jet. While contributing much to our understanding of turbulent phenomena in general, and of jets in particular, these investigations have experienced only limited success in:

---

*Present Address - State University of New York at Buffalo.

a) Deducing the dominant jet structure.
b) Accounting for the radiated noise.
c) Suggesting techniques for minimizing this noise.

The first step toward a satisfactory understanding of the radiated noise is clearly an understanding of the jet turbulence structure. At the 1971 Symposium on Aerodynamic Noise at Loughborough University, sponsored by the Royal Aeronautical Society and the British Acoustical Society "delegates were divided on the ultimate possility of reducing jet noise, but it seemed to be generally considered that understanding the underlying order in the turbulence would probably be the most fruitful path for jet noise control (Fisher and Lowson, 1971)." Recent work (Crow and Champagne, 1971, and Bishop et al 1971) indicated the existence of a large scale coherent structure in both subsonic and supersonic jets. In a subsonic jet this structure has a Strouhal frequency, fd/U_o, which corresponds to the observed peak in the far field radiated noise spectrum.

This paper describes an objective method for deducing the large eddy structure in a large jet. It is also suggested that any large, coherent structure in itself is probably a weak source of sound. Sound radiation probably occurs through the interaction of finer scale turbulence with the more coherent large scale structure.

Experimental Evaluation of Lighthill's Theory

The non-homogeneous wave equation for a flow without non-steady sources of mass or applied forces was obtained by Lighthill (1952) in the form

$$\frac{\partial^2 \rho}{\partial t^2} + a_o^2 \frac{\partial^2 \rho}{\partial x_i \partial x_i} = \frac{\partial^2 T_{ij}}{\partial x_i \partial x_j} \qquad (1)$$

where, in the case of a sub-sonic, high Reynolds number, turbulent flow, T_{ij} may be approximated by

$$T_{ij} \cong \rho u_i u_j \qquad (2)$$

A retarded time solution was offered by Lighthill in the form

$$(\rho-\rho_o)(x,t) = \frac{1}{4\pi a_o^2} \frac{\partial}{\partial x_i \partial x_j} \int \frac{[T_{ij}]}{(x-y)} [y, t - \frac{x-y}{a_o}] dy \qquad (3)$$

A more convenient expression for experimental work is the formulation of Proudman (1952):

$$\rho-\rho_o = \frac{1}{4\pi_o^4 x} \int [\frac{\partial^2}{\partial t^2}(\rho u_x^2)]_{t'} dy \qquad (4)$$

$$t' = t - \frac{\underset{\sim}{x}-\underset{\sim}{y}}{a_o} \tag{5}$$

wherein u_x is the velocity component in the direction of an observer.

Lighthill's theory has formed the basis for much additional theoretical work. Of particular interest to this study are the past experimental attempts to relate turbulence measurements to acoustic source strength, especially the distribution of sound source intensity within a jet. A direct evaluation of the Lighthill theory was first attempted by Chu (1966). He made his measurements at a single point in the flow ($x_1/d=4$, $x_2/d=0.5$) and attempted to predict the total jet noise characteristics with theoretical estimates of sound source distributions based on the similarity principles of Ribner (1958) and Powell (1959). Unfortunately, the intensity depends on the fourth time derivative of the two-point correlation of ρu_x^2. Chu's attempts to evaluate this from an experimental curve was inherently inaccurate. A similar attempt by Jones (1969) was also incomplete and only limited success was achieved.

Recently, the experimental evaluation of the Lighthill integral has taken a new direction. Lee and Ribner (1972) and more recently Seiner and Reethof (1974) report cross correlations of the fluctuating stress with the far field noise. The method is based on the Proudman form of the Lighthill integral:

$$I = \frac{\overline{p^2}}{\rho_o a_o} = -\frac{1}{4\pi a_o^3 r} \int \frac{\partial^2}{\partial t^2} \overline{\rho v_x^2 p} \; d\underset{\sim}{y} \tag{6}$$

Unfortunately the method is sensitive to phase differences in the two types of instrumentation. Lee and Ribner chose to perform their correlation in narrow bands. The data they present is questionable because of the very low value of correlation achieved. Seiner and Reethof (1974) chose to perform their correlations in octave bands which eliminated some of the problems experienced by Lee and Ribner. They also chose to reformulate the problem in terms of shear noise and self noise which meant working with both the correlation between far field pressure and velocity squared and the pressure-velocity covariance. They found that "shear noise" was the major contributor to the total power and that, oddly enough, the radial distribution of sound source strength peaked at the jet axis, even in the potential core.

An even more direct approach has been reported by Siddon and Rackl (1971) and Rackl (1973). This method depends on the cross correlation between "pseudo sound" and far field pressure using the Ribner dilation model as a basis:

$$\frac{\overline{p^2}}{\rho_o a_o} = - \frac{1}{4\pi\rho_o a_o^3 |\underset{\sim}{x}|} \int \frac{\overline{\partial^2 p^o(\underset{\sim}{y},t')p(t)}}{\partial t^2} d\underset{\sim}{y} \tag{7}$$

Their results agree qualitatively with Lee and Ribner but are in fundamental disagreement with Seiner and Reethof (1974). The errors inherent in pressure measurement were recognized and a unique pressure probe was developed for the purpose. However, this method is sensitive to current limitations of both high and low frequency response of pressure probes as well as the still unresolved, uncertainties associated with pressure measurement in turbulent flows.

Evidence of a Coherent Large Scale Structure

Of particular interest is the work of Crow and Champagne (1971). Their studies combined visual and hot wire investigations of jets with Reynolds numbers ranging from 2000 to 100,000. By imposing a periodic exitation on the jet with the aid of pressure transducer located in the settling chamber, they attempted to force the jet to act as a non-linear amplifier with maximum amplification occurring in the preferred modal frequency, presumably the large eddy structure. An initial series of ripples was observed to develop into a series of vortex "puffs" which could be detected even at the higher Reynolds numbers. These disturbances rapidly reached "saturation" and the final growth rate was a maximum at a Strouhal number, fd/U_o, of 0.3.

Additional confirmation of the existence of such a large coherent structure has been offered by Lau, Fisher and Fuchs (1972). Fluctuating pressures and velocities were measured in both the entrainment region and potential core of a subsonic jet. It was shown that these fluctuations have a relatively narrow band spectral content when compared to those in the mixing region. Furthermore, a high degree of correlation exists between fluctuations in the core and entrainment regions. The authors concluded that experimental results are consistent with a series of equally spaced toroidal vortices contained in the jet mixing region and convected at a speed of 0.6 times the jet efflux velocity. Similar conclusions concerning a coherent vortex ring structure are offered in papers by Fuchs (1972 a, b), Davies, Ko and Bose (1967), Scharton and White (1972), Wooldridge, Wooten and Amaro (1972) and Beavers and Wilson (1970). Mollo-Christensen (1967) observed that pressure fluctuations outside a fully developed turbulent jet came in rather well defined wave packets as though the jet column was undergoing sporadic oscillations. Similar conclusions have been made for high speed jets where there are indications that large scale pressure fluctuations may be associated with large unstable waves (Liu 1970, Bishop, Ffowcs - Williams and Smith 1971, and Tam 1972).

There is considerable evidence that a large scale coherent structure exists in a jet and, furthermore that it can play a major role in sound radiation. Cross correlation of sound with pressure fluctuations at the center of the mixing region will not necessarily isolate this structure and indeed, the cited attempts to directly evaluate the Lighthill integral have been singularly unsuccessful in this attempt.

Perturbation of the Large Eddy Structure

The possible favorable influence of perturbing the large eddy structure has been noted by Arndt, Tran and Barefoot (1972). They found that placement of a screen across the jet flow results in a substantial reduction in noise. The reduction in noise may be traced to the breaking up of the large eddy structure in the mixing zone as evidenced by the reduction in integral velocity scales. Corresponding measurement of the smaller pressure scales (via two point pressure correlations within the flow) indicate that the scale of the pressure field is similarly perturbed. (Barefoot 1972).

AN OBJECTIVE APPROACH TO THE LARGE EDDY STRUCTURE OF TURBULENT SHEAR FLOW

Townsend (1956) proposed that turbulent shear flows were characterized by the presence of large discernable, coherent structures which were designated as "large eddies." The large eddies were thought to contain no more than 20% of the turbulent energy and to exist in equilibrium with the mean flow and the smaller turbulent eddies. They have scales on the order of the scale of the mean flow and are responsible for the intermittency and spread of the turbulent-irrotational interface. By using simple arguments and measured correlations, Townsend proposed structures which semi-quantitatively accounted for the measurements available. These results were later modified and extended by Grant (1958) for turbulent wakes and by Bradshaw, et al. (1964) for the axisymmetric jet on the basis of extended measurements.

One of the major problems in determining the large eddy structure was the lack of an objective definition. The approach initiated by Townsend was the most objective in that it attempted to guess the structure which best explained the measured correlations. The other attempts to determine the large eddy structures by forcing, conditional sampling, and flow visualization while providing useful information appears to lack even this objectivity.

In 1965, Lumley proposed an objective definition of the large eddy structure (and in fact the smaller eddies as well!) based on a rational orthogonal decomposition of the turbulent velocity field. Lumley and his colleagues (Payne and Lumley 1967, Bakewell and Lumley 1967) succeeded in deducing the large eddy structure in the 2-dim. turbulent wake and in the viscous sublayer on the basis of very limited data. In spite of this success and the appeal of an objective approach to the large eddy definition, the orthogonal decomposition has been largely ignored.

In the remainder of this paper, Lumley's decomposition will be reviewed, an experimental program to apply Lumley's decomposition to the axisymmetric mixing layer of a jet will be outlined, and finally, a sketch will be given of how the radiated noise can be deduced from the characteristic eddies and their interaction.

The Orthogonal Decomposition

Lumley (1967) proposes the following approach to the large eddy identification. Suppose that we think that a candidate eddy, $\phi_i(x, t)$ is occurring in an identifiable manner in a given ensemble of random velocity fields,

$u_i(\underset{\sim}{x}, t)$. One way to test this hypothesis is to project ϕ_i on u_i and determine the extent to which they are parallel. Since we are interested only in parallelism, we remove the amplitude dependence by considering the following:

$$\alpha = \frac{\int \phi_i^{*}(\cdot)u_i(\cdot)d(\cdot)}{[\int \phi_j^{*}(\cdot)\phi_j(\cdot)d(\cdot)]^{1/2}} \tag{8}$$

where $(\cdot)$ indicates the dependence on a point in whatever space is relevant, e.g., (x_1, x_2, x_3, t), and $*$ denotes the complex conjugate. The integral is taken over all space.

Lumley suggests that the best choice for $\phi_i(\cdot)$ is that which maximizes the quantity $\overline{|\alpha|^2}$ where the overbar denotes the ensemble average. By the methods of the calculus of variations, it can be shown that the best ϕ_i is given by the solution to the following equation:

$$\int R_{ij}(\cdot, \cdot')\phi_j(\cdot')d(\cdot') = \overline{|\alpha|^2}\, \phi_i(\cdot) \tag{9}$$

where

$$R_{ij}(\cdot,\cdot') = \overline{u_i(\cdot)u_j(\cdot')} \tag{10}$$

Finite extent velocity field. If the velocity field is of finite extent and is of finite total energy, the following hold:

A. There are not one, but a discrete set of solutions of (2) which can be written as

$$\int R_{ij}(\cdot, \cdot')\phi_j^{(n)}(\cdot')d(\cdot') = \lambda^{(n)}\phi_i^{(n)}(\cdot),\ n = 1, 2, \ldots \tag{11}$$

B. We can choose the $\phi_i^{(n)}$ so that they are orthonormal

$$\int \phi_i^{(p)}(\cdot)\phi_i^{(q)}(\cdot)d(\cdot) = \delta_{pq} \tag{12}$$

C. The velocity field u_i can be expanded in the $\phi_i^{(n)}$

$$u_i(\cdot) = \Sigma a_n \phi_i^{(n)}(\cdot) \tag{13}$$

where

$$a_n = \int u_i(\cdot)\,\phi_i^{(n)}(\cdot)d(\cdot) \qquad (14)$$

and the series converges in mean square.

D. The coefficients of (13) are uncorrelated

$$\overline{a_n a_m} = \begin{cases} 0 & n \neq m \\ \lambda^{(n)} & n = m \end{cases} \qquad (15)$$

E. The two point Reynolds stress tensor can be decomposed into a double series in the $\phi_i^{(n)}$

$$R_{ij}(\cdot,\cdot') = \sum_{n=1}^{\infty} \lambda^{(n)}\phi_i^{(n)}(\cdot)\phi^{(n)*}(\cdot') \qquad (16)$$

and the series is uniformly and absolutely convergent.

F. The $\lambda^{(n)}$ are real and non-negative and their sum is finite and equal to the total energy in the flow.

The expansion of (13) is optimal in the sense that as little as possible is left to the remainder of each partial sum.

Lumley (1970) has shown that the number of terms necessary to adequately represent the energy variation of $u_i(\cdot)$ is

$$N \leq L/\mathcal{L} \qquad (17)$$

where L is a measure of the lateral extent of the velocity field and $\mathcal{L}$ is an estimate of the extent over which the process is correlated with itself. In a jet mixing layer N ~ 4, so only the first four eigenfunctions are necessary to obtain most of the turbulent energy.

It has been suggested by Lumley that the lowest order eigenfunction $\phi_i^{(1)}(x,t)$ be identified as the large eddy. The results of Payne and Lumley (1967) and Bakewell and Lumley (1967) indicate that the large eddy derived from this approach is in excellent agreement with that predicted by Townsend on intuitive grounds although considerably more detail is present. Moreover, the decomposition can be applied to the averaged velocity equations to obtain dynamical equations for the large eddy (Lumley 1967, 1971, Payne 1968).

Homogeneous Fields. From equation (17) it is clear that as the extent of the field L becomes large compared to the correlation distance $\mathcal{L}$, more and more terms are necessary to represent the velocity field. For homogeneous fields the number of terms becomes infinite and the eigenvalues are not discrete but continuous. The appropriate decomposition for a homogeneous field is the familiar Fourier decomposition. If u_i is homogeneous in $\underset{\sim}{x}$ and stationary in time we can write

$$u_i(\underset{\sim}{x},t) = \int_{-\infty}^{\infty} e^{i(\underset{\sim}{k},\underset{\sim}{x} + \omega t)} \hat{u}_i(\underset{\sim}{k},\omega)d\underset{\sim}{k}d\omega \qquad (18)$$

where $\hat{u}_i(\underset{\sim}{k},\omega)$ is the Fourier decomposition of $u_i(\underset{\sim}{x},t)$ and the $\hat{u}_i$ are uncorrelated at different wave numbers and frequencies.

$$\overline{\hat{u}_i(\underset{\sim}{k},\omega)\hat{u}_j(\underset{\sim}{k}',\omega')} = \Phi_{ij}(k,\omega)\delta(\omega-\omega') \qquad (19)$$

where $\Phi_{ij}(\underset{\sim}{k},\omega)$ is the velocity spectrum tensor. (The $\hat{u}_i$ are random functions and (18) is written in the sense of generalized functions [c.f. Lumley 1970]. This representation is equivalent to the Fourier-Stieltjes decomposition $dZ_i(\underset{\sim}{k},\omega)$ used by Batchelor (1953) and others.)

From (18) it is clear that in a homogeneous flow the large eddy structure will not be readily identifiable from the fluctuating Fourier components unless $\hat{u}_i(k,\omega)$ peaks strongly at a particular wave number frequency combination $(\underset{\sim}{k}^\circ,\omega^\circ)$. We will come back to this problem later under partially homogeneous flows.

Periodic Velocity Fields. If the velocity field possesses periodicities

$$u_i(\cdot,\theta) = u_i(\cdot, \theta + 2\pi) \qquad (20)$$

it can be expanded into a Fourier series or other appropriate harmonic functions. This has been recognized by Michalke (1972) who expanded the pressure field of an axisymmetric jet in a Fourier series.

For the turbulent velocity field we have

$$u_i(\cdot,\theta) = \sum_{n=-\infty}^{\infty} f_i^{(n)}(\cdot)\, e^{in\theta} \qquad (21)$$

where the $f_i^{(n)}(\cdot)$ are uncorrelated, that is,

$$\overline{f_i^{(m)}(\cdot)f_i^{(n)*}(\cdot')} = \begin{cases} 0; & n \neq m \\ B^{(n)}(\cdot,\cdot'); & n = m \end{cases} \qquad (22)$$

The two point Reynolds stress tensor can be similarly expanded

$$\overline{u_i(\cdot,\theta)u_j(\cdot',\theta')} = \sum_{n=-\infty}^{\infty} B^{(n)}(\cdot,\cdot')e^{in(\theta-\theta')} \qquad (23)$$

Fuchs (1972) has applied Michalke's decomposition to measurements of the turbulent pressure field in the jet mixing layer. Because the pressure field is strongly correlated around the jet the Fourier series representation was a natural method. The turbulent velocity correlations, however, fall off rapidly in the azimuthal direction (Bradshaw, et al. 1964). Therefore, it is not immediately obvious that the representation of equation (21) is preferable to that of equation (18) when applied to the azimuthal variable of the velocity field.

Partially Homogeneous and Stationary Fields. This special case is most often encountered in practice and is particularly relevant to the turbulent jet. Laboratory jet flows are stationary in time, homogeneous (and periodic) in the azimuthal direction, strongly inhomogeneous and of limited extent in the radial direction, and by comparison with the radial direction nearly homogeneous in the axial direction. The last statement is even more valid if the turbulence properties are normalized by the local turbulence scales. We consider here a velocity field which is homogeneous in x and z, stationary in time, and of bounded extent in y.

We first decompose the velocity field in the homogeneous directions and time according to

$$u_i(\underset{\sim}{x},t) = \int_{-\infty}^{\infty} e^{i(kx + k_3z + \omega t)} \hat{u}_i(k_1,k_3,\omega;\ y)dk_1dk_3d\omega \qquad (24)$$

where the $\hat{u}_i$ are uncorrelated for different frequencies and wave numbers.

$$\overline{\hat{u}_i(k_1,k_3,\omega;\ y)\ \hat{u}_i(k_1',k_3',\omega';\ y')}$$

$$= \Phi_{ij}(k_1,k_3,\omega;\ y,y')\delta(\omega-\omega',k_1-k_1',k_3-k_3') \qquad (25)$$

where Φ_{ij} is the Fourier transform of the two point Reynolds stress tensor.

We now seek an "eddy" $\phi_i(k_1,k_3,\omega;\ y)$ which maximally projects on the field $\hat{u}_i(k_1,k_3,\omega;\ y)$. The result is the following:

$$\int_{-V}^{V} \Phi_{ij}(k_1,k_3,\omega;\ y,y')\ \phi_j^{(n)}(k_1,k_3,\omega;\ y')dy'$$

$$= \lambda^{(n)}(k_1,k_3,\omega)\phi_i^{(n)}(k_1,k_3,\omega;\ y) \qquad (26)$$

V denotes the finite extent of the flow in the y-direction and is large enough to contain the range of variation of Φ_{ij} - in this case the mixing layer.

As before we identify $\phi^{(1)}(k_1,k_3,\omega; y)$ with the large eddy. The velocity field of this eddy is given by

$$u_i^{(1)}(\underset{\sim}{x},t) = \int_{-\infty}^{\infty} e^{i(k_1x + k_3z + \omega t)} a_1(k_1,k_3,\omega)\phi^{(1)}(k_1,k_3,)\omega)dk_1dk_3d\omega \tag{27}$$

where the a_1 is the random coefficient. Obviously the effect of the homogeneities has been to smear out the structure of the large eddy by the introduction of a fluctuating structure in both frequency and wave number. The large eddy $u_i^{(1)}(\underset{\sim}{x},t)$ can be visualized as a group of dispersive waves propagating in the homogeneous directions whose amplitude vary in the inhomogeneous and bounded directions. This interpretation is similar to the waveguide model of Landahl (1967) and is seen to be a special case of the orthogonal decomposition.

Lumley (1967) has observed that if $\phi_i^{(1)}$ has its energy concentrated about a single spectral value, say $(k_1°,k_3°,\omega)$, then that component can be chosen to be representative of the large eddy; that is $\phi_i^{(1)}(k_1°,k_3°,\omega°,y)$. In effect, this type of assumption has been made in those experiments which attempt to force a single component of the turbulence and seek the maximal growth rate identifying it as the large eddy, e.g., Crow and Champagne (1971), Hussain and Reynolds (1971). Other heuristis models for the jet turbulence structure have also implicitly assumed that the large eddy is concentrated about a particular wave number-frequency combination, for example, the roller eddies of Davies (1972) and the vortex pairs of Laufer (1973).

The observations reported by Crow & Champagne (1971) of a puff-like structure in the periodically forced jet is a simple statement that they were able to concentrate the large eddy energy to a narrow band to the point where it was recognizable. The observations reported by Laufer (1973) of a vortex-like structure in the plane mixing layer which resembled the last stages of a Kelvin-Helmholtz instability must be interpreted in light of the low Reynolds number. It is reasonable to expect the spectral content of the large eddy to broaden as the Reynolds number is increased because of the increased nonlinear interactions. This broadening with Reynolds number will proportionately reduce discernability of the large eddy.

A final comment is in order regarding the reputed axisymmetric structure in jets and the two-dimensional structure in the plane mixing layer. It was first observed by Townsend that for an eddy to extract energy from the mean flow its plane of circulation must be tilted against the mean flow. The structures proposed to date (Bradshaw et al., 1964 excepted) are defective in this regard. The structure deduced by Payne and Lumley (1967) by applying the orthogonal decomposition to Grant's (1958) measurements in a two-dimensional wake is shown in Figure (1). It is interesting to note that the eddy pairs are at nearly 90° to that which would have been expected from the symmetry alone (aligned parallel to the cylinder). Clearly some caution must be exercised in attacking significance to geometrically appealing models.

An alternate approach to partially homogeneous flows. For partially homogeneous flows, Lumley (1967, 1970) has suggested further decomposing each of the "eddies" obtained above into characteristic eddies occurring at uncorrelated locations in time and at uncorrelated locations in the homogeneous directions. This approach is similar to the shot effect representation of Rice (1948). We write for the large eddy (or any eddy)

$$u_i^{(1)} = \iiint g_i^{(1)}(x-\xi,\ y,\ z-\zeta,\ t-\tau)\,d\sigma(\xi,\zeta,\tau) \tag{28}$$

where

$$\overline{d\sigma(\xi,\zeta,\tau)d\sigma(\xi',\zeta',\tau')} = \begin{cases} 0\ , & (\cdot) \neq (\cdot') \\ d\xi d\zeta d\tau, & (\cdot) = (\cdot') \end{cases} \tag{29}$$

and where the $g_i^{(1)}$ is the characteristic eddy (or group) and is deterministic. It is easy to show that

$$\overline{u_i^{(1)}(\cdot)u_j^{(1)}(\cdot')} = \int g_i^{(1)}(x,y,z,t)g_j^{(1)}(x+\xi,y',z+\zeta,t+\tau)\,d\xi d\zeta d\tau$$

where $(\cdot') = (x + \xi,\ y',\ z + \zeta,\ t + \tau)$. (30)

Defining $G_i^{(1)}(k_1,\ k_3,\ \omega,\ y)$ to be the Fourier transform of $g_i^{(1)}(\underset{\sim}{x},\ t)$ we can show that

$$\phi_i^{(1)}(k_1,\ k_3,\ \omega,\ y)\phi_j^{(1)*}(k_1,\ k_3,\ \omega,\ y')\lambda^{(1)}(k_1,\ k_3,\ \omega) \tag{30}$$

$$= (2\pi)^3 G_i^{(1)}(k_1,\ k_3,\ \omega,\ y)G_j^{(1)*}(k_1,k_3,\omega,y')$$

Thus the large eddy can be identified as the inverse transform of

$$G_i^{(1)}(k_1,\ k_3,\ \omega,\ y) = \sqrt{\frac{\lambda^{(1)}(k_1,\ k_3,\ \omega)}{(2\pi)^3}}\ \phi_i^{(1)}(k_1,\ k_3,\ \omega,\ y) \tag{31}$$

or

$$g_i^{(1)}(x,y,z,t) = \int e^{ik_1x + k_3z + \omega t} \sqrt{\frac{\lambda^{(1)}(k_1,k_3,\omega)}{(2\pi)^3}}\,\phi_i^{(1)}(k_1,k_3,\omega,y)\,dk,dk_3d\omega \tag{32}$$

Clearly if the peak of $\lambda^{(1)}$ is distinct at some value $(k_1°,\ k_3°,\ \omega°)$, the value selected at the peak is representative and the eddy (or group) is easily discernable.

EXPERIMENTAL DETERMINATION OF THE LARGE EDDIES

In the previous section we have shown that the random velocity field of a jet mixing layer can be broken into a series of characteristic eddies, the lowest order one being the large eddy. These eddies can be obtained directly from the measured velocity covariance tensor $\overline{u_i(\underset{\sim}{x},t)u_j(\underset{\sim}{x}',t)}$.

The procedure for calculating the characteristic eddies is summarized below:

1. Measure the velocity covariance tensor

   $$R_{ij}(x-x', y,y', z-z', t-t')$$

2. Transform to get the velocity spectrum tensor

   $$\Phi_{ij}(k,m,\omega;y,y')$$

3. Calculate the eigenfunctions $\phi_i^{(n)}(k,m,\omega)$ and eigenvalues $\lambda^{(n)}(k,m,\omega)$.

4. Using this information in equations, calculate the characteristic eddies.

The techniques for carrying out the computations described above are straightforward and have been described in detail by Lumley (1970). The most difficult problem is of course to obtain sufficient information on the velocity covariance tensor R_{ij}. or its transform Φ_{ij}.

We can reduce the number of measurements required by recalling that the nine components of R_{ij} are related to each other by the mass conservation equations as follows:

$$\frac{\partial}{\partial x_i'} R_{ij}(\underset{\sim}{x},\underset{\sim}{x}') = 0 = \frac{\partial}{\partial x_j'} R_{ij}(\underset{\sim}{x},\underset{\sim}{x}') \qquad (31)$$

Fourier transforming in the homogeneous variables x and z and in the stationary variable t we have

$$\begin{aligned} ik_i \Phi_{ij} + \frac{\partial}{\partial y} \Phi_{2j} &= 0 \\ & \qquad i = 1,3 \qquad (32) \\ ik_i \Phi_{ij} + \frac{\partial}{\partial y'} \Phi_{i2} &= 0 \end{aligned}$$

Hence we have six equations in nine unknowns. If we use two x-wire probes and measure u_1 and u_3 at each location, it is straightforward to obtain Φ_{11}, Φ_{33}, Φ_{13}, and Φ_{31}. The missing terms may be readily obtained by integration from five of the six mass conservation equations.

The properties of the covariance function can also be used to reduce the number of measurements. Since the velocity covariance depends on progressively larger eddies as the spacial separation between the probes is increased, there appears to be little merit in making equally spaced measurements. Furthermore, since the covariance falls off in a nearly exponential fashion (Tennekes and Lumley 1971), it is clear that the optimum spacing is logarithmic. This has been previously used by Bakewell and Lumley (1967) in the viscous sublayer.

For a 12 inch jet at 30 m/s, the smallest spacing used will be 5 mm (corresponding to the peak in the dissipation spectrum). In spite of the loss of small scale structure, this will cause no problem because we are interested only in the large scales. There appears, at this point at least, no reason to measure correlations at separations greater than five integral scales. In the streamwise or x-direction, 5L - 0.3 m., and in the azimuthal, z-, and cross-stream or y-directions 5L - 0.15 m. The separations to be measured are then given by the following:

x-direction (mm.)

0, 5, 10, 20, 40, 80, 160, 320

y, z-directions (mm.)

0, 5, 10, 20, 40, 80, 160

This corresponds to a measurement grid of 8 x 7 x 7 on 392 probe separations for each choice of origin, y', in the inhomogeneous direction.

To complete the specification of the velocity covariance, this grid must be remeasured for different choices of the origin in the inhomogeneous direction. By choosing the same logarithmically spaced values for y as above, we see that the origin must be moved 13 times. The net result is a total of 13 x 392 = 5096 probe spacings. Since four channels of velocity signals are being recorded, the total number of correlations to be measured is 20,384 - a formidable task, but necessary if the large eddy structure is to be found unambiguously. An automatic stepping technique can be used for probe movement.

It will be recalled that the velocity covariance spectrum tensor Φ_{ij} $(k,m,\omega;\ y,y')$ is sought. Therefore it remains to Fourier transform the measured covariances in the x and z directions. This will be accomplished by first curve fitting the measured covariances with a modified Gram-Charlier expansion and then Fourier transforming analytically to obtain the spectrum. Such a procedure was used with success by Payne and Lumley (1967).

Once $\Phi_{ij}(k,m,\omega;\ y,y')$ is obtained for $i,j = 1.3$ by the procedures described above, it is straightforward to integrate the mass conservation equations to obtain the five missing terms $i,j = 3$.

CALCULATION OF RADIATED NOISE FROM THE ORTHOGONAL DECOMPOSITION OF THE VELOCITY FIELD

The pressure correlation for the far field can be written using the retarded time approximation to the solution of Lighthill's equation as

$$\overline{p(\underline{x},t)p(\underline{x},t+\tau)} \propto \frac{\partial^4}{\partial\tau^4}\iint \overline{T_{ij}(\underline{y},t-\frac{\underline{x}-\underline{y}}{a_o})T_{k\ell}(\underline{y}',t+\tau-\frac{\underline{x}-\underline{y}'}{a_o})}d\underline{y}d\underline{y}' \tag{33}$$

where we have for brevity left out the dependence on source distance and the directionality factor. The integrand can be abbreviated as

$$\overline{T_{ij}T_{k\ell}'} = \overline{u_i u_j u_k' u_\ell'} \tag{34}$$

where the prime denotes evaluation at y' and $t + \tau$.

Following Batchelor (1953), Kraichman (1956), Lilley (1958) and others, we assume that the 4th order moments are jointly normal and write

$$\overline{u_i u_j u_k' u_\ell'} = \overline{u_i u_j}\ \overline{u_k' u_\ell'} + \overline{u_i u_k'}\ \overline{u_j u_\ell'} + \overline{u_i u_\ell'}\ \overline{u_j u_k'} \tag{35}$$

(This will not be a valid approximation for the eddies corresponding to the scales of motion much smaller than those containing the turbulent energy.) The first term $\overline{u_i u_j}\ \overline{u_k' u_\ell'}$ is not interesting since it is independent of τ and will not contrubute to the noise. The remaining two terms are functions of τ and can contribute.

For simplicity in understanding we will restrict this discussion to completely inhomogeneous and bounded flows. The stationarity in time will, of course, introduce a fluctuating Fourier component in frequency. We define $\Phi_{ik}(\omega)$ as the cross spectral density

$$\Phi_{ik}(\omega) = F.T.[\overline{u_i u_k'}]$$

Transforming (33) with respect to τ we obtain the noise spectrum

$$S_{pp}(\underline{x},\omega) \propto \omega^4 \iint [\Phi_{ik} * \Phi_{j\ell} + \Phi_{i\ell} * \Phi_{jk}]d\underline{y}d\underline{y}' \tag{36}$$

where * denotes a convolution in frequency.

We have seen that Φ_{ik} can be decomposed into the characteristic eddies as follows

$$\Phi_{ik}(\omega;\underline{y},\underline{y}') = \sum_{n=1}^{\infty} \lambda^{(n)}(\omega)\phi_i(\underline{y})\phi_k^*(\underline{y}') \tag{37}$$

Using the fact that the $\lambda^{(n)}(\omega)$ are real and symmetric, substitution of (37) into (36) yields

$$S_{pp}(\underset{\sim}{x},\omega) \propto \omega^4 \sum_{m=1}^{\infty} \sum_{n=1}^{\infty} \int_{-\infty}^{\infty} \lambda^{(n)}(\omega_1)\lambda^{(m)}(\omega-\omega_1)\, d\omega_1 \tag{38}$$

$$\cdot \int \phi_i^{(n)}(\underset{\sim}{y})\phi_j^{*(m)}(\underset{\sim}{y})d\underset{\sim}{y} \cdot \int \phi_k^{*(n)}(\underset{\sim}{y}')\phi_\ell^{(m)}(\underset{\sim}{y}')d\underset{\sim}{y}'$$

$$+ \text{ similar term}$$

The diagonal terms of (38) $n=m$ clearly represent the noise generated by a particular eddy. If we take N terms to approximate the total flow energy there are N terms of what will call type 1 sources. The off-diagonal term of (38) $n \neq m$ represents the noise generated by the interaction of eddies of various sizes. Again if we take N terms in the decomposition there are N^2-N eddy interaction terms which we will call type 2 sources. The strength of these is dependent on the integrated "Reynolds stress" associated with the interacting eddies and the convolved integrated spectra of these eddies.

It is appropriate to recall at this point that Kraichman (1956), Lilley (1958) and others have treated the problem of noise generated by a homogeneous turbulence acted upon by a uniform mean shear. The result was a turbulence-interaction source and a turbulence-shear interaction source. From the above it is clear that in a bounded, inhomogeneous turbulent flow we have the same type of turbulent-shear interaction source terms as the eddies of various sizes interact with one another. This is not surprising since a large eddy appears as a quasi-uniform strain field to a smaller eddy imbedded in it. Clearly the analysis above could be extended to include the effects of a mean shear interacting with each eddy.

It has been speculated for several years by the present authors and independently by H. Tennekes (P.S.U. Acoustic Seminar, 1974) that the large eddies themselves cannot be primary sources of noise because of their long evolution times - at least at low Mach number. Rather, the short life times and high vorticities and strain rates of the dissipative scales make them ideal radiations if they were coherent over large enough distances. The type 2 mechanisms derived above provide a means by which the large eddies can interact with the smaller scales and perhaps provide the necessary coherence lengths.

These arguments are consistent with these of Townsend (1955) and Tennekes and Lumley (1972) regarding the energetics of the large eddies which are believed to obtain energy directly from the mean flow and then cascade it by means of vortex stretching to the smaller scales. It has been speculated that the larger eddies line up or orient the smaller eddies so that their principal axes of strain rate coincide. The small eddies then destroy the larger ones. It is this lining up and destructive process that will contribute to the type 2 interaction terms above.

The conclusions above should be regarded as tentative and confirmation awaits experimental evidence and further study. The important point to this discussion is the possibility that there may be a direct link between the coherence of the large eddy structure and the potentially noisy smaller scales.

Summary and Conclusions

A review of current suppressor technology indicates that further advances in jet noise reduction hinges on a more fundamental understanding of the noise generation mechanism. There has been considerable conjecture about the existence of a coherent structure in jet turbulence. Should such a structure exist, the opportunities for further jet noise reduction may be considerably enhanced.

It is suggested that Lumley's objective approach to large eddy definition may prove to be a fruitful way to deduce the jet structure in sufficient detail to allow calculation of the noise field. An experimental method for direct evaluation of these eddies has been proposed.

Several general observations on the mechanism of jet noise can be made by direct substitution of the characteristic eddy formulation into Lighthill's equation. Basically two types of noise terms are found which parallel the concept of shear noise and self noise suggested by Kraichman, Lilley, Ribner and others. Type 1 consists of the self interaction of the various eddies. Type 2 consists of interaction between eddies of various scales. Because of the preponderance of type 2 interactions and because of the possibility of obtaining both large coherence lengths and short lifetimes it is speculated that these may be the dominant source of jet noise. Thus, the existence of coherent structure in itself is not a priori evidence of a strong emitter of sound but rather such large structure may act as the catalyst for sound radiation from smaller scale, more vortical motions which feed off of the larger eddies.

ACKNOWLEDGMENTS

This work is sponsored jointly by NASA-Lewis under Grant #NGR 39-009-270 and the Naval Ordnance Systems Command under the Exploratory and Foundational Research Program at the Applied Research Laboratory. The authors are indebted to Dr. Hendrik Tennekes for his help and guidance during many enlightening discussions on this topic.

REFERENCES

Arndt, R. E. A., Tran, N. and Barefoot, G. L., "Turbulence and Acoustic Characteristics of Screen Perturbed Jets" AIAA Paper No. 72-644 (1972).

Bakewell, H. and Lumley, J. L., "The Viscous Sublayer and Adjacent Wall Region in Turbulent Pipe Flow" Physics of Fluids, 10,II,9, pp. 1880-92 (1967).

Barefoot, G., "Fluctuating Pressure Characteristics in the Mixing Region of a Perturbed and Unperturbed Round Free Jet," M.S. Thesis, The Pennsylvania State University, (1972).

Batchelor, G. K. (1953), Homogeneous Turbulence, Cambridge University Press, Cambridge.

Beavers, G. S. and Wilson, T. A., "Vortex Growth in Jets" J. Fluid Mech 44, pp. 97-112 (1970).

Bishop, K. A., Ffowcs-Williams, J. F. and Smith, W., "On the Noise Sources of the Unsuppressed High Speed Jet" J. Fluid Mech, 50, pt. 1, pp. 21-31 (1971).

Bradshaw, P., Ferriss, D. H. and Johnson, R. F., "Turbulence in the Noise Producing Region of a Round Jet" J. Fluid Mech, 19, pt. 4, pp. 591-624 (1964).

Chu, W. T., "Turbulence Measurements Relevant to Jet Noise" Univ. of Toronto UTIAS Report 119 (1966).

Crow, S. C. and Champagne, F. H., "Orderly Structure in Jet Turbulence" J. Fluid Mech, 48, pt. 3, pp. 547-591 (1971)

Davies, P. O. A. L., (1972), "Structure of Turbulence" Journal of Sound and Vibration, 28, p. 513-526.

Fisher, M. J. and Lowson, M. V., "Aerodynamic Noise" J. Fluid Mech, 48, pt. 3, pp. 593-603 (1971).

Fuchs, H. V. "Measurement of Pressure Fluctuations Within Subsonic Turbulent Jets' J. Sound and Vib., 22, (3)(1972a).

Fuchs, H. V. "Space Correlations of the Fluctuating Pressure in Subsonic Turbulent Jets" J. Sound and Vib., 23, (1)(1972b).

Grant, H. L., "Large Eddies of Turbulent Motion" J. Fluid Mech, 4, pt. 2, pp. 149-90 (1958).

Hussain, AKMF. and Reynolds, W. C. (1972), The mechanics of an organized wave in turbulent shear flow, pt. 2, Experimental results, J. Fluid Mech., 54, p. 241.

Jones, I. S. F., "Fluctuating Turbulent Stresses in the Noise Producing Region of a Jet" J. Fluid Mech, 36, pp. 529-543 (1969).

Landahl, M. T. (1967) "A Wave-Guide Model for Turbulent Shear Flow," J. Fluid Mech, 29, p. 441.

Lau, J. C., Fisher, M. J. and Fuchs, H. V., "The Intrinsir Structure of Turbulent Jets," J. Sound and Vib., 22, (4)(1972).

Laufer, J., (1973), Presentation on Aerodynamic Noise to the American Physical Society Fluids Division Annual Meeting, Nov. 1973, Hartford, Conn.

Lee, H. K. and Ribner, H. S., "Direct Correlation of Noise from a Jet" AIAA Paper No. 72-640 (1972).

Lighthill, M. J., "On Sound Generated Aerodynamically, Part I General Theory" Proc. Roy. Soc. Series A, 2111 (1952)

Lighthill, M. J., "On Sound Generated Aerodynamically, Part II Turbulence as a Source of Sound" Proc. Roy. Soc. Series A, 222, February 1954.

Liu, J. T. C., "On Eddy-Mach Wave Radiation Source Mechanism in the Jet Noise Problem" AIAA Paper No. 71-150 (1970).

Lumley, J. L. (1971), "Some Comments on the Energy Method," Developments in Mechanics, Vol. 6, Proceedings of the 12th Midwestern Mechanics Conference.

Mollo-Christensen, E., "Jet Noise and Shear Flow Instability Seen From an Experimenters Point of View" Jour. Appl. Mech, 34, March 1967.

Packl, R. "Two Causality Correlation Techniques Applied to Jet Noise," Ph.D Dissertation, The University of British Columbia, 1973.

Payne, F. R. (1968), "Predicted Large Eddy Structure of a Turbulent Wake," Report to Fluid Mechanics Branch, U. S. Office of Naval Research under Contract Number 656, The Pennsylvania State University, Univ. Park, Pa.

Powell, A., "Similarity Considerations of Noise Production from Turbulent Jets", J. Acoust. Soc. Am. 31, pp. 812-813 (1959).

Proudman, I., "The Generation of Noise by Isotropic Turbulence" Proc. Roy. Soc. Series A, 214, pp. 119-132 (1952).

Ribner, H. S., "Strength Distribution of Noise Sources Along a Jet" J. Acoust. Soc. Am. 30, September 1958.

Rice, S. O. (1948) "Mathematical Analysis of Random Noise," Bell System Technical Journal, Vols. 23 and 24.

Scharton, T. D. and White, P. H., "Simple Pressure Source Model of Jet Noise" J. Acoust. Soc. Am. 52, No. 1 (Part 2), July 1972.

Seiner, J. M. and Reethof, G., "On the Distribution of Source Coherency in Subsonic Jets" AIAA Paper 74-4 (1974).

Siddon, T. E., and Rackl, R. "Cross Correlation Analysis of Flow Noise with Fluid Dilatation as Source Fluctuation" Paper presented at 82 Meeting Acoust. Soc. Am. Oct. 1971 (J. Acoust. Soc. Am. 51, pt. 1, p. 36 (1972)).

Tam, C. K. W., "On the Noise of a Nearly Ideally Expanded Supersonic Jet" J. Fluid Mech, 51, pt. 1, pp. 69-95 (1972).

Wooldridge, C. E., Wooten, D. C., and Amaro, A. J., "The Structure of Jet Turbulence Producing Noise" AIAA Paper No. 72-158 (1972).

Payne, F. R. and J. L. Lumley, "Large Eddy Structure of the Turbulent Wake Behind a Circular Cylinder," Physics of Fluids Supplement, 1967.

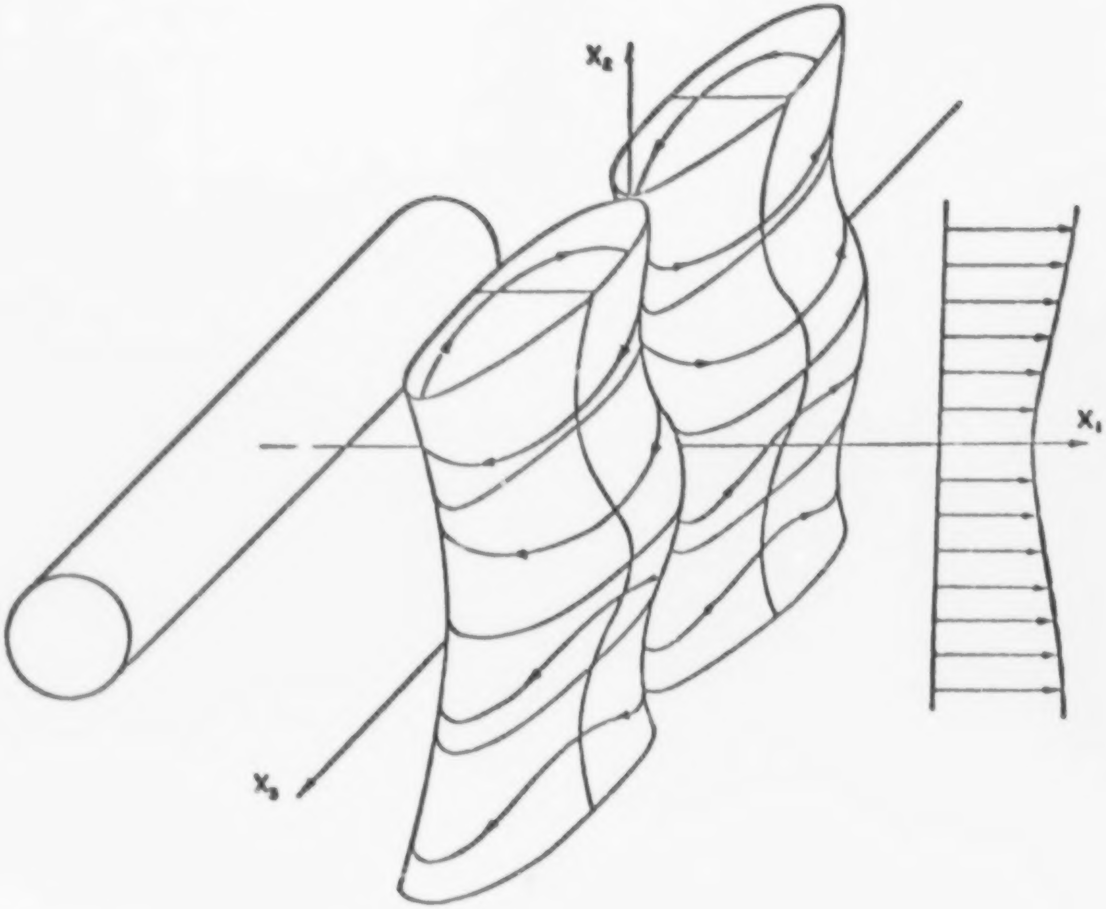

Artist's Conception of the Large Eddy Structure of a Cylinder Wake as Deduced from an Orthogonal Decomposition of the Velocity Field (Payne & Lumley 1967)

POTENTIAL OF COAXIAL MULTINOZZLE CONFIGURATIONS FOR REDUCTION OF NOISE FROM HIGH VELOCITY JETS.

by

D.S. Dosanjh, M.R. Bassiouni, P.K. Bhutiani and K.K. Ahuja
Department of Mechanical and Aerospace Engineering
Syracuse University, Syracuse, New York

Summary

Characteristics of radiated noise from coaxial multinozzle exhaust configurations (without any externally inserted mechanical devices in the exhaust flow) where high speed coaxial multiple jet flows interact just downstream of the nozzle exits, have been investigated and found to be potentially promising for supersonic jet noise suppression.

From acoustic 1/3 Octave Sound Pressure Level spectra and optical (shadow and schlieren) data for coaxial multinozzle configurations operated at a wide range of pressure ratios, it is concluded that as a result of interaction among coaxial multinozzle (two or three) high speed cold jet flows, the acoustic radiation from any of the individual single supersonic jets is substantially modified virtually eliminating the usual intense discrete frequency components of radiated noise. In addition, significant broadband reduction especially at higher frequency range of the radiated noise spectra is observed. Interacting coaxial multinozzle high velocity jet flows show substantial reductions in PWL (from 9 - 16 dB depending on the method of comparison). The correspondence between the observed noise reductions and shock and jet flow modifications evident in optical data is underscored.

Based on the comparison of radiated noise from multinozzle coaxial jets and that from a single 'equivalent' high speed jet issuing from a convergent nozzle with the mass flow rate, thrust and exit area the same as for the combined multinozzle jets, the effectiveness and potential of multinozzle high velocity coaxial jets for supersonic jet noise suppression with minimal thrust loss is examined.

INTRODUCTION

To develop a successful jet noise abatement approach, one must first locate as well as understand the nature, the distribution, the strength and radiation mechanisms of the dominant jet noise sources. Guided by this understanding, practical techniques to reduce the effectiveness of the dominant noise-generating sources need to be devised. It is commonly recognized, has often been stated, and is widely accepted by those interested and actively working in this research field that in high speed (supersonic) turbulent cold and/or heated free jet flows, the dominant noise sources and noise generating mechanisms are associated with (a) Supersonic and subsonic turbulent mixing, (b) Interaction between shock and flow fluctuations such as - shock-turbulence (vorticity); shock-temperature (entropy) fluctuations and shock-pressure fluctuations, (c) Shock unsteadiness and oscillations, (d) Shock induced acoustic resonance, (e) Mach wave radiations associated with flow eddies convected supersonically relative to the ambient medium. Therefore, any successful technique for supersonic jet noise suppression should modify, weaken, eliminate and/or shield some or all of these noise generating sources without resulting in an unacceptable thrust loss.

Various schemes and techniques for high speed jet noise suppression (as applied to turbo-fan or turbojet engines) have been investigated with varying degrees of success by an expanding number of research groups. These attempts may be enumerated in broad categories as (a) mechanical devices such as rods, wedges, screens, buckets and spades mounted or inserted in the exhaust flow at or close to the nozzle (engine) exit, (b) nozzles of different shapes and configurations to promote mixing; multi-tube nozzle exhaust systems; or multi-nozzle coaxial jet flows, (c) ejector-shrouds used in conjunction with approaches (a) and (b). Some of the experimental observations on use of the multinozzle (two and three) coaxial interacting high velocity cold jet flows are presented in this paper. The background material, important existing publications and contributions by others, germane to the experiments reported here are enumerated in references 1 and 2.

As opposed to the subsonic jet noise prediction, at present there is no single unified theory that predicts the noise radiation from supersonic turbulent jets with shock structure. The noise prediction gets even more complex and remote if mechanical devices are mounted or inserted in such supersonic turbulent jet flows. Hence, of necessity, several practical schemes of comparison of the acoustic performance have been attempted by various authors to assess the effectiveness of different noise suppression systems. The coaxial multinozzle jet flows offer a considerable flexibility in controlling the exit areas, mass flows, thrust, the operating pressure ratios, and mean flow Mach number or velocity for each of the individual jets. Thus the radiated noise performance of such multinozzle jets varies widely and for minimum noise operations, the operating pressure ratios of the individual nozzles are different (Ref. 1,2). Therefore the comparative evaluation of the observed noise reductions from multinozzle coaxial jets with that from say a single jet becomes more complicated than is normally the case with the usual comparative assessment of the acoustic performance of model jets or turbojet engine exhaust systems operated first with and then without some noise suppressing mechanical device such as the multi-tube nozzle exhaust or the spades mounted (or inserted) in the exhaust flow.

The mean flow Mach number which is a function of the nozzle operating pressure ratio and the nozzle exit area predominantly influence the character and intensity of the acoustic radiation from a supersonic jet flow. However, the parameters that govern the mechanical performance of any jet system are the thrust and the mass flow. Hence in making a comparison of say a multinozzle jet flow system with that of a single jet jet flow Mach number, nozzle exit area, mass flow rate and thrust of the two systems need to be matched. This suggests two basic schemes for comparing the acoustic performance of the coaxial multinozzle jets with that of a single jet. In the first scheme the total thrust, total mass flow and total exit area of the coaxial multinozzle system operated at the minimum noise condition were matched with that of a single underexpanded jet issuing from a convergent nozzle. However to match these parameters when the two-nozzle jets are operated at minimum noise condition the needed operating pressure for the single 'equivalent' jet was found to be lower than that of the outer jet of the coaxial system. The noise reductions achieved by using the coaxial two-nozzle jets and their comparison with the acoustic performance of an 'equivalent' single jet are reported here.

In the planned second scheme for comparison, the jet flow Mach number (i.e. operating pressure ratio of the outer jet), the total thrust and mass flow rate will be matched with those of the single 'equivalent' nozzle. For minimum noise operation of the multinozzle coaxial jets, the exit area/s of the single nozzle and the multinozzle systems will not be the same. In matching the flow Mach number of the two systems, the single 'equivalent' nozzle can either be a convergent nozzle operated in the underexpanded mode or a convergent-divergent nozzle which may be operated in the fully expanded mode. These experiments are currently being conducted.

Multinozzle Configurations, Experimental Procedure and Experimental Data.

The coaxial three-nozzle assembly, the two-nozzle assembly and the single 'equivalent' nozzle used in these investigations are shown in Fig. 1 where the important specifications and dimensions of each of the nozzles are given.

Each of the three jets are supplied through three separate plenum chambers, such that the stagnation pressure for each jet flow is independently adjustable and maintained constant. Therefore, the coaxial three-nozzle assembly can be used flexibly with either any one of the three nozzles operated independently as a single jet, or any two or all three nozzles operated simultaneously. Since the innermost (nozzle 1), the intermediate (nozzle 2) and the outermost (nozzle 3) jet flows are directed in the same direction, each of the three nozzles is thrust producing. The stagnation pressure for the innermost jet is measured in the plenum chamber. The stagnation pressures in nozzles 2 and 3 are measured by four pitot tubes mounted 90° apart along the circumference and inserted in the buffer reservoirs (supply chambers) of each nozzle. The air temperature in the reservoirs was almost ambient.

B & K acoustic instrumentation comprised: 1/8" condenser microphone (for the 'equivalent' nozzle investigations 1/4" microphone) with grid, cathode follower, microphone amplifier, 1/3 octave band filter set with frequency range 20 Hz to 200 KHz and a level recorder. The microphone was calibrated before each run with a piston phone which produces 124 dB re 0.0002 μbar at 250 Hz, and the ambient temperatures, and pressures were recorded. The far-field acoustic measurements were made in a horizontal plane containing the axis of the jet flow at eight stations from azimuth angle 15^o to 120^o in 15^o increments located on an arc of 6 ft. radius from the nozzle exit in the anechoic chamber of size approximately 10' x 12' x 9'. The microphone axis was oriented along the polar radius of the arc (zero degree incidence) along which the noise measurements were made. 1/3 octave sound pressure level spectral data were recorded for the single round jet alone (nozzle 1), the single annular jet alone (nozzle 2), two coaxial interacting jets (nozzles 1 and 2) and three coaxial interacting jets from three-nozzle configuration (nozzles 1, 2 and 3).

To select the operating pressure ratios at which the individual jets of the three-nozzle configuration were to be operated, initially the outermost jet (nozzle 3) was not used; the operating pressure of the intermediate (nozzle 2) $\zeta_2 = (P_{t_2} + P_a)/P_a$, where P_{t_2} is the reservoir gage pressure of nozzle 2 and P_a, the ambient pressure, was fixed at 3.04 and the pressure ratio ζ_1 of the innermost jet (nozzle 1) was varied. Similar 1/3 octave SPL data for the 'equivalent' convergent nozzle were also gathered. Corrections for microphone

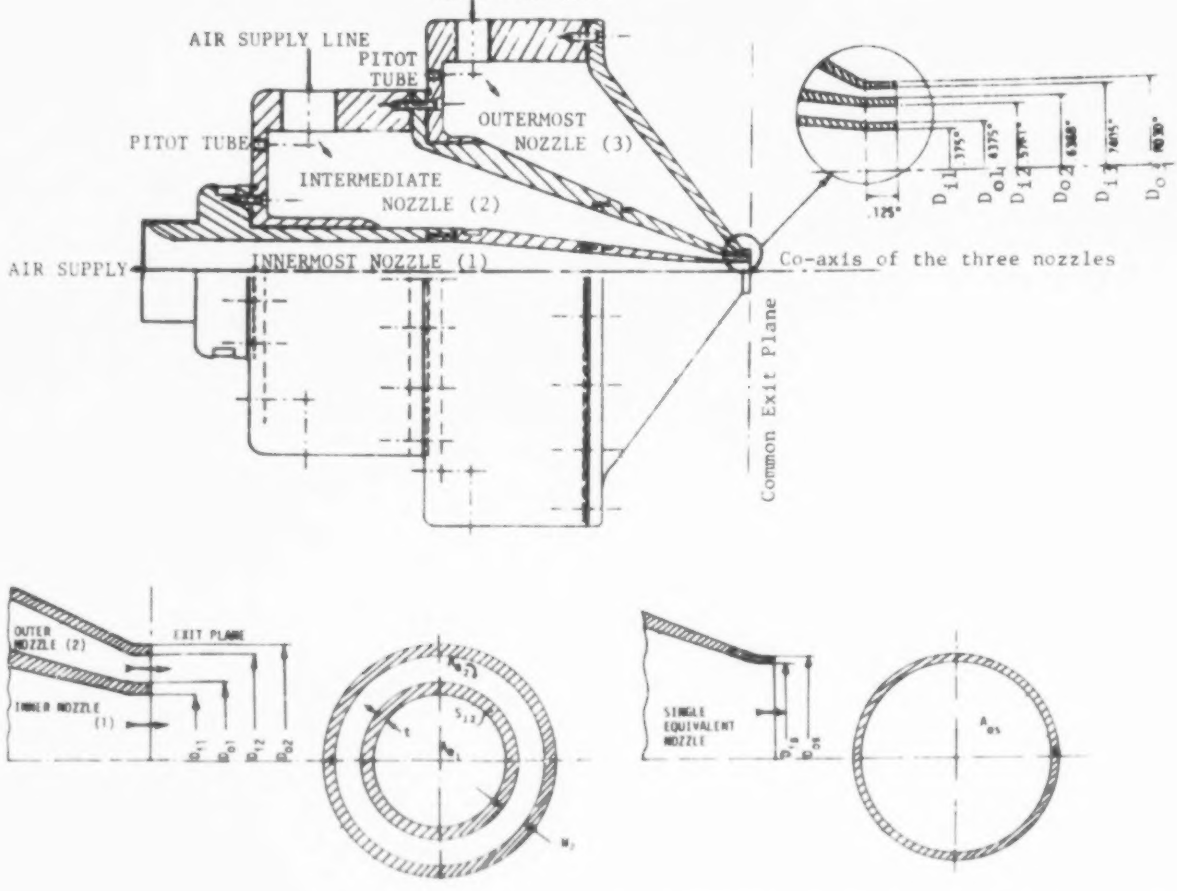
AIR SUPPLY LINE
AIR SUPPLY LINE
PITOT TUBE
PITOT TUBE
OUTERMOST NOZZLE (3)
INTERMEDIATE NOZZLE (2)
AIR SUPPLY
INNERMOST NOZZLE (1)
Co-axis of the three nozzles
Common Exit Plane
.125"
.375"
.4375"
D i1
D o1
D i2
D o2
D i3
D o3
OUTER NOZZLE (2)
EXIT PLANE
INNER NOZZLE (1)
D i1
D o1
D i2
D o2
t
S 12
SINGLE EQUIVALENT NOZZLE
A es

t = LIP THICKNESS

w = ANNULAR WIDTH AT THE EXIT

D_i = INNER EXIT DIAMETER

D_o = OUTER EXIT DIAMETER

A_e = EXIT AREA

S_{12} = SOLID ANNULUS EXIT AREA BETWEEN NOZZLES 1 AND 2

SUFFIX REFER TO NOZZLE USED

IMPORTANT SPECIFICATIONS OF THE NOZZLE ARRANGEMENTS (b) AND (c)

NOZZLE ARRANGEMENT	NOZZLE NO	INNER EXIT DIAMETER (D_i) (IN.)	OUTER EXIT DIAMETER (D_o) (IN.)	EXIT AREA (A_e) (SQ.IN.)	LIP THICKNESS (t) (IN.)	SOLID ANNULUS EXIT AREA (S) (SQ.IN.)
Coaxial Convergent Nozzles	1	0.3750	0.4375	0.1143	0.0313	0.040
	2	0.4375	0.5669	0.1039	0.0625	0.123
Single "Equivalent" Convergent Nozzle	1	0.5275	0.6525	0.2182	0.0625	0.116

FIG. 1. MULTINOZZLE CONFIGURATIONS AND SPECIFICATIONS.

a) THREE COAXIAL NOZZLES

b) TWO COAXIAL NOZZLES

c) 'EQUIVALENT' SINGLE CONVERGENT NOZZLE pressure response with frequency (from calibration curve provided by manufacturer with each microphone cartridge) and microphone free-field (from B & K handbook) were applied to all acoustic spectral data. Overall sound pressure and acoustic power levels were computed from the corrected 1/3 octave sound pressure level data.

Experimental Results:

1. Sound Pressure Level Spectra

For the innermost jet alone (nozzle 1) operated at pressure ratio ξ_1 = 3.04 and the intermediate jet alone (nozzle 2) operated at ξ_2 = 3.04, 1/3 octave sound pressure level vs. frequency are plotted for various azimuthal locations from 15° to 120° in Figs. 2a and 2b respectively . Generally for the single convergent nozzle operated in the underexpanded mode, over the frequency range 0.5 to 10 KHz the 1/3 octave SPL decreased with increasing azimuth angle. Therefore the radiated far-field noise at lower frequencies is progressively less intense at higher azimuth angles. Over the same low frequency range (0.5 to 10 KHz) and azimuth angles of 60° to 120°, 1/3 octave SPL at each azimuth angle increased by about 6 dB/octave.

For nozzles 1 and 2 operated alone the broad band SPL peaks occurred at 30° azimuth angle and in each case there are additional peaks at higher frequencies, around 90° for single jet from nozzle 1 (Fig. 2a) and at 30° to 90° from the annular nozzle 2 (Fig. 2b). For physical appearance of the underexpanded jet flow with cellular shock structure from nozzle 1 and nozzle 2, see schlieren records in Figs. 6a and 6b respectively. The inward tapering of the shock structure for the annular jet alone (with the innermost nozzle not operating, is worth noting. When the innermost (nozzle 1) and intermediate (nozzle 2) jets are operated simultaneously at pressure ratios ξ_2 = 3.04 and ξ_1 = 2.02 corresponding to the minimum noise mode of operation for two coaxial jets, the sharp peaks in 1/3 octave SPL vs. frequency plot (Fig. 2c) of the single supersonic jets are eliminated. The general peak still occurred at 30° but is shifted to a lower frequency around 5 kHz. However, similar to the single nozzle operation, over the frequency range 0.5 to 5 KHz the 1/3 octave SPL decreased with increasing azimuth angle and thus the lower frequency noise content predominates at smaller azimuth angles. For three-nozzle configuration of interacting coaxial jets operated at $\xi_1 = \xi_3$ = 2.02 and ξ_2 = 3.04, the 1/3 octave SPL peak still occurred at 30° but is shifted to even lower frequency at about 3 KHz. At azimuthal angles 60° to 120°, the 1/3 octave SPL increased by about 6 dB/octave. Similar to the single and two-nozzle operation, the spectral content of radiated noise from three interacting coaxial jets is stronger in low frequency components at smaller azimuth angles. In all four modes of operation the broad bank peak occurred at 30°. These peaks correspond to the same Strouhal number ≈ 0.16 if the Strouhal number for the single jet is defined as $f_p D/a_o$ where D is diameter of the single jet, a_o ambient sonic speed and f_p is the broadband peak frequency and the Strouhal number for the two or three coaxial jet flows is defined as $f_p D_{eq}/a_o$ where D_{eq} is the equivalent diameter of a single round nozzle calculated from the total exit area of the coaxial multinozzle configuration. This Strouhal number ≈ .16 agrees well with values obtained by Lush (Ref. 3) and Ahuja and Bushell (Ref. 4) for subsonic jets.

From the 1/3 octave SPL spectral data for all the modes of operation of the multinozzle jets reproduced in Fig. 2, the direction of maximum SPL in

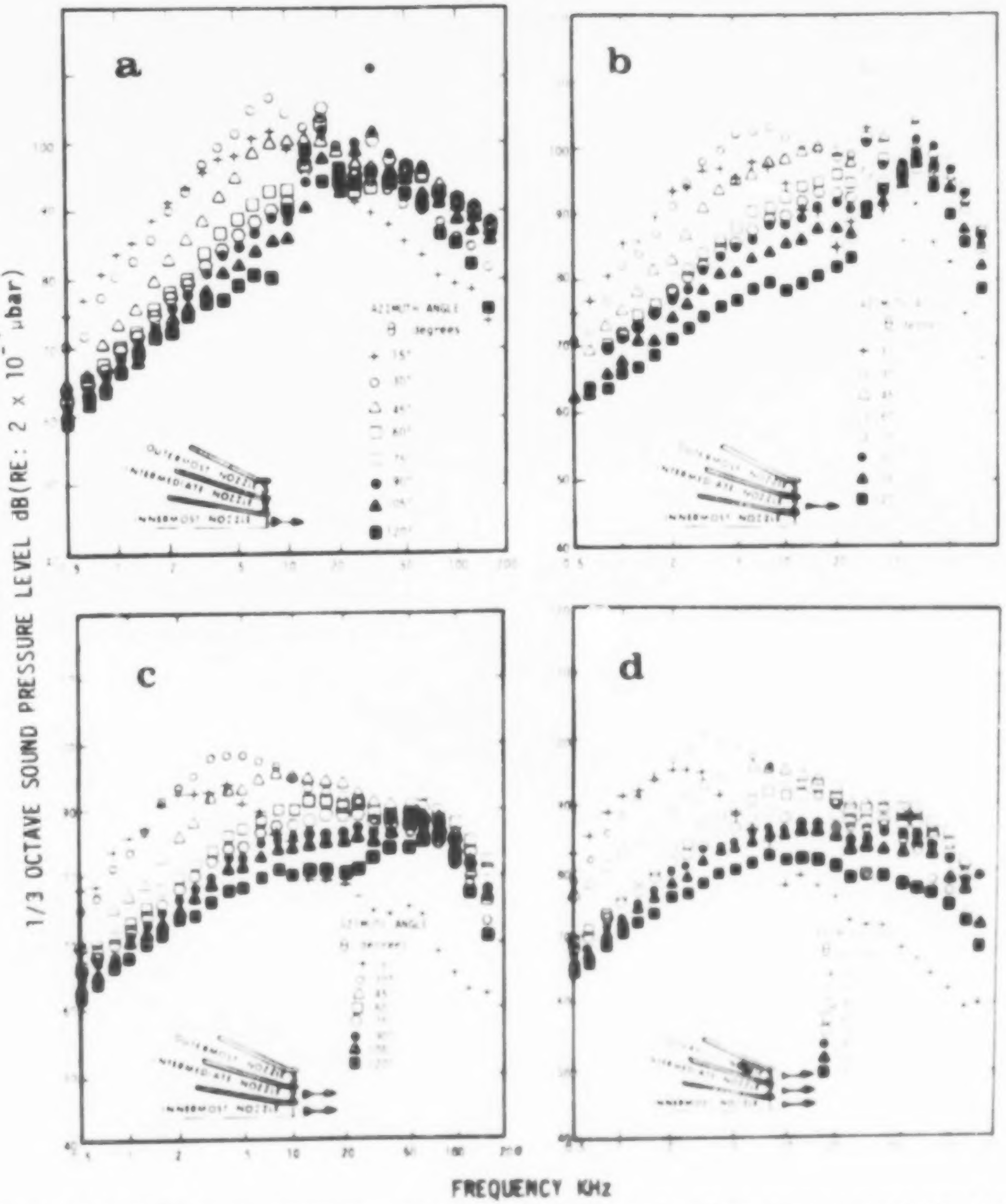

FIG.2 1/3 OCTAVE SOUND PRESSURE LEVEL VS. FREQUENCY FOR THREE-NOZZLE CONFIGURATION

(a) Only the innermost jet operated $\xi_1 = 3.04$: $\xi_2 = \xi_3 = 1$

(b) Only the intermediate jet operated $\xi_2 = 3.04$: $\xi_1 = \xi_3 = 1$

(c) Only two nozzles operated $\xi_2 = 3.04$: $\xi_1 = 2.02$: $\xi_3 = 1$

(d) All three nozzles operated $\xi_2 = 3.04$: $\xi_1 = \xi_3 = 2.02$

1/3 octave band vs. center frequency can be plotted (Ref. 5). It is observed that the higher the frequency band, the greater the azimuth angle for the peak noise; and that these angles increase in steps with frequency. However the peak noise data at different frequency bands do not exhibit any noteworthy difference in azimuth angles for the two and three coaxial jets when both configurations are operated under the respective minimum noise conditions. From comparison of earlier data on maximum SPL in 1/3 octave band vs. center frequency by Yu and Dosanjh (Ref.6) for a contoured nozzle (exit Mach number = 1.5)used at design (shock free jet) pressure ratio ξ = 3.57 and off-design (with shocks) pressure ratio ξ = 4.74, with that of the inner nozzle alone operated at pressure ratio ξ_1 = 3.04 and intermediate annular nozzle operated alone at ξ_2 = 3.04, it is observed that the shock-free jet exhibits the peak noise vs. 1/3 octave band center frequency very similar to the two or three coaxial jets operated for minimum noise when, due to flow interactions and modifications, there is hardly any strong cellular shock structure in the combined jet flows (for illustration see shadowgraphs of Figs. 5b, 5c and 6e and schlieren recording of Fig. 6c). On the other hand the single underexpanded supersonic circular or annular jets with shock structure (see shadowgraph of Fig. 5a and schlieren records of Figs. 6a and 6b) exhibit strong peaks at $\theta = 90^{\circ}$ at higher frequency bands. Similar peaks are observed at $\theta = 90^{\circ}$ to 120° for the contoured nozzle operated at off-design pressure ratios (Ref. 6) where shocks are present. From this comparison it is evident that the presence of shocks in turbulent free supersonic jet flows generates high frequency acoustic radiation which is more prevalent at higher azimuth angles, mostly around 90°.

2. Spectrum Level

Spectrum level at each 1/3 octave band center frequency were calculated for single, two and three interacting supersonic jets from 1/3 octave SPL spectral data corrected for microphone free field and pressure response using

$$L_p(f_c) = L_{p\ band} - 10 \log_{10} \frac{\Delta f}{\Delta f_o} \text{ dB re: } 2 \cdot 10^{-4}\ \mu\text{bar}$$

where $L_p(f_c)$ = the spectrum level dB (re: $2 \times 10^{-4}\ \mu$bar) at center frequency f_c; $L_{p\ band}$ = 1/3 octave band SPL (measured); Δf is the bandwidth for 1/3 octave band center frequency and Δf_o = 1 Hz. Spectrum level at each 1/3 octave center frequency are plotted in Fig. 3, where the operating pressure ratio for each mode of operation of the three-nozzle configuration are also given. Since the SPL peaks for single jets were observed at azimuth angles around $\theta = 30^{\circ}$ and 90° (Figs. 2a and 2b) and which were noticeably modified for two and three jet operation for minimum noise conditions (Figs. 2c and 2d), typical spectrum level data for one set of operating conditions are plotted only for azimuthal locations at $\theta = 30^{\circ}$ and 90°.

At azimuth angle $\theta = 30^{\circ}$ (Fig. 3), generally the slope of the spectrum level for low frequency range for minimum noise for the two and three nozzle configurations as well as the single supersonic circular or annular jets is equal to + 6 dB/octave. The spectrum levels for two and three interacting coaxial jets at respective minimum noise modes essentially have the same broad band peak at $f = 3150$ Hz. This shows that peak broad band noise of single annular supersonic jet observed at 5 KHz and for circular jet at about 8 KHz shifted to 3150 Hz for two or three coaxial interacting jets operated at their respective minimum noise conditions.

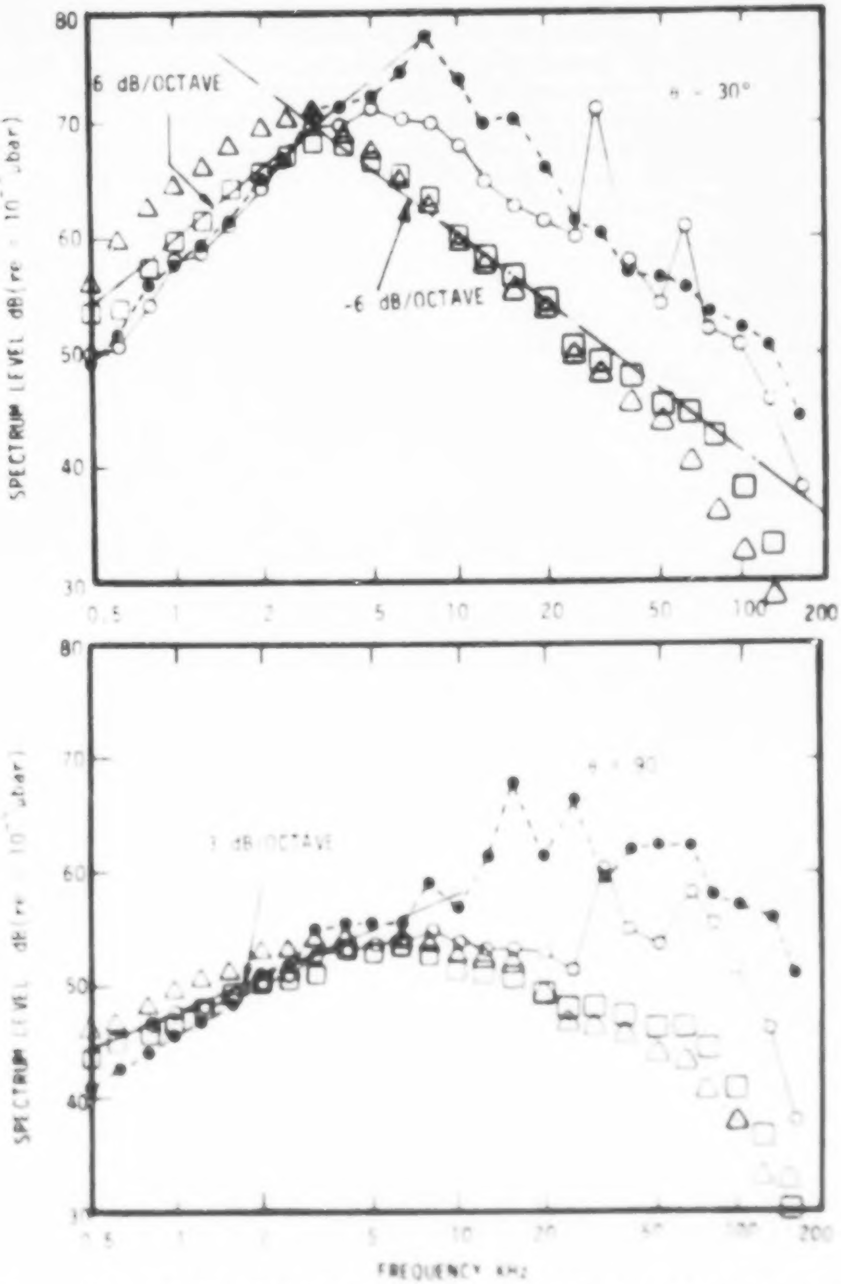

FIG. 5 1/3 OCTAVE SPECTRUM LEVEL VS. CENTER FREQUENCY FOR THREE-NOZZLE CONFIGURATION OPERATED AS SINGLE, TWO AND THREE-JETS

(—◆—) SINGLE SUPERSONIC CIRCULAR JET, [illegible] = 3.04,

(—○—) SINGLE ANNULAR SUPERSONIC JET, [illegible] = 3.04,

(□) TWO INTERACTING COAXIAL JETS, [illegible] = 3.04, [illegible]

(△) THREE INTERACTING COAXIAL JETS, [illegible] = 3.04, [illegible], The spectrum level drop-off for azimuth angle $\theta = 30^{o}$ was found to be about 6 dB/octave at 1/3 octave center frequencies up to about 20 KHz for the two and three nozzles operated in the minimum noise mode. The faster drop-off at higher 1/3 octave band center frequencies is most likely due to atmospheric absorption of sound at the relative humidity in the ambient medium in the anechoic chamber. Such absorption corrections at higher frequencies (Ref. 7) are currently being looked into. However the comparative magnitudes of the noise reductions obtained by using multinozzle schemes are not affected by these corrections.

At azimuth angle 90^{o}, the single supersonic jets exhibit strong discrete components at high frequencies in the spectrum level which for two and three interacting coaxial jet flows disappear. For frequency range of $f <$ 5 KHz, the two and three coaxial jets used at minimum noise conditions follow nearly + 3 dB/octave change in spectrum level. The nature of spectrum level variation with frequency at azimuth angles $\theta = 30^{o}$ and 90^{o} support the conclusion that the coaxial interacting jets from multinozzle configurations operated at about minimum noise conditions result in substantial reduction of broadband noise at higher frequencies as well as in the elimination of high frequency discrete (screech) components observed in radiated noise field of single supersonic circular (nozzle 1) and annular (nozzle 2) jets. The fundamental frequency of the discrete components can be roughly estimated by using Powell relation (Ref. 8).

3. Interpretation of Noise Reductions on the Basis of Thrust.

The three-nozzle configuration (Fig. 1) was operated either with nozzle 1 (innermost jet) operated alone or nozzles 1 and 2 operated simultaneously as two interacting jets in minimum noise mode or all three nozzles operated simultaneously, where the operating pressure ratios for nozzles 1 and 2 are kept fixed at values which yield minimum noise for two-jets and the operating pressure of the outermost jet (nozzle 3) is varied again to achieve minimum noise. The operating conditions for single, and combined two or three jets are listed in Fig. 4. The acoustic power levels for each mode of operation were calculated from the SPL spectral data corrected for microphone free field and pressure response. The total thrust/A_e (based on one-dimensional flow assumption) produced by coaxial jets was calculated at different operating conditions, where A_e is the total exit area of coaxial multinozzles i.e. $A_e = A_{e1} + A_{e2}$ if two nozzles are operated and $A_e = A_{e1} + A_{e2} + A_{e3}$ if three nozzles are operated. If a single jet is used, then A_e is the exit area of the single nozzle. It was assumed that the total thrust of the multinozzle configuration $T = \Sigma_i T_i$ where $i = 1, 2,$ and 3, is the sum of thrusts from each nozzle operating alone.

The variation of acoustic power level vs. thrust (both normalized with respect to the exit area/s) for the two-nozzle and three-nozzle configurations is reproduced in Fig. 4. The acoustic power levels of individual single jets from nozzles 1 and 2, the calculated total PWL of the two individual jets operated independently, 1 + 2, and the PWL of the two interacting coaxial jets used simultaneously are plotted in Fig. 4a. It is evident that for the same thrust/area, the use of the two interacting coaxial jets results in about 12 dB noise reduction when compared to the calculated total acoustic power level for the two individual jets operated independently, each at the same pressure ratio at which minimum noise for the two interacting coaxial jets was observed.

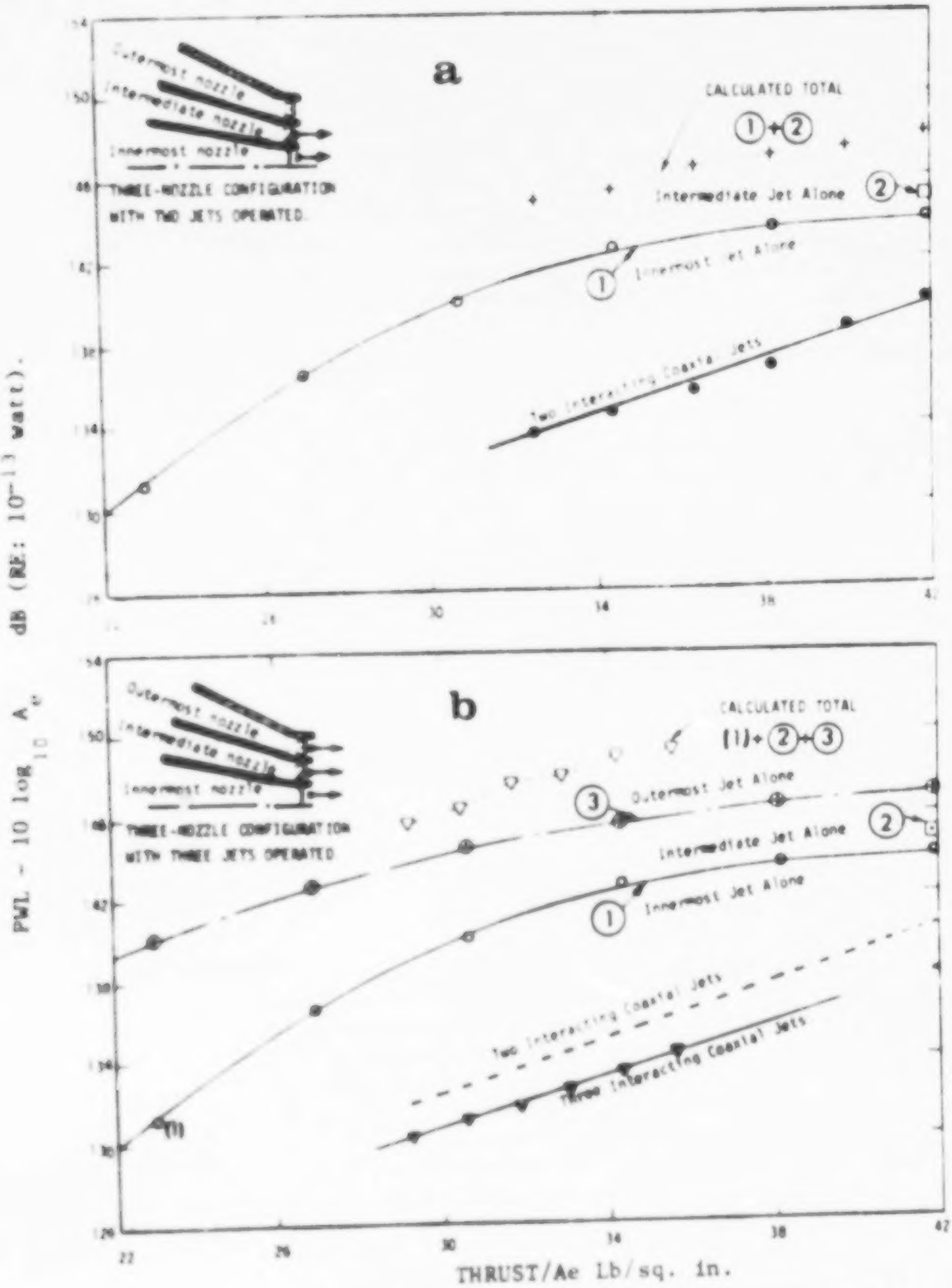

FIG. 4 TOTAL ACOUSTIC POWER LEVEL VS. CALCULATED THRUST, (both normalized with respect to nozzle exit area/s).

(—◆—) ξ_2 = 3.04 (fixed), ξ_3 = 1, ξ_1 variable (ξ_1 = 2.02 minimum noise).

(- + -) CALCULATED TOTAL ①+②·① ξ_1 variable, ② ξ_2 = 3.04 (fixed)

(—◆—) ξ_2 = 3.04 (fixed), ξ_1 = 2.02, ξ_3 variable (ξ_1 = 2.02 minimum noise).

(—○—) ① Innermost jet alone, ξ_1 variable,

(+ ● +) ③ Outermost jet alone, ξ_3 variable,

(▽) CALCULATED TOTAL (1) ② ③ (1) ξ_1 = 2.02 (fixed) ② ξ_2 = 3.04(fixed) ③ ξ_3 variable.

Starting with the two coaxial nozzles 1 and 2, each operated at the fixed pressure ratio at which minimum noise was recorded, the third nozzle is operated at various pressure ratios ξ_3, again resulting in minimum radiated noise for three coaxial jets at one value of ξ_3.

For the same thrust/area, acoustic power level reduction of about 16 dB may be claimed from the three interacting coaxial jets when compared with the calculated total acoustic power level from the three individual jets each operated independently at the pressure ratio at which it was used for achieving minimum noise from three interacting jets. However if for the same thrust/area, the comparison was to be based on the acoustic power level from the innermost jet alone (nozzle 1) and that from the three interacting jets, an acoustic power level reduction of about 8 to 9 dB will result.

The comparison of the acoustic power levels of the two- and three-nozzle coaxial jets at same thrust/area is shown in Fig. 4b. For acoustic power level reductions, the three-nozzle interacting coaxial jets are more effective than the two-nozzle interacting coaxial jets. However the potential usefulness of the three-nozzle configurations may inherently lie in that it offers additional flexibility of operation where the velocity gradients and the temperature gradients (if one or some of the jets were to be heated) may be systematically changed. These may result in favorable refraction and shielding phenomena yielding further noise reductions from interacting coaxial multinozzle jet flows. Such investigations are about to be initiated by the authors in the newly constructed acoustic and heated jet facilities.

4. Optical Investigations

Optical (schlieren and shadowgraphic) data gathered in these and earlier studies have been useful in exhibiting the nature and extent of the modifications in the shock structure and in the individual jet flows when coaxial supersonic jet flows from multinozzle configurations interact.

Two sets of typical shadowgraphs and schlieren records of coaxial supersonic jet flows from two-nozzle and three-nozzle configurations are reproduced in Figs. 5 and 6 where the operating conditions for each optical record are given. From comparison of the optical data and the radiated noise power level for interacting coaxial jets from two-nozzles where the operating pressure ratio of nozzle 2 is fixed at $\xi_2 = 3.04$ and operating pressure ratio ξ_1 of nozzle 1 is varied (Figs. 5a to 5h and Fig . 6c), it is evident that the observed noise variations and reductions from coaxial supersonic jets from two coaxial interacting jets correspond to the appearance of significant changes in the shock structure. The sequence of typical shadowgraphs in Fig. 5 (also see references 1 and 2) illustrates the modification of the shock structure of a single annular jet operated at $\xi_2 = 3.04$ (Fig. 5a) with progressively large values of the operating pressure ratio ξ_1 of the innermost jet (nozzle 1) achieving nearly minimum noise conditions for points A, B and C in the plot of PWL vs. ξ_1. The corresponding state of the interacting coaxial supersonic jet flows is shown by shadowgraphs (Fig. 5A, B and C) and schlieren records (Figs. 6a, 6b and 6c). Note the development of a composite shock structure just downstream of the nozzle exit with only weak shock and wave structure in the flow downstream. As the operating pressure ratio ξ_1 is increased, the shock structure reappears and with $\xi_1 \rightarrow \xi_2$ 3.04 (Fig. 5h), double cellular shock structure appears. It is worth noting that even when the two coaxial jets

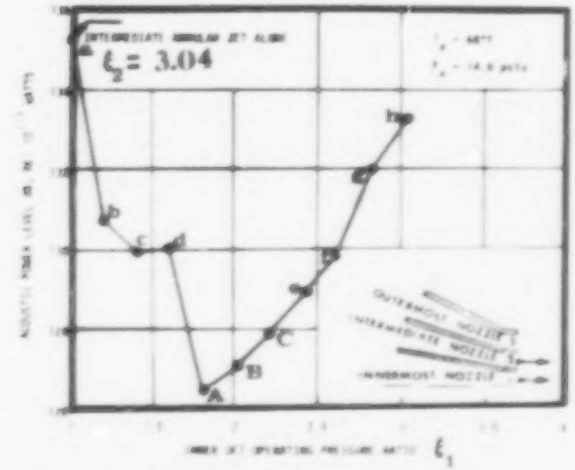

NOISE FROM TWO INTERACTING COAXIAL JETS

$\xi_2 = 3.04$ (Fixed)

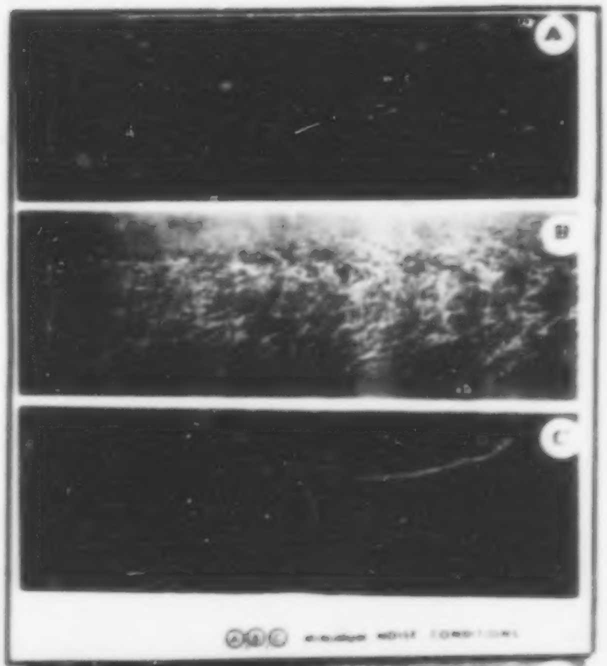
A
B
C
ABC MINIMUM NOISE CONDITIONS

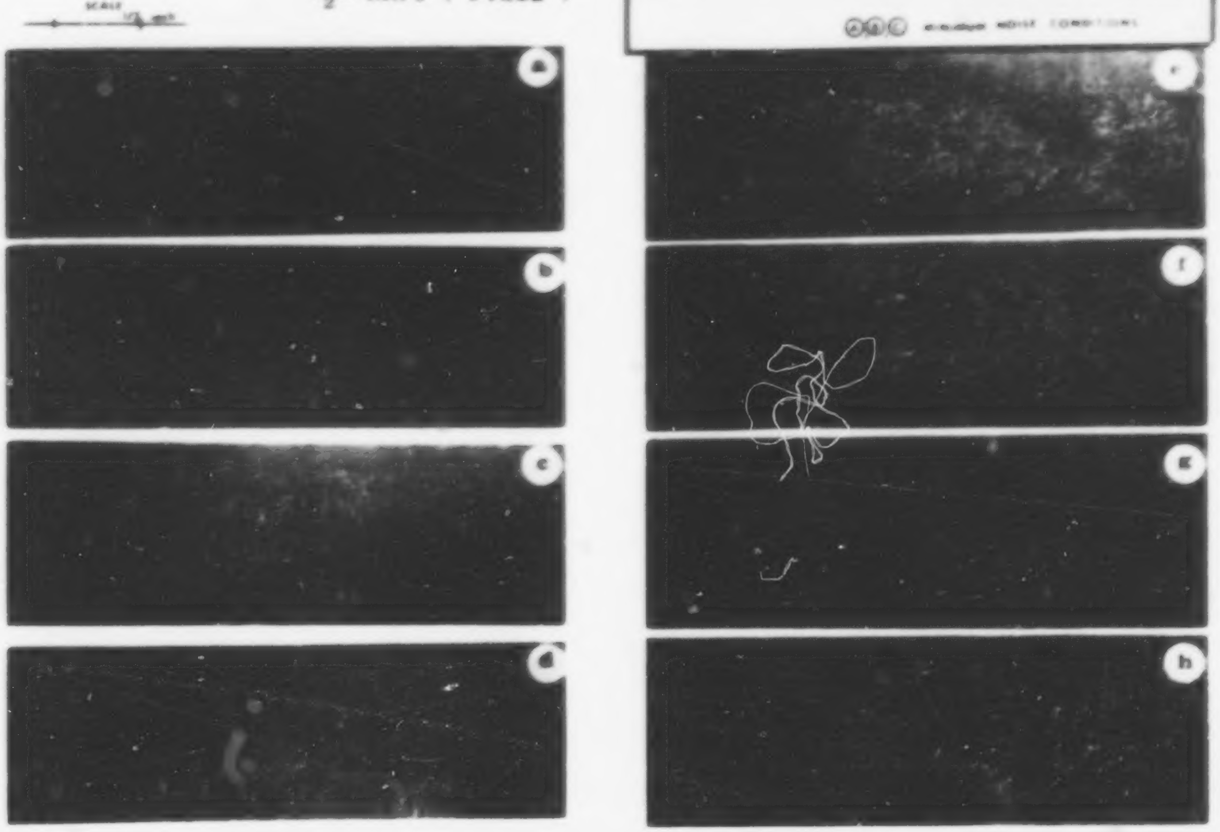
SCALE
a
b
c
d
e
f
g
h

FIG. 5 SEQUENCE OF SHADOGRAPHSOF TWO INTERACTING COAXIAL JETS : All NOZZLES CONVERGENT.

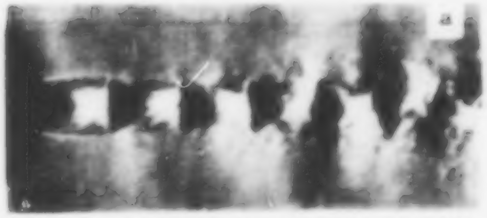

Single Circular Nozzle $\zeta_1 = 3.04$

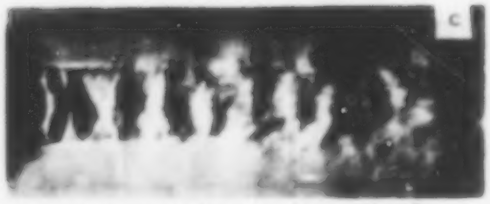

Minimum Noise (two-jets)
$\zeta_1 = 2.02$ $\zeta_2 = 3.04$

Single Annular Nozzle $\zeta_2 = 3.04$

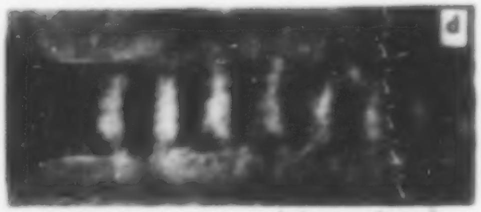

Minimum Noise (three jets)
$\zeta_1 = \zeta_3 = 2.02$ $\zeta_2 = 3.04$

(A) Typical Schlieren Records

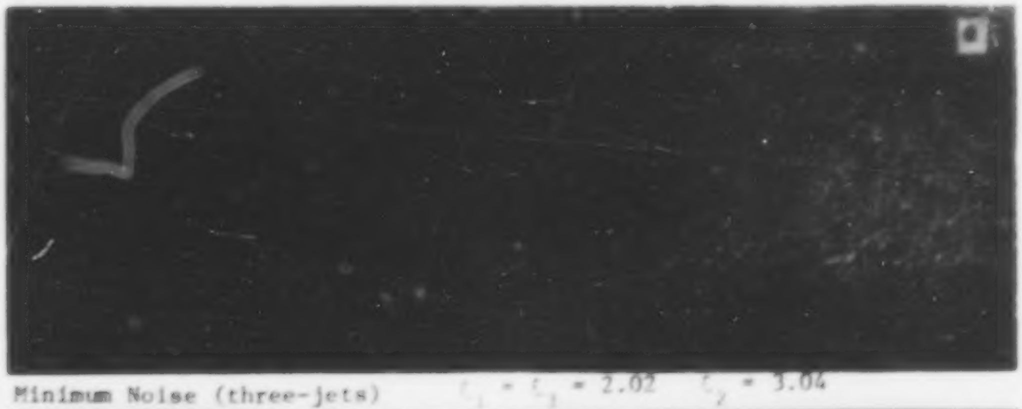

Minimum Noise (three-jets) $\zeta_1 = \zeta_3 = 2.02$ $\zeta_2 = 3.04$

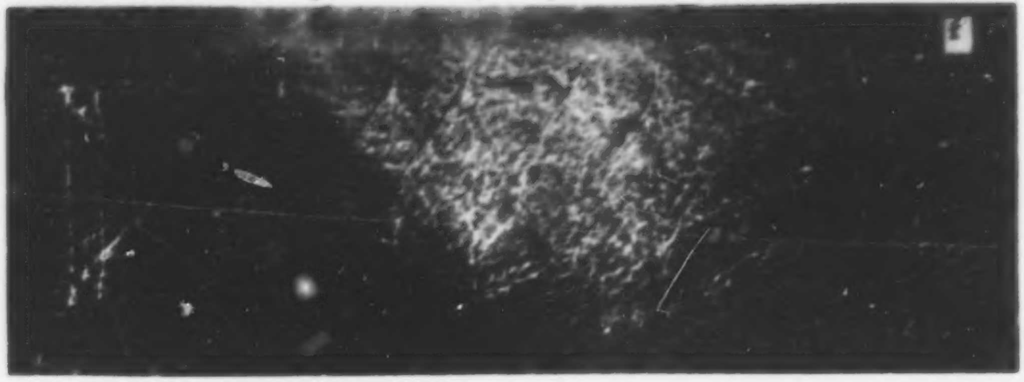

All three jets operated at same pressure $\zeta_1 = \zeta_2 = \zeta_3 = 3.04$

(B) Typical Shadowgraphs (three-jets)

Fig. 6. Typical Optical Records for Single and Multiple Jets.

(nozzle 1 and 2) are operated at the same pressure ratios, the radiated noise from the combined jet flows (Fig. 5, point h) is less than the single annular jet alone (point a) or the circular jet from nozzle 1.

Typical shadowgraphs and schlieren records for three coaxial jets where the intermediate jet (nozzle 2) is operated at $\xi_2 = 3.04$ and the innermost jet (nozzle 1) and the outermost jet (nozzle 3) are operated at the same pressure ratios $\xi_1 = \xi_3$, are reproduced in Fig. 6. For minimum noise operations the shock structure is quite modified (Fig. 6d & 6e) as compared to single jet (Fig. 6a or 6b) and it is located close to the nozzle exit with only weak wave system in the downstream jet flow. The combined coaxial jet flow downstream of this shock is similar to a nearly shock-free flow from a fully-expanded nozzle.

5. Single 'Equivalent' Jet

The single equivalent convergent nozzle was designed to have the exit area equal to the total exit area of the two-nozzle configuration and was operated at a pressure ratio that resulted in the same thrust and mass flow as that of the coaxial two-nozzle configuration operated at the minimum noise condition. 1/3 octave spectral data were recorded for both systems. Figure 7a shows a comparison of the wide band directionality pattern over the frequency band from 200 Hz to 100 KHz obtained for the coaxial two-nozzle configuration and the single equivalent convergent nozzle. The maximum reduction in OASPL of about 11 dB occurs at 90° to the jet axis. Along the direction of maximum noise propagation (30° with the jet axis) the reduction in OASPL is about 6 dB. As the single nozzle and the two-nozzle configurations have the same thrust ($T_s = T_1 + T_2$), same mass flow ($\dot{m}_s = \dot{m}_1 + \dot{m}_2$) and equal exit areas ($A_{e_s} = A_{e_1} + A_{e_2}$), it can be concluded that in this mode of operation the two coaxial supersonic jets radiate less noise than the single 'equivalent' convergent supersonic jet. This observation is even more noteworthy considering that the single convergent underexpanded jet is operated at a lower pressure ratio than the outer jet (dominant noise generator) of the coaxial jet arrangement, thus yielding a lower mean flow velocity for the single jet than that of the outer jet in the coaxial system.

The calculated 1/3 octave power spectra for the coaxial and single 'equivalent' systems are compared in Fig. 8a. As the exit areas, the thrust and the mass flow are the same, the difference in magnitudes of the PWL's in each 1/3 octave band represents a reliable measure of the noise reduction in that band. The single 'equivalent' jet and the coaxial jets have their respective peaks around 20 and 31.5 KHz. The maximum reduction of 12.5 dB occurs in the 20 KHz band. The spectra of the coaxial jets is quite flat over a wide frequency band as opposed to a continuous rise in the case of the single 'equivalent' jet. A reduction in OAPWL of about 9 dB is achieved where both the disappearance of the discrete components and reduction in broad band PWL are the contributing factors.

The same single nozzle was also operated at a pressure ratio $\xi_s = 3.04$ and the coaxial two-nozzle arrangement was operated at $\xi_1 = \xi_2 = 3.04$. 1/3 octave spectral data were gathered for both systems. Since the mass flow, the thrust and the operating pressure ratios of the two systems were the same, this mode of operation of the coaxial two-nozzle configuration is similar to the multi-tube suppressor when all tubes are operated at the same pressure ratio. It must be remarked here that these operating conditions for the coaxial two-nozzle

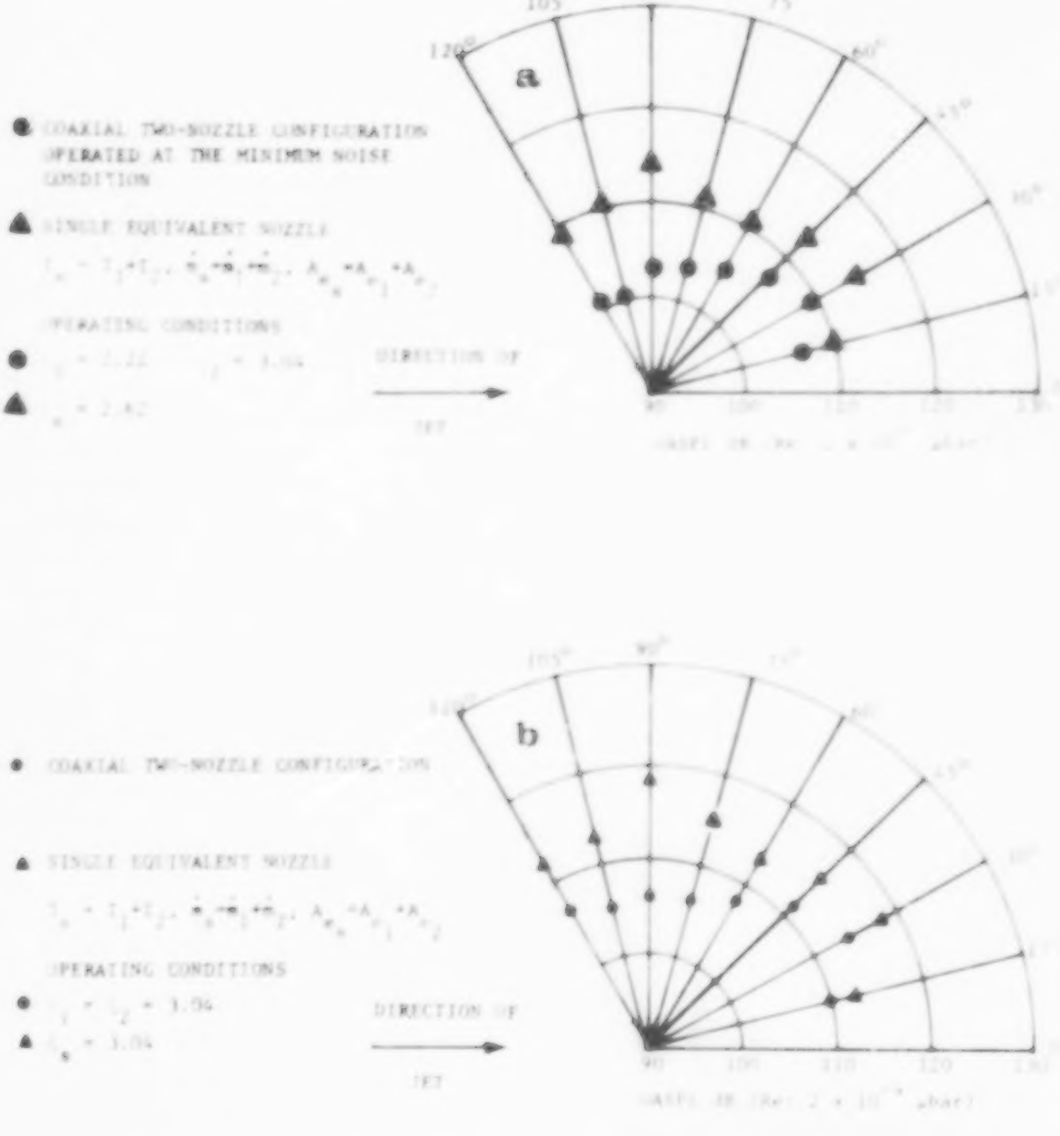

FIG. 7. COMPARISON OF RADIATED OASPL's OF JET FLOWS FROM A COAXIAL TWO-NOZZLE CONFIGURATION WITH THAT OF A SINGLE JET FROM AN EQUIVALENT CONVERGENT NOZZLE.

a) THRUST, MASS FLOW AND EXIT AREA SAME FOR BOTH SYSTEMS.

b) THRUST, MASS FLOW, EXIT AREA AND PRESSURE RATIO THE SAME FOR THE TWO SYSTEMS.

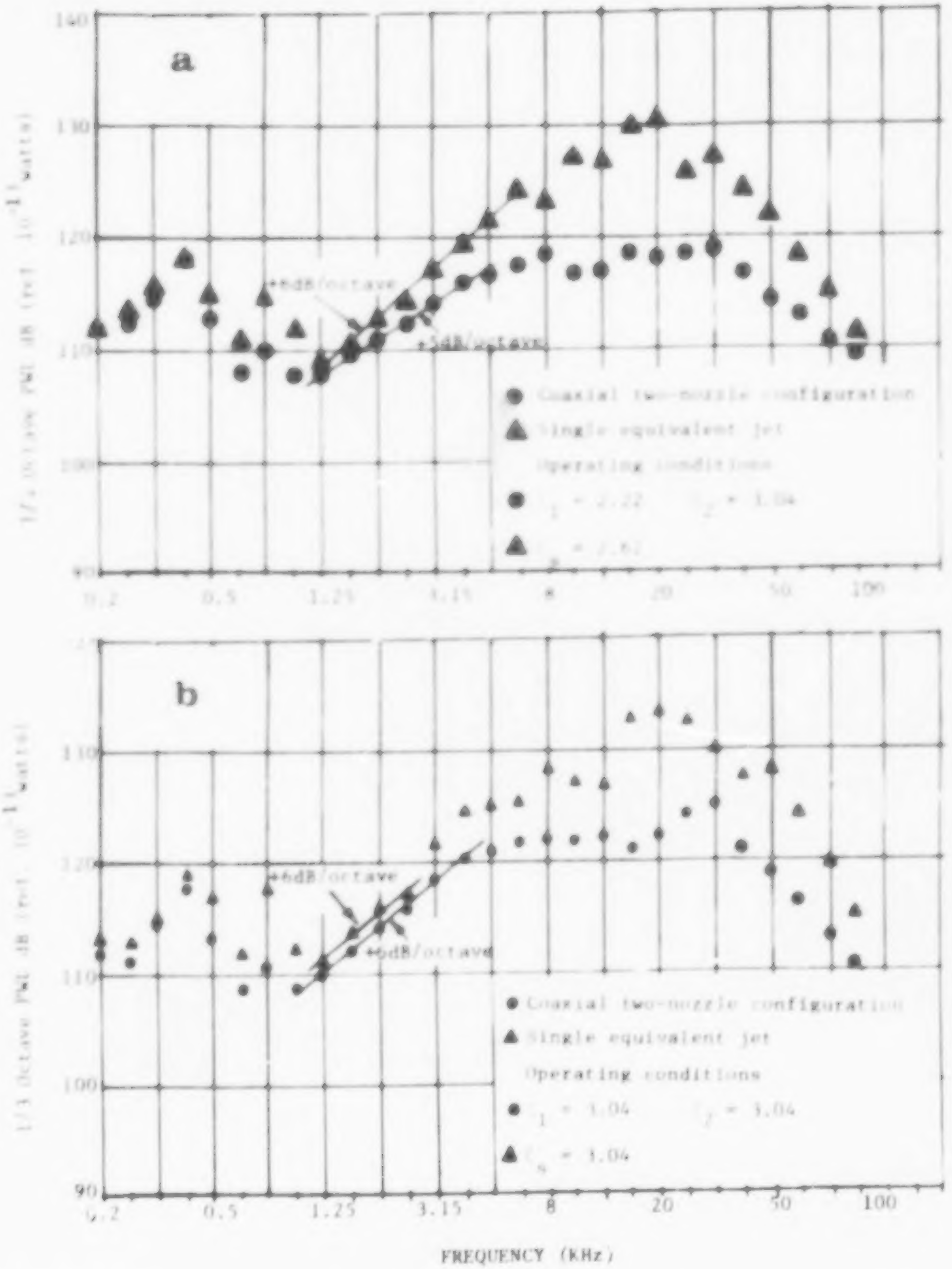

FIG. 8. COMPARISON OF 1/3 OCTAVE BAND POWER SPECTRA OF JET NOISE FROM COAXIAL TWO-NOZZLE CONFIGURATION WITH THAT OF A SINGLE JET FROM AN EQUIVALENT CONVERGENT NOZZLE.

a) THRUST, MASS FLOW AND EXIT AREA SAME FOR BOTH SYSTEMS.

b) THRUST, MASS FLOW, EXIT AREA AND PRESSURE RATIO THE SAME FOR THE TWO SYSTEMS.

system were chosen because only then could all the important physical parameters including the pressure ratio be matched for both the coaxial two nozzle and the single 'equivalent' nozzle jet flows.

The wide band directionality pattern plotted in Fig. 7b shows a maximum reduction of about 12.0 dB in the direction normal to the jet axis. This is partly because a peak acoustic radiation was observed at 90° to the jet axis in the case of the single jet, while shock and flow modification in interacting coaxial jets eliminated any such radiation in the coaxial two-nozzle configuration.

The calculated 1/3 octave power spectra for the two systems are compared in Fig. 8b. The single 'equivalent' jet has its peak PWL again at 20 KHz. However two peaks are now evident for the coaxial system, one at 12.5 KHz and the other at 31.5 KHz. The largest reduction in PWL of 11 dB was observed in the 16 KHz band. Here again the single 'equivalent' jet is seen to have a higher sound power level than the coaxial jet system in the entire 1/3 octave band spectrum from 1.25 KHz to 100 KHz. Total reduction in OAPWL of about 7 dB is achieved because of reductions in both the discrete and broad band noise components. Although this mode of operation is not the most favorable for achieving maximum noise reduction from a coaxial two-nozzle configuration, it still is an attractive system for noise reduction. The role of the solid annulus between nozzles 1 and 2 (Fig. 1) on the observed noise reductions and the assessment of the possible thrust loss is now being studied more systematically.

[This research work is supported by the Noise Abatement Office of the DOT under grant No. DOT-OS-20094. Some of the shadowgraphic data reproduced in Figs. 5 and 6 were recorded by M. Audi during his participation as a research assistant under the DOT research project.]

References

1. Yu, J. C. and Dosanjh, D.S., "Noise Field of Coaxial Interacting Supersonic Jet Flows", AIAA Paper No. 71-152, January, 1971.
2. Dosanjh, D.S., Yu, J.C., and Abdelhamid, A.N., "Reduction of Noise from Supersonic Jet Flows", AIAA Journal, Vol.9, No.12, Dec., 1971.
3. Lush, P.A., "Measurement of Subsonic Jet Noise and Comparison with Theory", Journal of Fluid Mechanics 46, 1971.
4. Ahuja, K.K., and Bushell, K.W., "An Experimental Study of Subsonic Jet Noise and Comparison with Theory", Journal of Sound & Vibration, 30 (3), 1973.
5. Dosanjh, D.S., Ahuja, K.K., Bhutiani, P.K., Bassiouni, M.R. "Noise Reduction from Supersonic Jet Flows", Quarterly Progress Report No.7, Feb.1974.
6. Yu, J.C. and Dosanjh, D.S., "Noise Field of a Supersonic Mach 1.5 Cold Model Jet", JASA Vol. 51, No. 5 Part I, May 1972, pp. 1400-1410.
7. Evans, L.B. and Bass, H.E., "Table of Absorption and Velocity of Sound in Still Air at 68°F", Wyle Laboratories Report WR 72-2, January 1972.
8. Powell, A., "On the Mechanism of Choked Jet Noise", Proc. Phys. Soc., LXVI, 12-B, 1953.

FLUID DYNAMIC ASPECTS OF JET NOISE GENERATION

by

S.Slutsky, Polytechnic Institute of New York, Brooklyn, N.Y.
S.Panunzio, New York University, New York, N.Y.
V.Barra, New York University, New York, N.Y.

An experimental investigation is underway under a NASA grant, directed toward a better understanding of the coupling between turbulent fluctuations in the mixing region of the jet and pressure fluctuations inside and outside the jet. The jet being studied at this time is comprised of an inner axisymmetric, supersonic flow and an outer concentric subsonic flow whose velocity can be independently varied. During the past year efforts have been directed to the aerodynamic and acoustic survey of the jet flow field, to developing procedures for introducing a test signal at the jet boundary, to the extraction of the signal within the jet from the intense ambient noise field in which it is imbedded and to the preliminary tracing of the wave field in the moving jet. Subsequent efforts are hoped to generate insight into the focussing effects of waves at the jet axis, to interaction of these waves with the shock structure of the jet and to the relative contribution of the several possible disturbance sources in an engine flow to the external noise field.

Introduction

One of the important objectives of this experimental investigation is to obtain qualitative and quantitative information on the propagation of a wave inside a jet (single or multiple) with particular attention to refraction of ray trajectories and distortion of wave profile due to nonlinear effects.

As discussed in Ref. 1, sound can originate in the disturbances of the mixing zone, propagate into the jet core, cross the sonic line and curve back upstream. This upstream propagation can reinforce the original mixing zone disturbance, and result in the phenomenon of supersonic screech.

Nonlinear steepening of large amplitude compression waves which focus at the axis, together with the separation of the expansion wave ray path from that of the compression wave, can play an important role in the intensification of emission from the neighborhood of shock surfaces as well as the sonic surface.

An experimental method is being used to study these phenomena, based on the introduction of one or more test signals whose subsequent history can then be monitored by means of pressure pickups and signal detection procedures. Principal tasks encountered in this phase of the effort have included

a) construction jet facility
b) development of suitable electroacoustic and pneumatic sound sources
c) construction of transducer mounts and supports
d) investigation of the aerodynamic flow field of the jet including mean velocity and pressure distribution and shock structure.

e) investigation of acoustic field within the jet, including a mapping of the rms static pressures and of the power spectral distribution along the axis.

f) development of signal recovery techniques for the extraction of test signals from the high Mach number flow and high ambient noise level acoustic field.

g) preliminary mapping of test field within jet.

Progress During the Year

Facility

The axisymmetric flow system described in Fig. 4 of Ref. 2 has been constructed and tested through its working range, which is M = 2 for the 7 inch inner region (T_o = 490°R, mass flow 60 lb.m/sec). The concentric outer nozzle is 10 inches in diameter, pressure balanced at M = 1, with mass flow of 20 lb.m/sec. A stand is located on a track oriented along the jet, on which the microphones and other probes are mounted. A traverse mechanism permits the transducers to make a vertical traverse of the jet (perpendicular to the flow direction).

Sound Sources

A pneumatic system has been constructed which uses a compressed air manifold (20 to 200 psig) to deliver six pulsed flows of air to six emission points spaced circumferentially around the jet. The pulsations are produced by cutting off the flow periodically in the six air supply lines connected with the manifold using a rotating valve (i.e., a disc with 24 windows driven by a variable speed electric motor). Phase of the signals can be controlled by a slight variation of the lead lines, and pulse repetition rates of 700 per second, currently, and 2000 per second with some modifications to the motor drive.

Experimentation with this source was postponed while using an electro-acoustic driver system consisting of an audio power source, a 100 watt Altec Lansing driver, and a 3" exit diameter catenoidal coupling horn. This source delivered adequate power for our initial exploratory studies, with the added convenience of higher signal repetition rate (significance discussed below) and ease of coupling with electronic reference signal generator. Source intensity reached about 154 dB at the horn exit plane at 5KHz and about 160 dB at 2KHz. The use of paired drivers to feed a single horn via a coupling T connection will be initiated within a few days of this writing, to increase power, and to decrease the small electromagnetic radiation field which is being sensed by the transducers.

Transducers

Transducers used in this study include a pitot tube and static pressure probe for pressure, Mach number and shock configuration surveys, condenser microphones (1/8" and 1/4") for sound field surveys outside of the jet, and

Kulite piezoresistive pressure transducers (type CQ125) for measurements within the jet flow. The Kulite transducer is mounted within a 1/4" diameter tube, and fitted with a Bruel and Kjaer ogival nose cone for measurement of static pressure fluctuations, or a nose cone, closed except for a hole at the stagnation point, for measurement of total pressure fluctuation. A blind cap was also made when it became apparent that noise other than the signal of interest was being picked up. The cap was used to identify and remove these noise sources.

It will be noted that the Kulite transducers are rather insensitive as compared to the usual acoustic microphones, and are operated at the lower end of their usual dynamic range. The electronic noise thereby experienced is much smaller than the jet noise signal, and is processed together with the latter. However, non random signals picked up by the microphone, such as the very small voltage induced by the magnetic field from the electroacoustic driver, cannot be ignored since it determines the practical signal level floor. As noted above, the pair of drivers arranged on a T-connection to feed into a single horn is expected to materially improve that condition, because of the opposed and rotated magnetic field orientations.

The transducers were mounted onto the traverse mechanism, and cables were fully enclosed within the streamlined support structure to minimize cable noise due to vibration.

Aerodynamic Flow Field

The manner in which the jet facility is arranged at this time permits a running time of 40 seconds at a chamber pressure, P_o, of 80 psia and nozzle exit pressure of 10 psia but a considerably shorter time at p_o = 115 psia (balanced exit pressure). The lower chamber pressure is being used until a modified valve arrangement is installed to give 40 seconds at the balanced condition. The present flow field is therefore associated with the shock structure of an overexpanded jet. The time average static pressure, velocity and mach number distributions were determined at axially spaced cross-sections. Shadowgraphs were also taken to confirm the discontinuity locations.

Acoustic Field Within Jet

Using the Kulite transducer with the static pressure nose cone, fluctuating static pressure levels were measured on the axis. The SPL varied from 160 dB at the jet exit, to a maximum of 176 at 8 1/2 diameters (60") downstream. Stagnation pressure fluctuations at the 8 1/2 diameter position were about 187 dB. (The measured chamber pressure for this case was 80 psia). Transverse static pressure surveys taken at six streamwise stations showed the pressure peaking at the edge of the jet, first moving out radially for 2 diameters, then moving in toward the axis and growing. Thereafter the SPL decayed fairly uniformly. These curves were found to be in reasonable agreement with those reported in the literature by Nagamatsu.

Narrow band spectra taken at various locations generally showed low frequency peaks at 50 to 100 Hz, dropping then by about 6 dB per octave, upon which is superimposed a second distribution peaking at from 1 to 3 KHz, (depending on position). Both peaks grow considerably in strength as the microphone is moved downstream, but the frequency at the upper peak decreases monotonically and markedly with distance along the axis. This contribution would appear to be related to the mixing induced turbulence whose scale increases monotonically with axial position and whose characteristic frequency drops correspondingly. The low frequency peak could then be due to initial turbulent flow thru the shock structure and to the dynamic interaction and amplification mechanisms associated with shock noise. This will be clearer when we survey in a balanced jet and in the mixing region.

Signal Recovery

Initial experiments with a purely electronic simulation of the signal extraction from noise established that processing on a SAICOR 42 would be feasible. This instrument can function in several modes including a signal enhance (ensemble averaging) mode.

The ensemble averaging procedure works by sensing a sample of the test signal, digitizing and storing the resulting sequence of magnitudes $f_i^{(1)}$ (i = 1 to 100) in a row of 100 "storage bins". This sensing process is initiated by means of a suitable trigger pulse. When the next trigger pulse comes along the process is repeated, and the second sequence of 100 values, $f_i^{(2)}$ is sensed and the i-th element is allocated to the i-th bin where it is added to the previous value. After N repetitions of this process the sum grows linearly with the number of repetitions; $\sum_{n=1}^{N} f_i^{(n)} = N f_i^{(1)} = N f_i$.

However, if the test signal is stationary random with zero mean and with $f_i^{(n)}$ uncorrelated with $f_i^{(m)}$, $m \neq n$, then the sum grows like $\sqrt{N}$; $\sum_{n=1}^{N} f_i^{(n)} \rightarrow \sqrt{N} f_{rms}$.

If our test signal is imbedded in random noise, the summing procedure will result in an N-fold growth of the test signal and a $\sqrt{N}$ increase in the summed random noise, i.e., an improvement in stored signal to noise ratio of $\sqrt{N}$, or 10 log N decibels.

It should be noted that this ideal gain is obtainable only when the processor is being used in the "clipped" mode (in which the signal is sensed either as plus or minus one). The condition for accuracy of this mode is that the random part of the signal is much stronger than the deterministic part. As noted before, this condition is amply satisfied in our case, whereas it could not be used if the signal to noise ratio were of the order of unity.

The feasibility of extracting a small test signal from a strong random noise background therefore depends on the initial signal to noise ratio (SNR) and on the number of repetitions. The number of repetitions N depends, in turn, on the repetition rate of the acoustic source, and the effective running time of the jet. Hence, the advantage of using a sound source at 5000 Hz (rather than 700) and a running time of 40 sec, giving N = 200,000 and a SNR gain of 53 dB. Note that the Altec Lansing driver is more efficient at 2KHz (6dB) so this lower frequency may be more desirable, by 6 - 4 = 2 dB.

Various electronic filtering possibilities were tried in order to cut out those parts of the noise frequency spectrum not essential to the detailed descriptions of the recovered signal shape. However, induced phase shifts for any filters with sharper than 6 dB/octave cutoffs proved unacceptable.

The foregoing procedures are being used for the study of the propagation of a test signal within the jet. Two Kulite microphones are being used, sting-mounted on the test stand. One microphone is currently located at the axis, the second 1 1/2" below, and the acoustic driver at 4" below the axis and centered 2" from the jet exit. Measurements were made with the Kulite microphones at a series of axial positions ranging from upstream of the mach cone of influence to about 7 3/8" downstream of the exit. Each signal was amplified and recorded on both FM and D/R channels of a Honeywell 5600 tape recorder together with a trigger signal activated by the electronic signal source feeding a Bogen power amplifier and thence the Altec Lansing driver. On playback from the tape recorder, the SAICOR ensemble averager, was used to recover the signal.

Signal sound pressure levels recovered to date ranged from a maximum of .015 psi (peak to peak) down to an apparent signal floor of .002 psi. However, since that latter amplitude was found to be almost exactly equal to that induced by the magnetic field of the driver (as well as other possible sources in the test signal generating sequence) it is expected that it will be soon removed. Note that the induced voltage corresponding to that field is quite small, order of 10[illegible] volts, but is significant because of the very high overall signal amplification entailed in the processing procedure. It appears then that recovery capability with present running times are adequate for r.m.s. signal to noise ratios down to 1/100.

Preliminary Mapping

The comparison of the test field within the jet to that in the absence of the jet shows the expected shift of the measured axial contours to a downstream position corresponding to the convection of the field. In addition the position upstream of the mach cone shows a zone which it appears now would be several decades down in amplitude from that within the cone, were it not for the above mentioned magnetic field.

The most downstream position found one of the microphones located at a shock. Here the ambient noise was so great that the signal could not be recovered in the available running time.

Efforts in the immediate future call for cleaning up of our instrumentation procedures, improvement of the jet flow, and more systematic test signal tracing.

Acknowledgement

The work reported herein was supported by the National Aeronautics and Space Administration under Grant #NGR-33-016-177. It was directed and guided by Professor Antonio Ferri of the New York University Aerospace Laboratory.

References

1) A. Ferri, L. Ting and J. Werner, "Supersonic Jet Engine Noise Analysis", Interagency Symposium on University Research in Transportation Noise, Vol. 1, p. 39.

2) A. Ferri, S. Slutsky and S. Panunzio, "Fluid Dynamic Aspects of Jet Noise Generation", Interagency Symposium on University Research in Transportation Noise, Vol. 1, p. 62.

NOISE FROM FLOW INTERACTION WITH SOLID BODIES

INVESTIGATION OF JET NOISE FROM SLOT NOZZLES WITH ATTACHED FLAPS

by

J. R. Maus, W. A. Dunnill, G. T. Patterson, and P. M. Yee
The University of Tennessee Space Institute
Tullahoma, Tennessee

INTRODUCTION

For short-haul STOL aircraft to be employed most effectively they must be able to take off and land within highly populated areas. Because of the nature of operation of these aircraft, they are likely to be subject to more restrictive noise regulations than conventional aircraft. These restrictions coupled with the aerodynamic requirements of a high lift propulsion system which are inherently noisy make the acoustic problems associated with STOL aircraft especially challenging.

One contender for a powered lift system for STOL aircraft is the internally blown jet-augmented flap or jet flap; a high aspect ratio rectangular nozzle exhausting over a flap. A simple representation of a jet flap is shown in Figure 1. Acoustically, one expects that a slot nozzle with a high aspect ratio will produce a lower sound power than a circular nozzle of the same area and shift the noise spectrum to the higher frequency regime. These expectations are confirmed by the experimental observations presented in this report and by those of other investigators (Ref. 1,2). A flap placed below the slot nozzle should act as a sound shield for high frequency noise generated above the flap with wave length short compared to the length of the flap. Thus, part of the aircraft exhaust noise could be directed away from the ground. Early experimental results (Ref. 1,3) seemed to substantiate these ideas but more recent investigations (Ref. 4,5,6) have indicated important noise sources associated with the interaction of the jet flow with the flap. Nonetheless, the jet flap appears to be one of the quieter of the powered lift systems currently being considered for STOL application (Ref. 7).

One of the goals of the present study is to investigate in some detail the aeroacoustic characteristics of the jet flap. This is being accomplished by a systematic variation of geometrical and fluid dynamic parameters of the jet flap and measurement of appropriate acoustic quantities. Some of the results of this study are presented in this paper.

A second goal of the study was to determine the location and strength of the principal noise sources in the jet flap exhaust. To date, efforts in this direction have consisted of hot wire anemometer measurements in the turbulent exhaust. From these measurements an attempt has been made to estimate the acoustic source strength distribution in the turbulent mixing layers developing from the nozzle exit and from the trailing edge of the flap. This work has been discussed extensively in previous publications (Ref. 6, 8) and will be described only briefly in this paper.

A third goal of the present study is to investigate techniques for suppressing or more effectively redirecting the noise generated from jet flap exhaust flows. The results of initial experimentation in this direction are also described in this report.

EXPERIMENTAL FACILITIES

The experimental facilities used to perform the investigations described in this report consist of three major parts: a high pressure blow-down facility for the generation of free jets, a reverberation chamber for the determination of overall sound power and a free field jet noise facility. Figure 2 is a schematic of the reverberation chamber and shows the principal elements of the air supply system and sound data acquisition system. The reverberation chamber has a volume of $10.2m^3$ and a lower cut off frequency of 500 Hz. In addition to providing an easy technique for obtaining overall sound power from a jet, the chamber provides a shelter for hot wire probes and thus facilitates the acquisition of turbulence data. Figure 3 shows an elevation view of the free field test facility used for obtaining the directional radiation characteristics of jet exhaust flows. The nozzle exit is located approximately 15 feet above the ground plane and the nozzle axis is oriented at an angle of 35.5° to the horizontal. At this angle, three microphone sweep arms located symmetrically about the nozzle exit may be used to measure the sound pressure level in the three principal planes of the nozzle. The three identical sweep arms permit microphone measurements along three great circles of a sphere centered at the nozzle exit as shown in Figure 4. The measurement sphere radius can be varied from 5 ft. to 20 ft. The stilling chamber of the free field facility can be lowered to a horizontal position to allow fluid dynamic measurements and permit rapid model changes (see Figure 3).

The operational limits of the aeroacoustics facilities are as follows: Nozzles up to 5 cm in diameter may be tested with cold flow in the reverberation chamber up to Mach 1. Nozzles up to 30 cm in diameter may be tested with cold flow in the free field up to Mach 1. A heater has been installed which allows hot gas testing in the free field at temperatures up to 1000°F.

EXPERIMENTAL RESULTS AND DISCUSSION

SOUND POWER MEASUREMENTS

Acoustical data were obtained for slot nozzles with straight flaps using both the reverberation chamber facility and the free field facility described in the previous section. Figure 5 gives a general picture of the overall sound power output as a function of the exit Mach number, nozzle aspect ratio and flap length.

The slot nozzles are generally quieter than the equivalent area 2 cm. diameter circular nozzles by some 3 dB or more for Mach numbers larger than approximately 0.5. Adding a flap to the slot nozzle results in an increase of the radiated sound power over the entire Mach number range covered. For low Mach numbers this increase is substantially greater than for the higher subsonic Mach numbers.

Figure 6 shows the overall sound power output of a 60 aspect ratio slot nozzle as a function of dimensionless flap length $\delta_f = \ell_f/h$, with Mach number as a parameter. In the range $0 < \delta_f \lesssim 8$, the overall sound power output increases with increasing flap length. The rate of increase is dependent on the exit Mach number being greatest for the lowest Mach number. For $\delta_f > 10$ the sound power decreases slightly over the range of flap lengths tested. These trends are also exhibited for other nozzles of different aspect ratio that were tested.

Figure 7 shows the behavior of the sound power spectral density functions as characterized by the peak frequency of these spectra. The addition of a flap increases the peak frequency of these spectral density functions indicating an increase in the high frequency noise. For $M_e = 0.9$ the peak frequency increases with increasing flap length up to $\delta_f \approx 10$ and then decreases for the longer flaps.

It should be noted that the change in radiation characteristics occurs at the flap length that is approximately equal to the maximum potential core length. When a flap is added to a slot nozzle the flow field is, of course, changed substantially. On the free side of the jet the mixing layer develops essentially in the same way as for a two dimensional jet. However, on the lower side of the jet the free mixing layer is prevented from developing by the presence of the flap, and instead, a boundary layer is formed along the flap surface. This boundary layer grows much more slowly than the free mixing layer and hence the potential core region of the jet is elongated. As the flap length changes, three different cases can be distinguished depending on whether the potential core extends beyond the end of the flap, terminates at the trailing edge, or is shorter than the flap (see Figure 8). For these three cases, the flow patterns will be substantially different and thus the characteristics of the radiated sound can be expected to be different. Downstream of the trailing edge of the flap a second free mixing region develops. There are indications that this secondary mixing region is a strong source of aerodynamic noise. It is believed that the increase in sound power with increasing flap length is due to a combination of the noise generated by the turbulent boundary layer on the flap surface, the elongation of the potential core, and the secondary mixing region.

ACOUSTIC SOURCE DETERMINATION

In an effort to better characterize the noise producing regions of jet flap exhaust flow, detailed hot wire measurements were taken in the turbulent mixing regions of a 60 aspect ratio slot nozzle with attached flaps of various length. The exit velocity for these measurements was 120 m/sec corresponding to an exit Mach number of .35. Figures 9 and 10 are examples of mean velocity profiles and turbulence intensity profiles taken for the slot nozzle with and without an attached flap. These profiles were taken at $x_1/h = 6.5$, just downstream from the trailing edge of flap with $\delta_f = 5.6$. Two important features of the flow field of a jet flap are readily apparent from inspection of these profiles. First, the mean velocity and the turbulence intensity distributions in the primary mixing region are unaffected by the addition of the flap. Second, a narrow region of very intense turbulence and very large mean velocity gradients occurs just beyond the trailing edge of the flap. This indicates a very strong source of aerodynamic noise in the secondary mixing region.

Additional measurements of space correlation coefficients yielding a scale of turbulence were combined with the mean velocity and turbulence intensity profiles, to give the acoustic source intensity of the shear noise as computed by using the following formula derived by Lilley (Ref. 9):

$$I(x_1,x_2) = C\left(\frac{\partial U_1}{\partial x_2}\right)^6 \overline{u_1^2}\, L_{x_1}^5 \qquad (1)$$

An example showing the results of this computation is given in Figure 11 where contours of equal source intensity are plotted in the x_1x_2 plane. It is clear from this figure that the secondary mixing region is a very strong source of aerodynamic noise. Approximate integration of the intensity distribution shown in Figure 11 reveals that the secondary mixing region for this configuration has approximately 10 times the sound power output of the primary mixing region. A similar calculation was made for longer flaps, $\delta_F = 8.95$ and $\delta_F = 15.4$. These computations show that the sound power of the secondary mixing region decreases with increasing flap length. However, even for the longer flap, $\delta_F = 15.4$, the total sound power of the secondary mixing region was almost five times that of the primary mixing region above the flap.

The existance of this strong acoustic source in the secondary mixing region must be regarded as a major disadvantage of the jet flap. Not only does this sound source increase the overall sound power of the jet but it also renders the flap ineffective as a sound shield since the secondary mixing region radiates noise unobstructedly toward the ground.

DIRECTIONAL RADIATION CHARACTERISTICS

Investigation of the directional radiation pattern and spectra for slot nozzles with and without attached flaps was carried out utilizing the free field facility. The slot nozzle investigated had an aspect ratio of 13.85 and an exit area of 7.06 cm^2 (equivalent to a 3 cm. diameter circular nozzle). Flap lengths corresponding to δ_f between 2.85 and 12.5 were investigated. Data were taken on a 220° circular arc of radius 13 ft., centered on the nozzle exit plane and in the plane X_1X_3 as shown in Figure 4.

The total sound pressure level directional characteristics at a Mach number of 0.9 is given in Figures 12 and 13. The convective and refractive effects of the jet are evident in the increased sound pressure levels in the vicinity of ± 30 to ± 40 degrees. Data is not presented in the -20° to +20° range since this data was very erratic due to the jet flow effects on the microphone. As was observed in reverberation chamber tests, the sound pressure level increases with increasing flap length up to a δ_f of 7.13. The larger value of δ_f however shows a decrease in SPL. The larger value of δ_f (12.5) is large enough such that the potential core does not extend to the flap trailing edge. Thus, the mean flow velocity at the trailing edge is reduced and the potential for producing a region of high noise source intensity in the secondary mixing region is also reduced. It is believed that this reduced effectiveness of the secondary mixing region is the reason for the reduced SPL for $\delta_f = 12.5$ versus $\delta_f = 7.13$.

As mentioned previously, it is hoped that the flap will act as a shield for the high frequency noise generated above the flap. Figures 12 and 13, however, do not indicate any shielding effect due to the flap. It is thought that this may be due to the flaps tested being too short to effectively shield the primary mixing region. Longer flaps would not only provide more effective sound shielding for the primary mixing region but would also reduce the intensity of the secondary mixing region as a sound source.

Figure 14 shows the power spectral density increase of the nozzle with flap over the nozzle without flap at +90° for a Mach number of 0.9. This shows that for the short flap the increased noise is in the high frequency region. As the flap is lengthened the noise increases in the lower frequencies. This is probably due to two factors. First the longer flap causes an extension of the potential core. This allows the primary mixing region to extend farther down the flap and although the essential character of this mixing region is not altered, the increased length will allow for the formation of the large scale turbulence necessary for low frequency noise production. Secondly, the boundary layer buildup as the flap is lengthened results in larger vortices being shed from the trailing edge thus also tending to produce larger scale turbulence.

Figure 15 shows the spectra for plus and minus 90° for a δ_f of 12.5 and Mach number of 0.9. It can be seen that there is a significant reduction in the very high frequencies at -90°

although the level is not sufficient to affect the overall level. This indicates that the flap is shielding the very high frequency noise as can be expected.

STRAIGHT FLAPS AT ANGLES

Acoustic measurements were made on jet flaps attached to slot nozzles with the flap deflected at small angles with respect to the normal flow direction at the nozzle exit. A slot nozzle. with an exit area of 3.14 cm^2 (equivalent to a 2 cm. diameter circular nozzle) and aspect ratio of 120 was used with different flap configurations. Flaps of three different lengths, $\ell_f = 2$, 3.5 and 5 cm (corresponding to a flap length to slot height ratio of $\delta_f = 12.4$, 21.5, and 31) and three different angles, $\alpha = 0$, 3, and 10° were tested at three different exit Mach numbers, .5, .7, and .9. In all tests the jet core length was less than the length of the flap. The measurements were carried out in the reverberation chamber and the results are shown in Figures 16 and 17.

The effect of flap angle on the power density spectrum is displayed in Figure 16. The spectra are mostly unaltered by a change in the flap angle. Figure 17 further indicates that the flap angle has no influence on the overall radiated sound power for all jet exit Mach numbers.

From these reverberation chamber tests conclusions reached are that the flap angle within the angle range tested does not appreciably alter the overall radiated sound power or the frequency spectrum of the radiated sound indicating that the secondary mixing region is unaffected by flap angle variation. It is believed that the jet tends to adhere to the flap surface - thus changing, in effect, only the mean jet exhaust direction.

ROUGH FLAP EFFECTS

Slot nozzles with straight rough flaps were investigated since this configuration has the potential for increasing the boundary layer thickness and subsequently reducing a dominant factor in the noise generating mechanism, the mean velocity gradient. The slot nozzle investigated had an exit area of 7.06 cm^2, an aspect ratio of 13.85, and a dimensionless flap length of 12.5. The flap was roughened by glueing sand paper to the upper surface taking care to always have the upper surface mounted parallel and coincident to the base of the slot nozzle. Four different sandpapers were used with roughness numbers of R_f of 36, 50, 80, and 100, the smaller numbers corresponding to a coarser surface.

Results of reverberation chamber tests are shown in Figures 18 and 19. Variation of the overall sound power with Jet exit Mach number is shown in Figure 18 for the rough flaps, the smooth flap and the basic slot nozzle. It is observed that the rough flaps are quieter than the smooth flap throughout the Mach number range. It is noisier, however, than the basic slot nozzle over a wide range of subsonic Mach numbers. In addition it is noted that the rate of increase of sound power with increase in exit Mach number is lower for the rough flaps. The plots also indicate that the rough flap might be quieter than the slot nozzle at near sonic Mach numbers. The effect of surface roughness on the sound power is shown in Figure 19. It is observed that, at constant pressure ratio roughness primarily decreases high frequency components.

Results of free field tests are shown in Figures 20, 21, and 22. Figure 20 is a plot of the angular distribution of the sound pressure level for smooth and rough flaps. It is observed that the sound pressure level is reduced at all angles for roughened flaps with a maximum reduction of 5 dB at 30 degrees below the axis (in the direction of maximum sound pressure level). Figures 21 and 22 compare the spectra of smooth and rough flaps at 30 and 90 degrees respectively below the flap. At minus 90 degrees the reduction in noise level is mainly due to the high frequency components above 10,000 Hz. At minus 30 degrees the reduction in noise level is mainly due to the reduced frequency components above 2000 Hz a result similar to the reverberation chamber sound power spectra shown in Figure 19. Above 10,000 Hz, the noise reduction is approximately equal at 30 and 90 degrees with maximum differences of 3 to 4 dB. The uniform reduction in high frequency indicates that the rough surface causes a reduction in the self-noise components. The additional reduction in noise from 2000 to 10,000 Hz at 30 degrees could be attributed to reduced shear noise since shear noise is dominant for low angular directions near the jet axis and is low pitched, at least when compared with self noise. These results indicate that the flap surface roughness affects the turbulence scale as well as the mean velocity gradient and thus alters the contribution of both the shear and self-noise.

CONCLUSIONS

From the experimental results on jet flap type exhaust flows presented in this paper the following conclusions can be made:

1. Addition of a flap causes an increase in sound output from a slot nozzle. The sound power increases with flap length up to a length approximately equal to the potential core and thereafter slowly decreases.

2. Part of this increase is due to the sound generated in the secondary mixing region downstream of the flap trailing edge. This mixing region is a strong source of aerodynamic sound.

3. For the nozzles investigated, short flaps ($\delta_F < 7$) show no benificial sound shielding effects. Longer flaps show some shielding of high frequency noise.

4. The overall sound power output is not affected by the deflection of the flap through small angles.

5. The effect of increased flap roughness is to reduce the over-

all sound power radiated. Directionally the greatest attenuation occurs at the maximum noise lobe about 30° below the jet axis.

ACKNOWLEDGEMENTS

The authors express sincere appreciation to the Federal Aviation Administration and to the National Aeronautics and Space Administration who supported this work under contracts DOT-FA72WA-3053, NASA-NGR-43-001-075 and NGR 43-001-135. Appreciation is also extended to Miss Vicky Parks who typed the manuscript and to Messers. M. C. Joshi and V. Veerasamy for their help in preparing the figures.

REFERENCES

1. Coles, W. D. "Jet-Engine Exhaust Noise from Slot Nozzles," National Aeronautics and Space Administration Technical Note D-70, Lewis Research Center, September 1959.

2. Maestrello, L. and E. McDaid, "Acoustic Characteristics of a High-Subsonic Jet," AIAA Journal, Vol. 9, No. 6, June, 1971.

3. Maglieri, D. J. and H. H. Hubbard, "Preliminary Measurements of the Noise Characteristics of some Jet-Augmented Flap Configurations," National Aeronautics and Space Administration Memorandum 12-4-58L, January 1959.

4. Hayden, R. E. "Sound Generation by Turbulent Wall Jet Flow over a Trailing Edge," Master's Thesis, Purdue University, August 1969.

5. Grosche, F. R., J. H. Jones and G. A. Wilhold, "Measurements of the Distribution of Sound Source Intensities in Turbulent Jets," AIAA Paper No. 73-989, October 1973.

6. Schrecker, G. O. and J. R. Maus, "Noise Characteristics of Jet Flap Type Exhaust Flows," NASA CR 2342, February 1974.

7. Dorsch, R. G., E. A. Kresja and W. A. Olsen, "Blown Flap Noise Research," American Institute of Aeronatucis and Astronautics, Paper No. 71-745, June 1971.

8. Goethert, B. H. and J. R. Maus, "Aeroacoustical Research on Circular and Slot Nozzles without and with Flaps," Proceedings, Interagency Symposium on University Research in Transportation Noise," March, 1973.

9. Lilley, G. M., "On the Noise from Air Jets," Aeronautical Research Council No. 20376, September 1958.

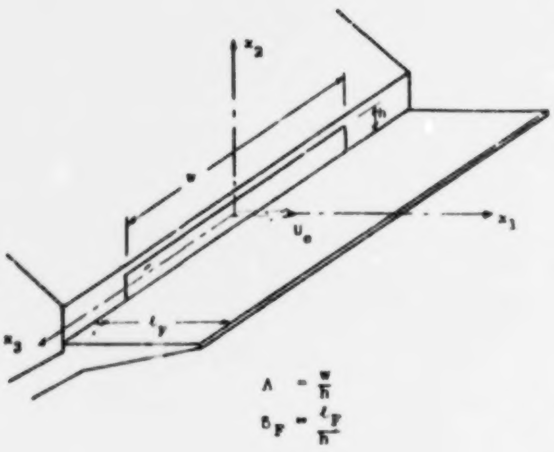

x_2
h
w
U_e
x_1
x_3
l_F
$\Lambda = \frac{w}{h}$
$\delta_F = \frac{l_F}{h}$

Figure 1. Jet Flap Geometry and Nomenclature.

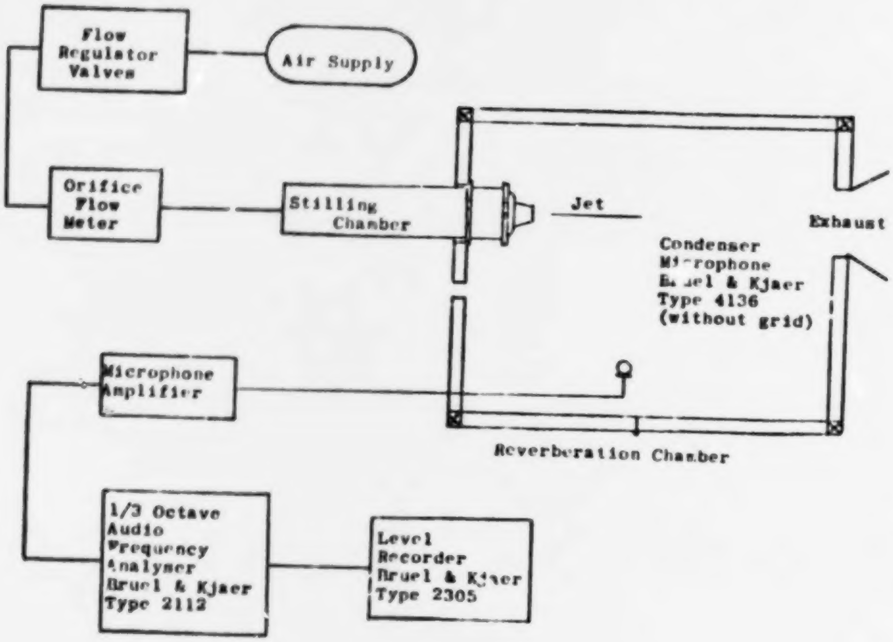

Flow Regulator Valves
Air Supply
Orifice Flow Meter
Stilling Chamber
Jet
Exhaust
Condenser Microphone Bruel & Kjaer Type 4136 (without grid)
Microphone Amplifier
Reverberation Chamber
1/3 Octave Audio Frequency Analyser Bruel & Kjaer Type 2112
Level Recorder Bruel & Kjaer Type 2305

Figure 2. Schematic of Reverberation Chamber Facility.

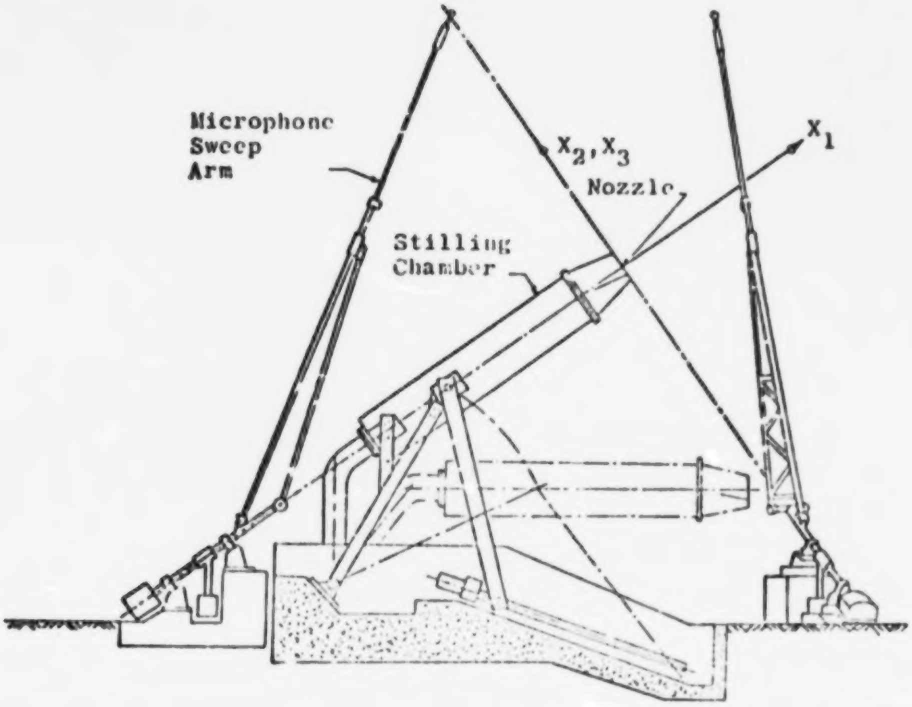
Microphone
Sweep
Arm
X_2, X_3
X_1
Nozzle
Stilling
Chamber

Figure 3. Elevation View of Free Field Facility

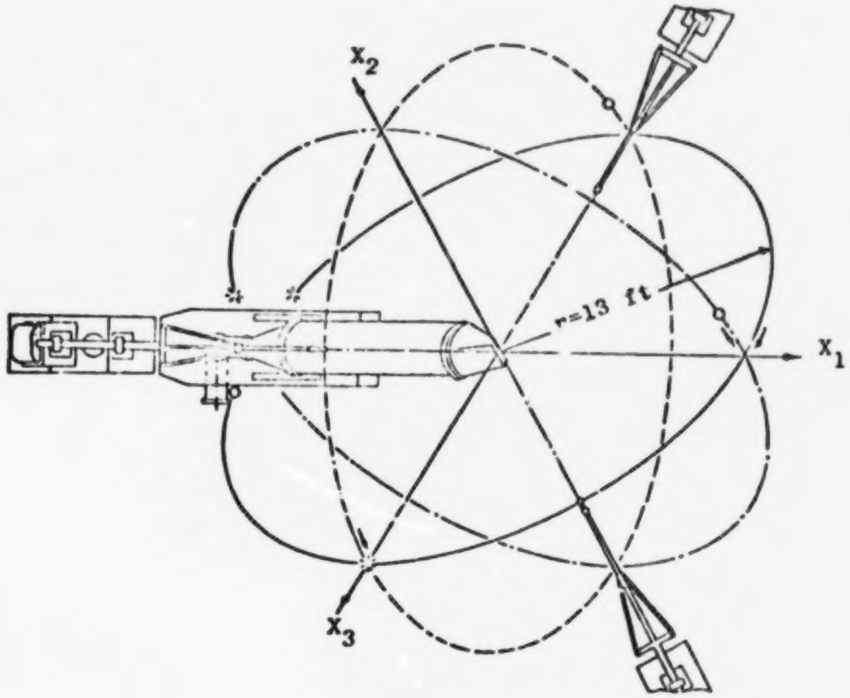
X_2
r=13 ft
X_1
X_3

Figure 4. Plan View of Free Field Facility

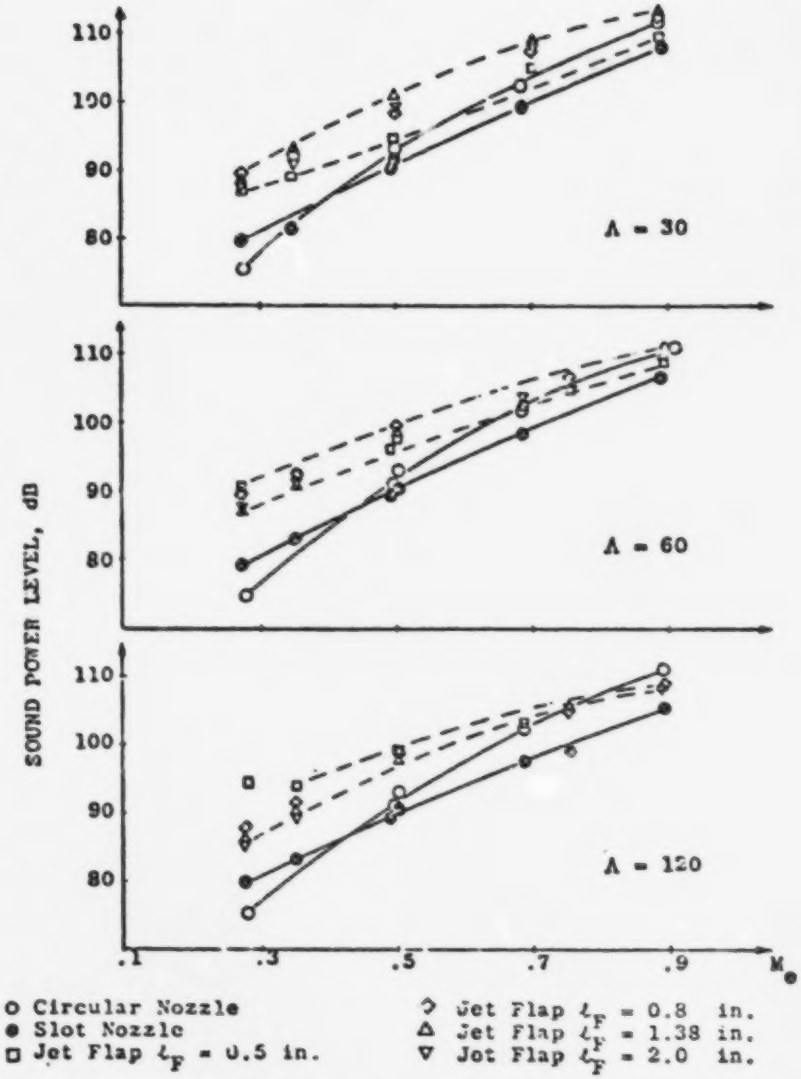

Figure 5. Overall Sound Power Level Versus Mach Number

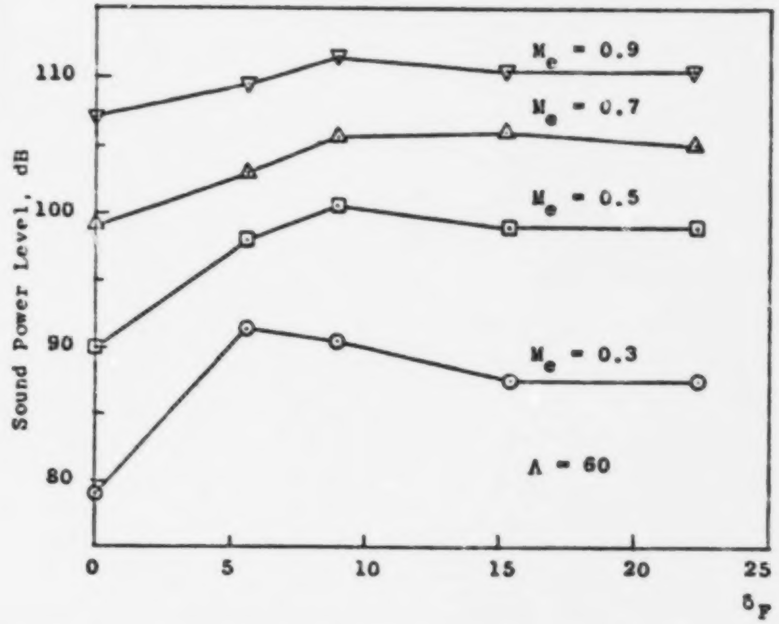

Figure 6. Overall Sound Power Level Versus Flap Length

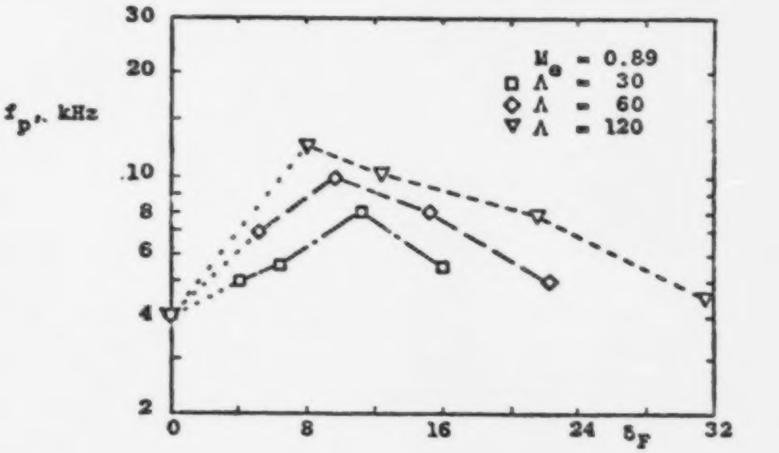

Figure 7. Peak Frequency of Power Density Spectra Versus Flap Length.

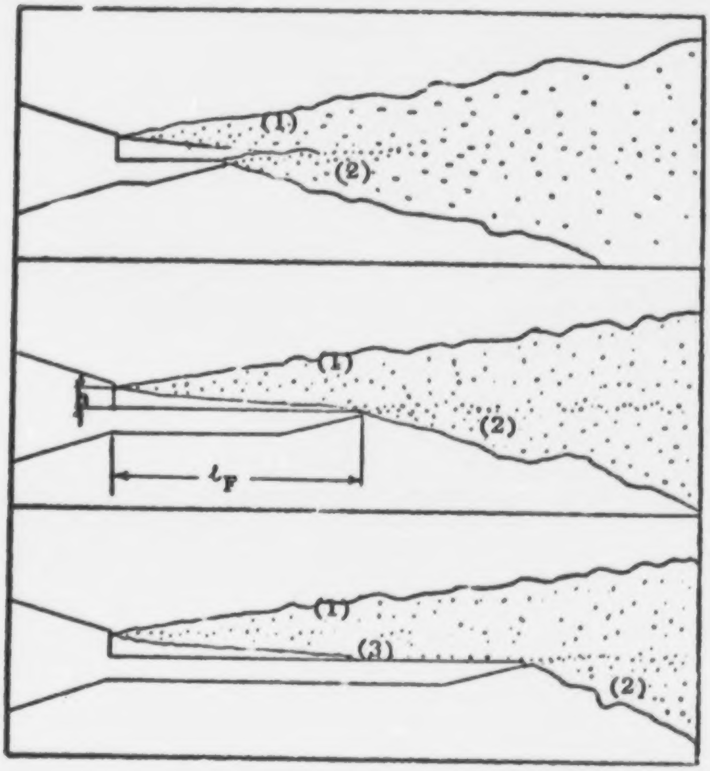

Figure 8. Three Flow Configurations encountered with Jet Flap. Three Noise Source regions are (1) primary mixing region, (2) secondary mixing region, (3) turbulent boundary layer.

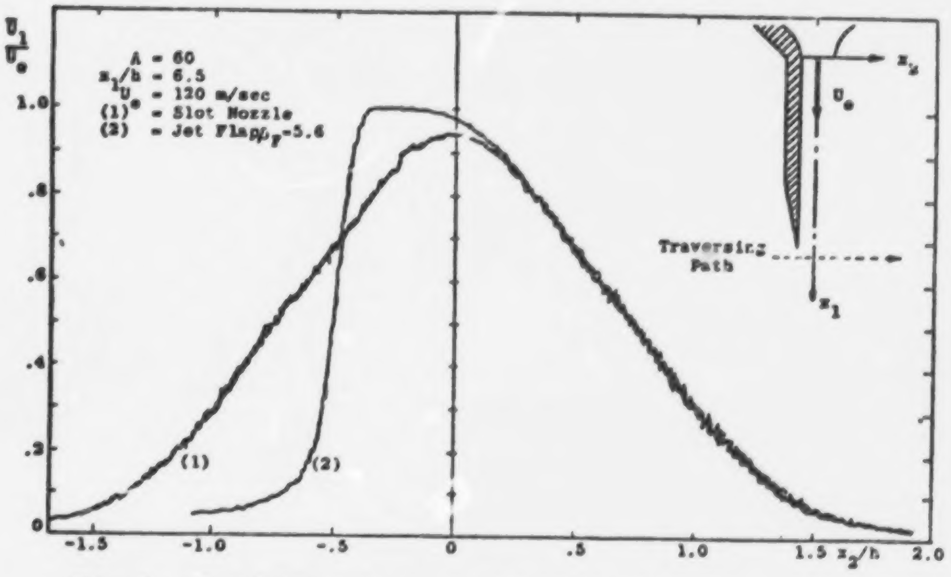

Figure 9. Mean Velocity Profiles of Slot Nozzle and Jet Flap at $x_1/h = 6.5$.

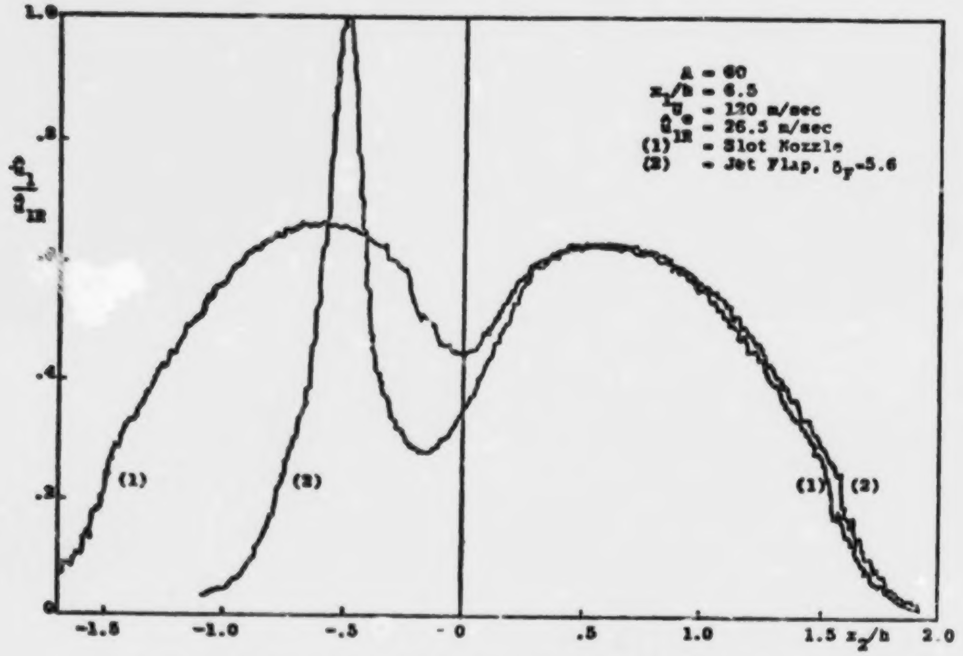

Figure 10. Turbulence Intensity Profiles of Slot Nozzle and Jet Flap at x_1/h=6.5.

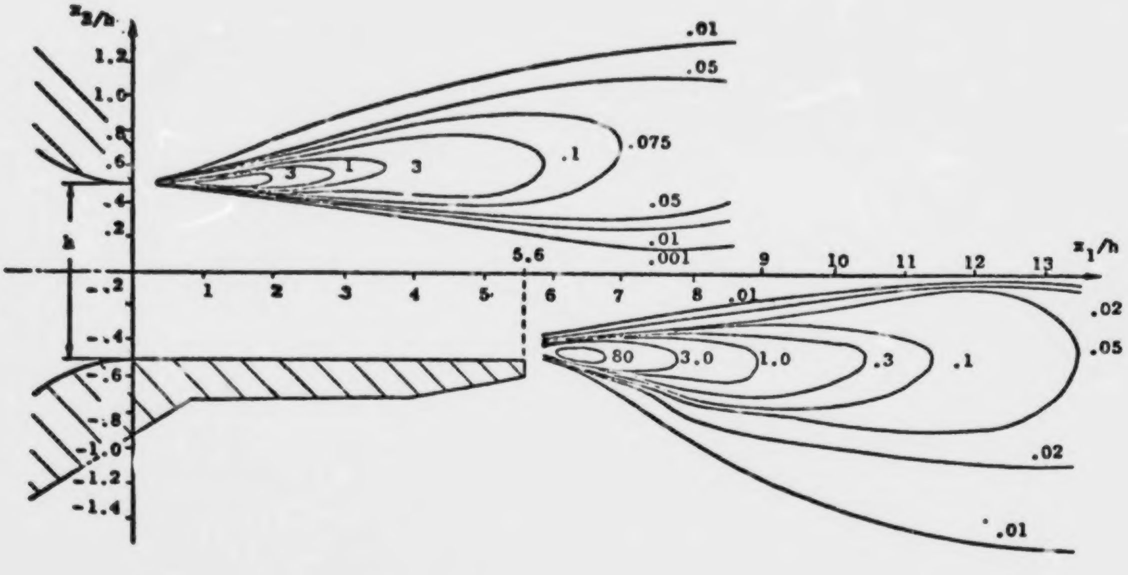

Figure 11. Acoustic Source Strength Distribution in Primary and Secondary Mixing Region for Jet Flap A = 60, δ_F = 5.6, versus Downstream Position.

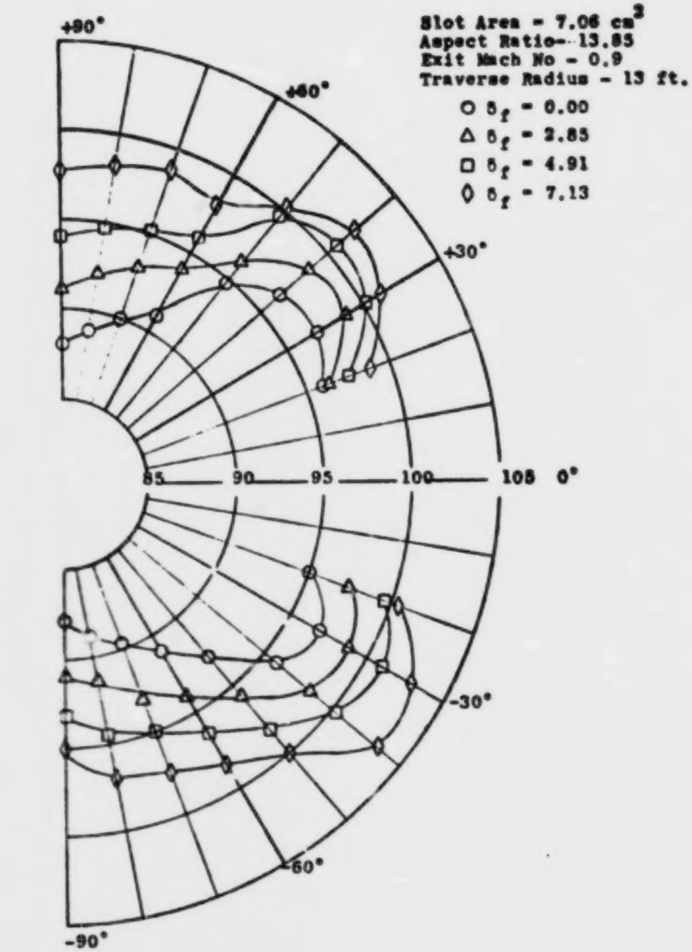

Figure 12. Sound Power Directivity Pattern of Slot Nozzle with Straight Flap.

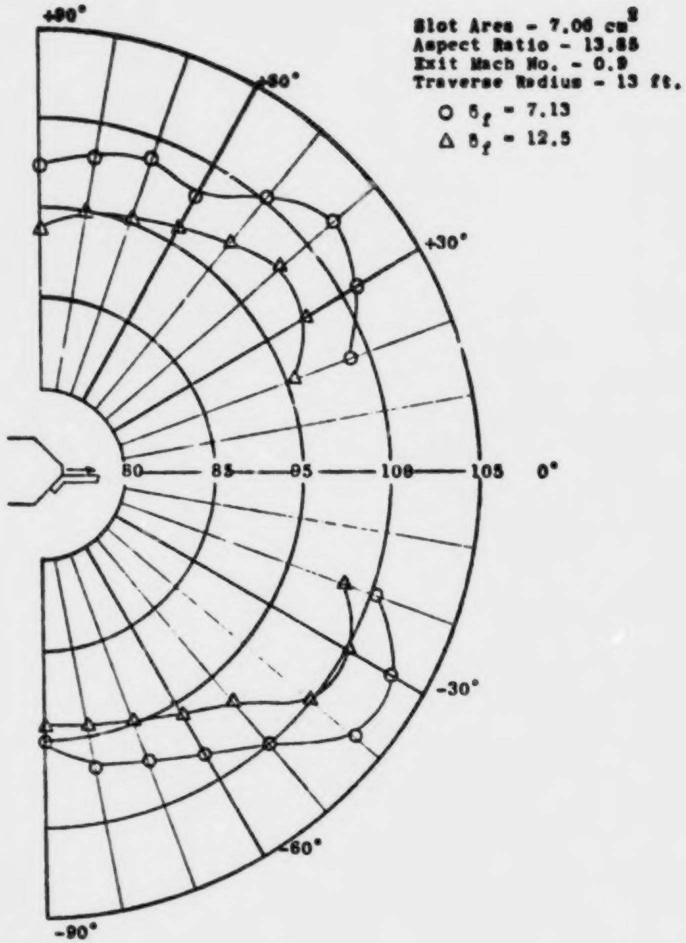

Figure 13. Sound Power Directivity Pattern of Slot Nozzle with Straight Flap.

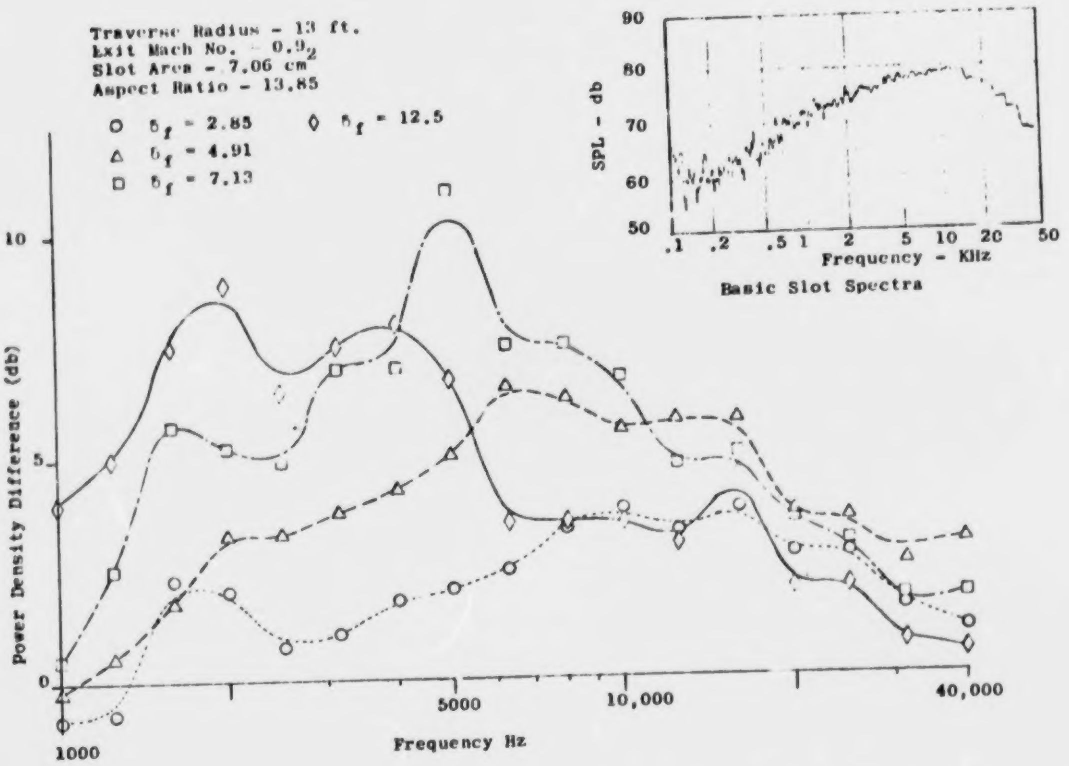

Figure 14. Difference Spectra, Slot with Flap minus Basic Slot, + 90°.

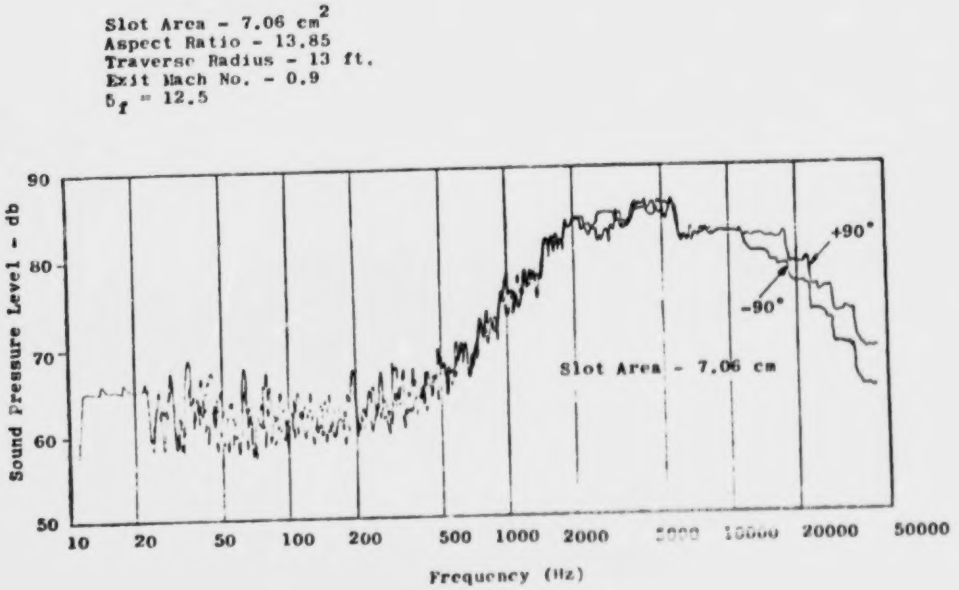

Figure 15. Spectra Comparison for Slot with Flap at Plus and Minus 90°.

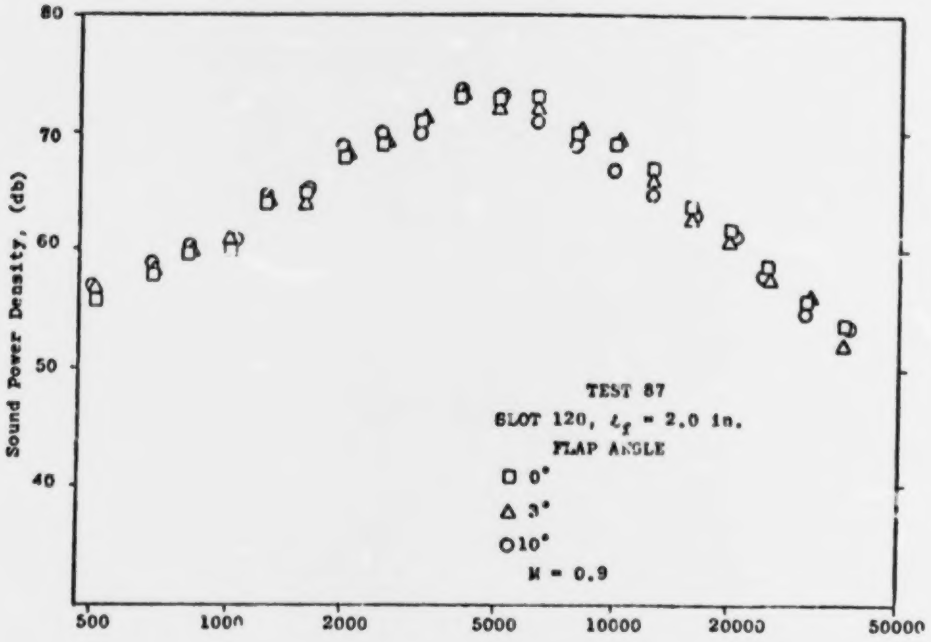

Figure 16. Effect of Flap Angle on Power Density Spectra.

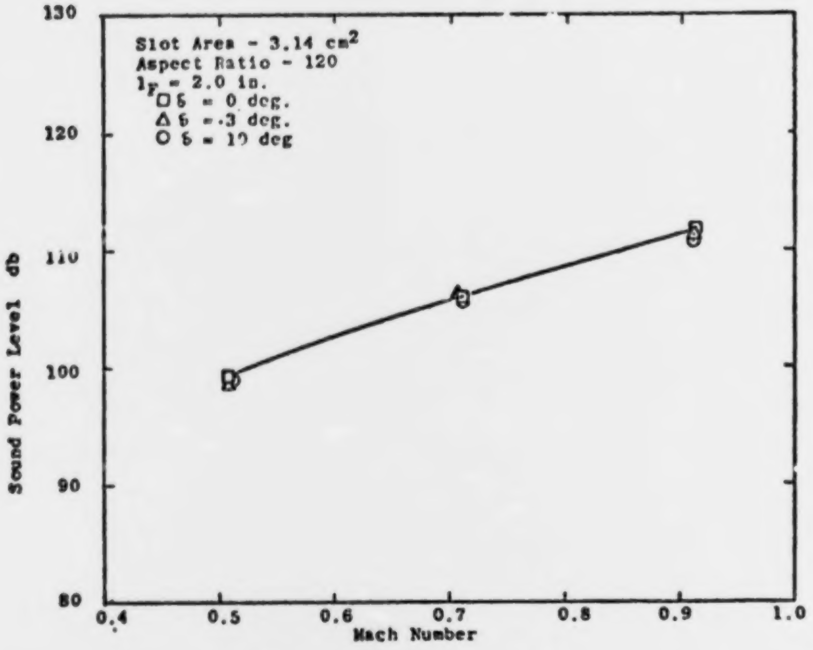

Figure 17. Sound Power vs. Mach Number for Flaps at Angle of Deflection

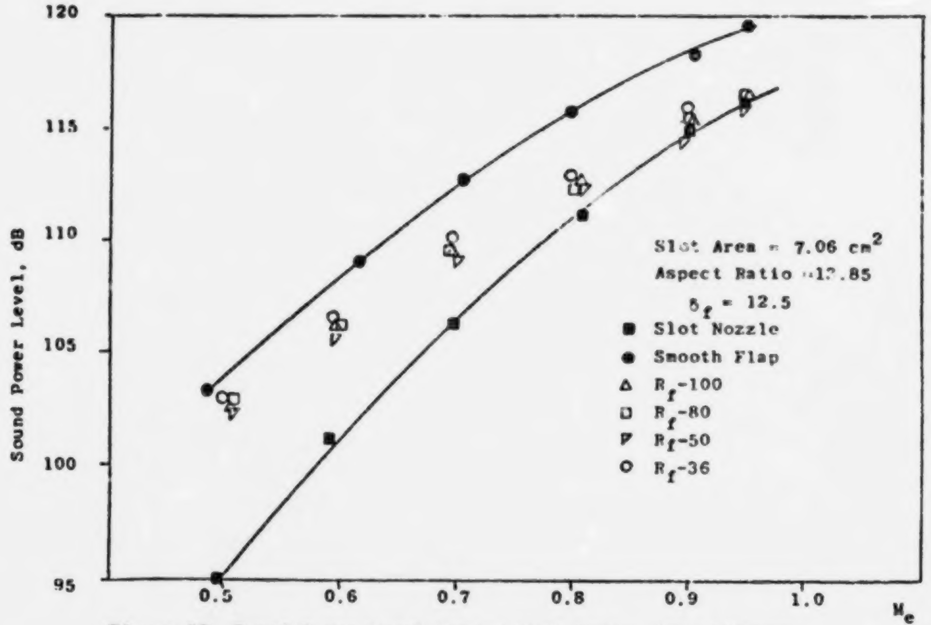

Figure 18. Sound Power Level Versus Mach Number for different Flap Roughness.

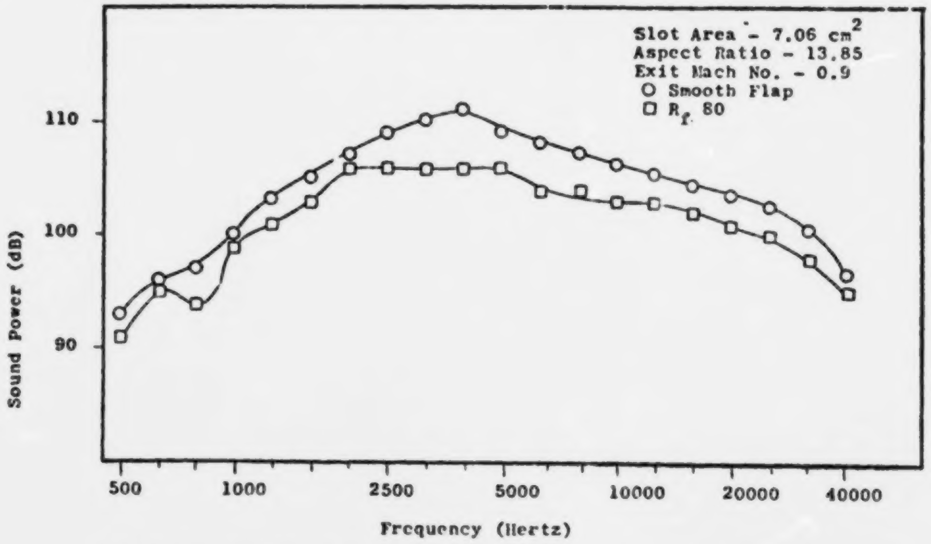

Figure 19. Effect of Roughness or 1/3 Octave Power Levels

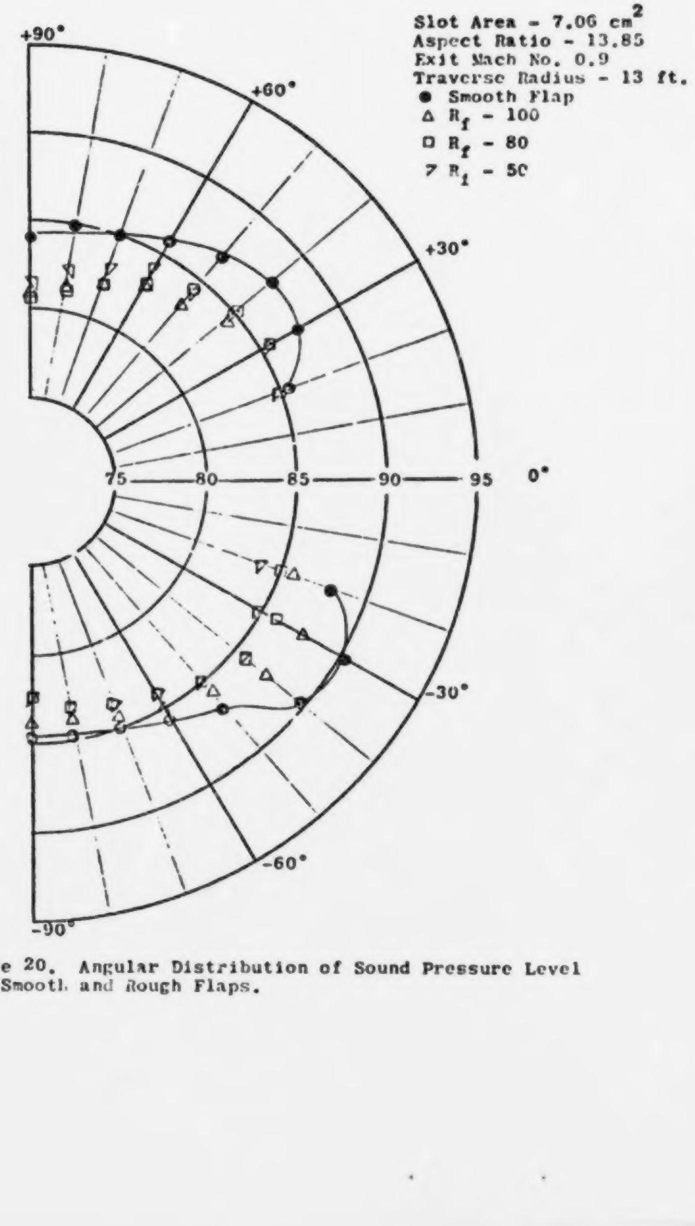

Figure 20. Angular Distribution of Sound Pressure Level from Smooth and Rough Flaps.

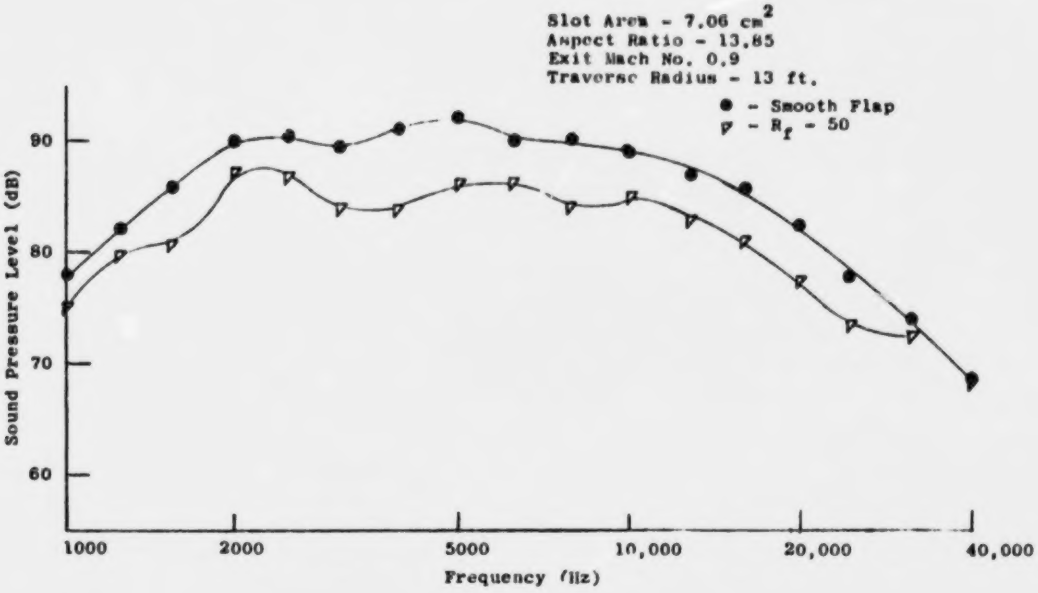

Figure 21. Comparison of Rough and Smooth Flap Spectra at -30°.

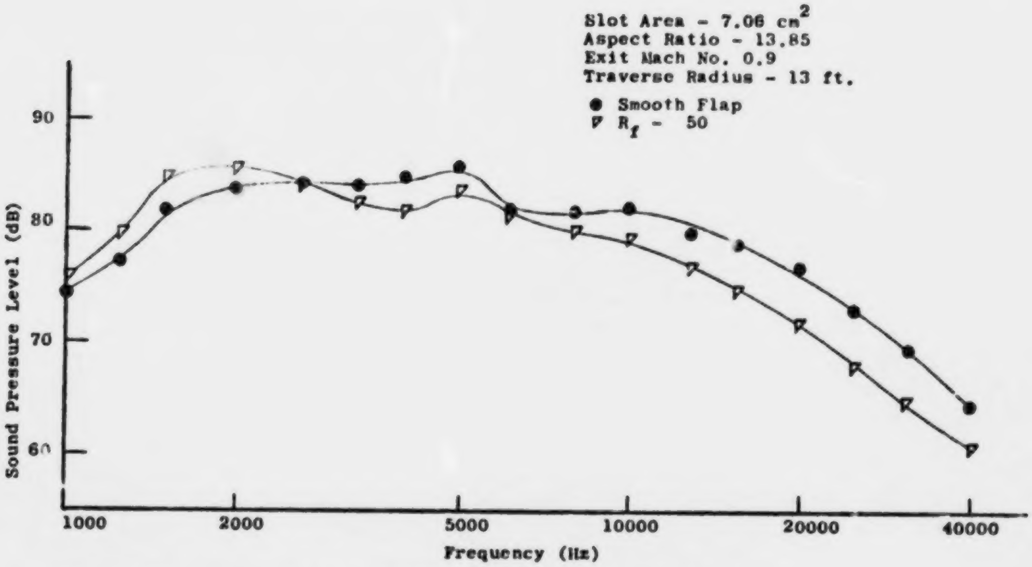

Figure 22. Comparison of Rough and Smooth Flap Spectra at -90°.

A STUDY OF IMPINGING JET-NOISE CHARACTERISTICS OF CROSS-CORRELATION TECHNIQUES

by

Y. S. Pan
Joint Institute for Acoustics and Flight Sciences
NASA-Langley Research Center
Hampton, Virginia 23665

ABSTRACT

A new method based on cross-correlation techniques is presented for experimental studies of near- and far-field noise characteristics of airflow and surface interactions. By cross-correlating appropriate two of three-kinds of microphone measurements: one flush-mounted on the solid surface, one located in the near field, and one placed in the far-field, far-field noise intensities and near-field acoustic energy fluxes can be determined. In both near and far fields, the noise characteristics due to the flow turbulence and surface fluctuating pressure contributions can be evaluated separately. Applications of the present method to several impinging jet problems are given and discussed. Experiments are being currently conducted at NASA Langley for a cold circular subsonic jet impinging on a large rigid surface.

I. INTRODUCTION

In recent years, the federal government and aircraft industries have been studying short take-off and landing (STOL) and vertical take-off and landing (VTOL) aircraft technologies in response to the increasingly pressing air-traffic problem faced by major metropolitan airports. One proposed method for STOL, which studies show could help alleviate the problem, is based on the lift-augmentation concept such that the engine exhaust is deflected downward by a wing with trailing-edge flaps. Experimental studies have shown, however, that the impingement of jet exhaust upon a flap surface generates considerable additional noise over a conventional jet. In the application of VTOL, additional noise is also generated when the engine exhaust is directed at the ground. Since STOL and VTOL aircraft will be designed to operate near heavily populated areas, the additional noise they generate during their operation becomes a major environmental concern and extensive research directed towards understanding and alleviating the problem is required.

Studies of noise generated by impinging jets upon a surface have been mainly experimental in the past. A rigorous theoretical study of this noise generation has not been possible to date because of the complexity of main flow fields and the lack of understanding of turbulence structures in the flow fields. Previous experimental investigations have been mainly on the general features of the far-field noise radiated by a jet blowing over a wing flap (for example [1,2] and a jet impinging upon a large flat surface (for example [3,4]). Most studies have been aimed at the additional noise over the conventional jet in the absence of the surface. No attempts have yet been made to examine systematically the various regions where the noise originates and their contributions to the near- and far-field noise characteristics.

In this paper, we shall present systematic methods for experimental studies of near- and far-field noise characteristics of a general jet interacting with a solid surface. In particular, we shall be concerned with the noise characteristics, both in near- and far-fields, due to the contributions of turbulence in the jet flow and fluctuating pressures on the solid surface.

The methods for determining the far-field noise intensity and near-field acoustic energy flux due to the surface contribution are developed in Sections II and III, respectively. In Sections IV and V, the developments of the methods for determining the near- and far-field due to the combined contributions of turbulence and surface are presented; then the noise contribution due to turbulence alone can be evaluated by subtracting the surface contribution from the combined contribution. Finally, applications of the present method to practical noise problems of current interest are illustrated and discussed in Section VI.

II. FAR-FIELD NOISE INTENSITY DUE TO SURFACE CONTRIBUTION

It is well known that flow turbulence generates noise[5,6] and also induces fluctuating pressures on a solid surface[7,8]. In addition, a solid surface reflects noise and fluctuating pressure on a surface itself radiates noise[9,10]. As shown in Fig. 1, a turbulent jet is assumed to be contained in a volume V_o which is interacting with the solid surface A at an area A_o. Noise received by an observer at $\vec{x}$ outside the turbulent jet may be radiated from the noise sources located at $\vec{y}$ in the turbulent jet V_o and on the surface A with the coordinate system fixed with the surface.

Based on Curle's solution of Lighthill's wave equation [9], the acoustic pressure p at $\vec{x}$ can be written in the following form.

$$p(\vec{x},t) = -\int_A \left[\frac{\partial}{\partial t}\rho u_n\right]_{\tau=\tilde{\tau}} \frac{dA(\vec{y})}{4\pi r} + \frac{\partial}{\partial x_i}\int_A \left[\rho u_i u_n + P_i\right]_{\tau=\tilde{\tau}} \frac{dA(\vec{y})}{4\pi r}$$

$$+ \frac{\partial^2}{\partial x_i \partial x_j}\int_V \left[T_{ij}\right]_{\tau=\tilde{\tau}} \frac{dV(\vec{y})}{4\pi r} \qquad (1)$$

where ρ is the density, $\tilde{\tau}=t-r/c$ the retarded time, c the sound speed and $r=|\vec{x}-\vec{y}|$. The first two surface integrals are associated with the noise generated by the interaction between the flow and solid surface which may be deform with an arbitrary surface velocity u_n. $\vec{n}$ is a unit outward normal vector with respect to the noise field. The quantity P_i represents the local resultant stress acting at each point on the surface and may comprise both shear stress and normal stress components. The volume integral is the Lighthill integral for turbulence-generated quadrupole-noise. The quantity T_{ij} is the effective stress tensor.

For a rigid surface ($u_n=0$) and under the circumstances where the shear stress component is small compared with the local surface fluctuating pressure p_s, Eq. (1) can be simplified,

$$p(\vec{x},t) = \frac{\partial}{\partial x_i}\int_A \left[p_s n_i\right]_{\tau=\tilde{t}} \frac{dA(\vec{y})}{4\pi r} + \frac{\partial^2}{\partial x_i \partial x_j}\int_V \left[T_{ij}\right]_{\tau=\tilde{t}} \frac{dV(\vec{y})}{4\pi r} . \tag{2}$$

In the acoustic and geometric far-field, namely $r \gg$ wave length and $r^2 \gg$ interaction region, respectively, the above expression can be further simplified,

$$p(\vec{x},t) = \frac{1}{4\pi c x}\int_A \cos\theta(\vec{y}) \left[\frac{\partial p_s}{\partial t}\right]_{\tau=\tilde{t}} dA(\vec{y}) + \frac{x_i x_j}{4\pi c^2 x^3}\int_V \left[\frac{\partial^2 T_{ij}}{\partial t^2}\right]_{\tau=\tilde{t}} dV(\vec{y}) , \tag{3}$$

with $\theta(\vec{y})$ the angle between the vector $\vec{x}-\vec{y}$ and the local normal vector with respect to the surface A.

To find the noise intensity in the far field, we multiply the acoustic pressure with its complex conjugate p^* at a new time t' and then take a time average,

$$\begin{aligned}\langle p(\vec{x},t)\,p^*(\vec{x},t')\rangle = {} & \frac{1}{4\pi c x}\int_A \cos\theta(\vec{y}) \left\langle \frac{\partial p_s}{\partial t}(\vec{y},\tilde{t})\,p^*(\vec{x},t')\right\rangle dA(\vec{y}) \\ & + \frac{x_i x_j}{4\pi c^2 x^3}\int_V \left\langle \frac{\partial^2 T_{ij}}{\partial t^2}(\vec{y},\tilde{t})\,p^*(\vec{x},t')\right\rangle dV(\vec{y}) .\end{aligned} \tag{4}$$

If p, p_s and T_{ij} are stationary random variables, a cross-correlation function can be defined; for example,

$$\begin{aligned}R_{pp_s}(\vec{x},\vec{y},\tau) & \equiv \langle p(\vec{x},t)\,p_s^*(\vec{y},t+\tau)\rangle \\ & \equiv \lim_{T\to\infty}\frac{1}{2T}\int_{-T}^{T} p(\vec{x},t)\,p_s^*(\vec{y},t+\tau)\,dt .\end{aligned} \tag{5}$$

Hence, in Eq. (4), the term on the left-hand side is the auto-correlation of the acoustic pressure R_{pp} which relates to the noise intensity. On the right-hand side, the first term represents the surface contribution due to surface fluctuating pressures, while the second term represents the volume contribution due to turbulence. Since the turbulence stress tensor T_{ij} is generally unknown and difficult to be measured reliably, the cross-correlation in the second integral is generally not possible to be obtained at present without making certain assumptions. On the other hand, surface fluctuating pressures can be measured by flush-mounted microphones on the surface; the integrand in the first term can be obtained by cross-correlating surface fluctuating pressures with the acoustic pressure measured in the far-field. Hence, we drop the second term on the right-hand side to account only the surface contribution.

Under the above argument, the far field acoustic pressure auto-correlation due to the surface contribution alone can be written in the following form,

$$R_{pp}(\vec{x},\tau) = -\frac{1}{4\pi x c}\int_A \cos\theta(\vec{y}) \left[\frac{\partial}{\partial\tau} R_{p_s p}(\vec{y},\vec{x},\tau)\right]_{\tau=\tau+x/c} dA(\vec{y}) . \tag{6}$$

The mean-square acoustic pressure is $R_{pp}(\vec{x},0)$ and the corresponding acoustic intensity $I(\vec{x}) \equiv R_{pp}(\vec{x},0)/\rho_o c$ with ρ_o the undisturbed density.

Defining the Fourier transform relations between the correlation function $R(\tau)$ and the power spectral density $S(\omega)$,

$$\begin{cases} S(\omega) = \displaystyle\int_{-\infty}^{\infty} R(\tau)e^{-i\omega\tau}\,d\tau \\ R(\tau) = \displaystyle\frac{1}{2\pi}\int_{-\infty}^{\infty} S(\omega)e^{i\omega\tau}\,d\omega \end{cases} \tag{7}$$

the power spectral density for the noise intensity $S_I(\vec{x},\omega)$ can be written in terms of the cross-power spectral density $S_{p_s p}(\vec{y},\vec{x},\omega)$,

$$S_I(\vec{x},\omega) = -\frac{i\omega}{4\pi x\rho_o c^2}\int_A \cos\theta(\vec{y})\, e^{i\omega x/c}\, S_{p_s p}(\vec{y},\vec{x},\omega)\, dA(\vec{y}) . \tag{8}$$

Once $S_I(\vec{x},\omega)$ is known, the total acoustic power can be obtained.

Reproduced from best available copy.

III. NEAR-FIELD ACOUSTIC ENERGY FLUX DUE TO SURFACE CONTRIBUTION

In this section, we shall present the theoretical development of a method for determining the near-field acoustic energy flux due to surface fluctuating pressures. By using the same argument used in the preceding section but without employing the far-field approximations, we can write the near-field acoustic pressure due to the surface contribution in the following form,

$$p(\vec{x},t) = \frac{1}{4\pi c}\int_A \frac{\cos\theta(\vec{y})}{r}\left[\frac{\partial p_s}{\partial t}\right]_{\tau=\tilde{t}} dA(\vec{y}) + \frac{1}{4\pi}\int_A \frac{\cos\theta(\vec{y})}{r^2}\left[p_s\right]_{\tau=\tilde{t}} dA(\vec{y}). \tag{9}$$

By taking an auto-correlation of $p(\vec{x},t)$, we have

$$\begin{aligned} R_{pp}(\vec{x},\tau) = &-\frac{1}{4\pi c}\int_A \frac{\cos\theta(\vec{y})}{r}\left[\frac{\partial}{\partial\tau} R_{p_s p}(\vec{y},\vec{x},t)\right]_{t=\tau+r/c} dA(\vec{y}) \\ &+ \frac{1}{4\pi}\int_A \frac{\cos\theta(\vec{y})}{r^2}\left[R_{p_s p}(\vec{y},\vec{x},t)\right]_{t=\tau+r/c} dA(\vec{y}) \end{aligned} \tag{10}$$

and the mean-square acoustic pressure $R_{pp}(\vec{x},0)$.

An acoustic energy flux across a surface element is defined by the real part of the generalized complex acoustic intensity,

$$I(\vec{x},\tau) \equiv \langle p(\vec{x},t)\, u_n^*(\vec{x},t+\tau)\rangle \equiv R_{pu_n}(\vec{x},\tau) \tag{11}$$

where u_n^* is the complex conjugate of the velocity component normal to the surface element. By cross-correlating p in Eq. (9) with u_n^* and using the linear momentum equation which relates $\frac{\partial u_n}{\partial t}$ with the normal pressure gradient denoted by ∇p, we have the relation between $I(\vec{x},\tau)$ and the cross-correlation function $R_{p_s \nabla p}(\vec{y},\vec{x},\tau)$,

$$\begin{aligned} \frac{\partial}{\partial\tau} I(\vec{x},\tau) = &\frac{1}{4\pi\rho c}\int_A \frac{\cos\theta(\vec{y})}{r}\left[\frac{\partial}{\partial\tau} R_{p_s \nabla p}(\vec{y},\vec{x},t)\right]_{t=\tau+r/c} dA(\vec{y}) \\ &- \frac{1}{4\pi\rho}\int_A \frac{\cos\theta(\vec{y})}{r^2}\left[R_{p_s \nabla p}(\vec{y},\vec{x},t)\right]_{t=\tau+r/c} dA(\vec{y}) . \end{aligned} \tag{12}$$

Again, by using Eq. (7), we have the power spectral density for the acoustic energy flux,

$$S_I(\vec{x},\omega) = \frac{1}{4\pi\rho_0 c}\int_A \frac{\cos(\theta_{\vec{y}})}{r}\left(1 + i\frac{c}{\omega r}\right)e^{i\omega r/c} S_{p_s\nabla p}(\vec{y},\vec{x},\omega)\, dA(\vec{y}) \tag{13}$$

Here, $R_{p_s\nabla p}$ and $S_{p_s\nabla p}$ can be obtained by cross-correlating surface fluctuating pressures with a pressure gradient at $\vec{x}$. Experimentally, the pressure gradient in the near field can be measured by a pressure gradient microphone such as one which has been developed at NASA Langley Research Center by Maestrello [12].

IV. NEAR-FIELD ACOUSTIC ENERGY FLUX DUE TO COMBINED CONTRIBUTION

To determine the noise characteristics due to turbulence, we shall determine firstly those due to the combined contribution of turbulence and surface; then the contribution due to turbulence alone is evaluated by subtracting the surface contribution from the combined contribution.

We choose an imaginary surface A_1 which encloses the major noise sources in the turbulent jet V_o and on the surface A (Fig. 1). Outside this imaginary surface A_1 and in the region V bounded by a solid surface A_2 (beyond where A_1 intersects with A) and a surface A_∞ at infinity, the simple wave equation is valid. The acoustic pressure at $\vec{x}$ can be expressed by the boundary conditions on the imaginary surface A_1 and on the solid surface A_2;

$$\begin{aligned} p(\vec{x},t) = {} & \int_{-\infty}^{t^+} dt_0 \int_{A_1} dA\, G(\vec{x},t|\vec{y},t_0)\,\frac{\partial p}{\partial n}(\vec{y},t_0) \\ & - \int_{-\infty}^{t^+} dt_0 \int_{A_2} dA\, \frac{\partial G}{\partial n}(\vec{x},t|\vec{y},t_0)\, p(\vec{y},t_0) , \end{aligned} \tag{14}$$

where G is the Green's function of the simple wave-equation and satisfies appropriate boundary and initial conditions [13].

To determine the acoustic energy flux $I(\vec{x},\tau)$ across a surface element on the imaginary surface A_1, we perform a cross-correlation of the acoustic pressure with the normal component of the local velocity.

Reproduced from best available copy.

$$I(\vec{x},t) = \int_{-\infty}^{t^*} dt_1 \int_{A_1} dA\, G(\vec{x}\,t\,|\,\vec{y},t+t_1)\, R_{\nabla p u_n}(\vec{y},\vec{x},\tau-t_1)$$

$$-\int_{-\infty}^{t^*} dt_1 \int_{A_2} dA\, \frac{\partial G}{\partial n}(\vec{x},t\,|\,\vec{y},t+t_1)\, R_{p_s u_n}(\vec{y},\vec{x},\tau-t_1) \qquad (15)$$

with $t_1=t_0-t$. By taking the Fourier transform of the above equation, we obtain the power spectral density of the energy flux,

$$S_I(\vec{x},\omega) \equiv \int_{-\infty}^{\infty} I(\vec{x},\tau)\, e^{-i\omega\tau}\, d\tau$$

$$= \int_{A_1} dA \int_{-\infty}^{t^*} dt_1\, G(\vec{x}\,t\,|\,\vec{y}\,t+t_1)\, e^{-i\omega t_1}\, S_{\nabla p u_n}(\vec{y},\vec{x},\omega) \qquad (16)$$

$$-\int_{A_2} dA \int_{-\infty}^{t^*} dt_1\, \frac{\partial G}{\partial n}(\vec{x}\,t\,|\,\vec{y},t+t_1)\, e^{-i\omega t_1}\, S_{p_s u_n}(\vec{y},\vec{x},\omega),$$

where $S_{\nabla pu_n}$ and $S_{p_s u_n}$ are, respectively, the Fourier transforms of $R_{\nabla pu_n}$ and $R_{p_s u_n}$.

By employing the linear momentum equation [14],

$$S_{\nabla p u_n}(\vec{y},\vec{x},\omega) = -\frac{1}{i\omega\rho_0} S_{\nabla p \nabla p}(\vec{y},\vec{x},\omega) \qquad (17)$$

and

$$S_{p_s u_n}(\vec{y},\vec{x},\omega) = -\frac{1}{i\omega\rho_0} S_{p_s \nabla p}(\vec{y},\vec{x},\omega) , \qquad (18)$$

and by using the relation [14]

$$G(\vec{x},t\,|\,\vec{y}\,t_0) = \frac{1}{2\pi}\int_{-\infty}^{\infty} G_k(\vec{x},\vec{y},\omega)\, e^{i\omega(t_0-t)}\, d\omega , \qquad (19)$$

we obtain

$$S_1(\vec{x},\omega) = -\frac{1}{i\omega\rho_0}\left[\int_{A_1} dA\ G_k(\vec{x},\vec{y},\omega)\ S_{\nabla p\nabla p}(\vec{y},\vec{x},\omega) - \int_{A_2} dA\ \frac{\partial G_k}{\partial n}(\vec{x},\vec{y},\omega)\ S_{p_s\nabla p}(\vec{y},\vec{x},\omega)\right] \tag{20}$$

Here, G_k, the Green's function of the Helmholtz equation, satisfies

$$\left(\nabla^2 + \frac{\omega^2}{c^2}\right) G_k(\vec{x},\vec{y},\omega) = -\delta(\vec{x}-\vec{y}) \tag{21}$$

and the boundary conditions:

$$\begin{aligned} &\frac{\partial G_k}{\partial n} = 0 && \text{on } A_1 \\ &G_k = 0 && \text{on } A_2 \\ &\text{radiation condition} && \text{on } A_\infty \text{ (infinity)} \end{aligned} \tag{22}$$

$S_{\nabla p\nabla p}$ and $S_{p_s\nabla p}$ can be obtained experimentally by space-time cross-correlating the normal pressure gradient with itself on A_1 and with surface fluctuating pressures on A_2 respectively.

V. FAR-FIELD ACOUSTIC ENERGY FLUX DUE TO COMBINED CONTRIBUTION

Far-field noise due to the combined contribution are usually measured directly by placing a microphone in the far-field. However, to obtain the information about significant noise-source regions, we can relate the far-field acoustic intensity in terms of near-field space-time cross-correlations.

To determine the acoustic intensity in the far field, we take an auto-correlation of Eq. (14) which consists of four terms [14]. Without loss of generality, we let t=0 and $t_0=t_0''-\tau$; the first term which relates to $R_{\nabla p\nabla p}$ on A_1 can be written in the following form,

$$R^{I}_{pp}(\vec{x},\tau) = \int_{-\infty}^{0^+} dt_0' \int_{-\infty}^{0^+} dt_0 \int_{A_1} dA' \int_{A_1} dA'' \, G(\vec{x},0|\vec{y}',t_0')\, G^*(\vec{x},\tau|\vec{y}'',\tau+t_0)$$

$$R_{\nabla p \nabla p}(\vec{y}',\vec{y}'',\tau+t_0-t_0') \, . \tag{23}$$

Taking the Fourier transform of the above equation and using Eqs. (17) and (19) yield (14)

$$S^{I}_{pp}(\vec{x},\omega) = \int_{A_1} dA' \int_{A_1} dA'' \, G_k(\vec{x},\vec{y}';\omega)\, G_k^*(\vec{x},\vec{y}'';\omega)\, S_{\nabla p \nabla p}(\vec{y}',\vec{y}'';\omega) \, , \tag{24}$$

where G_k and its complex conjugate G_k^* satisfy Eqs. (21) and (22). Similarly, other three terms in the auto-correlation of Eq. (14) can be carried out. Finally, the power spectral density of the noise intensity in the far field is written in terms of the cross-power spectral density of pressure gradients on A_1 and fluctuating pressures on A_2.

$$\begin{aligned} S_{pp}(\vec{x},\omega) = & \int_{A_1} dA' \int_{A_1} dA'' \, G_k(\vec{x},\vec{y}';\omega)\, G_k^*(\vec{x},\vec{y}'';\omega)\, S_{\nabla p \nabla p}(\vec{y}',\vec{y}'';\omega) \\ & + \int_{A_2} dA' \int_{A_2} dA'' \, \frac{\partial G_k}{\partial n}(\vec{x},\vec{y}';\omega)\, \frac{\partial G_k^*}{\partial n}(\vec{x},\vec{y}'';\omega)\, S_{p_2 p_2}(\vec{y}',\vec{y}'';\omega) \\ & + \int_{A_1} dA' \int_{A_2} dA'' \, G_k(\vec{x},\vec{y}';\omega)\, \frac{\partial G_k^*}{\partial n}(\vec{x},\vec{y}'';\omega)\, S_{\nabla p p_2}(\vec{y}',\vec{y}'';\omega) \\ & + \int_{A_2} dA' \int_{A_1} dA'' \, \frac{\partial G_k}{\partial n}(\vec{x},\vec{y}';\omega)\, G_k^*(\vec{x},\vec{y}'';\omega)\, S_{p_2 \nabla p}(\vec{y}',\vec{y}'';\omega) \, . \end{aligned} \tag{25}$$

VI. EXAMPLES AND DISCUSSION

The theoretical development of near- and far-field noise characteristics due to the surface contribution and due to the combined contribution of surface and turbulence has been presented. The noise characteristics due to surface contribution alone can be determined by the direct correlation of two microphone measurements: one flush-mounted on the solid surface and one placed in the far field for the far-field noise, Eq. (8) , or one pressure gradient microphone placed in the near field for the near-field noise, Eq. (13). The combined contribution, both in near and far fields, depends on the space-time cross-correlations of normal pressure gradients on an imaginary surface and fluctuating pressures on the solid surface, and also depends on the Green's function of the region outside the imaginary surface. In this section, we shall present only the application of the present method to the jet impinging problem; several other applications to surface blowing jets and edge diffraction are given in [14].

An impinging jet with an impinging angle Θ upon a large flat plate is considered. An imaginary surface A_1 may be chosen and is shown in Fig. 2. This surface consists of two parts: a spherical surface with a radius r_o enclosing the impinging jet and the impinging region and a conical surface with a half-cone angle θ_o enclosing the wall jet from r_o to infinity. The Green's function for the region V outside A_1 is [14]

$$G_0(\vec{r},\vec{r}\,') = \frac{ik}{4\pi}\left(1-\frac{\theta_0}{2}\right)\left[j_0(kr_<)h_0^{(1)}(kr_>) - h_0^{(1)}(kr)h_0^{(1)}(kr')j_0'(kr_0)/h_0^{(1)'}(kr_0)\right]$$

$$+\frac{ik}{2}\sum_{m=1}^{\infty}\cos m(\phi-\phi')\sum_{q>0}^{\infty}(2q+1)\frac{\Gamma(q-m+1)}{\Gamma(q+m+1)}\frac{1}{\sin(q+m)\pi}\frac{\frac{d}{d\theta_0}P_q^{m}(\cos\theta_0)}{\frac{\partial}{\partial q}P_q^{m}(\cos\theta_0)} \qquad (26)$$

$$P_q^{m}(\cos\theta)P_q^{m}(\cos\theta')\left[j_q(kr_<)h_q^{(1)}(kr_>) - h_q^{(1)}(kr)h_q^{(1)}(kr')j_q'(kr_0)/h_q^{(1)'}(kr_0)\right].$$

Here, r,θ,ϕ are the spherical coordinates with the z-axis perpendicular to the flat plate (Fig. 2). $\vec{r}$ and $\vec{r}\,'$ are, respectively, the position vectors of the field and source points, or vice versa. j_q and $h_q^{(1)}$ are, respectively, the spherical Bessel function and Hankel function of the first kind of order q; the prime on these functions denotes the differentiation with respect to their arguments. Γ is the Gamma function and P_q^m is the associated Legendre function. q's are determined by $\frac{d}{d\theta_o} P_q^m(\cos\theta_o)=0$ and $k=\omega/c$ the wave number. For this choice of A_1, the surface integrals over A_2 do not occur, so that only the space-time cross-correlation of pressure gradients on A_1 is required.

If the contribution from the wall jet is small, we may choose a hemi-spherical surface with a radius r_o as A_1 which encloses only the impinging jet and the impinging region (Fig. 3). The corresponding Green's function is [14]

$$G(\vec{r},\vec{r}') = \frac{ik}{\pi}\sum_{m=0}^{\infty} \epsilon_m \cos m(\phi-\phi') \sum_{n=m}^{\infty} (2\ell+1)\frac{(\ell-m)!}{(\ell+m)!} P_\ell^m(\cos\theta) P_\ell^m(\cos\theta')$$

$$\left[j_\ell(kr_<)\, h_\ell^{(1)}(kr_>) - h_\ell^{(1)}(kr)\, h_\ell^{(1)}(kr')\, j_\ell'(kr_o)/h_\ell^{(1)\prime}(kr_o) \right], \tag{27}$$

where $\epsilon_m=1/2$ for $m=0$ and $\epsilon_m=1$ for $m\neq 0$, and $\ell=2n-m+1$. By assuming a point noise source at the origin and using Eq. (27), the near-field acoustic energy flux, Eq. (20), has been checked numerically against the exact point source solution [15], the agreement is good. Currently, experiments for a cold, circular, subsonic jet impinging normally on a large rigid surface are being conducted at NASA Langley. Preliminary data are reported in [15].

Finally, it may be worthwhile to note that the present method can also be applied to the problems without having solid surfaces such as jet noise problems. The present method for the combined contributions gives the near-field acoustic energy flux and the far-field noise intensity of the jet. A semi-infinite circular conical surface, with its axis coinciding with the jet axis, enclosing the jet may be chosen as an imaginary surface. The Green's function for the region outside a semi-infinite cone is well-known (for example [16]).

VII. REFERENCES

1. W. A. Olsen, R. G. Dorsch, and J. H. Miles, "Noise Produced by a Small-Scale, Externally Blown Flap," NASA TN D-6636 (1972).
2. F. W. Gibson, "Noise Measurements of Model Jet-Augmented Lift Systems," NASA TN D-6710 (1972).
3. W. A. Olsen, J. H. Miles, and R. G. Dorsch, "Noise Generated by Impingement of a Jet Upon a Large Flat Board," NASA TN D-7075 (1972).
4. F. R. Wagner, "The Sound and Flow Field of an Axially

Symmetric Free Jet Upon Impact on a Wall," Ziet. fur Flugwiss. 19, 30-44 (1971); NASA TT F-13942 (1971).

5. M. J. Lighthill, "On Sound Generated Aerodynamically, I. General Theory," Proc. Roy. Soc. (London), A211, 564-587 (1952).
6. M. J. Lighthill, "On Sound Generated Aerodynamically, II. Turbulence as a Source of Sound," Proc. Roy. Soc. (London) A222, 1-32 (1954).
7. R. H. Kraichnan, "Pressure Fluctuations in Turbulent Flow over a Flat Plate," J. Acoust. Soc. Amer., 28, 378-390 (1956).
8. G. M. Lilley and J. H. Hodgson, "On Surface Pressure Fluctuations in Turbulent Boundary Layers," The College of Aeronautics, Cranfield, Note No. 101 (1960).
9. N. Curle, "The Influence of Solid Boundaries upon Aerodynamic Sound," Proc. Roy. Soc. (London) A231, 505-514 (1955).
10. P. J. F. Clark and H. S. Ribner, "Direct Correlation of Fluctuating Lift with Radiated Sound for an Airfoil in Turbulent Flow," J. Acoust. Soc. Amer., 46, 802-805 (1969).
11. T. E. Siddon, "Surface Dipole Strength by Cross-Correlation Method," J. Acoust. Soc. Amer., 53, 619-633 (1973).
12. L. Maestrello, "On the Relationship between Acoustic Energy Density Flux near the Jet and Far Field Acoustic Intensity," AIAA Paper 73-988 (1973).
13. P. M. Morse and H. Feshbach, "Methods of Theoretical Physics," (McGraw Hill, New York 1953) pp. 803-837.
14. Y. S. Pan, "Cross-Correlation Methods for Studying Near- and Far-Field Noise Characteristics of Several Flow-Surface Interaction Problems," to be presented at the 87th Meeting of the Acoustical Society of America, April 23-26, 1974 at New York City.
15. Y. S. Pan and J. S. Preisser,"A Method for Studying Near- and Far-Field Noise Characteristics of Impinging Jets," to be presented at the AIAA 7th Fluid and Plasma Dynamic Conference, June 17-19, 1974 at Palo Alto, California.
16. L. B. Felsen, "Alternative Field Representations in Regions Bounded by Spheres, Cones, and Planes," IRE Trans. on Antennas and Propagation, 109-121 (1957).

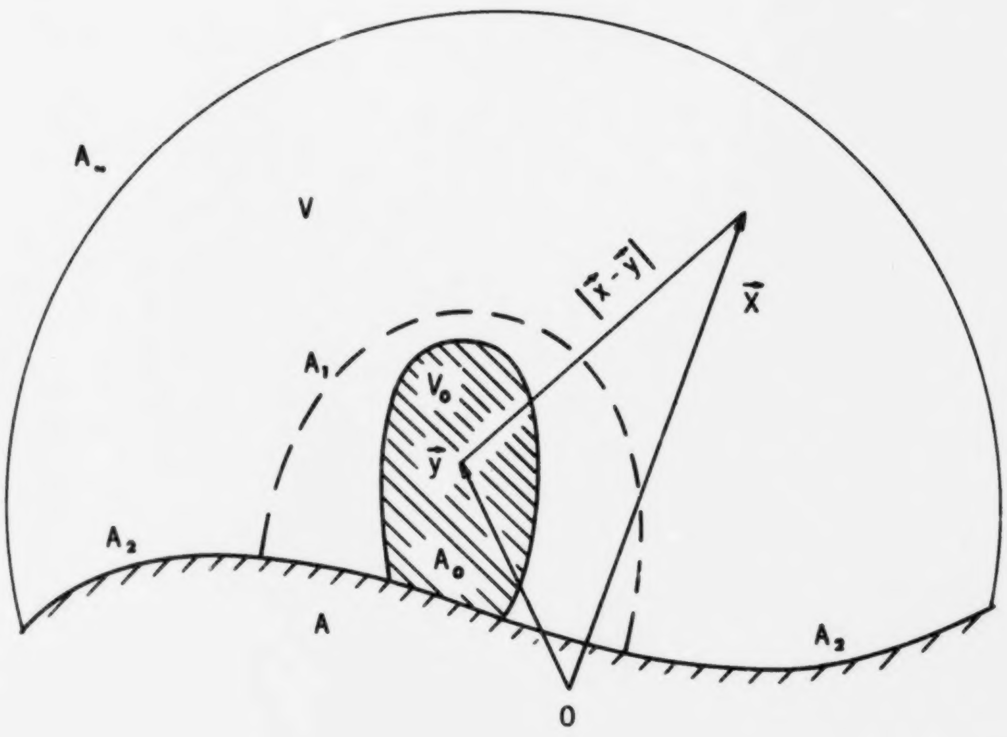
A_∞
V
A_1
V_0
$\vec{y}$
$|\vec{x}-\vec{y}|$
$\vec{x}$
A_2
A_0
A
A_2
0

Fig. 1 Sketch of Flow Volumes, Surfaces, and Coordinate System

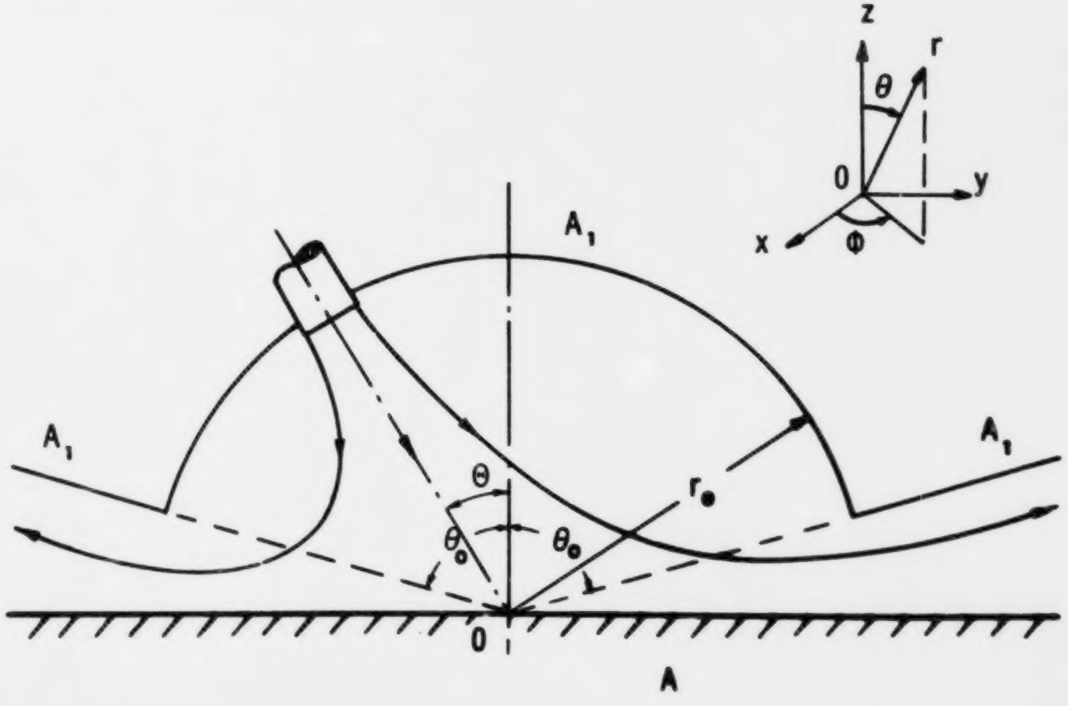
z
r
θ
0
y
x
Φ
A₁
A₁
A₁
Θ
θ₀
θ₀
r₀
0
A

Fig. 2 Sketch of Impinging Jet and Imaginary Surface

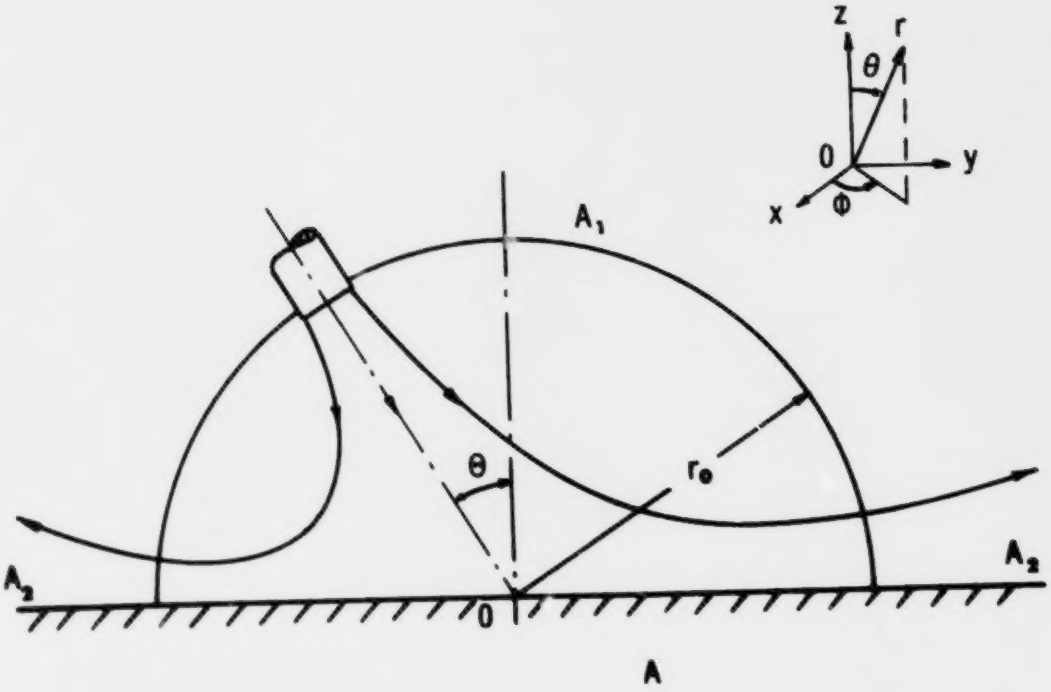
z
r
θ
0
y
x
Φ
A₁
θ
r₀
A₂
A₂
0
A

Fig. 3 Sketch of Impinging Jet and Imaginary Surface

NOISE AND FLOW CHARACTERISTICS OF AN EXTERNALLY BLOWN FLAP

by

J. C. Yu; N. N. Reddy; and J. L. Whitesides, Jr.

Joint Institute for Acoustics and Flight Sciences
NASA-Langley Research Center
Hampton, Virginia

ABSTRACT

Acoustical radiation characteristics, mean velocity field and fluctuating wall pressure field have been investigated experimentally for a subsonic air jet impinging on a simulated wing/flap configuration. The objective of the investigation is to identify the potential source mechanisms in the blown-flap noise generation. From the acoustic measurements, it was deduced that for flap extent greater than 12 nozzle diameters, the noise source is predominantly Reynolds fluctuating stress. For shorter flaps, the surface pressure fluctuation and the turbulence interaction with trailing edge are the important noise generators. Mean flow measurements made proved to be useful in defining the characteristic regions in an externally blown flap flow. Four different flow regions were delineated and discussed; the free jet region, the impingement region, the wall flow and the trailing edge jet. Surface fluctuating pressure measurements indicated the similarity of wall pressure spectra outside the impingement region. The two point space-time cross-correlation along the stream revealed that the pressure "spot" was convected by the local mean velocity. The characteristic frequency of the convected pressure "spot" coincided with the common spectral peak of the similar wall pressure spectra. Spatial correlation data indicated spanwise stretching of the wall pressure "spot" while being convected downstream. The probable dependence of wall pressure correlation on the turbulence structure is discussed. Based on experimental observations made in the present study, possible approaches for reducing blown flap noise are discussed.

I. INTRODUCTION

Quiet short take-off and landing (STOL) airplanes have been proposed by various air transportation study groups [1,2], as having large potential for alleviating the increasing congestion and delays of current air transportation systems. A number of approaches to achieving short field performance with aircraft capable of the cruise performance of the current jet transport have been considered [3]. The integrated lift-propulsion systems based on powered-lift concepts that are currently receiving the most attention are (i) under-the-wing externally blown flap system and (ii) over-the-wing upper surface blown flap system. Both systems achieve the additional lift requirement by utilizing flow turning and/or attachment to the wing/flap.

One of the main problems associated with these power-lift systems is the large amount of noise produced as a result of the interaction between the engine exhaust flow and the lifting surfaces. The resultant noise of the power-lift system during takeoff and landing could be several orders of magnitude higher than the noise produced by engine exhaust alone [4]. The seriousness of this noise problem becomes apparent in view of the expected STOL operation in close proximity to residential and commercial areas.

Faced with such a dilemma, it is not surprising that a large amount of research work has been carried out in recent years to explore the physical characteristics and mechanisms of noise generation from turbulent flow and surface interaction. Basically, the problem, like any other problem in aerodynamic noise, has three distinct and yet strongly coupled aspects; the acoustic far field, the fluctuating flow and the mean flow. Either from analytical or experimental standpoints, one would like to understand the nature of the mean flow field, the characteristics of the associated fluctuating flow field and their interdependence. With this knowledge, one could then be guided by the existing theories of aerodynamic noise generation and radiation to relate the flow field to the radiated sound.

Experimental investigations of the characteristics of noise radiated from model blown flap systems have been reported; for example in refernces 5-11. Mean flow field survey of jet impingement on large flat plate and upper surface blown flap flow have been conducted in references 8, 11-13. Surface pressure fluctuations in impinging jets and wall jets have been studied experimentally in references 14-18. Turbulent velocity fluctuations in the blown flap flow have been examined for example in references 8 and 11. The experimental findings reported in the work mentioned above proved to be invaluable in providing a general physical understanding of the nature of the problem. Unfortunately, however, in none of these studies was a systematic approach made so that all three aspects of the problem, the acoustic field, the mean and the fluctuating flow fields were investigated concurrently for a given experimental configuration. Since each flow configuration has its own special characteristics depending on the way it is generated, the experimental data can be best understood if complete information concerning the acoustic and flow fields of a given test configuration is obtained.

The purpose of this study is to experimentally investigate all three phases of the blown flap noise problem discussed earlier. The experimental configuration used is similar to that of an externally under-the-wing blown flap system. The velocity of the impinging jet used is in the subsonic range. Main experimental findings are reported and discussed.

II. EXPERIMENTAL FACILITIES AND INSTRUMENTATION

1. Blown Flap Configuration. A contoured circular converging

nozzle with 2" exit diameter and contraction ratio of 16 was used to generate the subsonic jet flow. The wing/flap combination used had a 45° turning angle with radius of curvature of the bend 16", see Fig. 1. The span of the wing/flap was 24". The flap length could be varied by changing the plate section downstream of the bend.

2. Acoustic Measurements. Total acoustic power and power spectrum of the blown flap noise were measured in a 10^5 cu. ft. vacuum chamber at NASA Langley Center. The chamber was calibrated by determining its reverberation characteristics. The reverberation time measured in 1/3 octave band varied from 12 seconds at 100 Hz to 0.4 seconds at 10 KHz. The vacuum capability and large volume of the chamber were utilized to generate the nearly steady jet flow through suction.

The directivity data of the blown flap noise were obtained by measuring sound pressure spectra over a semi-spherical surface enclosing the blown flap. Measurements were carried out in the Anechoic Chamber at NASA Langley Research Center. The design cutoff of the chamber is 100 Hz.

In both types of acoustic measurements, the instrumentation consisted of 1/4" condenser microphones, matched cathode followers, microphone amplifiers and a 1/3 octave band spectrum analyzer. The overall system response is flat within 1 dB from 50 Hz to 20 KHz. Averaging time used for the spectral analysis was 1~2 seconds. For power measurements, three microphones were used for spatial averaging.

3. Mean Flow Measurements. The mean velocity field of the impinging jet was surveyed by using a pitot-total tube mounted on a five degrees of freedom remotely-controlled traversing mechanism. The total pressure measured from the pitot tube was converted into electrical signal through a strain-gage type pressure transducer. Total pressure distribution for a given traverse was recorded on a x-y recorder. The mean velocity was calculated from the total pressure data. Majority of the velocity data were obtained by traverses made either parallel with or perpendicular to the wing/flap surface. The mean flow measurements and the fluctuating wall pressure measurements (see next section) were conducted using a small wind tunnel by fitting the jet nozzle downstream of the contraction section of the tunnel and with test section and diffuser section removed.

4. Fluctuating Wall Pressure Measurement. Two point space-time cross-correlation of the broadband wall pressure fluctuation and 1/3 octave band wall pressure spectra were measured over the wetted area of the wing/flap surface by using flush-mounted 1/8" condenser microphones. The bandwidth of the measurement was from 50 Hz to 40 KHz. Saicor Model SAI-42 correlation and probability analyzer was used to obtain the correlation data. Over the total delay range (nominally 2 msec), 100 discrete values of the correlation function were obtained. Auto-correlation function at

each microphone position was also recorded and their values at zero delay were used to normalize the cross-correlation function. The grid layout for spectrum and correlation measurements is given in Fig. 2.

For both acoustic and flow measurements, jet flow was generated from reservoirs at nearly room temperature.

III. RESULTS AND DISCUSSIONS

1. Acoustic Characteristics. Depending on the relative position between the jet exit and the wing/flap surface, the orientation of the jet and the extent of wing/flap surface, the flow field of the externally blown flap investigated may be divided into four different regions; (i) the free jet region which extends from jet exit to close to the wing/flap surface. In this region the flow behaves very similar to that of a jet discharging into a quiescent medium. (ii) the impingement region which surrounds the intersection (defined here as the geometrical impingement point) between the free jet axis and the wing/flap surface, which spans over a region of the size of the jet diameter. (iii) a short distance downstream of the geometrical impingement point is the wall jet region which may evolve into a self-similar state, and (iv) the edge jet region formed by the wall flow discharging from the trailing edge of the wing/flap. Based on this flow division, the possible physical mechanisms of noise generation are fluctuating Reynolds stresses[19], the fluctuating force caused by flow impingement [19] and turbulence interacting with the trailing edge of the flap [11,20]. If, however, the extent of the wing/flap is very large in comparison with the diameter of the free jet, it has been argued [21-23] that the surface plays a purely passive role and the fluctuating Reynolds stress is the dominant source mechanism.

With this physical understanding in mind, the radiated acoustic power and power spectrum were measured for four different flap length L_F, over a range of subsonic jet velocities in anticipation that various dominant source mechanisms may be delineated.

Fig. 3 shows the acoustic power dependence on the jet exit Mach number for a fixed jet exit position. For long flap length $L_F/D=24$, 12.75, the acoustic power variation is seen to be similar to that of a free jet, the magnitude, however, is increased by about two fold. This implies that in the absence of edge effects the source mechanism is basically the fluctuating Reynolds stress due to free jet mixing and the turbulent boundary layer formation over the flap surface. As the flap length was shortened, large increase in acoustic power was noted at lower jet exit Mach numbers. M^4 and M^5 dependences of acoustic power were observed, indicating the possible source mechanisms have changed in character, and the fluctuating force (pressure) due to jet impingement [19], and the turbulence-edge interaction [11,20] may be the primary candidates. It is also interesting to note that at nearly sonic velocities, the acoustic power radiated is nearly constant regardless of the length of the flap. If the observed power dependence on jet Mach number is extrapolated to supersonic range, it is possible that the acoustic power generated by shorter flap length may be less than that for long flap length.

Normalized power spectra are presented in Fig. 4 for $L_F/D=3.75$. This flap length is nearly equal to that proposed for the externally blown flap STOL system. The Strouhal No. $f.D/U_o$ of the spectral peak is nearly 0.15 where U_o is the jet exit velocity. The slopes of the spectrum are given by f^2 and between f^{-2} and f^{-3} for low frequency and high frequency respectively. The strong dependence of spectral distribution of acoustic power with Mach number of the impinging jet is evident. A substantial increase in low frequency spectral contents occurs as the jet Mach number is lowered.

Directional distribution of overall and 1/3 octave band noise intensity are given in Fig. 5a to 5c. The measurements were taken in a plane perpendicular to wing/flap surface containing the midspan. The directivity become more distinct as the flap length was decreased and/or the jet Mach number was increased. For long flap length, where the extent of the wing/flap is greater than the typical wave length of the radiated noise, the intensity in the back side of the flap is lower as compared to the flow side of the flap. This is believed to be a direct consequence of the acoustic shielding of the flap and the diminishing influence of the flap trailing edge both as a possible source of noise and a source of diffraction. For shorter flap length, however, the trend is reversed, at lower jet Mach numbers, see Fig. 5b. It is seen that relatively strong radiation takes place along $\theta=15°$ direction or about 65° from the plane of symmetry of the trailing edge jet. Directional patterns of intensity in selected 1/3 octave bands for $L_F/D=3.75$ are given in Fig. 5c, where $f_o=400$ Hz corresponds to the power spectral peak frequency for that test configuration (see Fig. 4). Strong radiation again occurred in the backside of the flap. The directional peak for $f_o=400$ Hz is very broad and occurs in a direction nearly perpendicular to the flap surface, at $\theta\approx40°$. For $f_o=800$ Hz and 1600 Hz, directivity exhibits lobe-pattern peaked at $\theta=0°$ and $\theta=50°$. The observed behavior of the directional pattern is believed to be in part due to the sound refraction by the flow gradients in the edge jet and in part due to the turbulence and edge interaction as an active source of sound. The turbulent and edge interaction discussed by Ffowcs Williams and Hall [20] and Hayden [11] is suspected to be mainly responsible for the intense radiation which occurred in the backside of the wing/flap.

2. Mean Flow Field. Mean velocity profiles of the blown flap investigated are presented for one typical test configuration with

flap length $L_F/D=3.75$ with jet positioned at X/D=6.75 and Y/D=2.0 (see Fig. 1). Results are obtained from pitot-pressure traverses made perpendicular to the flap surface at the mid-span (Z/D=0) and parallel to the flap surface respectively. Coordinate system used is illustrated in the insert of Fig. 6.

The free jet region was found within the first four nozzle diameters downstream of the jet exit. The velocity profiles obtain at different X/D stations from Z-traverse and W-traverse were almost identical and the axis of the jet coincided with the centerline of the nozzle. Results are presented in Fig. 6. For X/D>4, the locus of the maximum velocity determined from W-traverse deflected downward from the nozzle centerline indicating the turning of the impinging jet. At X/D=6.75, the location of the geometrical impingement point, this downward deflection was about 0.2D.

The characteristics of the stagnation region were also deduced from limited number of wall pressure measurements. The maximum wall pressure occurred at about 0.5D upstream of the geometrical impingement point. The chordwise extent of the deflected upstream flow was slightly greater than one D. Observations similar to these have also been reported in Reference 12,13.

The flow development in regions downstream of the geometrical impingement point is given in Fig. 7. The location of maximum velocity moved towards the wing/flap surface and spread laterally along the span. Slight local increase of the maximum velocity can also be noted from the figure.

The mean velocity distribution downstream of the flow turning is presented in Fig. 8a in non-dimensional form, where U_m is the maximum local velocity and $W_{1/2}$ is the half depth of the outer mixing region. In this region, the wall flow developed into a self-similar state and the velocity profile agreed closely with that of a wall jet [24,25]. Near the flap trailing edge, however, the velocity profile deviates slightly from the similarity. The variation of the maximum local velocity U_m, the location of maximum velocity from wall W_m and the half depth of outer region $W_{1/2}$ are plotted in Fig. 8b. The spanwise velocity distribution obtained from Z-traverse are presented in Fig. 8c-8e. The increase in lateral spread of the wall flow over the flap surface is illustrated in Fig. 8g. From the data presented in Fig. 8, it may be deduced that the wall flow spread laterally from 0.5D to 2D as determined from the half-width of the spanwise velocity distribution near the wall. This lateral spreading was accompanied by a vertical contraction with half depth decreased from 0.5D to 0.25D.

In the region downstream of the flap trailing edge, the development of mean velocity was found to be similar to a jet boundary flow characterized by steep shears near the trailing edge, see Fig. 9. Downstream of the adjustment region which extended to

1.5D from the trailing edge, the flow became similar and the velocity profile followed closely that of a fully-developed two-dimensional turbulent free jet. The steep shear at the flap trailing edge may play an important role in noise generation by a mechanism different from that discussed in Ref. 11 and 20. If the edge flow is inherently unstable, upon excitation by flow or acoustic disturbances,large lateral oscillation of the edge jet may result. This instability if propagated downstream would be amplified by the mean shear and radiate noise quite efficiently. Some shadowgraphs and high speed movie taken for the edge flow (results not presented) did indicate the oscillation of the edge flow. In order to reach more definite conclusions, additional fluctuating velocity measurements in the trailing edge jet are required.

3. Spectra of Fluctuating Wall Pressure. 1/3 octave band spectrum of the wall pressure was measured by using 1/8" condenser microphones flush-mounted on the wing/flap surface at positions shown in Fig. 2. Microphones were isolated from possible low frequency vibrations of the wing/flap by providing resilient material between microphone cartridge and mounting module.

The variations of broadband (50 Hz-40 KHz) fluctuating wall pressure are given in Fig. 10a and Fig. 10b. From Fig. 10a, it is seen that there are two regions of high level pressure fluctuations; one at the stagnation region of the impinging jet and the other near the trailing edge. At S/D= -1.0, Fig. 10a, the rms wall pressure was about 11% of the dynamic pressure at the nozzle exit, at S/D=3.5, the ratio was 6%. Similar observations have also been reported in reference 14 for a 4" low subsonic jet and in reference 15 for a 2.27" jet at Mach number comparable to that used in the present case. In both studies, however, the jet impingement was directed toward a large rigid flat plate. The observed overall variation of the rms wall pressure followed closely with that reported in reference 15. Particularly, the sharp drop-off for S/D<-1.0, i.e. outside of the impinging flow. For S/D>4, the rms wall pressure on a large flat plate was found [14] to decay very rapidly with distance.

In Fig. 10b, the spanwise variation of the rms wall pressure at three streamwise stations are given. At stations close to the impingement region, Z/D=0 and 2, the maximum values of rms wall pressure occurred along rays making a 25° angle with the central chord of the flap. The locations of the observed maxima are believed to be directly related to the turbulence intensity distribution in transition region of a free jet if the wing/flap were absent. Parallel to the flap trailing edge, at S/D=3.5, the wall pressure fluctuation remained nearly constant between Z/D=1.5 and Z/D=-1.5 and then decayed with the inverse square of Z.

Normalized power spectral density at various microphone locations are plotted as a function of Strouhal number based on the nozzle exit diameter and velocity, see Fig. 11a to Fig. 11d.

Several interesting observations can be made regarding the spatial and spectral distributions of the fluctuating wall pressure. Within the impingement region which is nearly a circular area centered at S/D=-0.5, the fluctuating wall pressure is characterized by high level low frequency components, see Fig. 11a at S/D=-1.0, 0 and Fig. 11b at Z/D=0, 0.5. The high level low frequency contents of the spectrum is indicative of the large scale interaction typical of an impinging jet. In the region immediately outside the impingement region, the flow undergoes a transition where the low frequency contents are reduced, see Fig. 11a at S/D=1.0 and Fig. 11b at S/D=1.0. In the wall flow region, where the velocity distribution became self-similar, the corresponding wall pressure spectrum also became similar especially for frequencies above the spectral peak. The common peak of the spectra in this similarity region occurs at $fD/U_o \approx .23$ See Fig. 11a for $S/D \geq 2$, Fig. 11b for $Z/D \geq 1.5$, Fig. 11c for $Z/D \leq 2.0$ and Fig. 11d for $Z/D \leq 2.0$. The slope of spectra for frequencies above the spectra peak follower f^{-2} relation indicating that the high frequency wall pressure fluctuation was governing by mechanisms similar to that found in the developed region of a free turbulent jet. Outside the similarity region, $S/D > 2.0$ and $|Z/D| \geq 2.5$ (see Fig. 11c and Fig. 11d), the spectral peak shifts with local maximum velocity. This is particularly evident near the trailing edge of the wing/flap. The peculiar appearance of the spectrum at S/D=-1.5 in Fig. 11a is due to the fact that the measuring microphone is outside the impinging flow. The apparent discrete peaks noted at S/D=-1.5 are suspected to be influenced by the vortex sheddings of the separated flow upstream of the stagnation region.

4. Wall Pressure Correlation. Correlation of wall pressures over the wing/flap surface serves the purpose to define the scales involved for the surface-related noise sources. This is true whether the surface is active in producing sound as a result of net reacting force exerted on the fluid or the surface plays merely a passive role in modifying the volume turbulence impressed and reflect sound so generated. In the latter case, however, the wall pressure measurement is useful in that some understanding of the turbulence convected over the surface may be gained as shown by Kraichnan [26] in his theoretical work on pressure fluctuations in a boundary layer flow. Quantitative understanding of the convected turbulence over the surface, however, needs also correlation between wall pressure and the turbulent velocity fluctuation, as has been done by Willmarth and Wooldridge [27].

In the present study, the broadband fluctuating wall pressures at two points were cross-correlated over a region which contains both the impinging flow and the wall flow. The output from the correlator was then normalized by the respective autocorrelations at zero time delay measured by the two microphones in a usual way. The normalized cross-correlation function is defined as the cross-correlation coefficient denoted by $\rho_{12}(\xi,\tau)$ where ξ is the space separation and τ is the time separation. By setting $\tau=0$ in

$\rho_{12}(\xi,\tau)$, one obtains the spatial correlation coefficient which may be used to define the spatial characteristics of a fluctuating wall pressure "spot".

Fig. 12a to Fig. 12c show the variations of the spatial correlation coefficient taken at three fixed microphone positions, S/D=0, 2.0 and 3.5 along the midspan Z/D=0. Measurements were taken along five rays θ=0°, 45°, 90°, 135° and 180°, originating from a fixed microphone position, where θ=0° is the stream direction. Nearly along all rays, the spatial correlation indicates a characteristic negative loop. Observation similar to this has also been reported in Reference 16 for surface pressure fluctuations induced by a radial wall jet. One simple way to interpret the double-loop behavior is to regard that the fluctuating pressures in the two regions are in phase opposition. On the basis of this interpretation, the wall pressure "spot" would then be characterized by a central region with, say, a positive phase surrounded by an outer region in phase opposite to the central region. Physically, the loop pattern observed for the wall pressure must be related to the turbulence convected over the flap surface. Willmarth and Wooldridge [30] measured p,u and p,v correlations in a thick turbulent boundary layer generated in a wind tunnel. They deduce that the vortices normal to the stream near the wall were of a hair-pin shape. The hair-pin shaped vortices may possibly explain the double-loop measured along θ=0° and 180°. Foss and Kleis [16] in their study of jet impingement on a large flat plate argued, based on Powell's earlier work [28], that the vorticity production and stretching due to flow impingement and deflection could be potential dominant sources of noise. They found, based on their mean static wall pressure and velocity measurements, that strong vortices exist in the impingement region both along and normal to the stream. It is suspected that the vorticity production along the stream direction is responsible for the double-loop found along θ=90°. If this is correct, the pressure correlation measured, Fig. 12a-12c at θ=90°, would indicate that the scale of streamwise vorticity is much larger as compared to that normal to the stream. If one follows the variations of the zero-crossing of $\rho_{12}(\xi,0)$ curves with θ, a rough idea of the shape of wall pressure "spot" is obtained. In the impingement region, Fig. 12a, the "spot" is about 0.3Dx0.5D along and normal to the stream respectively. In the wall flow region, S/D=2.0, Fig. 12b, the spot is stretched to 0.5Dx1.5D. Further downstream near the trailing edge, Fig. 12c, the "spot" size becomes 0.5Dx2.0D.

Variations of two-point space-time cross-correlation coefficient obtained along Z/D=0 is plotted against the non-dimensionalized time scale $U_o\tau/D$ in Fig. 13. The convection speed was calculated by dividing the separation distance between two adjacent microphones by time separation of the correlation peaks. Local variations of the convection speed were noted. On the average, however, the convection speed was nearly the same as the local maximum mean speed. Fig. 13 also shows that the decay rate of the moving-frame auto-correlation of the wall pressure became very slow for $U_o\tau/D>2.5$ and persisted to the trailing edge of the flap. The envelope is nearly symmetrical for $|U_o\tau/D|<2$. If the moving-frame auto-correlation is approximated by $e^{-c|\tau|}$, the time scale may be obtained by noting the value of τ at $\rho_{12}(\tau)=e^{-1}$. This is given by $U_o\tau/D=0.65$ or $\tau=1.9\times10^{-4}$ sec. The characteristic frequency corresponding to this time scale is about 800 Hz which agreed closely with the peak frequencies of the wall pressure spectrum in the similarity region (see Section III.3).

IV. CONCLUDING REMARKS

Main experimental observations reported in the earlier sections are recapitulated, and from which deductions are made regarding the physical nature of the noise sources in the blown flap configuration investigated. Possible approaches to reduction of blown flap noise are also discussed.

For long flap length, present results indicate that the blown flap noise is generated predominantly by volume quadrupole. For short flap length of practical applications in STOL systems, experimental findings revealed that the acoustic power radiation depends on 4th or 5th power of a typical velocity in the blown flap flow. The radiation directivity showed higher level noise in the back side of the wing/flap than that in the flow side, particularly at low jet Mach numbers. Fluctuating wall pressure survey indicated intense fluctuations existed in the impingement region and in the wall flow region near the flap trailing edge. The area over which the wall pressure was correlated was about six times larger near the trailing edge than in the impingement region. The spatial correlation was characterized by a double-loop which is indicative of the vorticity production and stretching due to jet impingement and deflection. Moving-frame auto-correlation had a time scale given by $U_o\tau/D=0.65$ which corresponded to the spectral peak frequency of the wall pressure spectrum over a large region on the wing/flap surface.

The major source mechanisms in blown flap noise for short flap length are therefore the intense wall pressure fluctuations induced by flow turbulence in the impingement region and the subsequent strong, large scale interaction between the turbulence and the trailing edge. Comparison was made on the spatial distribution of the fluctuating wall pressure between the present study for short flap length and that reported in reference 15 for oblique jet impingement on a large flat plate under similar test condition. From this comparison, it was found that the fluctuating surface pressure variations on a short flap agreed closely with the large plate results at corresponding locations. This observation is considered significant because it implies that the effectiveness of the flow interactions at the trailing edge as a source may be reduced if the trailing edge terminates at say, S/D>5, where the large plate results [15] indicated a rapid decay of the fluctuating wall pressure.

From the physical nature of the wall pressure fluctuation discussed above and its implications on the probable turbulence structure in the impinging flow, several approaches of possible noise reduction for blown flap noise are apparent. Apart from changing the flow characteristics in the free jet region (hence modifying the turbulence in the impinging flow) and reducing the magnitude of the wall pressure fluctuation in the impingement region and near the trailing edge, the idea based on reducing the scale of the flow fluctuations near the trailing edge appears to be very attractive. This may be achieved by, for instance, (i) dividing the trailing edge into a number of smaller separated sections along the span, (ii) providing small flow splitters installed near the trailing edge and perpendicular to the lifting surface or (iii) saw-toothing the trailing along the span. The basic idea is that if the scale of the flow fluctuation is reduced even if the magnitude of fluctuation remains the same, noise reduction may be obtained. Other approaches to blown flap noise reduction such as edge blowing [29] and acoustic treatment at the trailing edge [30] are believed to function based on the same physical argument discussed above, i.e. affecting the scale and/or magnitude of the flow fluctuation near the trailing edge.

In conclusion, the acoustic field, mean flow field and the fluctuating wall pressure of a simulated externally blown flap configuration have been experimentally investigated. The possible source mechanisms in blown flap noise generation and their physical characteristics are deduced. Possible approaches to reduction of blown flap noise are suggested.

REFERENCES

1. Simpson, R. W., "Summary and Recommendations NASA/MIT Workshop on Short Haul Air Transport," Rept. No. FTL-R71-4, MIT Flight Transportation Lab., Oct. 1971.
2. DOT/NASA "Civil Aviation Research and Development Policy Study," NASA SP-265, March 1971.
3. Riebe, J. M. and Kuhn, R. E., "Research on Future Short-Haul Aircraft at the NASA Langley Research Center," AIAA Paper No. 73-27.
4. Hubbard, H. H.; Chestnutt, D.; and Maglieri, D. J., "Noise Control Technology for Jet-Powered STOL Vehicles," Paper No. 72-50, The 8th Congress of the International Council of the Aeronautical Sciences, 1972.
5. Dorsch, R. G., et al, "Blown Flap Noise Research," AIAA Paper No. 71-745.
6. Dorsch, R. G., et al, "Externally-Blown-Flap Noise," AIAA Paper 72-129.
7. Olsen, W. A., et al, "Noise Produced by a Small Scale, Externally Blown Flap," NASA TN D-6636, March 1972.

8. Schrecker, G. O, and Maus, J. R., "Noise Characteristics of Jet Flap Type Exhaust Flows," NASA CR-2342, February 1974.
9. Maglieri, D. J., and Hubbard, H. H., "Preliminary Measurements of the Noise Characteristics of Some Jet-Augmented-Flap Configurations," NASA Memo 12-4-58L, 1959.
10. Clark, L. R., "An Experimental Study of the Noise Field Generated by Jet Flow Blowing over the Upper Surface of a Simulated Wing and Flap," Masters Thesis, George Washington University, April 1974.
11. Hayden, R. E., "Sound Generation by Turbulent Wall Jet Flow Over a Trailing Edge," Masters Thesis, Purdue University, August 1969.
12. Donaldson, C. D., and Snedeker, R. S., "A Study of Free Jet Impingement, Part 1. Mean Properties of Free and Impinging Jets," JFM, Vol. 45, Part 2, 1971.
13. Foss, J. F., and Kleis, S. J., "The Oblique Impingement of an Axisymmetric Jet," Second Annual Report NASA Lewis Research Center, Grant No. NGR 23-004-068.
14. Strong, D. R.; Siddon, T. E.; and Chu, W. T., "Pressure Fluctuations on a Flat Plate with Oblique Jet Impingement," NASA CR-839, February 1967.
15. Westley, R., et al, "Surface Pressure Fluctuations from Jet Impingement on an Inclined Flat Plate," AGARD Conference Pre-Print No. 113, Symposium on Acoustic Fatigue, Tallousee, France, September 1972.
16. Lilley, G. M., and Hodgson, T. H., "On Surface Pressure Fluctuations in Turbulent Boundary Layer," AGARD Rept. No. 276, April 1960.
17. Willmarth, W. W., and Wooldridge, E. E., "Measurements of the Fluctuating Pressure at the Wall Beneath a Thick Turbulent Boundary Layer," JFM, Vol. 14, 1962.
18. Bull, M. K., "Properties of the Fluctuating Wall-Pressure Field of a Turbulent Boundary Layer," U.S.A.A. Rept. No. 234, University of Southampton, 1963.
19. Curle, N., "The Influence of Solid Boundaries Upon Aerodynamic Sound," Proc. Roy. Soc., A231, 1955.
20. Ffowcs Williams, J. E., and Hall, L. H., "Aerodynamic Sound Generation by Turbulent Flow in the Vicinity of Scattering Half Plane," JFM, Vol. 40, Part 4, 1970.
21. Phillips, O. M., "On the Aerodynamic Surface Sound from a Plane Turbulent Boundary Layer," Proc. Roy. Soc., A234, 1956.
22. Powell, A., "Aerodynamic Noise and Plane Boundary," JASA, Vol. 32, No. 8, 1960.
23. Meecham, W. C., "Surface and Volume Sound from Boundary Layers," JASA, Vol. 37, No. 3, 1965.
24. Glauert, M. B., "The Wall Jet," JFM, Vol. 1, Part 6, 1956.
25. Bakke, P., "An Experimental Investigation of a Wall Jet," JFM, Vol. 2, Part 5, 1957.
26. Kraichnan, R. H., "Pressure Fluctuation in Turbulent Flow Over a Flat Plate," JASA, Vol. 28, No. 3, 1956.
27. Willmarth, W. W., and Wooldridge, C. E., "Measurements of the Correlation Between the Fluctuating Velocities and the Fluctuating Wall Pressure in a Thick Turbulent Boundary Layer,"

AGARD Rept. No. 456, April 1963.
28. Powell, A., "Vortex Sound," Univ. of California, Rept. No. 61-70, 1961.
29. Pinkel, B., and Scharton, T. D., "Reduction of Noise Generated by Flow of Fluid Over a Plate," 84th Meeting of the Acoustical Society of America, Miami Beach, November 1972.
30. Hayden, R. E., et al, "A Preliminary Evaluation of Noise Reduction Potential for the Upper Surface Blown Flap," NASA CR-112246, 1973.

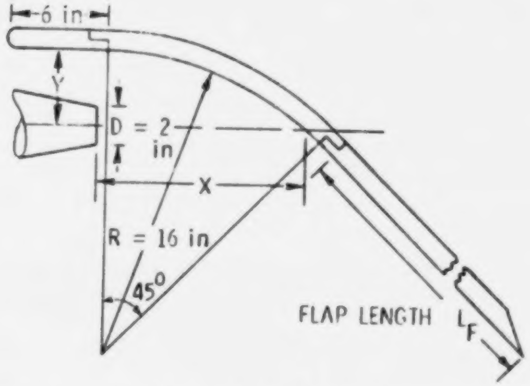
6 in
Y
D = 2 in
X
R = 16 in
45°
FLAP LENGTH L_F

FIG. 1 SKETCH SHOWING BLOWN FLAP CONFIGURATION INVESTIGATED

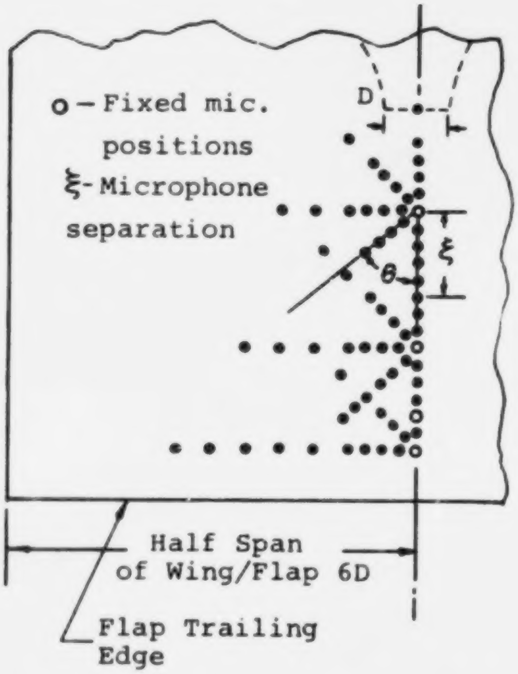
o – Fixed mic. positions
ξ - Microphone separation
D
ξ
θ
Half Span of Wing/Flap 6D
Flap Trailing Edge

Fig. 2 Sketch showing microphone arrangement for fluctuating wall pressure measurement

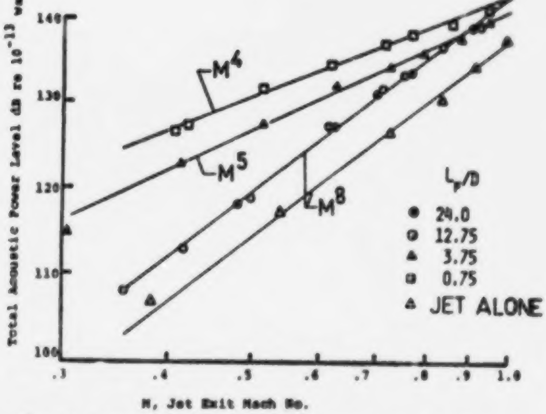

FIG. 3 VARIATION OF TOTAL ACOUSTIC POWER WITH FLAP LENGTH FOR JET POSITION x/D=5.75, y/D=2.0

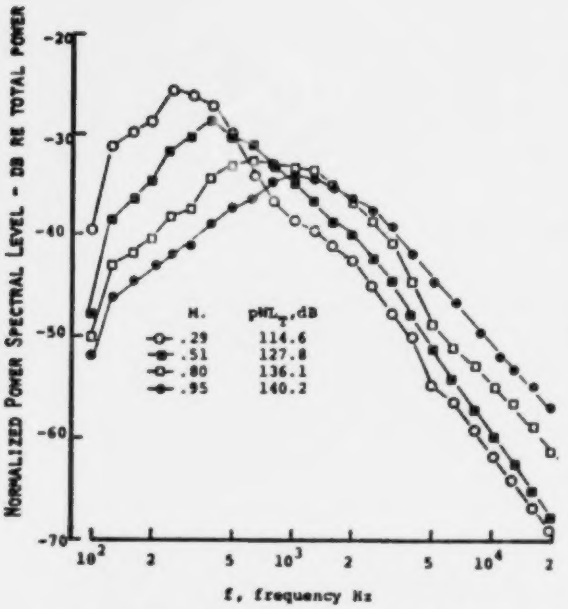

Fig. 4 Power Spectra Variation with Jet Exit Mach No. L_F/D=3.75, x/D=5.75, y/D=2.0

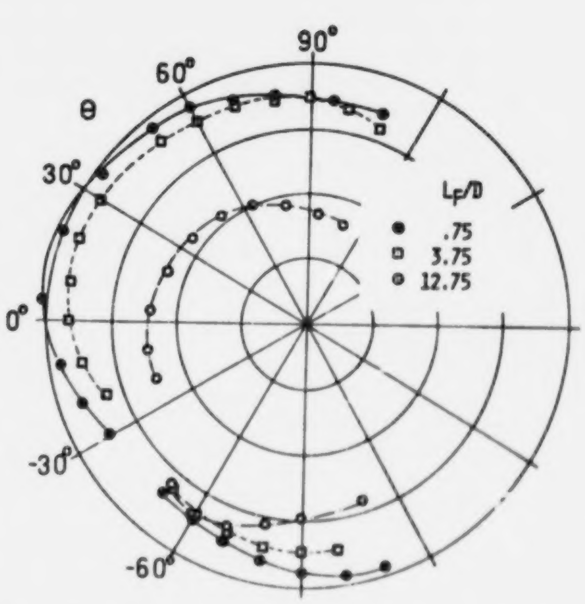

Fig. 5b Overall directional pattern of blown flap noise at different flap length. M=.49, X/D=5.75, Y/D=2.0.

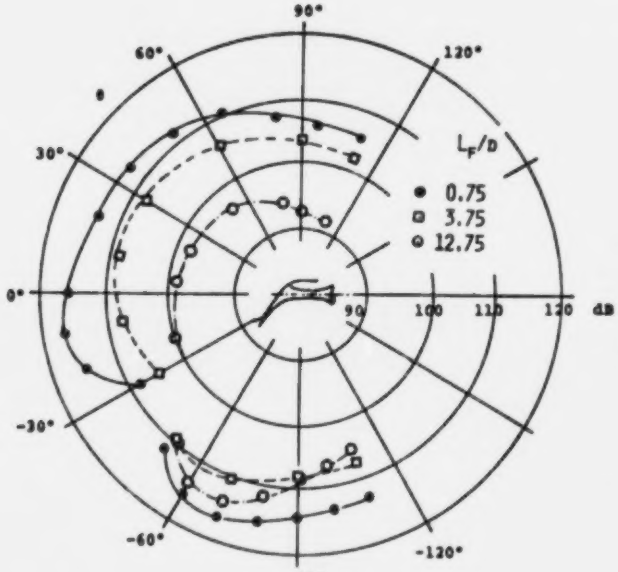

Fig. 5a Overall Directional Pattern of Blown Flap Noise at Different Flap Length. M=0.84, x/D=5.75, y/D=2.0

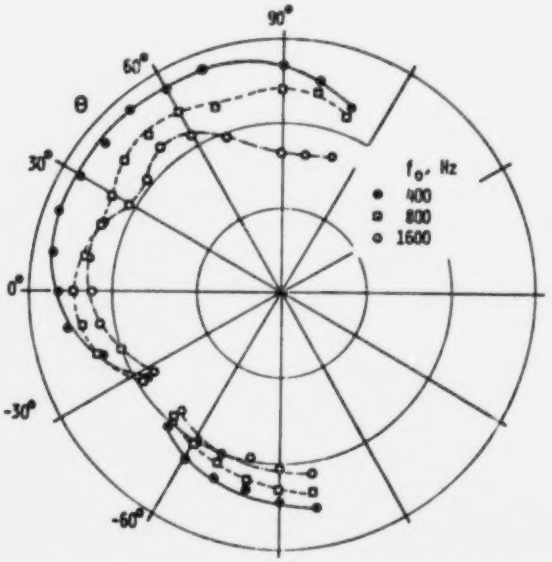

Fig. 5c 1/3 octave band directional pattern of blown flap noise, L_F/D=3.75, M=0.49, X/D=5.75, Y/D=2.0.

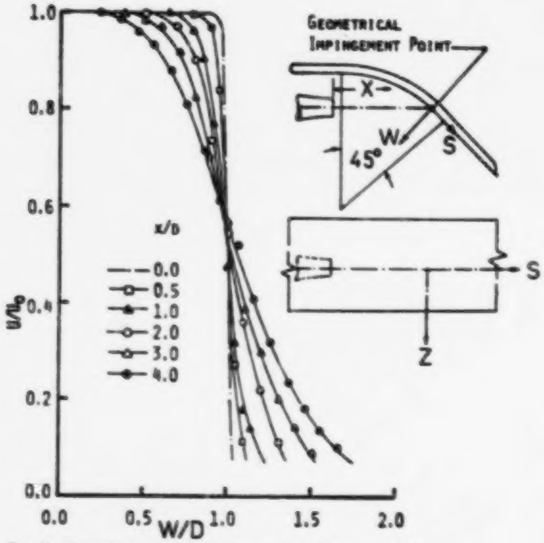

FIG 6 MEAN VELOCITY PROFILES IN THE FREE JET REGION OF THE BLOWN FLAP

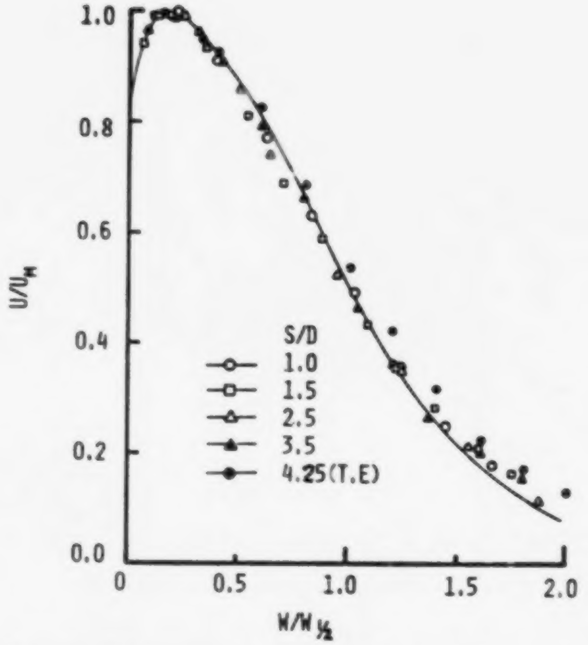

FIG. 8A NON-DIMENSIONAL VELOCITY PROFILE IN THE WALL FLOW REGION OF THE BLOWN FLAP SHOWING FLOW SIMILARITY, Z/D=0

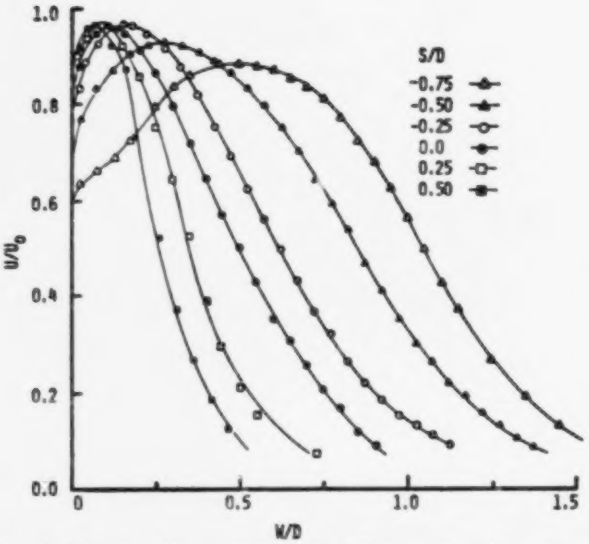

FIG. 7 STREAMWISE DEVELOPMENT OF THE MEAN VELOCITY IN THE IMPINGEMENT REGION OF THE BLOWN FLAP, Z/D=0

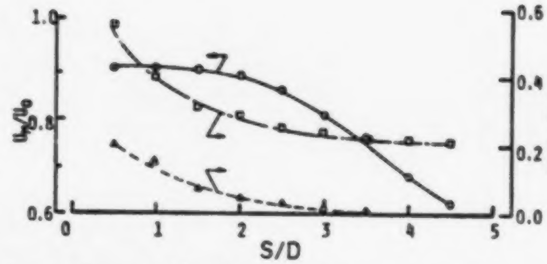

FIG. 8B STREAMWISE VARIATION OF FLOW CHARACTERISTICS IN THE WALL FLOW REGION OF THE BLOWN FLAP

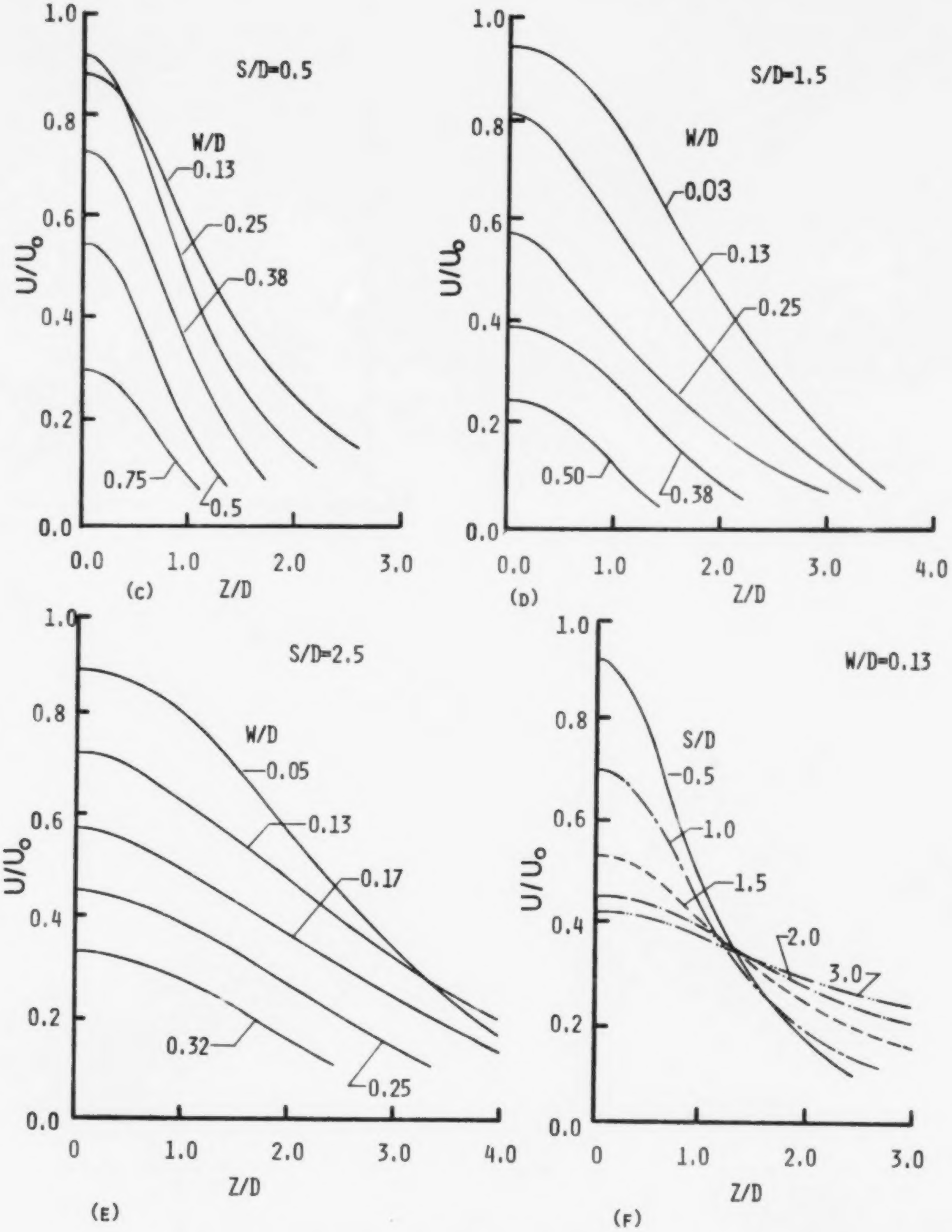

Fig. 8 Velocity Profiles in the Wall Flow Region of the Blown Flap

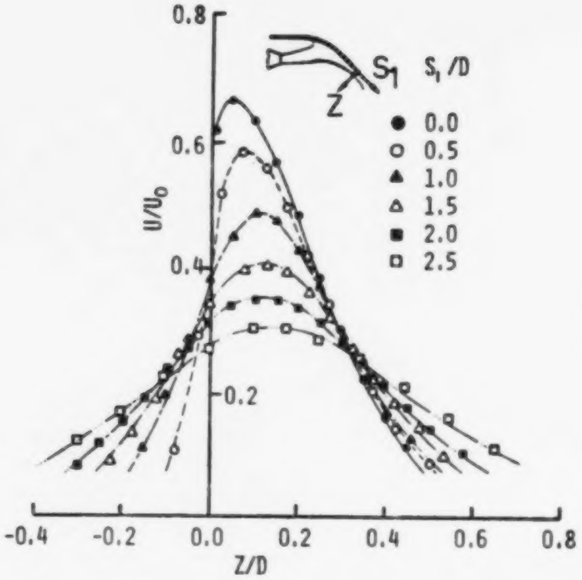

FIG. 9 VELOCITY PROFILES IN THE EDGE JET REGION OF THE BLOWN FLAP FLOW, U_0=570 FPS

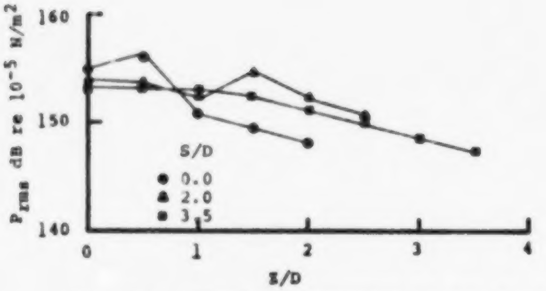

Fig. 10B Spanwise Distrbution of Broadband Fluctuating Wall Pressure

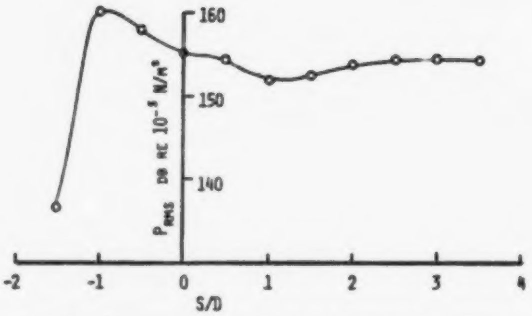

FIG. 10A STREAMWISE DISTRIBUTION OF BROADBAND FLUCTUATING WALL PRESSURE, Z/D=0

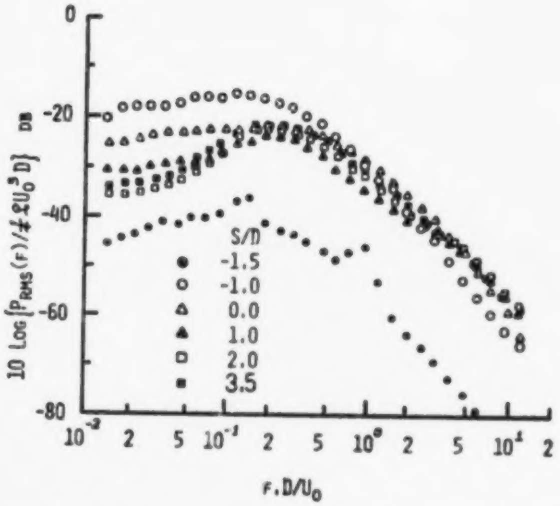

FIG. 11A NORMALIZED FLUCTUATING WALL PRESSURE SPECTRA STREAMWISE VARIATION Z/D=0

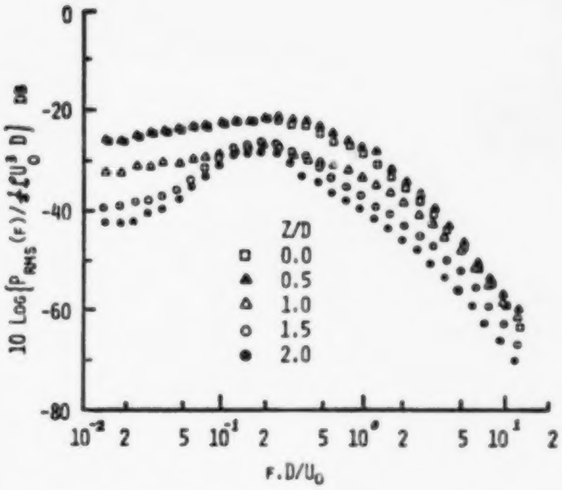

Fig. 11b Normalized Fluctuating Wall Pressure Spectra, Spanwise Variation in the Impingement Region, S/D=0.0

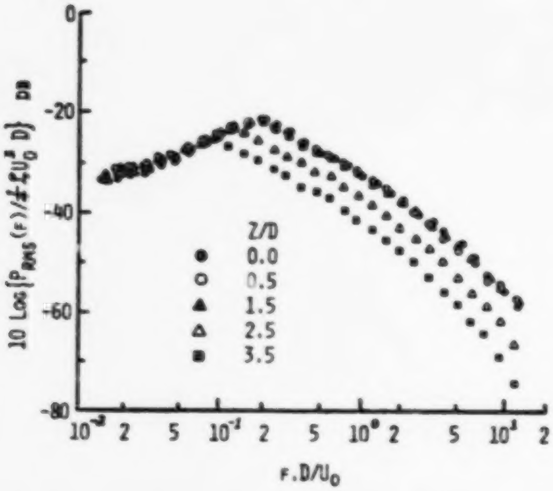

Fig. 11d Normalized Fluctuating Wall Pressure Spectra, Spanwise Variation Near the Trailing Edge of the Flap, S/D=3.5

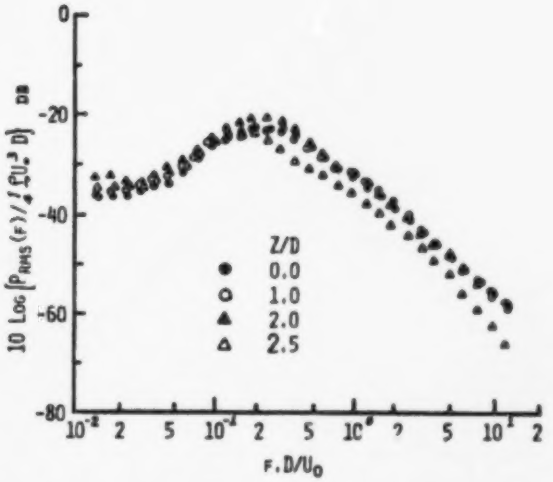

Fig. 11c Normalized Fluctuating Wall Pressure Spectra, Spanwise Variation in the Wall Flow Region, S/D=2.0

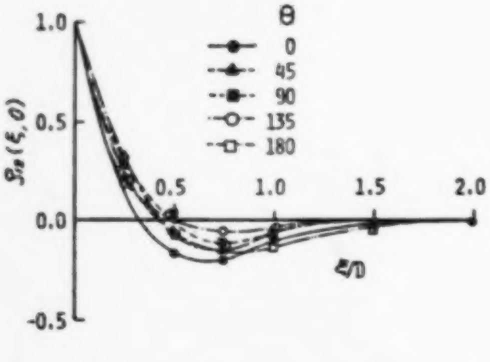

Fig. 12a Spatial Correlation Coefficients of the Fluctuating Wall Pressure in the Impingement Region. Fixed Microphone at S/D=0, Z/D=0

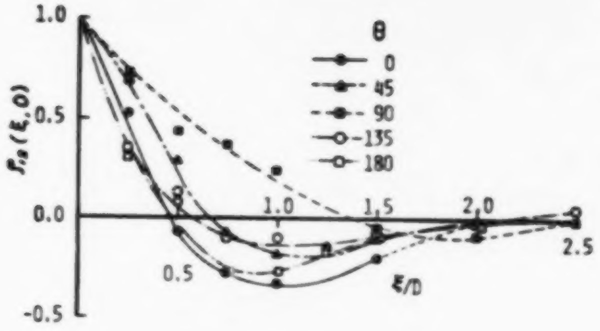

Fig. 12b Spatial Correlation Coefficients of the Fluctuating Wall Pressure in the Wall Flow Region. Fixed Microphone at S/D=2.0, Z/D=0

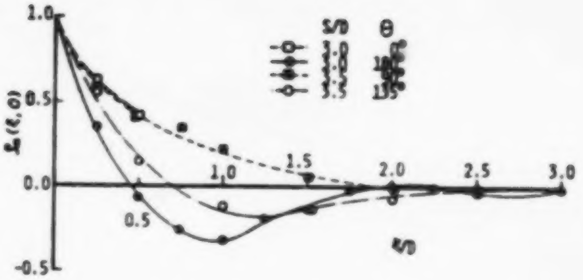

Fig. 12c Spatial Correlation of the Fluctuating Wall Pressure Near the Flap Trailing Edge. Fixed Microphone at S/D=3.0, 3.5, Z/D=0

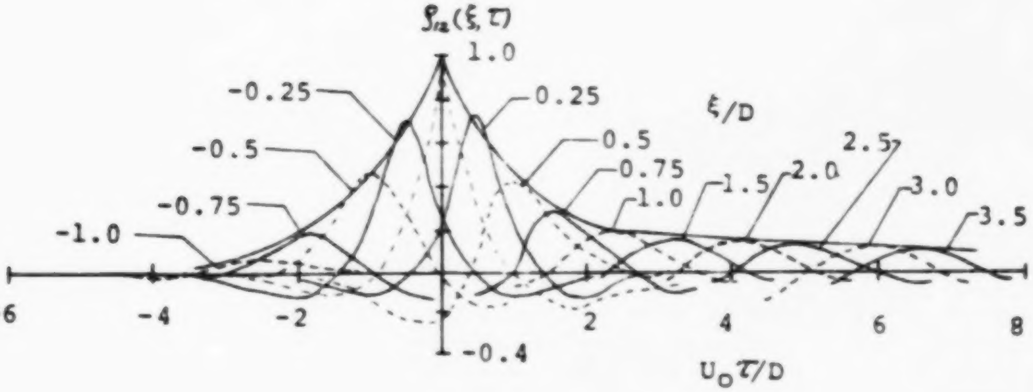

Fig. 13 Streamwise Variation of the Space-Time Cross-Correlation of the Fluctuating Wall Pressure. Fixed Microphone at Geometrical Impingement Point S/D=0, Z/D=0

PRESSURE FLUCTUATIONS ON THE SURFACE OF A CYLINDER IN A CROSS FLOW

by

K. Karamcheti* and Alfred Ayoub**

Joint Institute for Aeroacoustics
Department of Aeronautics and Astronautics
Stanford University
Stanford, California

INTRODUCTION

In the analysis of the aerodynamic noise generated by fluid flows involving solid bodies, a knowledge of the fluctuating pressures on the surfaces of the bodies and in the regions close to the bodies and in their wakes is required. A knowledge of such surface pressure fluctuations is of importance also in a wide range of problems such as the structural loading on an aircraft skin and the transmission of noise into the interior of an aircraft. From the point of view of aerodynamic noise radiation by flows involving solid surfaces, there are many problems in which the radiation may be considered to be dominated by that due to the surface pressure fluctuations.

The origin of the pressure fluctuations and also of the associated velocity fluctuations, depending on the particular flow problem under consideration, may lie in one or many factors such as a turbulent boundary layer or a jet past the surface of the body in the flow, its wake, vortex shedding from the body, and turbulence inherent in the main flow. In a variety of problems, it is possible to obtain, by proper experiments and approximate theoretical considerations, a satisfactory knowledge of the velocity field, rather than of the pressure field. Therefore, it is fruitful to explore the possibility of determining the pressure field near and on the body in terms of the knowledge of the velocity field which, although by necessity, may be empirical. Such a possibility presents itself readily for incompressuble flows.

Studies on this basis, determining the properties of the pressure fluctuations in terms of those of the velocity field in a number of problems have been undertaken at Stanford. The purpose of this paper is to describe the general analytical framework that forms the basis of these studies, and to discuss in particular the problem of the fluctuating pressure induced by the regular vortex wake of a rigid circular cylinder immersed in an originally uniform flow. Although the concern is with incompressible flow, the analysis described here is applicable under certain restrictions, to most general situations.

---

* Director, Joint Institute for Aeroacoustics, and Professor
** Ph. D. student

The notions presented here are similar to those employed by Kraichman (1956), and Lilley and Hodgson (1960), to determine the surface pressure fluctuations in turbulent boundary layer flow over a flat plate. The present study, however, appears to be the first attempt at determining the fluctuating pressure field in terms of the velocity field for a finite body in a flow, where the origin of the fluctuations may be due to one or many factors as enumerated before.

The next section deals with the general formulation and the mathematical problem. It is then followed by a presentation of the analysis for the particular case of circular cylinders.

GENERAL FORMULATION

We consider, for definiteness, flow past a fixed finite rigid body and assume that the flow is essentially incompressible.

It can be shown that if the Mach number $M = U_0/a_0$, where U_0 and a_0 are the mean speed of the flow and the mean speed of sound respectively far away from the body, is much less than unity

$$M = \frac{U_0}{a_0} << 1$$

and if the characteristic time scale T of the fluctuations is much greater than L/a_0 where L is a characteristic length scale of the fluctuations

$$T >> \frac{L}{a_0}$$

the unsteady surface-pressure is free from compressibiliby effects. This later condition is equivalent to

$$M << \frac{1}{S\ell}$$

where S is the Strouhal number defined by d/TU_0 and ℓ is L/d, d being a characteristic dimension of the body

By taking the divergence of the equation of momentum

$$\rho\left(\frac{\partial \vec{V}}{\partial t} + \text{div}\,\overrightarrow{VV}\right) = -\text{grad}\, p + \mu\nabla^2\vec{V}$$

and using the incompressibility condition

$$\mathrm{div}\ \vec{V} = 0$$

where the symbols have their usual meaning, we obtain in Cartesian tensor notation the following equation for the pressure in terms of the velocity field

$$\nabla^2 p = -\rho \frac{\partial}{\partial x_i} \frac{\partial}{\partial x} v_i v_j = -\rho \frac{\partial v_j}{\partial x_i} \frac{\partial v_i}{\partial x_j} \tag{1}$$

This is the basic equation for further considerations. We now express the flow field as composed of two parts, one a steady mean part and the other a time dependent fluctuating part. Thus, introducing $\overline{\vec{V}}$ and $\overline{p}$ as the mean velocity and the mean pressure respectively at any point, where the mean is taken as an appropriate time average, and $\vec{V}'$ and p' as the fluctuating velocity and pressure, we write

$$\vec{V}(\vec{x},t) = \overline{\vec{V}}(\vec{x}) + \vec{V}'(\vec{x},t)$$

or, in Cartesian tensor notation

$$v_i(\vec{x},t) = \overline{v_i}(\vec{x}) + v_i'(\vec{x},t) \tag{2}$$

and

$$p\,(\vec{x},t) = \overline{p}\,(\vec{x}) + p'\,(\vec{x},t) \tag{3}$$

We substitute (2) and (3) into (1) and take the time average of the resulting equation. Substructing the time average of this equation from itself we obtain

$$\begin{aligned} \nabla^2 p' &= -\rho \frac{\partial}{\partial x_i} \frac{\partial}{\partial x_j} \left(2\, \overline{v_i} v_j' + v_i' v_j' - \overline{v_i' v_j'}\right) \\ &= -\rho \left(2 \frac{\partial v_i}{\partial x_j} \frac{\partial v_j'}{\partial x_i} + \frac{\partial v_i'}{\partial x_j} \frac{\partial v_j'}{\partial x_i} - \overline{\frac{\partial v_i'}{\partial x_j} \frac{\partial v_j'}{\partial x_i}}\right) \end{aligned} \tag{4}$$

This equation, which is a Poisson equation, forms, with appropriate boundary conditions, the basis for determining the fluctuating pressure field in terms of the gradients of the mean and fluctuating velocity fields. It thus shows that the pressure fluctuation at any point is governed by the fluctuations in velocity throughout the entire flow and not just at the field point. The first term in Eq. (4) represents the amplifying effect of the mean velocity gradient on the fluctuations, while the second term denotes the effect of the interaction of the fluctuations on themselves. In regions of the flow where the mean velocity gradients are large, the first term on the right-hand side of (4) may be expected to dominate while in other regions, where the mean velocity gradients may be negligible, the other terms may become more important than or comparable to the first.

Now, we consider the solution of the equation

$$\nabla^2 p' = q(\vec{x},t) \tag{5}$$

where, $q(\vec{x},t)$ represents the right member of the equation (4). If R denotes the flow region exterior to a solid surface S fixed in the flow, and if p' and grad p' vanish satisfactorily at infinity, the formal integral representation of the solution of (5) may be expressed in terms of the boundary values of either p' or its normal derivative $\partial p'/\partial n$ only. For this purpose we introduce the Green's function which is a solution of the equation

$$\nabla^2 G(\vec{x};\vec{\xi}) = \delta(\vec{x}-\vec{\xi}) \quad \text{in} \quad R \tag{6a}$$

satisfying the boundary condition

$$\frac{\partial G}{\partial n} = n \cdot \nabla G = 0 \quad \text{on} \quad S \tag{6b}$$

and

$$\left|\nabla_x G\right| \to 0 \quad \text{as} \quad \left|\vec{x}\right| \to \infty \tag{6c}$$

where ∇_x is the gradient operator with respect to $\vec{x}$. In terms of $\partial p'/\partial n$ on the boundary, the case we shall be interested in, we have

$$p'(\vec{x},t) = + \iiint_R G(\vec{x};\vec{\xi})\, q(\vec{\xi},t)\, d\vec{\xi} + \oiint_S G(\vec{x};\vec{\xi})\, \vec{n} \cdot \frac{\partial p'}{\partial \vec{\xi}}(\vec{\xi},t)\, dS(\vec{\xi}) \tag{7}$$

where $(\partial/\partial\vec{\xi})$ denotes the gradient operator with respect to $\vec{\xi}$, $d\vec{\xi}$ is an element of volume around $\vec{\xi}$, and $\vec{n}$ denotes the outward normal from the region R into the surface S.

From the equation of motion

$$\rho\left(\frac{\partial\vec{V}}{\partial t} + \vec{V} \cdot \text{grad}\,\vec{V}\right) = -\,\text{grad}\,p + \mu\nabla^2\vec{V}$$

noting that on the surface of an impermeable rigid fixed surface the fluid velocity $\vec{V} = 0$, we find that

$$\vec{n} \cdot \text{grad}\,p = \vec{n} \cdot \mu\nabla^2\vec{V} \quad \text{on} \quad S$$

It follows that

$$\frac{\partial p'}{\partial n} = \vec{n} \cdot \text{grad}\,p' = \mu\,\vec{n} \cdot \nabla^2\vec{V}' \quad \text{on} \quad S \tag{8}$$

Equation (7) forms the basis for determining the fluctuating pressure field in terms of the mean and fluctuating velocity fields, assumed known emperically or otherwise. Before attempting the integrations in Eq. (7), the Green's function needs to be obtained, as the solution of the problem represented by Eqs. (6a,b,c) taking into account the particular geometry of the body into consideration. It may be noted that the Green's function is just the same as the velocity potential of a steady irrotational incompressible flow due to a source of unit strength situated at the point $\vec{\xi}$ in the region outside the body.

Usually, one is interested in the statistical properties of p', in particular its space-time covariance on the surface of the body from which other quantities of interest such as intensities, power spectra, scales, and convection speeds can be derived. The two point space-time cross-correlation for the pressure fluctuation, with the use of Eq. 7, may be expressed as

$$
\begin{aligned}
R_{p'p'}(\vec{x},\vec{x}',t) &= \overline{p'(\vec{x},t)\, p'(\vec{x}',t+\tau)} \\
&= \int_R\int_R G(\vec{x};\vec{\xi})\, G(\vec{x}';\vec{\xi}')\, R_{qq}(\vec{\xi},\vec{\xi}',\tau)\, d\vec{\xi}\, d\vec{\xi}' \\
&\quad + 2\int_R\oint_S G(\vec{x};\vec{\xi})\, G(\vec{x};\vec{\xi}')\, R_{qQ}(\vec{\xi},\vec{\xi}',\tau)\, d\vec{\xi}\, dS(\vec{\xi}') \\
&\quad + \int_S\int_S G(\vec{x};\vec{\xi})\, G(\vec{x}';\vec{\xi}')\, R_{QQ}(\vec{\xi},\vec{\xi}',\tau)\, dS(\vec{\xi})\, dS(\vec{\xi})
\end{aligned}
\tag{9}
$$

where, the bar denotes, as before, appropriate time average and q is given by the right member of Eq. (4), Q defined by

$$Q = \vec{n} \cdot \text{grad } p' \quad \text{on } S$$

is given by Eq. (8). The quantities such as R_{qQ} are defined in the same manner as $R_{p'p'}$.

Depending on the nature of the mean and fluctuating velocity fields, one can usually employ reasonable simplifications and approximations in evaluating the integrals in Eq. (7) or (9). These will crucially rest on the details of the spacial mean velocity gradients and on the intensities and correlation lengths of the fluctuations. We shall not enter here into a detailed discussion of these aspects. We note, however, that much will depend on the Reynolds number in question and the body shape. In utilizing Eq. (8), we should bear in mind that this is a consequence of the no-slip condition at the surface. If the mean flow over the whole or part of the surface were to be considered as that given by inviscid analysis appropriate modification of Eq. (8) should be done.

In several problems the contributions from the surface integrals in (7) (8) could possibly be shown to be negligible compared to those from the volume integrals.

Case of Two-Dimensional Mean Flow

We now consider the situation where an infinitely long cylinder of constant cross-section is placed in a stream, the mean velocity of which far away from the cylinder is normal to the cylinder axis. Although the mean flow is two-dimensional, the fluctuating flow in general may be three-dimensional. This will depend again on the Reynolds number in question, the cross-sectional shape of the cylindrical body, its attitude with respect to the stream and the nature of the fluctuations, if any, in the stream far away from the body.

For sake of definiteness and future considerations, let us consider a circular cylinder and restrict ourselves to the situation where the stream far ahead of the cylinder is free of any inherent turbulence. Consequently the fluctuations in the flow arise only from the boundary layer past it and the wake behind it. The nature of the boundary layer and the wake depends, as is well known, on the value of the Reynolds number R_e defined by

$$R_e = \frac{\rho U_0 d}{\mu}$$

where d is the diameter of the cylinder and U_0 is the undisturbed stream ahead of the cylinder. Here, we do not enter into a detailed description of the various flow patterns which correspond to different ranges of R_e. We shall merely point out the general features that are relevant to the determination of G, q, and Q. In this context, reference may be made to Kovasznay (1949), and Roshko (1954).

In the lowest range of R for which the wake of the body is unsteady the fluctuating flow field is two-dimensional and the wake consists of a regular pattern of vortices originating at some distance behind the cylinder and moving downstream. The boundary layer is laminar and the seperation may be assumed to be steady. The neighborhood of the body is in a practically steady state. In this case we may conclude that Q is essentially zero:

$$Q \equiv \vec{n} \cdot \text{grad}\, p' = \vec{n} \cdot \nabla^2 \vec{V}' \simeq 0$$

The terms represented by q (as given by the right member of Eq. 4) are all periodic in structure. At slightly higher Reynolds number the wake has, in addition to the regular component, a turbulent one which increases the tendency for three-dimensionality. However, for moderate values of R the correlation length in the axial direction is still large (for instance larger than the length of the cylinder in a practical situation) and the turbulence in the wake can be assumed homogeneous in that direction, in which case R_{qq}, R_{qQ}, and R_{QQ} are two-dimensional.

see, for instance, Phillips (1956). Under the conditions described, the fluctuation field may be regarded as essentially two-dimensional. Then Eq. (7) reduces to

$$p'(\vec{x},t) = -\iint_D g(\vec{x};\vec{\xi})\, q(\vec{\xi};t)\, d\vec{\xi} - \oint_C g(\vec{x};\vec{\xi})\, Q(\vec{\xi},t)\, ds \tag{10}$$

where D is the two-dimensional domain outside the cylinder, C is the circular contour of the cylinder cross-section and

$$g(\vec{x};\vec{\xi}) = \int_{-\infty}^{+\infty} G(\vec{x};\vec{\xi})\, d\xi_3 \tag{11}$$

Note that g is just the two-dimensional Green's function for the domain outside circle C and is readily obtainable. Equation (9) assumes a corresponding form.

When the mean flow past an arbitrary cylinder is two-dimensional and if the circumstances are such that the fluctuating field may be regarded as two-dimensional, the pressure fluctuation will be given by a relation of the same form as (10) except now C denotes the contour of the cylinder in the plane perpendicular to the axis and g is the two-dimensional Green's function associated with that contour. Employing the methods of conformal transformation one can derive g for this case from that obtained for the circle.

Returning now to the case of the circular cylinder, we observe that as the Reynolds number increases further the randomness and the three-dimensionality of the flow increase and the turbulence starts to move upstream toward the cylinder, and the boundary layer may become turbulent. Under these circumstances, the terms composing q may consist of both random and discrete components, and a careful assessment of the possibility of neglecting the contributions of the surface integrals in (7) and (9) is required. One must now consider the three-dimensional Green's function, even though the mean flow is two-dimensional.

PRESSURE FLUCTUATION ON A CYLINDER

We now consider the problem of a circular cylinder at low Reynolds numbers for which the wake behind the cylinder is two-dimensional and the boundary layers over the cylinder surface are laminar. In such a case the pressure fluctuations on the cylinder are entirely due to its wake which consists of a regular vortex street. We shall choose specifically the case of a Reynolds number of 56 for which the type of experimental data required in the present investigation are provided by Kovasznay (1949).

Kovasznay measured across the wake the magnitude of the mean velocity $\overline{\vec{V}}$ and the intensity of the velocity fluctuations, essentially in the direction of the undisturbed main stream, and their phases as functions of x_1 the coordinate along that direction. Based on those measurements and assuming that the measured velocity fluctuation v_1' was identical with that in the x_1 direction he expressed it as

$$\begin{aligned} v_1' = {} & \varphi_1(x_1,x_2) \cos 2\pi \left[\theta_1(x_1) + nt\right] \\ & + \varphi_2(x_1,x_2) \cos 4\pi \left[\theta_2(x_1) + nt\right] \end{aligned} \tag{12}$$

where n represents the vortex shedding frequency. The amplitude function φ_1 and φ_2 vary slowly with x_1 but rapidly with x_2. Function φ_1 is an odd function of x_2 while φ_2 is an even function of x_2. Functions $\theta_1(x_1)$ and $\theta_2(x_2)$ are almost linear functions of x_1.

Now, in expressing the source term $q(x_1,x_2,t)$, given by the right member of Eq. (4), explicitly we note that the contribution from the non-linear term namely $v_i'v_j' - v_i'v_j'$ is of higher order than that of the linear term and that it can thus be neglected. The source term then contains only the amplifying effect of the mean gradients; we have

$$q(x,t) = -2\rho \frac{\partial \overline{v_i}}{\partial x_j} \frac{\partial v_j'}{\partial x_i'} = -2\rho \frac{\partial}{\partial x_i} \frac{\partial}{\partial x_j} \overline{v_i} v_j'$$

We further note the following:

(1) the component $\overline{v_2}$ of the mean velocity is at most of the same order as the fluctuations,

(2) that the component $\overline{v_1}$ could be taken as the measured magnitude of the mean velocity,

(3) since measurements show that very near to the cylinder there is no fluctuation present, the term Q which is equal to $\vec{n} \cdot \mu\nabla^2\vec{V}'$ on the surface is essentially zero.

With these considerations in mind it can be shown* that the pressure fluctuations as given by Eq. (10) may now be expressed approximately as

$$p'(\vec{x},t) = -2\rho \iint_D \overline{v_1} \left(v_1' \frac{\partial^2 g}{\partial \xi_1{}^2} + v_2' \frac{\partial^2 g}{\partial \xi_1 \partial \xi_2} \right) d\xi_1 d\xi_2 \tag{13}$$

---

* For details reference should be made to a forthcoming JIA (Joint Institute for Aeroacoustics) publication

The Green's function is given by

$$g(\vec{x};\vec{\xi}) = \frac{1}{2\pi} \log \left|\vec{x} - \vec{\xi}\right| + \frac{1}{2\pi} \log \left|\vec{x} - \vec{\xi}'\right| - \frac{1}{2\pi} \log \left|\vec{x}\right|$$

where $\vec{\xi}'$ is the inverse point of $\vec{\xi}$ with respect to the circle. When $\vec{x}$ is on the circle C, g takes the simpler form:

$$g(\vec{x};\vec{\xi}) = \frac{1}{\pi} \log \left|\vec{x} - \vec{\xi}\right| - \frac{1}{2\pi} \log \left|\vec{\xi}\right| \tag{14}$$

The velocity fluctuation v_2' normal to the undisturbed main stream is not measured. It could be calculated using the continuity equation and physical considerations on the frequency of the lift and drag fluctuations to fix the limits of integrations.

The domain of integration is chosen as the square: $2 \le \xi_1 \le 12$; $-5 \le \xi_2 \le 5$. This domain includes a complete wavelength, in the ξ_1-direction of the dominant frequency and contains the major part of the unsteady region in the ξ_2-direction. The error involved in integrating on this finite domain was shown to be small due to the rapid decay of the integrands as the point of integration moves away from the cylinder.

Using Eqs. (12), (13), and (14), and the considerations discussed above, we obtain the following expression in the non-dimensional form for the pressure fluctuation on the surface of the cylinder:

$$\begin{aligned}
-\frac{\pi}{2} p'(x_1,x_2,t) = & \int_2^{12} \cos 2\pi\,(\theta_1+nt)\, d\xi_1 \int_0^{5} \left(\alpha_1 \bar{v}_1 \phi_1 + \beta_1 \bar{v}_1 \psi_1 - \gamma_1 \frac{\partial \bar{v}_1}{\partial \xi_1} \psi_1\right) d\xi_2 \\
& + \int_2^{12} \cos 4\pi\,(\theta_2+nt)\, d\xi_1 \int_0^{5} \left(\alpha_2 \bar{v}_1 \phi_2 + \beta_2 \bar{v}_1 \psi_2 - \gamma_2 \frac{\partial \bar{v}_1}{\partial \xi_1} \psi_2\right) d\xi_2 \\
& - \int_2^{12} \cos 4\pi\,(0_2+nt)\, d\xi_1 \int_0^{12} \left(\alpha \bar{v}_1 \phi_2 + \beta \bar{v}_1 \psi_2 - \gamma \frac{\partial \bar{v}_1}{\partial \xi_1} \psi_2\right) d\xi_2
\end{aligned} \tag{15}$$

where

$$\psi_1 = \int_{-\infty}^{\xi_2} \phi_1 \, d\xi_2$$

$$\psi_2 = \int_{0}^{\xi_2} \phi_2 \, d\xi_2$$

$$\alpha = \frac{\xi_2{}^2 - \xi_1{}^2}{\left(\xi_1{}^2 + \xi_2{}^2\right)^2}$$

$$\beta = \frac{2\xi_2\left(3\xi_1{}^2 - \xi_2{}^2\right)}{\left(\xi_1{}^2 + \xi_2{}^2\right)^3}$$

$$\gamma = \frac{2\xi_1\xi_2}{\left(\xi_1{}^2 + \xi_2{}^2\right)^2}$$

$$\alpha_1 = \alpha(\xi_1 - x_2,\ \xi_2 - x_2) - \alpha(\xi_1 - x_1,\ \xi_2 + x_2)$$

$$\alpha_2 = \alpha(\xi_1 - x_1,\ \xi_2 - x_2) + \alpha(\xi_1 - x_1,\ \xi_2 + x_2)$$

with similar expressions for β_1, β_2, γ_1, and γ_2; the pressure is nondimensionalized by $\rho U_0{}^2$, the distances by d, the time by d/U_0, and the velocities by U_0. Functions α_1, β_1, γ_1 are odd functions of x_2, while α_2, β_2, γ_2 are even functions of x_2. This implies that the fundamental frequency component of the pressure distribution p' on the cylinder is antisymmetric with respect to the x_1-axis while the double frequency component is symmetric. This is consistent with the physical notion that the lift oscillates with the fundamental frequency which is the shedding frequency while the drag oscillates with the double frequency. Note also that the last term in (15) is independent of x_1 and x_2 and has the double frequency.

The integrations are being carried out numerically. The results, however, are not available at the time of writing this paper. They will be reported later.

REFERENCES

Kovasznay, L. S. G., 1949. Proc. Roy. Soc. A, 198, 174.

Phillips, O. M., 1956. J. Fluid Mech. 1, 607-24 .

Roshko, A., 1954. Nat. Adv. Comm. Aero., Wash., Rep. No. 1191.

AN EXPERIMENTAL INVESTIGATION OF A JET IN A CROSSFLOW

by

Ivan A. Camelier* and Krishnamurty Karamcheti**
Joint Institute for Aeroacoustics
Department of Aeronautics and Astronautics
Stanford University
Stanford, California

INTRODUCTION

Most of the work done so far in the field of jet noise has been related particularly with the case of a free circular jet, that is a jet issuing into a medium at rest. Only recently with the prospective use of V/STOL airplanes is some interest being directed to the noise radiated from a jet in a cross wind. This kind of problem happens when a V/STOL airplane is landing or taking off with the lifting jet or fan producing a vertical thrust while the airplane is moving with a small horizontal velocity.

In a recent publication, Cole III (Ref. 1) studied theoretically the influence of a crossflow on the noise produced by a jet. The wave equation was solved for a moving medium to obtain the intensity of the noise radiated from the jet to the far field. As in the case of the free jet noise, the solution for which was first given by Lighthill (Ref. 2) in 1952, the noise radiated from a jet in a crossflow is also a function of measurable quantities inside the jet. Due to the lack of information about the jet in the crossflow, Cole III (Ref. 1) used in his analysis some results given in the literature for the free jet. Several experimental investigations have been done previously for a jet in a crossflow, however, these were not concerned with measurements directly related to noise production.

The present study is undertaken to obtain some preliminary data on the mean flow turbulence structure, and mapping of a high velocity jet issuing perpendicularly into a crossflow. The experiment has been performed in the 7 x 10 foot wind tunnel at NASA-Ames. The investigation has been confined to a region close to the jet exit where most of the noise is believed to be produced. Hot wire anemometry has been used for all the measurements of mean velocity and turbulent intensity in the plane of symmetry of the jet. The jet exit velocity is fixed at a Mach number of 0.6 (Reynolds number of 5.4×10^5), which is high enough to produce measurable levels of radiated noise in the far field. Various different ratios of jet and crossflow speeds [$r = \infty$, 10, 8, 6, 4] have been used in the experiment.

---

* Ph.D. Student and Research Assistant

** Professor of Aeronautics and Astronautics and Director of the Joint Institute for Aeroacoustics.

EXPERIMENTAL APPARATUS AND INSTRUMENTATION

The jet consists of air that comes from a high pressure tank through a remotely controlled valve to a settling chamber and then through a convergent nozzle to a circular orifice 1.5 inches in diameter on the surface of a wing with a symmetric profile. The wing is located inside the test section of the 7 x 10 foot wind tunnel in such a way that the jet direction is perpendicular to the wind tunnel flow.

Measurements in the jet were made using a DISA constant temperature hot-wire anemometer system with specifications as described below.

One	DISA	Type	55D01	Constant Temperature Anemometer
One	DISA	Type	55D10	Linearizer
One	DISA	Type	55D31	Digital Voltmeter
One	DISA	Type	55D35	RMS Voltmeter

The signals from the hot wire system were constantly monitored through a Tektronix type 502 Dual Beam Oscilloscope.

TEST PROCEDURE

Due to the crossflow the jet is deformed and altered in shape, bending in the direction of the wind. Following Keffer (Ref. 3) who gives a complete physical description of the interaction, the jet can be divided into three arbitrary regions. The first is the source flow region which is characterized by the presence of a mixing region surrounding a potential core. It goes from the jet exit up to the point where the potential core finishes. The curvilinear region which starts at the end of the potential core is the region where the jet flow is completely developed from the standpoint of the turbulence structure and is always changing its direction in a curvilinear trajectory. Finally in the far region the jet has the same direction as the mean flow and the mixing between the two flows is almost completely accomplished. Figure 1 shows a schematic representation of a jet in the crossflow.

For each value of the ratio r between the jet and the crossflow velocities a survey has been made in the source flow region and in the very beginning of the curvilinear region. One hot wire with its axis perpendicular to the plane of symmetry of the jet was placed at different vertical positions X_{1i}. For each one of these vertical positions the wire was traversed horizontally across the jet along the axis X_2, being stopped at several points X_{2j}. At each point X_{2j}, the signal from the hot wire anemometer was passed through a linearizer and both the DC and the true RMS components were registered. These measurements were then normalized by the DC component of the signal from the hot wire located at the center of the jet exit. From these measurements, plots of mean velocity and turbulent intensity profiles across the jet for several vertical points X_{1i} were obtained.

RESULTS

From the plots obtained by direct measurement as mentioned before in the Test Procedure section, the boundaries of the jet and the limits of the potential core were determined for each value of the ratio r. The mean velocity is low at the sides of the jet and increases toward the center. Where a potential core exists the mean velocity profile reaches a mazimum value and stays there for some extension X_2 in a flat shape. The two points where the mean velocity differs by 2% of the value of the mean velocity at the flat are chosen as determining the front and back edges of the core.

The limits of the jet were found with a criterion used previously by Keffer and Baines (Ref. 4), which defines the edges of the jet as the points "where the velocity excess above the external undisturbed flow, $(U-U_c)$, is 10% of the maximum excess $(U_m - U_c)$, at a given cross-section".

Figure 2 shows the mapping of the jet in the source flow region and in the beginning of the curvilinear region for the ratios of jet to crossflow velocities equal to 10, 8, 6, and 4.

The size of the potential core has a visible dependence on the ratio r, as can be clearly seen in Figure 3 where the curve $X_{1c} = 8 \tanh \frac{r}{13}$ was drawn for comparative purposes only. This variation of size of the potential core with the ratio r was also shown by Pratte and Baines (Ref. 5), and Figure 4 is a reproduction of Figure 3 of Ref. 5 with some points from the present experiment having been included. When comparing the two experiments one should, however, keep in mind that in Pratte and Baines work, a very low crossflow velocity of 3 fps was kept constant with the jet velocity being the variable for shanging the values of r, and the sizes of the jet diameters used were all smaller than the jet diameter used in the present test. Another observation pointed out in Ref. 5 is the fact that the length of the potential core varies with the size of the jet orifice.

Figure 5 shows the variation of the ratio X_{2c}/X_{1c}, between the coordinates of the tip of the potential core, as a function of r. This figure gives an idea of the deflection of the core by the crossflow. Notice that the tip of the potential core has a small deflection even for values of r as large as 10 in contrast with the result pointed out by Keffer and Baines (Ref. 4) that for velocity ratios greater than about four the potential core has the tip approximately above the center of the jet orifice. Again, it should be noted that also in Ref. 4 the value of the crossflow velocity was apparently very low [$U_c = 5$ fps, as can be concluded from Figure 1 of the mentioned reference] when compared to the values used in the present work.

Jet Axis

From Figure 2 one can see that the jet centerline is different for different values of the ratio r. However, when the coordinates X_1 and X_2 are normalized by X_{1c} and X_{2c} respectively, the jet centerline for all values of r investigated here are apparently reduced to only one curve in the source flow region, as shown in Figure 6. In a recent work, Chassaing et al. (Ref.6) have investigated the jet axis in the curvilinear and in the far regions. By using values of X_{1c} and X_{2c} taken from Figures 3 and 5 of the present report it was possible to normalize the jet centerlines corresponding to three different values of the ratio r presented in Ref. 6.

As can be seen in Figure 7, these centerlines were reduced to only one curve which seems to be the continuation, in the curvilinear region, of the normalized centerline curve obtained for the source flow region. For $r = 3.95$ in Ref. 4, the values of X_{1c} and X_{2c} corresponding to $r = 4$ were taken for normalizing the centerline. For $r = 2.35$ in Ref. 4, the values of X_{1c} and X_{2c} that brought the centerline to the desired position were those corresponding to $r = 3.2$ extrapolated from the results presented in Figures 3 and 5. In the case of $r = 6.35$ the values of X_{1c} and X_{2c} used were those corresponding to $r = 5.8$.

Axial Distribution of Mean Velocity and Turbulent Intensity

The axial distribution, along the jet centerline and also along the loci of the peaks of turbulence in the front and back mixing regions, of the mean velocity U and of the turbulent velocity u', both normalized by the jet velocity at the exit U_j, can be seen in Figures 8 to 11. One point to notice is the increase of turbulent intensity in the mixing region as the ratio r decreases. The plot for $r = 6$ seems to have the highest level of turbulence. Also notice that for $r = 10$ the turbulent intensity is higher in the front mixing region for all points investigated. For values of $r = 8$ and 6 (principally for $r = 6$) the maximum of the turbulent intensity is sometimes in the front mixing region and sometimes in the back mixing region. Finally for $r = 4$ the maximum of the turbulent intensity has changed to the back mixing region.

If in the abscissa of the previous figures (8 to 11) X_1 is stretched by the ratio $\frac{X_{1c}(r=\infty)}{X_{1c}(r)}$ between the X_1 coordinates of the tip of the potential core for the free jet and for the jet in the crossflow, and at the same time the mean velocity curves are replaced by $\frac{U + U_c}{U_j + U_c}$ instead of $\frac{U}{U_j}$, and the turbulent intensity curves are replaced by $u'/(U_j + U_c)$ instead of u'/U_j only two figures, 12a and 12b, result. (Observe that in Figures 12a and 12b the mean velocity and turbulent intensity in the mixing region correspond to the average between the values from the front and the back mixing regions). It seems that the axial distribution of the modified mean velocity $\frac{U + U_c}{U_j + U_c}$ can be reduced to just one curve for all values of the ratio r investigated including the free jet. The same is also true for the turbulent intensity $u' / (U_j + U_c)$ except for $r = 6$ where the results obtained in a zone close to the end of the potential core in both the centerline and in the mixing region are higher than the values for $r = \infty$ (free jet), 10, 8, and 4.

CONCLUSION

This report was concerned with a preliminary investigation of the source flow region of a jet issuing perpendicularly into a crossflow.

Because the principal interest of this work is related to the noise produced by the lifting jet or fan of a V/STOL aircraft, the jet velocity was kept constant at a high Mach number, with the crossflow velocity being changed to vary the values of the ratio r . However, the results seem to agree relatively well with those obtained by previous workers who used jets with smaller exit velocities. It was found that the size of the potential core is a function of the ratio r , increasing with the increase of r , approximating the value of the size of the core of the free jet as $r \to \infty$. The same conclusion was obtained before in Ref. 5 . Although the conclusions are similar, the initial rate of change of the core size is higher in the present experiment. Notice that in the experiments of Pratte and Baines (Ref. 5), the crossflow was kept constant and the jet velocity was changed to vary the values of r . This could imply that the potential core is not only a function of the jet diameter and of the ratio r , but is also dependent on the jet velocity; this would lead to the conclusion that the whole problem of the jet in the crossflow depends on r as well as on U_j itself. The dependence on U_j has never been considered before.

The representation of the jet centerline in the source region for different values of r by just one curve when the coordinates are normalized by the coordinates of the tip of the potential core is an evidence that a similarity law should exist for the source flow region of a jet in a crossflow. The existence of this evidence becomes stronger in the case of the axial distributions of the modified mean velocity and turbulent intensity along the centerline and along the locus of turbulence peak in the mixing region. From Figures 12a and 12b it seems that a jet with a velocity U_j, in a crossflow with a velocity U_c, could be taken as a free jet with an exit velocity $U_j + U_c$. Further work is needed to completely verify this important implication.

When the ratio r between the jet and the crossflow velocity is equal to 6, the turbulence of the jet, normalized by the modified velocity $U_j + U_c$, has a different behavior than that observed for other values of r , larger or smaller than 6 . As seen in Figure 12b, the turbulent intensity for $r = 6$ grows up and peaks, unexpectedly, close to the end of the potential core. It was also observed from Figures 8 to 11, that the turbulent intensity (U'/U_j) is slightly higher in the front mixing region than in the back mixing region for values of r larger than 6 , the inverse being true for r smaller than 6 . At $r = 8$ it looks like some sort of change is just beginning in a very mild way, while at $r = 6$ the maximum of turbulence actually jumps from the front to the back mixing region several times as the value of X_1 increases. Therefore, there seems to be some evidence that the value $r = 6$ is a kind of turning point in the behavior of the turbulence in a jet issuing in a crossflow. Much more investigation is clearly needed before any conclusions can be definitively reached.

More measurements are planned for the future. Measurements of the jet structure outside the source flow region for $r = 10$, survey of the jet for values of r less than 4 , and measurements of frequency spectra in the source flow region for several values of r are in consideration. For a study of what could be happening with the turbulence around $r = 6$ a natural suggestion would be an investigation of the jet with $r = 7$ and 5 . Measurement of noise in the far field for the same values of r considered in this report would complete the plans of the present investigation.

ACKNOWLEDGEMENT

The authors would like to acknowledge Mr. Brent Hodder and Mr. David H. Hickey of NASA-Ames Research Center, for coordinating this work between NASA-Ames and Stanford University, and for their very valuable assistance and discussions throughout the experimental part of this program.

The authors also want to thank Mr. Vadim Matte of Stanford University and Mr. Ray Schmorane of NASA-Ames for their valuable help in carrying out the experiments.

This work was supported by NASA grants NASA-NG-05-020-526 and NASA-NGR-05-020-676.

REFERENCES

1. COLE III, J. E., "The Influence of a Crossflow on Jet Noise", NASA CR-2169 (1972).

2. LIGHTHILL, M. J., " On Sound Generated Aerodynamically. I General Theory", Proc. of the Roy. Soc.,Series A, Vol. 211 (1952) pp. 564-587.

3. KEFFER, J. F., "The Physical Nature of the Subsonic Jet in a Cross-stream", NASA SP-218 (1969), pp. 19-36.

4. KEFFER, J. F., and BAINES, W. D., "The Round Turbulent Jet in a Cross-Wind", JFM Vol. 15, Apr. 1963, pp. 481-496.

5. PRATTE, B. D., and BAINES, W. D., "Profiles of the Round Turbulent Jet in a Crossflow", Journal of the Hydraulics Division, ASCE, Vol. 93, 1967, pp. 53-64.

6. CHASSAING, P., GEORGE, J., CLARIA, A., and SANANES, F., "Physical Characteristics of Subsonic Jets in a Cross-Stream", JFM (1974), Vol. 62, Part 1, pp. 41-64.

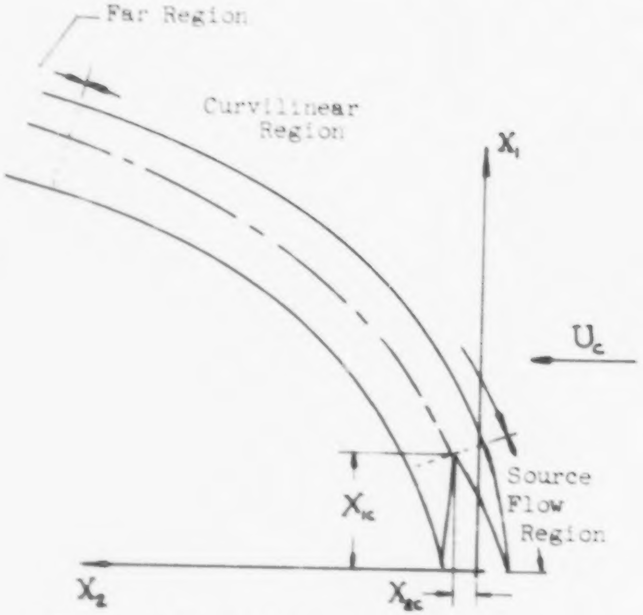
Far Region
Curvilinear Region
X_1
U_c
Source Flow Region
X_{1c}
X_2
X_{2c}

Fig. 1- Schematic view of a jet in a crossflow. (Plane of symmetry)

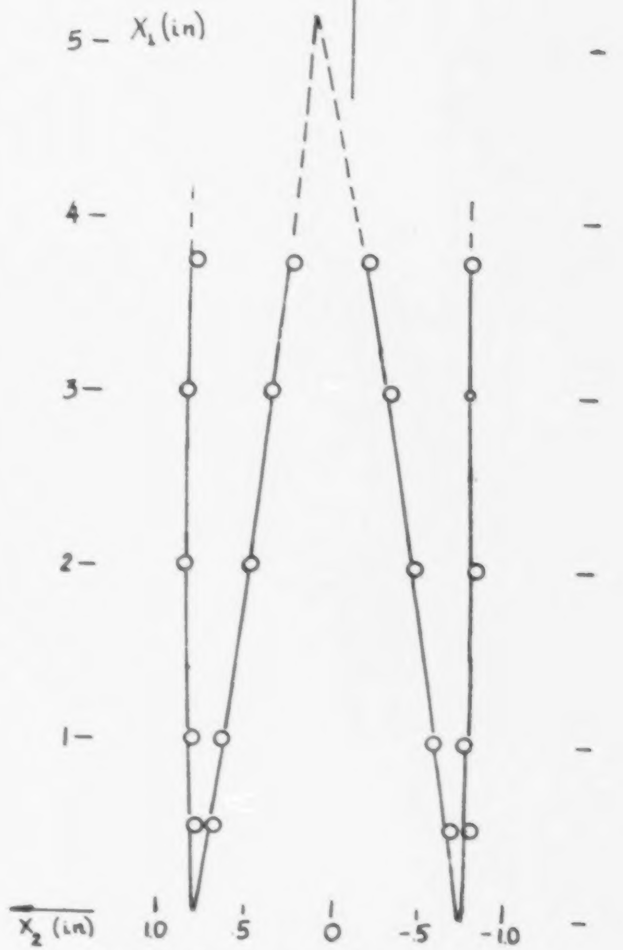

Fig. 2a-Boundaries of the jet.
M_j=0.6 r=10

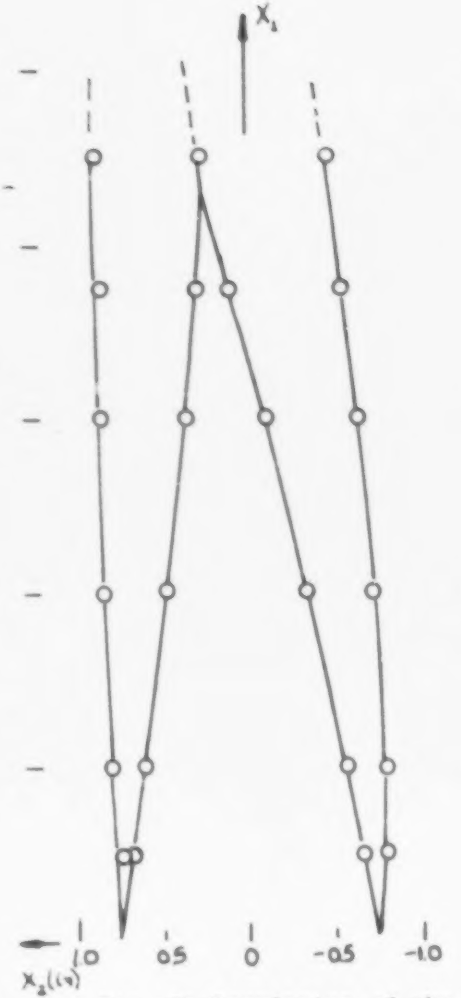

Fig. 2b-Boundaries of the jet.
$M_j=0.6$ r=[illegible]

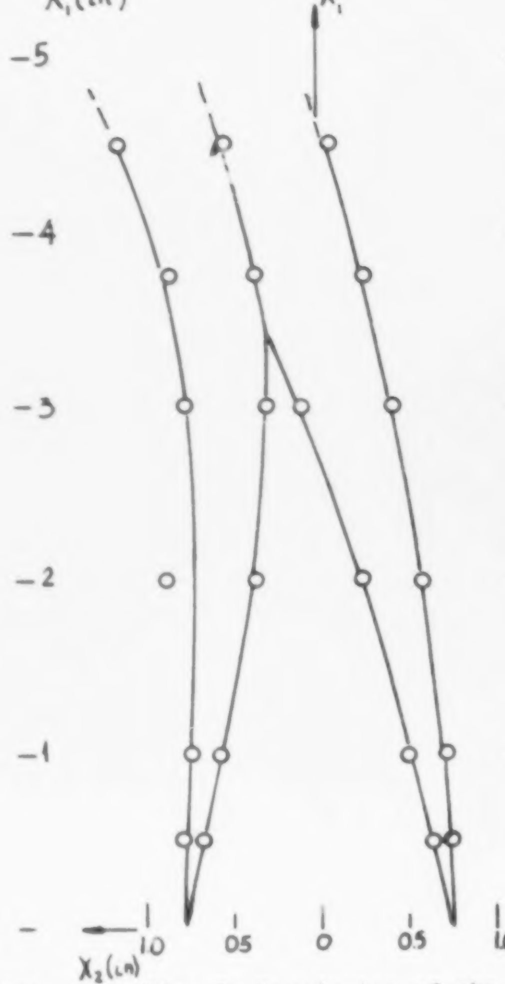

Fig. 2c-Boundaries of the jet.
$M_j=0.6$ r=6

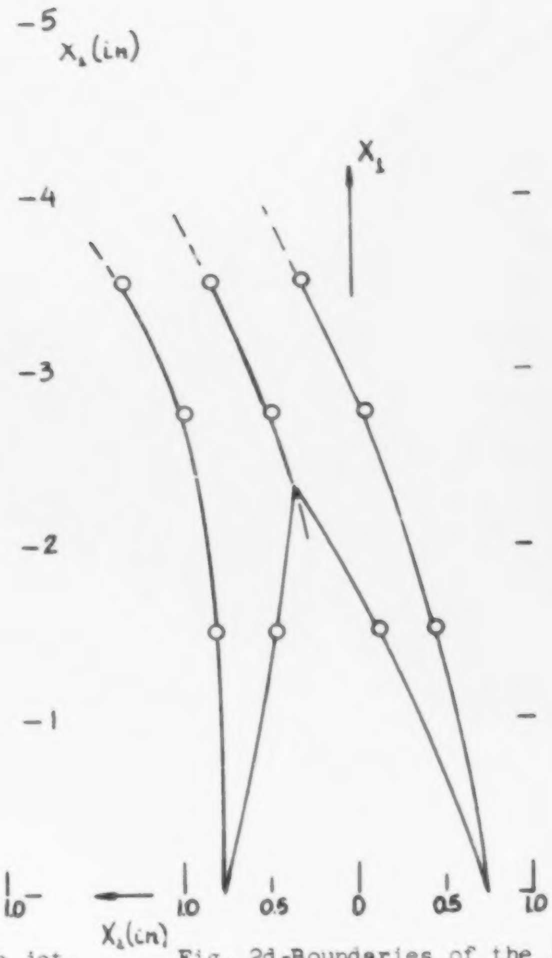

Fig. 2d-Boundaries of the jet.
$M_j=0.6$ r=4

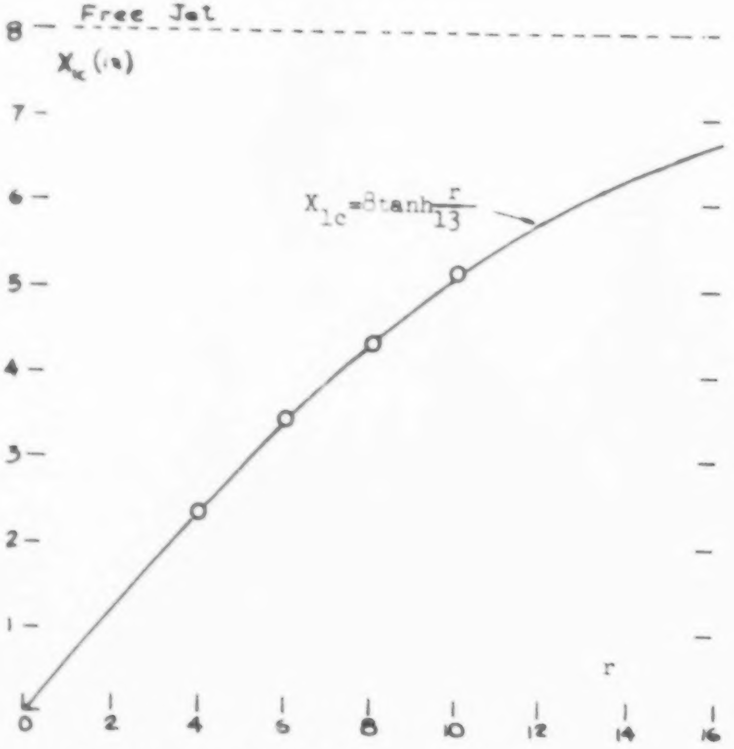

Fig. 3-Length of Potential Core
M_j=0.6 D=1.5 in.

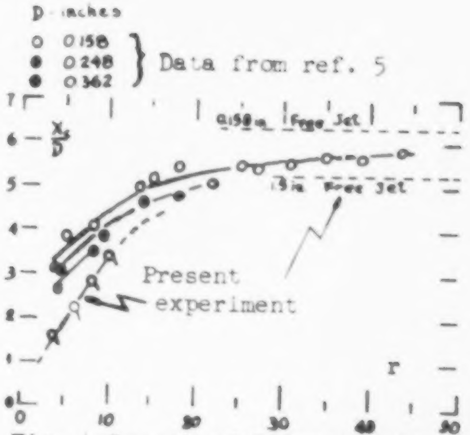

Fig. 4-Length of Potential Core
(Fig.3 ref.5)

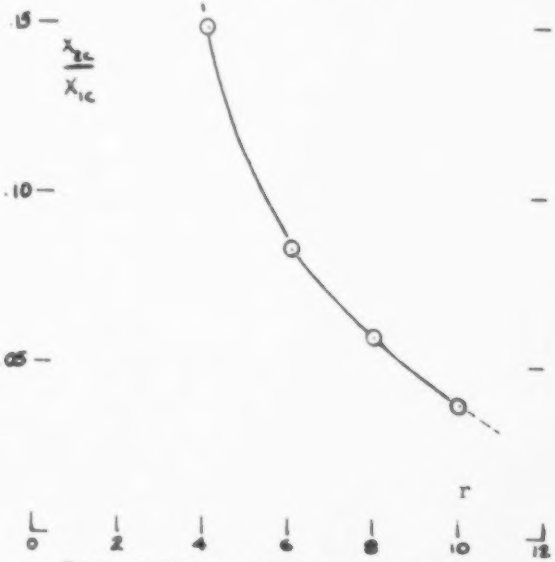

Fig. 5-Ratio of coordinates of end of Potential Core.

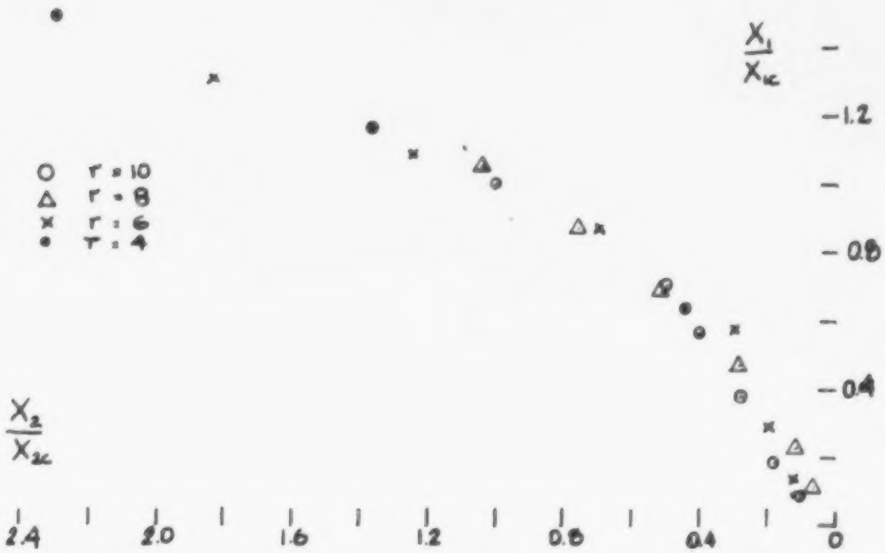

Fig. 6- Jet centerline.
M_j=0.6 D=1.5 in.

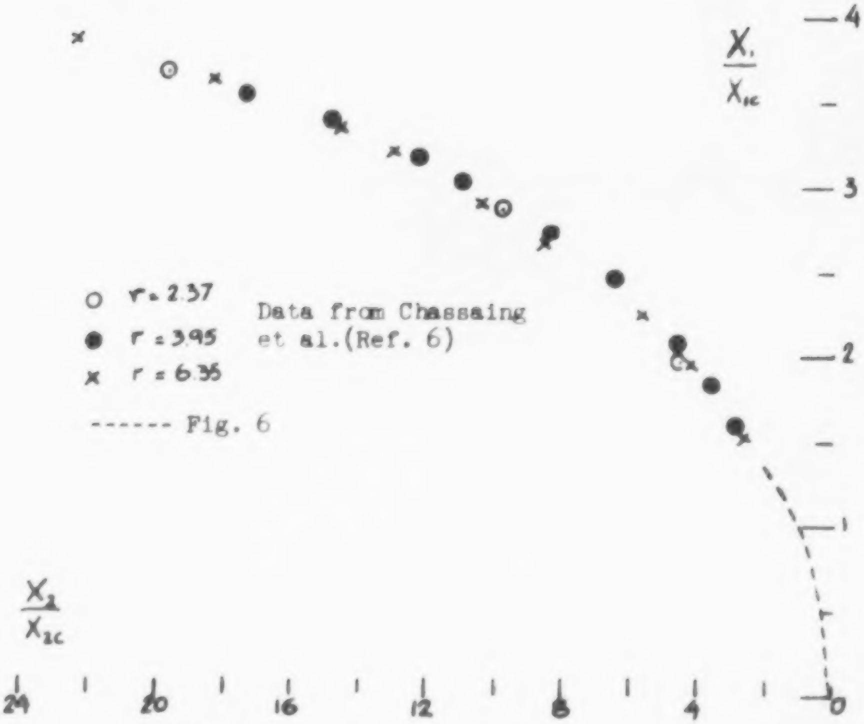

Data from Chassaing et al.(Ref. 6)

Fig. 7- Jet centerline.

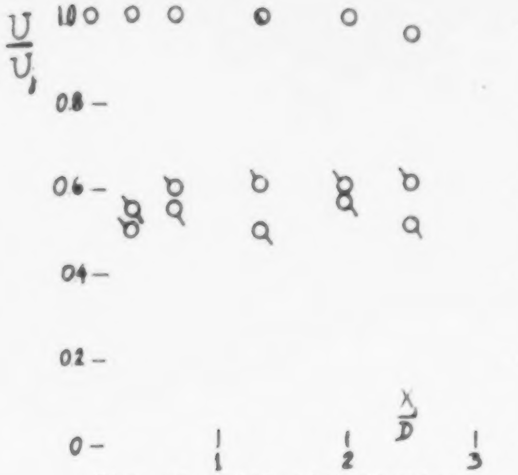

Fig. 8a-Axial distribution of mean velocity.

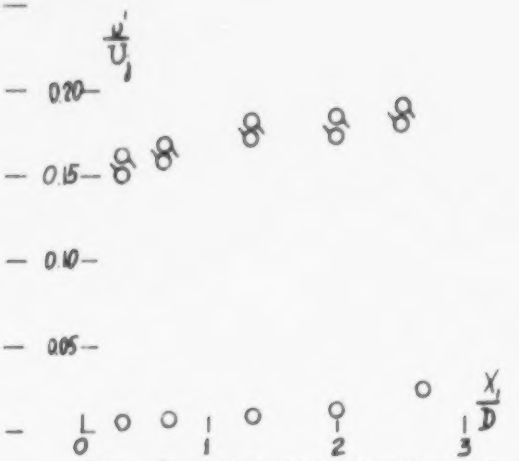

Fig. 8b-Axial distribution of turbulent intensity.

$M_j=0.6$ r=10

○ Center line
Front mixing region } (Point of turbulent peak)
Back mixing region }

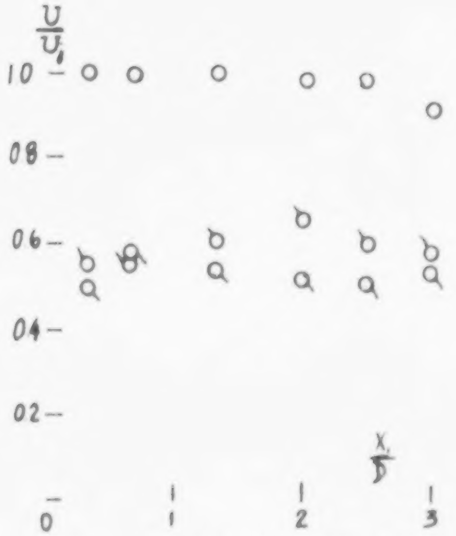

Fig. 9a-Axial distribution of mean velocity.

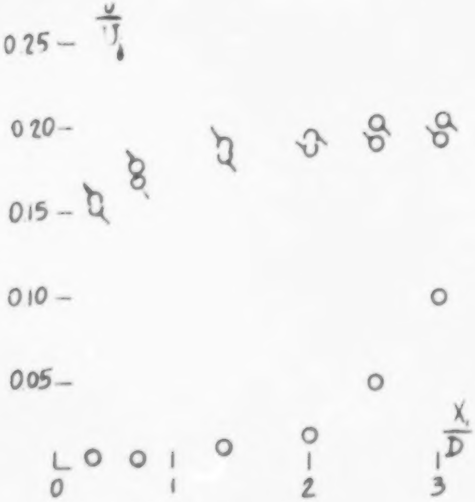

Fig. 9b-Axial distribution of turbulent intensity.

$M_j=0.6$ r=8

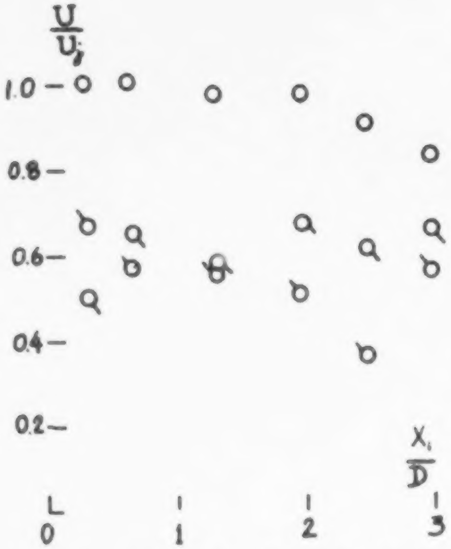

Fig. 10a-Axial distribution of mean velocity.

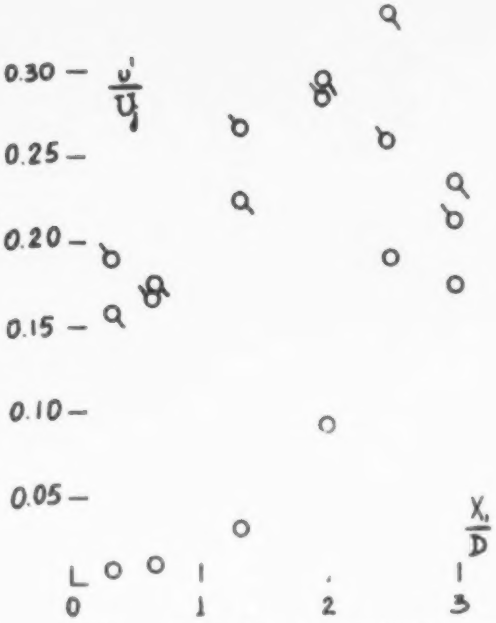

Fig. 10b-Axial distribution of turbulent intensity.

M_j=0.6 r=6

○ Center line
Q Front mixing region } (Point of turbulent peak)
ძ Back mixing region }

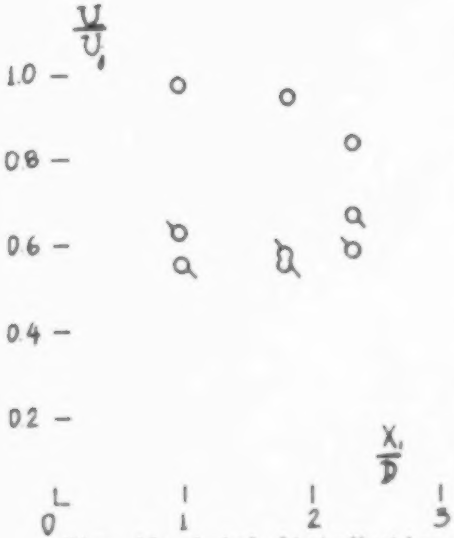

Fig. 11a-Axial distribution of mean velocity.

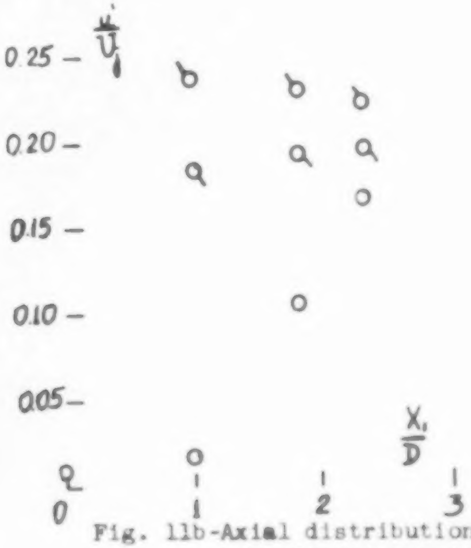

Fig. 11b-Axial distribution of turbulent intensity.

M_j=0.6 r=4

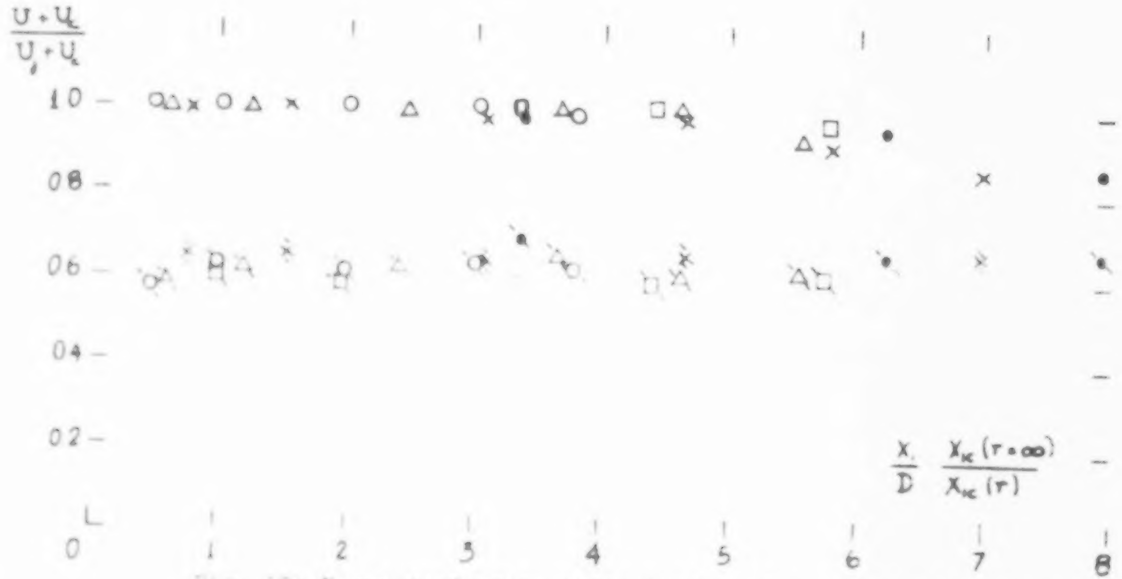

Fig. 12a-Normalized axial distribution of mean velocity. $M_j=0.6$.

r=∞ □ Center line □ Mixing region
r=10 ○ Center line ○ Mixing region
r=8 △ Center line △ Mixing region
r=6 ✖ Center line ✖ Mixing region
r=4 ● Center line ● Mixing region

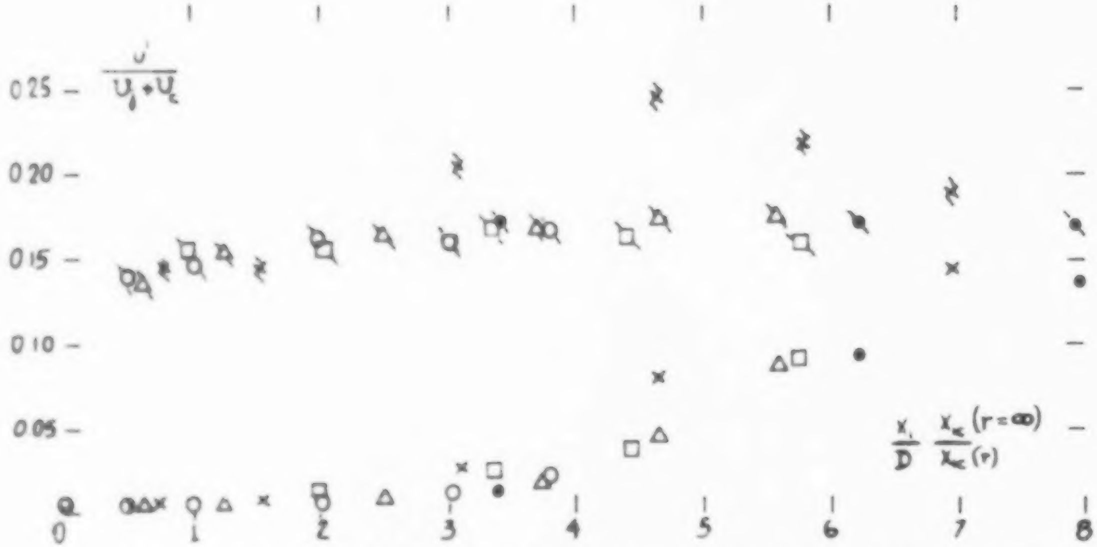

Fig. 12b - Normalized axial distribution of turbulent intensity. M_j=0.6.
(see Fig. 12a for explanation of symbols.)

VORTICITY EFFECTS IN A LARGE ANGLE OBLIQUE JET IMPINGEMENT FLOW

by

John F. Foss
Department of Mechanical Engineering
Michigan State University
East Lansing, Michigan 48823

Introduction

The externally blow flap, shown schematically in Figure 1, is one of the promising boundary layer control and powered lift schemes under consideration for STOL aircraft. However, the well documented significant increase in the acoustic noise associated with the impact of the jet on the deflecting flaps (see Refs. 1-4) presents a serious problem as regards the adoption of this configuration since its operation near population centers demands a sufficiently quiet operation of the aircraft. A multifaceted approach to the more precise identification of this problem and the possible means to reduce the noise level to a satisfactory value is both appropriate and, by means of numerous programs, is under way at this time. The work reported herein is one aspect of this total effort; the objectives of this study are to document and relate the pertinent characteristics of the fluid dynamic phenomena to the aerodynamic noise producing character of the impinging jet flow. For this, the idealized problem of an axisymmetric jet obliquely impinging on a large plane surface at an angle of $\pi/4$ radians was selected, see Figure 2. The purpose of this communication is to present the experimental data collected in this initial study and to interpret these results as regards the acoustic noise producing effects in the flow.

Background

The mean flow character of the shallow angle jet impingement flow field has been extensively documented and interpreted by Foss and Kleis [5]. In this, vorticity effects are shown to be quite important for the mechanics which govern the motion. That is, azimuthal vorticity of the approach jet is responsible for the maintenance of the basically circular character of the flow field isotachs except in the region near the plate where the vortex stretching and the flux of vorticity through the surface of the impact plate result in a concentrated and contra-rotating vortex structure. These features of the flow field, certain analytical considerations re the vorticity dynamics, and the relationship of these effects to the aerodynamic production of acoustic noise in terms of the Powell "vortex sound" [6] theory are discussed by Foss [7] in the first volume associated with this annual conference.

The essential character of the vortex sound theory is included here for reference; the original source is recommended for a complete explication including the relationship between the vortex sound concept and the well known convected quadrupole representation from Lighthill [8], [9].

Powell [6] has shown that the similarity between the dipole effect (Δp across the surface area s, which leads to a corresponding mass flux across the plane of the surface) and the circulation Γ, which characterizes the strength of the vortex whose axis forms the contour bounding the area, can be used to develop an expression for the far field velocity $u(\underset{\sim}{x}, t)$ as

$$u(\underset{\sim}{x}, t) = \frac{\hat{x}}{4\pi x c_a^2} \; \frac{d^2}{dt^2}\Big[\Gamma s\Big]^{*} \tag{1}$$

where c_a is the ambient speed of sound and * signifies a delayed time. A schematic representation of this relationship is shown in Figure 3. This expression can be used to infer what properties of the vorticity in the oblique jet impingement are most important for the noise generation. It should also be noted that arguments similar to those referenced here have been used by Hardin [10] to evaluate the acoustic characteristics of the orderly structures in the turbulent jets.

As suggested by (1) the contribution to the acoustic noise is from the unsteadiness with which the vortex loops change. (The solenoidal condition $\nabla \circ \underset{\sim}{\omega} = \nabla \circ (\nabla \times \underset{\sim}{v}) = 0$ requires that the vorticity appear in closed loops or terminate on the boundary of the flow.) The azimuthal vorticity of the approach flow will be distorted by the interaction with the plate and the surface flux of vorticity will require a modification of the vortex loop structures within the jet field. When viewed from the material coordinates of a portion of a given loop, the first time derivative of Γs can be expected to be large for those loops which are elongated by the interaction with the plate and/or for those loops in which significant migration of the loop into new fluid occurs. The contribution of $\underset{\sim}{u}(x, t)$ comes from the unsteadiness (i.e., the magnitude of the turbulent fluctuations) with which this occurs. These effects are shown schematically in Figure 4.

Donaldson and Snedecker [11] have also investigated the large angle oblique jet impingement flow. Their work and the present study are complimentary in that they report limited data for a very wide range of conditions including sub and supersonic jet exit velocities, various length/diameter ratios and various impact surface geometries. A pertinent result from their work is that the observed phenomena is weakly dependent upon L/d for L/d >7.

The next section identifies the experimental equipment and procedures used in the present study; the subsequent section presents the velocity and pressure data and interprets the behavior of the flow as revealed by these results. The final section interprets the noise producing characteristics in terms of the vortex sound theory and the present results.

The Experimental Program

Facility

The essential components of the experimental facility are shown in Figure 5. The surface static pressure and the hot-wire probe signals were processed on the T.I. 960 A minicomputer. (This allowed the calibration of the "linearized" anemometer to be stored as a fourth order polynomial in the computer memory and the velocity statistics $\bar{u}$, $\overline{u^2}$, etc., to be inferred from similar mean and mean square voltage signals digitally computed.) Velocity traverses were made under computer control by driving stepping motors

(Δy, Δz) and orienting the probe $\Delta\beta$ with respect to the mean velocity of the jet. The latter is accomplished by: (1) reading the average probe response at ±45, ±30, ±15, and 0 degrees from the presumed flow direction, (2) fitting this curve with a cosine function at the seven points (normalized upon the maximum reading) and then (3) orienting the probe at the computed mean flow direction to record $\overline{E}_s$, $\overline{E_s^2}$ and at ±45 degrees to allow the $\overline{u_t^2}$ and $\overline{u_s u_t}$ values to be inferred. Additional software routines were used to recover $\overline{u}_r$, $\overline{u}_\theta$, $\overline{u_r^2}$, $\overline{u_\theta^2}$, and $\overline{u_r u_\theta}$.

The length from the jet axis to the impact plate was seven diameters ($L/d = 7$) for all the data reported herein. The jet diameter was 1.9 cm and the jet Reynolds number was 5×10^4. A DISA gold plated probe was used to minimize pitch response effects; it was maintained parallel to the plate for all of the recorded data.

Results

Velocity traverses were originally made in the midplane ($\theta = 0, \pi$) of the flow field, see Figure 6. From these data, it appeared that $z/d \approx 0.05$ would be an appropriate plane to survey the velocity field near the plate since this was in the neighborhood of the maximum velocity for these traverses. In retrospect this was a good choice; this plane is in the neighborhood of the velocity maxima for the entire flow field as revealed by selected vertical traverses (see Figure 7). The latter were obtained at $r/d = 1$ and $r/d = 3$ at $\theta = 0$, $\pi/4$, $\pi/2$ radians. These locations for data acquisition are, of course, only a small fraction of that required for a complete documentation of the flow. However, they have provided the basis for interpreting the general character of the flow near the plate.

Figure 8 presents a composite plot of the magnitude and direction of the velocity field for $z/d = 0.05$. Two symmetry patterns are apparent in this figure; a stagnation region with a local symmetry effect is evident at the location $r/d \approx -1$ and $\theta = \pi$ and the flow is symmetric about the geometric intersection of the jet axis and the plate (the origin) for sufficiently large r ($r/d \geq 3$). Donaldson and Snedeker [3] note this latter effect; their data is for $r/d = 18.4$.

The surface static pressure measurements support the notion of a local symmetry pattern and the interpretation of this as the neighborhood of the stagnation point. The total pressure field is shown in Figure 9a and a detailed plot of the maximum pressure region is given by Figure 9b. The local symmetry point of this distribution is identified as $r/d = -0.89$ and $\theta = \pi$ and is marked on Figure 9b.

A rather striking results of the present data that is not apparent in the above figures is that the turbulence kinetic energy in the region near the plate is not larger than that which would have existed in the jet flow in the absence of the plate. This can be inferred by comparing the maximum turbulence intensity level of the approach flow with the maximum turbulence level near the plate in Figure 6. A possibly more relevant comparison would be the relative magnitudes of the volume integral over a segment of the undisturbed jet and in an equivalent length segment for the flow over the plate. The construction of the axisymmetric integral would not be difficult; the equivalent integral in the three-dimensional flow would be quite difficult to accurately evaluate since many traverses like those in Figure 7 would be required. An indication of the turbulence intensity level near the plate surface is proved by Figure 10.

The Generation of Acoustic Noise

The result that there is not a large production of turbulence kinetic energy in the impingement flow is, if not surprising, at least not incompatible with the significant acoustic emissions by such a flow. Specifically, since the acoustic noise production is a function of the rather subtle characteristics of the turbulence field and represents a small fraction of its energy, the orienting effects of the plate on the turbulence stress field are the apparent cause of the large noise generation. An alternative explanation is suggested by the vortex sound theory and the observed character of the flow.

By working "backward" from the supposed stagnation point, the approximate location of the stagnation streamline in the approach jet can be identified; this is shown in Figure 6. The ratio of the velocity at this location to the exit velocity at this location is 0.3; hence it is possible to identify the stream surface of the approach jet that contains the stagnation streamline as "the ≃ 0.3 isotach cone." This stream surface was qualitatively identified in Figure 4 in terms of its relationship to the "reconsitituion" of the vorticity loops which are exterior to this stream surface. This reconstitution leads to large values of $d^2(\Gamma s)/dt^2$ if this reconstitution participates in not only the viscous diffusion effects (as it must) but also the generally unsteady character of the turbulent flow field.

Based upon these considerations, the continuing studies of the jet impingement flow in our laboratory will focus on the vorticity field in the neighborhood of the stagnation point. Current developments involve a scheme to isolate the time varying transverse vorticity $\omega_t(t)$ by formulating the quantity

$$\omega_t = \frac{\partial w}{\partial s} - \frac{\partial u_s}{\partial z} \qquad (2)$$

from the "simultaneous" measurement of two adjacent wire pairs. That is, a vertical x-wire to isolate w(t) and

$$\frac{\partial w}{\partial s} \approx \frac{1}{u_s(t)} \frac{\partial w}{\partial t} \qquad (3)$$

and a vertically spaced pair of horizontal wires to isolate $\partial u_s/\partial z$ and the use of the T.I. computer to form the algebraic operations as well as to construct the appropriate statistical measures of ω_t will be utilized for this experimental investigation.

REFERENCES

1. Dorsch, R. G., W. J. Kreim, and W. A. Olsen, "Externally-blown-flap noise," Paper 72-129, Jan. 1972, AIAA New York, New York.

2. Putnam, T. W. and P. L. Lasagna, "Externally blown flap impingement noise," AIAA Paper No. 72-664, 1972.

3. Haas, M., "Blown flap noise," MIT Report FTL 72-5, 1972.

4. Olsen, W., J. Miles, and R. Dorsch, "Noise generated by impingement of a jet upon a large flat board," TN D-7075, 1972, NASA, Cleveland, Ohio.

5. Foss, J. F. and S. J. Kleis, "The oblique impingement of an axisymmetric jet," Second Annual Report, NASA Grant NGR 23-004-068, December 21, 1972.

6. Powell, A., "Theory of vortex sound," Jour. Acoustical Soc. of Am., 36, 1, 177-195, January 1964.

7. Foss, J. F., "Vorticity effects in oblique jet impingement flows as a background for the acoustics problem," Interagency Symposium on University Research in Transportation Noise, edited by G. Banerian and K. Karamcheti, Vol. I, 273, Stanford University (March 1973).

8. Lighthill, M. J., "On sound generated aerodynamically, I. General theory," Proc. of the Roy. Soc. of London, Ser. A, Vol. 211, No. 1107, March 20, 1952, pp. 564-587.

9. Lighthill, M. J., "On sound generated aerodynamically, II. Turbulence as a source of sound," Proc. of the Roy. Soc. of London, Ser. A, Vol. 222, No. 1148, February 23, 1954, pp. 1-32.

10. Hardin, J. C., "Analysis of noise produced by an orderly structure of turbulent jets," NASA TN D-7242, April 1973.

11. Foss, J. F. and S. J. Kleis, "The oblique impingement of an axisymmetric jet," Second Annula Report to NASA, NGR-23-004-068, Michigan State University, 1972.

ACKNOWLEDGEMENTS

This continuing study has been supported by NASA Lewis and Langley Research Centers on sequential Grants NGR 23-004-068 and NGR 23-004-091. Technical communication with the grant monitors, Dr. J. A. Albers and Dr. Jay Hardin, has been helpful in this work and it is appreciated. The special computer programing for this study was executed by Mr. T. Merrow; his support in this and the data acquisition has been of considerable importance in the completion of this work.

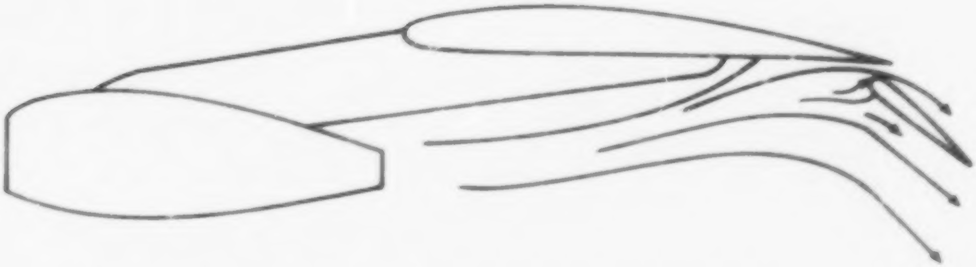

Figure 1. Externally-blown-flap configuration for STOL aircraft.

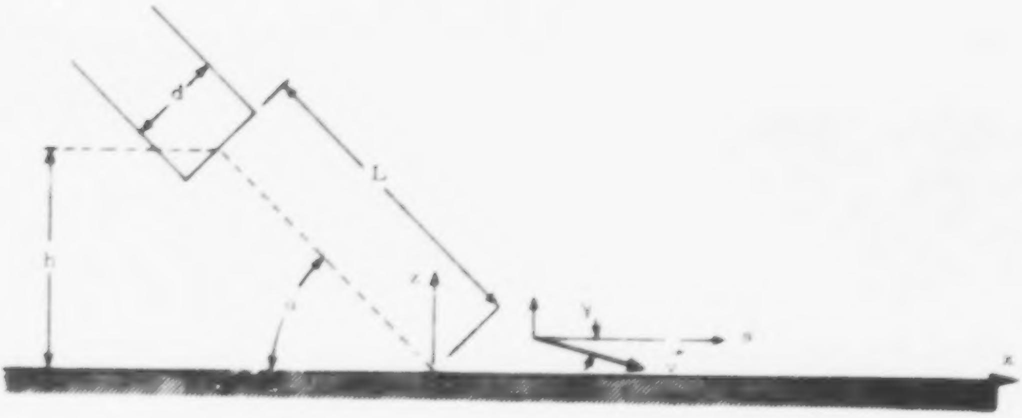

a. Side View

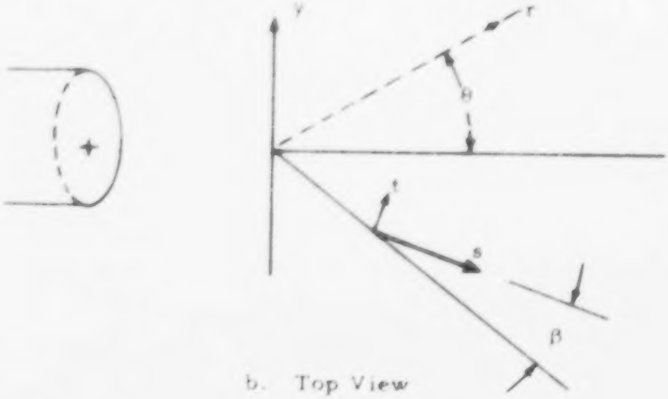

b. Top View

Figure 2. Coordinate system and definition of symbols for the large angle jet impingement studies.

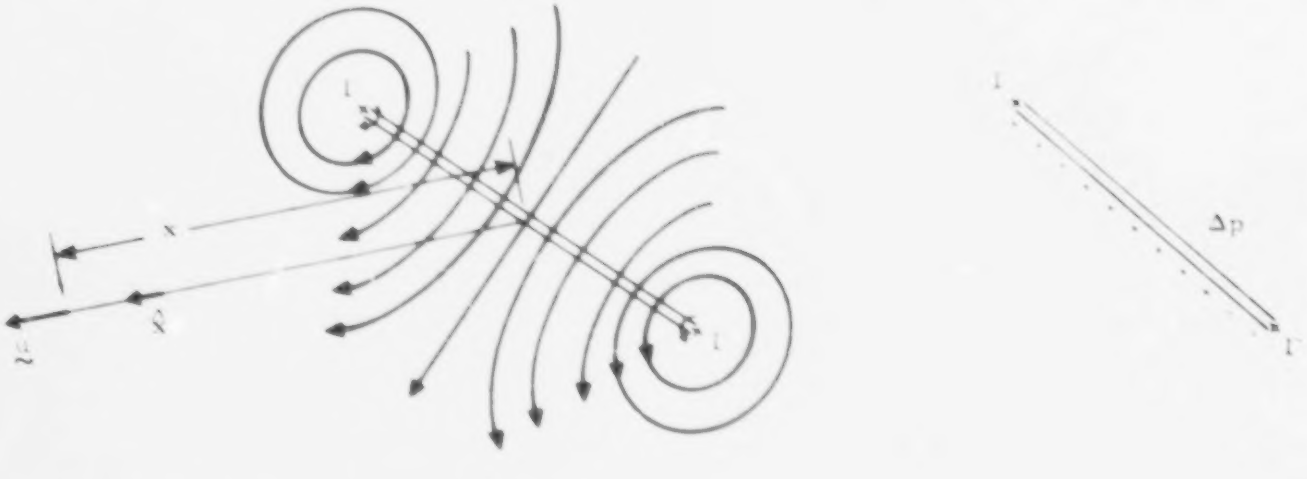

(a) Streamline flow pattern based upon vortex loop with strength Γ.

(b) Dipole sheet adjusted to yield the same flow field as in (a).

Figure 3. Terminology for Powell's vortex sound analysis. (Adapted from Figure 3 of [6].)

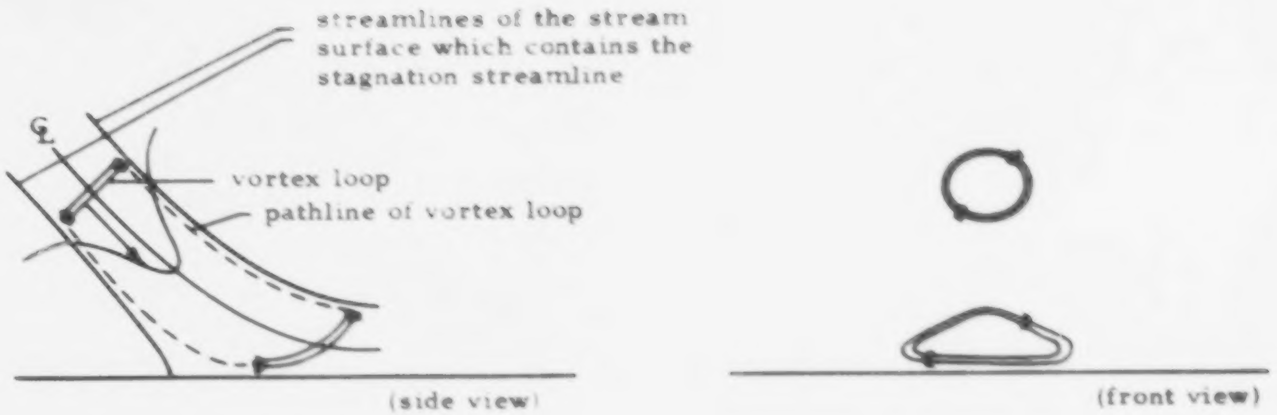
streamlines of the stream surface which contains the stagnation streamline
℄
vortex loop
pathline of vortex loop
(side view)
(front view)

(a) Vortex loop stretching "inside" the stagnation streamline.

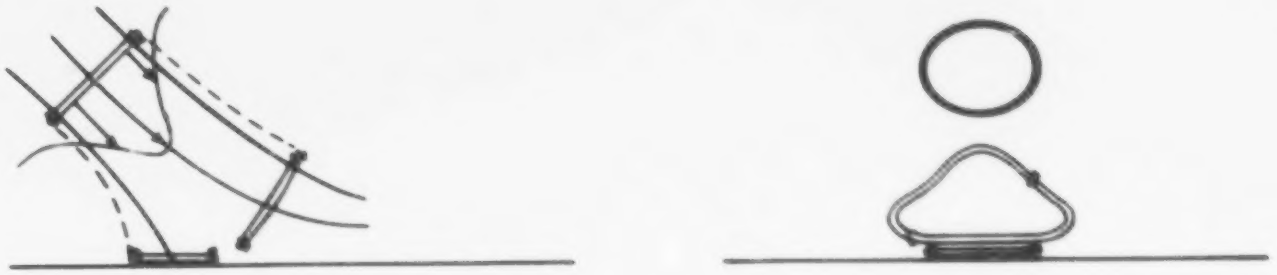

(b) Vortex loop exterior to the stagnation streamline which is reconstituted as a result of the surface vorticity flux.

Figure 4. **Schematic representation of vortex loop behavior which contributes to the quantity $d^2(\Gamma s)/dt^2$.**

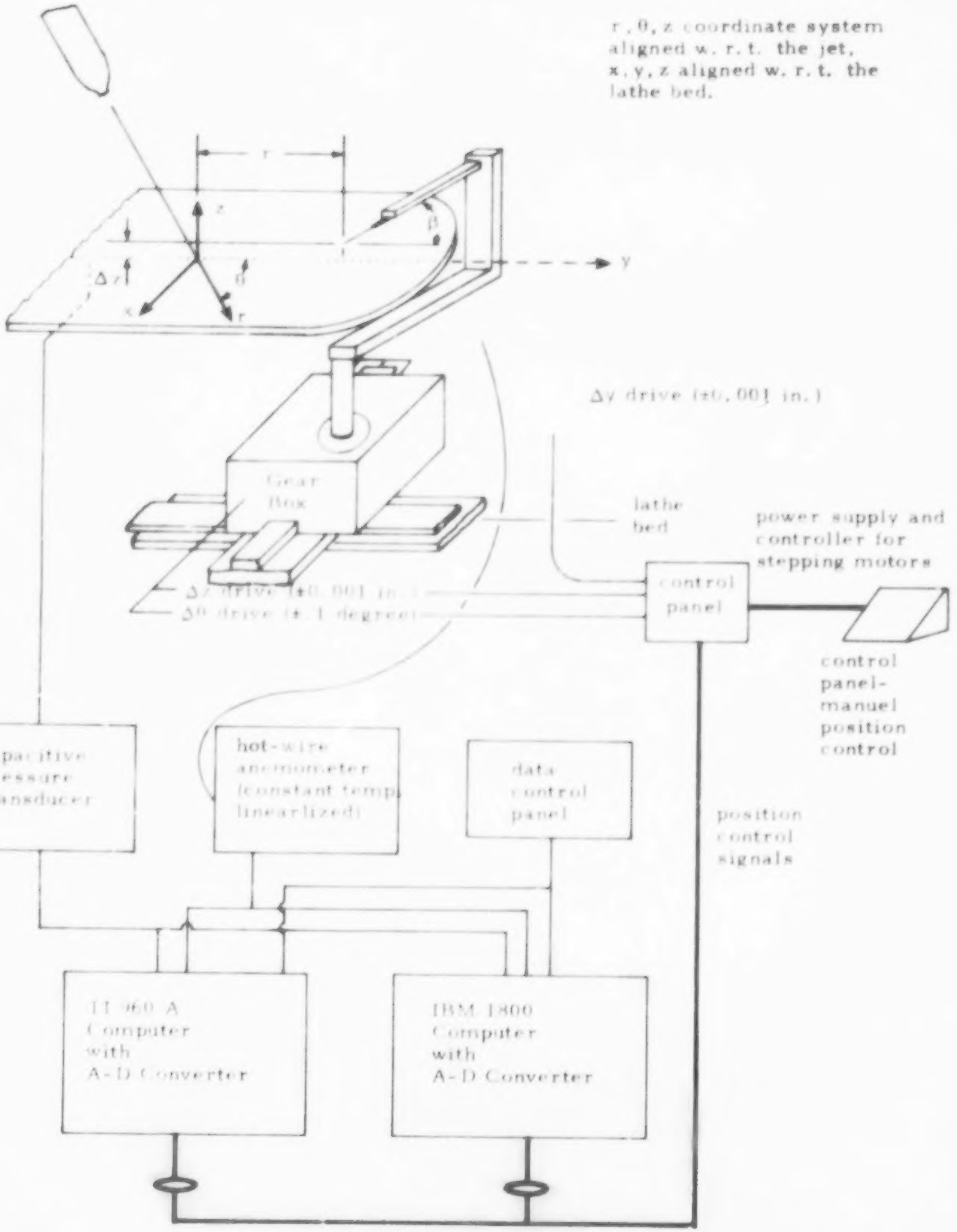

r, θ, z coordinate system aligned w. r. t. the jet,
x, y, z aligned w. r. t. the lathe bed.
r
z
β
y
Δz
θ
x
r
Δy drive (±0.001 in.)
Gear Box
lathe bed
power supply and controller for stepping motors
Δz drive (±0.001 in.)
Δθ drive (±.1 degree)
control panel
control panel-manuel position control
capacitive pressure transducer
hot-wire anemometer (constant temp. linearlized)
data control panel
position control signals
TI 960 A Computer with A-D Converter
IBM 1800 Computer with A-D Converter

Figure 5. Schematic of data acquisition facility.

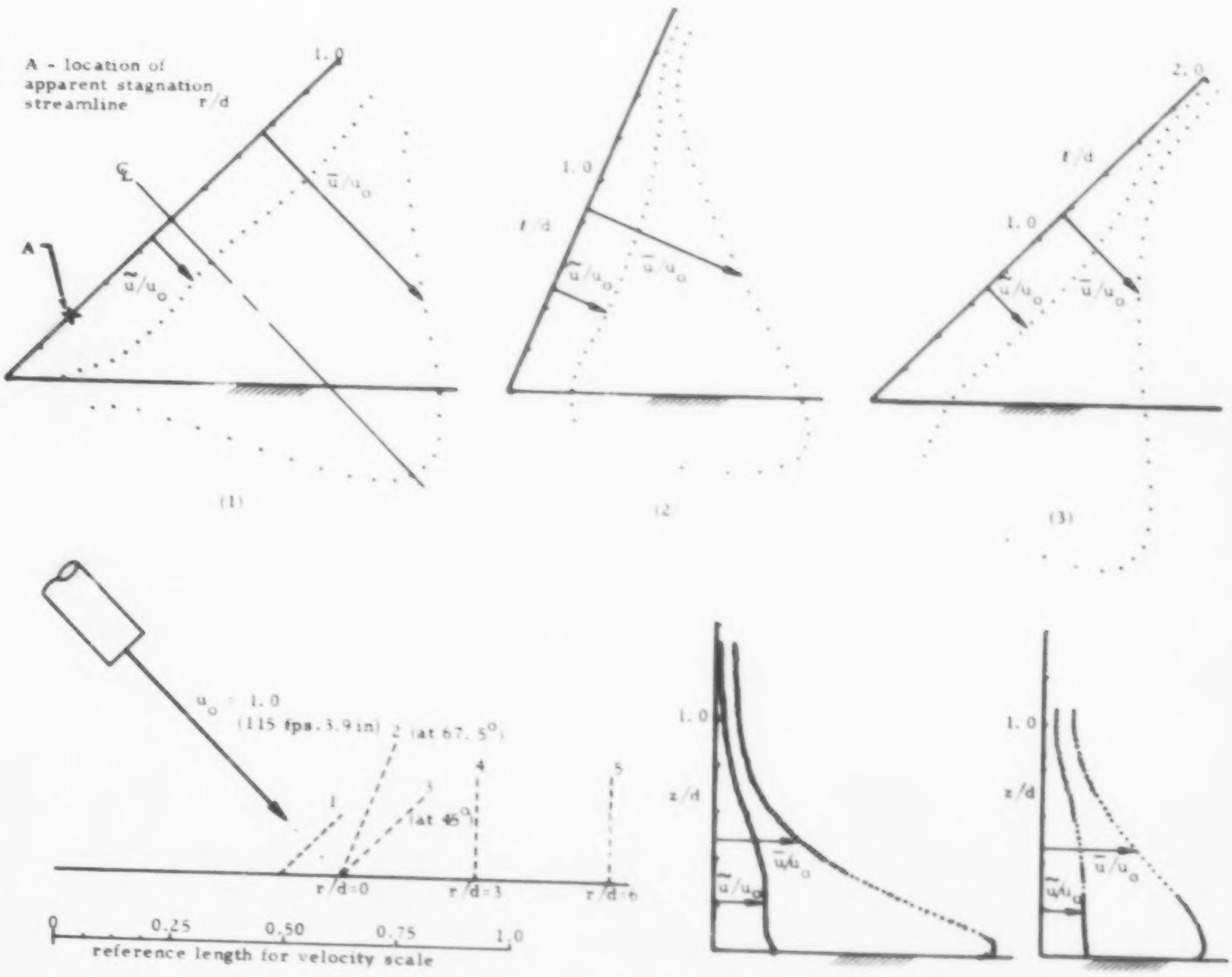

Figure 6. Velocity magnitude traverses in the $\theta = 0$, $\theta = \pi$ plane

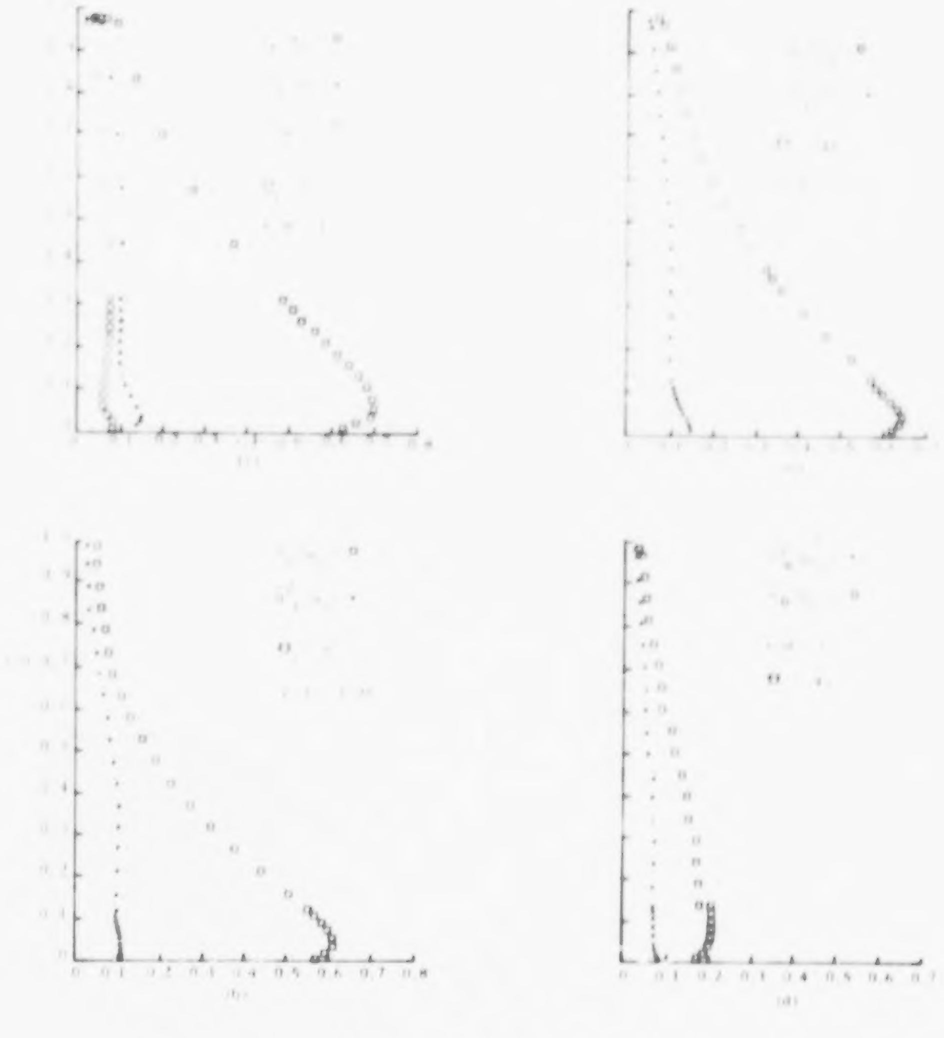

Figure 7. Vertical velocity traverses.

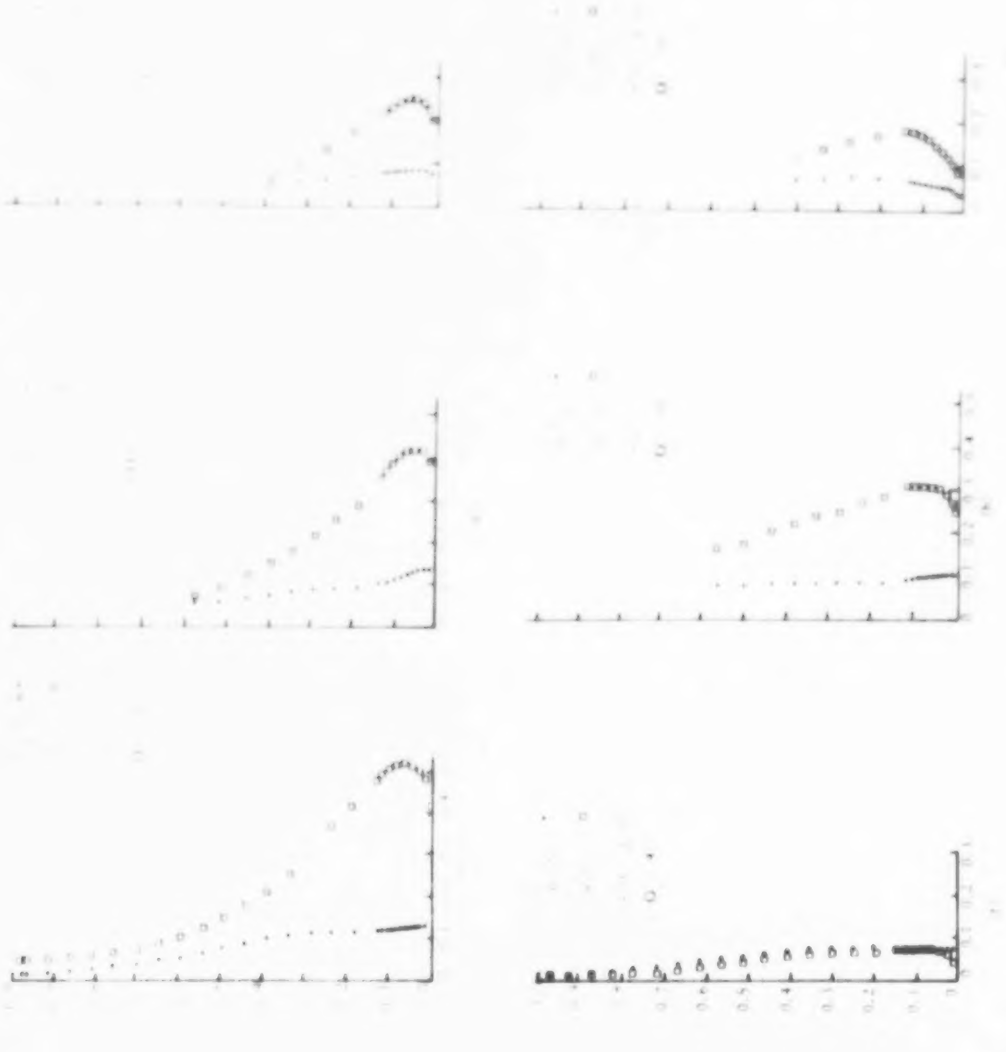

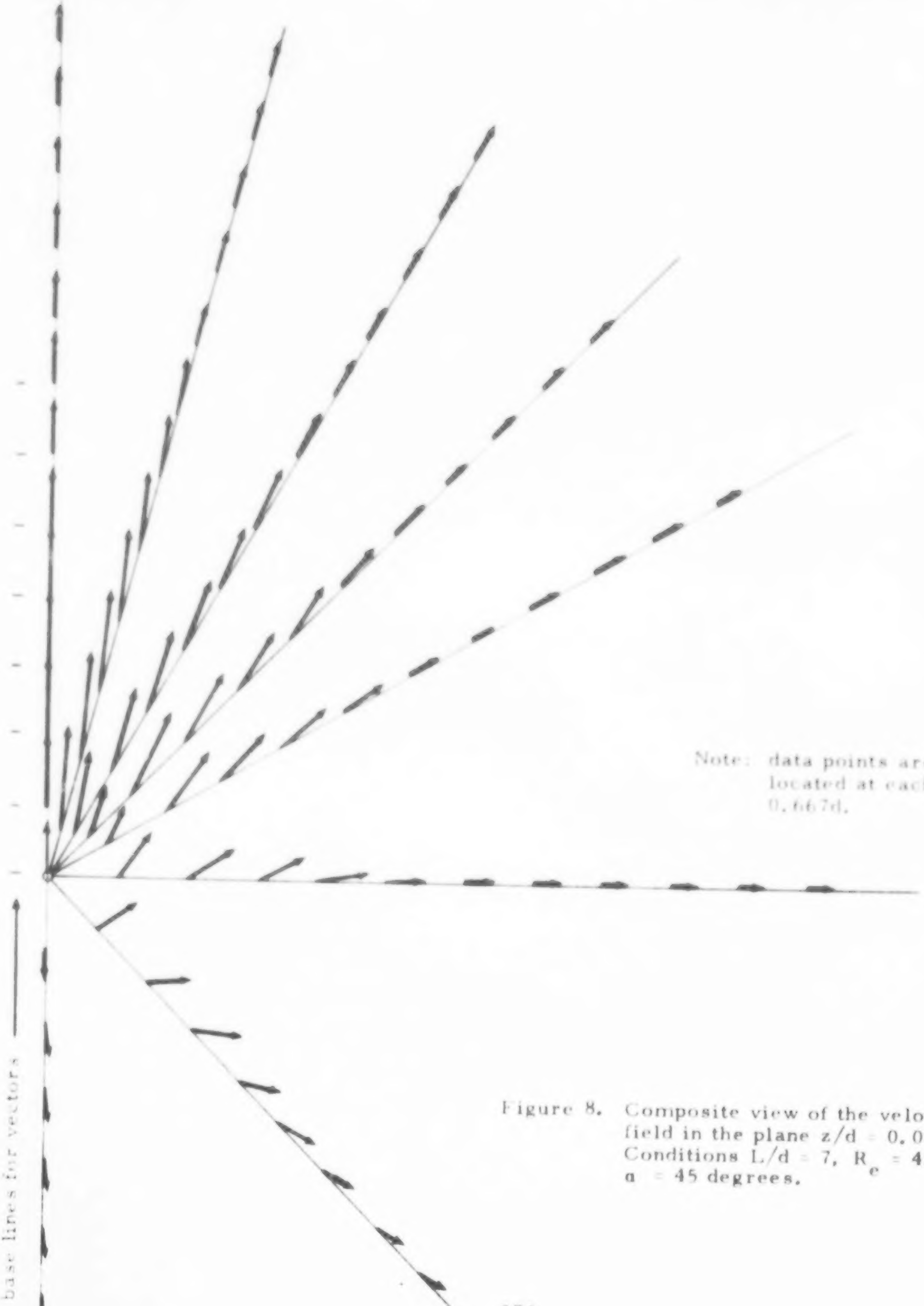

Note: data points are located at each 0.667d.

Figure 8. Composite view of the velocity field in the plane $z/d = 0.053$. Conditions $L/d = 7$, $R_e = 4.8 \times 10^4$, $\alpha = 45$ degrees.

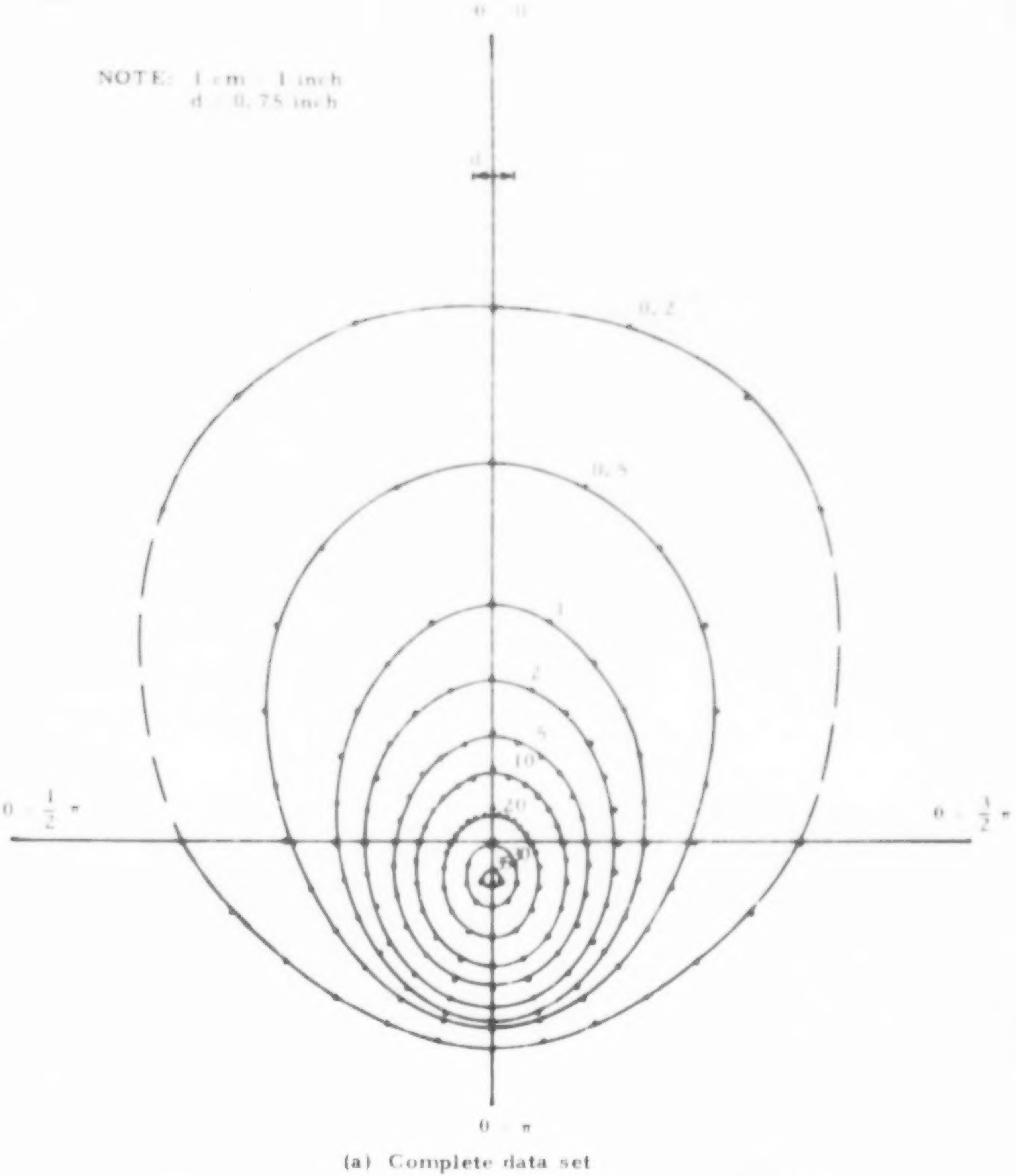

(a) Complete data set

Figure 9a. Surface pressure isobar contours. $\alpha = 45$ degrees, $L/d = 7$, jet Reynolds number $= 4.8 \times 10^4$.

Contours represent level curves of $100 \dfrac{(p - p_{atm})}{\rho u_o^2 \lambda \sin \alpha}$

$\lambda = \int_{A_{jet}} \rho u^2 dA / \rho u_p^2 A_{jet}$, $\lambda = 0.809$ taken from [5].

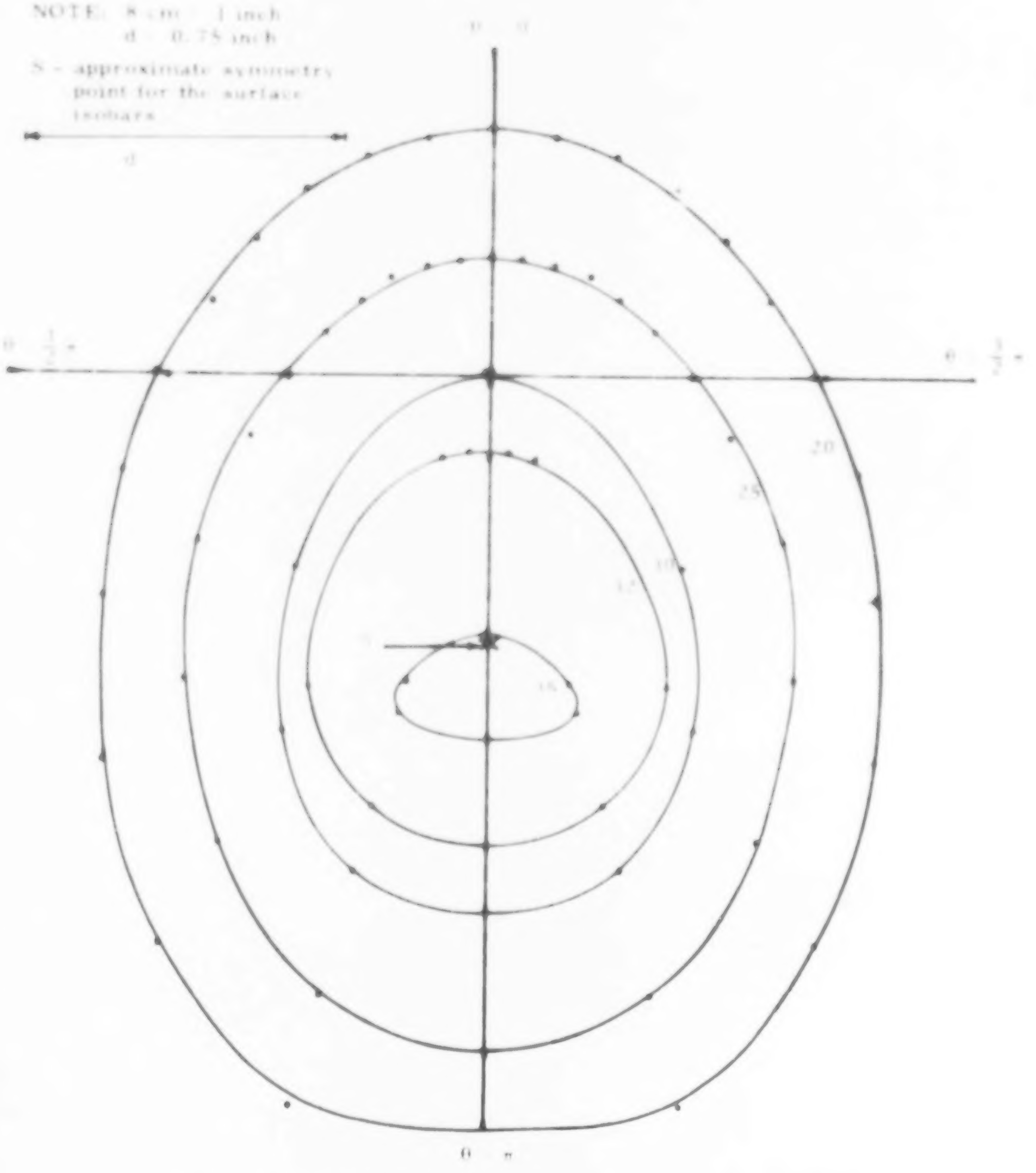

NOTE: 8 cm = 1 inch
d = 0.75 inch

S - approximate symmetry
point for the surface
isobars

Figure 9b. Expanded scale to show detail of the maximum pressure region.

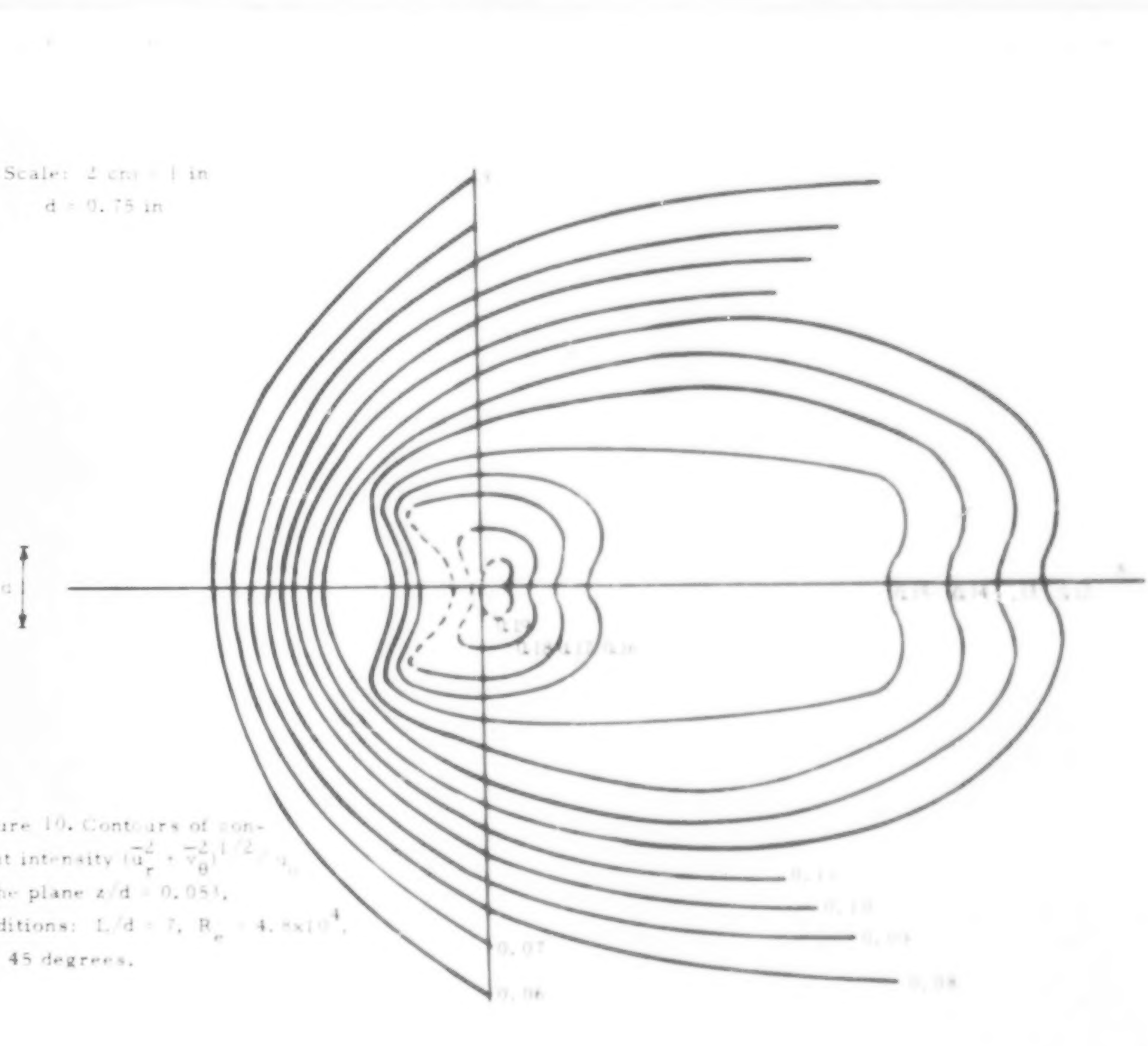

Scale: 2 cm = 1 in
d = 0.75 in

Figure 10. Contours of constant intensity $(\overline{u_r^2} + \overline{v_\theta^2})^{1/2}/u_0$ in the plane z/d = 0.051, conditions: L/d = 7, R_e = 4.8x10^4, α = 45 degrees.

BLANK PAGE

MEASUREMENT AND ANALYSIS OF THE UNSTEADY NORMAL FORCE AND PITCHING MOMENT ON AN AXIAL FLOW FAN ROTOR BLADE ELEMENT

by

Edgar P. Bruce

Applied Research Laboratory
Institute for Science and Engineering
The Pennsylvania State University
P.O. Box 30, State College, Pa. 16801

INTRODUCTION

In recent years, the radiated noise problem has emerged as one of the most serious problems associated with the design of axial flow turbomachines. Prediction of the noise radiated from a turbomachine is dependent upon a knowledge of the fluctuating forces on the blades as discussed by Morfey (1)[1] and Bragg and Bridge (2). One of the best known and most widely used methods for predicting the fluctuating forces on a turbomachine blade is that of Kemp and Sears (3), (4). This method is based on an adaptation of earlier work by von Kármán and Sears (5) which defines the fluctuating lift and moment on an isolated airfoil subjected to a small sinusoidal velocity disturbance in the direction normal to the chord. Horlock (6) analyzed the case of velocity perturbations parallel to the chord and combined his results with those of Sears (7) to treat the case of a generalized gust. Horlock (8) and Naumann and Yeh (9) considered the effects of camber and Naumann and Yeh produced a series of design charts which define the variation of unsteady lift as a function of blade camber and stagger angle. Holmes (10) extended these results by solving for the pressure distribution and the pitching moment. Even with these developments, the theory is inadequate for analysis of the flow in a real turbomachine since it applies only for low blade loading and no account is taken of the effect on a given blade of fluctuations occurring on other blades of the same blade row.

Several authors, for example Whitehead (11), (12), Mani (13), and Lotz and Raabe (14), have developed analytical methods which account for the unsteady effects of the entire cascade. However, these methods permit determination of the fluctuating lift only for a cascade of airfoils of one specific geometry, i.e., a flat plate, at a selected operating condition (zero incidence). The turbomachinery designer requires a knowledge of how the fluctuating forces and moments vary, both in magnitude and phase, with variations in cascade geometry and operating characteristics. In recently published results, Henderson and Daneshyar (15) and Yeh and Naumann (16) have attempted to solve the unsteady cascade problem when postulated in this frame of reference. Their results, and the extent to which the earlier results, i.e., those presented in (3) through (14), represent real turbomachinery flows, have never been subjected to evaluation by direct comparison with experimentally determined values of fluctuating forces and moments. In a closely related study, Henderson (17) has shown, both theoretically and experimentally, that the cascade effect on unsteady circulation can be significant under certain conditions.

---

[1] Numbers in parenthesis designate References at end of paper.

The ARL Axial Flow Research Fan (AFRF) was designed specifically to provide a capability for detailed research which will define the response of axial flow turbomachinery blade elements and/or blade rows to subsonic incompressible unsteady flow of the type encountered in practice. The facility has a hub radius of 4.75 inches, a hub-to-tip radius ratio of 0.442, and was designed to operate in the stagnation pressure ratio range from 1.0 to 1.1. At present, the facility can be operated with axial velocities up to 112 ft/sec with test rotor tip speeds up to 320 ft/sec. Hardware has been developed which permits generation of non-uniform rotor inflows and testing at reduced frequencies from 0.27 to 4.11. The purpose of this paper is to describe this facility and the specialized equipment that has been developed for use in it, and to present some preliminary unsteady force data.

NOMENCLATURE

A	Design ratio of maximum axial velocity increment to reference axial velocity
A_o, A_1, A_2, ..., A_n, ...	Fourier coefficients
B	Blade span
C	Blade chord
d	Wire diameter
K	Grid resistance coefficient
K_{MIN}	Minimum value of grid resistance coefficient
ΔK	$K - K_{MIN}$
N	Number of cycles of axial velocity variation per circumference
$\tilde{N}$	Unsteady normal force
n	Summation index (also harmonic number)
Re	Reynolds number based on grid interstitial velocity, $[V_{REF}/(1 - s)]\ d\ \rho/\mu$
R	Radial location
$\overline{R}$	Radial position at blade mid-span
S	Spacing between blades
s	Grid solidity (ratio of blocked area to total area)
t	Time
U	Blade rotational velocity
V	Strain gauge output voltage
V_R	Axial velocity at rotor inlet
$\overline{V}_R$	Circumferential average value of axial velocity at rotor inlet

V_{REF}	Axial velocity in annulus far upstream of rotor
W_m	Circumferential average value of relative velocity at rotor inlet
$\overline{w}_d$	Maximum axial velocity increment measured from $\overline{V}_R$
x_G	Distance from disturbance generating grid to rotor inlet
$\overline{\alpha}$	Circumferential average value of rotor inlet angle of attack
β_m	Mean value of rotor inlet relative flow angle
θ	Circumferential position measured in a plane normal to the facility centerline, positive for counterclockwise rotation when looking forward
λ	Stagger angle, the angle between the blade chord line and the axial direction
μ	Atmospheric viscosity
ν	Frequency with which waves pass any point on the reference blade
ρ	Atmospheric density
ϕ_n	Phase angle of n^{th} Fourier component
ω	Reduced frequency

THE ARL AXIAL FLOW RESEARCH FAN

The ARL Axial Flow Research Fan (18) was designed and built by personnel of the Fluids Engineering Unit. The facility became operational in January 1972. An artist's concept of the AFRF is presented in Figure 1.

The facility is 19 2/3-feet long and consists of an annular flow passage bounded at one end by a bellmouth inlet and at the other end by an exhaust throttle. The forward region, from the inlet to a point just upstream of the test rotor blade drive motor, is bounded by a 9 1/2-inch diameter cylindrical hub surface and a 21 1/2-inch inside diameter cylindrical outer casing. These surfaces are tapered to slightly larger diameters near the downstream end to permit housing the 70 HP test rotor drive motor inside the hub and to permit connection to the auxiliary fan outer casing. The auxiliary fan is a Joy Manufacturing Company Model No. 23 1/4-14-3450 Series 1000 Axivane Fan which delivers 15,000 cubic feet of air per minute at a pressure of 3.5 inches of water gauge at its nominal operation condition. The auxiliary fan drive motor and the 70 HP motor operational characteristics can be independently regulated at any speed up to 3400 RPM through the use of two Borg Warner Model No. BW1200 Solid State Adjustable Frequency Drive inverter units.

With a zero steady lift rotor of the type being used in the initial research programs, the auxiliary fan is used to provide the airflow. In this mode, two methods are available for final adjustment of the throughflow velocity: 1) adjustment of auxiliary fan RPM with fixed throttle setting, or 2) throttle position adjustment with the auxiliary fan operating at a fixed

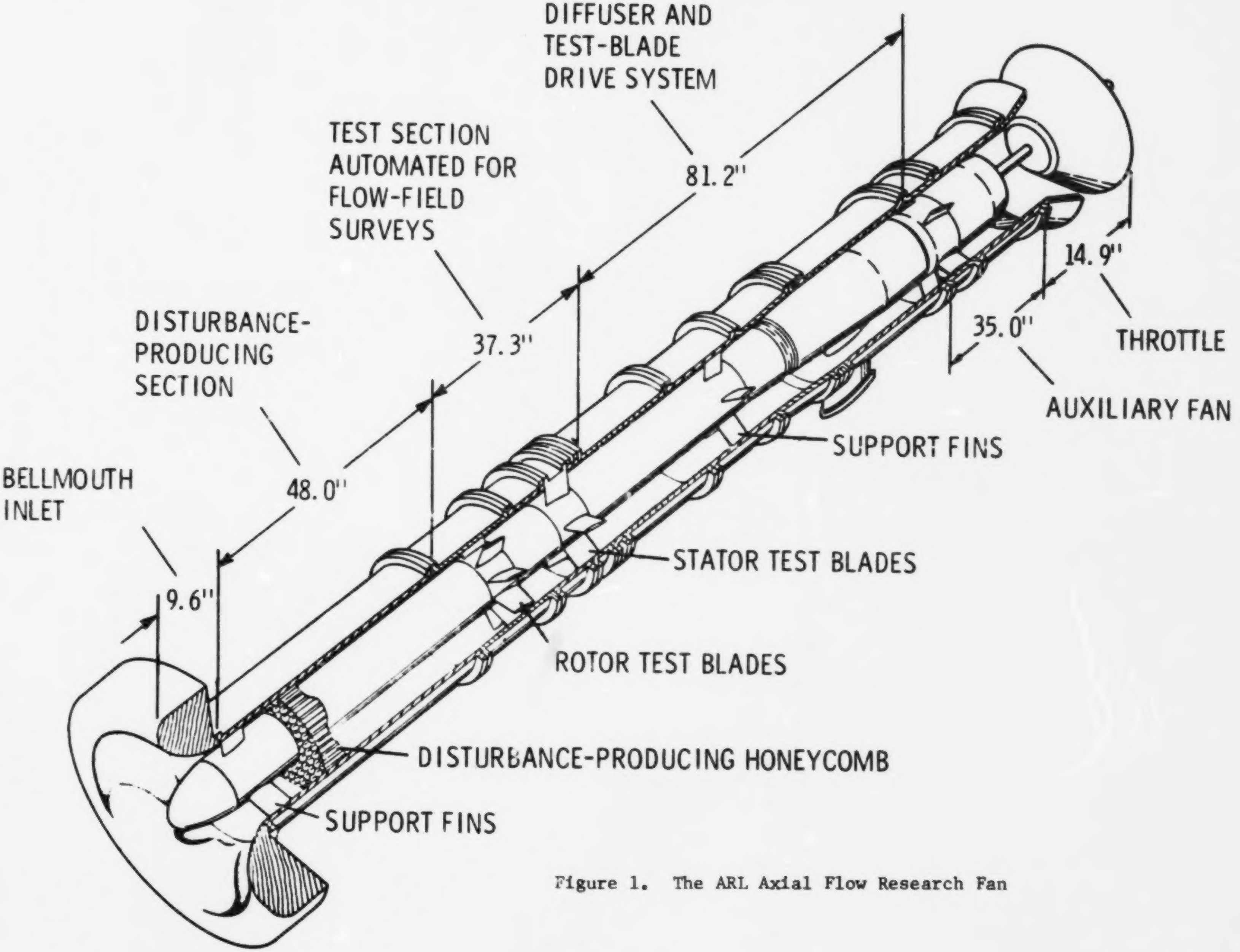
DIFFUSER AND
TEST-BLADE
DRIVE SYSTEM
81.2"
TEST SECTION
AUTOMATED FOR
FLOW-FIELD
SURVEYS
37.3"
DISTURBANCE-
PRODUCING
SECTION
48.0"
BELLMOUTH
INLET
9.6"
14.9"
THROTTLE
35.0"
AUXILIARY FAN
SUPPORT FINS
STATOR TEST BLADES
ROTOR TEST BLADES
DISTURBANCE-PRODUCING HONEYCOMB
SUPPORT FINS

Figure 1. The ARL Axial Flow Research Fan

speed. RPM adjustments are normally used with the throttle in the aft or full open position since this yields the highest throughflow velocity for a given frequency setting. Six inches of throttle travel is available. Throttle position is automatically set by operation of a 225 in-oz torque Slo-Syn Type SS250-1027 driving motor which is controlled by a Slo-Syn Preset Indexer. With this system, throttle movement can be limited to a step of 0.1 inch or can be as large as a step of 3.5 inches.

The two 24-inch long outer casing segments positioned just downstream of the bellmouth inlet house the disturbance generating section. This 48-inch long flow path was provided to permit the development of distorted flowfields, generated by placing honeycomb, wire grid, or cylindrical rod obstructions at selected positions within the cylindrical annulus, into a desired pattern at the rotor inlet.

The section immediately downstream of the disturbance producing section houses the test rotor-stator stage and is the heart of the AFRF. The outer casing of the part of this section forward of the stator housing is free to rotate about the AFRF centerline. This segment of outer casing is supported by two large bearings. Rotation was initially controlled manually and was accomplished by turning a wheel driven worm gear. This feature was provided to permit rotation of casing mounted flow surveying probes in the circumferential direction. This manual system has been replaced by an automated system in which the worm gear is driven by a 1800 in-oz torque Slo-Syn Type SS1800-1007 motor which is controlled by a Slo-Syn Preset Indexer. Outer casing rotation can be adjusted in 0.5 deg increments from a minimum step of 0.5 deg to a maximum step in excess of 360 deg.

The AFRF design utilizes split outer casing and hub sections both upstream of and downstream of the stator. By interchanging split sections of different lengths, it is possible to move the stator blade row axially relative to the rotor blade row. Thus, tests with rotor-stator spacings of 3, 6, 9 or 12 inches are easily achieved. For 6-inch chord blades, these dimensions correspond to nondimensional rotor-stator spacings from 1/2 to 2 blade chord lengths. When the stator is moved, part of the weight of the stator system is carried by cylindrical shafts mounted externally on the outer casing. The remainder of the weight is carried by a ball-bushing system mounted in the hub.

The components downstream of the stator at present are a 14-channel coin silver slip-ring unit, the 70 HP test rotor drive motor, the auxiliary fan, and the throttle. The motors and throttle were intentionally located at a downstream distance great enough to permit insertion of a silencer just downstream of the stator and thus upstream of the noise generating drive motors. An Industrial Acoustic Company Model No. 22 CL 44 Conic-Flow Silencer has been purchased for this purpose. An additional silencer of this type may be located downstream of the drive motors at a future date.

SPECIALIZED AFRF HARDWARE

Three special AFRF hardware items are described in this section. They are: 1) the zero mean lift test rotor, 2) the system for measuring rotor blade section unsteady normal force and pitching moment, and 3) the disturbance generating wire grids.

Zero Mean Lift Test Rotor

The first test rotor fabricated for use in the AFRF is unique in that it operates with no head input at design conditions. This feature was incorporated to permit investigation of unsteady flow effects with no steady rotor lift.

The rotor design was based on the relation

$$\lambda = \beta_m = \tan^{-1}\left[\frac{U}{\overline{V}_R}\right]$$

with $\lambda = 45$ deg at $R = \overline{R}$. The blades have a 10% thick uncambered C1 profile (19). The rotor produces zero head input at all operating conditions for which $\overline{V}_R$ is independent of radius and for which $U = \overline{V}_R$ at $R = \overline{R}$. The rotor can be assembled with 2, 3, 4, 6 or 12 blades, each of which has a chord C of 6.0 inches and a span B of 5.9 inches. Thus, space-chord ratios, S/C , defined at the mean radius $\overline{R}$ of 7.75 inches of 4.06, 2.71, 2.03, 1.35 and 0.68 can be tested. The rotor blades are made of aluminum.

When the rotor is operating at its design condition, the velocity V_R is controlled by the auxiliary fan RPM setting. The test rotor is driven by the 70 HP motor - hence control of the test rotor RPM setting is independent of the auxiliary fan RPM setting. By increasing the test rotor RPM while making minor adjustments to the auxiliary fan RPM setting to maintain V_R at a constant value it is possible to operate this rotor at preselected incidence angles (or angles of attack since the blades have no camber). Thus, the effects on unsteady flow quantities of incidence, ranging all the way to stall, can be investigated.

As noted above, the nominal stagger angle at the mean radius is 45 deg. The rotor can also be assembled with stagger angles at the mean radius of 35 or 55 deg by rotating the blades within hub attachment blocks. Operation at these stagger angle settings, or at positive incidence angles as described above, has the disadvantage of introducing three-dimensional flow effects.

This rotor has been used by Henderson (17) in a study of the time mean total pressure rise associated with operation in a sinusoidally varying inflow.

System for Measuring Unsteady Normal Force and Pitching Moment

A system has been developed and is being used to measure rotor blade section fluctuating normal force and pitching moment. The major features of this system, illustrated in Figure 2, are:

1) A 1-inch span blade segment is cantilevered from the blade hub at the mid-chord position by means of a beam that has the lower portion of its length machined as a torque tube and the upper portion of

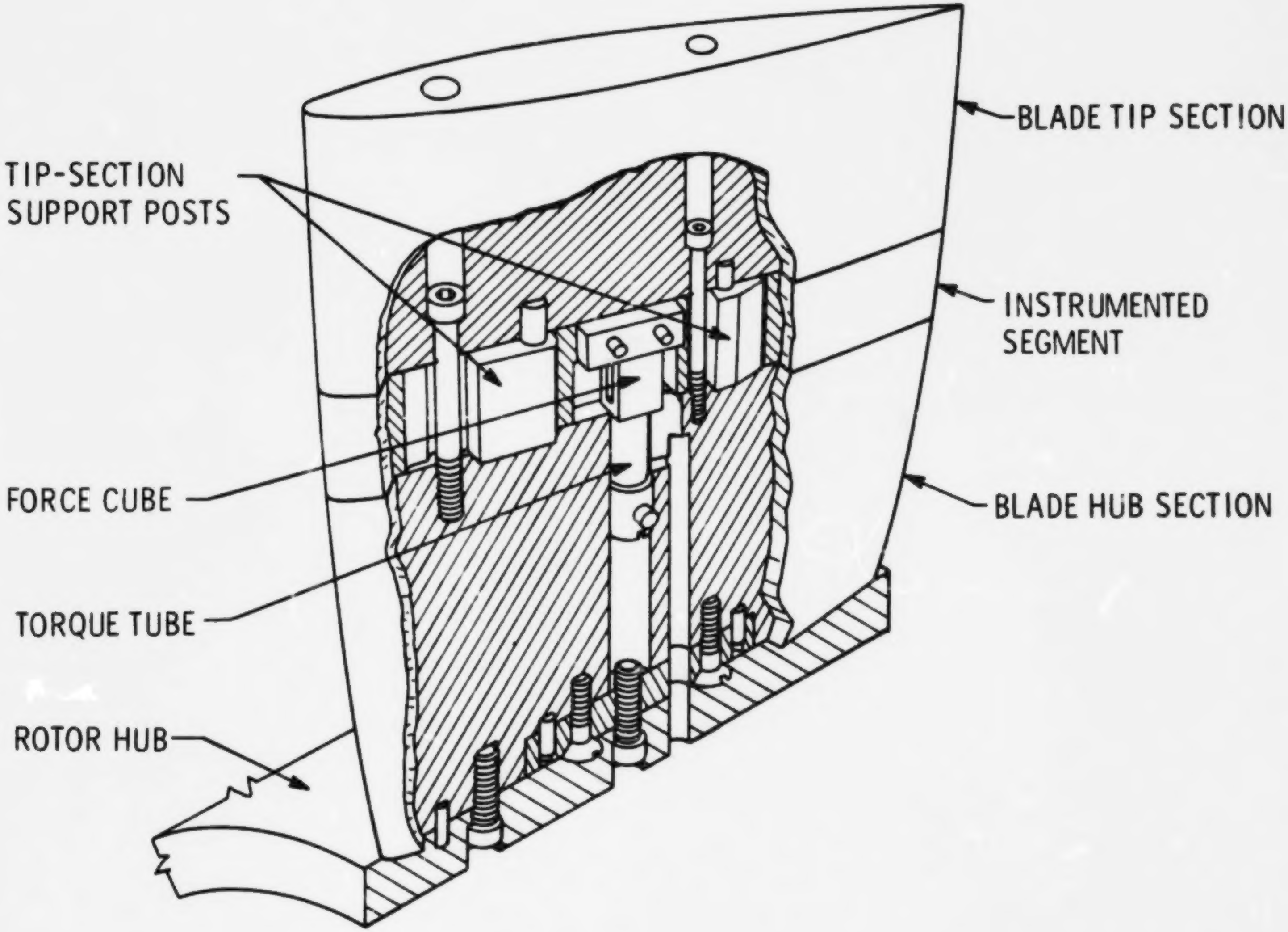
BLADE TIP SECTION
TIP-SECTION SUPPORT POSTS
INSTRUMENTED SEGMENT
FORCE CUBE
BLADE HUB SECTION
TORQUE TUBE
ROTOR HUB

Figure 2. Instrumented Blade-Strain Gauge Sensor Installation

its length machined as a force cube. The center section of the blade segment is located at the mean radius. The torque tube and force cube have been instrumented using Micro-Measurement 120 Ohm Foil Type Precision Strain Gages.

2) The 1-inch span segment is made of magnesium to minimize its mass and moment of inertia and is structurally independent of the rotor blade except for the cantilever mount. The aluminum tip portion of the blade attaches to posts on the aluminum hub section which pass through slots in the instrumented section. A minimum clearance of 0.005 inches has been specified for each mating surface for the initial measurement attempts. The magnesium segment has been mass-balanced to preclude uneven displacement.

3) Input power and signal transmission lines run from the rotor blade through the rotor hub to the hollow rotor shaft, downstream through the shaft to a coin silver slip-ring unit, and then out through holes drilled in the aft support fins.

The static sensitivities of the force and moment elements of this system are 0.119 volts/oz and 0.056 volts/in-oz, respectively. The results of dynamic calibration are shown in Figure 3. In the test program being conducted at present, the maximum fundamental frequency to be encountered will be on the order of 130 Hz. This frequency is low enough to avoid complications due to the measuring system resonance near 200 Hz.

Disturbance Generating Wire Grids

Disturbance generating wire grids (20) have been designed to produce one-, two-, four-, six-, nine-, twelve-, and fifteen-cycle 20% peak amplitude sinusoidal axial velocity variations at the rotor inlet. Based on the mid-span radius, a chord length C of 6-inches and an inlet relative flow angle β_m of 45 deg these grids provide a capability to conduct experiments at reduced frequencies ω from 0.27 to 4.11. For this case, $\omega = CN \sin \beta_m / 2R$ where N is the number of cycles of velocity variation per circumference produced by the screen.

The design of the grids was based on the method developed by McCarthy (21). This method defines the circumferential variation in grid resistance coefficient K required to produce a desired circumferential variation in rotor inlet axial velocity V_R. If $V_R = V_{REF.}(1 + A \sin N\theta)$ where $V_{REF.}$ is the uniform axial velocity in the duct far upstream of the grid, then the required circumferential variation in resistance coefficient is given by the solution of

$$A \sin N\theta = \frac{1.02(1 + X)}{(1 + X^3)^{2/3}} \left[\gamma_o - \frac{1 + 6X^3}{6X^2} \right]$$

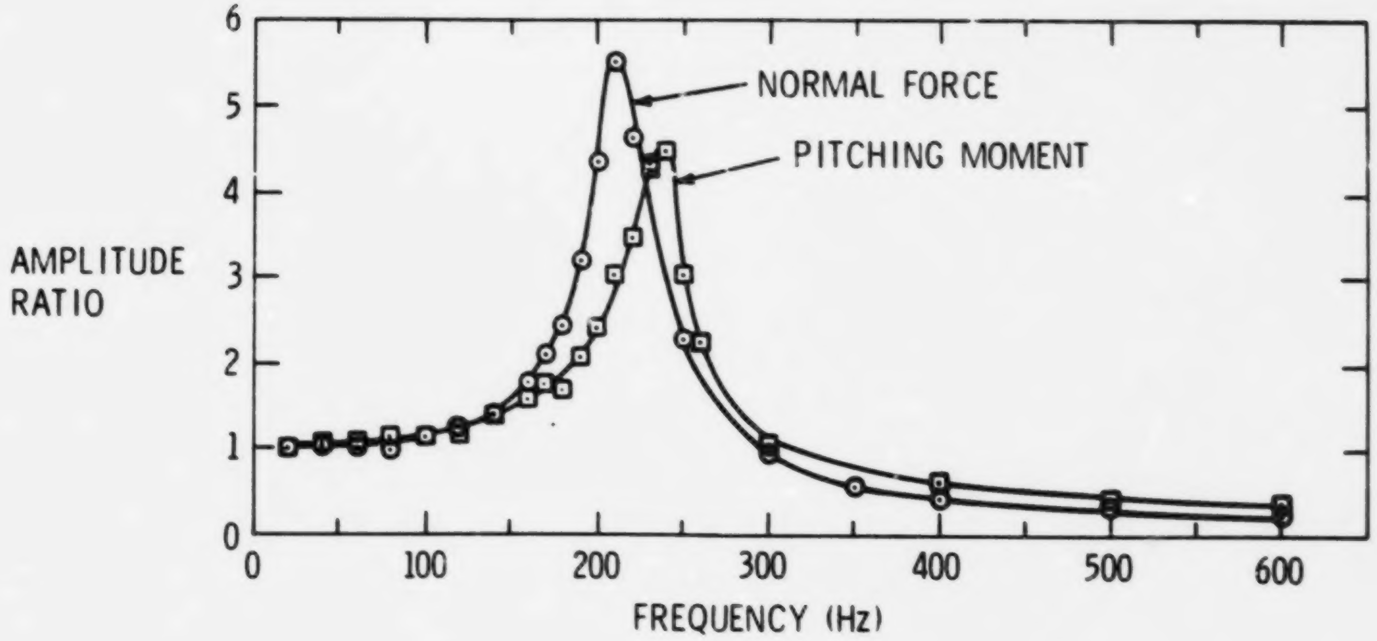

Figure 3. Strain Gauge Sensor Dynamic Response Characteristics

where

$$X = (1 + K)^{1/2}$$

$$Y_o = \frac{1 + 6\lambda_o^3}{6X_o^2} + \frac{A(1 + X_o^3)^{2/3}}{1.02(1 + X_o)}$$

and

$$X_o = (1 + K_{MIN})^{1/2}$$

At any circumferential location, the resistance coefficient is given by $K = K_{MIN} + \Delta K$ where K_{MIN} is associated with the large wire diameter, large wire spacing grid used to provide structural support for the assembly. The required increment in resistance coefficient, ΔK , is a function of circumferential position and is provided by overlay screen segments.

For operation at Reynolds numbers Re, based on the interstitial velocity through the grid $V_{REF.}/(1 - s)$ and wire diameter d, in the range $500 < Re < 15{,}000$ the grid resistance coefficient may be related to grid solidity s by

$$K = \frac{0.78\ s}{(1 - s)^2}$$

Detailed discussions of the effect of various parameters on the resistance of wire grids are presented by McCarthy (21) and by Cornell (22).

The rotor inlet velocity fields produced with the disturbance generating grids mounted against the centerbody support struts just downstream of the AFRF inlet have been measured. The measured flow field characteristics are in good agreement with the design values. The flow field produced by the four-cycle grid is shown in Figure 4. The measured data have been represented by a Fourier series of the form

$$\frac{V_R}{\overline{V}_R} = \frac{A_o}{2} + \sum_{n=1}^{\infty} A_n e^{i(n\theta + \phi_n)}$$

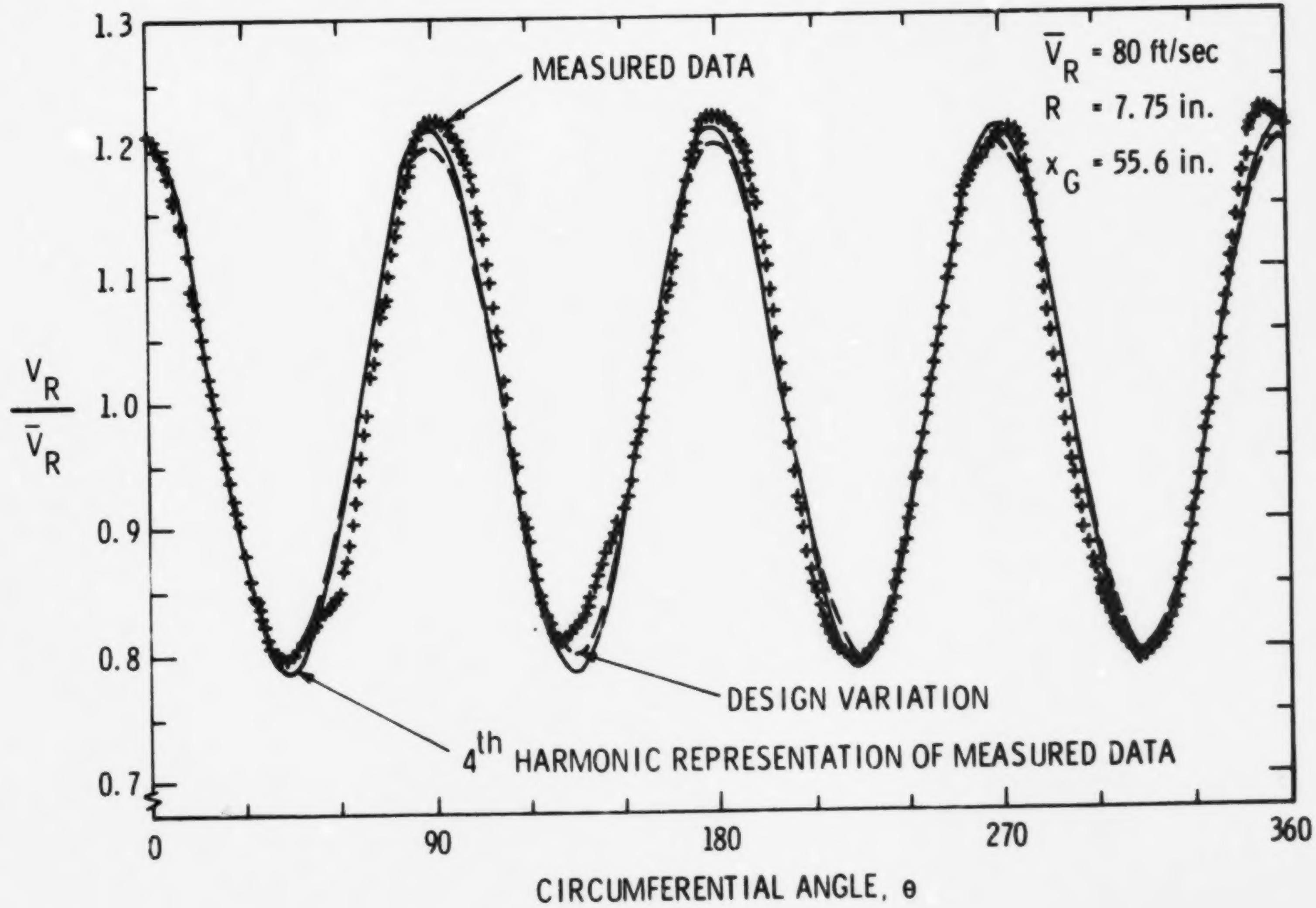

Figure 4. Velocity Profile at Rotor Inlet - Four-Cycle Screen

Comparison of the magnitudes of the coefficients A_n provides a good indication of the quality of the flow fields. Figure 5 shows the results of Fourier analysis of the flow field presented in Figure 4 and illustrates the high degree of success that was achieved in generating rotor inlet velocity fields that are dominated by a single harmonic.

The characteristics of the rotor inlet velocity fields are a function of the distance from the rotor inlet to the grid x_G, and of the average axial velocity $\overline{V}_R$. The dependence upon x_G is thought to be due to turbulent mixing and the dependence upon $\overline{V}_R$ is thought to be due to the variation in Reynolds number.

PRESENT RESEARCH PROGRAM

The objective of this program is to measure and analyze the unsteady normal force and pitching moment on the mid-span segment of a blade of an axial flow fan rotor operating in a flow whose axial velocity component varies sinusoidally in the circumferential direction. The program variables are reduced frequency, $\omega \approx 0.27$, 0.55, 1.10 and 1.64; blade space-to-chord ratio, $S/C = 0.68$, 1.35 and 2.03; blade stagger angle, $\lambda = 35$, 45 and 55 deg; and blade mean angle of attack, $\bar{\alpha} = 0$, 4 and 8 deg. The experimental results are being used to provide design information and to assess the validity of available theoretical models. The hardware described in the preceeding sections of this paper is being used in the experimental phase of this program.

Theoretical Analyses

Theoretical estimates of the unsteady normal force and pitching moment are being computed within the range of operational and geometric conditions outlined above using three different theoretical models--1) the infinite cascade model of Henderson and Daneshyar (15), 2) the infinite cascade model of Whitehead (11), and 3) the isolated airfoil model of Sears (7) and Horlock (6) as summarized and extended by Holmes (10).

The Henderson-Daneshyar model treats thin two-dimensional airfoils with small camber and small angles of incidence and includes the contribution to the unsteady normal force on the reference blade due to the presence of the other blades. The cascade of airfoils is represented by a vortex model with a continuous distribution of bound vorticity on the reference blade, a single bound vortex located at the quarter-chord point of the remaining blades, and a continuous distribution of wake vorticity for all of the blades. The Whitehead model is similar to the Henderson-Daneshyar model except that it applies to the case of uncambered blades at zero incidence and the bound vorticity is represented on all blades by a finite number of vortices spaced at regular intervals along the blade chord. The Sears-Horlock-Holmes isolated airfoil model represents the airfoil and its wake by continuous distributions of bound and trailing vorticity, respectively. The Whitehead model and the Sears-Horlock-Holmes model both permit prediction of the unsteady normal force and pitching moment.

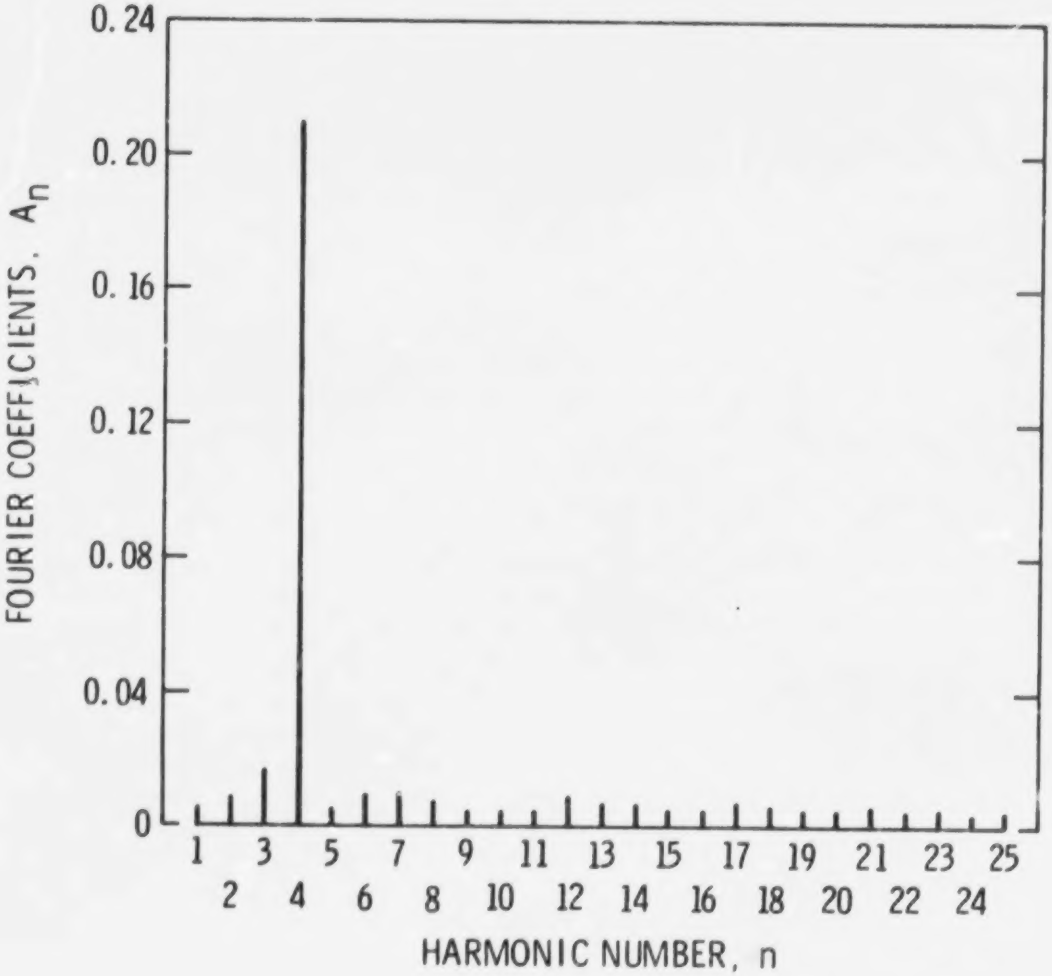

Figure 5. Magnitude of Fourier Coefficients for Four-Cycle Screen

Calculations of the unsteady normal force have been completed using the Henderson-Daneshyar model for all cases at $\overline{\alpha} = 0$ deg, and the calculations at $\overline{\alpha} = 4$ and 8 deg are nearing completion. Calculations, using Whitehead's model, of the unsteady normal force and pitching moment have been completed for the $\lambda = 45$ deg cases. All computations of unsteady normal force and pitching moment based on the Sears-Horlock-Holmes isolated airfoil model have been completed.

Experimental Program

Measurements of the unsteady normal force and pitching moment have been made for all of the $\lambda = 45$ deg cases. This series of measurements represented our first attempt at gathering data of this type; consequently, the results are regarded as preliminary at this time. No difficulties were encountered in this series of tests in facility operation or in obtaining a strong, repeatable signal from the strain gauges at the frequency corresponding to the fundamental excitation frequency.

A typical record of strain gauge output as a function of frequency is presented in Figure 6 for a reduced frequency $\underline{\omega}$ of 1.64. This record was obtained with the facility operating with $U = \overline{V}_R = 67$ ft/sec. The fundamental excitation frequency for this case is 99 Hz. Examination of the results shown in Figure 6 indicates that the gauge output is 15 - 20 dB above the background signal at this frequency.

A preliminary comparison of the measured unsteady normal force amplitude and predicted values given by the theoretical cascade model of Henderson and Daneshyar and the Sears isolated airfoil theory is presented in Figure 7. The "resonant" type variations in the performance predictions based on the Henderson-Daneshyar model occur at conditions where the spacing between blades S is equal to an integer multiple of the wavelength of the disturbance imbedded in the flow field. The measured data for S/C = 1.353 and 2.029 is in reasonable agreement with the Sears isolated airfoil theory at reduced frequencies above 1.0 and with the Henderson-Daneshyar model at all reduced frequencies. However, the data for high reduced frequencies with S/C = 0.676 disagrees with both prediction methods. The major differences between the predictions due to the two theoretical models are a difference in force level at low reduced frequencies and the presence of the "resonant" conditions in the cascade model.

The tests at $\lambda = 45°$ will be repeated, and the remainder of the program described above will be conducted during the Spring of 1974. A modified instrumentation system will be used in these experiments which will permit a more accurate evaluation of the strain gauge output.

SUMMARY

The facility and the special hardware items developed at the ARL for use in a study of the unsteady forces and moments developed on an axial flow turbomachine rotor due to operation in a flow field with a sinusoidally varying axial velocity component have been described. This equipment is being used in a research program in which the reduced frequency, blade stagger angle, blade

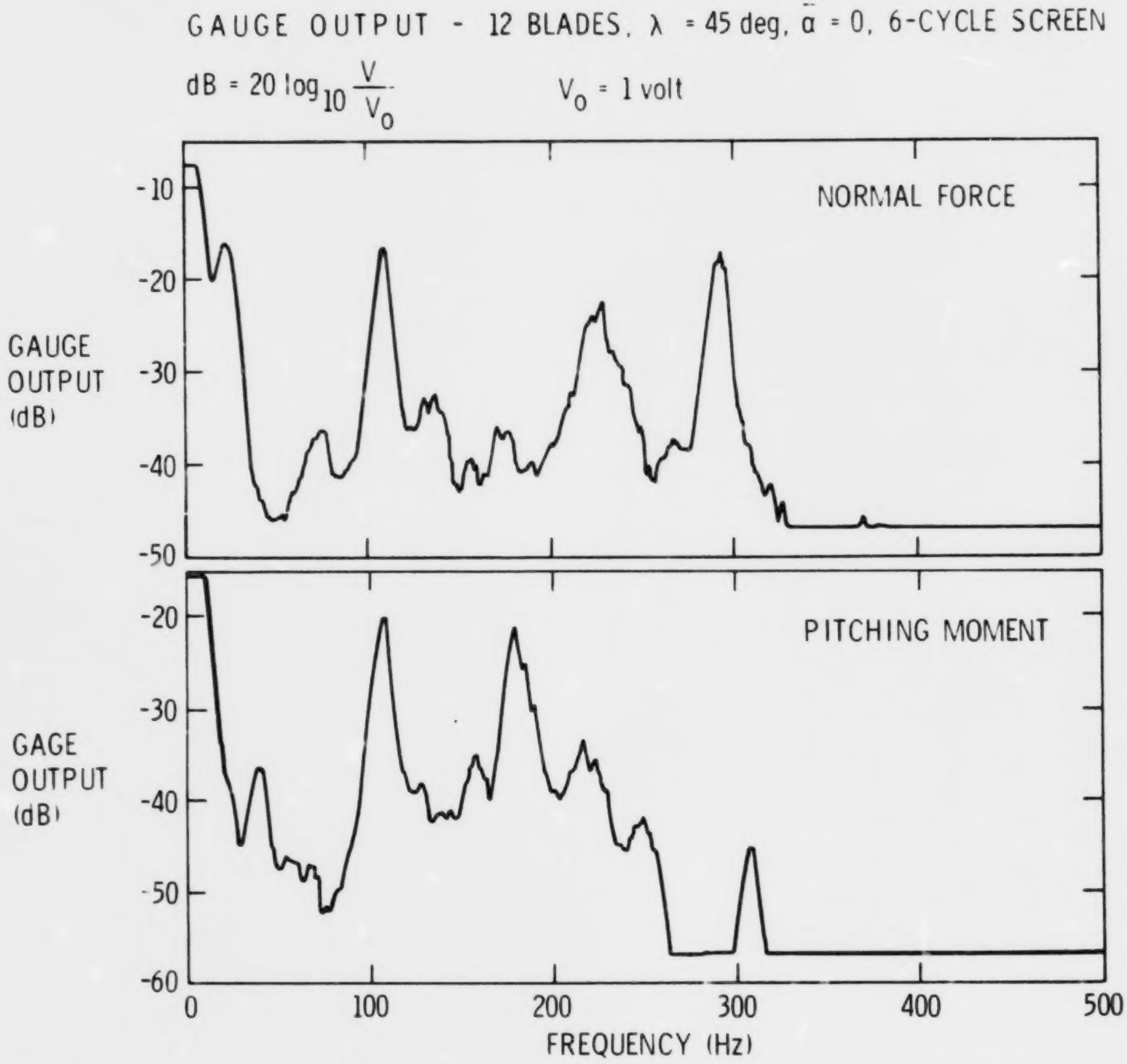

Figure 6. Typical Record of Strain Gauge Sensor Output

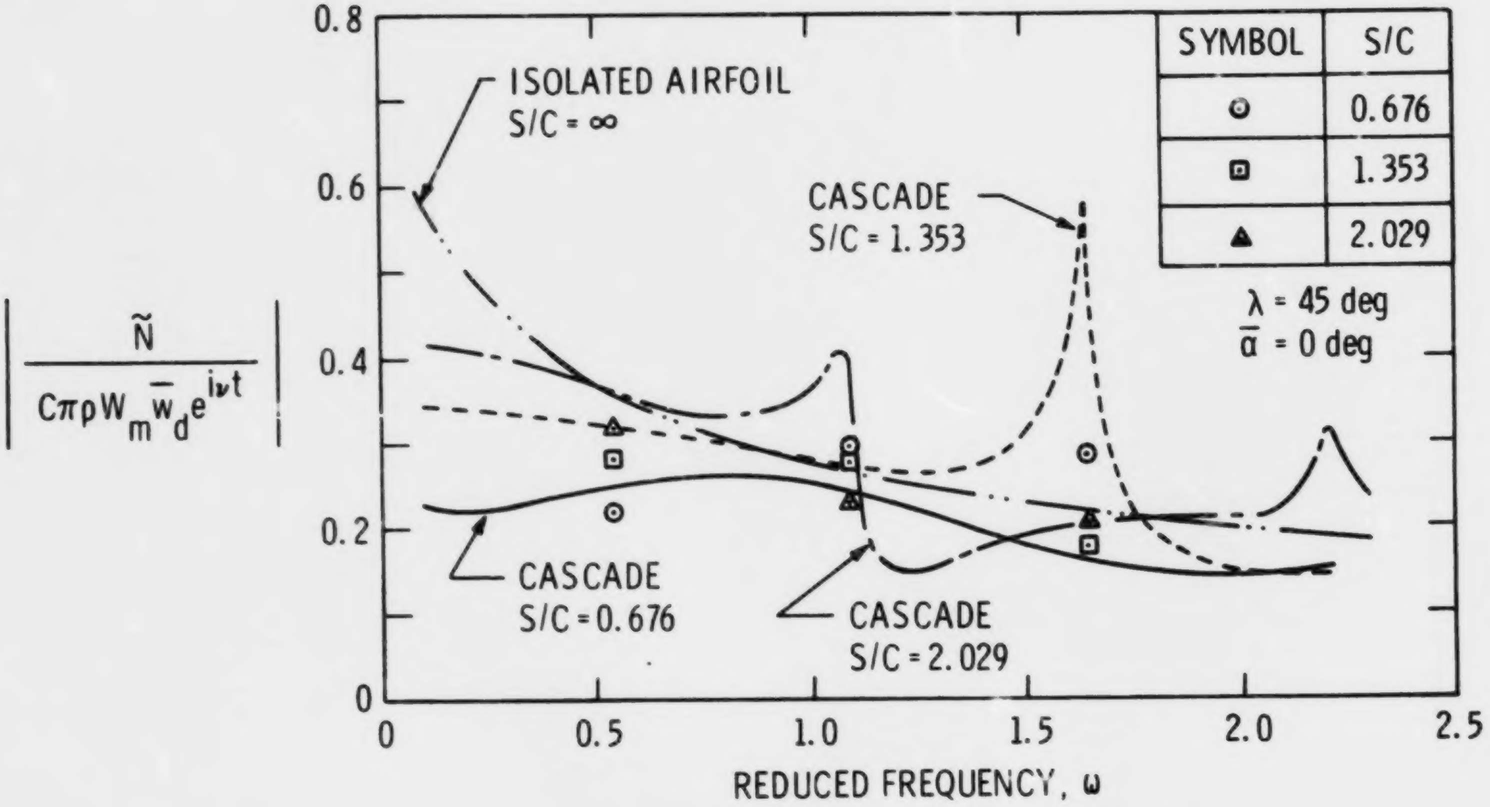

Figure 7. Preliminary Comparison of Predicted and Measured Values of Unsteady Normal Force

space-to-chord ratio, and mean angle of incidence are variable. Preliminary results have been presented which show reasonable agreement between the measured unsteady normal force magnitude and predictions based on existing isolated airfoil and cascade theoretical models.

[The ARL Axial Flow Research Fan was designed and brought to operational status under funding supplied by the U. S. Naval Ordnance Systems Command. The research program described herein is being funded by Project SQUID under Subcontract No. 4965-40. Project SQUID is an Office of Naval Research Program, Contract No. N00014-67-A-0226-0005.]

REFERENCES

1. Morfey, C. L., "Sound Generation in Subsonic Turbomachinery", Transactions of the ASME, Journal of Basic Engineering, September 1970, pp. 450-458.
2. Bragg, S. L. and Bridge, R., "Noise from Turbojet Compressors", Journal of the Royal Aeronautical Society, Vol. 68, No. 637, January 1964, pp. 1-10.
3. Kemp, N. H. and Sears, W. R., "Aerodynamic Interference Between Moving Blade Rows", Journal of the Aeronautical Sciences, Vol. 20, No. 9, September 1953, pp. 585-597 and 612.
4. Kemp, N. H. and Sears, W. R., "The Unsteady Forces Due to Viscous Wakes in Turbomachines", Journal of the Aeronautical Sciences, Vol. 22, No. 7, July 1955, pp. 478-483.
5. von Kármán, T. and Sears, W. R., "Airfoil Theory for Non-Uniform Motion", Journal of the Aeronautical Sciences, Vol. 5, No. 10, August 1938, pp. 379-390.
6. Horlock, J. H., "Fluctuating Lift Forces on Airfoils Moving Through Transverse and Chordwise Gusts", Transactions of the ASME, Journal of Basic Engineering, Vol. 90, Series D, No. 4, December 1968.
7. Sears, W. R., "Some Aspects of Non-Stationary Airfoil Theory and Its Practical Application", Journal of the Aeronautical Sciences, Vol. 8, No. 3, January 1941, pp. 104-108.
8. Horlock, J. H., "Unsteady Flow in Turbomachines", presented at the Third Australasian Conference on Hydraulics and Fluid Mechanics, Sydney, Australia, November 1968.
9. Naumann, H. and Yeh, H., "Lift and Pressure Fluctuations of a Cambered Airfoil Under Periodic Gusts and Applications in Turbomachinery", Transactions of the ASME, Journal of Engineering for Power, Vol. 95, Series A, No. 1, January 1973.
10. Holmes, D. W., "Lift Fluctuations on Aerofoils in Transverse and Streamwise Gusts", Ph.D. Dissertation, St. Johns College, Cambridge University, October 1972.
11. Whitehead, D. S., "Force and Moment Coefficients for Vibrating Airfoils in Cascade", Aeronautical Research Council R and M 3254, February 1960.
12. Whitehead, D. S., "Bending Flutter of Unstalled Cascade Blades at Finite Deflection", Aeronautical Research Council R and M 3386, October 1962.
13. Mani, R., "Compressibility Effects in the Kemp-Sears Problem", presented at the International Symposium on the Fluid Mechanics and Design of Turbomachinery, The Pennsylvania State University, August 1970, to be published in Proceedings.
14. Lotz, M. and Raabe, J., "Blade Oscillations in One-Stage Axial Turbomachinery", Transactions of the ASME, Journal of Basic Engineering, Vol. 90, Series D, No. 4, December 1968.

15. Henderson, R. E. and Daneshyar, H., "Theoretical Analysis of Fluctuating Lift on the Rotor of an Axial Turbomachine", Aeronautical Research Council R and M 3684, 1972.
16. Yeh, H. and Naumann, H., "Unsteady Induced Velocities in a Cascade", paper presented at the Second International JSME Symposium on Fluid Machinery and Fluidics, Tokyo, Japan, September 1972.
17. Henderson, R. E., "The Unsteady Response of an Axial Flow Turbomachine to an Upstream Disturbance", Ph.D. Dissertation, Engineering Department, University of Cambridge, 1972 (also Applied Research Laboratory, Technical Memo TM 72-218, October 1972).
18. Bruce, E. P., "The ARL Axial Flow Research Fan--A New Facility for Investigation of Time-Dependent Turbomachinery Flows", paper to be presented at the Combined Canadian Society for Mechanical Engineering and American Society of Mechanical Engineers Fluids Engineering Division Conference, La Chateau Champlain, Montreal, Quebec, Canada, May 13-15, 1974.
19. Howell, A. R., "The Present Basis of Axial Flow Compressor Design: Part I - Cascade Theory and Performance", Aeronautical Research Council R and M 2095, 1942.
20. Bruce, E. P., "Design and Evaluation of Screens to Produce Multi-Cycle ± 20% Amplitude Sinusoidal Velocity Profiles", paper to be presented at the AIAA 8th Aerodynamic Testing Conference, Bethesda, Maryland, July 8-10, 1974.
21. McCarthy, J. H., "Steady Flow Past Non-Uniform Wire Grids", Journal of Fluid Mechanics, Vol. 19, 1964, pp. 491-512.
22. Cornell, W. G., "Losses in Flow Normal to Plane Screens", Transactions of the ASME, Vol. 80, May 1958, pp. 791-799.

INVESTIGATION OF THE UNSTEADY PRESSURE DISTRIBUTIONS ON THE BLADES OF AN AXIAL FLOW FAN

By

Robert E. Henderson
Applied Research Laboratory and
Dept. of Mechanical Engineering
Pennsylvania State University
University Park, Pennsylvania 16801

INTRODUCTION

A major component in today's technological society is the turbomachine. This device experiences continual application in the conversion of rotating mechanical energy to fluid energy, a pump or compressor, or in the conversion of fluid energy into rotating mechanical energy, a turbine. One of the major problems in the employment of a turbomachine is the unsteady pressures, forces and moments which are generated on its blades and the excessive noise, vibration and performance degradation which can result. Thus, a major effort in current turbomachinery research is to better understand the generation of these unsteady pressures, forces and moments and the development of design data which will lead to their reduction in future turbomachinery applications.

For example, in present day high bypass ratio aircraft engines, the major source of noise is that generated by the fan. This noise arises as the result of the unsteady pressures (and, hence, lift and moment) on the blades due to potential interactions with other blade rows, interactions with the wakes from upstream blade rows, inlet flow distortions and inlet turbulence [1], [2]*. The prediction of this radiated noise, and its eventual reduction, is dependent upon an accurate knowledge of the unsteady response of the blades to these interactions [3], [4]. To reduce this source of fan noise, it is necessary that the designer be able to predict, with a known level of confidence, the unsteady pressures and forces acting on the fan blades as a function of the design parameters at his disposal and the known characteristics of the disturbance. These design parameters include: blade rotational speed, blade solidity, blade stagger angle, blade camber, blade thickness and spacing between adjacent blade rows.

To date, there is a lack of such unsteady design data. The reasons for this are twofold: (1) Most available theoretical design analyses represent the unsteady response of the turbomachine blades as isolated flat plate airfoils, thus ignoring the effects of camber, thickness and solidity, and (2) the acute lack of experimental measurements to demonstrate the validity of available analyses, and the effects of various design parameters. This paper describes a program of research directed toward filling these gaps by the development of an experimental capability for the measurements of the unsteady pressure distributions on a rotating blade as a function of the blade geometric parameters. Measurements conducted with this instrumentation will

---

*References page

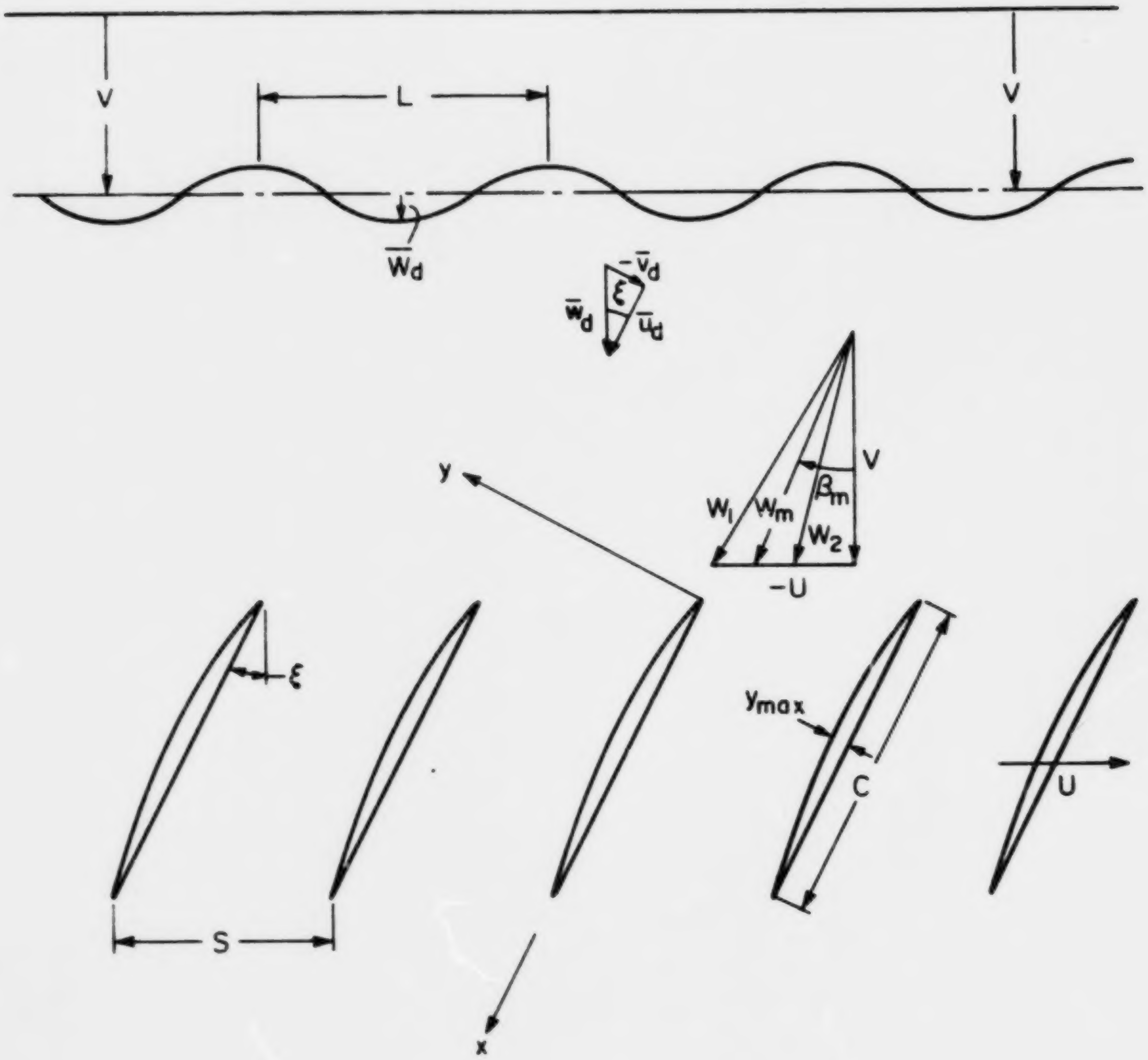

V
L
V
$\bar{W}_d$
$-\bar{v}_d$
ξ
$\bar{w}_d$
$\bar{u}_d$
y
V
W_1
W_m
β_m
W_2
-U
ξ
y_{max}
C
U
S
x

Figure 1: Interaction of a Two Dimensional Cascade and Inflow Axial Velocity Variations

be employed to verify a recent unsteady analysis for a moving cascade which, when verified, would provide predictions of unsteady design data. Considered will be the interaction of an axial flow stage with spatial variations of its inflow velocity field, as would be generated by the wakes of upstream blades and/or inflow velocity distortions. This type of interaction is shown in Figure 1 for a two-dimensional cascade of thin airfoils interacting with a simple circumferential variation in axial inflow velocity. For all cases the flow is considered to be incompressible.

UNSTEADY PRESSURE DISTRIBUTIONS IN A STATIONARY, TWO-DIMENSIONAL CASCADE

While the final goal of this program is the measurement of the unsteady pressure distribution on a rotating blade row which interacts with a spatially varying inlet flow, an ongoing program employing stationary cascades has provided some very pertinent results. This research was conducted in a special test apparatus at the SRC Turbomachinery Laboratory (SRC TL), Cambridge University, Cambridge, England, as a cooperative effort between that laboratory and the Applied Research Laboratory (ARL) of the Pennsylvania State University.

The SRC TL test apparatus is a cascade wind tunnel in which the top and bottom walls are flexible and can be positioned in a sinusoidal wave form which moves along the test section with time. As a result of this "wavy wall" motion, the flow through the test section appears as a mean velocity with a transverse sinusoidally varying disturbance velocity superimposed. If an isolated airfoil were installed in the tunnel, the flow would resemble a Sears [5] type gust, but more specifically, the non-convected type described by Kemp [6]. The resulting unsteady flow pattern interacting with a cascade of test blades is shown schematically in Figure 2.

The unsteady flow field of Figure 2 is not convected with the mean velocity W_m and, therefore, its interaction with the stationary cascade does not represent the interaction of a compressor rotor with a spatially varying inflow. However, the SRC TL cascade tunnel is a useful device for the development of experimental techniques for the measurement of unsteady pressure distributions and provides data for comparison with unsteady cascade analyses for non-convected gusts. A series of measurements of the unsteady pressure distributions on the central airfoil of a stationary cascade with no steady lift, a 45-degree stagger angle and two values of space-to-chord ratio have been conducted. In addition, the isolated airfoil experiments of Holmes [7] were repeated.

To compare these experimental results with an unsteady cascade analysis, the unsteady pressure distributions were integrated to give both the magnitude and phase of the unsteady lift. The theoretical analysis of Henderson and Danesheyar [8] was then altered to give predictions of the unsteady lift in a non-convected gust. This analysis assumes the flow to be incompressible and inviscid with the cascade represented by thin, slightly cambered airfoils. Figures 3 and 4 present comparisons of the experimental and predicted variation of the magnitude and phase angle of the unsteady lift as a function of reduced frequency, based on the mean velocity, W_m, and space-to-chord ratio. Also shown is the case of an isolated airfoil which is equivalent to the problem presented by Kemp [6] and Holmes [7]. These measurements, together with the method of data analysis and a discussion of the non-convected theory are presented in reference [9].

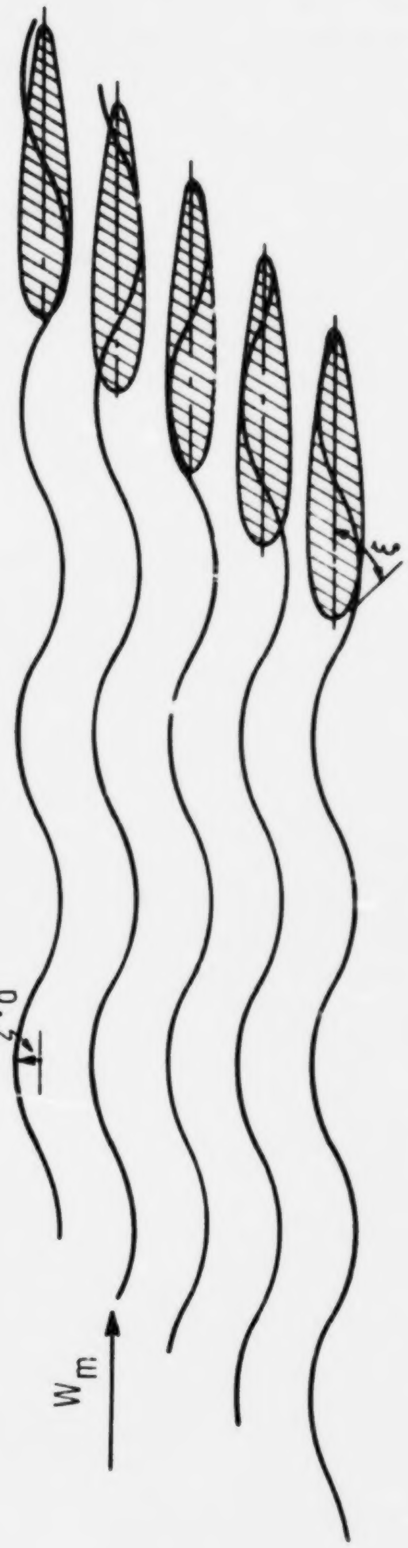
W_m
V_d
ε

Figure 2: Unsteady Flow in Stationary Cascade Tunnel

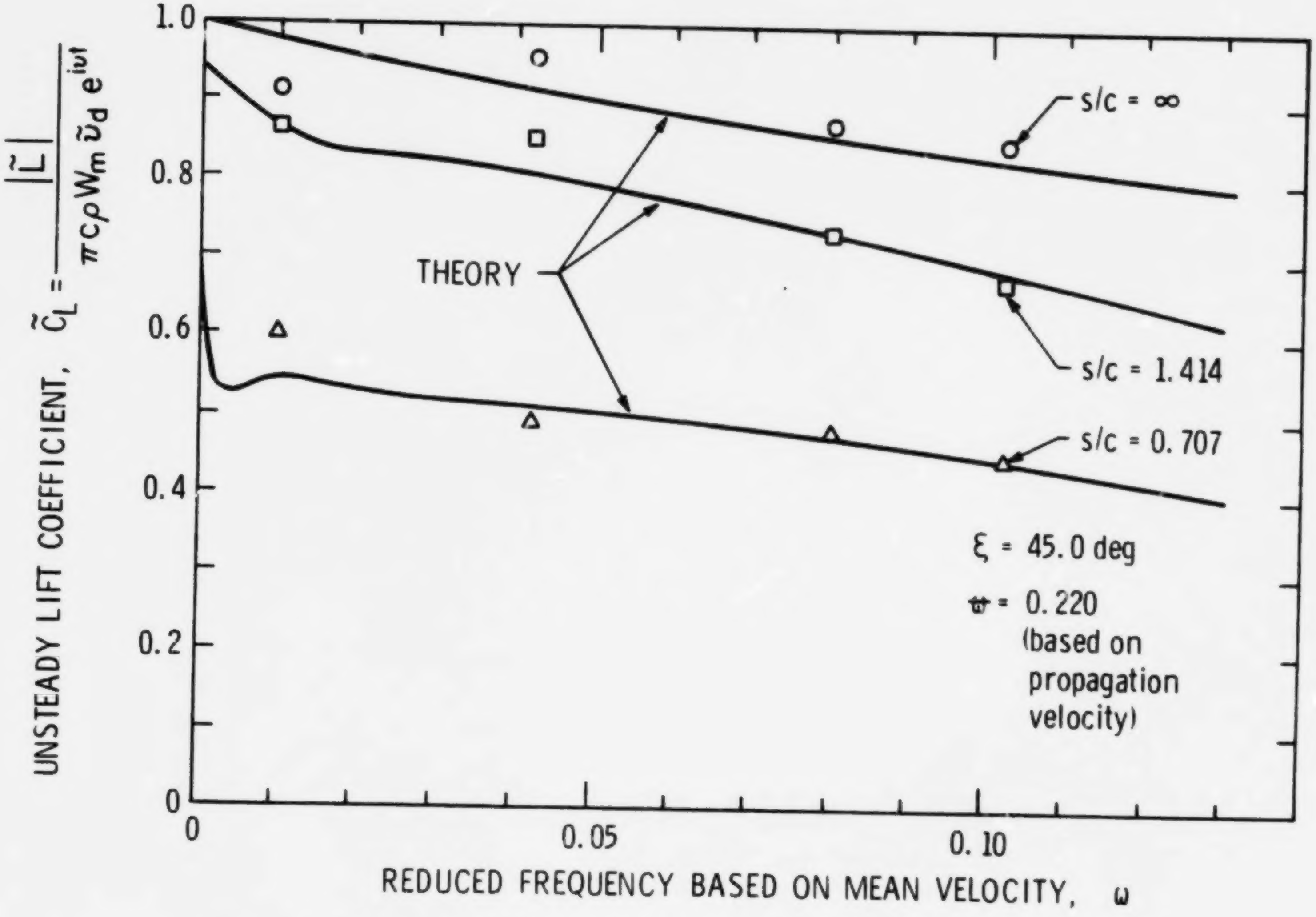

Figure 3: Magnitude of Unsteady Lift Coefficient Variation in Non-Convected Transverse Disturbance

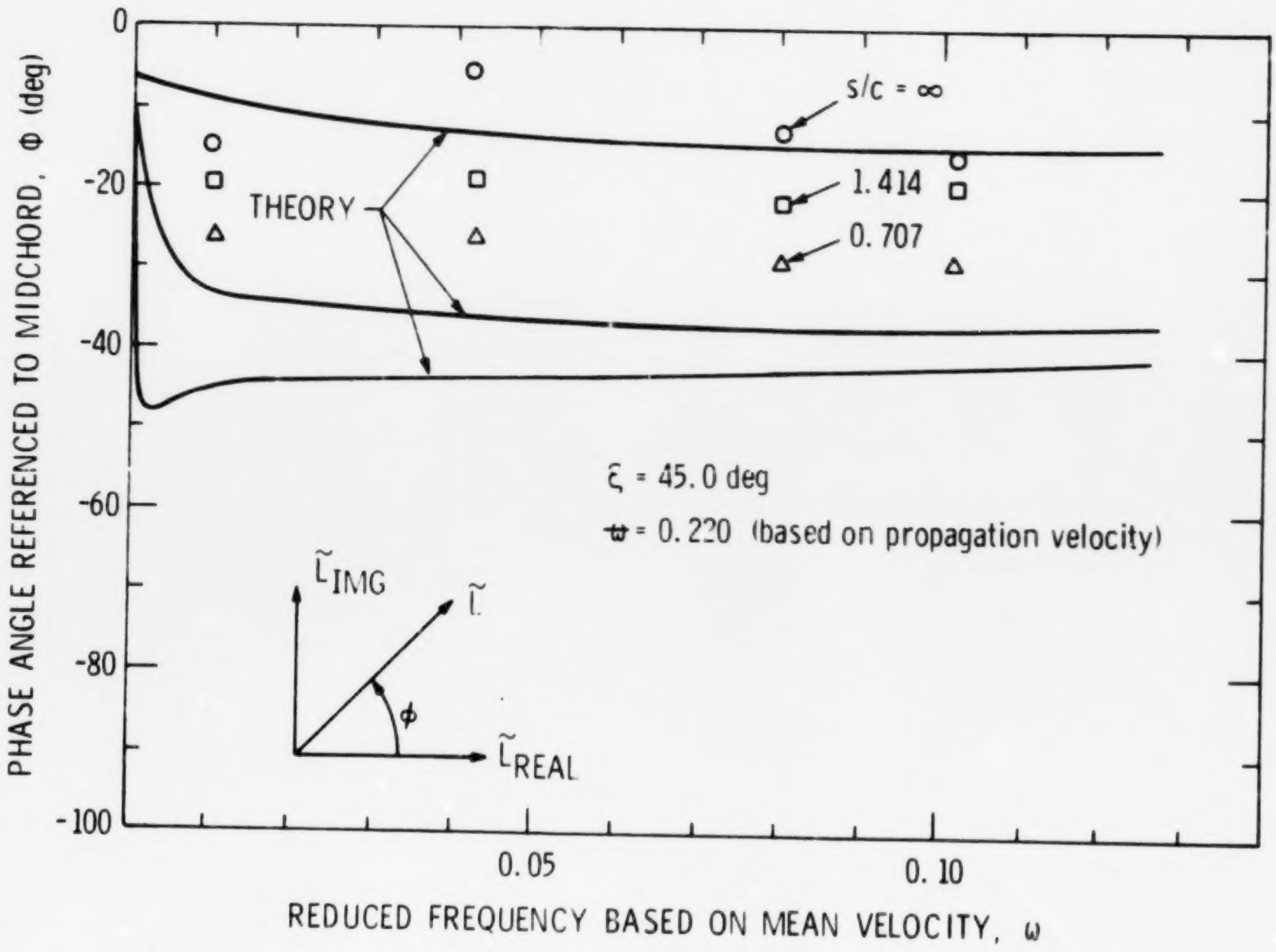

Figure 4: Phase Angle Variation in Non-Convected Transverse Disturbance

These results, while not simulating the case of a compressor or fan rotor, serve a very useful purpose. In a simplified experimental setup using a stationary cascade, methods of data reduction and analysis which are applicable to measurements with a rotating blade have been developed. As discussed in [9], this includes the use of "phase lock" averaging and on-line computer data reduction. In addition, the unsteady cascade effects on the unsteady lift predicted by the analysis of reference [8] have been experimentally observed. While exact agreement with measurements was not obtained, very satisfactory agreement with predicted trends were obtained. This gives credence to the analysis of [8] for use in developing unsteady design data.

PROGRAM OF RESEARCH IN ANNULAR CASCADE

The study of unsteady pressure distributions on the blades of an axial flow state was initiated in the Department of Mechanical Engineering, the Pennsylvania State University in September, 1974. This program is being conducted in an existing experimental facility, which is termed the Axial Flow Research Fan (AFRF) [10], and which was constructed specifically for the study of the unsteady response of an axial flow stage. The AFRF shown schematically in Figure 5, is located in the Applied Research Laboratory and permits the operation of a single stage having large blades, 6.0 inch chord, in different spatially varying inflow velocity fields. This program is directed toward the measurement of the unsteady pressure distributions on both the rotor and stator of an existing test stage, and complements two other programs which have been, or are being conducted in the AFRF. These other programs are concerned with the measurement of the total unsteady normal force and moment [11] and the measurement of the unsteady circulation on the rotating blades of the test stage [12]. Each of these complemented programs provides measurements of the unsteady response of the rotating blade row to different circumferential sinusoidally varying inflow velocity fields, at different blade stagger angles and solidities. The current program will also provide measurements of the unsteady response of the test stage, but in the form of detailed unsteady pressure distributions on both the rotor and stator blades.

The blades in the existing AFRF test stage are designed to operate at zero mean angle of incidence, and hence, with no steady lift. The stator blades are similar to the rotor blades but are not twisted. The measurement of the unsteady pressure distributions on these blades will be conducted at the blade mean-radius, thus approximating a two-dimensional annular cascade. A series of miniature, fast response pressure sensors fitted into the blade will be employed to obtain the unsteady pressure distributions. This instrumentation is described in the following sections.

Sensor Mounting in Test Blade

The first step in the development of instrumentation to permit the measurement of the unsteady pressure distributions on the test blades of the AFRF was the selection of a satisfactory pressure sensor. In light of the size constraints presented by the blades, a Stow Laboratories PITRAN differential pressure transducer has been selected for use in this program. The PITRAN is a silicone NPN planar transistor that has its emmiter-base junction mechanically coupled to a flexible diaphragm. The major advantage of the PITRAN over other transducers of comparable size is its high-level output signal. The output of at least 2.0 volts at the maximum linear pressure is much greater than that

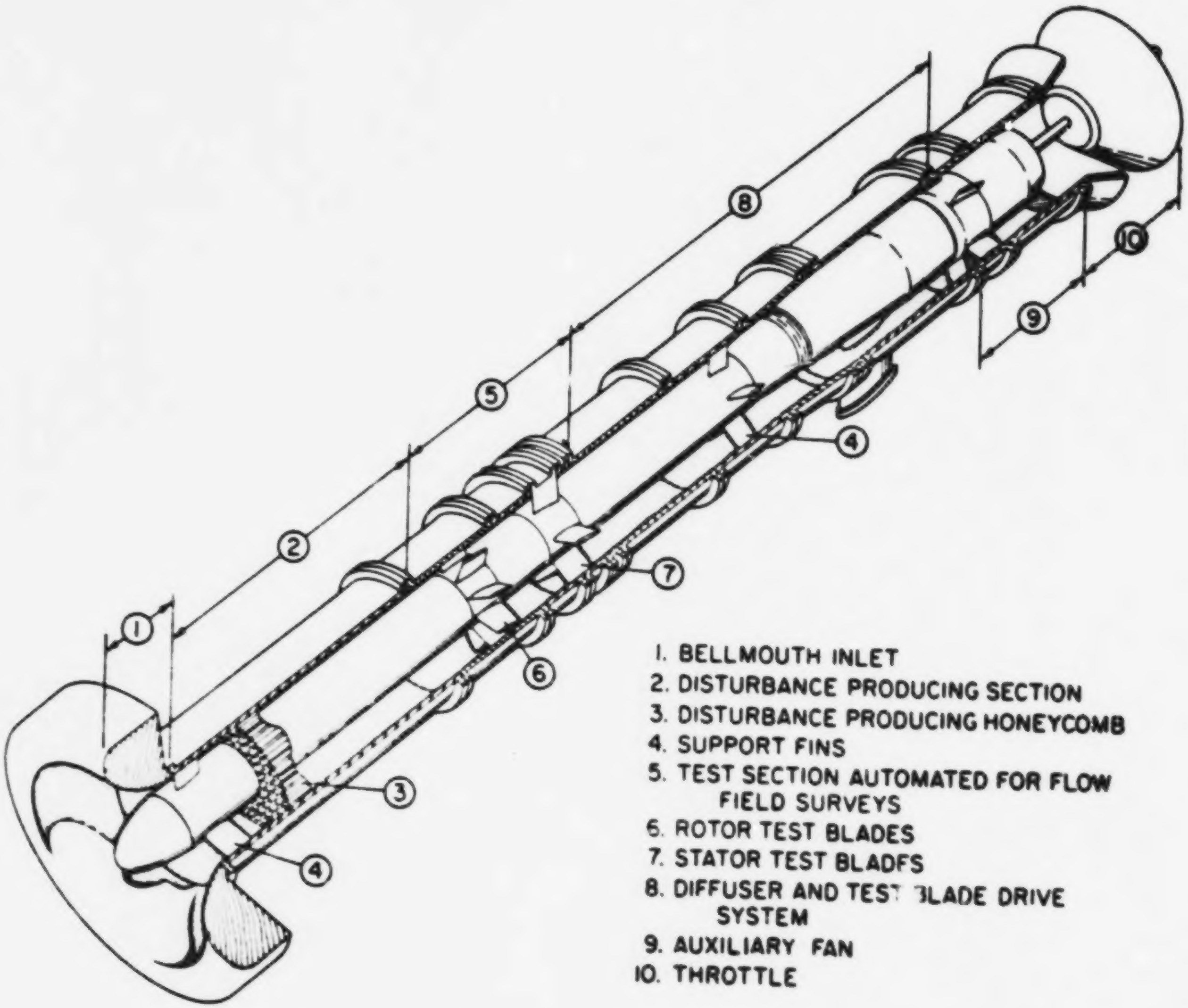

1
2
5
8
9
10
4
7
6
3
4
1. BELLMOUTH INLET
2. DISTURBANCE PRODUCING SECTION
3. DISTURBANCE PRODUCING HONEYCOMB
4. SUPPORT FINS
5. TEST SECTION AUTOMATED FOR FLOW FIELD SURVEYS
6. ROTOR TEST BLADES
7. STATOR TEST BLADES
8. DIFFUSER AND TEST BLADE DRIVE SYSTEM
9. AUXILIARY FAN
10. THROTTLE

Figure 5: ARL Axial Flow Research Fan

obtained with other transducers. In addition, the PITRAN has an extreme overload capability, in which overloads of 700 per cent of its linear range can be tolerated without damage. This capability is considered important in this program, as the exact magnitude of the unsteady pressures to be experienced on the blades is not known.

The first phase of testing which is to be conducted in the AFRF will consider a stator blade. This instrumented blade will be mounted downstream of the existing rotor and thereby operate in the moving (relative to the stator blade) wakes from the rotor. The reason for conducting the initial tests on a stator is to eliminate the effects of centrifugal force on the transducer and the problems of the transmission of the sensor output signal from the rotating to stationary frame of reference.

Figure 6 shows the arrangement which will be employed for mounting the PITRAN transducers in the blade. This arrangement was selected, as it permits the simple replacement of a malfunctioning transducer with another transducer. It also will permit an interchange of transducers between different test blades. The reference, or back pressure, for all of the differential gauges will be obtained by a common channel or manifold along the chord of the airfoil. This manifold will be directed along the span of the blade and out of the stator hub to atmospheric pressure. In the case of the rotor blade which will be evaluated at a later time, the reference will be a pressure applied to the manifold by a sealed container which rotates with the blade. The reference manifold will also be employed for the passage of the electrical leads from the PITRANs to the outside of the blades. For the rotating blades this system must also include a slip ring unit to get from the rotating to stationary frame of reference.

The unsteady static pressure will be sensed through static pressure taps connecting the surface of the airfoil and the cavity containing the transducer. The sizing of this cavity is such as to maintain its Helmhaltz resonating frequency well above the maximum anticipated disturbance frequency of 250 hz. The pressure on each side of the blade will be sensed by sealing the taps on the opposite side with tape or wax.

Pressure Transducer Dynamic Calibration

Prior to the acquisition of unsteady pressure distribution measurements on the blades of the AFRF, each PITRAN/cavity assembly must be dynamically calibrated to determine its unsteady response to a known unsteady pressure signal. This calibration will include the determination of the effects of the cavity enclosing the transducer and the static pressure taps connecting the cavity and the blade surface.

An important part of this calibration is the determination of a satisfactory calibration device. Initial investigations to determine such a device have been conducted and are reported in [13]. This study has resulted in the development of an acoustic coupling device which can generate a very accurately known unsteady pressure signal. To date, the calibration of a PITRAN transducer with and without an enclosing cavity has been conducted using this device. Prior to the calibration of the PITRAN/cavities shown in Figure 6, the present acoustic coupler must be redesigned to improve a mechanical resonance problem and to accept this particular cavity arrangement. This effort is presently in progress.

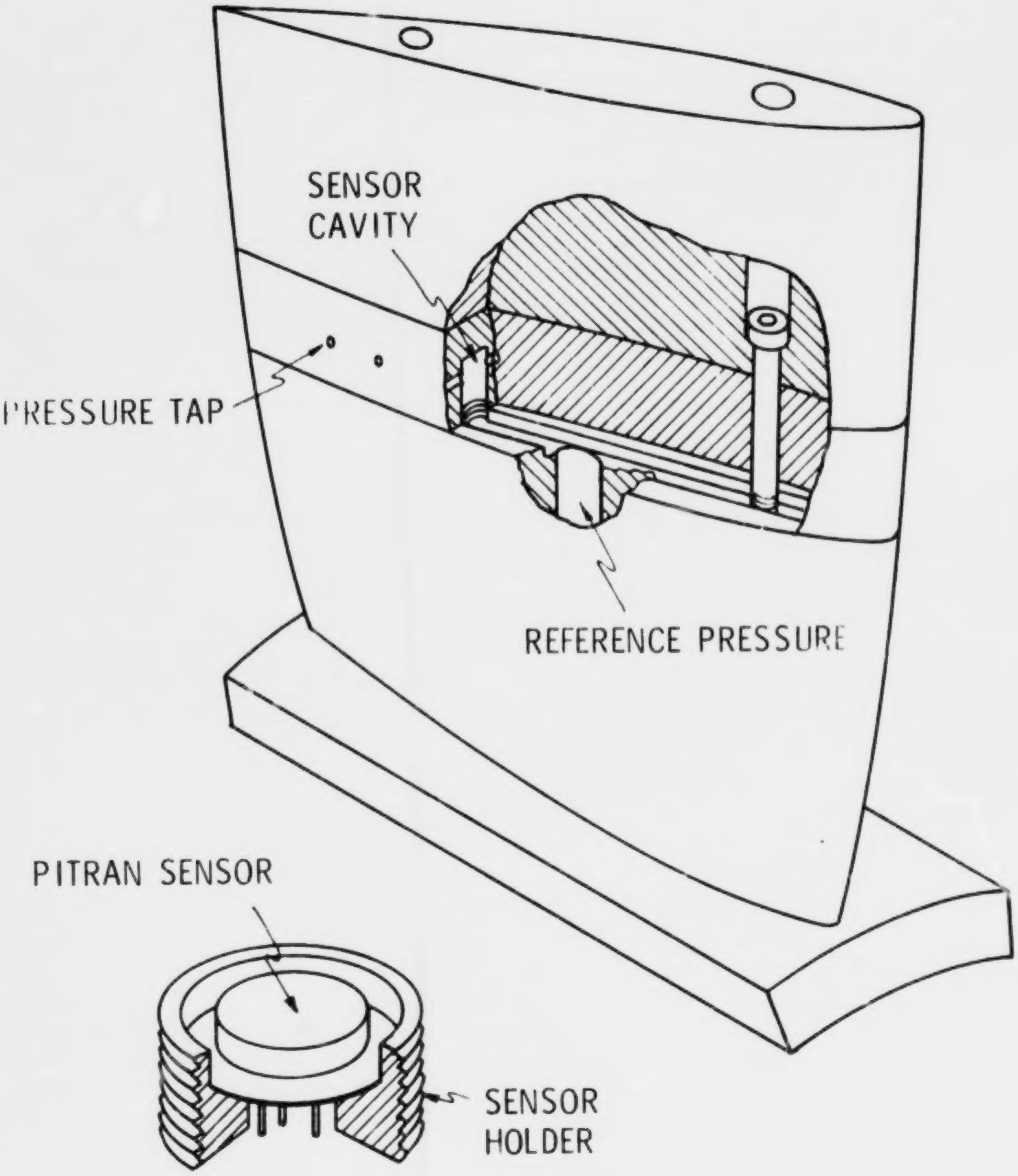
SENSOR CAVITY
PRESSURE TAP
REFERENCE PRESSURE
PITRAN SENSOR
SENSOR HOLDER

Figure 6: Mounting Arrangement of PITRAN Transducers in Stator Blade

SUMMARY

A program of research is in progress at the Pennsylvania State University to obtain both experimental and theoretical data related to the minimization of the unsteady pressures, forces, and moments on axial flow turbomachinery blade row operated at low Mach numbers. A portion of this program is concerned with the determination of the unsteady pressure distributions on both the stationary and rotating blades of an axial flow stage which operates in a spatially varying velocity inflow field. This program is presently in progress and, thus, a large portion of the material presented here represents a report on work in progress. The most significant points of progress to date include:
(1) The completion of an initial series of experimental measurements of the unsteady pressure distributions at Cambridge University on a stationary cascade operated in a non-convected gust velocity field. These experiments demonstrated the feasibility of conducting such measurements and the procedures to be employed in the analysis of data.
(2) The comparison of experimental values of unsteady lift determined by integration of the pressure distributions obtained on the stationary cascade and predictions using the theoretical analysis of [8] demonstrate the ability of the theoretical analysis to predict the unsteady lift in a cascade. While these comparisons were for a non-convected disturbance, the analysis was developed for use with convected disturbances such as experienced in aircraft compressors. Such an application is intended to provide unsteady cascade design data for use in reducing the unsteady interactions experienced in future turbomachines.
(3) The selection of an unsteady pressure sensor and the design of a mounting system to incorporate these sensors into both a stator and rotor blade for the Penn State Axial Flow Research Fan. The manufacture of the instrumented stator blade is presently in progress.

After completion of the initial tests with the instrumented stator blade operated in the wakes of an upstream rotor scheduled for September, 1974, an instrumented rotor blade will be assembled. The rotor blade will be operated in different inflow velocity disturbance flows and at different stagger angles and space-chord ratios. The theoretical analysis of [8] will also be extended to permit the prediction of the unsteady pressure distributions on a blade in a stationary or moving cascade.

[The cooperative research effort between SRC TL and ARL was supported by the British Ministry of Defense (Procurement Executive) and NOSC, U. S. Navy. Travel monies were provided by a NATO Research Grant. The program employing the Penn State AFRF is supported by a NASA Research Grant.]

NOMENCLATURE

C	Chord length (ft)
L	Disturbance wavelength (ft)
$\tilde{L}$	Unsteady lift (lbs)
S	Spacing (ft)
U	Blade rotational velocity (fps)
$\bar{u}_d$	Half-amplitude of disturbance velocity parallel to chord (fps)
V	Time-averaged axial velocity (fps)
$\bar{\nu}_d$, $\bar{v}_d$	Half-amplitude of disturbance velocity normal to chord (fps)
W	Time-averaged relative velocity (fps)
₩	Gust Propagation velocity (fps)
$\bar{\omega}_d$	Half-amplitude of axial disturbance velocity (fps)
y_{max}	Maximum camber (ft)
ν	Disturbance frequency (cps)
ξ	Stagger angle (deg)
ρ	Mass density (slugs/ft^3)
ϕ	Phase angle (deg)
ω	Reduced frequency based on mean velocity ($= \frac{\nu C}{2W_m}$)
ϖ	Reduced frequency based on propagation velocity ($= \frac{\nu C}{2₩}$)

Subscripts

d	Disturbance
m	Mean

REFERENCES

[1] "Aircraft Engine Noise Reduction," Proceedings of a Conference at Lewis Research Center, May 16-17, 1972, NASA SP-311.

[2] Mugridge, B. D., and C. L. Morfey, "Sources of Noise in Axial Flow Fans," Journal of the Acoustical Society of America, Vol. 51, No. 5 (Part I), 1972.

[3] Bragg, S., and R. Budge, "Noise From Turbojet Compressors," Journal of the Royal Aeronautical Society, Vol. 68, No. 637, pp. 1-10, January, 1964.

[4] Morfey, C. L., "Sound Generation in Subsonic Turbomachinery," ASME Transactions, Journal of Basic Engineering, Vol. 92D, pp. 450-458, September, 1970.

[5] Sears, W. R., "Some Aspects of Non-Stationary Airfoil Theory," Journal of Aeronautical Sciences, Vol. 8, 1941, pp. 104-108.

[6] Kemp, N. H., "On the Lift and Circulation of Airfoils in Some Unsteady Flow Problems," Journal of Aeronautical Sciences, Vol. 19, No. 3, 1952, pp. 713-714.

[7] Holmes, D. W., "Lift and Pressure Measurements on an Airfoil in Unsteady Flow," ASME Preprint No. 73-GT-41, Presented at Gas Turbine Conference, Washington, D. C., April 8-12, 1973.

[8] Henderson, R. E., and H. Daneshyar, "Theoretical Analysis of Fluctuating Lift on the Rotor of an Axial Turbomachine," Aeronautical Research Council R & M 3684, 1972.

[9] Satyanarayana, B., R. E. Henderson, and J. P. Gostelow, "A Comparison Between Experimental and Theoretical Lift on Cascades at Low Frequency Parameters," ASME Preprint 74-GT-78, Presented at Gas Turbine Conference, Zurich, Switzerland, March 30-April 4, 1974.

[10] Bruce, E. P., "The ARL Axial Flow Research Fan-A New Facility for Investigation of Time-Dependent Turbomachinery Flows," To be presented at the Canadian and American Society of Mechanical Engineering Fluids Engineering Conference, Montreal, Canada, May 13-15, 1974.

[11] Bruce, E. P., "Measurement and Analysis of the Unsteady Normal Force and Pitching Moment on an Axial Flow Fan Rotor Blade Element," Proceedings of Second Interagency Symposium on University Research in Transportation Noise, North Carolina State University, Raleigh, N. C., June 5-7, 1974.

[12] Henderson, R. E., "The Unsteady Response of a Blade Row Using Measurements of the Time-Mean Total Pressure," ASME Preprint No. 73-GT-94, Presented at the 18th International Gas Turbine Conference, Washington, D. C., April 8-12, 1973.

REFERENCES (Cont'd.)

[13] Atkins, G. B., "Development and Calibration of a Probe/Sensor System to Measure Unsteady Total Pressures," Applied Research Laboratory, Pennsylvania State University, Technical Memorandum TM 74-75, April 12, 1974.

TIME-DEPENDENT THRUST GENERATED BY A PROPELLER OPERATING IN A TURBULENT INFLOW

By

Donald E. Thompson
Applied Research Laboratory
State College, Pennsylvania 16801

INTRODUCTION

The blades of both marine and aircraft propulsors can operate in both a spatially varying steady inflow and a turbulent inflow. For instance, the rotor blades of an aircraft propulsor operate in the wakes shed by upstream guide vanes, support struts, or stator blades. These wakes introduce spatial variations in the steady velocity and turbulence due to the shed wakes.

Due to these variations in velocity, the local angle of attack of the blades vary with time and the local blade pressures vary with time. As a consequence of these time-dependent pressures, sound is radiated from the propulsor. In addition, blade vibrations result and time-dependent forces and moments are exerted on the rotor drive shaft. Each of these results in undesirable conditions and, therefore, has been the subject of much research.

The emphasis of the present investigation is on the response of propellers to turbulent inflows. The time-dependent thrust generated by a propeller due to operation in turbulent inflows with various length scales and intensities was measured. The resulting time-dependent thrust spectra are compared to the spectra predicted by several theories. Results show that blade-to-blade lift correlations are important for predicting the spectra levels and the peaking of the spectra at blade passing frequency and multiples.

Theoretical Considerations

It is desired to determine the spectrum of the time-dependent thrust generated by a given propulsor due to operation in a given turbulent inflow. An approach very similar to that employed by Sevik [1] has been used in the present investigation.

The quantities involved are tensors, consequently, the index notation is used. Directions are denoted by superscripts and subscripts denote elements of the propulsor involved. For example, $u_k^\beta(\tau')$ denotes the component of the fluctuating velocity at time τ' in the direction β of the rotating reference frame, Figure 1, at the element k. Also, $F_{ik}^{\alpha\beta}(t,\tau')$ denotes the aerodynamic force acting on the i^{th} element in the direction α at the instant of time t caused by the velocity fluctuation of unit magnitude in the direction β to to which the k^{th} element was subjected at the instant of time τ'.

Consider the propulsor blades to be subdivided into an arbitrarily large number of spanwise elements and consider a typical element located at r_i, as shown in Figure 1. The fluctuating aerodynamic forces acting on the various surface elements are interdependent by virtue of induction effects, as well as by virtue of spatial and temporal correlation of the turbulent velocity fluctuations. Neglecting higher order terms, the lift force, $\ell_i^{\alpha}(t)$, on the i^{th} element at time t in the direction α is given by

$$\ell_i^{\alpha}(t) = \int_o^{\infty} F_{ik}^{\alpha\beta}(t)\ u_k^{\beta}(t-\tau)d\tau \tag{1}$$

where the aerodynamic force tensor is time invariant,

$\alpha, \beta = 1,2,3$;
$i,k = 1,2,\ldots,m$;

and $\tau' \leq t$.

The total force acting on the propulsor is obtained by summing the forces acting on each individual blade element,

$$L^{\alpha}(t) = \sum_{i=1}^{m} \ell_i^{\alpha}(t) \tag{2}$$

Since $L^{\alpha}(t)$ is a random function, a statistical approach must be employed. In this particular application, the correlation tensor $\langle L^{\alpha}(t)\ L^{\beta}(t+\tau)\rangle$ and its Fourier transform are of importance. The random processes are assumed to be stationary and ergodic in forming average values of the forces and fluid velocities.

In terms of the velocity correlation tensor $R_{kr}^{\gamma\delta}(\tau-\tau_2+\tau_1)$ for the points located at $\overline{r}_k$ and $\overline{r}_r$, the cross-correlation tensor of the forces becomes,

$$\phi_{\ell_i \ell_i}^{\alpha\beta}(\tau) = \int_o^{\infty} F_{ik}^{\alpha\gamma}(\tau_1)d\tau_1 \int_o^{\infty} F_{jr}^{\beta\delta}(\tau_2)d\tau_2\ R_{\kappa r}^{\gamma\delta}(\tau-\tau_2+\tau_1)\ . \tag{3}$$

The spectrum tensor of the force fluctuations is then obtained as the Fourier transform of the cross-correlation tensor of the forces,

$$G_{\ell_i \ell_j}^{\alpha\beta}(\omega) = \frac{1}{\pi} \int_o^{\infty} \phi_{\ell_i \ell_j}^{\alpha\beta}(\tau)e^{-i\omega\tau}d\tau\ . \tag{4}$$

Taking the Fourier transform of equation (3) results in

$$G^{\alpha\beta}_{\ell_i \ell_j}(\omega) = \{H^{\alpha\gamma}_{ik}(\omega)\}^{*} \, \{H^{\beta\delta}_{jr}(\omega)\} \, G^{\gamma\delta}_{kr}(\omega) \ . \tag{5}$$

where $G^{\gamma\delta}_{kr}(\omega)$ is the spectrum tensor of the velocity fluctuations and where $H(\omega)$ is the aerodynamic frequency response function and where * denotes the complex conjugate of this quantity.

Equation (5) is the spectrum tensor of the force fluctuations in terms of the aerodynamic frequency response function and the spectrum tensor of the velocity fluctuations as derived by Sevik [1]. The application of this equation requires choosing an appropriate aerodynamic frequency response function which is consistent with the given propulsor and velocity fluctuations. In addition, the spectrum tensor of the velocity fluctuations must be determined.

Application to a Propulsor

A brief description of the approach taken by Sevik [1] will be given followed by the new approach taken in this paper.

Sevik [1] considered a propeller of low solidity with blades of high aspect ratio operating in a homogeneous, isotropic turbulent flow. For this type of flow, the velocity correlation tensor can be expressed in terms of the distance $\underline{r}$ between two points in the flow field and the mean square value of the velocity fluctuations $\overline{u^2}$ as follows:

$$R^{\alpha\beta}_{kr}(\underline{r}) = \overline{u^2} \left\{ -\frac{1}{2r} r^{\alpha} r^{\beta} \frac{\partial f(r)}{\partial r} + \left(f(r) + \frac{1}{2} r \frac{\partial f(r)}{\partial r}\right)\delta^{\alpha\beta} \right\} \tag{6}$$

where $\delta^{\alpha\beta}$ is the Kronecker delta and f is the coefficient of longitudinal correlation. The coefficient of longitudinal correlation, as measured by Stewart and Townsend [2], is shown in Figure 2. An approximate expression

$$f(r) = e^{-\frac{r}{\Lambda}} \tag{7}$$

where Λ is the integral scale of the turbulence has been used by Sevik [1]. This approximation is shown in Figure 2.

The aerodynamic frequency response function employed is that given by Sears [3], as follows:

$$H_j(\omega) = 2\pi\rho V_j b_j \, \{C(k_j)[J_o(k_j) - i \, J_1(k_j)] + i \, J_1(k_j)\}\delta R_j \tag{8}$$

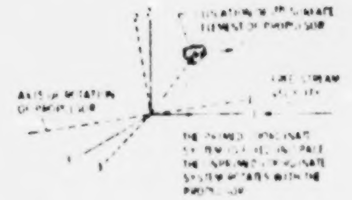

Figure 1: Coordinate System

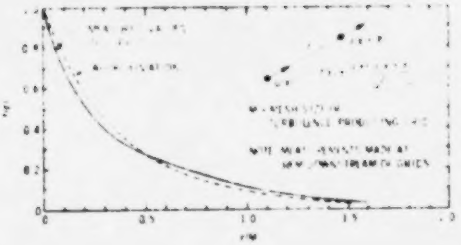

Figure 2: Correlation Curve for Isotropic Turbulence

where V_j is the resultant velocity at the j^{th} element of the propeller, J_o and J_1 are Bessel functions, C(k) is Theodorsen's function, and $k_j = \omega b_j/V_j$ is the reduced frequency.

Using the relationships given by equations (6), (7), and (8) in equation (5) permits the calculation of the response of a propulsor to turbulence by numerical means. Sevik [1], however, by making certain approximations and assumptions was able to obtain relatively simple expressions for the RMS thrust coefficient and the spectrum tensor of the thrust fluctuations. These approximations and assumptions are as follows:

1. The axis of rotation of the propeller is colinear with the free-stream velocity vector.
2. The resultant velocity and chord of the various propeller elements may be represented by those of a single "typical section" located at some fraction of the blade span.
3. The velocity correlation tensor is approximated by

$$R^{\alpha\beta}_{kr}(\underline{r}) = e^{-\frac{q}{\Lambda}} R^{\alpha\beta}_{kk}(C_x\tau) \qquad (9)$$

where q is the distance between the elements k and r of the propeller.

Using the equations (6), (7), (8), and (9) in equation (5), Sevik [1] has derived on expression for the spectrum tensor of the fluctuating thrust:

$$G^{11}(\omega) = \sum_i \sum_j \{H^*_i(\omega)\, H_j(\omega) \cos^2\beta_i \cos^2\beta_j\, G^{11}_{ij}(\omega)$$

$$+ \frac{1}{4} H^*_i(\omega)\, H_j(\omega) \sin 2\beta_i \sin 2\beta_j\, G^{22}_{ij}(\omega)\} \quad , \qquad (10)$$

where

$$G^{11}_{ij}(\omega) = \frac{2\overline{u^2}}{\pi} \left\{ \frac{C_x/\Lambda}{(C_x/\Lambda)^2 + \omega^2} \right\} e^{-\frac{q}{\Lambda}}$$

and

$$G^{22}_{ij}(\omega) = \frac{2\overline{u^2}}{\pi} \left\{ \frac{C_x/\Lambda}{(C_x/\Lambda)^2 + \omega^2} \right\} \left\{ 1 + \frac{1}{2} \left[\frac{(C_x/\Lambda)^2 - \omega^2}{(C_x/\Lambda)^2 + \omega^2} \right] \right\} e^{-\frac{q}{\Lambda}}$$

The angle β is that between the resultant velocity vector and the direction of rotation and is given by

$$\tan\beta = \frac{V}{R\Omega} .$$

The "typical section" concept mentioned in the second assumption above is now employed with respect to the aerodynamic frequency response functions

$$H_i^{\star}(\omega)\ H_j(\omega) \simeq H_T^{\star}(\omega)\ H_T(\omega) = \left|H_T(\omega)\right|^2 =$$

$$= (2\pi\rho V_T b_T)^2 \left[\frac{1}{1 + 2\pi\dfrac{\omega b_T}{V_T}}\right] \delta R_i \delta R_j \qquad (11)$$

where an approximation to Sears' function has been used.

Substituting equation (11) into equation (10), Sevik [1] ultimately expresses the spectrum of the thrust fluctuations as

$$G(\Gamma) = \pi(\rho C_x^2 R^2)^2 \left(\frac{2bB}{R}\,\frac{u}{C_x}\right)\left(\frac{1}{1+\phi^2}\right) f(\Gamma)\ S\left(\frac{R}{\Lambda}\right) \qquad (12)$$

where $\phi = \frac{c_x}{V}$ is the flow coefficient

B = number of rotor blades

$\frac{u}{c_x}$ = turbulence level in the approach stream.

The function $S\left(\frac{R}{\Lambda}\right)$ represents a "correlation area" and is given by

$$S\left(-\frac{R}{\Lambda}\right) = \frac{1}{B^2R^2}\int\int e^{-\frac{q}{\Lambda}}\, dr_i\, dr_j ; \qquad q = \left|\underline{r}_i - \underline{r}_j\right| \qquad (13)$$

The integration is performed from the hub radius r_h to the tip radius R.

The function, as computed by Sevik [1] for propellers having various numbers of blades and hub-to-tip ratios, is shown plotted in Figure 3. The variation of the total thrust driving the rotor with frequency is given by $f(\Gamma)$, as follows:

$$f(\Gamma) = \left(\frac{1}{1 + e\,\Gamma}\right)\left(\frac{1}{1+\Gamma^2}\right)\left(C + \frac{1-\Gamma^2}{1+\Gamma^2}\right) \qquad (14)$$

where $\Gamma = \frac{\omega\Lambda}{c_x}$

$$e = \pi \frac{2b}{\Lambda} \cos \beta$$

and

$$C = 2 \left(1 + \frac{1}{\phi^2}\right) \quad .$$

Equation (12) represents the results obtained by Sevik [1]. He proceeded to describe an experiment in which a propeller was operated in a turbulent inflow generated by a square mesh grid. The spectrum of the resulting fluctuating thrust was measured and compared to that resulting from equation (12). The same experimental apparatus and procedure is employed in the present paper, so that details will be presented later. A typical result due to Sevik [1] is shown in Figure 4. It is noted that the experimentally determined spectrum exhibits a peak whereas the computed spectrum does not.

It has been shown, Mani [4], that the radiated sound spectrum from propulsors operating in a turbulent inflow exhibits peaks centered at blade passing frequency and integer multiples. Mani [4] has shown that the width of the peaks is related to the ratio of the turbulence length scale to the blade spacing. At small values of this ratio, no peaks appear. As the value of the ratio is increased, peaks appear and become sharper. This peaking of the spectra for large values of length scale to blade spacing is due to blade-to-blade correlation of time-dependent lift as a result of the fluctuating velocity being correlated.

An attempt to incorporate blade-to-blade correlation of time-dependent lift into Sevik's theory is presented in the following. Consider the aerodynamic frequency response functions of equation (10). The subscript on this function refers to a particular spanwise element of a propeller blade and the summation is over all spanwise elements. There is a blade-to-blade phasing associated with the aerodynamic response functions which can be written as

$$H_h(\omega)^* \, H_\ell(\omega) \, e^{i\omega \frac{2\pi}{B\Omega}(n-m)}$$

where the h and the ℓ subscripts now refer to radial locations of elements only and the n and m indices refer to circumferential locations of the blades. Also, B is the total number of blades and Ω is the rotational speed of the propeller. In equation (10) a double summation is used, however, with the new aerodynamic frequency response functions a quadruple summation is needed, i.e., over h, ℓ, m and n. Using the new response functions, equation (10) for the spectrum tensor of the fluctuating thrust becomes,

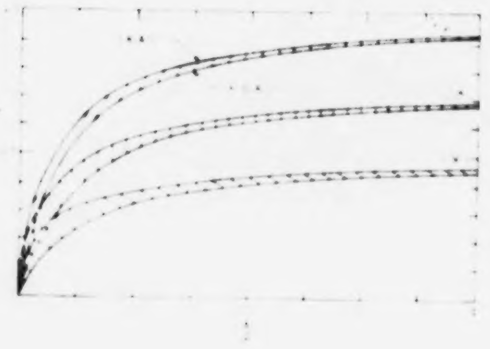

Figure 3: The "Correlation Area" Function $S(R/\Lambda)$ From Equation (13)

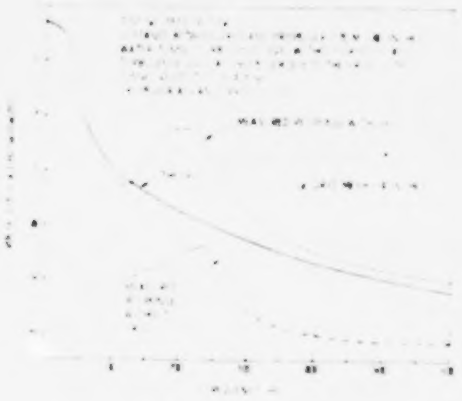

Figure 4: Power Spectral Density of the Response of a 10-Bladed, 8-inch Diameter Propeller to Turbulence Generated by a 4-inch Mesh Grid

$$G^{11}(\omega) = \sum_h \sum_\ell \sum_m \sum_n \{H_h^*(\omega)\, H_\ell(\omega) \cos^2\beta_h \cos^2\beta_\ell\, G_{h\ell}^{11}(\omega)\, e^{i\omega \frac{2\pi}{B\Omega}(n-m)}$$

$$+ \frac{1}{4} H_h^*(\omega)\, H_\ell(\omega) \sin 2\beta_h \sin 2\beta_\ell\, G_{h\ell}^{22}(\omega)\, e^{i\omega \frac{2\pi}{B\Omega}(n-m)} \} \qquad (15)$$

Let us now employ the "typical section" concept, expressed by equation (11), in equation (15).

$$G^{11}(\omega) = (2\pi\rho V_T b_T)^2 \left[\frac{1}{1 + 2\pi \frac{\omega b_T}{V_T}} \right] \sum_h \sum_\ell \sum_m \sum_n \{[\cos^2\beta_T \cos^2\beta_T\, G_{h\ell}^{11}(\omega) +$$

$$+ \frac{1}{4} \sin 2\beta_T \sin 2\beta_T\, G_{h\ell}^{22}(\omega)\,]\, e^{i\omega \frac{2\pi}{B\Omega}(n-m)} \} \qquad (16)$$

Using the definition of $G_{h\ell}^{11}(\omega)$ and $G_{h\ell}^{22}(\omega)$ from equation (10), an equation similar to equation (12) can be derived as

$$G(\Gamma) = \pi(\rho C_x^2 R^2)^2 \left(\frac{2bB}{R} \frac{u}{C_x} \right) \left(\frac{1}{1+\phi^2} \right) f(\Gamma)\, S_T \left(\frac{R}{\Lambda}, \frac{2\pi\omega}{B\Omega} \right) \qquad (17)$$

where

$$S_T \left(\frac{R}{\Lambda}, \frac{2\pi\omega}{B\Omega} \right) = \frac{1}{B^2 R^2} \sum_{n=1}^{B} \sum_{m=1}^{B} \sum_{\ell=1}^{P} \sum_{h=1}^{P} \exp\{i \frac{\omega}{\Omega} \frac{2\pi}{B} (n-m) -$$

$$- \frac{R}{\Lambda} [r_\ell^2 + r_h^2 - 2\, r_\ell r_h \cos [\frac{2\pi}{B}(m-n)]]^{1/2}\} \quad \delta r_\ell \delta r_h$$

The function $S_T \left(\frac{R}{\Lambda}, \frac{2\pi\omega}{B\Omega} \right)$ is similar to Sevik's function $S(R/\Lambda)$ except that the new function includes the effects of blade spacing and is frequency dependent. Figures 5 and 6 shows the important features of the function S_T. Figure 5 is a plot of S_T versus $\omega/B\Omega$ for various values of R/Λ for a 5-bladed propeller with a hub-to-tip ratio of 0.25. It is seen that for a particular propeller, i.e. with a given tip radius, as the turbulence length scale increases,

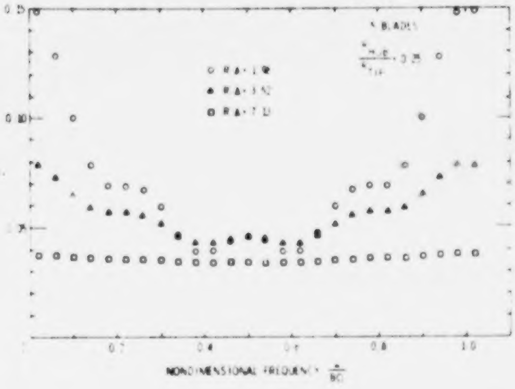

Figure 5: The Function $S_T(R/\Lambda, 2\pi\omega/B\Omega)$ Versus $\omega/B\Omega$ for Various Values of R/Λ

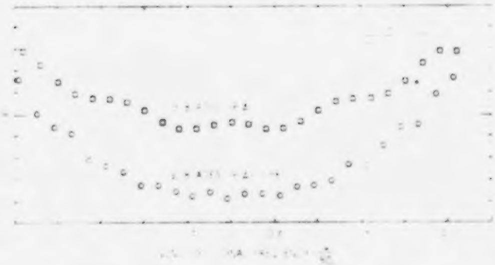

Figure 6: The Function $S_T(R/\Lambda, 2\pi\omega/B\Omega)$ Versus $\omega/B\Omega$ for Various Blade Numbers

i.e., as R/Λ decreases, the function S_T has a peak of increasing amplitude and width centered at blade passing frequency. Figure 6 is a plot of S_T versus $\omega/B\Omega$ for a 5-, and 10-bladed propeller for an R/Λ of 3.5. For propellers having the same radius, the turbulence length scale remains the same for each curve. As the blade number is increased, the peaks become sharper since the blade spacing-to-turbulence length scale ratio is decreasing. Not surprisingly, this is the same phenomenon as observed by Mani [4] for the spectrum of radiated sound, and the reason for its occurrence is the same.

Experimental Investigation

In order to investigate the time-dependent thrust response of propellers due to operation in various turbulent inflows, a series of experiments were conducted. The experiments were conducted in the 48-inch diameter water tunnel at the Applied Research Laboratory.

The time-dependent thrust due to operation in various turbulent inflows of a 5-bladed propeller was measured. The propeller used had a diameter of 8 inches. The blades had a span of 3 inches and a constant chord of 1 inch. The design static thrust coefficient based on propeller disc area is 0.183, and the advance ratio at the design thrust coefficient is 1.17.

The propeller was mounted in the water tunnel on a dynamometer. The housing contained a drive motor and drive shaft. A balance to measure time-dependent thrust was constructed internal to the shaft as shown in Figure 7. A piezoelectric crystal was used as the sensing element. It was positioned on the shaft centerline and a hemispherical piece of steel was used to transmit forces so that bending moment interactions were minimized.

The signal generated by the piezoelectric crystal had to be transmitted through slip rings. In order to maintain a good signal-to-noise ratio, the signal was conditioned by an MB N400 Line Driver System. This system converts the output of a piezoelectric transducer to a form less sensitive to noise. By dynamic calibration it was shown that the time-dependent thrust balance output is both flat with frequency over the desired range of frequencies and linear with applied force in the thrust direction. Calibration was performed in air.

Measurements of the time-dependent thrust generated by each propeller due to operation in turbulent inflows having different length scales and intensities were made. A series of square mesh grids composed of round rods was used to generate the turbulent inflows to the propellers. Since in the theoretical approach the assumption of homogeneous, isotropic turbulence has been made, an attempt to generate this type of turbulence was made by maintaining the ratio of rod diameter to mesh size of 0.2 and by always operating with the grid-to-propeller spacing greater than 20 mesh sizes. Two grids were used having mesh sizes of 2, 4, and 6 inches.

The length scales and intensities of turbulence, generated by each grid which exists in the propeller plane have been investigated by Naudascher [5]. He correlates measurements made by a large number of investigators. The values of the turbulence integral length scale and intensity for each particular grid configuration and free-stream mean velocity for which time-dependent thrust measurements were made have been based on the work of Naudascher [5].

A block diagram of the data acquisition and analysis system is shown in Figure 8. The high pass filters, Krohn-Hite, were used to remove the strong shaft rate frequency component from the signal. The filtered signal was then narrowband, 10 Hz, analyzed with a General Radio Wave Analyzer and Level Recorder on site in order to monitor the output. The signal was also recorded on magnetic tape for later analysis on a real-time analyzer, Federal Scientific Ubiquitous Analyzer. The spectra from the real time analyses are those presented here. Spectra levels were put in terms of force by using the calibration curves.

Measurement of the time-dependent thrust generated by the propeller due to operation in turbulent inflows having various length scales and intensities were made. For each test the propeller was operated at its design advance ratio of $J = 1.17$ in a free-stream mean velocity of 18 ft/sec. The length scale and intensity of the turbulent inflow was varied by using different grid sizes and by placing each grid at certain upstream locations respectively.

The measured spectra are compared to predicted spectra based on both the original theory due to Sevik [1] and the modified theory as presented in the present paper. Typical results are presented in Figures 9 through 11.

It is shown that the original theory due to Sevik [1] predicts levels that are too high compared to those of experiments. In addition, the original theory does not predict a spectrum which has peaks at blade passing frequency, as discussed previously. The theory, as developed in the present paper predicts both the levels of the spectra fairly accurately and the peaks which appear in the experimentally determined spectra.

Summary and Conclusions

The theory for the time-dependent thrust response of a propulsor to a turbulent inflow developed by Sevik [1] has been modified to include blade-to-blade correlation of time-dependent lift. With this modification, the spectra of the time-dependent thrust exhibits peaks at blade passing frequency and multiples.

Measurements of the spectra of the time-dependent thrust generated by a 5-bladed propeller due to operation in turbulent inflows with various intensities and length scales have been made.

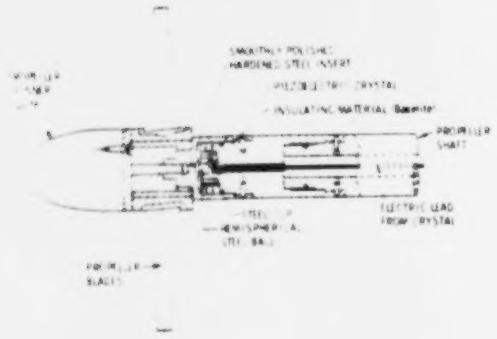
SMOOTHLY POLISHED
HARDENED STEEL INSERT
PIEZOELECTRIC CRYSTAL
INSULATING MATERIAL Bakelite
PROPELLER
SHAFT
ELECTRIC LEAD
FROM CRYSTAL
STEEL CUP
HEMISPHERICAL
STEEL BALL
PROPELLER
BLADES

Figure 7: Time-Dependent Thrust Balance

Figure 8: Data Acquisition and Reduction System

A comparison of the time-dependent thrust spectra as predicted by Sevik's [1] theory, the new theory presented in this paper, and as measured has been made. This comparison shows that the levels of the measured spectra are better predicted by the new theory presented here than by Sevik's [1] theory. In addition, the peaks in the measured spectra at blade passing frequency are predicted by the theory presented in this paper, whereas, Sevik's [1] theory does not.

Acknowledgments

[The work presented has been done under contract to the Naval Ship Systems Command.]

References

1. Sevik, M. M., "The Response of Propulsors to Turbulence," Proc. 7th Symposium on Naval Hydrodynamics DR-148, pp. 291-311, 1971.

2. Stewart, R. W., and A. A. Townsend, "Similarity and Self-Preservation in Isotropic Turbulence," Transactions of the Royal Society, Vol. 243, pp. 359-386, 1951.

3. Sears, W. R., "Some Aspects of Non-Stationary Airfoil Theory and Its Practical Application," Journal of the Aeronautical Sciences, Vol. 8, No. 3, January 1941.

4. Mani, R., "Noise Due to Interaction of Inlet Turbulence with Isolated Stators and Rotors," J. Sound Vib., Vol. 17, No. 2, pp. 251-260, 1971.

5. Naudascher, E., and C. Farell, "Unified Analysis of Grid Turbulence," J. Eng. Mch. Div., Proc. ASCE, pp. 121-141, April 1970.

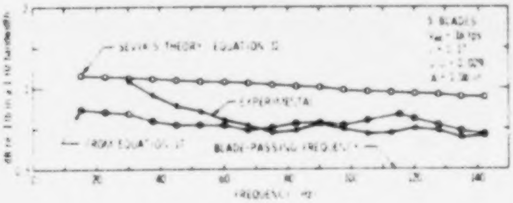

Figure 9: Power Spectral Density of the Time-Dependent Thrust Response of a 5-Bladed Propeller, u/U = 0.029, Λ = 1.06 in.

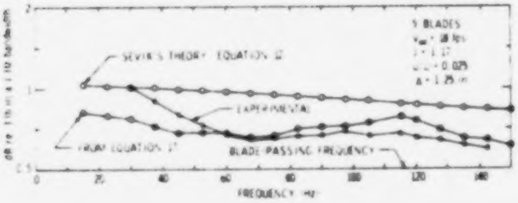

Figure 10: Power Spectral Density of the Time-Dependent Thrust Response of a 5-Bladed Propeller, u/U = 0.025, Λ = 1.25 in.

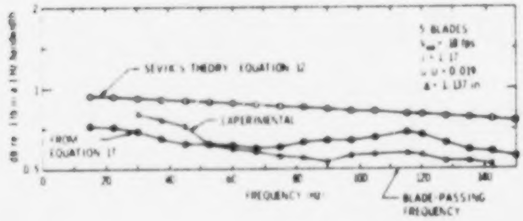

Figure 11: Power Spectral Density of the Time-Dependent Thrust Response of a 5-Bladed Propeller, u/U = 0.019, Λ = 1.137 in.

RESEARCH ON HELICOPTER-ROTOR NOISE

by

A. R. George, G. F. Homicz, Y. N. Kim,
C. Kitaplioglu, W. S. Pien, and W. R. Sears

Cornell University
Ithaca, New York

I Noise Field of High-Speed Rotor

Our research, reported earlier (References 1-3), has led us to the conclusion that the study of such phenomena as "high-speed blade slap", related to motion of rotors at substantial Mach numbers, is best carried out in the formulation originated by Ffowcs Williams and Hawkings (Ref. 4) and applied to solid bodies in arbitrary motion by Farassat (Ref. 3). In this formulation the solution of the governing equation, specifically the formula for the sound pressure $p(\underline{x},t)$ at an arbitrary observer's position $\underline{x}$ in a fluid-fixed coordinate system, is obtained by an integration, with respect to time, of contributions swept up by a contracting sphere as it collapses at the speed of sound c toward its center at $\underline{x}$, where it arrives at time t. At every instant τ during the collapse of this sphere, these contributions are found by integrating over the sphere's surface; the contributions are found wherever the sphere passes through disturbed regions of the flow or intersects with the solid bodies. This is expressed by Farassat in a formula for $p(\underline{x},t)$, valid in the far field, consisting of the sum of three definite integrals and four contributions that may arise (from "Leibniz terms") at the instants when the contracting sphere enters and leaves the body and its shock waves (if any).

In the work reported at this Symposium, Farassat's general formulas are specialized for the following specific situation:

(a) Reynolds number is assumed to be large, so that viscous effects may be neglected (except, of course, for the presence of such gross features as circulation and shock waves).

(b) Solid bodies are slender, so that second-order effects in the flow field may be neglected, except for the presence of shock waves.

(c) The angular velocity of the body, $\underline{\omega}$, is constant.

Under these assumptions, Farassat's general expression for $p(\underline{x},t)$ is much simplified. Let us consider first the contributions that are not related to shock waves; these are, for observer-positions $\underline{x}$ in the far field,

$$p(\underline{x},t) = I_1 + I_2 \tag{1}$$

where

$$I_1 = \rho_o \, \omega_N^2 \int_{\tau_1}^{\tau_2} \frac{1}{r} S(\tau) \, d\tau \tag{2}$$

$$I_2 = \rho_o \int_{\tau_1}^{\tau_2} \frac{1}{r} \oint_{\Gamma} \dot{v}_r \cot\theta \, d\Gamma \, d\tau$$

$$- \int_{\tau_1}^{\tau_2} \frac{1}{r} \frac{\partial}{\partial \tilde{R}} \oint_{\Gamma} (\rho_o v_r^2 + p)\cot\theta \, d\Gamma \, d\tau \tag{3}$$

(Symbols are defined in a table at the end of this paper.)

The integral I_1: The evaluation of I_1 [Eq.(2)] is purely a matter of kinematics. For large r (far field), the surface of the contracting sphere is approximated as a plane. Let the $\underline{x}$ coordinate system have its origin at the center of the rotor disk, and let the x_1 and x_2 axes lie in the plane of the rotor. In the special case of hovering, of course, the observer may be positioned in the plane $x_2 = 0$ with no loss of generality. The quantity $S(\tau;\underline{x},t)$ is then the cross-sectional area intercepted at time τ by a plane perpendicular to $\underline{r}$ moving with speed c toward the observer at $\underline{x}$, arriving at the observer's position at time t.

The integral I_2: Consider the factor $\cot\theta \, d\Gamma$, which appears in both integrals of I_2 [Eq. (3)]. Referring to Fig. 1, we see that the cross-hatched element of area is $d\Gamma$, the dotted element of area is $d\Gamma \cos\theta$, and $d\Gamma \cot\theta$ is the quotient of this element divided by the element $\Delta\tilde{R}$. Thus $d\Gamma \cot\theta$ is just the increment of cross-sectional area divided by $\Delta\tilde{R}$ and, for example,

$$\oint \cot\theta \, d\Gamma = \frac{\partial S}{\partial \tilde{R}} \quad (\tau \text{ fixed})$$

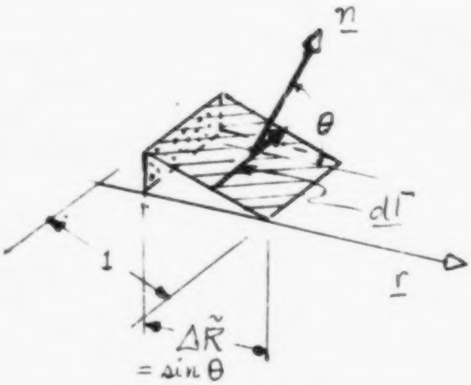

Fig. 1

There are three terms in I_2 containing the factor $\cot\theta \, d\Gamma$; consider first the terms $\oint \dot{v}_r \cot\theta \, d\Gamma$ and $\oint v_r^2 \cot\theta \, d\Gamma$. For a rotor,

$$v_r = (\underline{\omega} \times \underline{n})_1 = -\omega n_2 \tag{4}$$

$$\dot{v}_r = [\underline{\omega} \times (\underline{\omega} \times \underline{n})]_1 = \omega^2 n_1 \tag{5}$$

Consequently,

$$\oint \dot{v}_r \cot\theta \, d\Gamma = \omega^2 n_1 \frac{\partial S}{\partial \tilde{R}} \tag{6}$$

and

$$\int v_r^2 \cot\theta \, d\Gamma = - \omega^2 \frac{\partial N_3}{\partial \tilde{R}} \tag{7}$$

where N_3 denotes the moment of inertia of the intercepted cross-section; viz.,

$$N_3 \equiv \int_S \eta_2{}^2 \, dS \tag{8}$$

We also have $\oint p \cot\theta \, d\Gamma$. By means of the arguments above, we see that $p \cot\theta d\Gamma$ is equal to the $\tilde{R}$-component of the pressure force on the element of area $d\Gamma$ (Fig. 1) divided by $\Delta\tilde{R}$, so that the integral gives the $\tilde{R}$-force increment on the cross-section per unit $\tilde{R}$. In the special case of the helicopter rotor, where the loading is almost pure lift, the $\tilde{R}$-force is just a component of lift, namely (r_3/r) L; thus

$$\oint p \cot\theta \, d\Gamma = \frac{r_3}{r} \times \{\text{lift loading per unit } \tilde{R}\} \tag{9}$$

$$= \frac{r_3}{r_1} \times \{\text{lift loading per unit } \eta_1\} \tag{10}$$

and

$$\frac{\partial}{\partial \tilde{R}} \oint p \cot\theta \, d\Gamma = \frac{r}{r_1} \frac{r_3}{r_1} \frac{\partial}{\partial \eta_1} \{\text{lift loading per unit } \eta_1\} \tag{11}$$

Contribution of Shock Waves: The contribution I_3 to the far-field pressure at $\underline{x}$,t due to shock fronts is given in Ref. 3 as

$$I_3 = \int_{\tau_3}^{\tau_4} \frac{d\tau}{r} \left\{ \oint_\sigma \cot\psi \, \Delta\left(\frac{\theta T_{rr}}{\partial R}\right) d\sigma + \frac{\partial}{\partial \tilde{R}} \oint_\sigma \cot\psi \, \Delta T_{rr} \, d\sigma \right\} \tag{12}$$

Now, a shock front involves a jump ΔT_{nn}, where n denotes the normal to the front; namely

$$\Delta T_{nn} = - c^2 \Delta\rho \tag{13}$$

because $\rho u_n{}^2 + p$ is conserved across the front. Thus,

$$\Delta T_{rr} = - \cos^2\psi \, c^2 \Delta\rho \tag{14}$$

A Numerical Example: To acquire some experience in the use of this technique, Mr. W. Pien has carried out calculations of I_1 and I_2 for an idealized helicopter rotor in hover. The characteristics assumed for this rotor are as follows:

Blade profile: double-circular arc
Blade diameter/chord ratio: (40 ft)/(1 ft)
Tip Mach numbers: 0.7 and 1.0

The calculation of I_1 for an observer in the plane of the disk becomes purely kinematic. For various t it is found that the integration over τ

involves different intervals characterized by different types of intersections of the contracting sphere (plane) and the blade: first the plane intersects with the blade tip and trailing edge, then with leading and trailing edges, etc. For some values of t, depending on the tip Mach number, an interval occurs during which the plane intersects with both blade tips. The numerical calculation requires systematic determination of these intervals and, of course, different formulas for the contributions (integrands) that result. Construction of a simple mechanical model was found to be of assistance to the programmer.

Some results of Mr. Pien's computations will be presented at the Symposium. His complete report will constitute a Master's thesis at Cornell University.

II Noise Due to Acceleration of a Solid

The formula for far-field sound pressure [Eq.(1) of the preceding section of this report] contains a term explicitly involving the acceleration of the body; viz., the first term in the contribution called I_2. For a solid body in rectilinear motion it becomes

$$\rho_o \int_{\tau_1}^{\tau_2} \frac{1}{r} \dot{v}_r \, d\tau \oint_{\Gamma} \cot\theta \, d\Gamma = \rho_o \int_{\tau_1}^{\tau_2} \frac{1}{r} \dot{v}_r \frac{\partial S}{\partial \tilde{R}} \, d\tau \qquad (15)$$

It is interesting that this contribution is probably important in most cases of rotor noise, since the acceleration component v_r is appreciable. Suppose, for example, that a body accelerates uniformly; the term in question is then easily identified with the term mentioned by Lighthill (Ref. 5, p. 160).

It has occurred to us that in cases where the body's velocity is always small but its acceleration large, this may easily be the dominant source of noise — as, in fact, Lighthill also suggests. A typical example might be the sound of billiard balls colliding, which we believe is often attributed to other effects, such as vibration of the balls.

To verify this idea and to develop an experimental technique that might be used with other bodies, such as rotating helicopter blades, Mr. C. Kitaplioglu has carried out a series of measurements of acceleration-history of spheres set into motion by being struck, together with far-field measurements of the resulting sound-pressure signatures. While not professing complete disinterest in billiards, Mr. Kitaplioglu discarded the case of two spheres in collision, in favor of the case of a sphere struck by a thin rod whose opposite end is struck by a hammer — actually by a second ball, for convenience. The set-up is sketched in Fig. 2. It has the advantage that the signature resulting from the deceleration of the hammer arrives at the microphone at a distinctly later time; thus, if the noise caused by the thin rod is neglected, as seems appropriate when the rod is loaded symmetrically (axially), the signature due to the acceleration of the sphere can be identified and compared with the calculated prediction of Eq. (15).

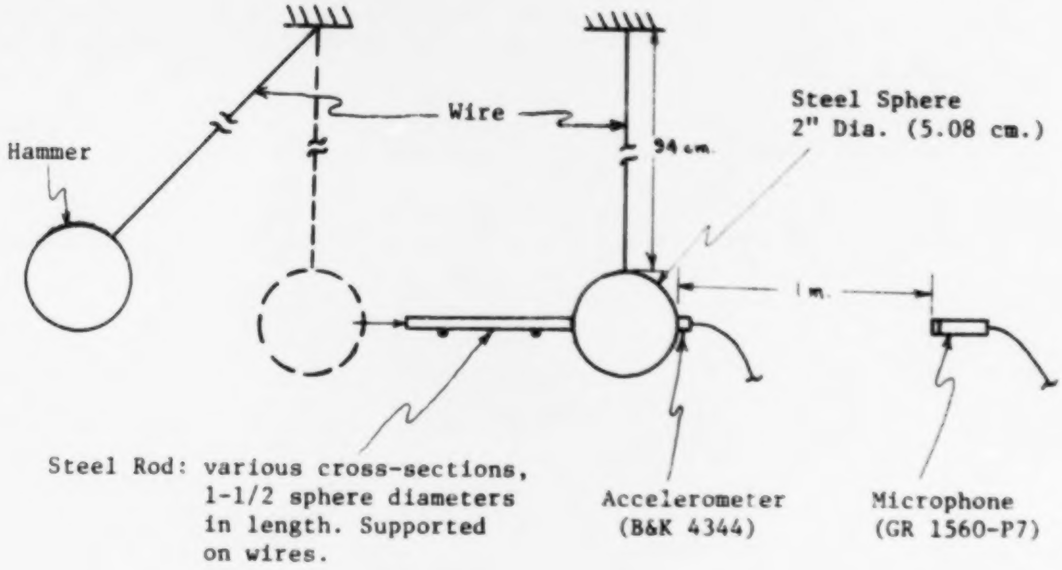

Fig. 2 Sketch showing experimental set-up for simultaneous measurement of acceleration and sound-pressure.

As shown, the sphere's acceleration was measured by a piezo-electric accelerometer silver-soldered to the "front" of the sphere. A variety of thin steel rods was used to strike the "back" of the sphere, all 1.5 sphere diameters long, but differing in cross-section; viz. 7/64", 11/64", and 1/4" solid squares, and a 11/64" hollow square.

Fig. 3 presents typical oscillograms recorded. The unfiltered acceleration record (Fig. 3a,) exhibits considerable high-frequency content, presumably due to sphere vibration and accelerometer resonance. The load actually applied to the sphere by the steel rod is, of course, unsteady, as elastic waves pass back and forth in the rod (Ref. 6); nevertheless, the above-mentioned high-frequency content is believed to be extraneous and/or unimportant in determining the sound-pressure signature received by the microphone. A filter circuit was therefore introduced in the accelerometer output, which eliminated frequencies above about 45 kHz. The lower trace in Fig. 3a is the corresponding filtered record. This record was used in connection with Eq. (15) to calculate the pressure signature plotted (solid curve) in Fig. 4. The observed microphone record of Fig. 3b is replotted (dashed curve) in Fig. 4 for comparison.

It is our conclusion that the agreement of computed and measured sound-pressure is satisfactory, at least during the first 0.2 msec of the signature. The reason for the subsequent substantial disagreement between measured and calculated pressure before $t \approx 3.3$ msec is not known; the sound due to

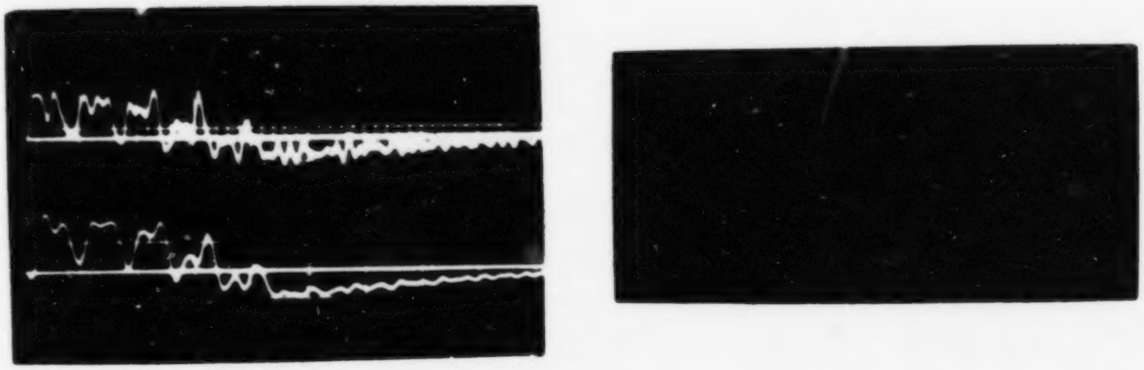

(a) Acceleration
1 V/cm., 50 μsec/cm.

(b) Sound-pressure
5 mV/cm., 50 μsec/cm.

Fig. 3 Typical oscillograms

deceleration of the hammer is estimated to arrive at the microphone at t ≈ 3.3 msec. At any rate, we conclude that the acceleration contribution does indeed dominate the signature in the far-field.

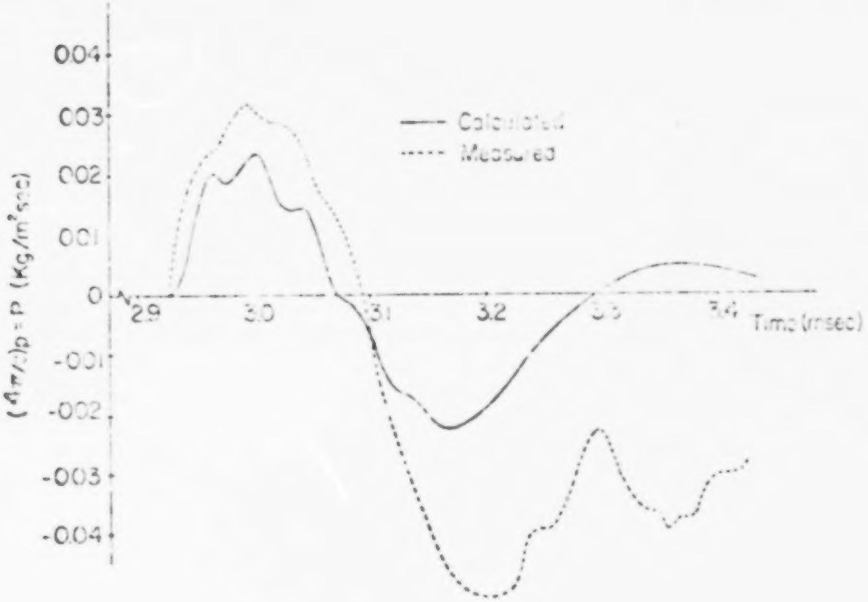

Fig. 4 Sound-pressure signature

Mr. Kitaplioglu plans to present more detailed results in a report of the Cornell University School of Mechanical and Aerospace Engineering.

III Noise Due to Random Blade Loading

A general method of analysis of noise from a rotor due to periodic or random loadings has been developed (Refs. 10-12). The analysis of noise due to inflow turbulence indicates that it is probably the major contributor to broadband noise and that some of the noise previously interpreted as discrete tones is also a result of blade-turbulence interactions.

The noise radiated by a rotor may be conveniently separated into two categories according to the type of Fourier spectrum it exhibits. The first and often most noticeable noise is discrete frequency radiation consisting of pure tones at harmonics of the blade passing frequency. This radiation is created by disturbances on the blades which repeat themselves identically with every revolution. The second category of noise is broadband radiation covering a continuous spectrum of frequencies and created by random disturbances whose behavior cannot be described deterministically. The theoretical groundwork for rotor noise studies was laid by Gutin [Ref. 7), who successfully predicted the magnitude of the tones generated at the first few blade passing harmonics by the steady loading (both thrust and torque forces) on a propeller. Later experimental results indicated that such loading could not account for the magnitude of higher harmonics observed in the spectrum. Subsequent analytical work by Lowson and Ollerhead (Ref. 8), and Wright (Ref. 9), convincingly demonstrated that a source of higher harmonic discrete tones is unsteady, but still periodic, loading on the blades. However, observed rotor-noise spectra are not made up of discrete tones but are made up of finite-bandwidth peaks and a broadband background. At lower frequencies the peaks are fairly narrow, but at higher frequencies the widths of the peaks begin to overlap, resulting in a smooth spectrum shape. Broadband loadings can be generated by the blades' passage through a turbulent (and thus randomly varying) velocity field. This may be atmospheric turbulence or turbulence due to some upstream obstruction in the flow. This is the point of view taken in our present analysis, although other broadband source mechanisms are also being investigated.

When rotor blades interact with turbulent eddies the lower frequencies are generated by the interactions with the larger eddies. These large eddies take a relatively long time to be convected through the rotor disk. As a result the nearly periodic loading due to the interactions of the eddy with the periodic blade motion is only slowly modulated by the convection, leading to a narrow-band spectrum. On the other hand, the smaller turbulent eddies, which cause the high-frequency noise, are convected rapidly through the rotor plane due to their small spatial extent. Thus the resulting loading seen by any blade is random in nature, leading to a wide-band or smooth spectrum shape at high frequencies. The details of the analysis have been presented in References 10 and 12. The general approach will be briefly reviewed below and some applications and results will be presented.

The model is that of an unducted axisymmetric rotor in hover, operating in some ambient turbulence pattern, which is assumed given. This pattern is convected through the rotor face with a mean convection velocity V_c, resulting from the rotor thrust. For simplicity each blade is initially represented by a point acoustic dipole at radius R_o. Subsequent modifications are made to account for the effects of compressible unsteady aerodynamics and distributed loading. The analysis is carried out in coordinates fixed with respect to the observer, thus taking account of blade-to-blade correlations in a rigorous manner.

Linearized small-perturbation theory is used throughout. This allows the overall problem to be divided into two sub-problems. The first is that of determining the radiated noise in terms of the loading experienced by a fixed point in the rotor disk. The second problem is the determination of this loading in terms of some given turbulence input.

We model the rotor disk as a localized planar distribution of acoustic dipole singularities which are fixed with respect to an observer positioned at $\underset{\sim}{x}$. These are switched "on" and"off" as dictated by the blades' passage over that point. Mathematically, we must solve the equation

$$\frac{1}{a_o^2} \frac{\partial^2 \rho}{\partial t^2} - \nabla^2 \rho = \frac{1}{a_o^2} \nabla \cdot \underset{\sim}{F}$$

where $\underset{\sim}{F}$ represents a force/volume, and a_o the undisturbed sound speed. Under the usual isentropic and far-field approximations, the time averaged acoustic spectrum is obtained:

$$< S(r_i,f) > = \frac{f^2}{4\rho a_o^3} \frac{r_i \ r_j}{r^4} \iiint d^3\eta < P_{L_i L_j} (\eta, - \frac{f}{a_o} \hat{r}_i, f) >$$

where $P_{L_i L_j}$ is the generalized four-dimensional cross-spectral density of the load fluctuations L_i as viewed in fixed coordinates. These fluctuations are then expressed in terms of angle-of-attack variations due to the turbulent upwash. Linearized aerodynamics is used, and the influence of horizontal perturbation velocities in the plane of the rotor is neglected. Both are reasonable approximations for thin airfoils away from stall. Because of the assumed linearity, the thin airfoil response to the mean (harmonic) and random components of the angle of attack may be separated. The turbulence pattern is convected through the rotor plane with velocity V_c, which we assume to be constant across the disk. We also employ Taylor's hypothesis, i.e., that the turbulence pattern remains frozen in the convected reference frame as it passes through the rotor.

Although the analysis can be extended to any turbulent spectrum the present results assume a homogeneous isotropic upwash spectrum of the Dryden form. Recently experiments by Hanson (Ref. 13) have shown that inflow turbulence can be quite anisotropic due to the distortion of the inlet flow. We intend to modify our analysis to account for these effects.

As discussed in detail in References 10 and 12, it was found that a reasonable approximation to the unsteady, compressible, airfoil lift response could be obtained for each turbulent wave number by averaging the chordwise and spanwise wave-number components over a blade revolution and using Osborn's compressible extension of the two-dimensional Sears function (Ref. 14).

For any given wavenumber disturbance it can be shown that the effective correlated length of the spanwise loading is of the order of the wavenumber. Thus the spanwise loading is modelled as independently radiating, uncorrelated strips of this width. It was found that chordwise-loading effects are highly directional, having maximum effect in the rotor plane but that these effects are not very important for typical helicopter-rotor applications. Thus chordwise-loading effects analysis was not included in our calculations.

The final expression for $< S_1 >$, the one-sided acoustic spectrum, for a B-bladed rotor with chord c and radius b , at angular velocity Ω, in turbulence with integral scale Λ, is

$$\frac{< S_1 >}{\rho_o a_o^3 \Omega^{-1} M_t^2 (R_T/r)^2} = \frac{16\pi^4 B^2 M_o^4}{1 - M_o^2} \left(\frac{bc}{R_T^2}\right)^2 \left(\frac{R_T}{R_o}\right)^2 \left(\frac{\Omega\Lambda}{V_c}\right)^3 \left(\frac{f}{\Omega}\right)^2 \cdot$$

$$\int_{\xi_{MIN}}^{\infty} \lambda\xi \; \xi \sum_{n=n_1}^{n_2} \sum_{\ell=-\infty}^{\infty} E_{INT} \, E_{\ell} \, E_{TURB} \, E_{AERO} \, E_{SPAN}$$

$$\xi_{MIN} = \frac{\left|\frac{f}{\Omega} - \hat{n}B\right|}{(V_c/\Lambda\Omega)} \quad , \quad n_{1,2} = \frac{\frac{f}{\Omega} \mp (V_2/\Lambda\Omega) \; \xi}{B}$$

where

$$E_{INT} = \left[\cos\mu\sin\phi - \frac{(nB-\ell)\sin\mu}{M_o(f/\Omega)}\right]^2 J_{nB-\ell}^2 \left(M_o \frac{f}{\Omega} \cos\phi\right)$$

$$E_{\ell} = J_{\ell}^2 \left(\frac{M_o}{M_c}\sqrt{(V_c/\Lambda\Omega)^2 \xi^2 - (f/\Omega - nB)^2}\right)$$

$$E_{TURB} = \frac{(V_c/\Lambda\Omega)^2 \; \xi^2 - (f/\Omega - nB)^2}{(1 + 4\pi^2 \; \xi^2)^3}$$

$$E_{AERO} = \frac{J_o^2(M_o^2\tilde{k}_T/1-M_o^2) + J_1^2(M_o^2\tilde{k}_T/1-M_o^2)}{1 + (2\pi/1-M_o^2)\tilde{k}_T}$$

$$E_{SPAN} = (1 + \tilde{k}_c b/\pi c)^{-1}$$

M_o, M_c, and M_t are the rotational, convective, and r.m.s. turbulence Mach numbers, respectively. $\xi = \nu\Lambda$ is the dimensionless turbulence wave number magnitude; R_T and R_o represent the tip radius and effective radius of rotation of the point dipoles, respectively. The notation $\hat{n}B$ denotes the BPH nearest to f/Ω. The range of n is over all integers lying within the given limits. $\tilde{k}_T(\xi)$ and $\tilde{k}_c(\xi)$ are averaged nondimensional turbulent wave numbers.

This expression has been numerically evaluated for several cases of interest. First, however, some simple implications of the analysis are evident. The noise scales directly with the turbulence intensity $M_t{}^2$ and as the fourth power of the blade Mach number M_o. Thus for fixed $(V_c/\Lambda\Omega)$ the velocity dependence is not the traditional M_o^6, unless the turbulent velocities scale with the blade velocities. This is not the case for the inflow of atmospheric turbulence. It may be the case for a rotor in recirculation, for turbulence from the wakes of other blades (Ref. 15), or in turbulent tip vortices (Ref. 16). Note also that the radiation does not scale with blade loading except, quite indirectly, through its influence on V_c. However, the radiation is proportional to blade-area squared (neglecting unsteady aerodynamic effects). This is because turbulent angle-of-attack fluctuations give lift fluctuations independent of existing steady loads but proportional to blade area.

The shape of the spectrum can be inferred from simple considerations. Assume a turbulence component or "eddy" of size λ. For blade velocity V_o, large compared to the convection velocity V_c, the blade loading fluctuations due to the turbulent component will occur at a frequency $f \approx V_o/\lambda$. Including the Doppler effect, this will radiate at acoustic frequencies up to $f \approx V_o/\lambda(1-M_o\cos\theta)$. As the eddy will be convected through the rotor plane with velocity V_c, the bandwidth Δf of the loading and radiation will be approximately $\Delta f \approx V_c/\lambda$. The spectrum will become smooth when Δf is of order of the frequency spacing $B\Omega$ between blade-passing harmonics. Thus the spectrum will be smooth for $V_c/\lambda \approx B\Omega$. Using this as an estimate for λ, the frequency at which the radiation becomes broadband is

$$f \approx \frac{B(V_o/V_c)\Omega}{1 - M_r}$$

An overall parameter governing the spectrum is that associated with λ of order Λ, the turbulence integral scale. Thus if $V_c/\Lambda\Omega$ is small, narrow sidebands appear at low frequencies, whereas for large $V_c/\Lambda\Omega$ the spectrum will be smooth everywhere. These considerations are easily extended to anisotropic turbulence.

In comparing the present analysis to experimental measurements several difficulties arise. The most important is that many parameters needed for the calculations were not measured in the experiments. This forced us to estimate quantities such as turbulent intensities, and integral scales. In addition the experiments generally contain other additional noise sources such as steady inlet flow distortion, tail rotor noise, etc. Comparison to the experiments of Lowson et al. on a low speed fan (Ref. 16), to those of Johnson and Katz on a full scale helicopter (Ref. 17), and those of Leverton on an inverted rotor (Ref. 18) are given in Figures 5 through 7. The values used for the parameters in the theory are indicated on the figures. Complete discussions of the comparisons have been given in References 7 and 9. Agreement is quite good considering the questionable reliability of the estimated turbulence input data. The theory

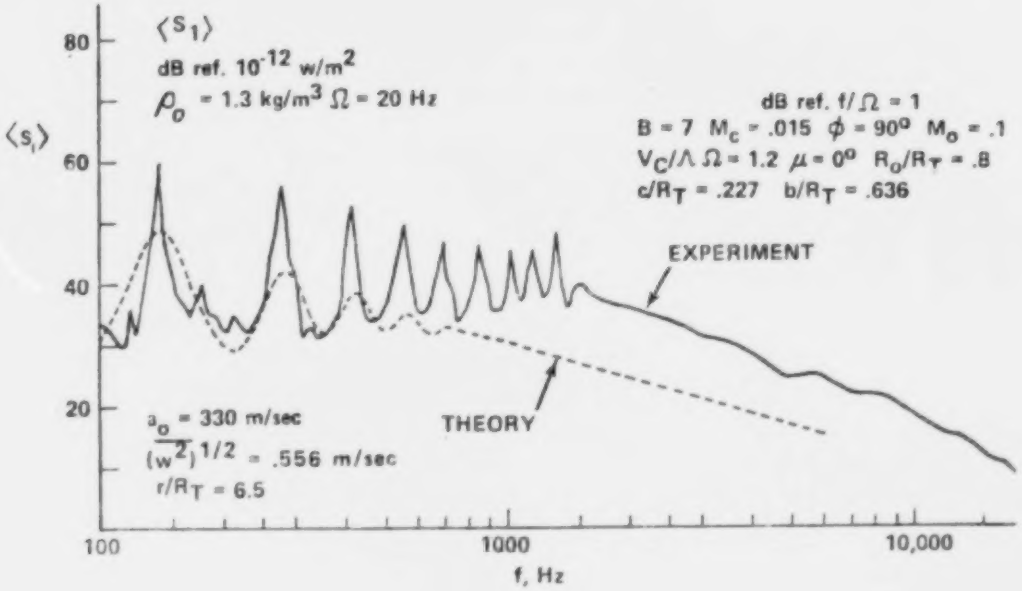

Figure 5. Comparison between theory and low speed fan data (Ref. 16).

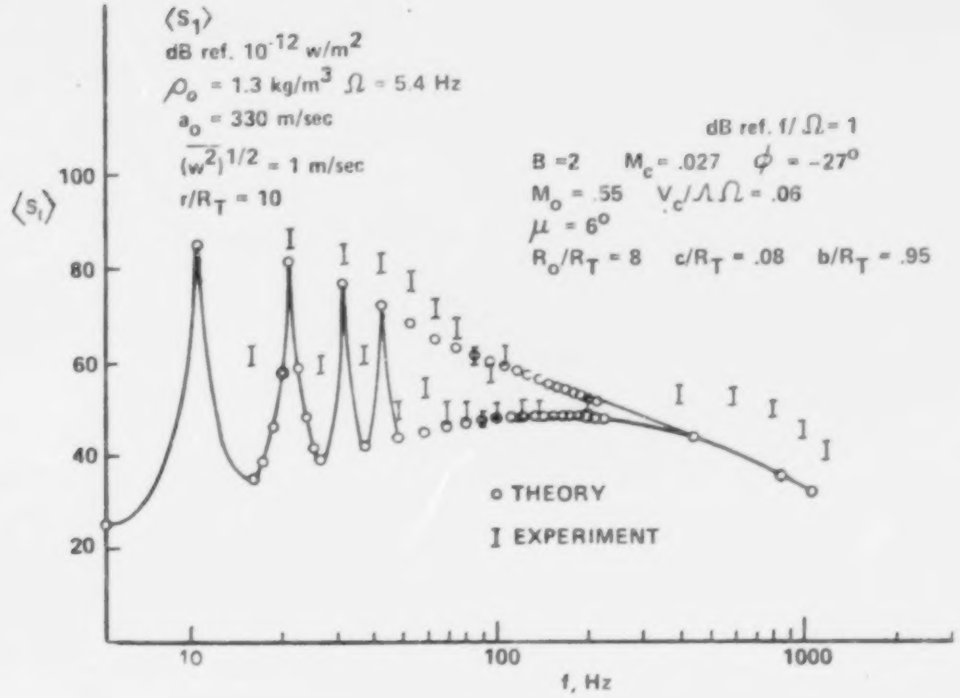

Figure 6. Comparison between theory and full scale helicopter data (Ref. 17).

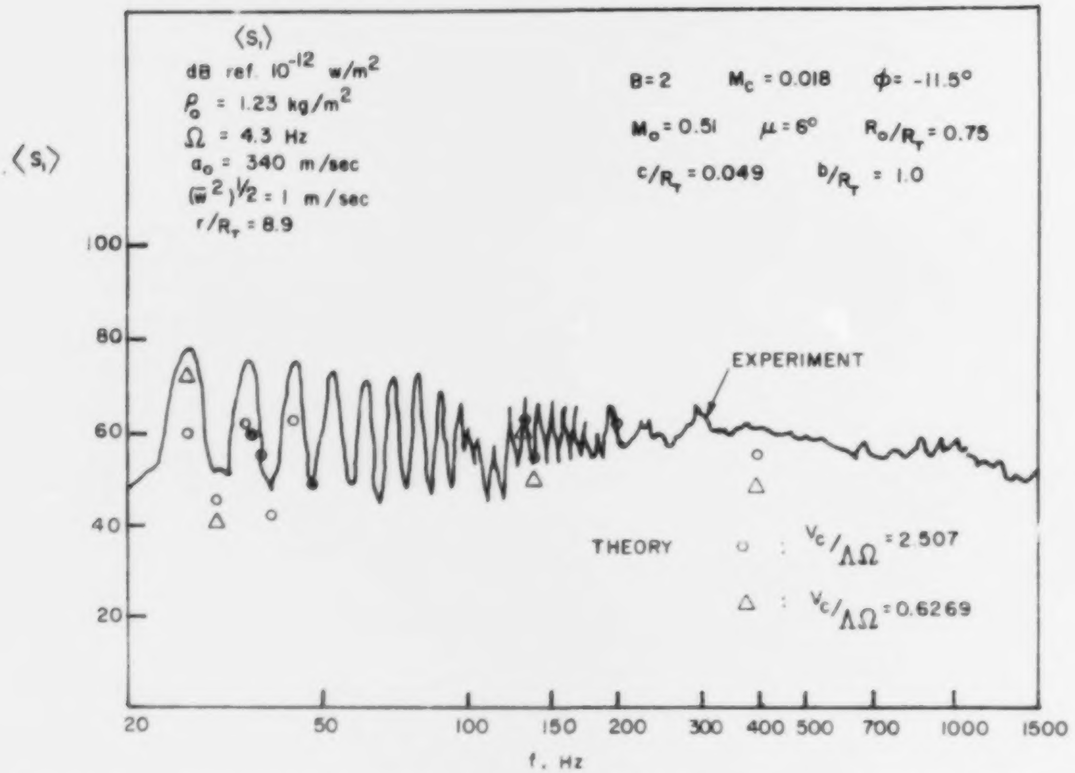

Figure 7. Comparison between theory and data from inverted rotor on tower (Ref. 18).

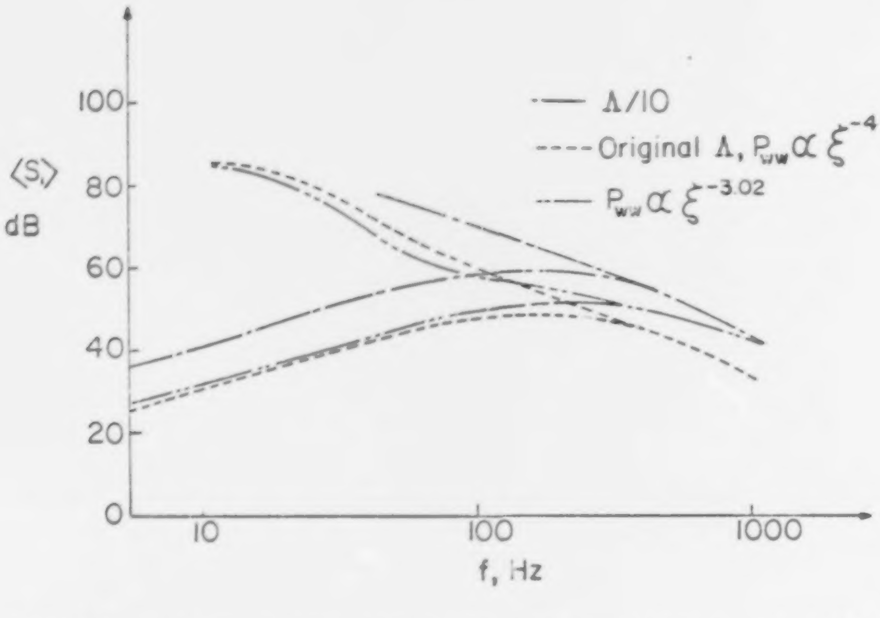

Figure 8. Effect of turbulent scale and spectrum shape on acoustic spectrum envelopes.

tends to fall below the experimental data, but this may be ascribed to poor modelling of the turbulence, or to additional noise sources at high frequencies. It is also true that the absolute levels of the factors accounting for unsteady aerodynamics and distributed loading are only order of magnitude estimates. The fact that reasonable agreement was obtained with data from both a small low speed fan and from full-scale helicopter rotors operating under quite different conditions makes a strong case for inflow turbulence/blade interaction as a significant source of broadband rotor noise, at least in the low to mid-frequency range. In addition the analysis shows that inflow turbulence can result in a highly peaked noise spectrum at low frequencies. Thus some of the noise previously attributed to discrete tones from periodic loading may actually be due to turbulent loading. Indeed, it is difficult to imagine the physical origin of any purely harmonic load variation mechanism for a hovering helicopter rotor.

Our present efforts are directed toward the development of a simplified model of the high frequency broadband noise and toward calculating the effects of inlet flow distortion on noise due to atmospheric turbulence. We are also working toward an analysis of the noise due to self interaction between blade tips and their turbulent tip vortices.

In Reference 10 a study was made of how variations in one or more of the operating parameters used as input for the theory would change the predicted noise output of a rotor. Such trends serve as guidelines to the design engineer trying to effect a noise reduction; only the most salient points are presented here.

1. In addition to the major role it plays in determining spectral shape, the tone broadening parameter ($V_c/\Lambda\Omega$) also influences acoustic levels, the broadband noise increasing with increasing ($V_c/\Lambda\Omega$). Since this ratio may be written as

$$\frac{V_c}{\Lambda\Omega} = 2\pi \; \frac{M_c}{M_o}\,\frac{R_o}{\Lambda}$$

one should work toward a lightly-loaded rotor operating in large scale non-uniformities (see also 2-5 below).

2. As can be seen from figure 8, decreasing either the turbulence integral scale or the turbulent decay rate at high wave numbers while holding the rotor parameters constant leads to increased high frequency noise, as one would expect.

3. For a given thrust level, lowering the rotational Mach number is a very efficient way to decrease the radiation as shown in Figure 9.

4. For a given rotational Mach number, a change in convection Mach number (and hence indirectly the thrust) wields much less influence on acoustic levels, particularly at high frequencies.

5. The effects of blade number B and chord c are compared in Figure 10 for a constant thrust.

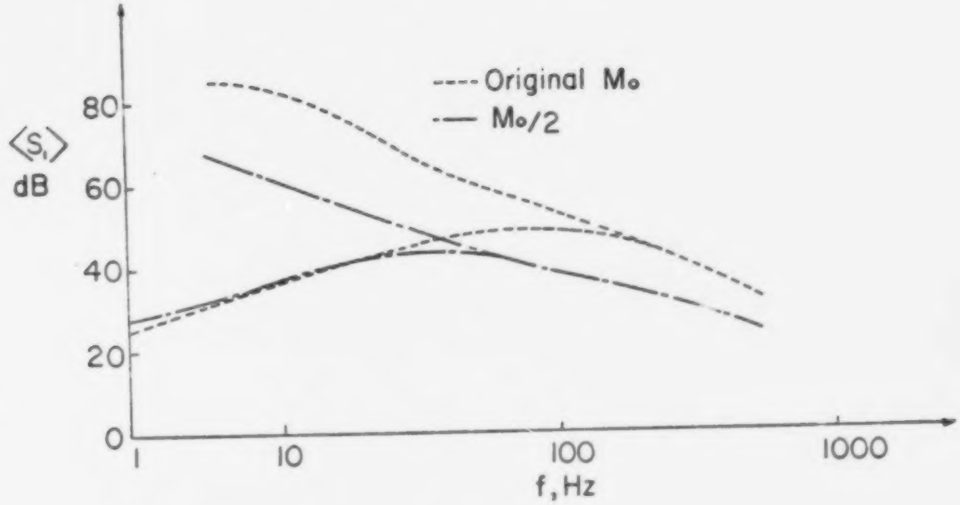

Figure 9. Effect of change in rotor speed at constant thrust on acoustic spectrum envelopes.

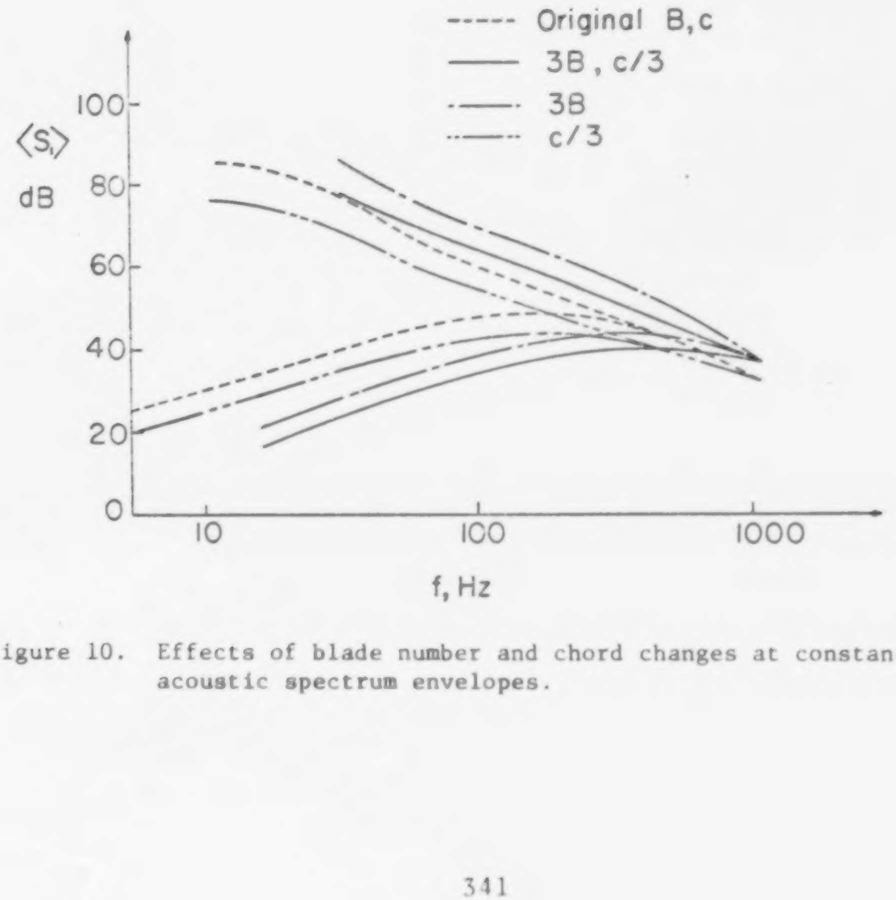

Figure 10. Effects of blade number and chord changes at constant thrust on acoustic spectrum envelopes.

An increase in blade number is often quoted as a means of reducing the low frequency BPH Gutin signature. However, this tends to raise the high frequency broadband content roughly in proportion to B as more blades are present for turbulence induced loads to act upon.

A decrease in chord length with thrust held constant through a pitch increase will lower the low frequency levels, with practically no effect at high frequencies; the latter results because of the competing influences of blade area effect and unsteady aerodynamics ($E_{AERO} \propto c^{-2}$ at high frequencies). For typical helicopter conditions, this conclusion should be only slightly affected by chordwise distributed loading considerations.

This research was supported by the U.S. Army Research Office, Durham, under contract DAHC04-74-C-001.

References

1. Farassat, F.,"The Sound From Rigid Bodies in Arbitrary Motion,"Ph.D. Thesis, Cornell University, 1973. (University Microfilms, Ann Arbor, Mich.)

2. Farassat, F., and Sears, W. R. "The Far-Field Sound of Rigid Bodies in Arbitrary Motion", Proc. Interagency Symposium on Univ. Research in Transportation Noise,Vol I, pp. 259-272, Stanford 1973.

3. Farassat, F., "The Acoustic Far-Field of Rigid Bodies in Arbitrary Motion", J. Sound and Vib. 1974.

4. Ffowcs Williams, J. E., and Hawkings, D. L., "Sound Generation by Turbulence and Surfaces in Arbitrary Motion", Phil. Trans. Roy. Soc. London (A). Vol. 264, pp. 321-342, 1969.

5. Lighthill, M.J., "Sound Generated Aerodynamically" (The Bakerian Lecture, 1961). Proc. Roy. Soc. London (A) Vol. 267, pp. 147-182, 1962.

6. Burr, A. H., "Longitudinal and Torsional Impact in a Uniform Bar with a Rigid Body at One End", J. Applied Mechanics, June 1950, pp. 209-217.

7. Gutin, L., "On the Sound Field of a Rotating Propeller", NACA TM 1195, 1948.

8. Lowson, M.V. and Ollerhead, J. B., "A Theoretical Study of Helicopter Rotor Noise", J. Sound and Vibration, 9, 197-222, 1969.

9. Wright, S. E., "Sound Radiation From a Lifting Rotor Generated by Asymmetric Disc Loading", J. Sound and Vibration, 9, 223-240, 1969.

10. Homicz, G. F., "Broadband and Discrete Frequency Noise Radiation From Subsonic Rotors", Ph.D. Thesis, Cornell University, 1973.

11 Homicz, G. F. and George, A. R., "Broadband Radiation From Rotors in Turbulent Flow", Proc. of Interagency Symp. on Univ. Res. in Transportation Noise, sponsored by U. S. Dept. of Transportation and Stanford Univ., Stanford, California, 1973.

12. Homicz, G. F., and George, A. R., "Broadband and Discrete Frequency Radiation from Subsonic Rotors", submitted for publication, 1974.

13. Hanson, D. B., "The Spectrum of Turbomachine Rotor Noise Caused by Inlet Guide Vane Wakes and Atmospheric Turbulence", Report HSER 6191, Hamilton Standard Division, United Aircraft Corporation, Windsor Locks, Conn.,1973.

14. Osborne, C., "Unsteady Thin Airfoil Theory for Subsonic Flow", AIAA J., 11, 205-209, 1973.

15. Scheiman, J., Hilton, D. A., and Shivers, J. P., "Acoustical Measurements of the Vortex Noise for a Rotating Blade Operating With and Without its Shed Wake Blown Downstream", NASA TN D6364, 1971.

16. Lowson, M. V., Whatmore, A., and Whitfield, C. E., "Source Mechanisms for Rotor Noise Radiation", Loughborough Univ. of Tech. Rept. TT 7202, 1972.

17. Johnson, H. K., and Katz, W. M., "Investigation of the Vortex Noise Produced by a Helicopter Rotor," USAAMRDL Tech. Rept. 72-2, 1972.

18. Leverton, J. W., "The Noise Characteristics of a Large 'Clean' Rotor", J. Sound and Vibration, 27, 357-376, 1973.

Nomenclature

a_o	speed of sound.
B	blade number.
b	blade span.
c	chord. (Section III)
c	undisturbed speed of sound.(Section I)
$\underset{\sim}{F}$	force/volume.
f	acoustic frequency, Hz.
I_1,I_2,I_3	integrals, Eqs. (1)-(3), (12).
k	acoustic wave number $f/a_o = \lambda^{-1}$.
$\tilde{k}_c,\tilde{k}_T$	averaged reduced aerodynamic frequencies.
M_o	rotational Mach number at effective radius, $2\pi\Omega R_o/a_o$.
M_c	axial convection Mach number, V_c/a_o.
M_t	r.m.s. turbulence Mach number.
$\underline{n} = (n_1,n_2,n_3)$	unit vector normal to surface.
N_3	moment of inertia of intercepted area (Eq. (8)).
$P_{L_iL_j}$	loading cross spectral density.
p	pressure
$\underline{r} = (r_1,r_2,r_3)$	position vector from arbitrary point to observer's position $\underline{x}$.

$\hat{\underline{r}}$	unit vector $\underline{r}/r$.
R,R	defined by $\partial/\partial R = -\hat{r}_i\ \partial/\partial r_i$, i.e., derivative in $\underline{r}$ direction (toward observer). When quantity differentiated is inside the integral over $d\Omega$ or $d\Gamma$, the symbol R is used; when outside, the symbol $\tilde{R}$.
R_o	effective radius of rotation in point dipole model.
R_T	rotor tip radius.
$\langle S(x,f)\rangle$	acoustic spectral density.
$\langle S_1(x,f)\rangle$	one-sided acoustic spectral density, $f > o$.
S	area intercepted by intersection of contracting sphere (plane) and body.
t	time.
T_{ij}	Lighthill's stress tensor, $\rho u_i u_j + \delta_{ij}\ (p-c^2\rho)$.
T_{nn}	component of T_{ij} where $\underline{n}$ = normal to shock front.
$\underline{u} = (u_1,u_2,u_3)$	fluid velocity.
$\underline{v} = (v_1,v_2,v_3)$	body velocity.
v_r	component of $\underline{v}$ in direction of $\underline{r}$.
$\dot{v}_r$	time rate of change of v_r.
V_c	axial convection velocity.
V_o	rotational speed, $2\pi\Omega R$.
w	vertical component of random turbulent velocity.
$\underline{x}$	position vector of observer.
$\Delta(\ )$	jump of quantity ( ) across shock front.
$\Gamma, d\Gamma$	Γ denotes curve of intersection of contracting sphere (plane) and body; $d\Gamma$ is element of arc length of Γ.
$\eta = (\eta_1,\ \eta_2,\ _3)$	position vector of point of integration.
θ	angle between $\hat{\underline{r}}$ and $\underline{n}$ (normal to body surface)
Λ	turbulence integral scale.
μ	blade lift inclination angle from vertical.
$\underline{\nu}$	turbulence wave number vector.
ξ	dimensionless wave number.
ρ	fluid density.
ρ_o	density of undisturbed fluid.
$\sigma, d\sigma$	σ denotes curve of intersection of contracting sphere (plane) and shock front; $d\sigma$ is element of arc length of σ.
τ	time (variable of integration).
$\tau_1,\ \tau_2$	values of τ at which contracting sphere (plane) first enters and last leaves the body and/or disturbed flow.

τ_3, τ_4	values of τ at which contracting sphere (plane) first enters and last leaves the shock front.
ϕ	observer elevation angle.
ψ	angle between $\hat{\underline{r}}$ and normal to shock front
ω	angular velocity of body
ω_N	component of $\underline{\omega}$ perpendicular to $\underline{r}$ and lying in plane of $\underline{\omega}$ and $\underline{r}$; thus $\omega_N^2 = \omega^2 - (r_i \omega_i)^2$.
$\Omega, d\Omega$	Ω denotes surface of contracting sphere (plane) intercepted by body or flow; $d\Omega$ denotes element of this area (Part I).
	shaft rotational frequency (Part III).

COMPRESSOR AND FAN ROTOR WAKE CHARACTERISTICS

by

B. Lakshminarayana and R. Raj

Department of Aerospace Engineering
The Pennsylvania State University
University Park, Pa. 16802

ABSTRACT

The objective of this research is to study, both analytically and experimentally, the characteristics of the wake behind a compressor and fan rotor. The analytical approach would include the approximate solution of the equations of motion as well as numerical solution of coupled equations of motion and turbulent energy equation. The former model employs several approximations consistant with the physics of the flow through an axial compressor or fan blade row. The latter approach, commonly referred to as "turbulent field method" utilizes turbulent energy equation (along with the mean equations of motion), simplified using assumptions for Reynolds stress, pressure velocity correlation and dissipation. The equations will be solved numerically. It is anticipated that these solutions will lead to an analytical model, which includes the rotor flow and blade geometry as well as turbulence characteristics of the flow.

The experiment will be carried out at the exit of a compressor and fan rotor using a rotating triaxial probe and conventional probes, mounted on a rotating traverse gear operated by two step motors. The experimental program would include the measurement of mean velocities, turbulence quantities across the wake at various radial locations and downstream stations. The ultimate objective is to provide a rotor wake model, based on theoretical analysis and experimental measurements, which the acousticians could use in predicting the discrete as well as broadband noise generated in a fan rotor. This investigation will also be useful to turbomachinery aerodynamists in evaluating the aerodynamic losses, efficiency and optimum spacing between a rotor and stator in turbomachinery.

This paper is intended to present our method of approach. In addition, an attempt will be made to summarize briefly the progress achieved so far.

INTRODUCTION

Compressor and fan rotor wakes play a significant role in the study of improved blade design, noise generating mechanism and flow induced vibrations in rotating fluid machinery. Because of the complicated nature of the problem, compressor and fan rotor wakes still continue to be one of the least understood problems in rotating fluid machinery. The complications involved in the analytical and experimental investigations are many. Firstly, the flow field behind the rotor is highly three-dimensional and turbulent. Secondly, the flow field behind the rotor is a function of a number of parameters such as: radial and axial pressure gradients, speed of rotation, incidence, solidity, hub/tip ratio, blade geometry, blade outlet angle, free stream turbulence and the distance from the trailing edge. Both the boundary layer that develops on a rotating blade and the wakes that result from them are three dimensional in nature. There are centrifugal and coriolis forces, which in addition to pressure gradients (especially in the radial direction) and viscous forces, make the direction of the flow inside the boundary layer and wake different from the flow outside, thus forming a three dimensional wake as shown in Fig. 1.

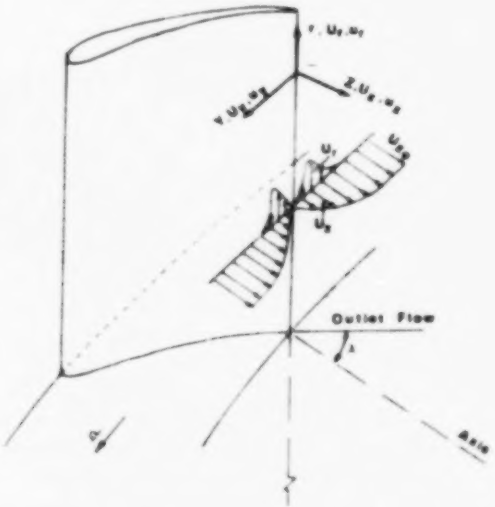

FIG 1 NATURE OF COMPRESSOR ROTOR WAKE AND NOTATIONS USED

Knowledge of the effects of coriolis and centrifugal forces on the mean as well as turbulent quantities is an essential prerequisite for the analysis of the rotor wake. In addition, it is essential to know the three dimensional turbulent boundary layer characteristics at the trailing edge of the rotor blade. Considerable advance has been made in the study of the boundary layer growth in a rotating channel (References 1 and 2) and the blade (Reference 3).

Due to rotor wake, the subsequent stator will see time dependent incident flow. A knowledge of the mean and turbulence properties in the rotor wake is essential not only in predicting the periodic and random unsteadiness in the stator blade pressures but also the consequent noise generated. Thus, an adequate knowledge of the rotor wake characteristics is essential not only for the prediction of the aerodynamic and acoustic performance of the compressors but also in building more efficient and quieter compressors or fans used in jet engine, and propulsors used in underwater application.

The classical analysis of blade passing frequency (BPF) noise in axial flow fans, compressors, and propulsors due to defect in mean velocities is well-known. A random source such as turbulence in the wake is suggested as the cause of the 'fluttering' signal at BPF as opposed to 'steady and piercing' signal (4). The sound spectrum due to wake turbulence is likely to depend on the kinetic energy, length scale and velocity correlations of the turbulence wake. Sofrin and McCann (4) examined the noise due to inlet wakes as a function of axial spacing between the rotor and stator. As the axial spacing is increased, the customary fall off in noise with spacing is noticed, but the fall off leveled off after certain spacing Upon complete removal of the wake, however, the noise dropped off abriptly. These observations by Sofrin and McCann indicate that the turbulence level in the wake has appreciable influence on the sound field.

Downstream of the trailing edge, a mixing takes place between the wake and the free stream flow, and the wake is eventually reenergized through turbulent mixing. The loss of energy due to complete mixing represents the "mixing loss." The present day analysis used for calculating the wake mixing loss is based on semi-theoretical expressions derived mainly from isolated airfoil experiments. Even with this crude model, the mixing losses are found to be a considerable percentage of total viscous losses.

Due to complexity and economic reasons, it is not feasible to study the effect of all the parameters on which compressors or fan wake depends in a compressor or fan setup. However, some of the parameters on which compressors or fan rotor wakes depend can be easily simulated, theoretically and experimentally, in a cascade. Unfortunately, the literature survey carried out on two and three-dimensional wakes indicated that even a two-dimensional model for predicting the wake characteristics close behind a cascade of blades was not yet developed and most aerodynamists and acousticians still use the isolated airfoil wake model developed by Silverstein and Katzoff (5) for prediction of mixing losses and noise in compressors.

Realizing the above stated difficulties an extensive cascade near wake study (theoretical and experimental) was undertaken and a cascade near wake model was developed for prediction of mean and turbulence quantities (6). The cascade study has given a thorough insight into the behavior of structure of turbulence in the near, asymmetric wake of a cascade. The concepts of self-preservation, variation of eddy viscosity and decay rate of turbulence quantities were also investigated. The effect of solidity and incidence on wake centerline velocity and the pressure gradient was also investigated. Cascade wake investigation will be very useful and helpful in constructing a theoretical model for the rotating wake. A brief summary of this investigation is given in the next section.

The effect of remaining parameters such as rotation, curvature, swirl and the associated pressure gradient and spanwise effects, which cannot be simulated in a cascade, will have to be investigated in a compressor setup. In order to understand the wake development (theoretically and experimentally) more clearly, it is essential to carry out similar analytical and experimental investigation in a fan or compressor rotor. This is the objective of the research briefly described in this paper. The present and future investigations is directed towards the development of a rotor blade wake model and to study the nature and magnitude of mean velocities and turbulence quantities (such as intensity, velocity correlations, length scales etc.) in a rotor wake. In addition, it is proposed to study the rotor wake characteristics with different inlet turbulence levels.

CASCADE WAKES

A systematic investigation of the characteristics of the cascade wake was carried out and the results are reported in reference 6. The mean velocities, turbulence intensities and stresses across the wake were measured at various axial locations of the cascade at the Applied Research Laboratory. These measurements were repeated at several inlet incidences. The important conclusions of this investigation are:

(a) The wake is asymmetrical and when two different length scales are used, one for each side of the wake, mean velocity profiles become symmetrical about the wake center line. The mean velocity profiles are of the type $(1-\eta^{3/2})^2$, where $\eta = y/L_{os}$ or y/L_{op}, and L_{os} and L_{op} are length scales on the suction side and pressure side of the wake respectively.

(b) The wake edge velocity (U_e) changes continuously, giving rise to slower decay of wake center line than an isolated aerofoil. The wake center line velocity (U_e) is well represented by

$$\frac{U_c}{U_e} = 1 - \frac{1.25\ (c_d)^{1/2}}{(z/c + 0.02)^{(1/2)(1-m)}} \qquad (1)$$

where C_d is the profile drag coefficient, z is the streamwise distance from the trailing edge and m is the exponent in the free stream velocity variation ($U_e \sim Z^{-m}$).

(d) The width of the wake is given by

$$\frac{b - b_o}{c\ C_d^{1/2}} = 1.35\ (z/c + z_o/c)^{0.58} \qquad (2)$$

where b is the wake width, b_o is the wake width at the trailing edge, c is the chord length. Z_o is the virtual origin.

(e) The turbulence intensities are found to be higher than those of a flat plate wake and the decay in maximum longitudinal turbulence intensity is given by

$$I_{u\,max}\ \% = 8\ (z/c + z_o/c)^{-0.35} \qquad (3)$$

(f) The maximum shear stress at any location is given by

$$[\tau/\rho U^2]_{max} = 0.005\ (z/c + 0.05)^{-0.72} \qquad (4)$$

(g) The effect of solidity and incidence is to change the drag coefficient and the wake edge velocity and equation 1 thus takes these effects into consideration.

These investigations indicate that the cascade wake is appreciably different from those of an isolated aerofoil. Equations 1-4 should thus enable the acousticians to attempt a better prediction of the unsteady forces and the noise generated due to rotor-stator viscid interaction.

ROTOR WAKE

As indicated earlier, the rotor wake is three dimensional and the three dimensionality induced by coriolis and centrafugal forces, and radial pressure gradient cannot be simulated in a cascade. Hence we have undertaken a systematic study of the rotor wake in a real environment. The mean velocities and turbulence properties will be predicted using equations of motion in rotating coordinates and the measurements will be taken at the exit of a compressor and fan in a rotating (relative) frame of reference.

Analytical Investigation

The objective of the analytical investigation is to predict the mean properties of the wake at various radial and downstream locations of the rotor. The characteristics of the rotor wake is a function of the properties of the blade row (solidity, stagger angle, lift coefficient, hub/tip ratio etc.) as well as flow properties (Reynolds number, flow coefficient, inlet turbulence properties etc.). In addition, the wake characteristics is a function of the coordinates, with variation in radial as well as downstream locations. The governing equations, which include all these variables, are extremely difficult to solve. In view of this, it is essential to invoke practically realistic assumptions and derive simpler solutions of the wake equations. The theoretical solution can then modified and extended continuously from the information derived from the measurements. The prediction scheme can be catagorized, in order of complexity, as follows.

(a) Approximate Solutions: In this method, the concept of eddy viscosity is invoked to replace the turbulent shear stress terms by velocity gradients. The wake properties, when normalized with respect to characteristics velocity and length, can be assumed to be self similar. The simplified equations of motion can be solved to provide expressions for the mainstream and radial velocity profiles. This is the method adopted in deriving a solution for the wake of two types of rotor blades discussed in the next section.

(b) Turbulent field method: In this method, the closure problem is resolved through the introduction of an assumed turbulence equation of state; which relates the turbulence quantities to the properties of the mean field. Such equations can be "local" or "global" in nature. The 'local' equation of state is used in the turbulence field method developed by Bradshaw et al (Reference 7). This method is based on the hypothesis that the properties of the turbulent fluctuations at a given position are uniquely specified by the shear stress profile. Three functions relating the local turbulent stress to normal intensity, viscous dissipation and pressure velocity correlations are used to simplify the turbulent kinetic energy equation. This equation in combination with three momentum and one continuity equation has to be solved simultaneously. Extension of this method to rotating three dimensional boundary layer is described in Reference 8. It is proposed to pursue this approach to three dimensional rotating wakes.

In the exact solution pursued by various turbulence groups (e.g. Lumley and Nouri - Reference 9), a turbulence dissipation equation is employed. This equation in combination with continuity, three momentum and six stress equations are solved simultaneously. Enormous computational difficulties are encountered in this method. Raj (10) has derived the turbulent dissipation equation valid for three dimensional wakes and modeled the rotation and curvature terms. The objective is to provide a complete set of constitutive equations governing the rotor wake flow. It is anticipated that this effort will lay an important ground work for the eventual exact solution of the rotor wake and boundary layer equations in distant future.

The analytical solution has been carried out for two types of rotors; (a) The rotor in which the downstream external flow has no tangential (relative) component, (b) The rotor with staggered blades of large length (or radius). A brief description of these two analyses is given below.

(a) Rotor with zero free stream relative tangential velocity at the exit:

It should be remarked here that this investigation was undertaken solely as a basic step in the eventual analysis of the more generalized rotor wake. The authors realize that this is not a practical rotor and the centrifugal forces, which are likely to dominate the wake decay characteristics, is not present in this configuration. The coriolis forces, which are very small in this case, arises due to wake diffusion. Detailed analytical development is given in Reference 11. Equations of mean motion and Reynolds stress in rotating coordinate system is employed. The equations are simplified considerably due to various assumptions made. The major conclusions of this analysis are (See Figure 1 for notations used);

(1) The decay of the wake defect is given by

$$U_s = (U_{z_o} - U_z) \sim z^{-1/2} \qquad (5)$$

(2) The mean radial velocity is given by,

$$U_r = \phi\, g(\eta) \qquad (6)$$

Where $\phi = \Omega U_s \ell / U_{zo}$, Ω is the angular velocity of the rotor, ℓ is the characteristic length scale and U_{zo} is the free stream velocity. It should be noted that the wake defect (U_s) is the same as two dimensional cylinder or an aerofoil and is not affected by rotation or centrifugal forces.

Using the assumption that the wake is quasi-homogeneous, two main effects of rotation have been found. (1) The effect of rotation is to redistribute the energy in the three components of fluctuating velocity. When there is weak or no rotation, $\overline{u_z^2} > \overline{u_r^2} > \overline{u_y^2}$, where u_z, u_r, u_y are fluctuating components of velocity in z, r and y directions respectively (Figure 1). When there is large rotation, $\overline{u_y^2} > \overline{u_z^2} > \overline{u_r^2}$. It has also been proved that the rotation introduces additional isotropy.

(b) Wakes of staggered rotor blades:

A more general case is considered by R. Raj (10) since rotor wake model developed in the previous section is valid only for a particular case i.e., when the wake leaves the trailing edge of the rotor blade axially. However, that is not the case in actual compressors or turbines. In all those cases of axial flow turbomachinery where the flow leaves the trailing edge at some stagger angle, the velocity distribution in the main stream as well as radial direction is affected by the Coriolis forces i.e. there is distortion of velocity profiles in both of these planes in contrast to previous case where the Coriolis forces distort only the velocity distribution in the radial plane.

Equations of motion for a rotor wake in which the flow outlet angle is at an angle λ to the axis of rotation can be written in rotating coordinate system as follows (employing the usual boundary layer approximations - see Reference 2 for details and Figure 1 for notations used).
r direction (Figure 1)

$$U_r \frac{\partial U_r}{\partial r} + U_y \frac{\partial U_r}{\partial y} + U_z \frac{\partial U_r}{\partial z} - \sin^2\lambda \frac{U_z{}^2}{r} - 2\Omega U_z \sin\lambda$$

$$- 2\Omega U_y \cos\lambda = - \frac{1}{\rho}\frac{\partial p^*}{\partial r} + \frac{1}{\rho}\frac{\partial T_r}{\partial y} \quad . \tag{7}$$

Z direction (Figure 1).

$$U_r \frac{\partial U_z}{\partial r} + U_y \frac{\partial U_z}{\partial y} + U_z \frac{\partial U_z}{\partial z} + 2\Omega U_r \sin\lambda$$

$$+ \frac{(\sin^2\lambda) U_z U_r}{r} = - \frac{1}{\rho}\frac{\partial p^*}{\partial z} + \frac{1}{\rho}\frac{\partial T_z}{\partial y} \tag{8}$$

where U_z, U_r, and U_y are mean velocities in z, r and y directions (Figure 1). The coordinate z is along the flow outlet angle, y is normal to radial direction (r) and z axis. T_r and T_z are shear stresses in the r and z directions respectively. p^* is the reduced pressure given by

$$p^* = p - (\underline{\Omega} \times \underline{r}) \cdot (\underline{\Omega} \times \underline{r}) \cdot$$

The following assumptions are now made to simplify the equations of motion with a view to construct a simplified wake model to predict the mean axial and radial velocity profile. The assumptions are:

1. The boundary layer does not separate from the trailing edge and the boundary layer thickness (δ), the mid radius (R) and the distance (L) downstream which the flow is investigated are such that

$$\delta << L << R$$

2. The turbulence of the rotor wake is weekly anisotropic and homogeneous such that

$$\overline{u_y^2} \sim \overline{u_z^2} \sim \overline{u_r^2} \sim O(\overline{u^2})$$

$$\overline{u_y u_r} \sim \overline{u_r u_z} \sim \overline{u_z u_y} \sim O(\overline{u^2})$$

3. The distance from the trailing edge where the boundary layer approximations begin to apply is small.

4. The choice of the coordinate loads to,

$$U_y << U_z \text{ and } U_r.$$

5. It is assumed that hub/tip ratio of the rotor is large so that any variation in the radial direction is negligible.

6. The turbulent stresses can be represented by

$$T_r = -\overline{u_y u_r} = \nu_T \frac{\partial U_r}{\partial y}$$

$$T_z = -\overline{u_y u_z} = \nu_T \frac{\partial U_z}{\partial y}$$

where ν_T = Eddy viscosity

Using the above equations, the equations of mean motion (equation 7 and 8) can be simplified to,

$$U_z \frac{\partial U_r}{\partial z} - 2\Omega U_z \sin\lambda = -\frac{1}{\rho}\frac{\partial p^*}{\partial r} + \nu_T \left(\frac{\partial^2 U_r}{\partial y^2}\right) \qquad (9)$$

$$U_z \frac{\partial U_z}{\partial z} + 2\Omega U_r \sin\lambda = -\frac{1}{\rho}\frac{\partial p^*}{\partial z} + \nu_T \left(\frac{\partial^2 U_z}{\partial y^2}\right) \qquad (10)$$

Equations (9) and (10) are non-linear equations. Therefore only a numerical solution is possible. Since, the wake defect decays to about 60 to 70 percent in a very short distance (referred to chord length) behind the trailing edge (Reference 6), it is possible to apply the far wake approximation. Also assuming that the external pressure gradient is impressed on the wake flow,

$$\frac{\partial p^*}{\partial z} = 0$$

$$\frac{\partial p^*}{\partial r} = 2\Omega \; U_{z_o} \sin\lambda$$

With these assumptions, equations (9) and (10) reduces to

$$U_{z_o} \frac{\partial U_r}{\partial z} + 2\Omega \, (U_{z_o} - U_z) \sin\lambda = \nu_T \left(\frac{\partial^2 U_r}{\partial y^2}\right) \tag{11}$$

$$U_{z_o} \frac{\partial U_z}{\partial z} + 2\Omega \, U_r \sin\lambda = \nu_T \left(\frac{\partial^2 U_z}{\partial y^2}\right) \tag{12}$$

Eliminating U_r from equation (11) and (12) and writing

$$U_{z_o} - U_z = u_s \, f\,(\eta) \;, \quad \eta = y/\ell \tag{13}$$

ℓ is the length scale

the following equation results.

$$\left[\frac{\ell^2}{u_s} \frac{d^2 u_s}{dz^2}\right] f - \left[\frac{2\ell}{u_s} \frac{d\ell}{dz} \frac{du_s}{dz}\right] [\eta f']$$

$$+ \left[\frac{d\ell}{dz}\right]^2 [\eta^2 f'' + 2\eta f'] - \left[\ell \cdot \frac{d^2\ell}{dz^2}\right] [\eta f']$$

$$+ \left[\frac{2\nu_T}{U_{z_o} \ell} \frac{d\ell}{dz}\right] [\eta f'''] - \left[\frac{2\nu_T}{U_{z_o} u_s} \frac{du_s}{dz}\right] f''$$

$$+ \left[\frac{4\nu_T}{U_{z_o} \ell} \frac{d\ell}{dz}\right] f'' + \left[\frac{\nu_T^2}{\ell^2 U_{z_o}^2}\right] f'''' = - \left[\frac{4\Omega^2 \ell^2}{U_{z_c}^2} \sin^2\lambda\right] f \tag{14}$$

where u_s is the defect in center line velocity $(U_{zo} - U_z \text{ min})$.

The condition of self similarity in longitudinal velocity (U_z) profile is satisfied only if coefficient of f, ηf^1, f'', $\eta^2 f''$, $\eta f'''$ and f'''' are constant. This is a remote possibility in the present form of equation (14). However, some simplification can be made at this point. Assume that the rotor we are considering is of high solidity i.e. the wake of two adjacent blades start interacting. In this case the wake width is constant and is equal to blade spacing (S) width. Under such circumstances it is possible to consider blade spacing as the characteristic length so that $d\ell/dz = 0$. This situation also corresponds to that of a far wake. Equation (14) with these considerations take the following form

$$[\frac{s^2}{u_s} \frac{d^2u_s}{dz^2}] f + [\frac{2\nu_T}{U_{z_o} u_s} \cdot \frac{du_s}{dz}] f''$$

$$+ [\frac{\nu_T^2}{s^2U_{z_o}^2}] f'''' = - [\frac{4\Omega^2 s^2}{U_{z_o}^2} \sin^2\lambda] f. \tag{15}$$

If similarity exists, coefficients of f and f" in the first two terms of equation (15) should be constant. Hence

$$u_s \sim e^{-z/s}$$

$$\text{or} \quad u_s/U_{zo} = A_1e^{-z/s} \tag{16}$$

It is evident that $(\frac{\nu_T}{sU_{zo}})^2 <<1$.

So that equation (15) along with equation (16) can be written as

$$(A + \phi)\ f + Bf'' = 0 \tag{17}$$

Where A and B are constants of order unity and $\phi = [\frac{4\Omega^2 s^2}{U_{z_o}^2} \sin^2\lambda]$

The solution of equation (17) is

$$f = A_2 \cos \{[\frac{A+\phi}{B}]^{1/2}\ \eta\} \tag{18}$$

Therefore, substituting equations (18) and (16) in (12) we get,

$$\frac{U_r}{U_{z_o}} = \frac{u_s}{U_{z_o}} \{\frac{(A+\phi)\ \nu_T - U_{z_o} SB}{2B\ \Omega(\sin\lambda) S^2}\} A_2 \cos\ (\sqrt{A+\phi}\sqrt{B}\ \ \eta) \tag{19}$$

Although the analysis is over simplified, it provides very important information.

1. The rate of decay of U_r is the same as that of velocity defect in longitudinal direction.

2. Radial velocity profile is a function of longitudinal velocity profile, speed of rotation, rotor cascade parameters and the turbulence characteristics.

3. The decay law for the rotor wake is much different than that of a cascade or isolated airfoil for the same case and is the fastest of the three.

Experimental Program

The main objective of the experimental program is to measure the mean and turbulent properties of the wake of different rotors in a rotating frame of reference and establish the profile and decay laws for the mean and turbulent properties of the wake.

Test Facilities

The experimental program will be carried out at the turbomachinery laboratory, Department of Aerospace Engineering and at the Applied Research Laboratory, The Pennsylvania State University. The axial flow compressor and axial flow fan research facilities to be used in this program are described below.

The axial flow research fan facility to be used in this program is described by Bruce (Reference 12). This facility has already been used to measure the wakes of a twelve bladed rotor operating at zero loading using a stationary triaxial probe. The method of measuring the wakes in a stationary system is described by Lakshminarayana and Poncet (Reference 13). However, some modifications are being done to the facility for measurement of the wake in relative rotating coordinate system.

The major modifications are being done just upstream and downstream the rotor. Upstream the rotor a pressure transfer device and a mercury slip ring unit is being mounted on the shaft to transfer signals from a relative rotating coordinate system to a stationary system for further processing the data. The pressure probe and the three-sensor hot wire probes to be used for measurements will be rotating with the speed of the shaft. Downstream of the rotor a traversing mechanism will be installed to control the motion of the probe in rotation.

The outer hub diameter of the AFRF rotor is 9.50" and the inner annulus diameter is 21.50". The drive unit for the rotor is a 70 horsepower motor enclosed in the hub of the AFRF. The speed of the motor can be regulated up to 3600 rpm giving a maximum relative tip mach number of 0.338. The flow through the facility is controlled by the axial flow fan and the throttle arrangement provided at the exit of the facility. Steady lift on the rotor can be produced by controlling the relative speed of the fan and the rotor. Detailed information on the facility is given in Reference 12.

A twelve bladed rotor to be used in the test program. The rotor blades are symmetrical aerofoils with zero camber. The blade is twisted from hub to tip so that the blade has no loading at every radial location. The rotor blades have a 10 percent thick, uncambered C1 profile which has the maximum thickness at the 33 percent chord point. The blades have a chord of 6 inches and a span of 5.9 inches. The stagger angle at the mean radius is 45°.

Axial Flow Compressor Facility

A schematic of the compressor facility is shown in Figure 2.

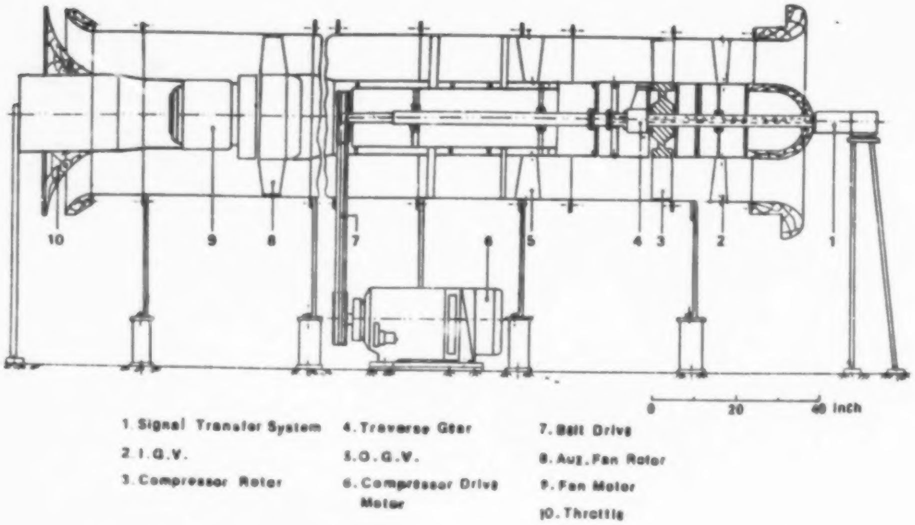
10
9
8
7
6
5
4
3
2
1
0
20
40 inch
1. Signal Transfer System
2. I.G.V.
3. Compressor Rotor
4. Traverse Gear
5. O.G.V.
6. Compressor Drive Motor
7. Belt Drive
8. Aux. Fan Rotor
9. Fan Motor
10. Throttle

FIG 2 AXIAL FLOW COMPRESSOR TEST FACILITY

The overall characteristics of the compressor stage, which consists of inlet guide vanes, rotor and stator are:

Hub/tip ratio	0.5	Design flow coefficient	0.516
Outer diameter	36 inches	Design pressure rise coefficient	0.61

The inlet guide vanes are of aluminum casting and has 45 blades. The rotor has 21 blades of cast aluminum with tee shaped roots. The hub is machined from an aluminum forging. The stator vane construction is similar to IGV and has 25 blades.

The modified compressor facility is highly flexible and could be used to study the rotor wake at various inlet levels of turbulence intensity, flow coefficient and back pressures (with the use of auxiliary fan at the outlet), with and without inlet guide vanes. The stater-rotor spacing can be varied to study the interaction effects. The speed of the auxiliary fan and compressor rotor can be varied independently, thus providing wide range of Reynolds number, inlet flow, tip speed, blade loading etc. Most importantly, the facility has provision to carry out rotating probe measurements at the exit of the rotor and blade static pressure measurements.

An auxiliary fan and corresponding ducting is incorporated into this facility. This provides a greater flexibility in the operating range of the compressor and also facilitates testing of annular cascades. The selection of the auxiliary fan was based on the variables to be investigated and the flow losses through the facility. The auxiliary fan chosen is an axial type with variable blade pitch, providing a pressure rise of up to 5 inches of water. The auxiliary fan (Figure 2) is driven by a fixed speed 40HP motor.

The compressor drive is a 50HP variable speed motor, whose speed can be varied continuously from 175RPM to 1695RPM. The belting will be housed inside streamlined supports spanning the annulus.

A detailed aerodynamic analysis was carried out to determine the blade element performance with and without inlet guide vanes. It is concluded that the blades near the tip would stall at a flow coefficient of 0.516, without IGV. Several trial calculations have indicated that, at a flow coefficient of 0.612, the rotor can be operated without stall for both the geometries (with and without IGV). A three-dimensional calculation, using the streamline curvature method, is underway to determine the accuracy of these two-dimensional calculations.

Traversing Mechanism

Two types of traversing mechanisms have been developed for carrying out measurements in a rotating frame of reference. The first one is described by Anand and Lakshminarayana (Reference 2).

The second type of traversing mechanism available was built for this project at the Applied Research Laboratory for the measurement of rotor wake. It consists of more than 100 parts and can provide four degrees of freedom, two manual and two automated, as follows.

i) motion of the probe about its own axis

ii) motion of the probe along the circumference

iii) motion of the probe along the radius

iv) motion of the probe along the axis of the shaft.

The first two degrees of freedom of movement can be realized in rotation and are controlled by the two remotely controlled step motors. The remaining two are realized manually. The traversing mechanism is at present being balanced only for three-degrees of freedom of which only one can be realized in rotation due to complications involved in the balancing. However, at a later date, the second degree of freedom in rotation will also be realized.

The probes to be employed in this program are;

(a) A triaxial hot wire probe. The probe to be used for the rotor wake measurements is similar to the one used for the measurement of mean velocities and turbulence quantities in a rotor channel (Reference 8). The hot wire equations developed in reference 8 are being modified to include the second order terms.

(b) A Kiel probe for measuring the total pressure.

(c) A spherical static pressure probe for the measurement of static pressure in the wake.

The Method

The wake will be surveyed at several radii and at several stations downstream using both the conventional probes and the hot wire probes. The measurements from the conventional probes (Kiel probe and static pressure probe) will be transferred through a pressure transfer device to a manometer or a transducer to derive the static pressure and stagnation pressure at various locations. Thr triple sensor hot wire probe will be used for the measurement of mean velocity and turbulence quantities such as intensity and shear stress. A schematic of the instrumentation to be used is shown in Figure 3.

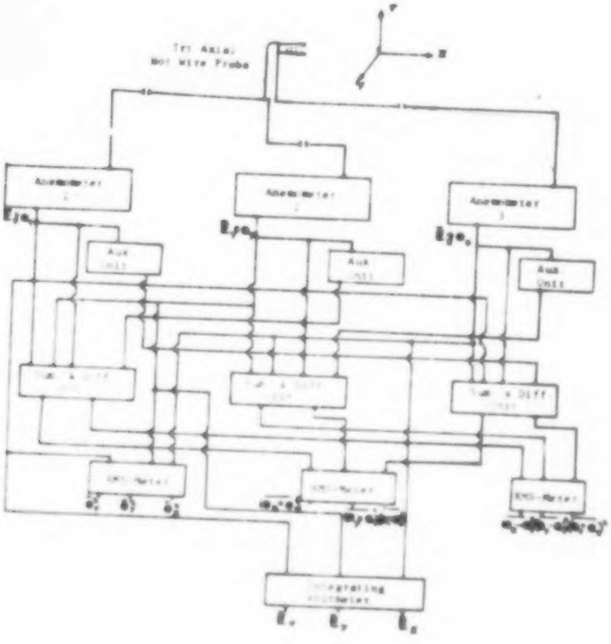
Tri Axial
Hot Wire Probe
Anemometer
Anemometer
Anemometer
3
Aux Unit
Aux Unit
Aux Unit
Sum & Diff Unit
Sum & Diff Unit
Sum & Diff Unit
RMS-Meter
RMS-Meter
RMS-Meter
Integrating Voltmeter

Fig. 3 Block Diagram of Turbulence Instrumentation for Mean Velocity, Turbulence Intensity and Shear Stresses

The output voltages consisting of three mean voltages $(\bar{E}_z, \bar{E}_y, \bar{E}_r)$, rms values of fluctuating voltages $(\overline{e_z^2}, \overline{e_y^2}, \overline{e_r^2})$ and correlations $(\overline{e_z e_y}, \overline{e_r e_z}, \overline{e_y e_r})$ will thus be used in the hot wire equations to derive the three mean velocities, turbulence intensity and correlations in r, z and y directions. The method is similar to that described in reference 8, with modifications to include the second order terms in the hot wire equation.

Preliminary Measurements

Some preliminary measurements of the wake at the exit of the twelve blade rotor in the axial flow research fan using the method developed in reference 13 have been completed. The data is being processed to derive the wake characteristics.

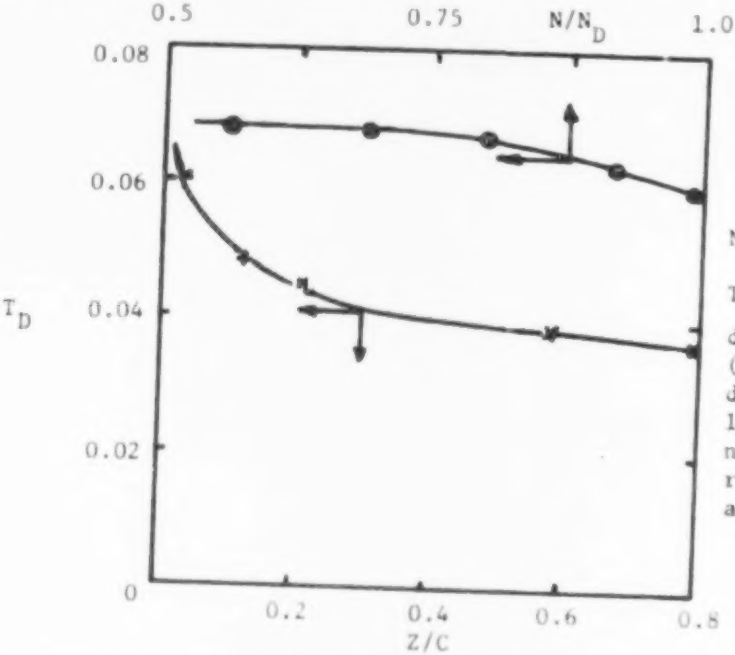

N_D = design speed

T_D = RMS value of disturbance level (including wake defect and turbulence fluctuation) normalized with respect to time averaged velocity.

Figure 4: Variation of overall disturbance level (T_D) with distance downstream and the speed of rotation

A single sensor probe was used to measure the overall disturbance level (turbulence and wake defect) at the exit of the rotor. The results are plotted in Figure 4. The rotor speed was varied to determine the effect of rotation on the overall disturbance level. As indicated in Figure 4, it is clear that the overall disturbance level is independent of the rotor speed.

ACKNOWLEDGMENTS

The cascade work and the initial phase of the rotor wake program was sponsored by the Applied Research Laboratory of the Pennsylvania State University, which operates under contract with the Naval Systems command.

The rotor wake program is presently sponsered by NASA Lewis Research Center through the contract NAS3-17855 with technical management by M. Heidmann.

REFERENCES

1. Johnston, J. P., "Effects of Rotation on Boundary Layers in Turbomachinery Rotor," In "Fluid Mechanics, Acoustics, and Design of Turbomachinery," NASA SP 304, 1974.

2. Anand, A. K. and Lakshminarayana, B., "Three Dimensional Turbulent Boundary Layer in a Rotating Helical Channel," ASME Paper 74-FE-25 (To be published in J. Fluids Engineering).

3. Lakshminarayana, B., Jabbari, A. and Yamoaka, H., "Turbulent Boundary Layer on a Rotating Helical Blade," J. Fluid Mechanics, Vol. 52, p. 545, 1972.

4. Sofrin, T. G., McCann, J. C., "Pratt Whitney Experience in Compressor Noise Reduction," 72nd meeting of the Acoustical Society of America, 1966.

5. Silverstein, A., Katzoff, S., and Bullivant, W., "Downwash and Wake Behind Plain and Flapped Airfoils," NACA Report 651, 1939.

6. Raj, R., and Lakshminarayana, B., "Characteristics of Wake Behind a Cascade of Airfoils," Journal of Fluid Mechanics, Vol. 61, pp. 707-730, December 1973.

7. Bradshaw, P., Ferris, D. H. and Atwell, N. P., "Calculation of Boundary Layer Development using Turbulent Energy Equation, J. Fluid Mechanics, Vol. 28, pp. 593-616, 1967.

8. Anand, A. K., Gorton, C., Lakshminarayana, B., and Yamaoka, H., "Investigation of Boundary Layer and Turbulence Characteristics Inside the Passages of an Axial Flow Inducer," NASA CR 121248, July 1973.

9. Lumley, J. L. and Khajeh-Nouri, B., "Modeling Homogeneous Deformation of Turbulence," Symposium on Turbulence in Planetary Boundary Layer of Atmosphere, Moscow, 1973.

10. Raj, R., "Characteristics of Cascade and Rotor Wakes," Ph.D. Thesis (in preparation), Department of Aerospace Engineering, The Pennsylvania State University, 1974.

11. Raj, R. and Lumley, J. L., "Characteristics of Turbulent Wakes Behind Rotating Fans with Zero Free Stream Relative Tangential Velocity," (in preparation).

12. Bruce, E. P., "The ORL Fluids Engineering Unit Axial Flow Research Fan," ORL TM 72-109, The Pennsylvania State University, 1972.

13. Lakshminarayana, B., Poncet, A., "A Method of Measuring Three-Dimensional Wakes in Turbomachinery," ASME Paper 73-FE-31 (to be published in J. Fluids Engineering).

SOME RESEARCH ON HELICOPTER ROTOR NOISE
THICKNESS AND ROTATIONAL NOISE

by

F. Farassat
Joint Institute for Acoustics and Flight Sciences
NASA-Langley Research Center
Hampton, Virginia

ABSTRACT

Thickness noise from a helicopter rotor appears to be significant in a forward region of flight at high tip speed. A new formula, valid at transonic speed, has been obtained which is suitable for numerical computation. The sound pressure signature will be obtained through the use of a computer program currently under development based on this new formulation. It is highly probable that thickness noise is the cause of high speed blade slap. The program will be used to test the validity of this conjecture.

Lowson's formula has been usually used in frequency domain. However, it can be used to compute the acoustic pressure signature due to steady and periodic forces on the rotor. This pressure time history can be Fourier analyzed. A computer program using experimental force measurement has been worked out to compute rotational noise of a helicopter in hover or at low speed flight. The results will be compared with those available which use frequency analysis. Apart from inclusion of forward speed, one advantage appearing from this program is the speed and ease of computation.

INTRODUCTION

The noise from a helicopter rotor at high tip speed is very directional, loud and peaks in the rotor plane. It is frequently referred to as compressibility noise. Several attempts have been made to explain the source of this noise. Arndt and Borgmann [1] propose that the cause is the increase in the rotor drag at transonic speed. However, their use of compact acoustic source model to represent rotor forces renders their conclusion doubtful. In Lyon's analysis [5], the rotor tip region is replaced by an equivalent torpedo-shaped body in terms of rotor cross sectional area. The use of this axisymmetric body is dictated by the mathematical technique employed. He finds that thickness noise is significant at high tip speeds. However, it will be shown that the acoustic field due to body thickness defines the shape of the body uniquely. This means that Lyon actually finds the thickness noise of torpedo-shaped bodies which does not correspond to that of the rotor. His mathematical approach is unnecessarily cumbersome and complicated.

In this paper an integral representation for the thickness noise is developed which can be shown to reduce to the known formulas obtained previously on this subject.

When conditions of compactness of acoustic sources apply, the rotational noise can be calculated by a fairly simple formula due to Lowson [4]. Thus far, the main use of this equation has been in the frequency domain. This approach does quickly get involved with series of Bessel functions. Bessel functions are familiar tools of workers in this field. But no one seems to be worried about convergence characteristics of these series. Another objection to the common approach is that it is hard to use intuition with involved manipulations. A study of Lowson's original paper [4] reveals that the Bessel functions appear as the result of the non-linear relation between the source and the observer times when this relation is used in the Fourier expansion of the acoustic pressure. It is therefore suggested that Lowson's formula be applied in the time domain and the resultant pressure signature be then Fourier analyzed. This approach turns out to be easy to program and fast on computer.

THICKNESS NOISE OF A SLENDER BLADE SYSTEM

The governing equation for the sound generation by a moving body in an inviscid medium with the sound speed C is [2,3]:

$$\frac{1}{c^2}\frac{\partial^2 p}{\partial t^2} - \nabla^2 p = \frac{\partial}{\partial t}\left[\rho_0 v_n |\nabla \tilde{f}|\, \delta(\tilde{f})\right] - \frac{\partial}{\partial y_i}\left[p n_i |\nabla \tilde{f}|\, \delta(\tilde{f})\right] \qquad (1)$$

where p is the pressure, ρ_o is the density of the undisturbed medium, $\tilde{f}(\vec{y},\tau)=0$ is the equation of the surface of the body, V_n and $\vec{n}$ are the normal velocity and the unit normal to the body surface, respectively. The function $\tilde{f}$ is defined negative inside the body and positive outside it and $\delta(\tilde{f})$ is the delta-function. This equation was originally derived by Ffowcs Williams and Hawkings [3]. Due to the assumption of slenderness of the blades, we have neglected a third term on the right side of (1) involving Lighthill's stress tensor T_{ij}. Several forms of solutions of (1) exist which are equivalent [2,3]. A closed form solution of (1) is obtained by dropping the contributions from T_{ij} terms in the solution by Farassat [2]. For computational purpose , we develop a different formula for the problem under the consideration.

The solution of (1) is given by:

$$p(\vec{x},t) = \frac{\partial}{\partial t}\int \frac{\rho_0 v_n}{4\pi r} |\nabla \tilde{f}|\, \delta(\tilde{f})\, \delta(g)\, d\vec{y}\, d\tau - \frac{\partial}{\partial y_i}\int \frac{p n_i}{4\pi r} |\nabla \tilde{f}|\, \delta(\tilde{f})\, \delta(g)\, d\vec{y}\, d\tau \qquad (2)$$

where $g=\tau-t+\frac{r}{c}$, $r=|\vec{x}-\vec{y}|$ and τ is the source time. We use the following relation to integrate the products of the two delta-functions:

$$d\vec{y} = \frac{d\bar{f}\,dg\,dy_1}{\dfrac{\partial(\bar{f},g)}{\partial(y_1,y_2)}} = \left\{ \frac{dy_1}{\dfrac{\partial(\bar{f},g)}{\partial(y_1,y_2)} \Big/ |\nabla\bar{f}\times\nabla g|} \right\} \frac{d\bar{f}\,dg}{|\nabla\bar{f}\times\nabla g|}$$

$$d\vec{y} = \frac{c\,d\bar{f}\,dg\,d\Gamma}{|\nabla\bar{f}|\sin\theta} \qquad (3)$$

Here Γ is the curve of intersection of the sphere $g=0$ and the surface $\bar{f}=0$ and θ is the angle between $\nabla\bar{f}$, the normal to the surface, and radiation direction $\vec{x}-\vec{y}$, $\vec{y}$ being the point on the element of Γ-curve under consideration. Substituting (3) in (2) and integrating with respect to $\bar{f}$ and g, we get:

$$p(\vec{x},t) = \frac{\rho_0 c}{4\pi}\frac{\partial}{\partial t}\int_{\tau_1}^{\tau_2}\frac{d\tau}{r}\int_{BODY}\frac{v_n}{\sin\theta}\,d\Gamma - \frac{c}{4\pi}\frac{\partial}{\partial y_i}\int_{\tau_1}^{\tau_2}\frac{d\tau}{r}\int_{BODY}\frac{p\,n_i}{\sin\theta}\,d\Gamma \qquad (4)$$

Here τ_1 and τ_2 are the times that the sphere $g=0$ enters and leaves the body, respectively. We first consider one blade only.

Let us now fix a new coordinate system $\vec{\eta}'$, to a blade in such a way that $\eta_1'\eta_2'$-plane coincides with the rotor plane and the origin is at the center of the rotor disc. Let the η_2' - axis be along the span of the blade parallel to the leading edge. For simplicity we assume that we have a rectangular planform with uniform airfoil section across the span. Then the function $f(\vec{\eta}')=f(\vec{y},\tau)=0$ describing the blade surface is given by:

$$f(\vec{\eta}') = \begin{cases} \eta_3' - [h(\eta_1') + F(\eta_1')] = 0\text{, UPPER SURFACE} \\ [h(\eta_1') - F(\eta_1')] - \eta_3' = 0\text{, LOWER SURFACE} \end{cases} \qquad (5)$$

where $\eta_3'=h(\eta_1')$ and $\eta_3'=F(\eta_1)$ are the camber and thickness functions of the airfoil section. Note that the above definition is consistent with the requirement that $f<0$ inside the body. Note that the $\vec{y}$-frame is fixed with respect to the undisturbed medium. Let the helicopter speed be given by $\vec{V}_H(\tau)$ and let a non-rotating coordinate system $\vec{\eta}$-frame be fixed to center of the rotor disc. Assume that the three coordinate systems coincide at the time $\tau=0$. Then the transformation rules between these systems are:

$$\vec{y} = \vec{\eta} + \int_0^{\tau}\vec{V}_H(\sigma)\,d\sigma \equiv \vec{\eta} + \vec{\xi}(\tau)$$

$$\begin{bmatrix}\eta_1' \\ \eta_2'\end{bmatrix} = \begin{bmatrix}\cos\phi & \sin\phi \\ -\sin\phi & \cos\phi\end{bmatrix}\begin{bmatrix}\eta_1 \\ \eta_2\end{bmatrix}$$

$$\eta_3' = \eta_3$$

where $\phi = \Omega\tau$ and Ω is the angular velocity of the rotor. From these we obtain:

$$\begin{aligned} \eta_1' &= (y_1 - \xi_1)\cos\phi + (y_2 - \xi_2)\sin\phi \\ \eta_2' &= -(y_1 - \xi_1)\sin\phi + (y_2 - \xi_2)\cos\phi \\ \eta_3' &= y_3 - \xi_3 \end{aligned} \qquad (6)$$

To calculate v_n, we use the relation $v_n = -(\partial\tilde{f}/\partial\tau)/|\nabla\tilde{f}|$. Using Eqs. (5) and (6), we obtain:

$$\frac{\partial\tilde{f}}{\partial\tau} = \begin{cases} -\dot{\xi}_3 - (h' + F')(\eta_2'\Omega - V_1') & \text{UPPER SURFACE} \\ \dot{\xi}_3 + (h' - F')(\eta_2'\Omega - V_1') & \text{LOWER SURFACE} \end{cases} \qquad (7)$$

In this relation $(\dot{\ }) = d/d\tau$, $F' = dF/d\eta_1'$, $h' = dh/d\eta_1'$ and $V_1' = (V_H)_1\cos\phi + (V_H)_2\sin\phi$, that is the helicopter speed along the η_1'-axis. We also have:

$$\begin{aligned} |\nabla\tilde{f}| &= \begin{cases} [1 + (h' + F')^2]^{1/2} & \text{UPPER SURFACE} \\ [1 + (h' - F')^2]^{1/2} & \text{LOWER SURFACE} \end{cases} \\ &\approx [1 + F'^2]^{1/2} \end{aligned} \qquad (8)$$

We are interested to simplify (4) in the region where the sources are non-compact, i.e. in the forward region of the flight and on or near $\eta_1'\eta_2'$-plane. That is the observer is located in the near or far-field but close to the plane which includes the rotor disc. In this case, sin θ will be nearly the same for a point on the upper surface and a point directly below it on the lower surface and by slenderness assumption $n_1 \approx 0$, $n_2 \approx 0$, $n_3 \approx 1$. Using (7) and (8), we write (4) as:

$$\begin{aligned} p(\vec{x},t) &= \frac{\rho_0 c}{2\pi}\frac{\partial}{\partial t}\int_{\tau_1}^{\tau_2}\frac{d\tau}{r}\int_{\substack{\text{UPPER}\\\text{SURFACE}}}\frac{F'(\eta_1')(\eta_2'\Omega - V_1')}{[1+F'^2]^{1/2}\sin\theta}\,d\Gamma \\ &+ \frac{c}{2\pi}\frac{\partial}{\partial y_3}\int_{\tau_1}^{\tau_2}\frac{d\tau}{r}\int_{\substack{\text{UPPER}\\\text{SURFACE}}}\frac{P_L - P_U}{\sin\theta}\,d\Gamma \end{aligned} \qquad (9)$$

where P_L and P_U refer to the pressure on the lower and upper surfaces of the blade respectively. For the rotor system, we sum the individual contributions of each blade.

We note that for a non-lifting blade the contribution from the second term on the right side of (9) is zero so that we define the first term on the right side of (9) as the thickness noise. The term $\eta_2'\Omega - V_1'$ is the local blade velocity relative to the undisturbed medium, V_B and $F'(\eta_1')$ is the local derivative of the thickness function. Therefore the thickness noise is given by:

$$p(\vec{x},t) = \frac{\rho_0 c}{2\pi} \frac{\partial}{\partial t} \int_{\tau_1}^{\tau_2} \frac{d\tau}{r} \int_{\substack{\text{UPPER}\\ \text{SURFACE}}} \frac{F'(\zeta'_1) V_\theta}{[1+F'^2]^{1/2} \sin\theta} \, d\Gamma \qquad (10)$$

In computation, the time derivative must be carried out numerically.

To see that the blade cannot be replaced by another body for acoustic calculations as proposed by Lyon, we demonstrate that in the above case we can actually find the shape of the body from the acoustic field. To do this we first note that we need to determine $F(\zeta'_1)$. Let us divide the chord into n points at which points we will demonstrate that $F'(\zeta'_1)$ can be calculated. Since n is at our disposal and we know that $F(\zeta'_1) = 0$ at the trailing edge, the airfoil shape will then be known. Let us put the observer in $\zeta'_1 \zeta'_2$-plane so that $\sin\theta \approx 1$. Then we can approximate the integral in (10) as follows:

$$I(\vec{x},t) = \int_{\tau_1}^{\tau_2} \frac{d\tau}{r} \int F'(\zeta'_1) V_\theta \, d\Gamma \qquad ; [1+F'^2]^{1/2} \approx 1$$

$$\approx \sum \frac{\Delta\tau}{r} \sum F'(\zeta'_1) V_\theta \, \Delta\Gamma$$

Let us assume that we have sharp leading edge so that we can safely approximate $\Delta\Gamma$ by $[(\Delta\zeta'_1)^2 + (\Delta\zeta'_2)^2]^{1/2}$. Then I is a linear equation in n unknowns $F'(\zeta'_1)$ at the n points along the chord. We also approximate $p(\vec{x},t)$ by

$$p(\vec{x},t) = \frac{\rho_0 c}{2\pi \Delta t} \left[I(\vec{x}, t+\Delta t) - I(\vec{x},t) \right] \qquad (11)$$

which is again linear in the n unknowns we are seeking. Thus if the acoustic pressure at a point $\vec{x}$ is given at n distinct times for a rotor system whose motion is known, then by applying (11) at these times we get n linear equations which would determine $F'(\zeta'_1)$ at the n points along the chord of the airfoil section.

It is seen from (10) that the thickness noise depends on airfoil shape and the blade kinematics. No aerodynamic data are required other than the blade geometry. For this reason, thickness noise calculations are taken up first to determine whether this is the mechanism of generation of the high speed blade noise. One can demonstrate that in the region under consideration, the second term in (10) is negligible.

Rotational noise (compact model)

Lowson's formula is the solution of the wave equation

$$\frac{1}{c^2} \frac{\partial^2 p}{\partial t^2} - \nabla^2 p = -\frac{\partial}{\partial y_i} F_i(\tau) \, \delta(\vec{y} - \vec{\xi}(\tau)) \qquad (12)$$

where $\vec{F}(\tau)$ the force on the medium whose location is given by $\xi(\tau)$. The formula is

$$p(\vec{x},t) = \frac{1}{4\pi}\left[\frac{\dot{F}_r(\tau)}{c(1-M_r)^2 r} + \frac{F_r(\tau)}{c(1-M_r)^3}\frac{\partial M_r}{\partial \tau} - \frac{(M^2-1)F_r}{r^2(1-M_r)^3} - \frac{\vec{F}\cdot\vec{M}}{r^2(1-M_r)^2} \right]_{RET.} \tag{13}$$

The usual notation is used. To apply this formula for multiple source systems in the time domain, each source is followed separately and its pressure signature calculated. The overall signature is the sum of the pressures from individual sources at the required observer time. In executing this procedure on the computer, care must be taken that the arrival times of the pressure signals from all the sources overlap to get meaningful result. This can be done as follows. At the start of calculation, find the nearest source to the observer. Determine the arrival time t_1 of the signal from this source. Then let each source retrace its path back in time until its signal arrives within a specified range of t_1. From here on follow each source individually to the desired observer time t. Due to irregular arrival times of the signals, the stored values for each source must be interpolated at specified observer times and summed up to get the overall signature.

A program is developed using the above procedure for the rotational noise of a helicopter in hover or low speed forward flight. It uses experimental force data. It is being compared with other programs which give the acoustic pressure spectrum directly.

SOME PRELIMINARY RESULTS

A computer program utilizing Eq. (10) to calculate thickness noise of a helicopter in flight or in hovering is under development. Fig. (1) shows the pressure signature of a hovering helicopter at almost sonic blade tip speed. The rotor has two rectangular blades with 8 per cent thickness ratio. The airfoil section is a symmetric parabolic arc. The observer is in the rotor plane at 250 meters from the center of the rotation. Other relevant information is: blade chord=0.70 meters, blade radius=6.71 meters and RPM=480. The pressure signature corresponds to one period (0.0625 seconds). It is seen that one actually gets sharp pulses from blades rotating at high tip speed. The propagation effects of these pulses must be considered. These effects are not included in the program at the present. The available computation seems to support the conclusion of Lyon [5] that thickness noise is significant in or near the plane in which the rotor disc lies. Probably, what is frequently referred to as compressibility noise or high speed blade slap is the same phenomenon caused by blade thickness and high tip speed. If this is true, then the terminolog compressibility noise is a misnomer.

One effective means of reducing thickness noise is to reduce the thickness ratio and the chord of the tip region of the blade. Everything else remaining the same, reducing the thickness ratio to half of its original value scales down the pressure signature by a factor of two.

A test run of the program of rotational noise has been reproduced in Fig. 2. The blade forces are located at an effective radius of about 0.8 times the blade radius. The experimental force spectrum from a test on the whirl tower at NASA Langley Center was used. Unfortunately all the phase information was not available at the time of the computation. Fifty force harmonics are used which obviously are not sufficient for the range of the acoustic frequencies we are interested in. Nevertheless, there is some similarity between Fig. (2) and the pressure signature commonly observed. The observer is at the distance of 51.1 meters from the center of the rotor disc and at an angle of 26.5 degrees above the plane of rotation. The other data are: number of the blades=4, effective radius=5.34 meters, RPM=355 and the net thrust=18556 Newtons=4171 lbs.

The above results are only preliminary and must not be considered final. Both programs are under evaluation at the present.

The author would like to thank the staff of the Acoustics and Noise Reduction Division of NASA Langley Research Center for their help during the development of these programs. Thanks are due to Mr. J. Mall of Computer Sciences Corporation for work on the thickness noise program and Ms. L. C. Parks of NASA for work on the rotational noise program. This work was carried out under NASA Grant Number NGR 03-010-085.

REFERENCES

1. R. E. A. Arndt; D. C. Borgmann (1971) J. Am. Helicopter Soc., 16, 36-45; Noise radiation from helicopter rotors operating at high tip Mach numbers.
2. F. Farassat (1974), J. Sound and Vib., 32, 3, 387-405; The Acoustic far-field of rigid bodies in arbitrary motion.
3. J. E. Ffowcs Williams and D. L. Hawkings (1969), Phil. Trans. of Roy. Soc. of London, Series A, 264, 321-342; Sound generation by turbulence and surfaces in arbitrary motion.
4. M. V. Lowson (1965), Proc. of the Roy. Soc. of London, Series A, 286, 559-572; The sound field for singularities in motion.
5. R. H. Lyon (1971), J.A.S.A., 49, 3, 894-905; Radiation of Sound by airfoils that accelerate near the speed of sound.

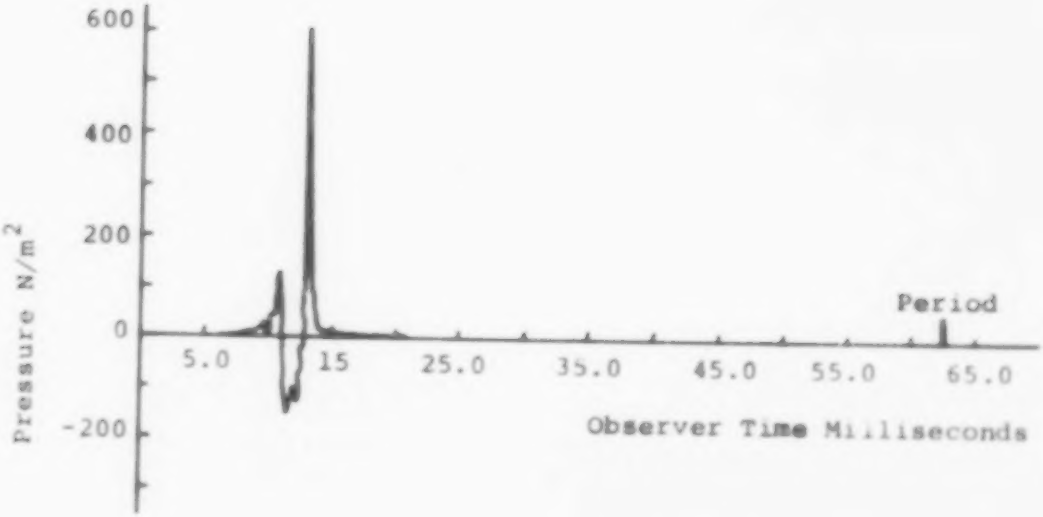

Fig. 1 - Thickness Noise of a Helicopter Rotor at Sonic Tip Speed. No. of Blades - two.

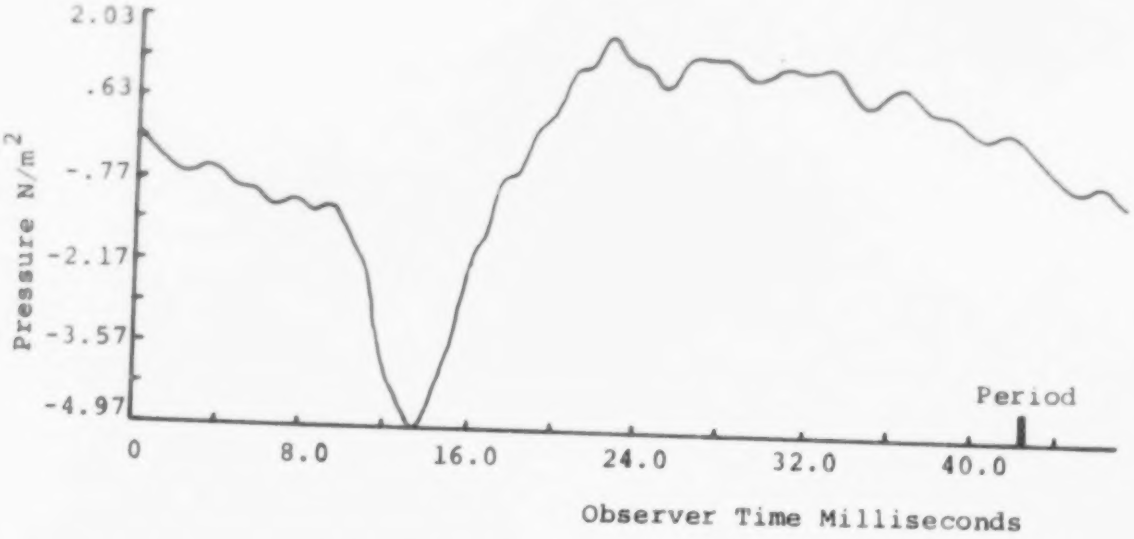

Fig. 2 - Rotational Noise of a Helicopter rotor. No. of Blades - 4.

EFFECT OF STEADY AND UNSTEADY SPANWISE CIRCULATION DISTRIBUTION ON ROTOR NOISE - PROGRESS REPORT

by

Edward Lumsdaine
Mechanical and Aerospace Engineering
University of Tennessee
Knoxville, TN 37916

ABSTRACT

The purpose of this project is to determine the influence of steady and unsteady loading on rotor noise generation. The theoretical study shows that steady-loading rotor noise increases with increasing rpm and increases rapidly with increasing hub-tip ratio. The noise decreases with increasing number of blades and decreases slightly with increasing taper angle. Also for minimum noise, there exists an optimum twist angle (optimum radial loading) for a given stagger angle. For the case of unsteady loading, the combination of optimum stagger and twist angle depends on whether the rotor is subject to an axial or transverse disturbance. Rotor design for minimum noise for an unsteady disturbance also depends on rotor rpm and disturbance-reduced frequency. Thus, the optimum design must use a statistical study of the disturbances to the rotor and a compromise combination of twist and stagger that will result in an optimum steady and unsteady spanwise loading distribution. An experimental program is now under way to attempt to verify these results and to extend the theoretical study. Although the immediate purpose of this project is to determine the influence of steady and unsteady spanwise loading on compressor noise, the overall objectives of this research are to study the influence of blade geometry on noise and compressor efficiency.

INTRODUCTION

This program was initiated to attempt to determine the influence of blade design characteristics on axial turbomachinery noise and to evaluate performance resulting from low-noise design. Although in recent years the understanding of turbomachinery noise and methods for noise reduction has increased markedly, theoretical and experimental studies have concentrated on the gross parameters (such as mass flow, rpm, pressure ratio, rotor-stator spacing, number of blades, etc.) rather than on the specific blade characteristics. Whether it is possible to design blades with a geometry that would significantly reduce the far-field noise without sacrifice in performance remains presently an open question. However, it is a fact that the volume of research, both theoretical and experimental, on the influence of blade geometry on noise is very small. The reason for this can best be illustrated by an example: in the solution of the linear wave equation for sound propagation, the rms pressure involves the circulation term (steady or unsteady) as one of its parameters. Most authors use a two-dimensional approach, either using a modified constant [1] or calculating the radial circulation at the root, midspan and tip using the two-dimensional theory [2]. Although these methods will allow the calculation of the influence of overall parameters on noise generation, they will not provide information on blade design characteristics and their effect on noise.

Three-dimensional theories must be used if information on the influence of blade design characteristics on noise is required. Without violating any aerodynamic laws, there are numerous ways of twisting the blades on an axial turbomachine. The question of blade twist in design has not yet been answered satisfactorily, but it appears that this parameter can be exploited in designing compressors with low noise. Thus one of the first objectives of this program was to extend the present methods to include the spanwise circulation distribution.

Experimentally, without a definite theoretical basis to serve as a guide, there are infinite combinations of design geometries possible; systematic variations of parameters will provide some information but would be extremely costly. This is particularly the case in turbomachinery noise research since the two-dimensional cascade tests used so successfully for aerodynamic performance studies cannot be used for noise studies. Numerous empirical equations have been derived through the years by industries and others to estimate noise for a given turbomachinery design. A large number of these equations show that there is little or no dependence of noise on blade characteristics. However, one cannot automatically conclude that blade design has little or no influence on noise just because a group of fans which have similar aerodynamic performance design (which means similar selection of optimal blade characteristics) will undoubtedly result in noise characteristics that will depend only on gross parameters.

The present results and future aims of this project will be placed in a more logical perspective if a brief summary of the empirical, experimental and theoretical results of previous work on the effect of blade design characteristics on noise is given.

1. Empirical Equations

Most empirical methods relate overall rather than blade characteristics to noise. These correlation studies, using normalized sound power levels, show that there is little dependence of blade characteristics on noise. However, as mentioned above, this technique is somewhat self-fulfilling because correlation studies are usually done using fans of similar design; since the fans were designed with little initial consideration of blade characteristics on noise (but rather are based on similar aerodynamic performance studies) it would seem reasonable that the noise would not noticeably deviate from overall parameters related to the performance of the fan. Thus for example for several fans operating at different tip speeds, the trend of data in a recent paper [4] showe that there was no evidence that fan design parameters such as loading or tip speed influence the noise. Rather, overall parameters such as pressure ratio, etc. seem to define the noise. The normalized equation from that study is

$$\mathrm{PwL} = 121.9 + 14 \log (\mathrm{PR} - 1) + 10 \log F$$

Other typical empirical formulas are given by Peistrup and Wesler [5] for axial fans

$$\mathrm{PwL} = 105 + 17.7 \log (\mathrm{HP}/B) + 15 \log (B/6)$$

by Beranek [6] for ventilating fans

$$\text{PwL} = 98.5 + 10 \log \Delta T + 10 \log \text{HP}$$

by Lowson's formula [7] (at 200 ft sideline)

$$\text{PwL} = 20 \log D + 50 \log V_t - 75$$

and by Morfey's formula [8] for a multistage axial compressor

$$\text{PwL} = 95 + 10 \log w + 20 \log \Delta T + 10 \log n$$

where PwL = sound power level, PR = pressure ratio, F = unit thrust, HP = shaft horsepower, B = number of blades, ΔT = stage temperature rise, D = rotor diameter, V_t = rotor tip speed, H = stagnation enthalpy, and w = mass flow.

However, studies by Sower [9] and General Electric using a large class of fan/compressors showed that there exists an empirical formula to account for the effect of certain design parameters on noise. For fans of a given power requirement, the formula

$$\text{PwL} = 10 \log [(A_a n/B)(r_h/r_t)^2] + F(Hw/A_a)$$

$$\text{where } F(Hw/A_a) = 107 + 43.3 \log (Hw/A_a) \qquad \text{for } 0.5 \leq Hw/A_a \leq 3.5$$

$$= 123 + 13.3 \log (Hw/A_a) \qquad \text{for } 3.5 \leq Hw/A_a \leq 10$$

may be evaluated to obtain blade characteristics to minimize noise. This formula shows that a reduction in rpm (n), annulus area (A_a), hub-tip ratio (r_h/r_t) and an increase in the number of blades will reduce the noise. Although these are only some of the parameters that affect the noise, they show that radial loading (hub-tip ratio) and circumferential loading distribution (number of blades) have a substantial influence on noise. Here it should be noted that the sound power level can be divided into blade design parameters (first term) and overall parameters (second term). Looking at the relative magnitudes of these terms, fans of certain design (i.e. large mass flow) may not change significantly in their noise characteristics by changing the blade design.

2. Experimental Studies

It appears that there are relatively few detailed experimental studies on effects of blade characteristics on noise in axial compressors. Studies done by Boeing [10,11] using a small fan with several blade configurations and under numerous operating conditions did not reach any conclusive evidence that could be used to design blades to minimize noise. One notable conclusion, within the limits of the experimental setup, was that the noise generating mechanism from the rotor is primarily due to lift or loading, with vortex and thickness noise being of secondary importance. Recent studies [12], however, showed that for low static pressure ratio, thickness noise may be equally if not more important than lift noise. Further work is required since changing blade designs that would favorably influence the noise from one source may adversely affect others, since the three subdivisions of noise according to source (lift, vortex, thickness) are interrelated.

Projected tests on this program will attempt to determine some of the details of the influence of changing blade design on loading noise. Since one of the key items is the influence of spanwise circulation, tests will be conducted with a small fan, and blades with the same spanwise circulation will also be tested in a cascade to separate the loading noise from the vortex noise. Present experimental evidence shows that changing spanwise circulation will not increase vortex noise for the same overall lift [13]. Therefore, the present study concentrated on the influence of spanwise circulation distribution on lift noise. Figure 1 is a schematic of the experimental setup being used for tests on blade characteristics. Particular attention is being paid to changes in noise due to changes in axial loading (aspect ratio, camber, etc.), radial loading (twist, taper, hub-tip ratio, etc.) or circumferential loading (solidity, etc.).

3. Theoretical Analyses

It is now well established that noise from the fan/compressor is due to the rotor and rotor-stator interaction; this noise generation can be due to viscous and/or non-viscous effects. In other words, considering the lift noise being the primary noise source, the noise is a result of steady or unsteady loads. In the case of unsteady loads, it can be periodic or random. The periodic loads are due to such mechanisms as rotor-stator interaction, and the non-periodic loads are due to inflow and self-induced turbulence. The periodic loads generate the discrete tones whereas turbulence generates broadband noise. For example, if the vortex noise due to the periodic shedding of the vortices induces a periodic force on the blade, and this periodic force generates noise, then the result would be discrete noise. But if the vortices themselves create the noise, then this would be more broadband in nature.

Recently there have been numerous theoretical studies on the problem of turbomachinery noise. These include the papers by Sharland [14], Large [1], and Benzakein [2,15,16] and recent review papers by Morfey [8], Lowson [7], and Reethof [17]. The findings of these references (for the purposes of design) can be summarized as follows, assuming that the tip speeds of the rotor are reasonably high: the sound pressure level of the blade passage frequency of a rotor increases with blade pitch, thickness, rate of mass flow, rpm, pressure ratio, and it decreases with increasing number of blades for a given mass flow. It should be noted that because two-dimensional theories were used in the determination of steady and unsteady circulation, most of the results relate noise to overall parameters rather than to blade characteristics.

Within the limitations of linear acoustic theory, the lift noise is a function of the steady and unsteady circulation of the rotor. Since the steady circulation is a special case of the unsteady circulation (when the disturbance frequency is zero), the unsteady circulation will be discussed only.

Early attempts to solve the two-dimensional unsteady circulation in a cascade of airfoils were made by Kemp and Sears [18,19]. However, in those models, the unsteady part of the circulation and the wakes of neighboring blades were neglected. Horlock [20] analyzed the case of a single rotating blade subject to upstream disturbances, and subsequently Henderson and Horlock [21] extended the analysis to a two-dimensional cascade subject to axial disturbances in the incoming flow, but their analysis is limited to cascades with very high

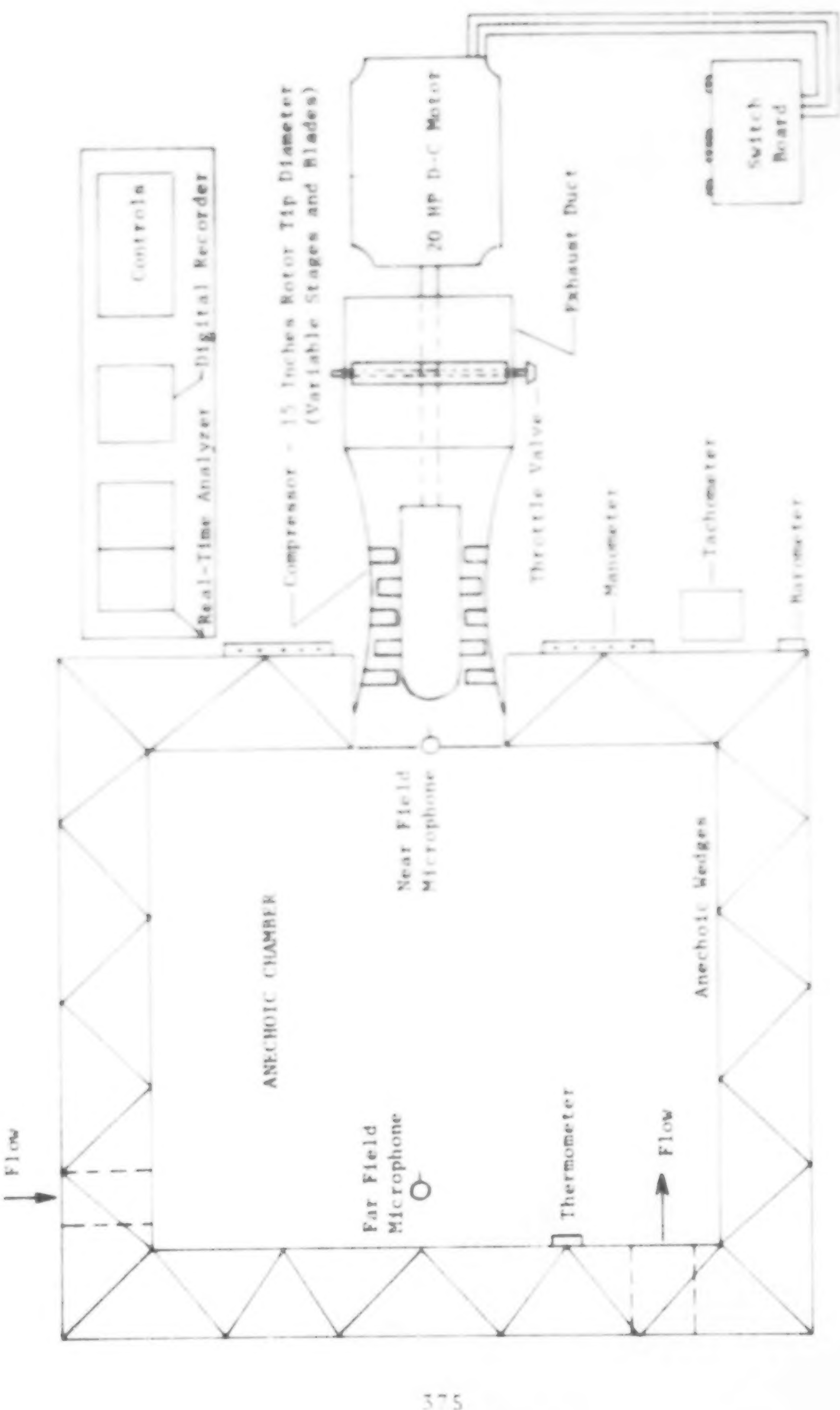
Flow
Far Field Microphone
Thermometer
Flow
ANECHOIC CHAMBER
Near Field Microphone
Anechoic Wedges
Real-Time Analyzer
Digital Recorder
Controls
Compressor - 15 Inches Rotor Tip Diameter (Variable Stages and Blades)
Throttle Valve
Exhaust Duct
20 HP D-C Motor
Manometer
Tachometer
Barometer
Switch Board

Figure 1 Plane View of Experimental Setup

solidity and a blade spacing which is small compared to the wavelength of the disturbances. A further restriction imposed in that work is the coupling between the frequency of the disturbance and its wavelength in the lateral direction. This restricts the use of the method to potential interaction and similar problems and makes it unsuitable for the solution of problems involving arbitrary disturbances such as inlet turbulence. Furthermore, some of their results are difficult to resolve, especially when the disturbance frequency tends to zero.

Whitehead obtained approximate solutions to the fluctuating lift problem, first using the actuator disk approach [22] and subsequently studying the case of a two-dimensional cascade of flat plates by replacing the blades with concentrated vortices [23]. Along the same lines, Henderson and Daneshyar [24] also studied the problem of a two-dimensional cascade by replacing the reference blade with a continuous distribution of vorticity, the adjacent blades by concentrated vortices and the wake by a continuous distribution of vorticity. On the other hand, Yeh and Eisenhuth [25] and later Neumann and Yeh [26] studied the unsteady pressure distribution on a two-dimensional blade as a result of incoming periodic disturbances. But they too had to neglect the interaction between the reference blade and other blades. Their solution is "exact" only for isolated airfoils and is expected to lead only to qualitative results for the case of low solidity cascades; it is completely inaccurate for high solidity cascades. Finally Mugridge [27] studied qualitatively the noise generated from a three-dimensional gust encountering a two-dimensional isolated thin airfoil.

In all these analyses several approximations were made and in many instances generality was sacrificed for the sake of obtaining closed-form solutions. The most important approximations commonly made in almost all of these works are:

a. The rotor is represented by a two-dimensional infinite cascade.

b. The interaction between the reference blade and the neighboring blades and their wakes is neglected.

As a result these methods are mainly suitable for application only with low solidity cascades and completely fail to show the effects of any radial variations in rotor geometry.

PRESENT STUDY

The mathematical analysis for the determination of the steady and unsteady spanwise circulation distribution for a rotor with finite blades is given in References 28 and 29. In this analysis the classical representation of the rotor by a two-dimensional infinite cascade is eliminated. Instead the more realistic case of a radial cascade with blades of finite length is considered. Blade interference effects are also taken into account, thus making the solution valid for rotors with different geometries and any number of blades.

Although the solution is quite general and the method basically three-dimensional, the assumptions of thin slightly cambered blades, inviscid incompressible flow with disturbance frequency small compared to the average steady flow and with negligible secondary flow effects are imposed in order to obtain a tractable but useful solution. For the determination of noise, the results of the steady and unsteady circulation are substituted into the solution of the linear acoustic equation (see for example Benzakein's papers). All the results are evaluated at the fan face. The solution is too lengthy to present here.

Summaries of the noise calculations are given in References 30 and 31.

Noise due to Steady and Unsteady Spanwise Circulation Distribution

A typical fan was selected for which detailed experimental information was available. The fan used for comparison purposes is listed in References 10 and 11. The standard case selected has the following properties:

Hub-tip ratio = 0.33
Number of blades = 8
Blade chord = root chord/blade length = 0.375
Stagger angle = 30°
Tip clearance/blade length = 0.04
Twist angle = taper = camber = 0
Blade length = 4 in.
Blade chord = 1.5 in.
Duct Mach number = 0.325

$$\text{Dimensionless Velocity Parameter} = \frac{\text{Angular Velocity x Blade Length}}{\text{Reference Velocity}} = 0.774$$

Magnitude of disturbance velocity = 5%

$$\text{Reduced Frequency} = \frac{1}{2}\,\frac{\text{Disturbance Frequency x Chord}}{\text{Reference Velocity}} = 0.1$$

The computer program that was developed can be used to calculate rotor noise, rotor-stator interaction noise, periodic and non-periodic disturbances, and axial or circumferential disturbances. By inputing a periodic circumferential disturbance which is calculated from the wake of the upstream stator, rotor-stator interaction noise can be determined [32].

Figure 2 shows the results of different hub-tip ratios for the case of steady rotor and for the same rotor subject to a circumferential or axial disturbance. It appears that changing hub-tip ratio influences the steady lift noise component but varying the hub-tip ratio has no effect on the unsteady lift. Figure 3 shows the influence of rpm on noise. For this fan, the unsteady circulation produces noise levels far below that of the steady component. Of course this changes if the magnitude of the disturbance velocity is increased. The effect of taper is given in Figure 4 which shows that the taper angle changes the circulation distribution but is not particularly significant in changing the noise generation from a rectangular blade to a near-triangular blade. Since increasing the taper appears to decrease the noise, this means that uniform radial loading distribution is more desirable. Figure 5 shows the noise reduction as the number of blades is increased. This result is of course consistent with two-dimensional theories.

These figures show that circumferential disturbances in general result in higher noise than axial disturbances. The influence of two other parameters was also calculated. Although not graphically presented here, they show qualitatively that increasing the gap decreases the noise slightly. Since near the tip the viscous effects would dominate (such as the shear noise), the results are of only secondary importance. Another parameter is the influence of a distorted profile subject to an axial or circumferential disturbance; the results show that a uniform velocity profile is more desirable. The general trend of these results seem to be consistent with the empirical result of Sower: noise increases due to increasing rpm and decreases with increasing number of blades, both at about the same rate of change, whereas a change in hub-tip ratio for

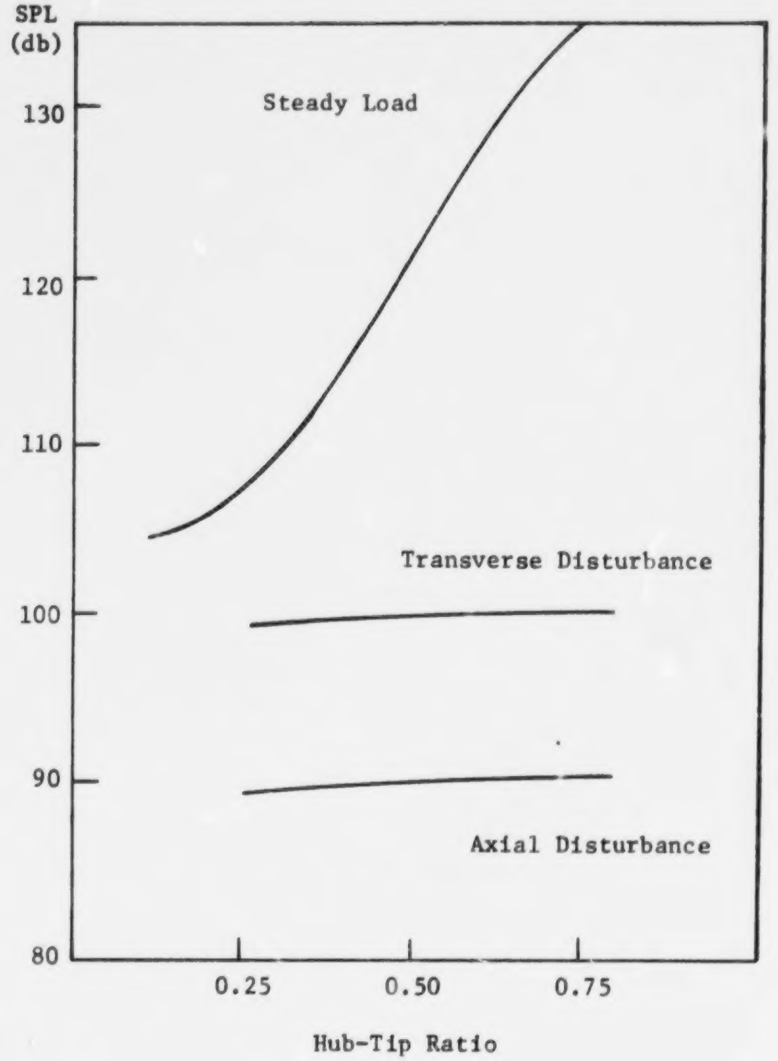

Figure 2. Effect of Hub-Tip Ratio on the Sound Power Level Generated

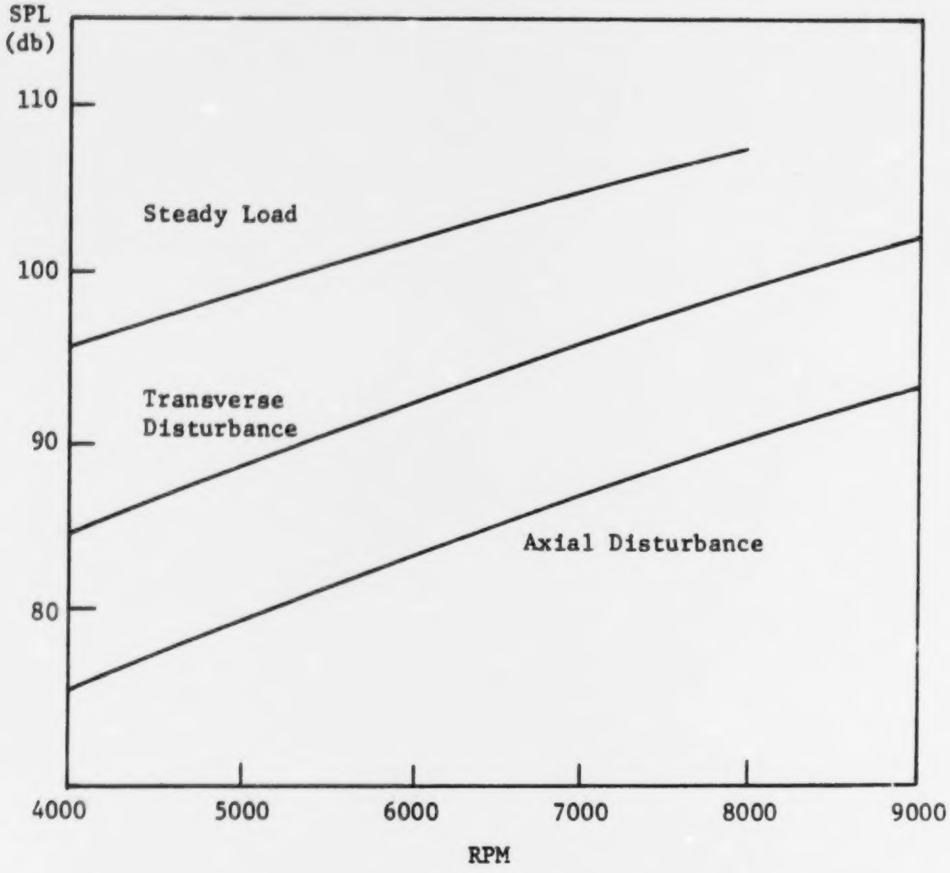

Figure 3. Effect of RPM on the Sound Power Level Generated

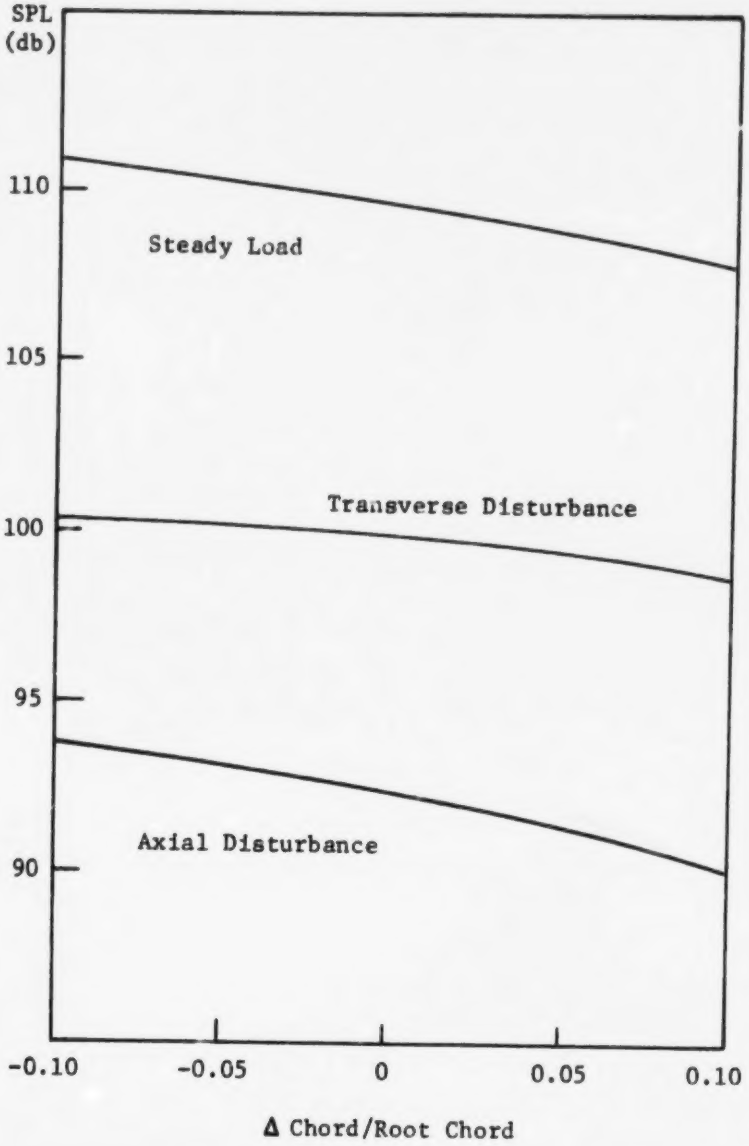

Figure 4. Effect of Taper on the Sound Power Level Generated

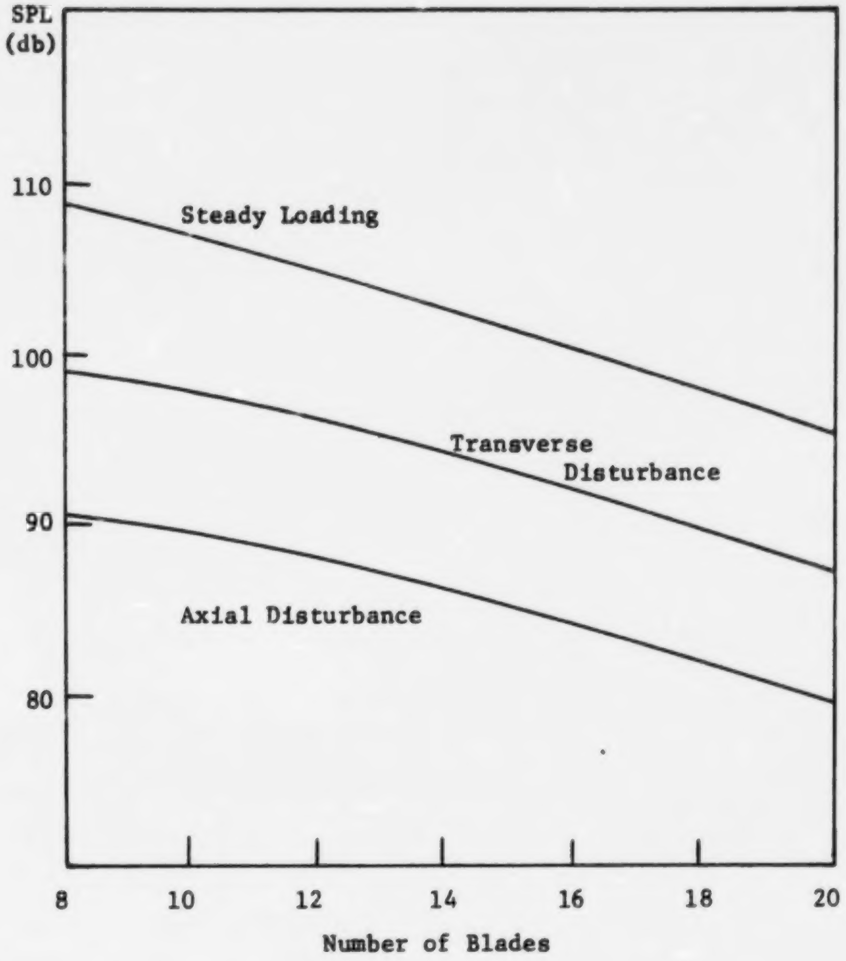

Figure 5. Effect of Number of Blades on the Sound Power Level Generated

steady circulation increases the noise at a much higher rate.

One of the interesting results was the noise change due to changes in twist angle, as shown on Figure 6. The results indicate that for an optimum design it is necessary to know something about the type of disturbance anticipated before a decision is made on the combination of twist and stagger to minimize noise. Since this result opens interesting and useful possibilities, further work (both theoretical and experimental) is being done to expand and verify this result. Figure 7 shows the influence of the disturbance frequency. From the study of the effect of reduced frequency it was found that the higher the rpm, the more important the steady loading noise becomes.

Although comparisons with the experimental results from References 10 and 11 show good agreement, and variation of these parameters show certain trends as seen from Figures 2 to 7, extrapolation, even qualitatively, can be done only with extreme caution. However, within the limits of the assumptions made in the solution, the results can show the influence of blade design characteristics on noise. More work is being carried out including a combined program where the results of a particular blade design for low noise are input into thethe streamline curvature program [33] to determine its aerodynamic performance.

[Acknowledgment: A portion of this work was supported by NASA grant NGR-43-001-134. Special thanks go to Mrs. Monika Lumsdaine for typing the manuscript.]

REFERENCES

1 Hulse, B.T. and Large, J.B., "The Mechanism of Noise Generation in a Compressor Model," Trans. ASME, Journal of Engineering for Power, April 1967, pp. 191-198.

2 Benzakein, M.J. and Kazin, S.B., "Fan Compressor Noise Reduction," ASME Paper No. 69-GT-9, 1969.

3 Dzung, L.S. (ed.), Flow Research on Blading, Proceedings of the Symposium on Flow Research on Blading, Brown-Boveri and Co., Lmtd., Baden, Switzerland, 1969.

4 Feiler, C.E. and Conrad, E.W., "Noise from Turbomachinery," AIAA 5th Aircraft Design, Flight Test and Operations Meeting, St. Louis, Missouri, August 6-8, 1973.

5 Peistrup, C.F. and Wesler, J.E., Journal of the Acoustical Society of America, Vol. 25, 1953, p. 322.

6 Beranek, L.L. (ed.), Noise Reduction, McGraw Hill Book Co., New York, 1960.

7 Lowson, M.V., "Theoretical Studies of Compressor Noise," NASA Report No. CR1287, March 1969.

8 Morfey, C.L., "A Review of the Sound-Generating Mechanism in Aircraft-Engine Fans and Compressors," AFORS-UTIAS Symposium on Aerodynamic Noise, Toronto, 1968; University of Toronto Press, 1969, pp. 299-329.

9 Sowers, H.D., "Investigation of Methods for the Prediction and Alleviation of Lift Fan Noise," USATRECOM TR 65-4, 1965.

10 Bateman, D.A., Chang, S.C., Hulse, B.T and Large, J.B., "Compressor Noise Research," FAA-ADS-31, Jan. 1965.

11 Hulse, B., Pearson, C., Abbona, M. and Andersson, A., "Some Effects of Blade Characteristics on Compressor Noise Level," FAA-ADS-82, Oct. 1966.

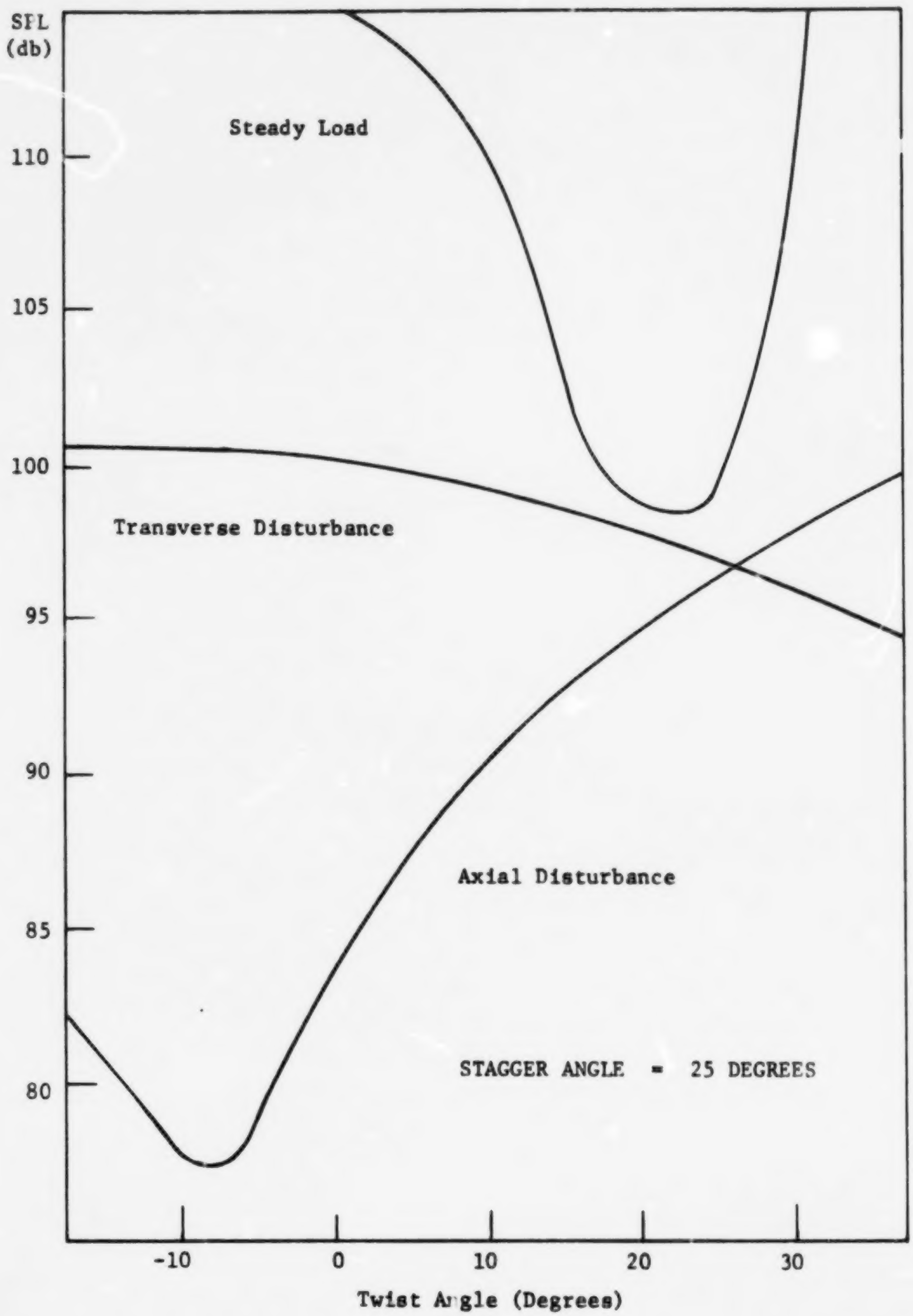

Figure 6. Effect of Twist on the Sound Power Level Generated

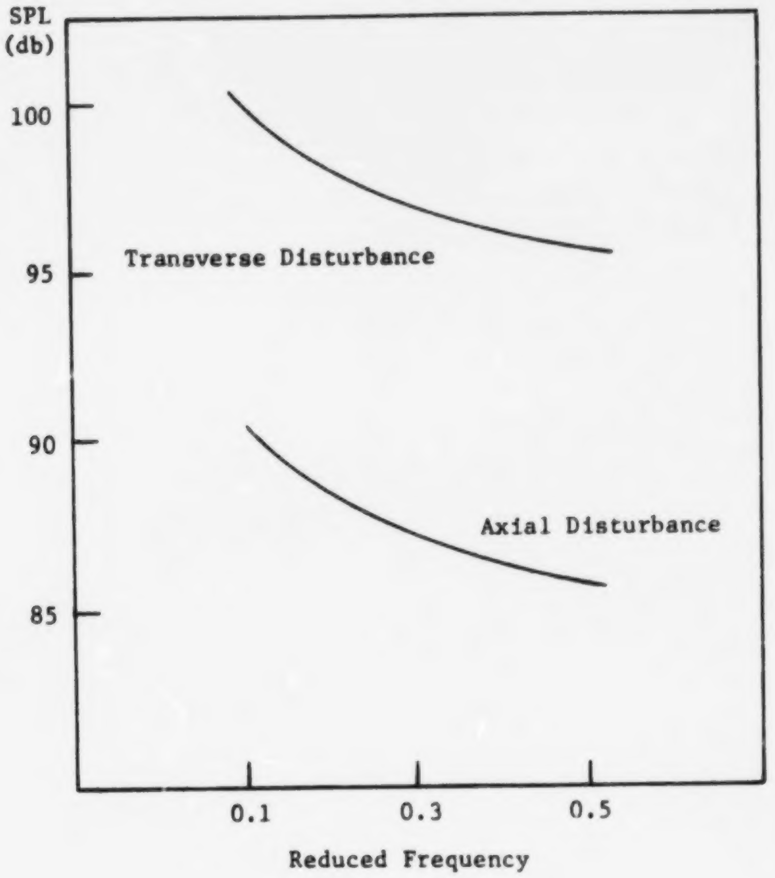

Figure 7. Effect of Reduced Frequency on the Sound Power Level Generated

---

12 Lordi, J.A., "Noise Generation by a Rotating Blade Row in an Infinite Annulus," 4th AIAA Conference on Fluid and Plasma, 71-617, 1971.

13 Flot, R., private communications, Laboratoire de Mechanique des Fluides, Ecully, France.

14 Sharland, I.J., "Sources of Noise in Axial Flow Fans," Journal of Sound and Vibration, Vol. 1, No. 3, 1964.

15 Benzakein, M.J. and Kazin, S.B., "A Theoretical Prediction of Aerodynamically Generated Noise in Fans and Compressors," presented at the November 1968 meeting of the Acoustical Society of America.

16 Benzakein, M.J., Claes, H.P., Coward, W.E., Hoshheiser, R.M., Kazin, S.B. and Knott, P.R., "Fan/Compressor Noise Research," Rept. No. FAA-RD-71-85, Vols. I,II,III, May 1972.

17 Reethof, G., "Aircraft Fan and Compressor Noise Generation, A Review," Noise and Vibration Control Engineering, Proceedings of the Purdue Noise Control Conference, July 1971.

18 Kemp, N.H. and Sears, W.R., "Aerodynamic Interference Between Moving Blade Rows," Journal of Aeronautical Sciences, Vol. 20, 1953, pp. 585-598.

19 Kemp, N.H. and Sears, W.R., "The Unsteady Forces Due to Viscous Wakes in Turbomachines," Journal of Aeronautical Sciences, Vol. 22, 1955, pp. 478-483.

20 Horlock, J.H., "Unsteady Flow in Turbomachines," Third Australian Conference on Hydraulics and Fluid Mechanics, Paper No. 2674, Nov. 1968.

21 Henderson, R.E. and Horlock, J.H., "An Approximate Analysis of the Unsteady Lift on Airfoils in Cascade," ASME Paper No. 72-GT-5, 1972.

22 Whitehead, D.S., "Vibration of Cascade Blades Treated by Actuator Disk Methods," Proceedings, Institute of Mechanical Engineers, Vol. 173, Nov. 21, 1959.

23 Whitehead, D.S., Bending Flutter of Unstalled Cascade Blades at Finite Deflection," Aeronautical Research Council, R and M 3386, 1962.

24 Henderson, R.E. and Daneshyar, H., "Theoretical Analysis of Fluctuating Lift on the Rotor of an Axial Turbomachine," Cambridge University Report TR17, 1970.

25 Yeh, H. and Eisenhuth, J.J., "The Unsteady Wake Interaction in Turbomachinery and Its Effects on Cavitation," Journal of Basic Engineering, Series D, Vol. 81, No. 2, June 1959, pp. 181-189.

26 Naumann, H. and Yeh, H., "Lift and Pressure Fluctuations of a Cambered Airfoil Under Periodic Gusts and Applications in Turbomachinery," ASME Paper No. 72-GT-30, 1972.

27 Mugridge, B.D., "Gust Loading on a Thin Aerofoil," The Aeronautical Quarterly, Vol. XXII, Aug. 1971.

28 Lumsdaine, E. and Fathy, A., "A Three-Dimensional Theory for Calculating Circulation in Axial Turbomachines (Direct Problems)," presented at the 1974 Gas Turbine Conference (ASME), Zurich, Switzerland, and published in ASME Trans., Journal of Engineering for Power.

29 Fathy, A. and Lumsdaine, E., "Unsteady Circulation Distribution in Rotors," submitted for publication in ASME Trans., Journal of Engineering for Power.

30 Lumsdaine, E. and Fathy, A., "Effect of Spanwise Circulation Distribution on Compressor Noise," presented at the 1972 International Conference on Noise Control Engineering, Washington, D.C., Oct. 4-6; published in 72 Inter-Noise Proceedings, pp. 482-487.

31 Fathy, A. and Lumsdaine, E., "Effect of Unsteady Loading on Rotor Noise," 73 Inter-Noise Proceedings, Lyngby, Denmark, August 1973, pp. 186-190.

32 Fathy, A., "The Unsteady Distribution in Rotors and its Application to Noise Studies," Ph.D. Thesis, South Dakota State University, Brookings, South Dakota, 1973.

33 Daneshyar, H. and Shaalan, M.R.A., "The Off-Design Analysis of Flow in Axial Compressors," Aeronautical Research Council, D.P. 1234, University of Cambridge, England, 1972.

AERODYNAMIC DESIGN OF A ROTOR BLADE FOR MINIMUM NOISE RADIATION

by

K. Karamcheti* and Yung H. Yu**

Joint Institute for Aeroacoustics
Department of Aeronautics and Astronautics
Stanford University
Stanford, California

ABSTRACT

An analysis of the aerodynamic design of a hovering rotor blade for obtaining minimum aerodynamic rotor noise has been carried out. In this analysis, which is based on both acoustical and aerodynamic considerations, attention is given only to the rotational noise due to the pressure fluctuations on the blade surfaces. A functional relation between the pressure distribution along the blade span and the radiated noise is developed. From this relation, along with constraint equations concerning given levels of aerodynamic performance such as given total lift and drag, one may deduce, by utilizing the variational method, an optimum shape of the lift distribution. Utilizing an appropriate theory for the lift distribution along a blade, one may further deduce the aerodynamic characteristics such as the blade section profiles and their disposition in order to achieve the lift distribution required for minimum noise radiation. The lift distribution obtained in this analysis has different characteristics from those of the conventional distribution. The present distribution shows negative lift values over a quarter of the span from the blade tip, and a maximum lift at about the mid-span. Results are presented to show that the noise field is considerably affected by the shape of the lift distribution along the blade and that noise reduction of about 5dB may be obtained by designing the rotor blade to yield minimum noise. The nature and method of analysis pursued here are of general interest in different problems concerned with the reduction of aerodynamically generated noise.

INTRODUCTION

We are concerned with the problem of the noise generated aerodynamically by hovering rotor blades. Specifically, the study is directed towards the contribution to the noise produced by the steady lift forces distributed along the span of a blade rotating with a constant angular velocity. The objective is to determine analytically, satisfying certain given constraints such as total lift and total drag, that spanwise distribution of lift which yields the minimum far field noise intensity, and with the knowledge of such a distribution the corresponding characteristics such as the blade section profiles and their disposition.

---

* Director, Joint Institute for Aeroacoustics, and Professor

** Research Assistant and Ph. D. student

This aspect has not received any attention in the earlier studies of rotor rotational noise. The noise analysis is usually carried out assuming a concentrated lift to be situated at an effective radius of the rotating blade. Thus, little is known at present concerning how the sound field is affected by the different types of lift distribution.

In this paper we shall first describe briefly the formulation of the mathematical problem, and the method of solution. The solution for the lift distribution yielding the minimum noise is then presented and the characteristics of the corresponding noise field are discussed in comparison with the fields given by other distributions. A possible blade shape to obtain the desired distribution is derived.

MATHEMATICAL FORMULATION

Let us consider, as shown in Fig. 1, a rigid rotor rotating with a constant angular velocity Ω, and concern ourselves with the noise radiated by only the pressure forces distributed over the blade surfaces. The noise field is simply that due to pressure forces distributed over rigid surfaces rotating with a constant angular velocity. We shall furthermore neglect the contribution from the drag components of these forces and thus restrict ourselves to the contribution from only the lift components.

Choose the origin of coordinates and the space fixed axes $\vec{e}_1$ and $\vec{e}_3$ as shown in Fig. 1, such that the spherical coordinates of the fixed position vector $\vec{x}$ to the field point P are

$$\vec{x} : (x,\ \psi,\ \theta = 0)$$

Consider a surface element of the blade $ds(\vec{y})$ situated at a radius $\vec{y}$ along the blade. The position vector from this element to the field point is denoted by

$$\vec{R} = \vec{e}_R \, R$$

The velocity at the element is $\Omega y \, \vec{e}_\theta$ and the corresponding Mach number vector is

$$\vec{M} = \frac{\Omega y}{a_0} \, \vec{e}_\theta$$

where $\vec{e}_\theta$ is the unit vector corresponding to θ and a_0 is the speed of sound in the undisturbed fluid.

Acoustical Considerations

Following Ffowcs Williams and Hawkings(1), the acoustic denisty perturbation ρ' at the field point is given by

$$4\pi a_0^2\, \rho'(\vec{x},t) = -\text{div} \int_S \left[\frac{p\vec{n}}{kR}\right] ds(\vec{y}) \qquad (1)$$

where p is the pressure

$k = 1 - \vec{e}_R \cdot \vec{M} = 1 - M_R$

$\vec{n}$ is the outward normal to the surface into fluid

$[\alpha] \equiv \alpha(\vec{y},\ t - \frac{R}{a_0})$

and S denotes the blade surfaces.

Denoting by $\ell(y)\, \vec{e}_3$ the spanwise distribution of the lift forces measured per unit length. Carrying out the divergence operation in relation (1), neglecting the contributions from the drag forces, assuming that $R \gg \lambda > b$, where λ is a typical acoustic wave length, and neglecting retarded time, we may approximate (1) for the far field as

$$4\pi a_0^2\, \rho'(\vec{x},\ t) = \frac{nx_3}{a_0 x^2} \int_0^b \frac{1}{k^2} \left(\frac{\partial \ell}{\partial t} + \frac{\ell}{k}\frac{\partial M_R}{\partial t}\right) dy \qquad (2)$$

where b is the span length of a blade and n is the number of blades. Note that $x = |\vec{x}|$ and $x_3 = \vec{e}_3 \cdot \vec{x}$.

In the present problem the forces on a blade are steady. Hence relation (2) reduces to

$$4\pi a_0^2\, \rho'(\vec{x},\ t) = \frac{nx_3}{a_0 x^2} \int_0^b \frac{\ell}{k^3} \frac{\partial M_R}{\partial t}\, dy \qquad (3)$$

denoting noise radiation due to the acceleration of the dipole sources.

The noise intensity in the far field is defined by

$$I\ (\vec{x}) = \frac{a_0^3}{\rho_0} < \rho'^2 >$$

where ρ_0 is the density in the undisturbed fluid and the brackets denote appropriate time average. With the use of (3), this becomes

$$I(\vec{x}) = \left(\frac{n}{4\pi}\right)^2 \frac{1}{\rho_0 a_0^3} \left(\frac{x_3}{x^2}\right)^2 \int_0^b\!\!\int_0^b H(y_1, y_2)\ \ell(y_1)\ \ell(y_2)\ dy_1\ dy_2 \qquad (4)$$

where

$$H(y_1,y_2) = \left\langle \frac{1}{\left\{1-M_R(y_1,t)\right\}^3} \, \frac{1}{\left\{1-M_R(y_2,t)\right\}^3} \, \frac{\partial M_R}{\partial t}(y_1,t) \, \frac{\partial M_R}{\partial t}(y_2,t) \right\rangle$$

The integral relation (4) forms the basis for further considerations.

Preliminary Mathematical Considerations

Our problem now is to determine $\ell(y)$ such that $I(\vec{x})$ is a minimum while at the same time satisfying certain constraint relations such as keeping the total lift and total drag on a blade constant. The constraint relations may be written as:

$$n \int_0^b \ell(y)\, dy = L \tag{5}$$

$$n \int_0^b f(y)\, dy = D \tag{6}$$

where $f(y)$ denotes the spanwise drag distribution and L and D are constants respectively, denoting the total lift and drag on the rotor. Assuming that the sectional lift and drag are related in the same manner as in the lifting line theory, we write

$$f(y) = \ell(y)\,\frac{w(y)}{\omega y}$$

where, $w(y)$ is the induced downwash velocity. Then relation (6) becomes

$$n \int_0^b \ell(y)\,\frac{w(y)}{\omega y}\, dy = D \tag{7}$$

Thus the problem is to determine $\ell(y)$ such that $I(\vec{x})$ is a minimum while satisfying relations (5) and (7). We note, however, that the induced velocity $w(y)$ is not known a priori. It is, in fact, related to the lift distribution in form of an integral of the later. We shall, therefore, discuss next a few pertinent aerydynamic relations.

Some Aerodynamic Considerations

In order to obtain the relation between the induced velocity and the lift distribution we assume, based on the experimental observations of Landgrebe(2), a simple wake model which consists of only strong vortex filaments emanating from the blade tips, as shown in Fig. 2. It is assumed, for simplicity, that the vortex sheets emanating from the trailing edges of the blades roll up rapidly into the tip vortices. The axial displacement of a vortex filament, based on the experimental observations, is sketched in Fig. 2b.

With this wake model and the use of Biot-Savart law, the induced velocity $w(y)$ is given by (3)

$$w(y) = \frac{1}{4\pi}\left\{\int_0^b \left[\frac{\ell(\xi)}{\rho\Omega\xi}\right] d\xi\right\} \sum_{j=1}^{n} \int_{C_j} \frac{d\vec{s}_j \times (\vec{y}-\vec{s}_j)}{\left|\vec{y}-\vec{s}_j\right|^3} \qquad (8)$$

where, the integral from 0 to b is the circulation around a vortex filament, C_j denotes the filament from the tip of blade j, and $\vec{s}_j$ is the position vector to an element of the filament C_j.

The Final Mathematical Problem

We wish to determine $\ell(y)$ such that the intensity integral given by relation (4) is a minimum and such that the constraint relations (5) and (7), where $w(y)$ is given by (8), are satisfied. Since the lift vanishes at both the root and the tip of the blade, we shall assume that the lift distribution is of the form

$$\ell(y) = \ell^*(y)\, y(1 - y) \qquad (9)$$

METHOD OF SOLUTION

The solution is to be constructed following variational methods. Since $w(y)$ in the constraint condition (7) is not known a priori but is given by (8) which involves an integral of the lift distribution, mathematical difficulties are encountered. In order to surmount these difficulties, we attempt the solution of the problem by iteration. Accordingly, we assume a suitable distribution of the induced velocity $w(y)$, solve for $\ell(y)$, assuming the form given in (9), by variational methods, from the equations (4), (5), and (7). Utilizing this solution for $\ell(y)$ we compute using equation (8) a new distribution for $w(y)$, which then is used for another evaluation of $\ell(y)$. This iterative procedure is repeated until satisfactory convergence is reached.

To initiate the procedure, we assumed for the first downwash distribution one that is given by the experimental results of Landgrebe(2). The variation of the induced angle of attack which is $w(y)/\Omega y$ along the span according to Landgrebe's results is shown in Fig. 3. In the same figure we also show the computed downwash distribution obtained a few iterations.

In carrying out the actual solution, the various equations are first cast in a non-dimensional form. The following are the main non-dimensional parameters that are of interest:

$$\begin{aligned} \eta &= \frac{y}{b}\,, \quad 0 \le \eta \le 1 \\ \bar{x} &= \frac{x}{\lambda} \qquad\qquad (10) \\ \bar{\ell}(\eta) &= \frac{\ell(\eta)}{L/bn} \end{aligned}$$

Cont.

tip Mach number $M_b = \frac{\Omega b}{a_0}$

$$\bar{I} = \frac{I}{L^2/b^4 \rho_0 a_0}$$

At each stage of the iteration, the lift distribution yielding the minimum intensity and satisfying the constraint conditions turns out to be a Fredholm integral equation of the first kind with a symmetric kernel, and thus it can be determined without undue mathematical difficulties. The solution is obtained in closed form but is too lengthy to be presented. We shall not enter here into the details; they can be found in a forthcoming JIA report*.

BLADE CHARACTERISTICS

Once the lift distribution for the minimum noise radiation has been determined, as discussed in the previous sections, one can proceed, by employing a consistent and suitable theory of lift, the aerodynamic characteristics of the rotor blade. Here, we shall confine ourselves to the simplest considerations. Accordingly, we shall assume "strip" theory, as in the case of a finite wing of large aspect ratio, to be applicable and take as our basic relation for this part of the analysis the following

$$\ell(y) = \beta_0 \left\{\alpha(y) - \alpha_i(y)\right\} c(y) \frac{1}{2} \rho V^2 \tag{11}$$

where

β_0 : slope of the lift versus angle of attack curve

$\alpha(y)$: angle of zero lift

$\alpha_i(y)$: induced angle of attack

$c(y)$: chord length

$V(y) = \Omega y$

From previous analysis we know $\ell(y)$ and $\alpha_i(y)$. Assuming a thin airfoil for the blade section the value of β_0 usually does not differ very much from the value 2π . Then, equation (11) becomes the basis for determining $c(y)$ and $\alpha(y)$, i.e., the variations of the chord length and the twist along the span.

---

* JIA stands for the Joint Institute for Aeroacoustics

SOME RESULTS AND DISCUSSION

On the basis of the closed form solution, numerical results are obtained for a two bladed rotor $(n = 2)$ using an IBM 360-67 computer, for $\bar{x}$ equal to 30, and for various values of the angle ψ and the tip Mach number M_b. We now present some of the results.

Optimum Lift Distribution

The lift distribution yielding the minimum intensity and satisfying the constraint equations, which we shall refer to as the optimum lift distribution, has been computed for different values of ψ and M_b (see Fig. 1). There is no marked difference between the various cases. The optimum distribution thus found is shown in Fig. 4.

It is seen that the optimum distribution is characteristically different from the conventional distribution which is of a triangular form as sketched below. It is to be noted that the optimum distribution indicates a negative lift over about quarter of the span at the blade tips, and a maximum lift at about the mid-span. This is physically understandable since we are seeking a distribution that yields a minimum intensity and to achieve such a situation it is necessary to arrange the distribution so as to lead to distructive interference of the acoustic radiation from the rotating blade.

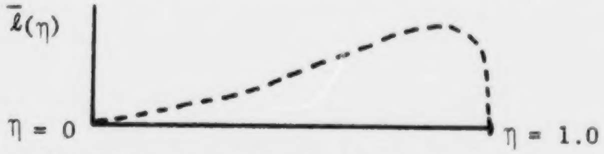

Schematic of a triangular distribution

Comparison of Acoustic Intensities for Different Lift Distributions

Figure 5 shows the variation of the non-dimensional intensity with the angle ψ for a given tip Mach number M_b for different shapes of the lift distribution. It is seen that the optimum distribution yields to the minimum intensity for all values of the angle ψ. The ratio of the intensity for a triangular distribution is that for the optimum varies over the range 3.1 to 3.6 as ψ varies from 10 to 90 degrees. This means that the optimum distribution will lead to a noise reduction of about 5 dB compared to the conventional triangular distribution.

Figure 6 shows the variation of the intensity with the tip Mach number for a fixed angle ψ. We notice, as expected, all distributions lead to increasing intensities as the tip Mach number increases. However, we note that the optimum distribution is the one that yields the lowest intensity at all tip Mach numbers.

Determination of Blade Characteristics

Having known the optimum lift distribution and the variation of the induced angle of attack along the span from the previous section, one can determine, on the basis of (11), the aerodynamic characteristics of the rotor blade such as the variations of the chord length and the twist along the span.

Equation (11), however, is one equation for two unknowns $c(y)$ and $\alpha(y)$; thus additional requirements need to be stipulated. First, $c(y)$ should always be positive. Second, we may stipulate, for instance, the ratio of the maximum chord to the span. Assuming this ratio to be 0.1 and the angle of zero lift $\alpha(\eta)$ should not exceed 0.35 radians, we deduce from equation (11), the distribution shown in Fig. 7 for $c(\eta)$ and $\alpha(\eta)$.

CONCLUDING REMARKS

It is seen that the shape of the spanwise distribution of lift over a rotor blade affects considerably the intensity of the noise radiated. The "optimum" distribution, as obtained in this analysis indicates that it yields the minimum intensity for all values of the angle ψ and for different tip Mach numbers.

This study appears to be the first attempt at analytically determining the aerodynamic characteristics of a body moving through a fluid which lead to minimum intensity of the far field. The nature of the inquiry and the methodology concerned in this study should be of general interest, and hopefully will stimulate more detailed and complete analyses of a similar nature.

ACKNOWLEDGEMENTS

This work is carried out under the sponsorship and financial support of the U. S. Army Mobility Research and Development Command, Ames Directorate under Contract NAS 2-6158. The authors gratefully acknowledge this support. They wish to express their appreciation to Mr. Andrew H. Morse, Dr. Fredric H. Schmitz, Mr. Rande C. Vause, and Mr. Donald A. Boxwell for their continued interest in basic research in rotor aerodynamic noise and for many valuable discussions.

REFERENCES

1. FFOWCS WILLIAMS, J. E., and HAWKINGS, D. L., Sound Generation by Turbulence and Surfaces in Arbitrary Motion - Phylosophical Transactions of the Royal Society of London, Vol. 264A, pp. 321-342, 1969.

2. LANDGREBE, A. J., The Wake Geometry of a Hovering Helicopter Rotor and its Influence on Rotor Performance - 28th Annual National Forum of the American Helicopter Socity, May 1972.

3. KARAMCHETI, K., Ideal Fluid Aerodynamics - John Wiley & Sons, New York, 1966.

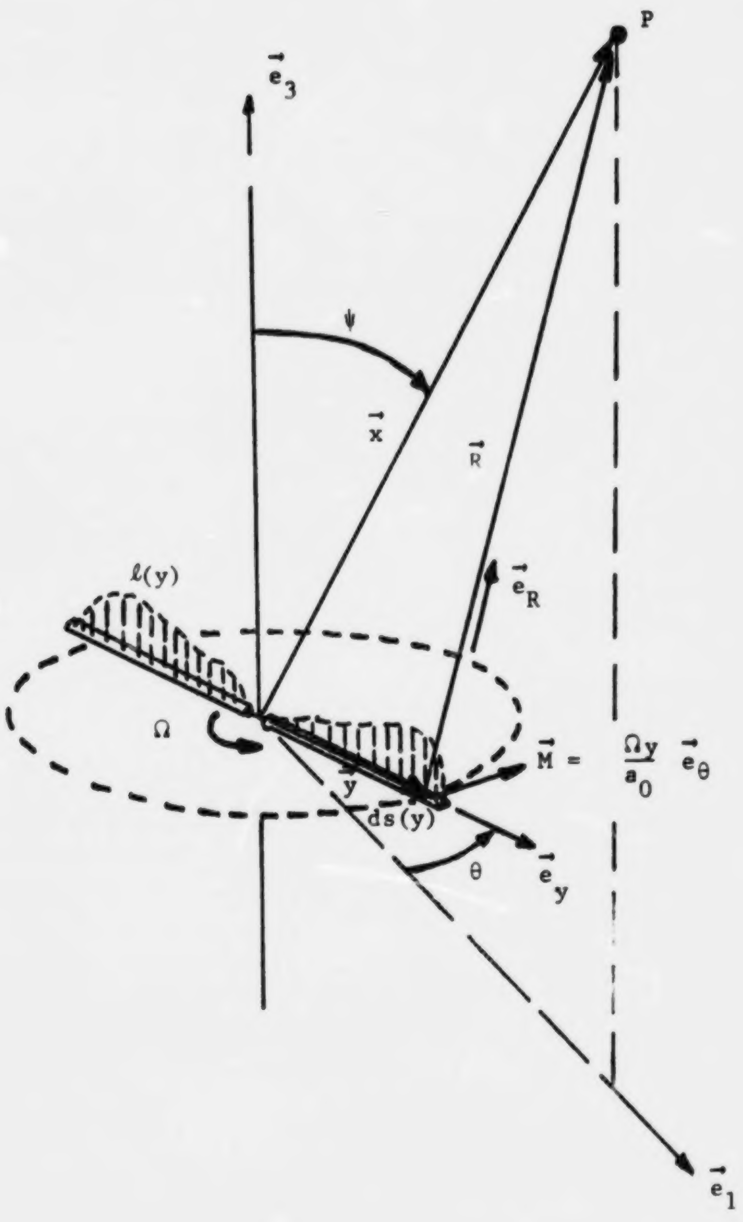
P
$\vec{e}_3$
ψ
$\vec{x}$
$\vec{R}$
$\vec{e}_R$
$\ell(y)$
Ω
$\vec{M} = \frac{\Omega y}{a_0} \vec{e}_\theta$
$\vec{y}$
ds(y)
θ
$\vec{e}_y$
$\vec{e}_1$

Fig. 1 Illustrating the Formulation of the Problem

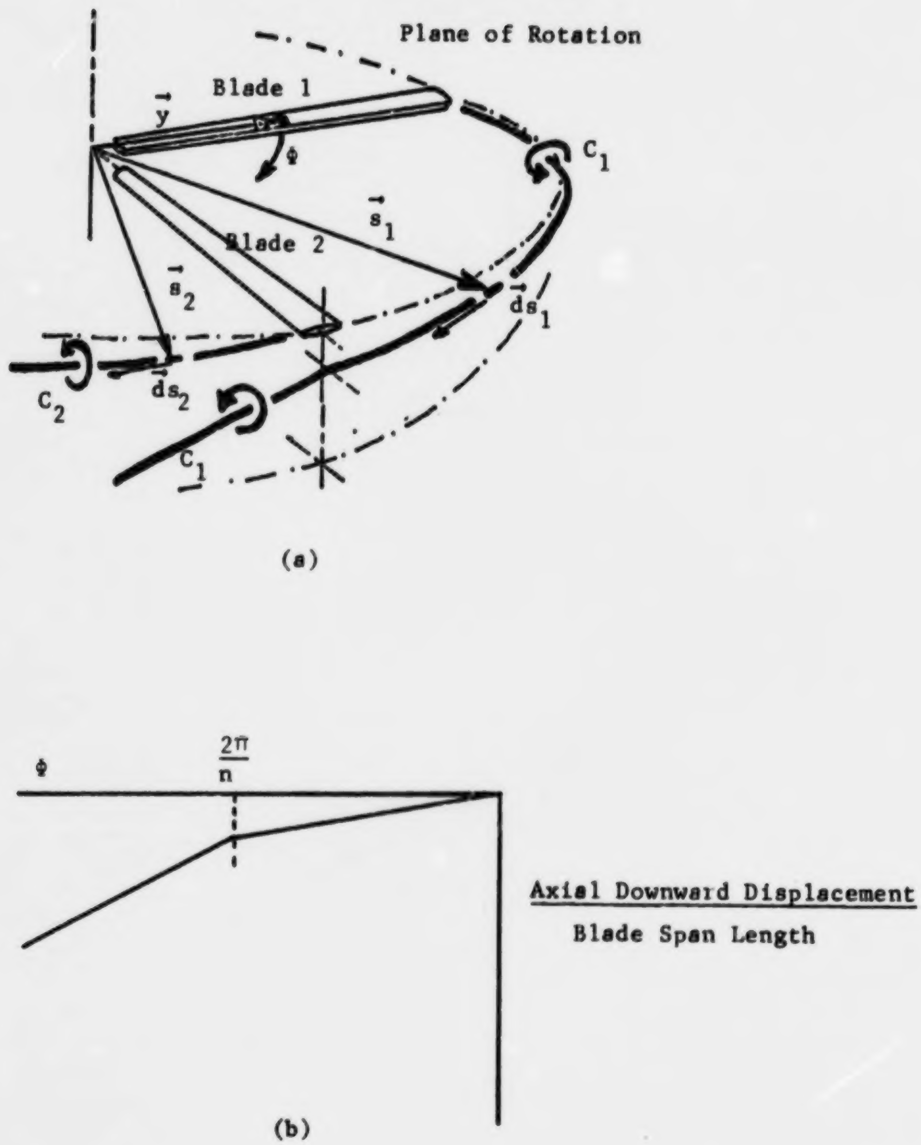
Plane of Rotation
Blade 1
$\vec{y}$
Φ
C_1
$\vec{s}_1$
Blade 2
$\vec{s}_2$
$\vec{ds}_1$
C_2
$\vec{ds}_2$
C_1
Φ
$\frac{2\pi}{n}$
$\frac{\text{Axial Downward Displacement}}{\text{Blade Span Length}}$

(a)

(b)

Fig. 2 General Schematic of the Wake System

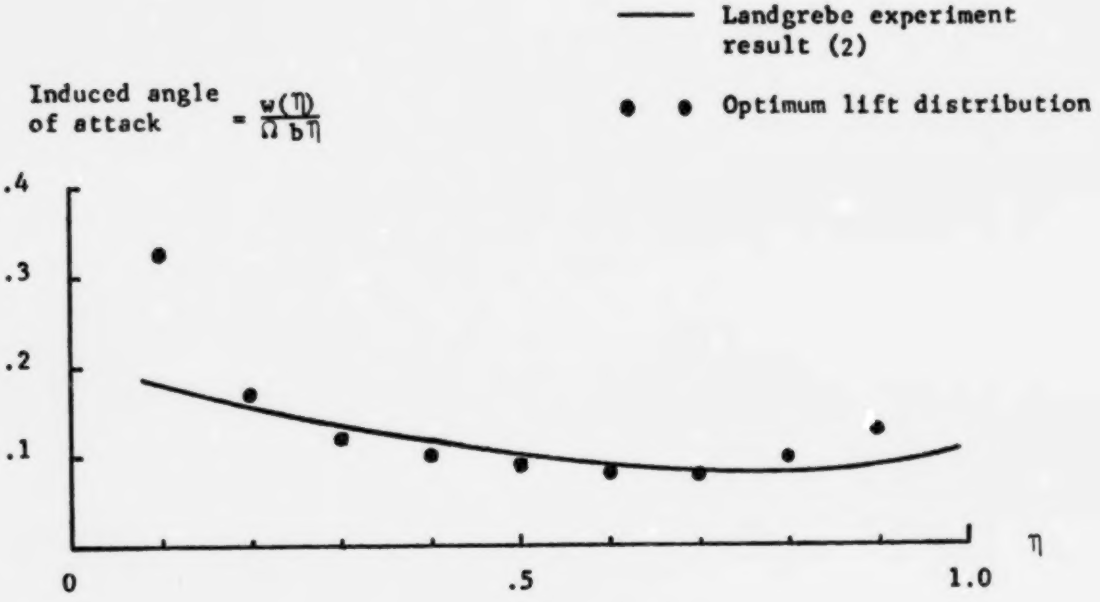

Fig. 3. Comparison of the induced angle of attack

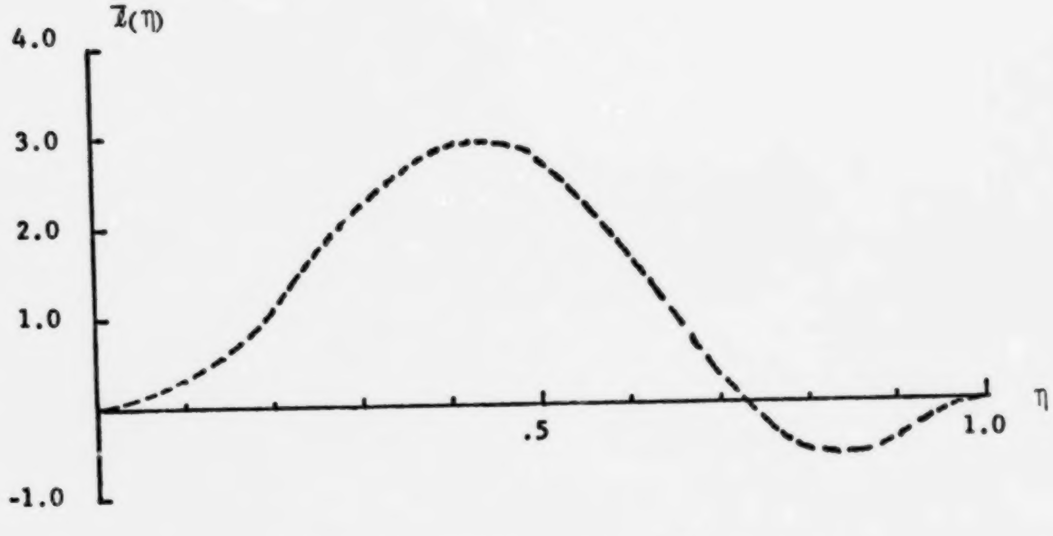

Fig. 4. Optimum lift distribution ($\psi = 50^\circ$, $M_b = 0.4$)

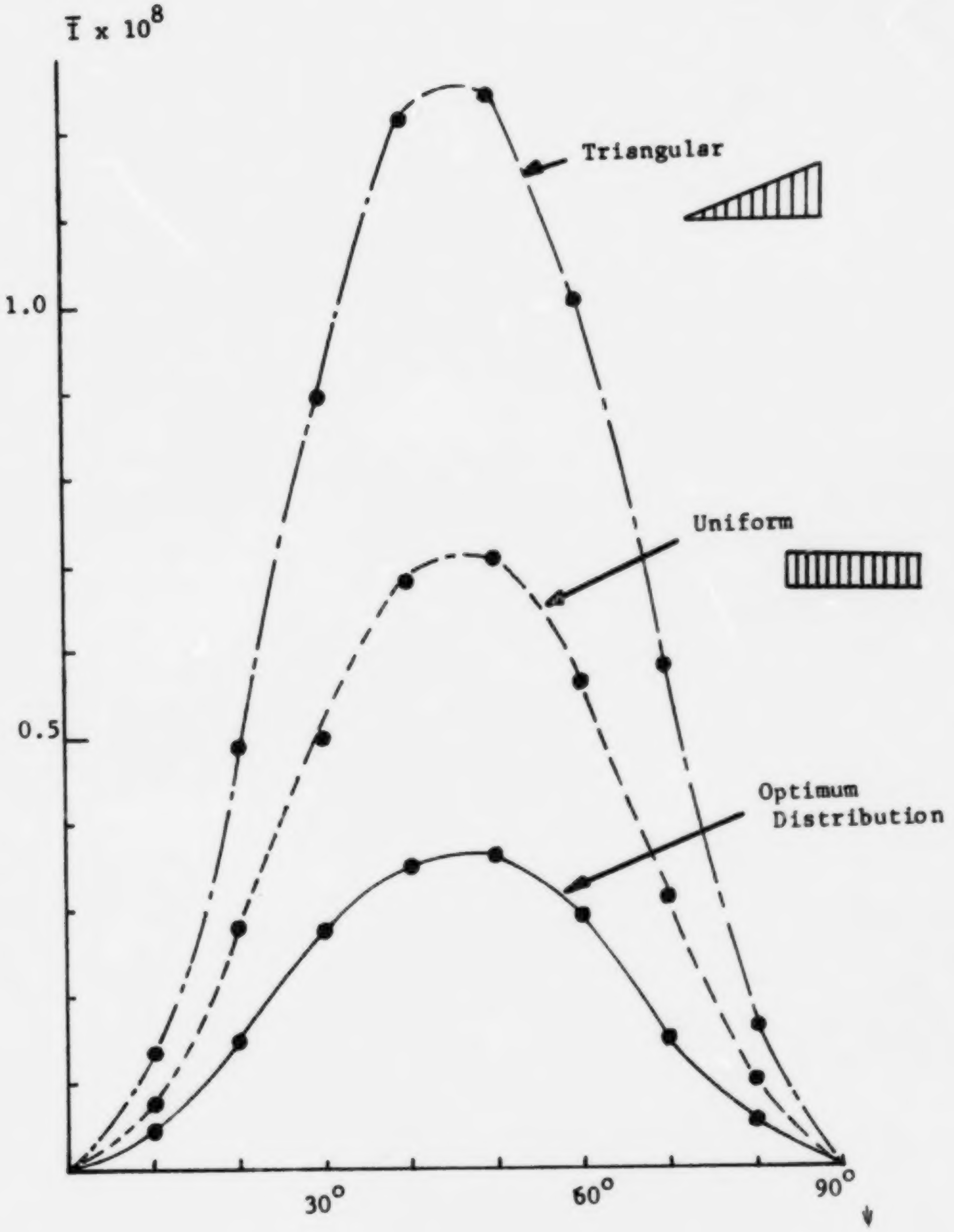

Fig. 5 Non-dimensional Intensities of Different Distriubtions with Respect to the Angle ψ (M_b = 0.3)

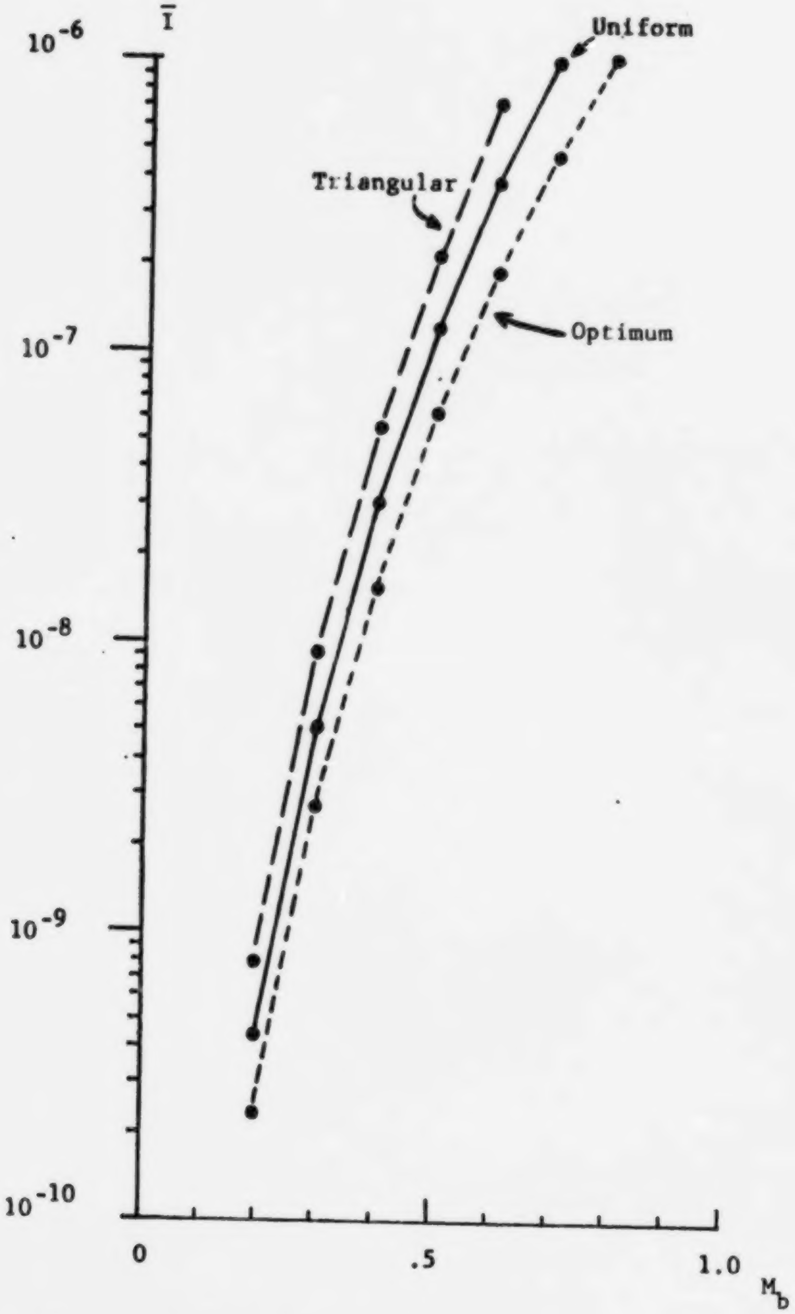

Fig. 6 · Intensities of several types of distribution
(ψ = 30°)

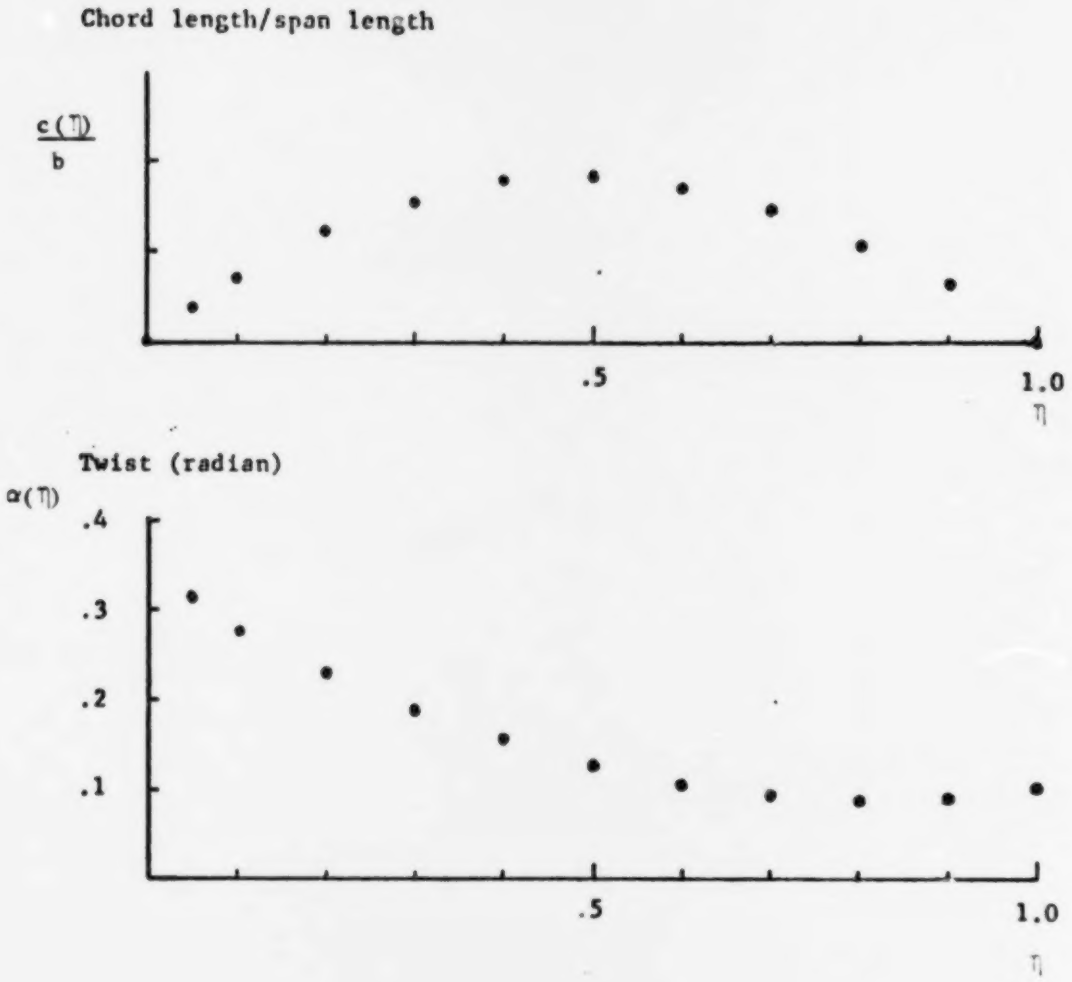

Fig. 7 Variations of the Chord Length and the Twist of a Flat Plate

SELECTED PROBLEMS I

DYNAMICS OF WEAK SHOCK WAVES AT A FOCUS

by

B. Sturtevant and V. A. Kulkarny

California Institute of Technology
Pasadena, California

ABSTRACT

Experimental observations of the behavior of focussed weak shock waves in air are reported. Incident plane shocks of Mach numbers from 1.005 to 1.3 are reflected from parabolic reflectors. Spark shadowgraphs exhibit the wavefront dynamics and pressure measurements provide supplemental information. It is shown that wavefront folding and crossing, a distinctive feature of linear geometrical acoustics, occurs even when the wave propagation in the neighborhood of the focus is predominantly nonlinear. The transition from folded to unfolded wavefronts as shock strength increases can be predicted by considerations of nonlinear shock diffraction, in which it is necessary to account for diffracted waves behind the leading disturbance. It is concluded that the fact that wavefront folding occurs cannot be taken to mean that the maximum overpressure at focus is limited by essentially linear diffraction processes. Indeed, it appears that in a majority of observations nonlinear shock diffraction is the limiting process.

I. INTRODUCTION

A pressure wavefront, such as a shock wave or acoustic pulse, if generated by a non-uniform source, or if propagating in a non-uniform medium or reflecting from a curved surface, may become concave toward the direction of propagation and so focus. The occurrence of greatly magnified wave amplitudes in the focal region is a matter of concern in many applications, and it is important to be able to calculate the maximum overpressure that will occur. Furthermore, it may be equally important in certain applications to predict the shape of the wavefront during and after focus.

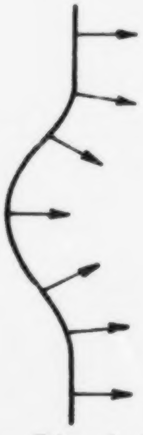

Figure 1. Dimpled Wavefront

This problem has arisen recently with the realization that maximum overpressures observed in the sonic boom may be caused by effects of aircraft manouver, by wave propagation through atmospheric thermal inhomogeneities, winds or turbulence, or by reflections from valleys and buildings. Indeed, this phenomenon occurs in such a variety of problems and over such a large range of physical scales that the study of the physical processes that limit the amplitude near a focus is of fundamental importance.

Consider a plane weak shock front or acoustic pulse which by one of the aforementioned processes has become locally concave (Fig. 1). The theory of geometrical acoustics predicts that the rays normal to the concave portion of the wavefront form a caustic or a focus and that the amplitude of the wave is infinite on the caustic. Furthermore, it is predicted that after focus the wavefront is folded. The central question is, what physical processes serve to limit the maximum amplitude to finite values at the focus? Two possibilities are diffraction and gasdynamic nonlinearity.

According to linear theory, if the pressure at the wavefront is discontinuous geometrical acoustics is exact and the singularity exists. Previously, we have speculated (Ref. 1) that on the scale of the (actual) shock-wave thickness wave-acoustic effects (diffraction) limit the amplitude. If the magnitude of the maximum amplitude so determined is so small that gasdynamic nonlinearity is negligible, then the maximum amplitude near focus can be predicted by linear theory, and far from the focus the wavefronts are folded as predicted by geometrical acoustics. At the focus, instead of converging to a point, the wavefront becomes locally plane (Ref. 2). The details of the calculation for an incident N-wave have recently been carried out by Obermeir (Ref. 3).

On the other hand, for stronger waves the amplitude may be limited by a completely different process; namely, the increase of wavespeed with amplitude described by Whitham's shock-diffraction theory (Ref. 4). In this case, perfect focus is prevented because the more strongly amplified portions of the wavefront accelerate, so the front flattens. Furthermore, because of the supersonic-subsonic character of finite-amplitude waves, wavefront folding is precluded by nonlinear effects and the geometry of the wavefront turns out to be quite different. Indeed, Whitham predicted an overshoot of the initially concave portion of the front to form a bulge in the direction of propagation.

Until now it has been assumed that in the neighborhood of some critical wave strength the maximum amplitude and the geometry of the wavefront change from those predicted by linear wave theory to those described by nonlinear theory. The central result of the experiments reported here is to show that this is not the case. Though for very weak waves the wave amplitude may undergo such a transition, the transition from folded to unfolded wavefronts occurs for much stronger waves, under conditions such that the focussing process is dominated by nonlinearity. That is, it is shown that there is a region of incident wave strengths and shapes in which the amplitude near focus is limited by nonlinear shock-diffraction effects but the wavefront beyond focus is folded. The transition from folded to unfolded wavefront is determined by purely kinematical considerations in which it is necessary to account for the diffracted fronts behind the leading disturbance. Therefore, it is seen that shock-diffraction theory contains the essential elements for describing the mechanism for amplitude limitation in the nonlinear regime. The paradox implied by previous observations (e.g., Ref. 5) of folded wavefronts when they were not expected is resolved; folded fronts may occur in the nonlinear regime (depending on the kinematics of shock diffraction), and the fact that folded wavefronts are observed cannot be taken to mean that linear theory holds in the focal region. In fact, it is evident that linear diffraction-limited focussing occurs in a rather limited range of conditions in practice and that nonlinear shock diffraction describes most observations of shock focussing. It is significant that wavefront geometry plays an important role in determining the behavior at a focus. This confirms the importance of shock diffraction and suggests that any successful analysis of focussing must account for these geometrical effects.

After describing the experimental apparatus (Section II) and the results (Section III) a simple model is proposed (Section IV) which explains the observations.

II. EXPERIMENT

Of the large variety of phenomena that may occur in focussing of shock waves, the simple and basic phenomenon of a perfect focus is investigated, especially to study nonlinear effects. The focus is created by reflecting a plane shock wave from a parabolic reflector on the endwall inside a large shock tube. Fig. 2 shows a schematic drawing of the setup. The transient wave patterns as they pass the focus are recorded through the windows by spark shadowgraphs. Also, wave amplitudes are independently measured in the flow field with a pressure transducer mounted on a probe.

The GALCIT 17" shock tube yields very plane shocks and the flow conditions behind them are quite uniform. Shocks of Mach number as low as 1.005 can be created with $\frac{1}{4}$ mil mylar diaphragms, and have been found to be well converged (i.e., with risetimes of less than one microsecond). Conditions in the test section are normally atmospheric except for strong shocks; for $M_s=1.2$ and 1.3 the initial pressure is 10 psia.

A simple spark light is used as an instantaneous point source at the focus of a concave mirror to generate a parallel beam of light which passes across the shock tube through the windows and directly exposes a fast Polaroid film on the other side.

Two solid reflectors are used, an axi-symmetric parabolid (a glass reflector embedded in epoxy on a wooden backing) with a point focus and a parabolic cylinder (a machined and polished piece of hardwood) with a line focus. Both have 2-3/8" focal length and 8" aperature. The reflectors are moved along the axis of the shock tube to examine different sections of the flow field. The experiment is initiated when the incident shock wave passes over a pressure transducer in the shock-tube wall, triggering a time-delay generator which, in turn, controls the spark discharge. Thus different stages of focussing are observed by changing the delay time and firing a shock for each setting.

Five different incident shock strengths are used (M=1.005, 1.03, 1.1, 1.2 and 1.3) to exhibit the full range of behavior. Only the shadowgraphs of the 2-dimensional line focussing are presented, as the shadowgraphs of 3-dimensional point focussing are found to be qualitatively identical.

Pressure histories at points on the axis of symmetry are recorded with piezoelectric pressure transducers on oscillograms. A small $\frac{1}{4}$" diameter sensor (PCB Piezotronics 113A21, risetime 1 microsecond) is mounted on a streamlined probe to minimize scattered disturbances and

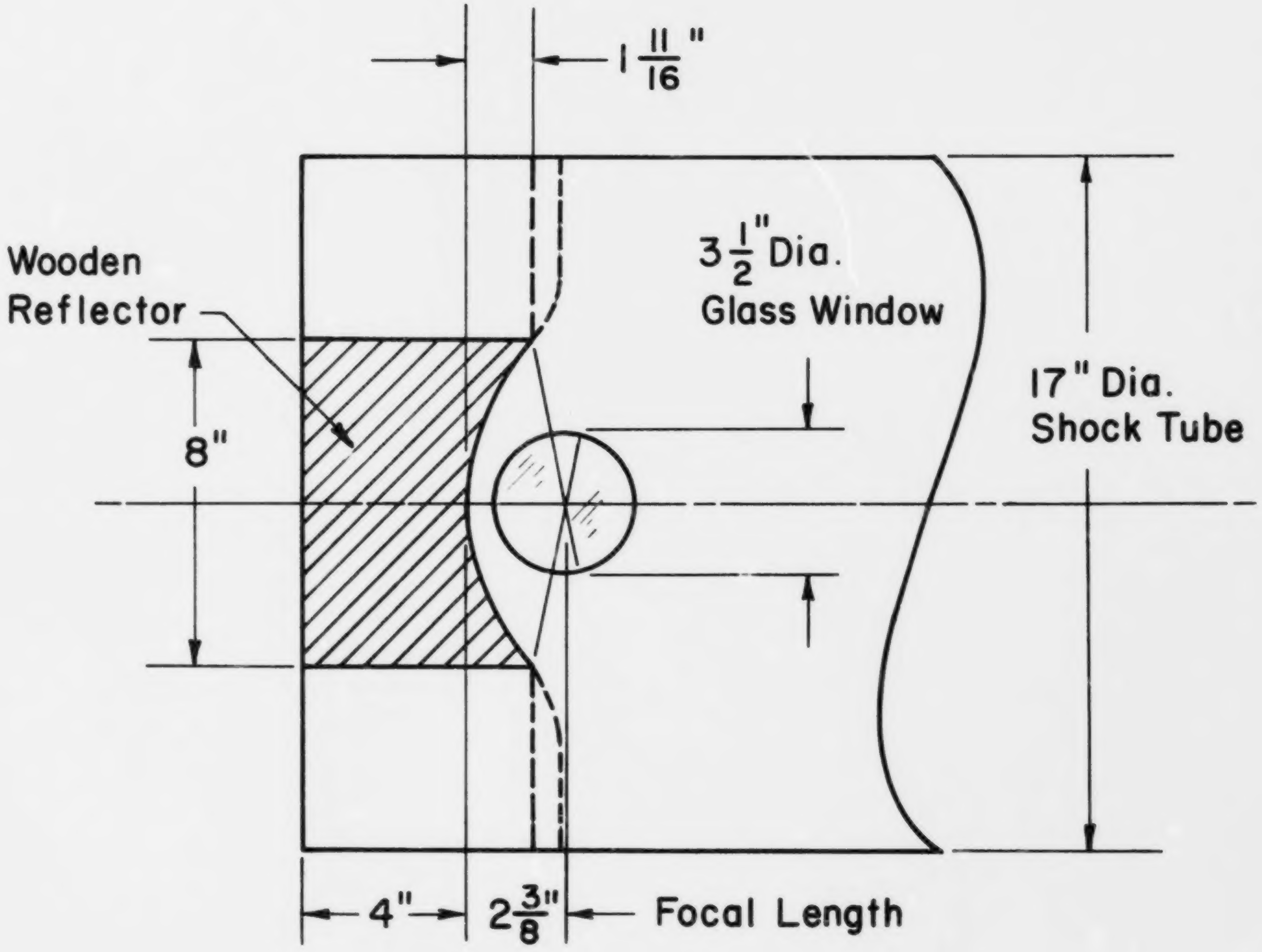
1 11/16"
Wooden
Reflector
8"
3 1/2" Dia.
Glass Window
17" Dia.
Shock Tube
4"
2 3/8"
Focal Length

Figure 2. Schematic of Experiment

wake. Some typical waveforms of both 2- and 3-dimensional focussing are shown.

The influence of the shape and strength of the diverging (diffracted) part of the reflected shock has been examined by changing the shape of the reflector at its edges; two different configurations are used, a flat baffle with sharp corners and a smooth rounded baffle (shown by dotted lines in Fig. 2). Shadowgraphs and pressure measurements show that these changes have little effect on the behavior near the focus.

III. RESULTS

The results presented here include spark shadowgraphs of waves focussed by the 2-dimensional reflector of Fig. 2 and pressure traces observed at a point beyond the focus of 2-dimensional and 3-dimensional reflectors.

Figure 3 is a sequence of shadowgraphs at six successive times showing a wave initially of strength $M_s = 1.1$ which has reflected from the 2-dimensional reflector. The processes exhibited in this sequence are typical of "weak" focussing shocks and lead to crossed and folded wavefronts beyond focus, despite the fact that nonlinear phenomena are evident near the focus. In the first photograph ($t=0$) may be seen a) the reflected front (dark, concave to the right), b) the outer compressive segments of the diffracted wavefront from the corners of the reflector (dark, convex to the right), and c) the inner expansion segments (light) of the diffracted wave. In the second picture ($t=0.05$) the expansion or negative diffracted waves have crossed; e.g., the upper light-colored front originated at the bottom corner and is propagating upward. An important nonlinear effect is exhibited in this picture; the intersections of the negative diffracted waves with the reflected shock wave have reached the axis of symmetry well before focus of the shock. The subsequent pictures in this figure show how the compressive diffracted waves cross ahead of the focussed wave and show that a hot lenticular focal spot is left behind. The boundaries of the dark spot are the trajectories of the intersections of the diffracted and reflected waves (the shock-shocks). These photographs show that wave crossing occurs because the shock-shocks are turned around (at $t=0.08$) and are "forced" (by shock dynamics) back to the axis of symmetry. The second crossing of the shock-shocks is the point at which the leading diffracted waves first cross. Beyond this point nonlinearity is too weak to uncross the waves. Thus, a criterion is established for the occurrence of crossed and folded wavefronts; for all cases in which the shock-shocks cross twice the wavefronts will also cross.

Fig. 4 is a similar sequence for an incident wave of $M_s=1.3$. This case exemplifies the focus of a "strong" shock. The inner diffracted waves reach the axis much sooner and the shock-shocks never turn back toward the axis, so crossed wavefronts do not occur. In the last two pictures, after the waves have left the field of view, the tracks of the shock-shocks, which are shear layers, suffer a spectacular instability!

Fig. 5 summarizes the behavior of shocks of five different strengths, including the ones already discussed. It may be seen that there is a case intermediate between the two already described, namely the focus of a

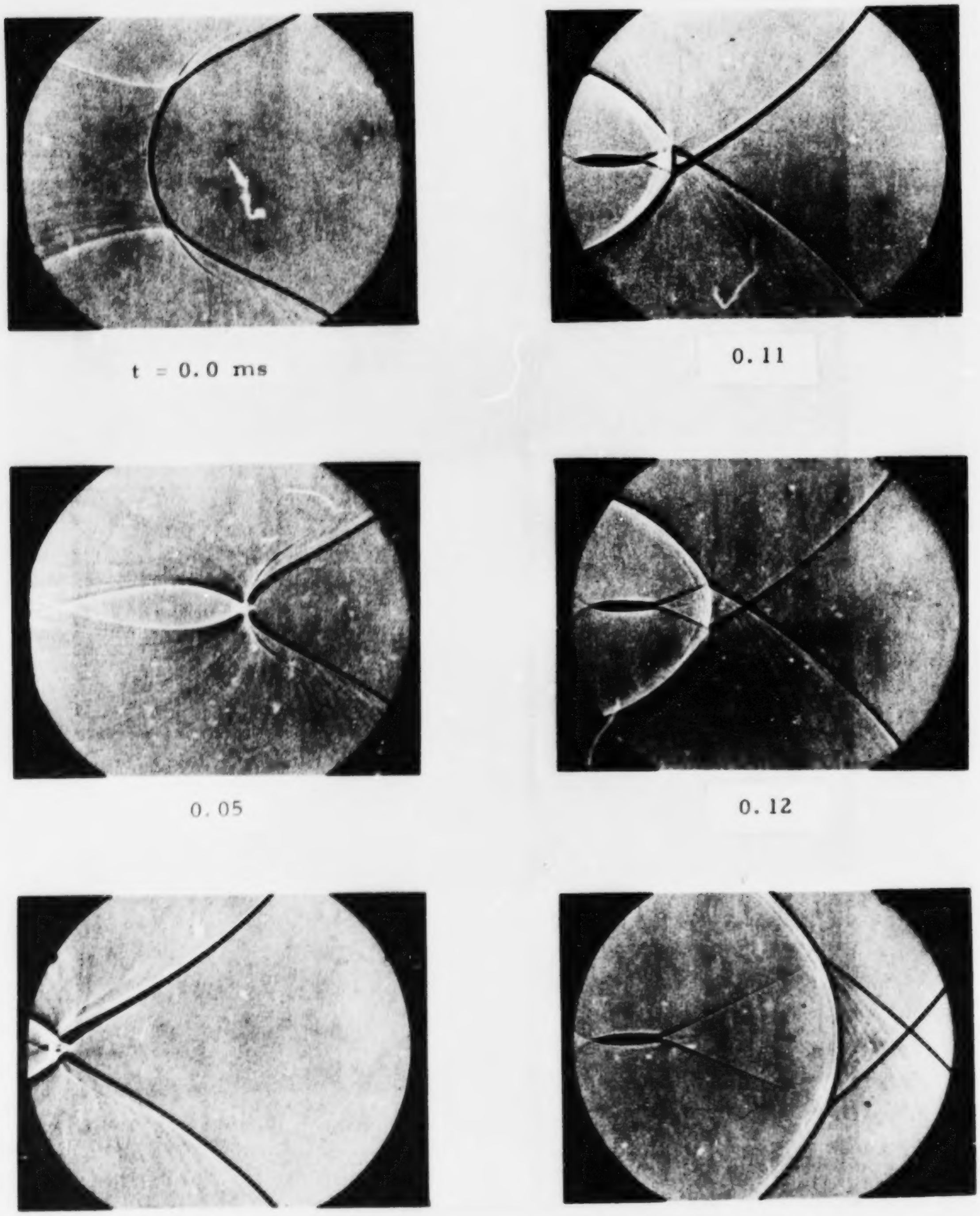

t = 0.0 ms

0.11

0.05

0.12

0.08

0.19

Figure 3. Focussing wave at six successive times. Incident Mach No. = 1.10. Focussing wave is propagating from left to right. Reflector is at left side of the first two pictures.

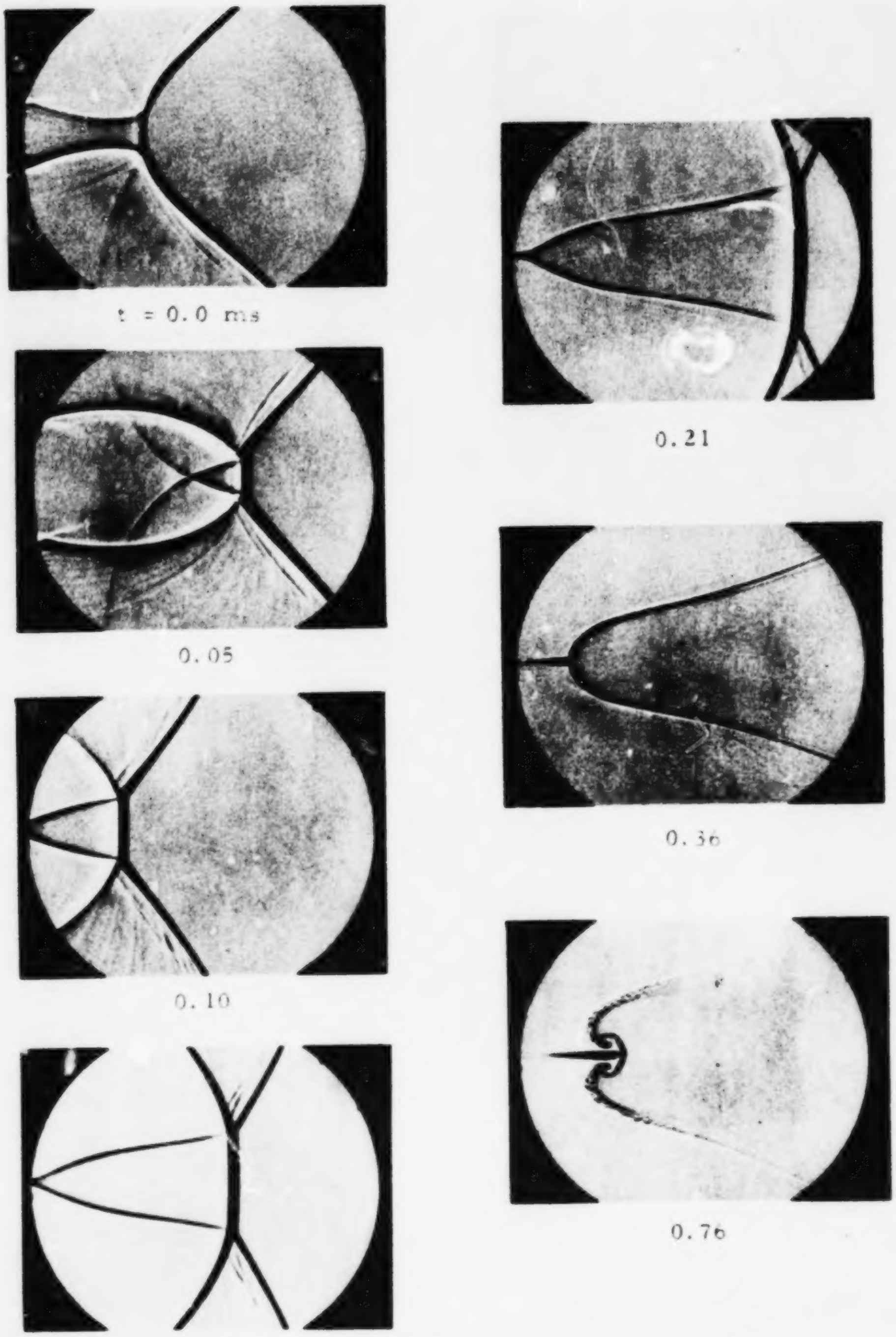

t = 0.0 ms

0.05

0.10

0.16

0.21

0.36

0.76

Figure 4. Focussing wave at seven successive times. Incident Mach No. = 1.3. Focussing wave is propagating from left to right, is out of picture in last two pictures. Reflector is at left side of first two pictures.

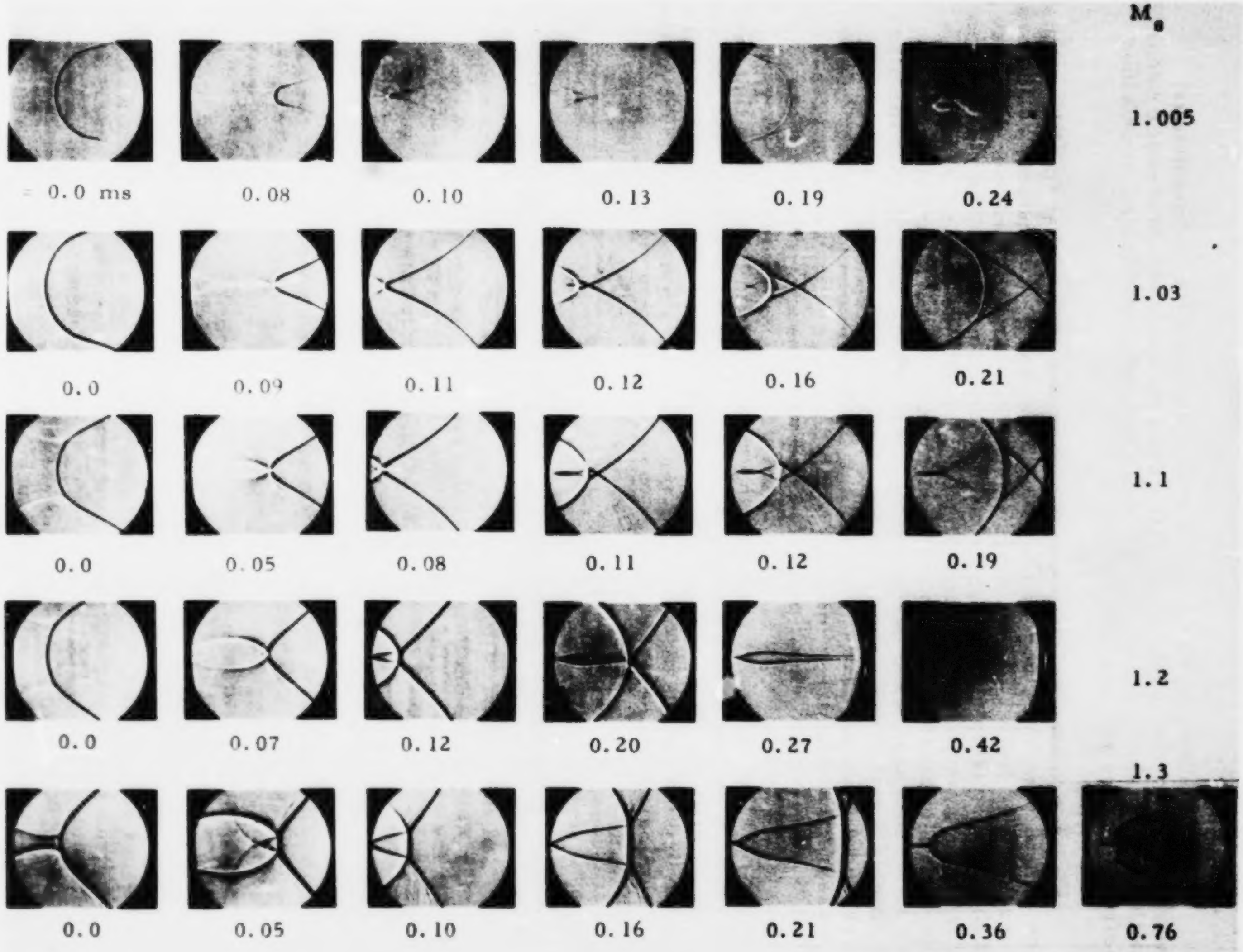
M_s
1.005
= 0.0 ms
0.08
0.10
0.13
0.19
0.24
1.03
0.0
0.09
0.11
0.12
0.16
0.21
1.1
0.0
0.05
0.08
0.11
0.12
0.19
1.2
0.0
0.07
0.12
0.20
0.27
0.42
1.3
0.0
0.05
0.10
0.16
0.21
0.36
0.76

Figure 5. Sequences of focussing waves at corresponding locations for 5 different incident Mach numbers. Focussing waves propagate from left to right.

"medium strength" shock (M_s= 1.2 in these figures), in which the shock-shocks are turned back toward the axis but do not quite make it, with the result that the waves beyond focus do not cross!

Spark shadowgraphs of waves reflected from the 3-dimensional axially symmetric reflector show that precisely the same processes occur as with 2-dimensional focus, though the transition from folded to unfolded wavefronts occurs for weaker waves.

Fig. 6 exhibits typical pressure histories observed at fixed locations on the axis of symmetry beyond the focus of 2- and 3-dimensional reflectors. For weak waves from 2-D reflectors (upper left-hand picture) one observes first the compressive rise of the crossed diffraction waves (the rise is slow because the waves pass over the transducer at oblique incidence) and then a compression-expansion spike which corresponds to the logarithmic singularity at the focussed wave predicted by linear theory (Ref. 6). On the other hand, for 3-D reflectors (upper right-hand picture) the compression from the crossed diffracted waves (complicated in this picture by diffraction over the pressure transducer) is followed by a steep expansion wave, corresponding to the inverted shock predicted by linear theory. Though these waveforms are qualitatively similar to the predictions of linear theory, it should be recalled that the corresponding shadowgraphs have shown that the waves actually spring from a complicated nonlinear shock diffraction process at focus. Strong shock waves (bottom pictures) show a simple compression-expansion spike after focus, indicating that there is a single wavefront on the axis of symmetry, as observed in the shadowgraphs.

IV. DISCUSSION

Fig. 7 summarizes schematically the predictions of geometrical acoustics for the reflection of a plane acoustic pulse from a finite parabolic reflector. At the instant of focus the reflected wave has focussed to a point and the only wavefronts visible are the diffracted waves generated at the corners of the reflector. Beyond focus the diffracted waves are ahead of the focussed wave because the shortest propagation distance along a ray from the incident wavefront before reflection to a point on the axis of symmetry beyond focus is through the corners rather than along the axis.

It is important that the formation of diffracted waves behind the focussing wavefront is a general phenomenon and is not unique to our particular method of producing a focus. For example, if a smooth, curved wavefront of uniform strength (e.g., Fig. 1) is given as initial condition, immediately after initiation of the flow a diffracted wave forms at the inflection point on the wavefront, dividing the region of decreasing pressures behind the convex expanding portions of the front from the region of increasing pressures behind the concave focussing portion. In acoustic theory the diffracted front is circular and touches the leading disturbance at the inflection point, while in nonlinear theory, the disturbances propagate outward from the inflection point along the wavefront. Therefore, in general, diffracted fronts occur behind dimpled wavefronts. Since, as we have seen in the previous section, the focussing process is primarily controlled by the dynamics of the diffracted fronts, it is anticipated that no matter how the concave wavefront is formed, the behavior near a focus will in general prove to be the same as observed in our experiments. An important

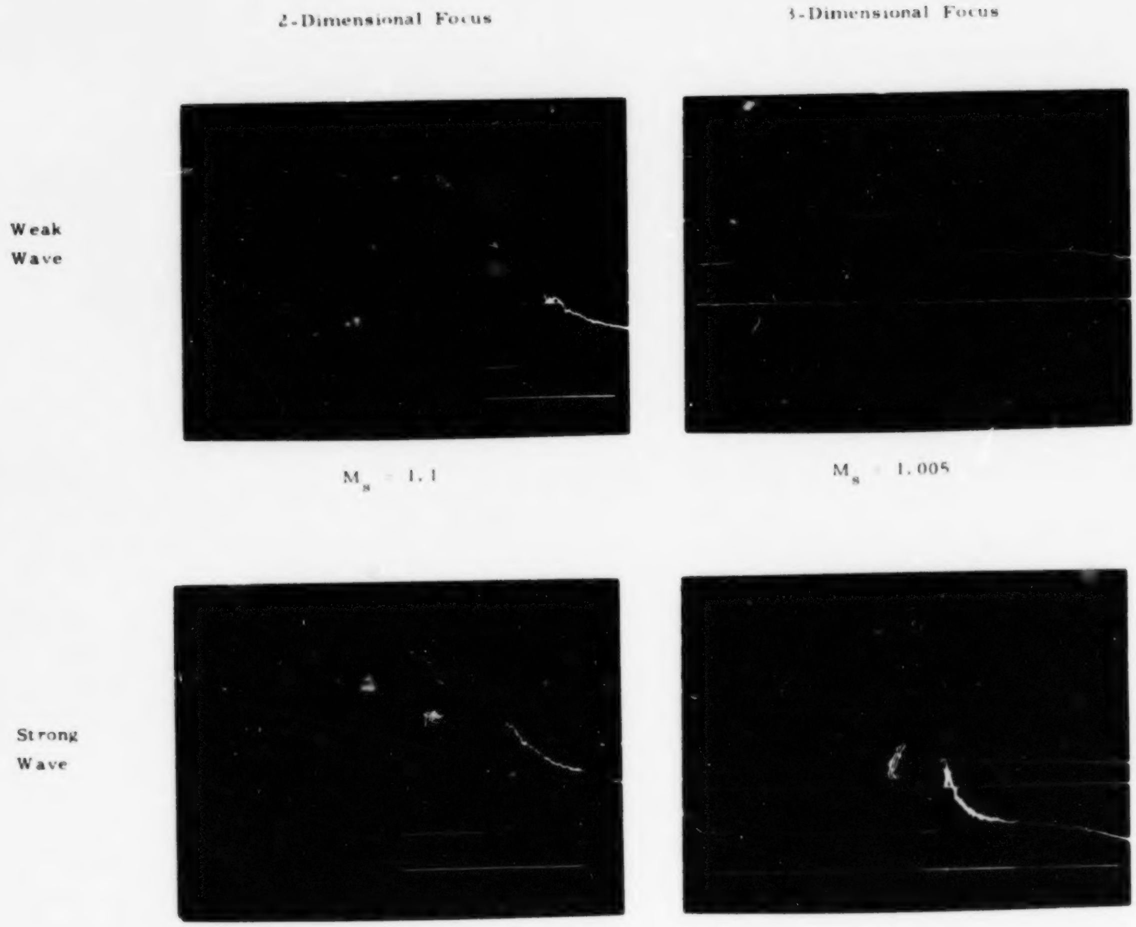

M_s = 1.1

M_s = 1.005

M_s = 1.3

M_s = 1.1

Figure 6. Typical pressure histories (upper traces) observed for 2- and 3-dimensional focuses. Time (abscissa) increases to right, pressure (ordinate) increases upward. Transducer is spaced 3 in. from reflector for 2-D pictures and 4-3/4 in. from reflector for 3-D.

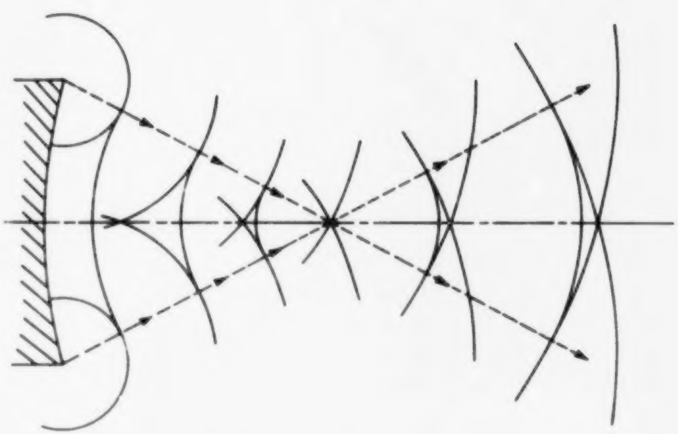
Figure 7. Focussing of a Wavefront of Sound

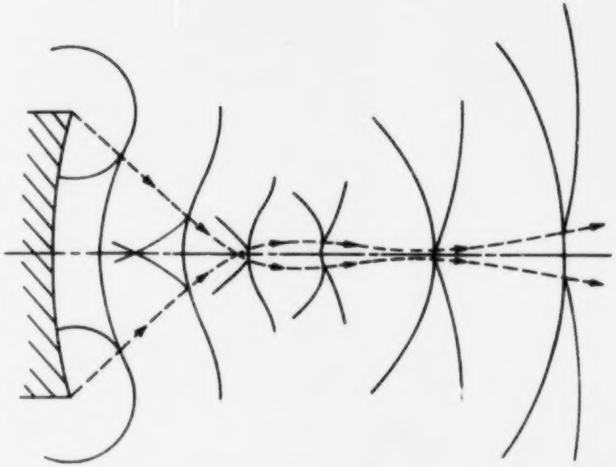
Figure 9. Focussing of a Medium Strong Shock Wave

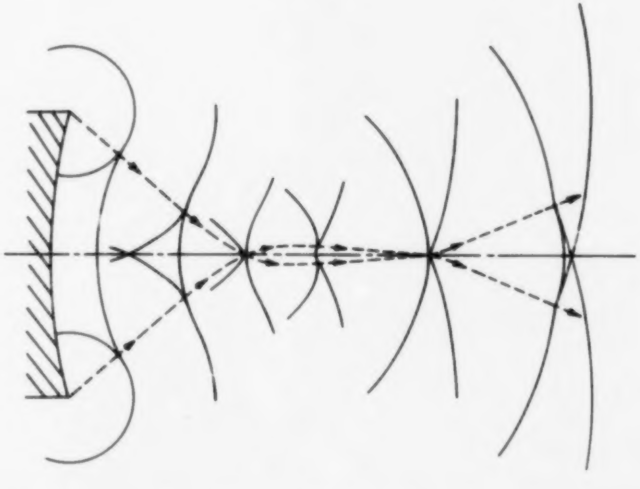
Figure 8. Focussing of a Weak Shock Wave

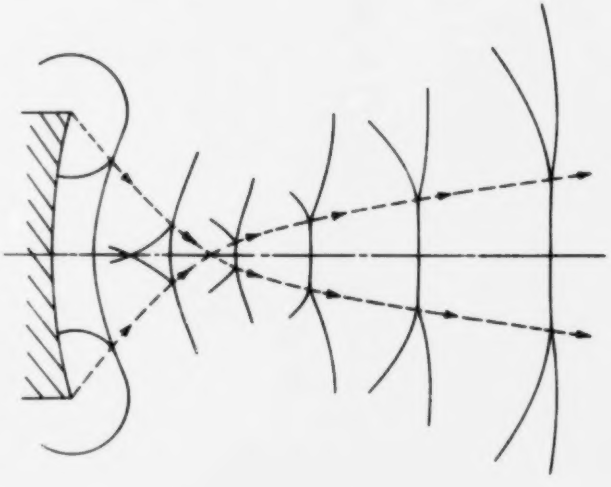
Figure 10. Focussing of a Strong Shock Wave

question in this regard is how results of the present work are to be scaled to apply to other situations. Experiments are presently being conducted with reflectors of different apertures to answer this question.

The behavior of "weak", "moderate", and "strong" focussing shocks is summarized in Figs. 8-10. The dashed lines indicate schematically the trajectories of the three-wave intersections. In all observed cases the intersection of the diffracted wave with the converging front reaches the axis of symmetry substantially before the geometrical focus and before focus of the shock. For weak waves (Fig. 8) a second crossing occurs beyond the geometrical focus. In all cases, just beyond the first crossing of the axis the wavefront at the axis of symmetry is astonishingly straight and normal (cf. Fig. 5); this emphasizes the close relationship between nonlinear shock diffraction and acoustic diffraction, which also predicts normal wavefronts at focus (Ref. 2).

The principal questions which must be answered before the focussing process is understood are a) what is it that causes the wavefronts far beyond focus to be crossed in the case of weak shocks and uncrossed in the case of strong shocks, and b) how does this process serve to limit the maximum amplitude? We address the first question in this paper.

Unfortunately, the dynamical processes which determine the nature of a focus include diffraction of curved, weak shock fronts propagating into nonsteady, nonuniform media, so a complete description of the problem is very difficult. However, it is clear from the sketches (Fig. 8-10) that the final effect of the focussing process is to provide a situation in which either regular reflection (for weak shocks) or Mach reflection (for strong shocks) occurs. After the three-wave intersections first cross at the axis of symmetry Mach reflection is always observed to occur, but if a second crossing occurs regular reflection is observed.

In view of the strong dependence of the focussing process on the behavior of the three-wave intersections it seems clear that, as a first step, the trajectories of the intersections should be investigated. Accordingly, we have developed a crude hypothesis which simplifies some of the geometrical aspects of shock-diffraction theory, yet which embodies the essential nonlinearity. It is assumed that the strength of the converging wavefront is given by geometrical acoustics and that the diverging (leading) diffracted front propagates at sonic velocity. The resulting misfit between the two curved wavefronts is filled in with a straight-line segment tangent at each end to the curved fronts. The intersection of the third wave behind the converging front is assumed to propagate at local sonic velocity, and an equation for the trajectory of its intersection with that front is derived.

Trajectories calculated for a reflector of the same aperture as in our experiments and for three different Mach numbers are shown in Fig. 11. It may be seen that the agreement with the pictures of Fig. 5 is better than qualitative. These calculations suggest that the axial extent of the focal spot is an important parameter. For example, the transition from crossed to uncrossed wavefronts occurs when the spot attains its maximum (finite) length and this length is seen to be of the order of the focal length of the original concavity. As another example, it might be expected that if the calculated length of the focal spot turns out to be less than the shock

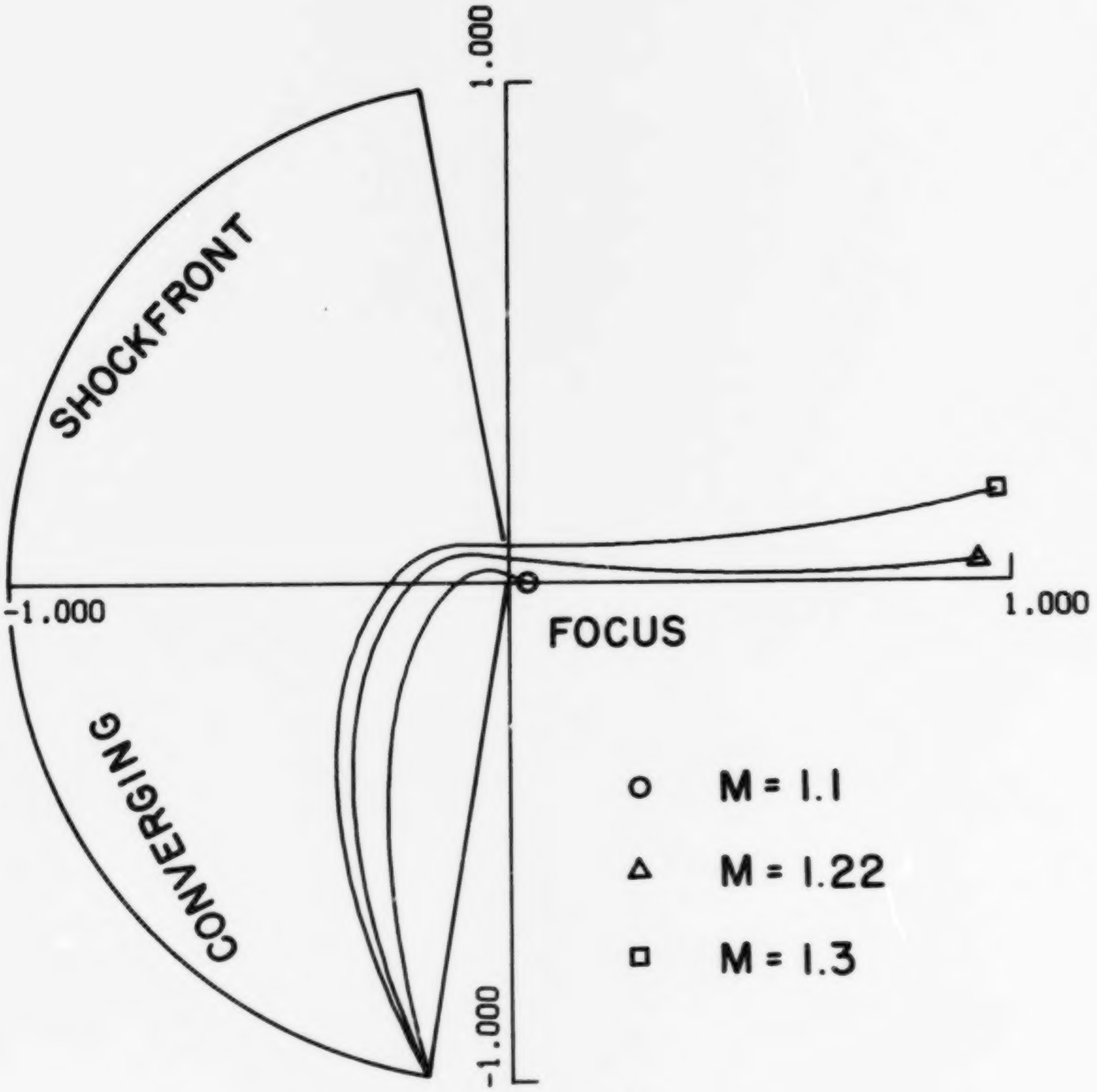

Figure 11. Calculated three-wave intersection trajectories.

thickness, then linear wave acoustics would yield the correct maximum amplitude at focus. Otherwise, nonlinear effects limit the amplitude. Methods for obtaining precise measurements of wave amplitudes are presently being developed in our laboratory, and experiments will be conducted to develop this point more fully.

V. CONCLUSIONS

It has been shown that wavefront folding occurs beyond an acoustic focus even when the wave propagation in the neighborhood of the focus is essentially nonlinear. Wavefronts fold if the intersection of the diffracted wave with the leading disturbance crosses the axis of symmetry twice. They do not fold if the wave intersection crosses the axis only once. In the former case conditions are apparently such that regular reflection is possible, while in the latter Mach reflection occurs. A crude hypothesis on shock-diffraction theory explains the qualitative behavior of the observed focal spot. Scaling of the phenomenon is presumed to depend on the wave strength, aperture and focal length of the concavity and shock wave thickness, and is being investigated further.

[The authors gratefully acknowledge a helpful discussion with Prof. J.B. Keller. This work was supported by a grant from the AFOSR (71-2092).]

VI. REFERENCES

1. Sturtevant, B., "Studies of Shock Focussing and Nonlinear Resonance in Shock Tubes", in Recent Developments in Shock Tube Research (D. Bershader and W. Griffith, eds.), p. 23, Stanford Univ. Press (1973).

2. Debye, P., Ann. d. Phys. 30, 755 (1909). Cf. also Sommerfeld, A., Optics, p. 318, Academic Press, N.Y. (1954).

3. Obermeier, F., "Sonic Boom Behavior Near a Caustic", in Noise Mechanisms, AGARD CPP 131 (1973).

4. Whitham, G.B., Jour. Fluid Mechs., 2, 145 (1957).

5. Beasley, W.D., Brooks, J.D. and Barger, R.L., NASA TN D-6306 (1969).

6. Friedlander, F.G., Sound Pulses, Cambridge Univ. Press (1958)

LABORATORY INVESTIGATION OF SONIC BOOM FOCUSING[*]

by

M. Sanai[**] and T. Y. Toong[***]

Department of Mechanical Engineering
Massachusetts Institute of Technology
Cambridge, Massachusetts 02139, U. S. A.

ABSTRACT

A two-part investigation of shock focusing as related to sonic booms has been conducted in a ballistic range with the objective of studying the nonlinear effects. Part I deals with focusing due to an increase in body Mach number. Projectiles at supersonic speeds are fired into a gaseous medium with decreasing sound speed along the flight axis, producing converging shocks with higher overpressures in focal regions. Focus factors of up to 2.0 have been measured. Flow field features (including shock folding) agree qualitatively with the linear theory for weak shocks. But for strong shocks, folding does not occur, possibly due to the presence of dominant nonlinear effects.

In Part II, focusing due to refraction is investigated. Projectiles at low supersonic speeds are fired into a stratified medium, producing a Y-shaped shock configuration in the vicinity of the sonic cut-off altitude due to total reflection. A maximum focus factor of 1.7 has been measured at the triple point of the leading shock.

---

[*] Supported by NASA Grant NGR-22-009-618

[**] Research Assistant

[***] Professor of Mechanical Engineering

1. INTRODUCTION

Two of the more common cases in which enhanced sonic booms or superbooms are expected to result are:

(I) Acceleration of aircrafts at supersonic speeds, giving rise to the acceleration superbooms, and

(II) Steady flight of a supersonic aircraft at threshold Mach numbers in the real inhomogeneous atmosphere, the refraction superbooms.

Accordingly, two separate series of laboratory experiments have been conducted to simulate each of the above phenomena. Experimental procedure and some preliminary results from the acceleration-superboom experiments have been reported in the last year's meeting [1] and are not repeated here. Major results obtained since then are briefly summarized below with full details to be given in Ref. 2.

Acceleration superbooms are simulated by firing projectiles of different sizes and shapes at constant supersonic speeds into gaseous media with decreasing sound speed along the trajectories (resulting in increasing Mach numbers). Signatures from pressure transducers have been studied in conjunction with dual-schlieren pictures obtained simultaneously during the same experiment. It is observed that converging shocks are produced, containing a concave region in which the overpressures are higher than those in the adjacent regions. Focus factors of up to 2.0 have been measured. Observed flow-field features (including shock folding) for weak shocks (shock Mach numbers of less than 1.03) agree qualitatively with those predicted by the linear theory. But for the stronger shocks (shock Mach numbers above 1.30), folding has not been observed, possibly due to the presence of dominant nonlinear effects. Defocusing of strong shocks has also been observed and was reported in Ref. 1.

The remainder of this paper is devoted to the refraction superboom problem. Theoretical description of the flow field resulting from a steady flight of a supersonic aircraft in a stratified atmosphere has been discussed by several authors [3-6]. Of particular interest are cases in which the aircraft speed is less than the sound speed at the ground level. The aircraft is then said to be flying at a "threshold" Mach number. Although qualitative features of the flow field resulting from such a flight seems to be fairly well understood, a complete theoretical treatment is still lacking. The following is a brief description of those features that are related to the simulation experiments reported in this paper.

Figure la illustrates the effect of a refracting medium on the propagation of the leading shock as predicted by the linear theory of geometrical acoustics. The part of the shock which propagates towards the ground does not reach the ground if the aircraft speed is less than the sound speed at the ground level. The shock is totally reflected at the caustic surface, which is defined as the envelope to all the acoustic rays. The caustic is located at the sonic cut-off altitude where the aircraft speed equals the local sound speed. The incident and reflected shocks form at the caustic

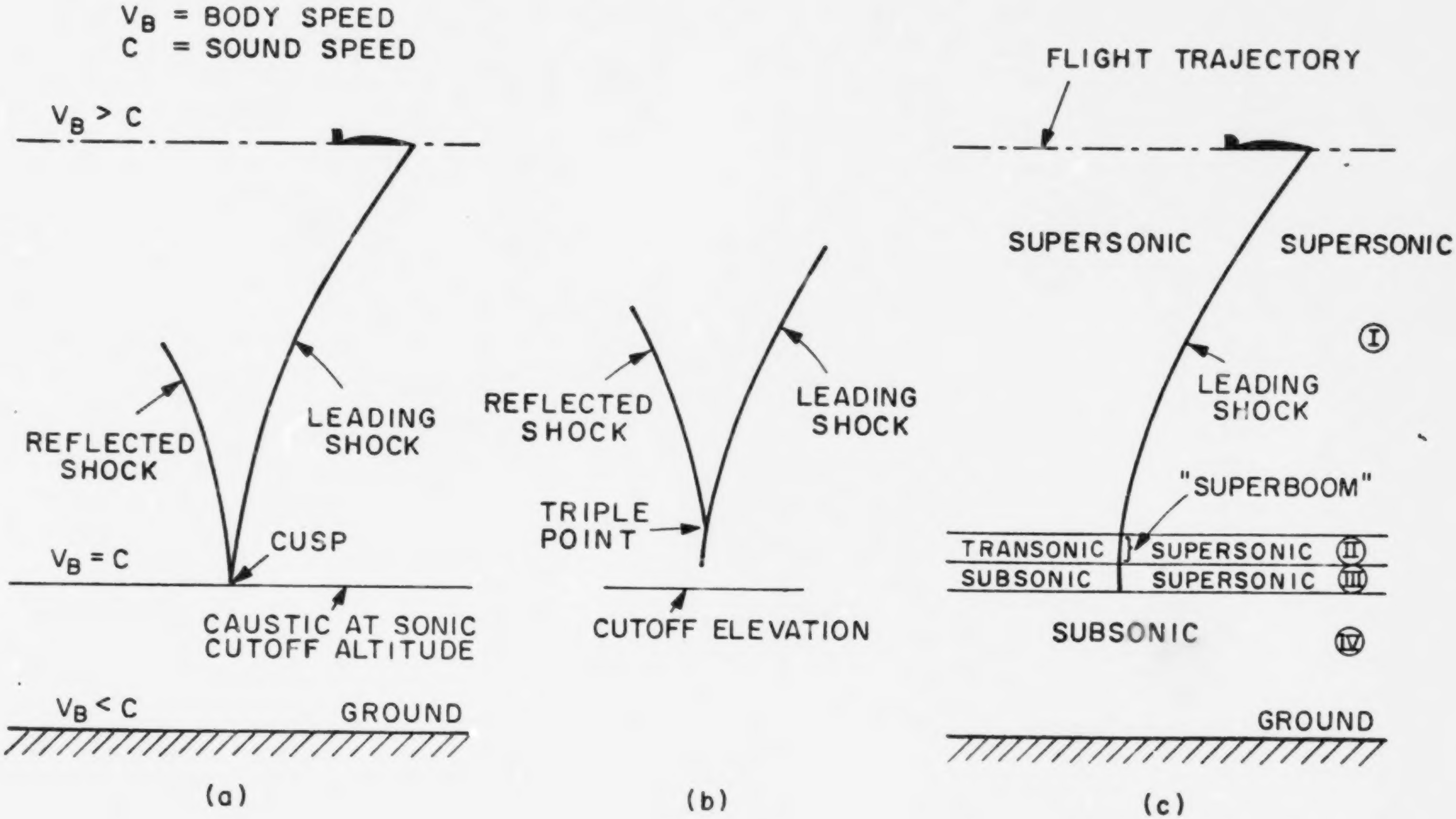
V_B = BODY SPEED
C = SOUND SPEED
$V_B > C$
REFLECTED SHOCK
LEADING SHOCK
CUSP
$V_B = C$
CAUSTIC AT SONIC CUTOFF ALTITUDE
$V_B < C$
GROUND
(a)
REFLECTED SHOCK
LEADING SHOCK
TRIPLE POINT
CUTOFF ELEVATION
(b)
FLIGHT TRAJECTORY
SUPERSONIC
SUPERSONIC
Ⓘ
LEADING SHOCK
"SUPERBOOM"
TRANSONIC
SUPERSONIC
Ⓘ Ⓘ
SUBSONIC
SUPERSONIC
Ⓘ Ⓘ Ⓘ
SUBSONIC
Ⓘ Ⓥ
GROUND
(c)

Fig. 1 Shock refraction in a stratified medium: (a) prediction of geometrical acoustics theory; (b) shock configuration observed near the sonic cut-off altitude in simulation experiments and (c) various flow regions identified along the leading shock.

a cusp that moves along with a speed equal to that of the aircraft. The cusp region represents a zone in which the energy density becomes large (it is infinite according to the acoustic theory) so that the finite-amplitude or nonlinear effects are expected to play an important role near the cusped shock.

The geometrical-acoustic theory discussed above is strictly valid for shocks that are of infinitely small strength. For shocks with finite strengths, a configuration other than a cusp results when the reflection takes place near the cut-off altitude. Experiments reported in Section 3 indicate that the leading shock and its reflected portion form a Y-shaped shock structure near the cut-off elevation, as sketched in Fig. 1b. The difference between this triple-shock complex and the cusped-shock of Fig. 1a predicted by the linear theory is attributed mainly to the finite-amplitude effects near the caustic region. These are not accounted for in the geometrical-acoustic theory.

Relative to the leading shock, the incoming flow has a constant speed equal to that of the aircraft. But the flow Mach number decreases with decreasing altitude because of the corresponding increase in the sound speed. Coupled with the local shock inclination, this determines the flow produced behind the leading shock. According to the type of flow that exists behind the leading shock, four regions have been identified in Fig. 1c. In Region I, the flows both ahead of and behind the shock are supersonic. In Region II. the incoming flow Mach number and the shock inclination are such that the flow behind the leading shock becomes very nearly sonic. At the lower altitudes contained in Region III, the shock is very nearly normal to the flight axis, with subsonic flow behind it. Finally, in Region IV, the flow is subsonic everywhere and contains no shock waves. A series of compression waves similar to those occurring below a subsonic aircraft exists in this region.

Of considerable importance in the present investigation is the pressure variation across the incident shock at different altitudes. In Region I, shock overpressure decreases with decreasing altitudes, as predicted by Whitham's theory [7,8]. In Region II, the shock overpressure increases despite the fact that the incoming flow Mach number is decreasing. Whitham's theory breaks down and full nonlinear theories become essential for describing the pressure field in this region. The oblique-shock analysis developed by Friedman [4] and the characteristic theory of Ref. 6 apply to part of this region[*] and predict a magnified shock overpressure. However, these theories are not complete because they do not consider the effect of the reflected shock. Experiments reported in Section 3 indicate that the reflected shock joins the leading shock at a point which is very near to where the maximum shock intensity is measured. In other words, the triple-point of Fig. 1b is located near or inside Region II. A complete theory must account for the possible effects that the presence of the reflected shock may have on the overpressure magnification. Therefore, at best, the above theories provide an estimate of the lower bound to the magnitudes of the superbooms.

---

[*] These theories apply as long as the flow speed behind the leading shock is supersonic. The largest shock overpressure results at the altitude where the flow behind the shock becomes just sonic. From there on, the theories cease to be applicable.

In Region III, the overall flow field is quite complicated and none of the theories discussed above can predict the shock intensity. The major source of complication is that the disturbances caused by the aircraft arrive before the bow wave; i.e., a compression field is formed in front of the bow shock so that the shock is propagating into an already disturbed medium [4]. In Region IV, there is no abrupt pressure increase and no boom is heard. The pressure is spread out into a continuous rise so that a rumble similar to that caused by a subsonic aircraft is experienced.

Region II discussed above warrants special attention because it contains the zone in which the superboom is expected to be experienced. The magnified shock overpressure in this rather narrow zone is believed to be caused by two complementary effects [4]. First, there is a focusing of wave energy caused by the simultaneous arrival of many of the pressure waves emitted by the aircraft. Second, these pressure disturbances cannot propagate away from the transonic zone behind the shock and will therefore remain in the immediate vicinity of the shock. They tend to "accumulate" and give rise to the enhanced shock overpressure or the superboom.

It should be pointed out that the borderline between Regions I and II or II and III is not clear-cut because the extent to which the flow speed behind the leading shock in Region II deviates from sonic speed has not been specified. A convenient way of fixing the above borderlines is to center Region II at the altitude where the flow behind the leading shock becomes just sonic and extend it by an arbitrary small amount to either side of this altitude.

2. EXPERIMENTAL INVESTIGATION

A schematic diagram of the experimental apparatus is shown in Fig. 2a. A standard 17 caliber bullet is fired into a stratified medium produced in a ballistic range, instrumented with a fast-response dynamic pressure transducer and schlieren photographic equipment. The stratified medium is obtained by a slow injection of CO_2 into air through a porous rubber sheet stretched over a container located at the bottom of the test section. (Experiments similar to these have also been conducted by the ISL Group [9] in France as reported by Wanner, et al. [10]). Since the speed of sound is lower in CO_2 than in air, the sound speed increases with increasing elevation in the test section. The flow configuration which results from the passage of the bullet is therefore upside down as compared to that produced by flights in a real atmosphere.

By regulating the flow rate of CO_2 and the time elapsed before the projectile is fired, the sound-speed variation may be controlled to suit the test conditions. For all the experiments reported here CO_2 has been introduced at the rate of 3,750 cc/min for 7 mins. before the projectile was fired. For this combination of flow rate and mixing time, the medium

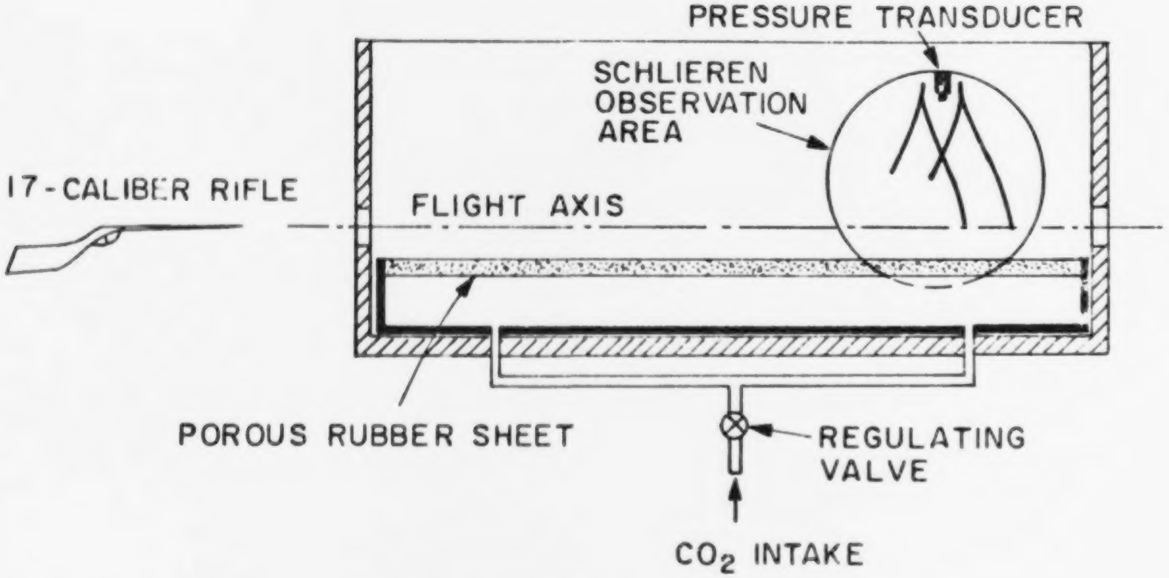
PRESSURE TRANSDUCER
SCHLIEREN OBSERVATION AREA
17-CALIBER RIFLE
FLIGHT AXIS
POROUS RUBBER SHEET
REGULATING VALVE
CO_2 INTAKE

Fig. 2a Schematic diagram of test apparatus.

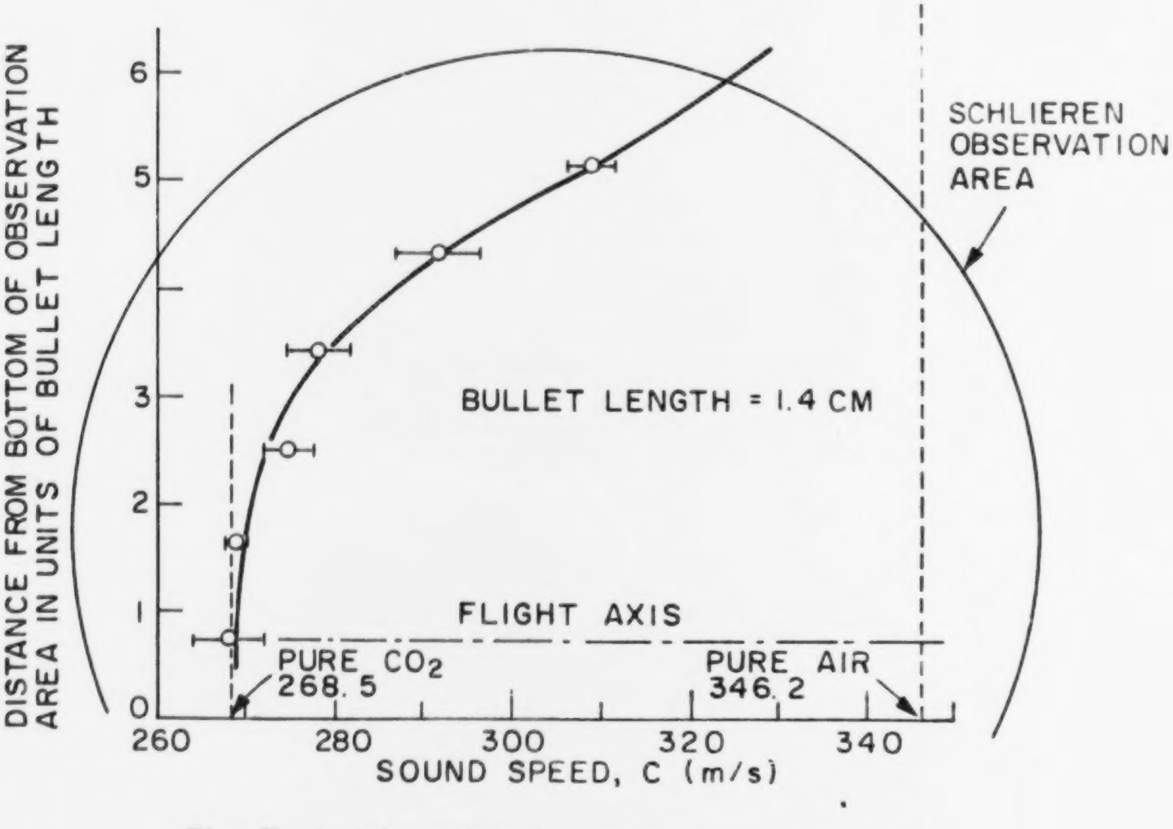

Fig. 2b Sound speed variation in cut-off experiments.

sound speed has the distribution shown in Fig. 2b. The way this distribution has been measured is described in detail in Ref. 2. The method is based on the assumption that a unique and distinguishable shock configuration is produced around the body for each body Mach number so that an unknown Mach number can be inferred by examining the resulting shock pattern in the schlieren pictures. Knowing the Mach number, the sound-speed at the flight axis is calculated by dividing the body speed (measured separately) by its Mach number. This has been repeated for several elevations in the test section and the resulting measurements have been represented by the smooth curve shown in Fig. 2b.

3. DISCUSSION OF RESULTS

A pair of dual-schlieren pictures (taken at 15 μs apart) and a simultaneous pressure record obtained when the bullet moves in the stratified medium of Fig. 2b at a Mach number of 1.15 are shown in Fig. 3. The shock configurations produced by the leading and wake shocks resemble that of Fig. 1a, discussed in conjunction with flights in a real atmosphere.

The rod-shaped black extension appearing at the top of the schlieren pictures is the tubular support on which the transducer is mounted. The pressure-sensitive surface is horizontal and parallel to the flight axis. This particular way of mounting has been found to minimize the distortion in the pressure signal due to the effect of diffracted shocks at the transducer surface [2]. The container used to introduce CO_2 is responsible for the black portion at the bottom of the picutres. The porous surface is located approximately 5 mm below the dark border. Propagating shocks below the flight axis are reflected at this surface and produce additional shocks. For example, shock number 2 is the reflection of the lower half of the leading shock and has produced a Y-shaped shock configuration just as the leading shock itself.

Both schlieren pictures are shown here to indicate that the shock shapes are identical in both pictures. This has been found to be the case in all the runs conducted in the present series of experiments. One implication of this observation is that no appreciable axial variations in medium properties exist so that the sound speed varies essentially in the vertical direction only. This substantiates the one-dimensional variation shown in Fig. 2b and simplifies the shock-shape computations greatly.

Shock-Shape Comparison

Fig. 4a shows the wave front positions as predicted by the geometrical acoustic theory super-imposed on the shock front positions observed in the schlieren picutres of Fig. 3. The overall shapes of the computed and observed shocks are found to be in reasonable agreement. The major difference that exists between the shock shapes is the triple-point configuration which is observed experimentally but is not predicted by the linear theory. This seems to be due to the presence of nonlinear effects near the cut-off region, as discussed in Section 1.

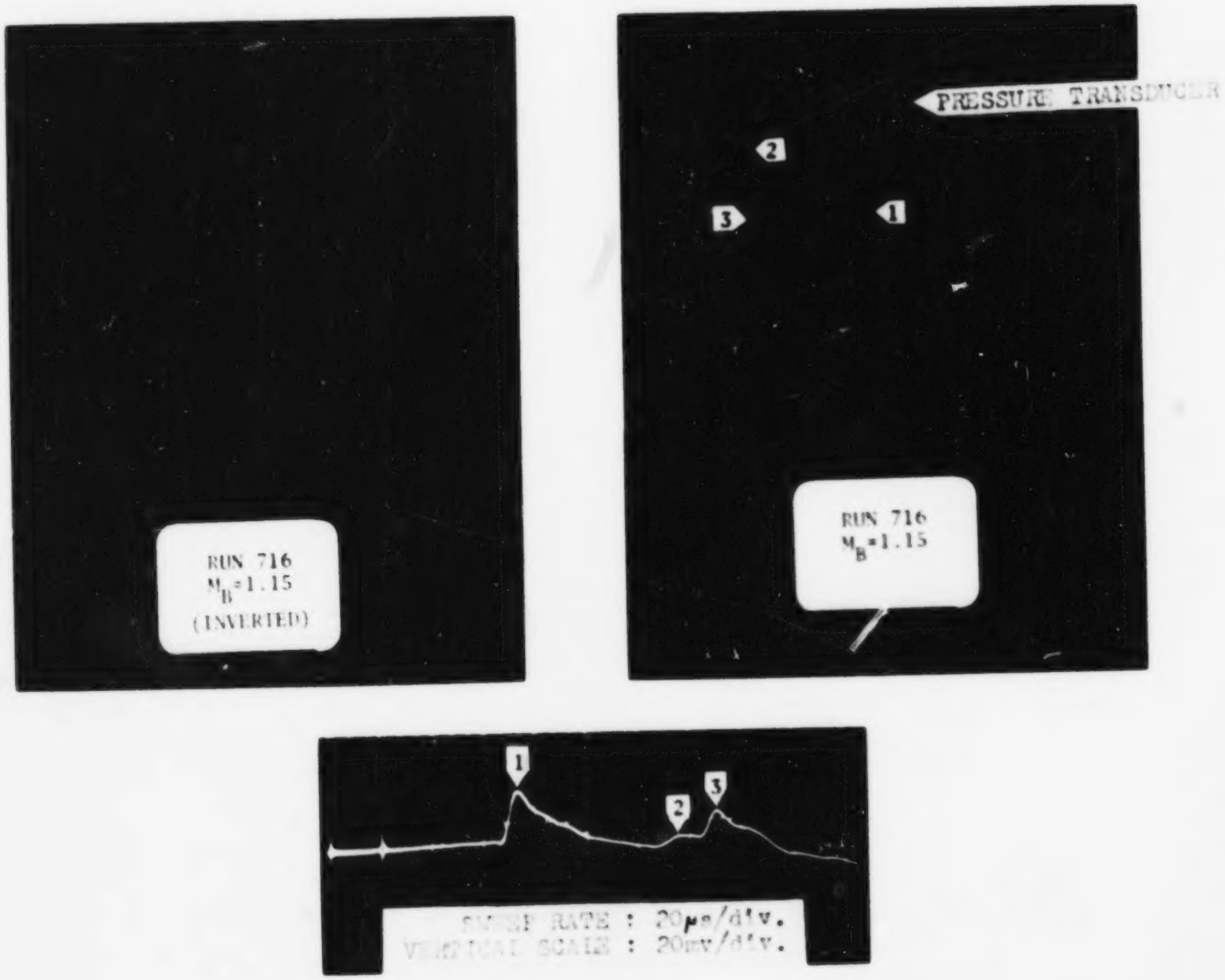
RUN 716
M_B=1.15
(INVERTED)
PRESSURE TRANSDUCER
2
3
1
RUN 716
M_B=1.15
1
2
3
SWEEP RATE : 20μs/div.
VERTICAL SCALE : 20mv/div.

Fig. 3 Dual-schlieren pictures (taken 20 μs apart) and pressure signature from a 17 caliber bullet in a stratified medium.

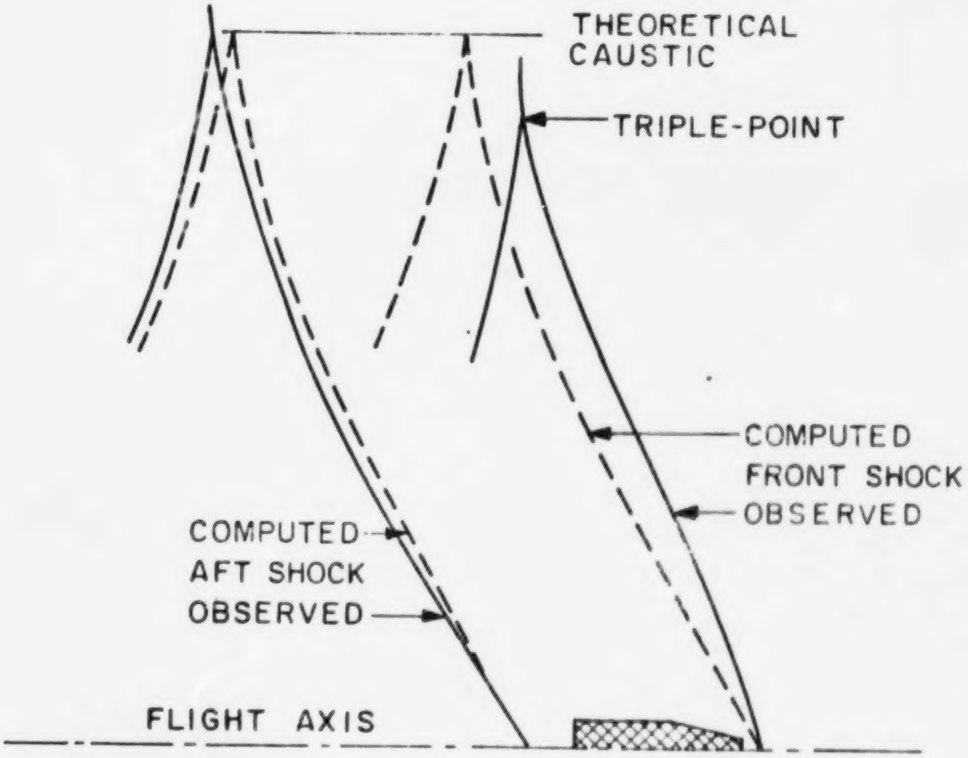
THEORETICAL CAUSTIC
TRIPLE-POINT
COMPUTED
FRONT SHOCK
OBSERVED
COMPUTED
AFT SHOCK
OBSERVED
FLIGHT AXIS

Fig. 4a Comparison between observed and computed shock positions for the run of Fig. 3.

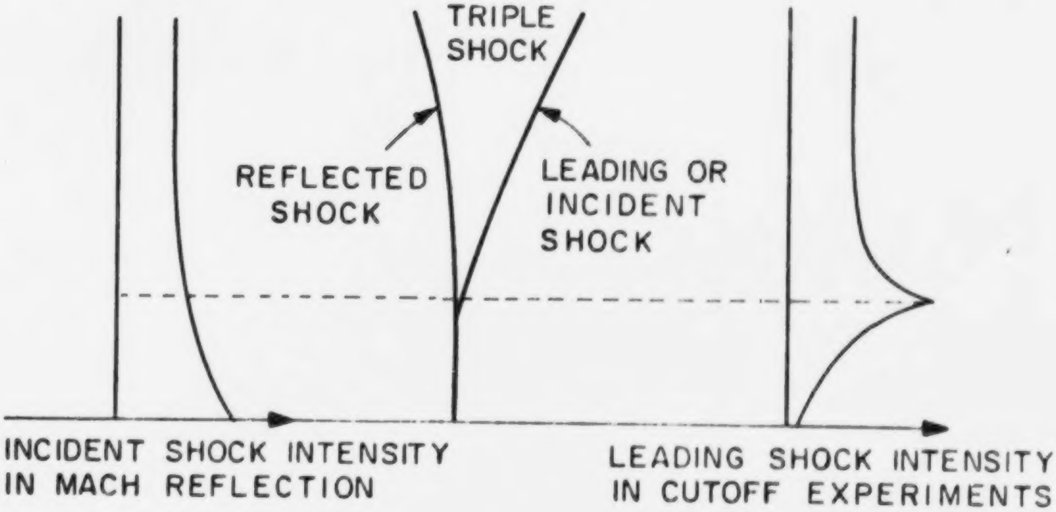
TRIPLE SHOCK
REFLECTED SHOCK
LEADING OR INCIDENT SHOCK
INCIDENT SHOCK INTENSITY IN MACH REFLECTION
LEADING SHOCK INTENSITY IN CUTOFF EXPERIMENTS

Fig. 4b Comparison between shock intensities in Mach reflection and cut-off experiments.

It is noted in Fig. 4a that the shock bends rather sharply near the triple-point and approaches the normal. But the more the shock approaches the normal, the more the flow behind it approaches the sonic speed, a condition to be recalled that identifies Region II in Fig. 1c. It is therefore expected that Region II containing the magnified shock overpressure be in the vicinity of the triple-point. This will be seen to be in agreement with the experimental measurements, indicating that the triple-point altitude is an important radial position as far as the pressure variations are concerned.

A remarkable similarity in shape exists between the triple shocks observed here and that produced by a Mach or irregular reflection of a shock at a solid surface [11]. However, detailed comparison with several studies of Mach reflection [11-13] indicates that the similarity is restricted to the shape alone and does not extend to other important flow field features such as the shock strenght. Variation of shock intensity as inferred from the interferograms of Mach reflections reported in Ref. 13 is sketched at the left of Fig. 4b. It is noted that the Mach stem has a nearly constant intensity and is at least as strong as the incident shock. On the right of Fig. 4b, the variation of shock intensity in the cut-off experiments is sketched. (Measured values are to be reported later). Unlike the previous case, the shock intensity peaks near the triple-point and decreases rapidly along the normal portion. It is therefore obvious that the Mach-reflection phenomenon alone cannot describe the flow field associated with the present experiments. It may, however, supplement any theory that predicts the flow field on the basis of a different theoretical notion (e.g. from that of theories of Refs. 4 or 6) and may account for the effect of shock reflection at the caustic, not considered in any of the above theories.

Shock Intensity

To facilitate visual comparisons, Fig. 5 has been prepared where schlieren pictures and pressure traces from several runs at approximately the same Mach number in both the stratified and the homogeneous media are presented. Each column contains a run in air-CO_2 medium and its corresponding run in air for the same radial position of the pressure transducer. As before, the first peak on each pressure trace corresponds to the passage of the leading shock. For runs in air, the peaks decrease in magnitude monotonically as the transducer is moved away from the flight axis. But for the refracting medium runs (bottom row) a peaking of the overpressure is observed when the transducer is positioned near the triple-point. (Compare heights of the first peaks in pressure signatures of Runs 709, 669 and 711). In the shock-free region far above the triple-point, a rounded peak is recorded as seen in Run 742. (This corresponds to Region IV of Fig. 1c.).

The above observations are in complete qualitative agreement with the flow field description given in Section 1. They also indicate that the enhanced shock strength is solely due to the presence of a refracting medium.

Focus Factor

To facilitate the quantitative comparisons between the cases of the refracting and the homogeneous media, a focus factor, K, is defined as follows:

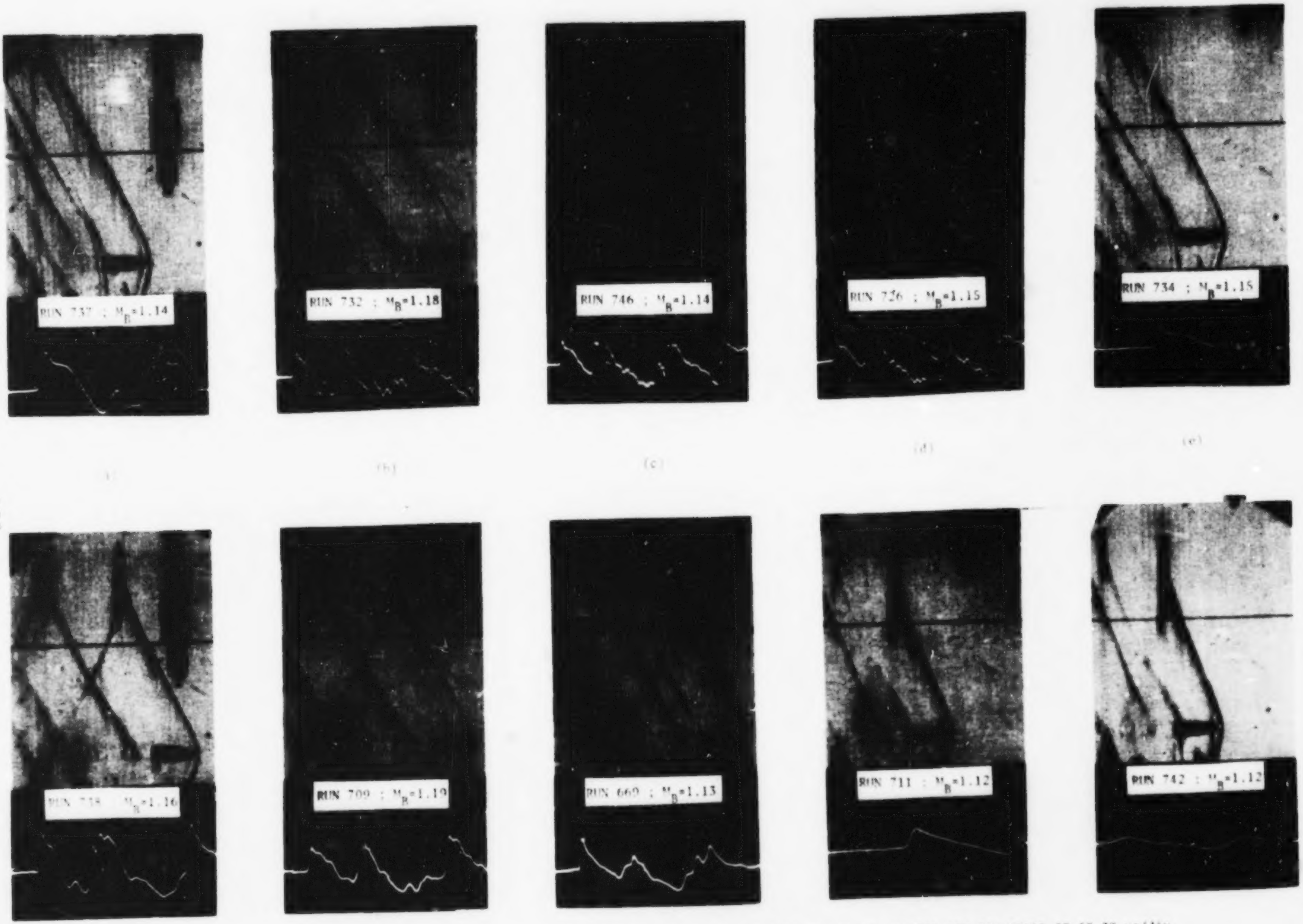

RUN 737 : M_B=1.14
RUN 732 : M_B=1.18
RUN 746 : M_B=1.14
RUN 726 : M_B=1.15
RUN 734 : M_B=1.15
(a)
(b)
(c)
(d)
(e)
RUN 738 : M_B=1.16
RUN 709 : M_B=1.19
RUN 669 : M_B=1.13
RUN 711 : M_B=1.12
RUN 742 : M_B=1.12

FIG. 5 COMPARABLE RUNS IN HOMOGENEOUS AND STRATIFIED MEDIA. SCOPE SWEEP RATE IS 50 μs/div IN ALL RUNS EXCEPT IN 711 AND 734 WHERE IT IS 20 μs/div.

VERTICAL SENSITIVITY IS 20 mv/div IN ALL RUNS.

$$K = \left[\frac{(\Delta P/P_o)_{\text{REF. MED.}}}{(\Delta P/P_o)_{\text{HOM. MED.}}} \right]_{\text{Same } M_B \text{ and } r} \tag{3.1}$$

where $\Delta P/P_o$ represents the shock intensity, M_B is the body Mach number and r denotes the radial position at which the pressure measurement is made.

To avoid uncertainties due to the presence of the reflected shocks from the porous surface, only the leading shock is considered here. Fig. 6 shows the radial variation of the focus factor and the approximate positions of the flow region boundaries for the leading shock. Four values as inferred from the experimental results reported in Ref. 10 are also shown for comparison. The leading shock intensity in these experiments is nearly equal to what is encountered in the present investigations. Each point in the plot represents a pair of runs similar to those depicted in one column of Fig. 5. The small difference between the body Mach numbers of the homogeneous and the refracting media runs has been accounted for by assuming that at a fixed radial distance, the shock intensity in the homogeneous case, $(\Delta P/P_o)_{\text{HOM. MED.}}$, is proportional to $(M_B^2 - 1)^{1/8}$, as predicted by Whitham's theory [7, 14].

The rather good correlation obtained for the experimental results is believed to be due to measuring the radial distances in terms of r_t, the triple-point height above the flight axis. This is consistent with the observation made earlier that r_t is a significant radial position as far as the pressure variations are concerned. The peaking of the focus factor curve near $r/r_t = 1$ (or the triple-point) is a purely experimental finding and is in general agreement with the earlier prediction made on the basis of the shock shape.

The largest focus factor detected in the present experiments is 1.7 and has been observed at $r/r_t = 0.98$. (This may be compared to $K = 1.8$ at $r/r_t = 0.93$ of Ref. 10). But this value has been obtained for a leading shock which is very much stronger than a typical sonic boom. Furthermore, the sound-speed gradient in the present simulation experiments is much greater than that in a typical atmosphere. Therefore, some scaling is required for applying the present result to the case of real flights. Possible effects of the sound-speed gradient on the magnification factor is currently being investigated. A suitable scaling law to account for the effect of shock strength is that of Guiraud [15, 16], which prescribes that the focus factor be scaled according to the negative one-fifth (-1/5) power of typical shock intensities far from focal regions. Assuming a value of 0.5 mbar (1 lb/ft^2) for a typical sonic boom [17] and noting that the typical shock intensity in the present experiments is 45 mbar, the present maximum focus factor observed scales to K_s given by:

$$K_s = 1.7 \left(\frac{0.5}{45}\right)^{-1/5} = 4.2 \tag{3.2}$$

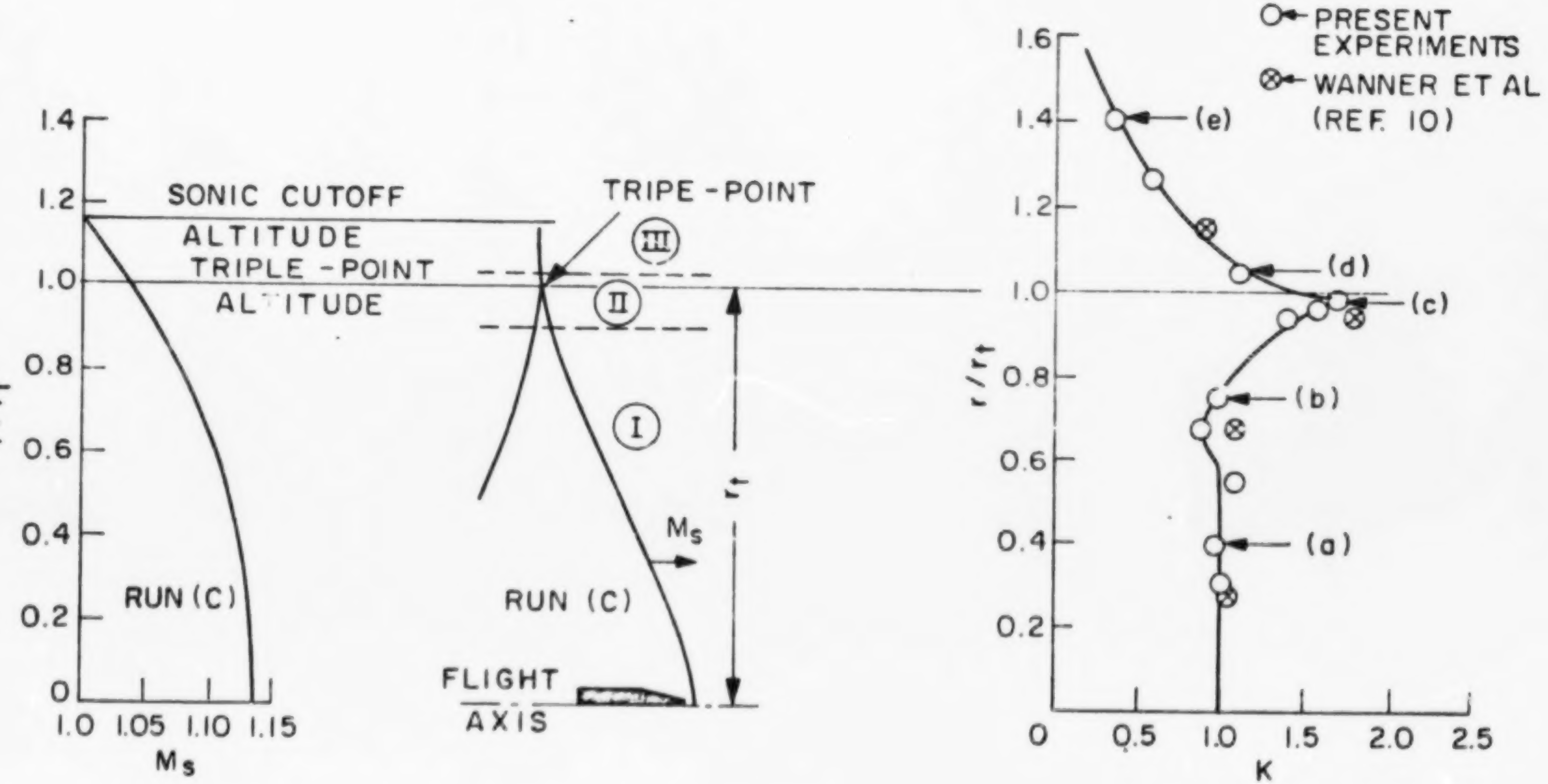

Fig. 6 Radial variations of the magnification factor, K, and the incoming flow Mach number, M_s, for the leading shock. Letters correspond to runs depicted in Fig. 5. Circled Roman numbers refer to flow region identified in Fig. 1c.

This is 1.4 times larger than the value of 3 measured in real flight tests by Maglieri et al. [17] and 1.1 times larger than the value of 3.7 obtained from the characteristic theory of Ref. 6.

4. CONCLUSIONS

A two-part investigation of shock focusing as related to sonic booms has been reported. Part I deals with the enhanced sonic booms generated by accelerating supersonic aircrafts. For laboratory simulation of such "acceleration superbooms", projectiles at constant supersonic speeds are fired into a gaseous medium with decreasing sound speed along the line of flight, thus resulting in trajectories with increasing Mach numbers. Experimental details have been given in Refs. 1 and 2. Major results reported here include the presence of converging shocks with higher overpressures in their concave portions. Focus factors as large as 2.0 have been detected. Other observations include folding of weak shocks (shock Mach numbers below 1.03) and defocusing of strong shocks (shock Mach numbers above 1.30).

In the second part, focusing due to refraction has been investigated. To simulate such "refraction superbooms", projectiles at low supersonic speeds are fired into a stratified medium produced by mixing CO_2 and air. Schlieren observations of the resulting flow fields indicate that the generated shocks are reflected near the sonic cut-off altitude (altitude at which the local sound speed equals the body speed), provided that such an altitude exists. The incident shock and its reflected portion join to form a Y-shpaed shock configuration near the cut-off elevation. This has been compared to the linear theory which predicts that the incident shock is totally reflected at a caustic located at the sonic cut-off altitude and that the reflected shock joins the incident shock to form a cusp at the caustic. The difference between the two shock configurations near the caustic has been attributed to the presence of nonlinear effects which are not accounted for in the linear theory.

Depending on the flow field behind the leading shock, several regions have been identified. The most interesting one is the region in which the flow speed behind the leading shock is transonic because the theories of Refs.4 and 6 predict enhanced shock overpressures (or superbooms) in this region, as discussed in Section 1. Experimental results obtained seems to agree with this prediction. However, they show that the maximum shock intensity occurs very near the triple-point, indicating that the presence of the reflected shock may have had an appreciable effect on the magnitude of the enhanced shock overpressures detected. By noting that the theories mentioned above disregard the presence of the reflected shock, it has been asserted that these theories are incomplete and, at best, they can only provide an estimate of the lower bound to the magnitudes of the overpressure for such superbooms.

The largest focus factor detected in the present refraction superboom experiments is 1.7. By correcting this value for the difference in shock intensities according to Guiraud's scaling law [15, 16], a focus factor of 4.2 has been predicted for a typical sonic boom of 0.5 mbar or 1 lb/ft^2.

(Corrections that may be required for the difference in sound-speed gradients are currently being investigated). This value is 1.4 times larger than the value of 3 measured in field tests of Ref. 17 and 1.1 times larger than the value of 3.7 predicted by the theory of Ref. 6.

REFERENCES

1. Sanai, M., Pierce, A.D., Toong, T.Y., and Salant, R.F., "Acceleration Superbooms: Some Preliminary Results", Proceedings of the Inter-Agency Symposium on University Research in Transportation Noise, Stanford University, Stanford, Calif., March 28-30, 1973, Vol. I, pp. 351-368.
2. Sanai, M., "Generation and Propagation of Focused Shock Waves", M.I.T. Ph.D. Thesis, in progress.
3. Friedman, M.P., Kane, E.J., and Sigalla, A., "Effects of Atmosphere and Aircraft Motion on the Location and Intensity of a Sonic Boom", AIAA J., Vol. I, No. 6, pp. 1327, 1963.
4. Friedman, M.P. and Chou, D.C., "Behavior of the Sonic Boom Shock Wave Near the Sonic Cut-off Altitude", NASA CR-358, December 1965.
5. Schorling, M., "A Nonlinear Theory for Sonic Boom Calculations in a Stratified Atmosphere", NASA TN D-7105, March 1973.
6. Auriol, A., Thery, C., Noyere, J.B., et Rothea-Laurent, C., "Réfraction des Ondes de Choc Aériennes", ISL Note Techniques Nos. T 14/66, T 29/66, T 44/66, N 11/68 et T 48/68 (in French).
7. Whitham, G.B., "The Flow Pattern of a Supersonic Projectile", Comm. Pure and Appl. Math., Vol. V, pp. 301, 1952.
8. Whitham, G.B., "On the Propagation of Weak Shock Waves", J. Fluid Mech., Vol. I, pp. 290, 1956.
9. Peter, A., Pfister, M., Stimpfling, A. et Devaud, M., "Etude Expérimentale de la Réfraction d'une Détonation Balistique dans une Atmosphère Stratifiée", Institut Franco-Allemand de Recherches de Saint-Louis, Report No. 17/71 (in French).
10. Wanner, F.C., Vallee, J., Viver, C. and Thery, C., "Theoretical and Experimental Studies of Focus of Sonic Booms", J. Acoust. Soc. Am., 52, 1972, pp. 13-32.
11. Bleakney, W. and Taub, A.H., "Interaction of Shock Waves", Rev. Mod. Phys., Vol. 21, 1949, p. 584.
12. Fletcher, C.H., "Mach Reflection of Weak Shock Waves", Technical Report II-4, Dept. of Phys., Princeton Univ., 1951.

13. White, D.R. and Bleakney, W. "Experimental Survey of Mach Reflection of Shock Waves", Technical Report II-10, Dept. of Phys., Princeton Univ., 1951.

14. Collins, D.J., "On the Experimental Determination of the Near-field Behavior of the Sonic Boom, and its Application to Problems of N-Wave Focusing", AIAA Paper No. 71-185, January, 1971.

15. Guiraud, J.P., "Acoustique Géométrique, Bruit Balistique des Avions Supersonique et Focalisation", Journal de Mécanique, Vol. 4, No. 2, 1965, pp. 215-267 (in French).

16. Thery, C., Lecomte, C. et Reggiani, F., "Remarques Concernant les Renforcements du Bang des Avions Supersoniques au Voisinage des Zones de Focalisation", ISL Note Technique, T 51/68 (in French).

17. Maglieri, D.J., Hilton, D.A., Huckel, V. and Henderson, R.H., "Measurements of Sonic Boom Signatures from Flights at Cut-off Mach Numbers", Third Conference on Sonic Boom Research, I.R. Schwartz, ed., SP-255, Oct. 1970, NASA, Washington, D.C., pp. 243-256.

NOISE SUPPRESSION WITH SONIC AND NEAR-SONIC INLETS

by

Edward Lumsdaine
Mechanical and Aerospace Engineering
University of Tennessee
Knoxville, Tennessee 37916

and

Lorenzo R. Clark
NASA-Langley
Hampton, Virginia

SUMMARY

The purpose of this research project is to develop some fundamental aerodynamic and acoustic information on the sonic and near-sonic inlets. The sonic inlet is a device that can be used to eliminate inlet noise from fans (or compressors) by means of the classical principle that sound cannot propagate upstream of a fluid flowing at sonic velocity. The sound attenuation produced by the near-sonic inlet is quite complex and not yet understood. Several inlets have been tested using a small ejector as a source, and a large inlet was tested using a single-stage transonic compressor. The test program is continuing. Presently the results show that:

(a) Substantial inlet noise reduction occurs before the inlet is aerodynamically choked with an inverse relationship between pressure recovery and degree of noise attenuation.

(b) Subsonic (acoustic) choking is more effective in reducing higher frequency noise than blade passage frequency noise, and more effective in attenuating blade passage frequency than overall noise.

(c) Exhaust noise does not increase significantly as a result of choking.

(d) An inlet with a larger pressure gradient produces larger attenuation than one with the same overall pressure difference but a more gradual pressure gradient.

(e) Pressure distortion can be kept at a safe, low value by designing the inlet with a sharp pressure gradient near the throat which produces also good acoustic characteristics at some sacrifice in pressure recovery.

(f) Choked inlets even with large area ratios can operate safely from the compressor surge margin during choked operation and do not change the operating characteristics of the compressor during unchoked operation.

(g) Near sonic velocities there is an optimum length/diameter ratio for a given area ratio.

(h) Tests with an automatic control system to maintain a specific noise reduction level (depending on location, other noise sources, etc., where maximum noise reduction is not required) show that it is feasible to provide specific amounts of noise reduction as indicated by circumstances.

(i) For small area ratios ($A_{exit}/A_{throat} < 1.5$) the collapsing cowl appears to be a better choice for choked inlet applications. For larger area ratios the centerbody type is better.

INTRODUCTION

Inlet noise attenuation by means of the so-called choked or sonic inlet can be divided into two general classifications. In the first case, the flow in the inlet is accelerated until a sonic surface exists near the throat of the inlet and the inlet is aerodynamically (or nearly) choked, with corresponding complete acoustic choking. In the second case the inlet is not choked aerodynamically, yet substantial noise reduction occurs; in fact some noise reduction is observed when the flow in the diffuser is everywhere subsonic. The term subsonic choking refers to such acoustic attenuation.

Sonic inlets are acoustically very effective; the problems are aerodynamic: how to achieve a sonic surface with the shortest inlet, with low distortion and negligible instability while still maintaining high pressure recovery. To achieve a sonic surface, there will exist in the inlet supersonic regions and also partial shocks which create large losses and instability problems. Contrary to some existing opinion (see for example References 1 and 2), using a very long inlet with low diffusion angle is not the answer even if it were practical, because for transonic flow and a given area ratio there is an optimum length/diameter ratio; extending the diffuser length beyond this point would increase the loss. This will be discussed in a later section.

Increased exhaust noise can also result when using the sonic (or near-sonic) inlets because of the increase in circumferential and radial distortion and turbulence which changes the blade loading characteristics of the rotor, leading to an increase in rotor noise and therefore rear-ward radiated noise. This noise increase is not due to reflected acoustic energy from the choked plane since it appears that the forward energy is largely dissipated. Experimental evidence indicates that the increase in exhaust noise is not significant under normal engine operating conditions.

For near-sonic inlets, the noise reduction is not physically well understood. It has been suggested that the combination of large axial and radial velocity gradients could result in large reflections, refractions, and viscous and heat dissipation of the sound. The present tests show that the axial velocity gradients seem to have a rather dominant effect. Because of the obvious aerodynamic advantages (stability, high recovery) when the flow in the inlet is predominantly subsonic, the interaction of the high velocity flow field with acoustic modes is being studied both experimentally and theoretically in order to exploit this interaction to minimize noise transmission. This paper will give a brief summary of results of work on the sonic and near-sonic inlet. Aerodynamically, there is no sharp line of demarcation between the two; acoustically, however, much more detailed measurements are required in order to understand and exploit the near-sonic inlet noise reduction phenomenon.

DISCUSSION

1. Sonic Inlets

The investigation of the sonic inlet requires a study of steady and unsteady aerodynamics since acoustically this type of inlet is effective. A crucial problem in the operation of the sonic and near-sonic inlet is the problem of instabilities. Instabilities due to shock boundary layer interaction and flow oscillations as a result of gust or thrust variation could cause engine surge and stall. It has been found in some experimental tests, where the pressure gradient was distributed in the diffuser, that for diffusers of low area ratio and high pressure recovery some instabilities occurred with no noticeable upstream disturbance. There are two instability problems, one

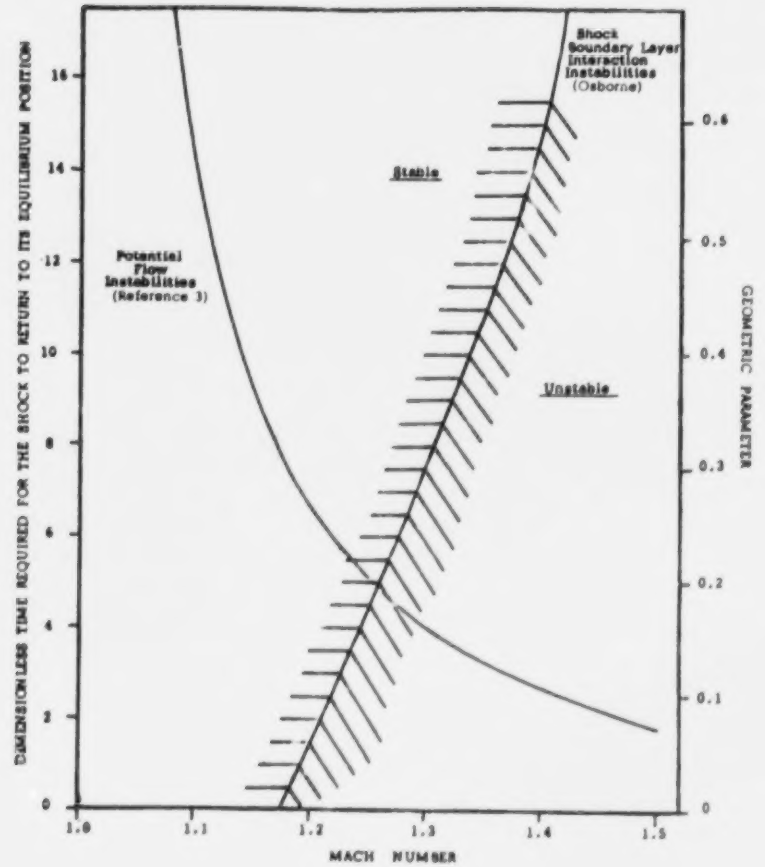

Fig. 1 Stability criteria for a choked inlet

associated with the free stream and the other with the shock boundary layer interaction. Figure 1 shows that the time required for a shock to return to its original position increases with decreasing Mach number, which means that for potential flow the stronger the shock the more stable the system (see Reference 3). However, with increasing Mach number the tendency toward shock boundary layer interaction increases. Of course, at transonic velocities, even without the existence of the shock, instabilities can occur in the free stream triggered by flow separation due to the adverse pressure gradient.

For steady state operation, the problem of boundary layer control was studied both theoretically and experimentally. Distributed suction and injection are effective in controlling the boundary layer. A detailed discussion with results for injection at different shock strengths is given in Reference 4. Vortex generators appear to be effective when properly designed and placed and when separation is not too severe. Although the preceding sentence appears obvious, it is very crucial for transonic flows. Most of the experimental studies reported here are without boundary layer control to establish the minimum level of aerodynamic performance since boundary layer control can be added if necessary or advantageous. Another problem is to find an optimum

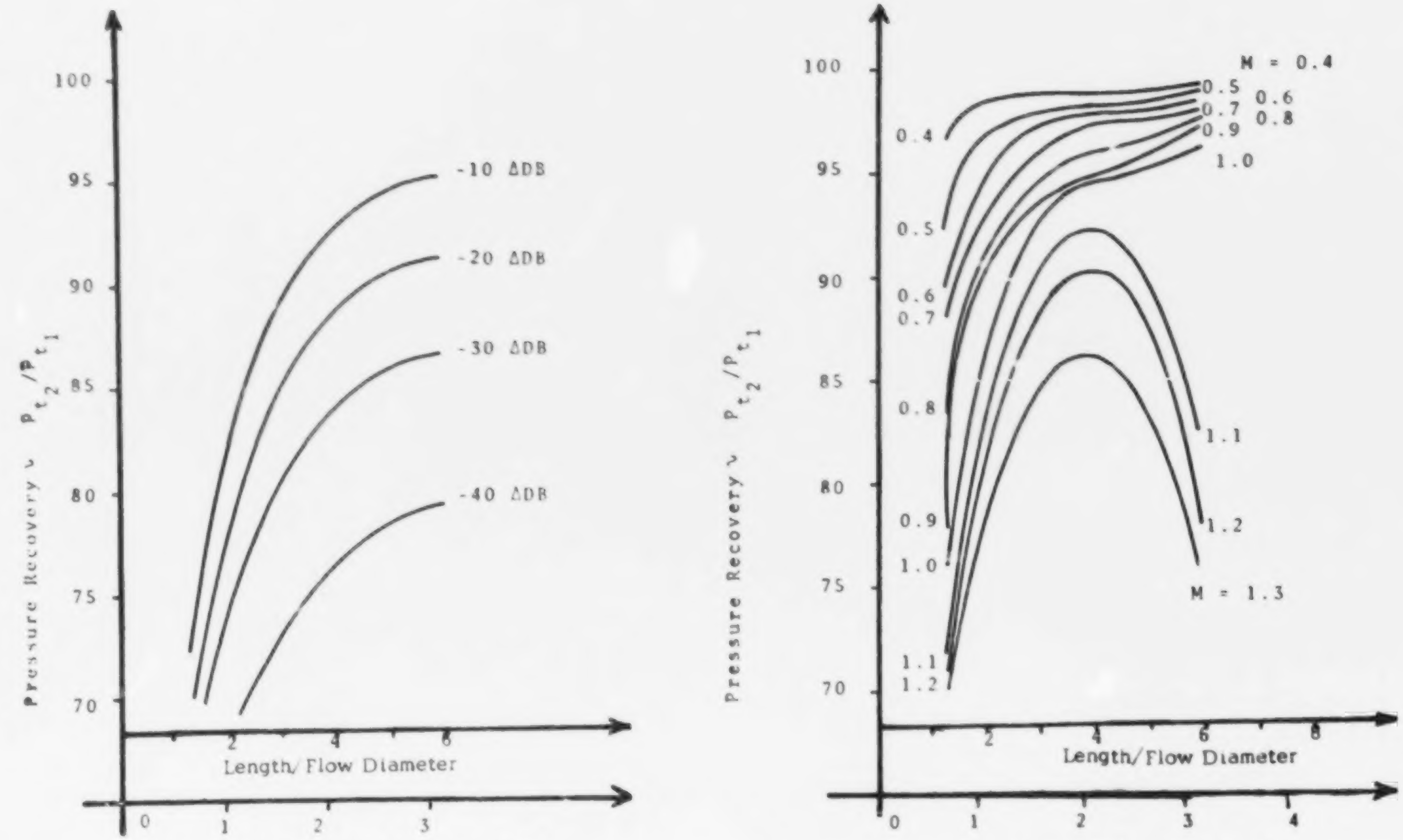

2a. Length/Diameter Ratio L/D

2b. Length/Diameter Ratio

Fig. 2 Results from choked inlet studies

length for a given area ratio. Unfortunately, the theoretical work on the inverse transonic flow problem has not been completed. In the absence of a good theoretical design method, some tests were conducted and combined with a literature search which revealed some interesting results. Figure 2 shows the results of tests conducted with six inlets of different lengths with area ratio of 3.2 and the same contoured lip. They clearly show that there is an optimum length/diameter ratio for a given area ratio. Repeated tests changed the shape of the curve for M = 1, but the optimum appears to be at approximately the same place. Figure 3 presents curves for the optimum for annular and straight circular and square diffusers. For the case of annular diffusers the data is rather limited and further tests are being conducted to compare with this curve. The usefulness of these curves is simply that they provide an initial starting point for the design, since for a given area ratio to achieve a specified mission for a particular type of aircraft, the approximate L/D can be obtained. From this result the direct problem is solved to obtain refinements since transonic solutions and computer programs for solving the direct problem are readily available. The testing phase then confirms or refines this result.

Several conclusions were brought out as a result of constructing these curves. Although boundary layer blockage is a very important parameter in pressure recovery, it does not affect the optimum point very significantly. The scatter in the points is largely due to the method of selecting the optimum as seen in Figure 2b, particularly for subsonic flow. However, the results clearly show a trend apparently independent of throat Mach number. Figure 2a shows the attenuation characteristics as a function of pressure recovery; it is quite clear that subsonic choking will not produce large noise attenuation, which can be obtained only at a cost to pressure recovery. The maximum Mach number here is the maximum wall Mach number, and it is seen that large noise reduction is obtainable when the inlet is nearly aerodynamically choked.

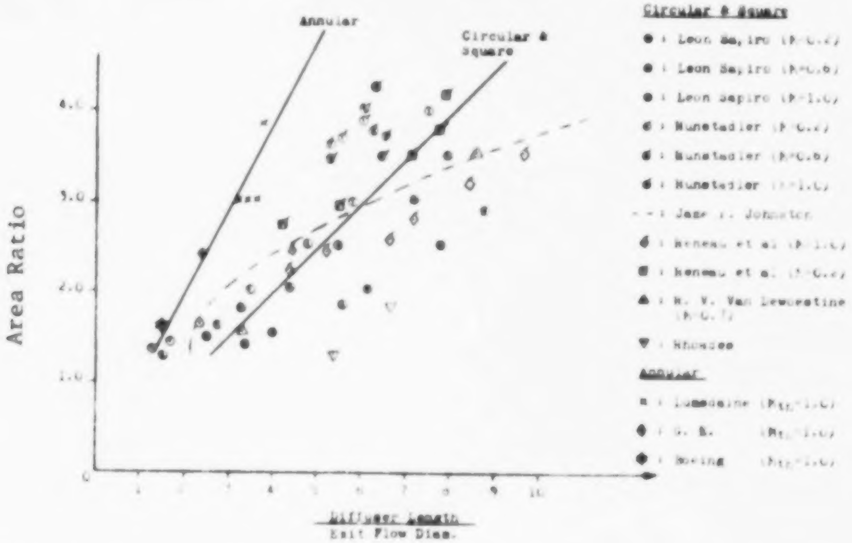

Fig. 3 Optimum L/D for a given area ratio at different throat Mach numbers for circular and square diffusers

2. Near-Sonic or Accelerating Inlets

Aerodynamically, near-sonic inlets pose problems similar to sonic inlets, although this depends on the amount of attenuation required. If a moderate amount of attenuation is required, this type of inlet can operate with high pressure recovery, low distortion and stable flow. A theoretical and experimental program was set up to investigate the aerodynamic and acoustic characteristics of the near-sonic inlet. The work is still in progress; some specific objectives are: obtain information on the effect of axial velocity gradient on noise propagation; design inlets with low distortion and instabilities; investigate compressor operation characteristics during choke; compare translating centerbody inlets with other types, and verify theoretical as well as empirical results (such as the optimum L/D for a given area ratio).

The early experimental study consisted of small model tests using an ejector (see Reference 5 for details of the experimental setup) and showed that for an inlet with the same overall pressure difference (overall area ratio) and the same flow conditions to the throat, but with different L/D (different pressure gradient) the attenuation characteristics near Mach one are very different, as shown on Figure 4. Subsequent tests with several translating-type centerbodies (see Reference 5) have also shown that the velocity gradient rather than the maximum velocity is the controlling factor in noise attenuation. Presently, several configurations are scheduled for tests on the NASA-Langley transonic compressor anechoic-chamber facility. The 12-inch tip speed single-stage compressor has 19 rotor blades and 30 stator blades with a maximum rpm of 25,000. Results from testing the first inlet (Figure 5) at the

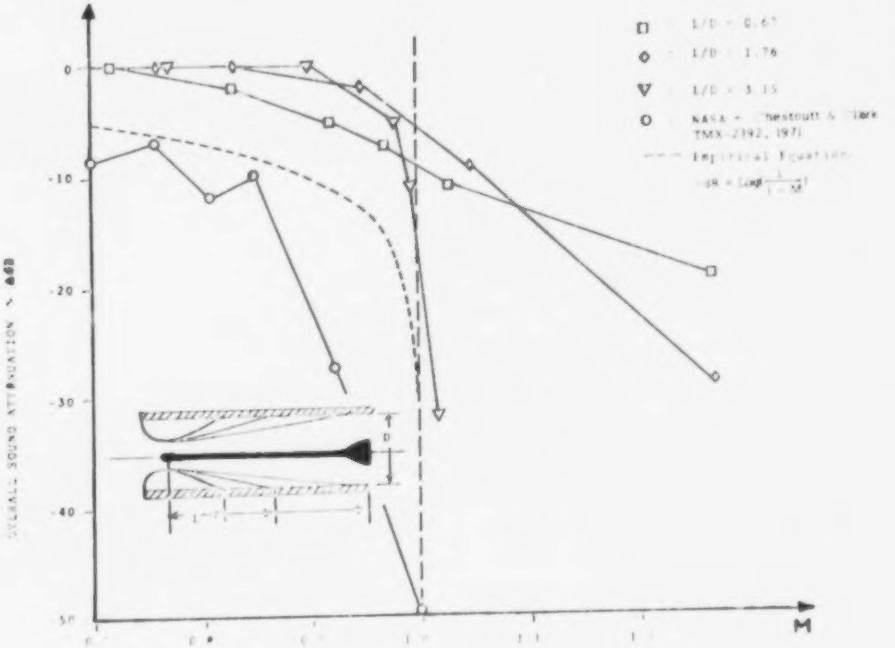

Fig. 4 Sound attenuation versus average maximum axial Mach number for inlets with different L/D

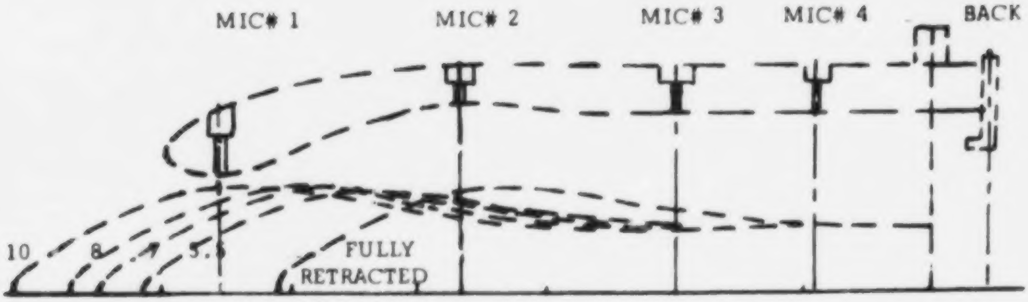
MIC# 1
MIC# 2
MIC# 3
MIC# 4
BACK
10
8
7
5.5
FULLY RETRACTED

ACOUSTIC MICROPHONE POSITIONS

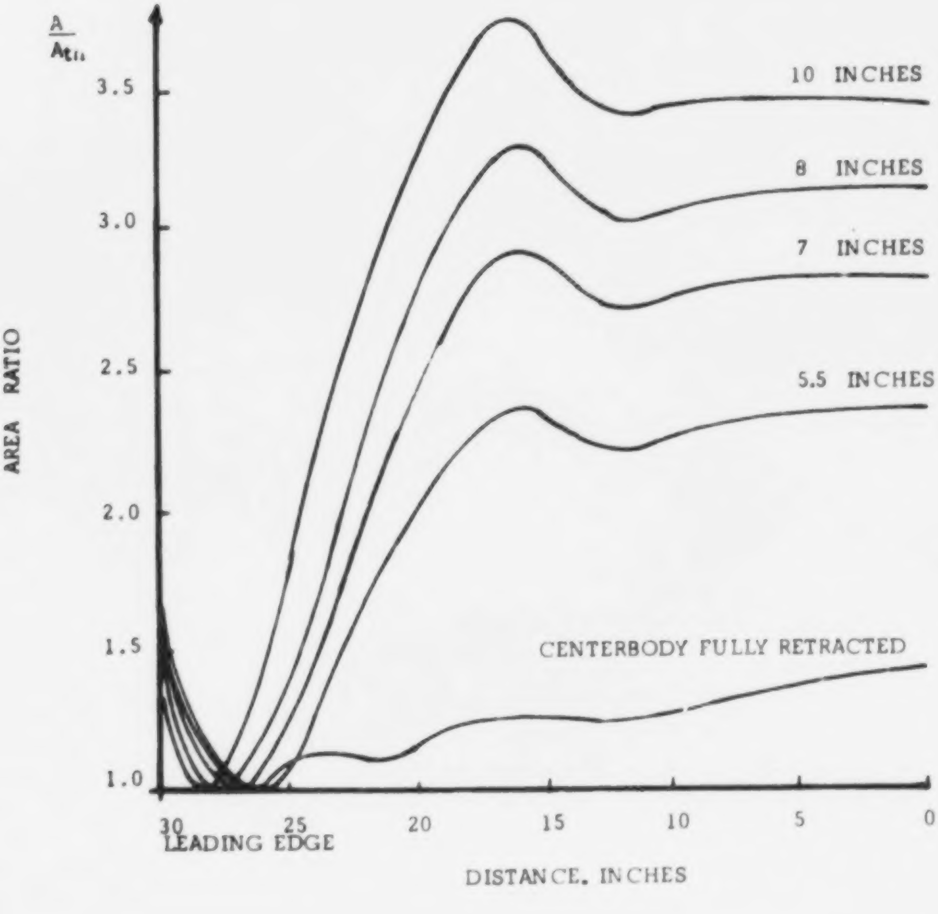

Fig. 5 Centerbody positions for inlet I tested at NASA-Langley

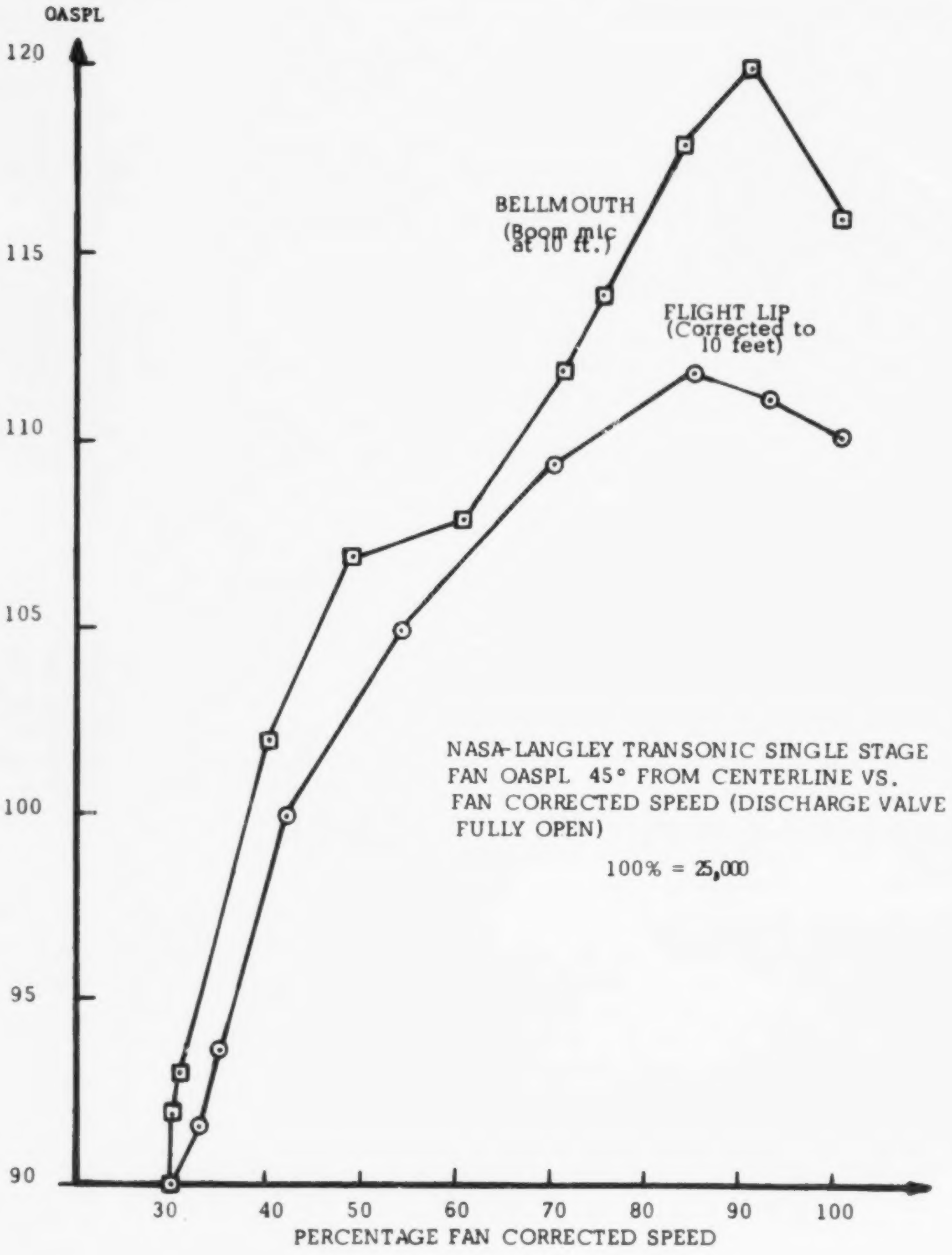

NASA-LANGLEY TRANSONIC SINGLE STAGE FAN OASPL 45° FROM CENTERLINE VS. FAN CORRECTED SPEED (DISCHARGE VALVE FULLY OPEN)

100% = 25,000

Fig. 6 Lip effect on radiated noise

NASA-Langley facility are included here. They support the results from the model tests which show tentatively that:

1. The geometry of the inlet is not as crucial to the aerodynamic performance as was suspected. However, lip geometry has a significant effect on noise attenuation, as indicated by the results presented in Figure 6.

2. Larger pressure gradients near the throat produce larger noise reduction and substantially lower distortion but a slightly higher pressure loss than a gradual pressure gradient for the same overall pressure difference. The question of stability is still undetermined.

3. High Mach number inlets are more effective in attenuating high-frequency noise; they are not as effective against the fundamental blade passage frequency. Yet in comparison to the overall noise reduction levels, these inlets seem to be relatively more effective in reducing blade passage frequency noise than overall noise. Also, the amount of noise reduction by a given inlet is amplitude-dependent.

4. The velocity gradient rather than the velocity itself plays a dominant role in noise attenuation for subsonic choke. Thus graphs showing the attenuation of sound at different Mach numbers are not very meaningful without also showing the velocity gradient.

5. For mechanical, control, and aerodynamic reasons a translating centerbody appears to be the best choice for sonic and near-sonic inlets, especially for high area ratios. The use of a collapsing cowl for choking results in large radial gradients with high distortion. The inlet would also have to be longer (see Figure 3) to achieve optimum attenuation as compared to a centerbody-type inlet. Tests are being run to make further assessment of the aerodynamic and acoustic performance of the different types of inlets. Radial vanes create a large increase in drag with increases in circumferential distortion and back noise, but have low radial distortion. The expanding centerbody has the same advantages as the translating centerbody, except that the translating centerbody is easier to design and control. For inlets using a combination of high velocity and some acoustic treatment (hybrid inlets), the presence of the centerbody reduces the channel height and increases the treatment area and effectiveness.

6. There appears to be no significant increase in back noise from the present type of translating centerbody inlets, since increase in back noise occurs with increased circumferential distortion.

Figures 7 to 9 show some preliminary results of the aerodynamic and acoustic performance of the inlet tested at NASA-Langley at three positions of centerbody translation. Although there was a large reduction in noise between the back and front wall microphones at five inches of translation, as compared to the completely retracted position, only a small difference appeared in the far-field results (see Figure 10). This information together with near-field microphone results tends to confirm earlier findings that high Mach number inlets are not as effective in attenuating lower frequencies. Figure 11 gives the operational characteristics of the compressor at different translation positions of the centerbody. This information can be useful in selecting the design of a high Mach number inlet with acoustic liners.

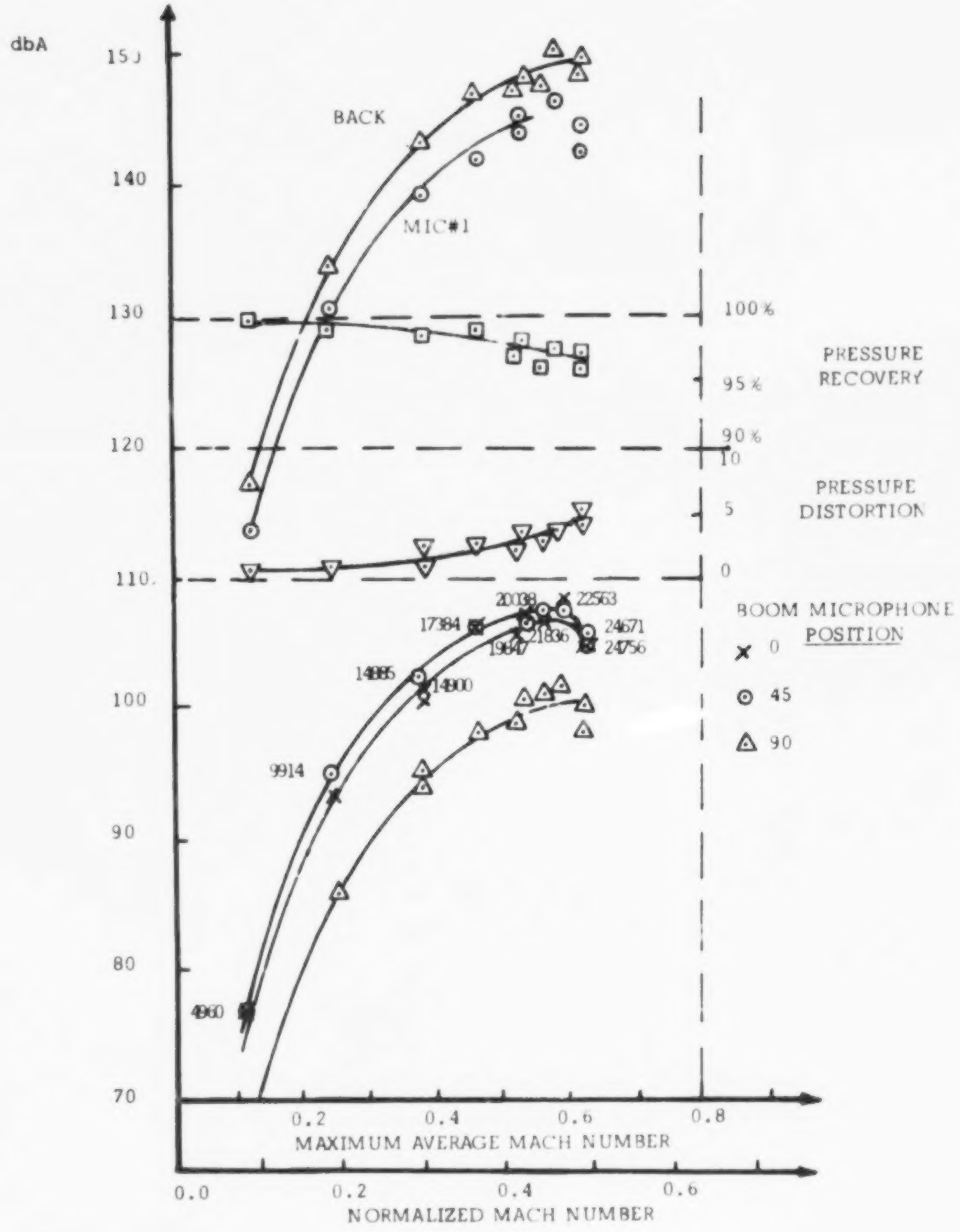

Fig. 7 Acoustic and aerodynamic performance of inlet I with fully retracted centerbody

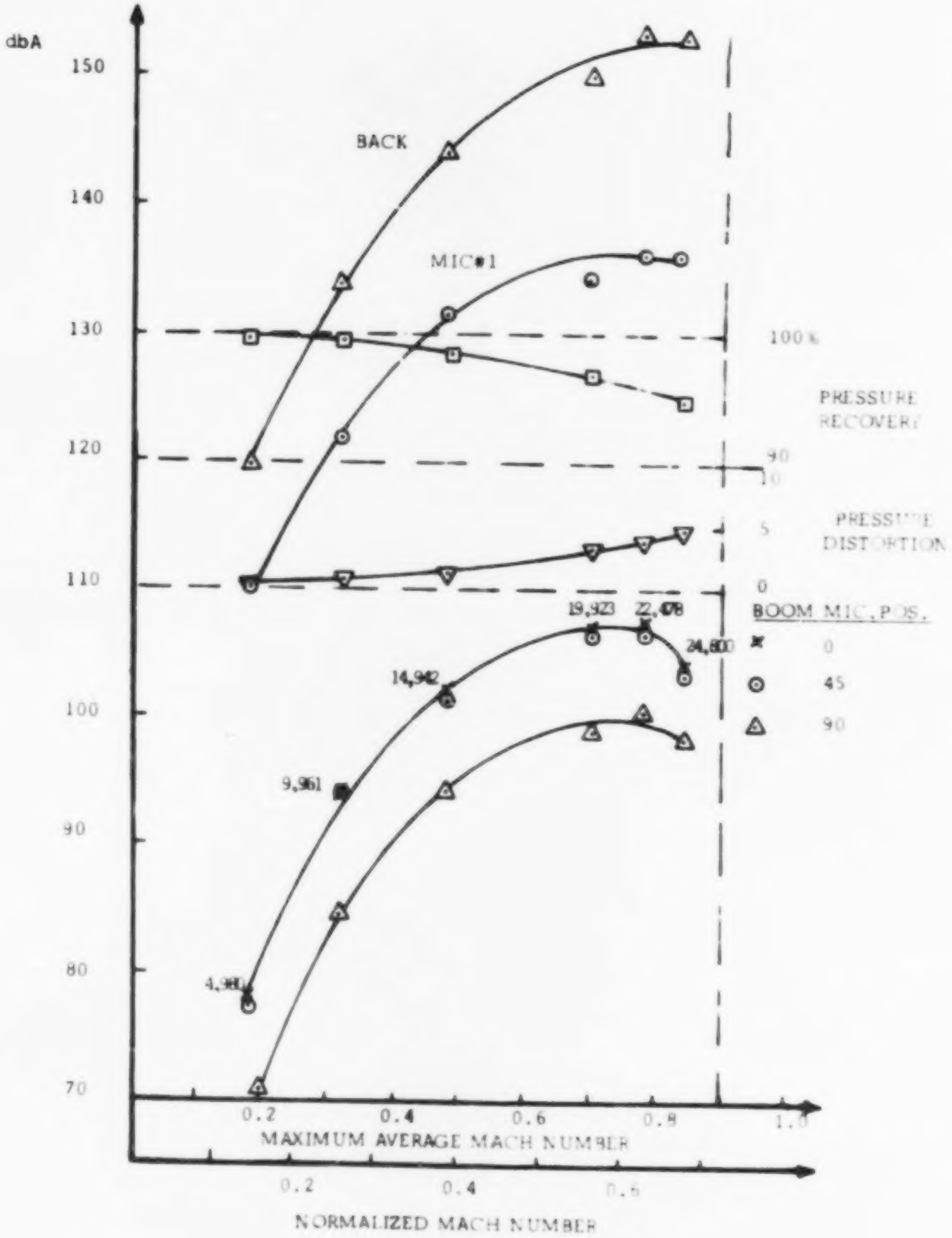

Fig. 8 Acoustic and aerodynamic performance for 5-inch centerbody translation (inlet I)

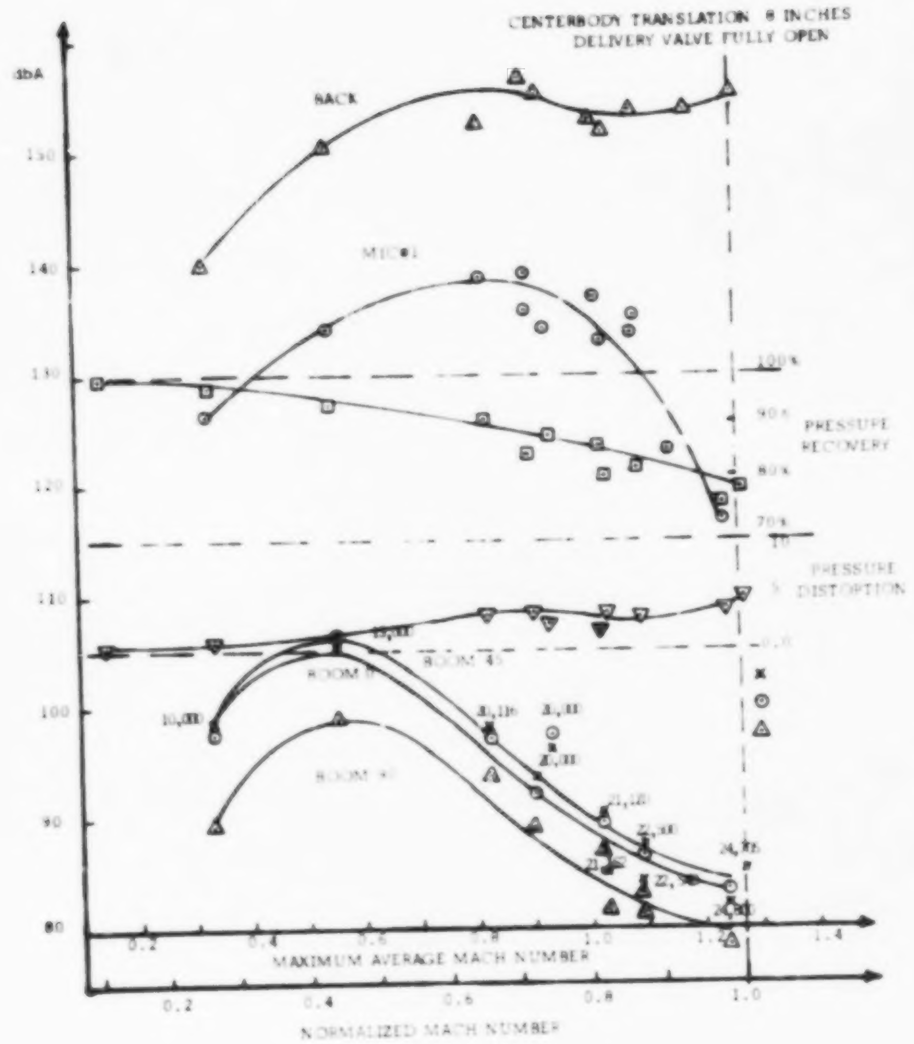

Fig. 9 Acoustic and aerodynamic performance for 8-inch centerbody translation (inlet I)

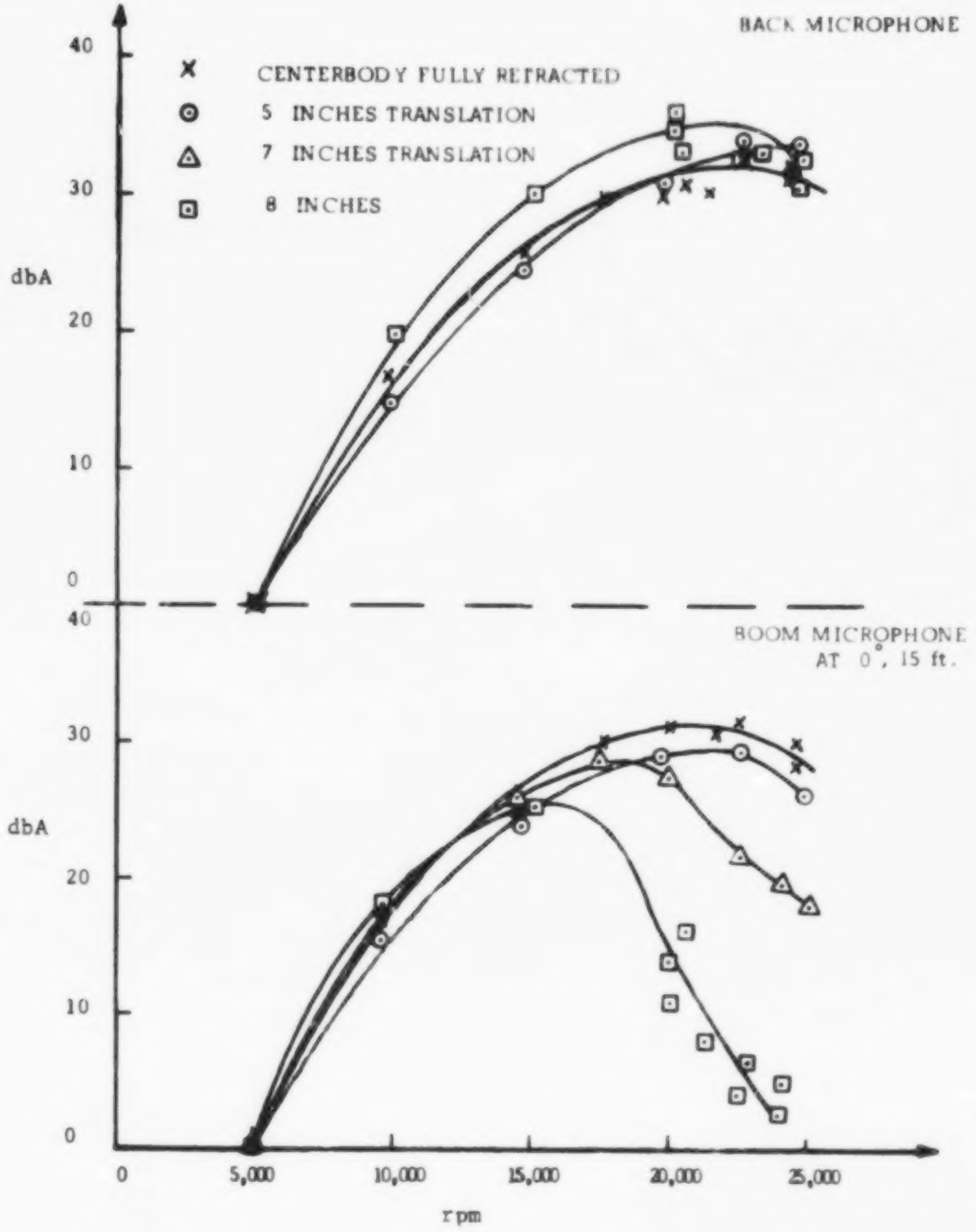

Fig. 10 Corrected speed versus dbA with delivery valve fully open (far field)

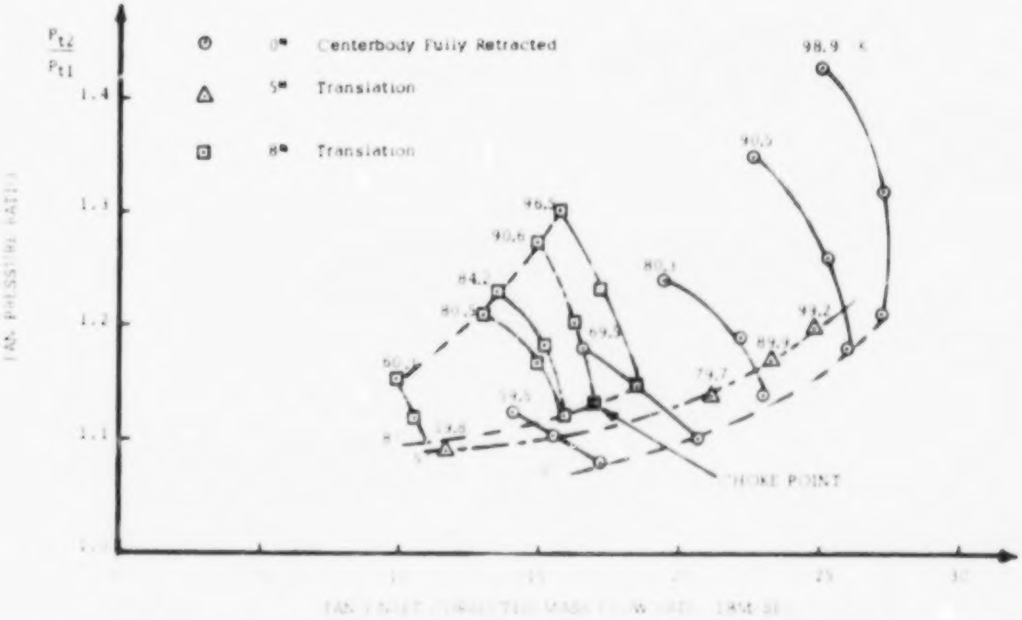

Fig. 11 Operational characteristics of the NASA-Langley transonic compressor at three centerbody positions (inlet I)

Figure 12 is a comparison of three inlets with different area ratios. An important feature of this result is that although higher area ratio inlets have higher pressure loss, the pressure distortion is much lower than for both of the lower area ratio inlets. This is largely due to the design philosophy of this inlet with a higher pressure gradient to obtain larger noise reduction at subsonic Mach numbers with low distortion. This is similar to using vanes when the area change takes place over a relatively small region. Of course the present inlet does not have the added drag, increased circumferential distortion, and mechanical and other disadvantages of the vane-type inlet. Tests are continuing with other area ratios and configurations, and a detailed comparison will be made upon completion with other results in the literature as well. Preliminary tests have been completed on an automatic control system to maintain a preset amount of noise reduction consistent with environmental requirements and the noise floor of the aircraft.

[Acknowledgment: Financial support for this research was provided by NSF under grant GK-38342. The equipment and personnel support provided by NASA-Langley in its transonic compressor facility, and particularly the cooperation of Mr. D. Maglieri, are gratefully acknowledged. Special thanks go to Monika Lumsdaine for typing and layout of this manuscript.]

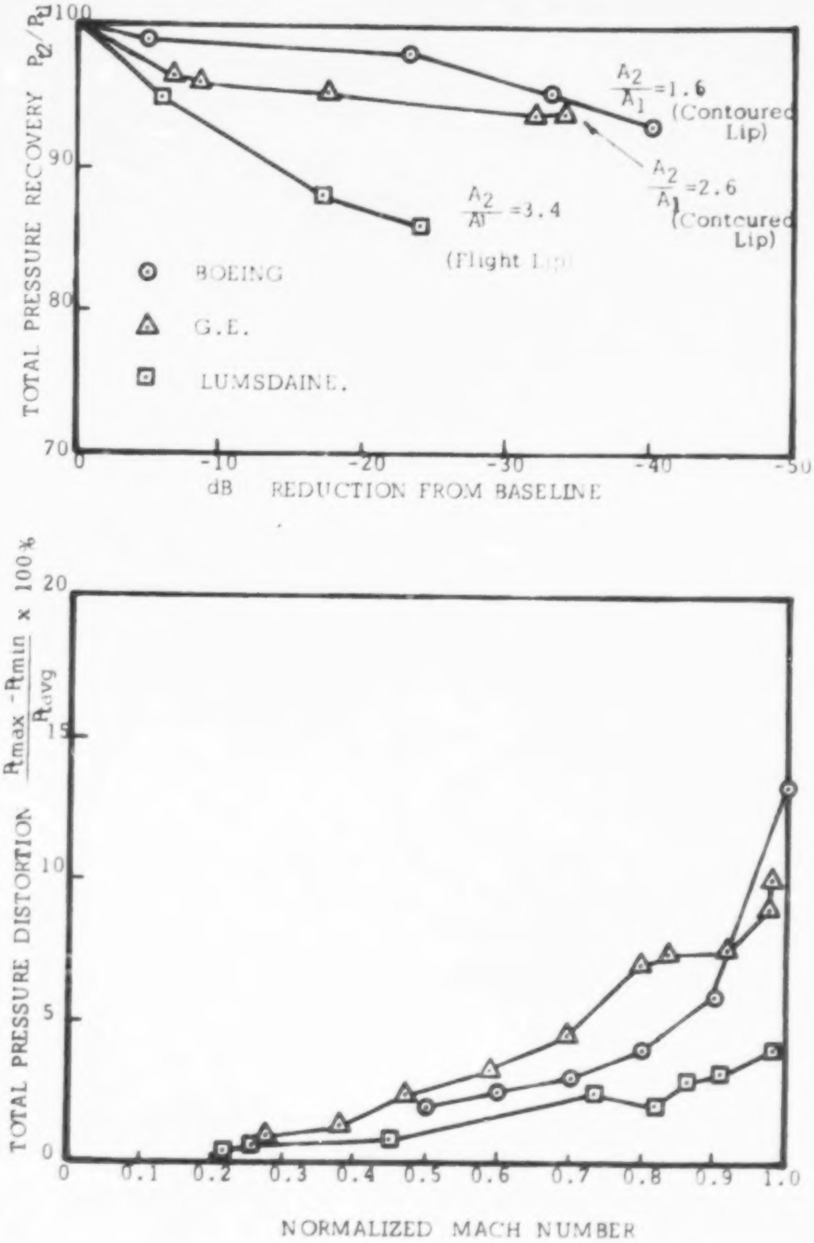

Fig. 12 Comparison of aerodynamic performance of choked inlets with different area ratios

REFERENCES

1 A.H. Marsh, I. Elias, J.C. Hoehne and R.L. Frasca, "A Study of Turbofan-Engine Compressor-Noise-Suppression Technique," Douglas Aircraft Company Contract Report No. NAS1-5256.

2 T.G. Sofrin and J.C. McCann, "High Bypass Ratio Engine Noise," Paper presented at the International Noise Conference, London, Nov. 22-30, 1966.

3 A. Fathy and E. Lumsdaine, "A New Method of Solving One-Dimensional Unsteady Flow Equations and Its Application to the Shock Wave Stability in Sonic Inlets," Developments in Mechanics, Vol. 7, Aug. 1973, pp. 153-165.

4 E. Lumsdaine and A. Fathy, "Theoretical Study of Boundary Layer Control by Blowing for Axisymmetric Flow and Its Application to the Sonic Inlet," Engineering Experiment Station Bulletin 16, South Dakota State University, Oct. 1970.

5 E. Lumsdaine, "Results of the Development of a Choked Inlet," presented at the 1972 International Conference on Noise Control Engineering, Washington, D.C., October 4-6; published in 72 Inter-Noise Proceedings, pp. 501-506.

EFFECT OF NONLINEARITY ON NOISE PROPAGATION

by

F. M. Pestorius, S. W. Williams, and D. T. Blackstock

Applied Research Laboratories
The University of Texas at Austin
Austin, Texas 78712

Introduction

At the Stanford Symposium last year[1] we reported a study of the propagation of finite-amplitude noise in a tube (for a more detailed and complete description see Ref. 2). Previously Pernet and Payne[3] had investigated the propagation in tubes of narrowband noise at low and moderate intensities (generally, initial bandwidths less than 1 octave at sound pressure levels in the range 120-140 dB). We considered broadband noise at high intensity (initial bandwidth approximately 3 octaves and sound pressure levels up to 160 dB). Theoretical predictions were obtained by means of a computer algorithm based on weak-shock theory. Incorporated in the algorithm was a provision for including the effects of tube wall attenuation and dispersion. Experimental measurements of noise pulses traveling down a 100-foot long, 2-inch (i.d.) tube confirmed the theoretical predictions. A typical set of results is shown in Fig. 1. The noise waveform distorts rapidly as propagation distance increases. The distortion leads to formation and growth of shocks. As the larger shocks advance or retreat in the waveform, they encounter and "eat up" small irregularities and weaker shocks. A random sawtooth wave evolves. The random sawtooth is much simpler in appearance than the original noise signal in that the number of zero crossings is greatly reduced.

The effects of nonlinearity on the propagating noise may also be described in terms of changing spectra. At first, associated with the formation of shocks, there is an enhancement of the high-frequency end of the spectrum. Later the low-frequency end experiences a buildup as the number of zero crossings decreases. The net result is a substantial transfer of energy out of the midfrequency region. The transfer is accompanied by an overall increase in absorption due mainly to dissipation at the shocks. Experimentally observed spectra shown in Fig. 2 illustrate the effects described.* The fact that there is comparatively little change from 48 ft to 72 ft indicates that by 48 ft the random sawtooth has apparently become well formed. Changes thereafter reflect (1) the slow migration of some energy to low frequencies as the remaining shocks vie for control of the waveform, and

---

*Computed spectra associated with the noise waveforms shown in Fig. 1 (but with the effects of tube wall attenuation and dispersion omitted) exhibited similar behavior. Both the figure showing these results and Fig. 2 were presented in the oral version of our report at the Stanford Symposium but did not appear in the written Proceedings.[1] The two figures may be found in Ref. 2.

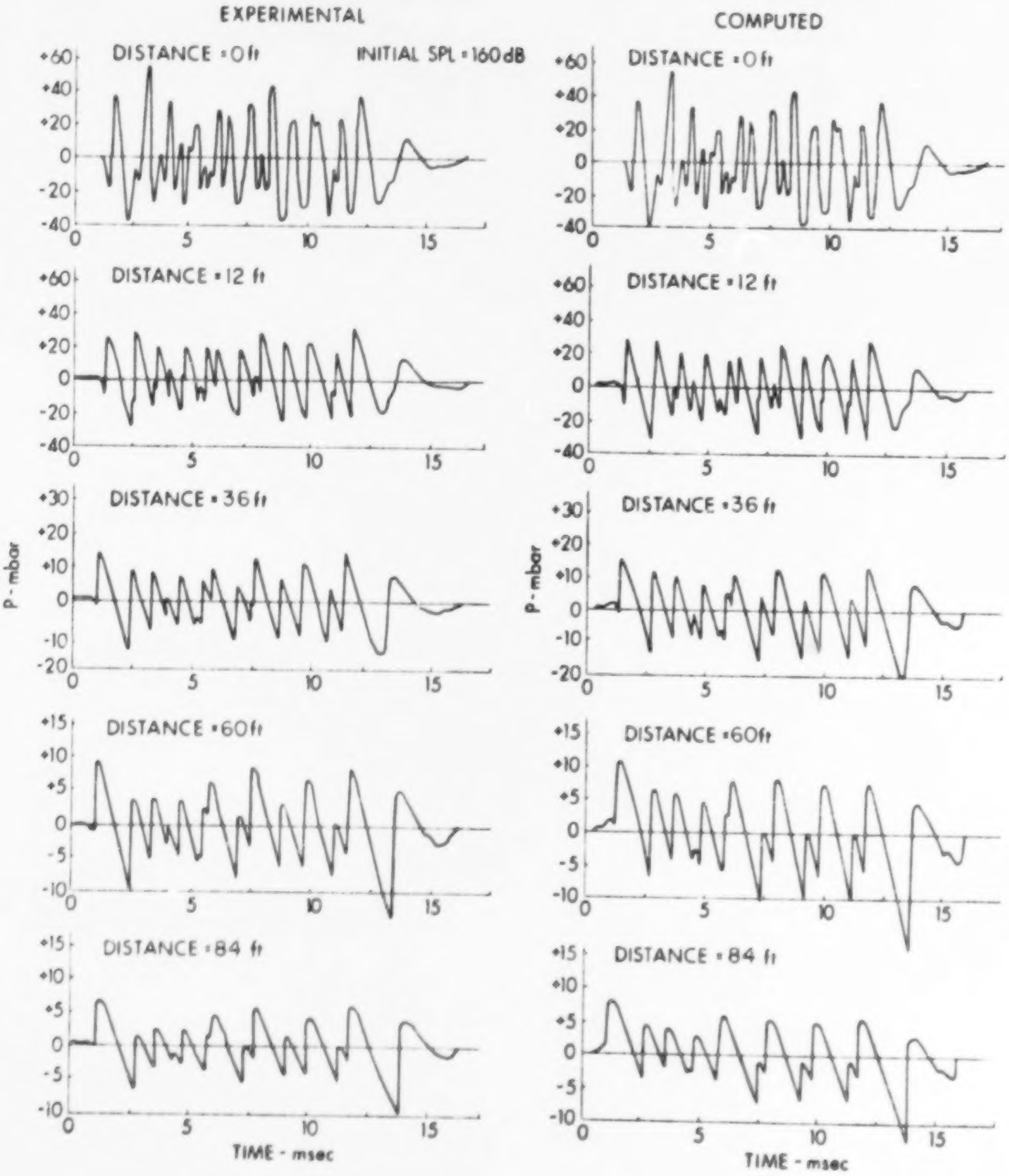

FIG 1. Nonlinear distortion of a pulse of noise as it propagates down a tube (from Refs. 1 and 2, with minor revisions).

AS-74-1717
DTB C-0015

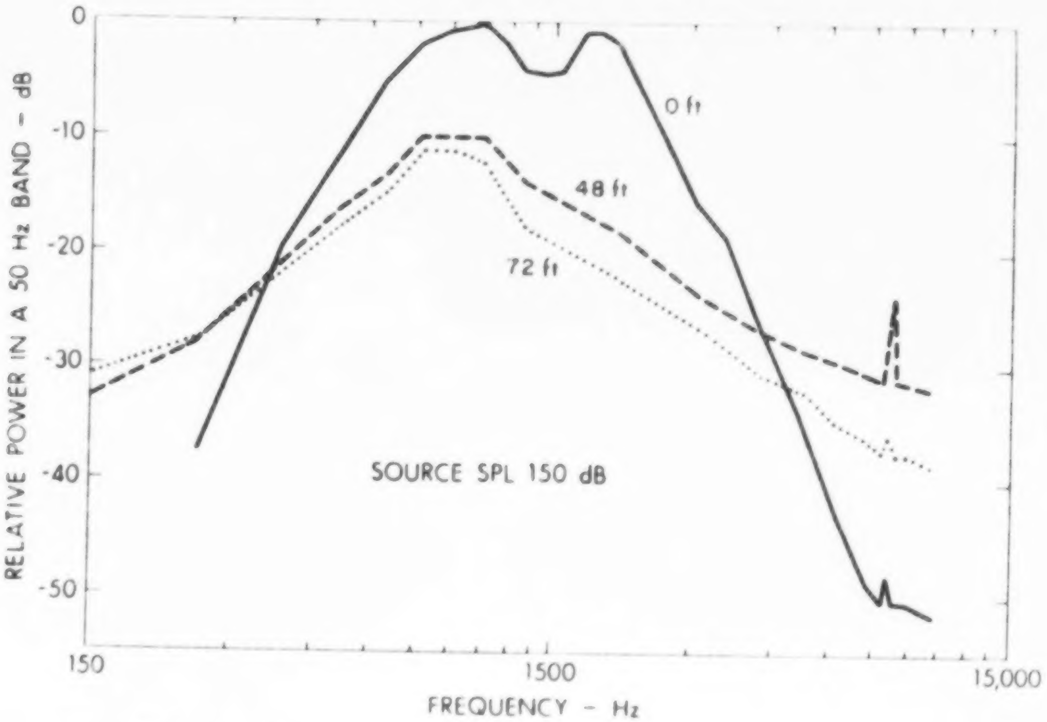

FIG. 2. Spectra of CW noise at various distances (from Ref. 2, with minor revisions).

(2) the gradual general decay of the wave caused by tube wall absorption. Incidentally, tube wall effects, in particular, dispersion, are responsible for the asymmetry of the shocks in Fig. 1, i.e. the rounded peaks and sharp troughs. To show this, we ran our computer program without the correction for tube wall effects. Starting with the same initial noise pulse shown in Fig. 1, we obtain the waveforms shown in Fig. 3. The shock peaks here are as sharp as the troughs. These waveforms are of particular interest for the present study because they pertain to planar noise in an open medium.

The initial study, summarized above, showed that nonlinearity produces remarkable effects in the propagation of intense plane waves of noise. However, most intense noise encountered in practice spreads spherically, and spherical spreading sharply reduces the rate of distortion. Thus how important are nonlinear propagation effects, really, in technology? In particular, how important are nonlinear effects in the propagation of jet noise? Furthermore, if nonlinear effects are important, what role do characteristics of the noise, such as bandwidth, spectral shape, peak frequency, phase, overall SPL, and so on, play? We found that the noises we studied experienced a great deal of spectral broadening and increased absorption. But what about other noises, with different characteristics? Is it necessary to run every noise in which one is interested through our computer program in order to determine the effect of nonlinearity on that noise? Or can scaling laws be developed that will permit one to make estimates based on, say, overall SPL coupled with an octave band analysis? We are now in the process of trying to answer

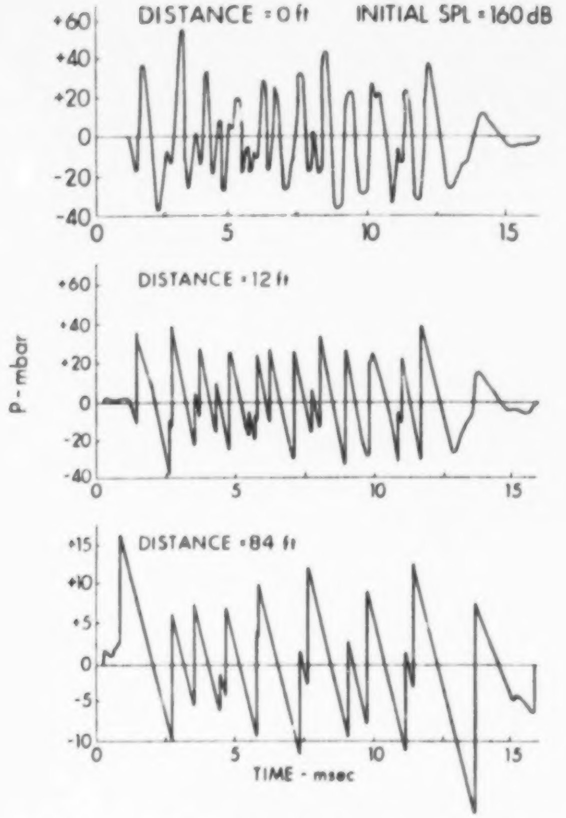

FIG. 3. Nonlinear distortion of the same noise pulse shown in Fig. 1 but without the effects of tube wall absorption and dispersion (from Refs. 1 and 2, with minor revisions).

some of these questions along with others that became apparent in the course of our initial study. The present paper represents a very early progress report.

The Basic Model: Weak Shock-Theory

For our study of jet noise in the open air we use weak-shock theory without any modification of the sort employed in the previous study. In weak-shock theory one assumes that decay of a wave is due entirely to dissipation at whatever shocks are present in the waveform; ordinary absorption is neglected. Thus lossless theory is used for continuous sections of the waveform. This means that the propagation speed dx/dt of a wavelet (a wavelet is a point on a waveform identified by the value of its ordinate) is

$$dx/dt = c_o + \beta u,$$

where c_o is the small-signal sound speed, u is the particle velocity, and $\beta = (\gamma+1)/2$ (γ is the ratio of specific heats). Therefore, the law governing the relative time of arrival $t' = t - x/c_0$ of a wavelet is

$$\frac{dt'}{dx} = \frac{dt}{dx} - \frac{1}{c_0} \doteq - \frac{\beta u}{c_0^2} \quad . \tag{1}$$

In the case of a shock the analogous relation is, to the same degree of approximation,

$$\frac{dt_s'}{dx} = \frac{\beta(u_a + u_b)}{2c_0^2} \quad , \tag{2}$$

where t_s' is the relative arrival time of the shock, and u_a and u_b are the particle velocities immediately ahead of and immediately behind the shock, respectively. Equations 1 and 2, which form the basis of our computer algorithm, describe the way the distortion of a waveform develops with distance. For example, if the wave is of infinitesimal amplitude, i.e. $u \to 0$, the equations show that t' does not depend on the distance x. All wavelets travel at the same speed; consequently there is no distortion.

The use of weak shock theory leads to accurate results when the waves are neither too strong nor too weak. The upper limit is approached when the sound pressure level reaches about 165 dB.[4] The lower limit is set by the validity of the assumption about the importance of shock dissipation. For sufficiently weak waves (weakness depends upon frequency as well as amplitude) ordinary absorption is more important then losses at shocks, and, in fact, shocks may never even form.*

Extension to Nonplanar Waves

For spherically spreading waves the equations of motion and the shock relations may be reduced to equations having the same form as Eqs. 1 and 2 simply by applying the transformation[5]

$$x \to z = r_0 \ln (r/r_0) \tag{3a}$$

$$u \to w = (r/r_0)u \quad , \tag{3b}$$

where r is the radial coordinate and r_0 is a reference distance, usually source radius or effective source radius, i.e., the distance at which the time waveform of the signal is known. Although the independent variable t' is not stretched in this transformation, it is usually convenient to redefine it as $t-(r-r_0)/c_0$ to reflect the fact that the wavelet begins its journey at the source, not the origin. The reduction to plane-wave form via the transformation given by Eqs. 3 is valid provided $kr \gg 1$, where $k = \omega/c_0$ is the wave number corresponding to a typical angular frequency ω of the acoustic signal. Although originally developed for omridirectional spherical waves, the transformation also applies, with certain restrictions, to directional spherical waves as well.[6] Noise from jet engines probably meets these restrictions in large part.

---

*Our earlier study[1,2] was not hampered by any such lower limit because, as noted previously, our weak-shock model was a modified one wherein explicit account was taken of tube wall absorption and dispersion.

We may illustrate the use of Eqs. 3 by applying them to the noise waveforms in Fig. 3 (the waveforms in Fig. 1 would do if it were not for the fact that they include the effects of tube wall absorption and dispersion). From Eq. 3a we see that if a plane wave suffers a certain distortion in traveling a distance x, then a spherical wave having the same source waveform will suffer the same distortion when it reaches the distance

$$r = r_o e^{x/r_o} \quad . \tag{4}$$

For example, if a spherical source 3 ft in radius emits the source signal shown at the top of Fig. 3, then the waveform designated "Distance = 12 ft" in Fig. 3 will be observed at a range $r = 3 \exp (12/3) = 164$ ft. From Eq. 3b, the amplitude of the spherical wave will be less than that of the plane wave by the factor $r_o/r = 3/12 = 1/4$. Thus spherical spreading modifies the distortion process only by slowing it down. Note that the size of the effective source has a great deal to do with the rate of slowdown. If $r_o = 2$ ft, the "12 ft" waveform will be observed at a range of about 800 ft; if $r_o = 6$ ft the range will be about 44 ft. (In these examples we are holding the amplitude constant at r_o, which means that the sound power is being varied.)

If near the source the spreading is cylindrical rather than spherical, the appropriate transformation is[5]

$$\begin{aligned} x \to z &= 2\sqrt{r_o}\,(\sqrt{r} - \sqrt{r_o}\,) \\ u \to w &= \sqrt{(r/r_o)}\; u \quad . \end{aligned} \tag{5a}$$

Thus the distortion observed for a plane wave at distance x will be observed for a cylindrical wave at range

$$r = r_o + x + x^2/4r_o \quad . \tag{6}$$

If the wave first spreads cylindrically and later spherically, one transformation can be used first and then the second. Or a smooth transition can be effected by using the more general transformation[5]

$$x \to z = \int_{x_o}^{x} \sqrt{A_o/A}\; dx' \tag{7a}$$

$$u \to w = \sqrt{A/A_o}\; u \quad , \tag{7b}$$

where A is the cross sectional area of the ray tube through which a given element of the wave propagates (for example, for spherical waves $A \propto r^2$, for cylindrical waves $A \propto r$, etc.).

Effects of Frequency and Amplitude

Consider wavelets 1 and 2 in the arbitrary source waveform (time waveform at x=0) shown in Fig. 4. Using Eq. 1, we find that the difference in

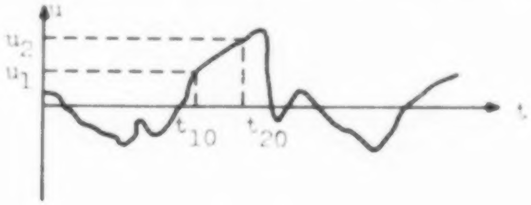

FIG. 4. Two wavelets in a source waveform.

arrival times $\Delta t = t_2 - t_1$ of the two wavelets at a given distance x is, normalized to the initial difference $\Delta t_o = t_{20} - t_{10}$,

$$\frac{\Delta t}{\Delta t_o} = 1 - \frac{\beta x \Delta u}{c_o^2 \Delta t_o} \quad , \tag{8}$$

where $\Delta u = u_2 - u_1$. The dimensionless group of factors

$$\sigma = \frac{\beta x \Delta u}{c_o^2 \Delta t_o} \tag{9}$$

is the fractional phase shift; its size is a direct measure of the distortion of the waveform. For example, the fractional phase shift can be doubled by doubling the distance x, by amplifying the waveform so that Δu is doubled, or by time scaling the waveform so that Δt_o is halved. Thus the wave shapes displayed in Fig. 3 would not change if at the source the sound pressure level were lowered to 154 dB and the noise pulse were compressed in time by a factor of 2. Compression of the pulse would, of course, shift the peak of the initial frequency spectrum up an octave (from 1 kHz to 2 kHz in this case).

Although we are not able to say anything at this time about how the shape of the initial spectrum affects the distortion, there are some indications about the asymptotic shape of the spectrum after considerable nonlinear distortion has taken place. It will be seen that in the random sawtooth in Fig. 3 the line segments connecting the shocks all have the same slope. This is no accident.[7,8] A straight line segment in a waveform may be described by

$$u = m\,(t' - t_o') \ ,$$

where m is the slope of the segment. We shall be concerned here with line segments whose slope is negative, i.e. $m<0$. Using the solution of Eq. 1,[5] we find that the segment remains straight as the wave propagates, but that the slope changes with distance as follows:

$$m = \frac{m_o}{1-\beta x m_o/c_o^2} \quad , \qquad (10)$$

where m_o is the slope at x=0. As x becomes large the slope becomes independent of m_o,

$$m \approx -\frac{c_o^2}{\beta x} \quad , \qquad (11)$$

which explains the uniformity of the segments behind the shocks in the random sawtooth. Now because of this uniformity, the random sawtooth can be thought of as a ramp function, of slope given by Eq. 11, to which is added a series of step functions of random occurrence and random amplitude. See Fig. 5. The high frequency characteristics of the random sawtooth are determined by the step functions. Because the step functions are independent events, their power spectral densities, which have an ω^2 dependence, add. Thus the spectrum of the random sawtooth is expected to have a high frequency rolloff of 6 dB/octave. This rolloff is in fact close to what is observed for the 48 ft and 72 ft waveforms in Fig. 2. We have also observed the 6 dB/octave slope in many of our computed spectra.

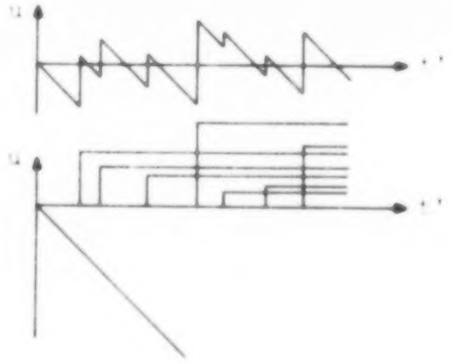

FIG. 5. Decomposition of a random sawtooth wave into a ramp function and a series of step functions.

Effect of Phase

We now take up the question of the importance of phase in nonlinear propagation distortion. In the case of deterministic, or mainly deterministic, waveforms phase is very important. For example, an N wave and an inverted N wave have grossly different propagation properties.[9] We also know from the phenomenon of multiple tones in jet engines that small phase variations from cycle to cycle in an otherwise periodic signal can have a very great effect on the waveform after a long propagation distance.[10] On the other hand, phase would not seem to be very important for random waveforms. For example, when the spectra shown in Fig. 2 were measured, they proved quite stable with time despite the fact that the source signal had an ever changing waveform (recall that the noise in this case was CW, not repeated pulses). In the case of stationary random noise the observed spectrum at a given receiver location may be thought of as a time average (which we assume to be equivalent to an ensemble average) of spectra associated with successive sections of the noise time waveform. Since each section is different, each experiences a different distortion as it travels to the receiver. Nevertheless, there is evidently an "average distortion," as the measured spectra show.

If phase considerations can be ignored, the analysis of propagation distortion for practical cases may be greatly simplified. Given a noise source in the field, say of omnidirectional spherical waves, one needs only the spectrum of the noise, not its time signature, in order to predict the effect of propagation distortion on the noise. In particular, one can recreate a suitable (random) time waveform in the laboratory simply by requiring its spectrum to match that of the field noise and then "computer propagate" the recreated noise using the algorithm we have developed. We have not, however, determined how long the recreated noise signature should be to assure that the recreated noise and the field noise experience comparable nonlinear distortion.

As a rather extreme test of the proposition that phase is unimportant in the distortion of random noise, we performed the following computer experiment: First we generated a random noise sample, which we shall call WAVE I. Waves II, III, and IV were then derived from WAVE I by specifying the phase of the harmonics in the FFT representation of WAVE I. The phase properties of the four signals are as follows (ϕ_n is the phase of the nth harmonic):

WAVE I: ϕ_n = random
WAVE II: $\phi_n = -\pi/2$
WAVE III: $\phi_n = (-1)^n \pi/2$
WAVE IV: $\phi_n = (-1)^n \pi/2 + \pi$.

Thus although all waves have the same power spectra, their phases are grossly different. In fact, Waves II, III, and IV are not really random signals because their phases have been made so regular. This is why the test is characterized above as "extreme."

The four waves were computed propagated (as plane waves) over a distance of 200 ft. Their waveforms and power spectra were plotted at intermediate points. A sampling of the results is shown in Figs. 6 and 7. At top and bottom of each series are the spectra at 0 ft and 100 ft, respectively. It will be seen that despite the fact that Waves II, III, and IV have been rendered nonrandom by the phasing chosen for them, the spectra at 100 ft do have much in common, particularly at the high frequencies, where, as expected, the slopes are approximately 6 dB/octave. There is, however, a spread of about 7 dB in the overall sound pressure levels at 100 ft. Wave IV experienced the most attenuation, Wave I the second most, Wave III the third most, and Wave II the least. Although no definitive conclusions can be drawn from this test, it is clear that very drastic changes in phase did not produce drastic changes in the effect of nonlinear distortion on the propagation, at least over the distance considered.

The distortions suffered by the various waves are interesting in themselves. The phasing chosen for Waves II, III, and IV produced strong transients in each waveform. The transient dominates the distortion of Waves II and III but disappears in Wave IV. In Wave II the transient is a pair of "end effect" pulses. Because of their polarity these pulses "grow" toward each other, rapidly gobbling up smaller shocks in the process. It can be

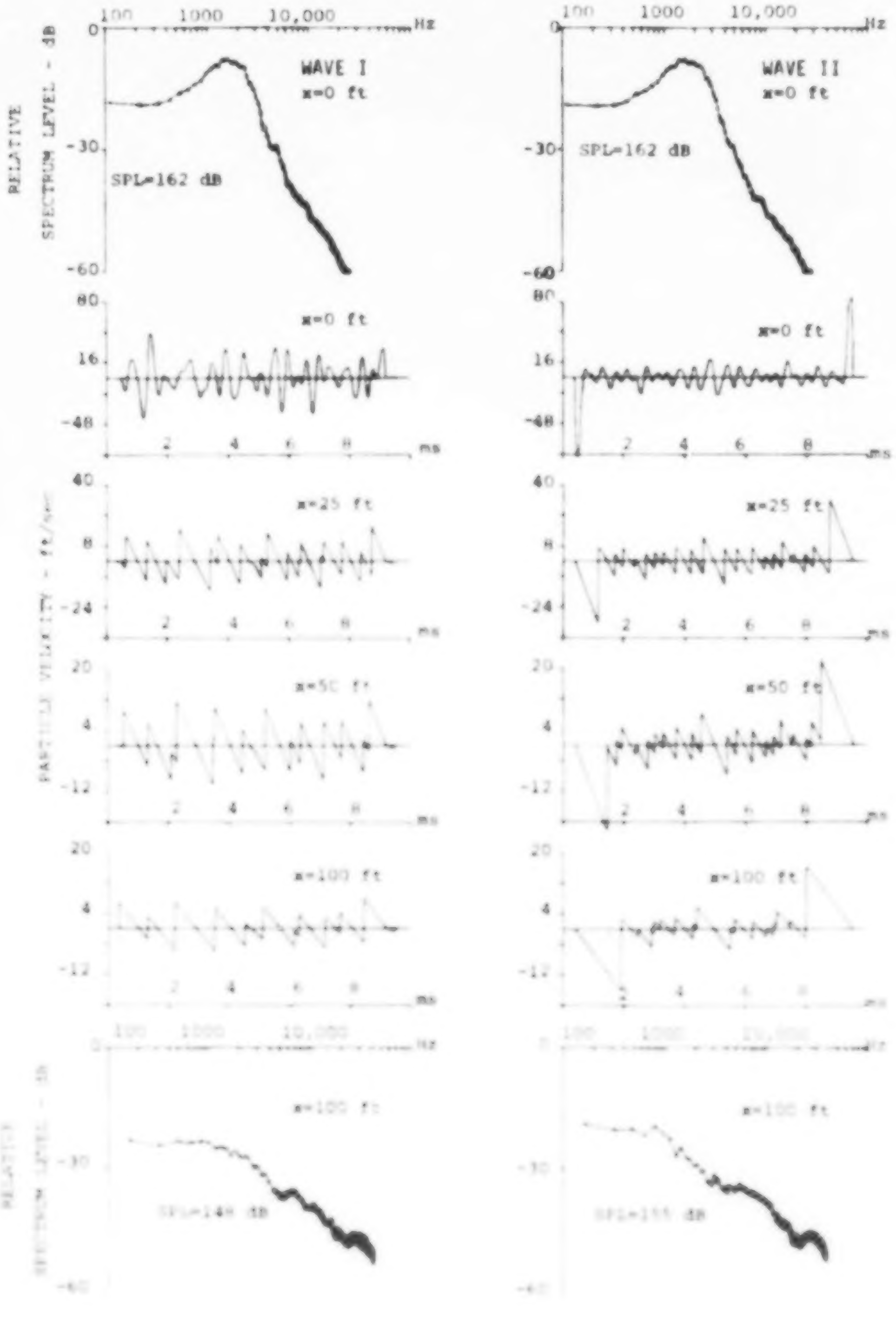

FIG. [illegible] Waveforms and spectra for WAVE I (random) and WAVE II ($t_0 = -\tau/2$).

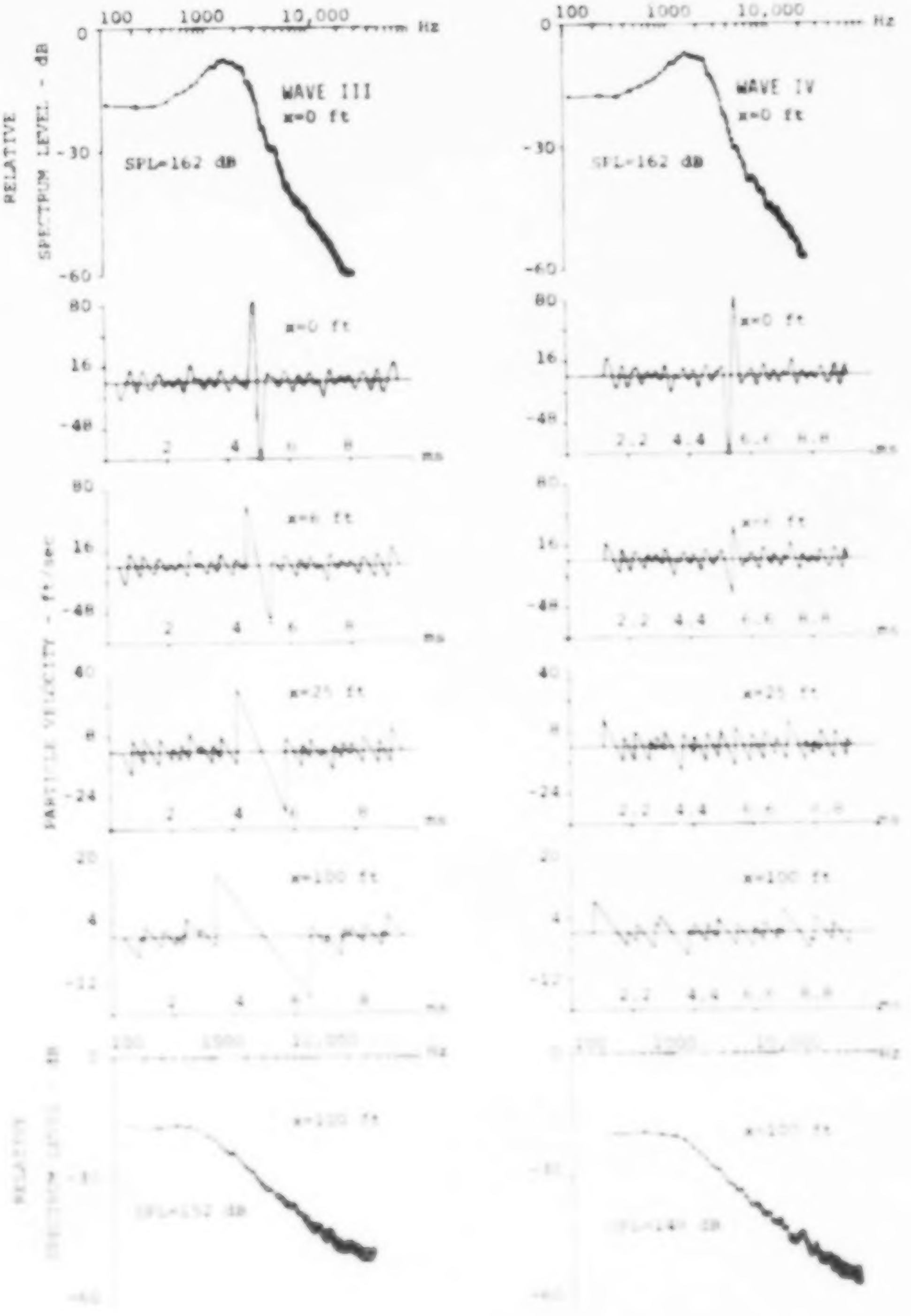

[illegible] Waveforms and spectra for WAVE III [illegible]
and WAVE IV [illegible]

seen that the asymptotic waveform will be a single cycle of a sawtooth wave, the shock wave in the middle. Such a wave decays very rapidly (amplitude proportional to $1/x$), just like a CW sawtooth. Thus the fact that Wave II has experienced the least attenuation at 100 ft is probably not significant; eventually its decay will probably be the most rapid. By contrast, the doublet in the center of Wave III becomes an N wave, which will eventually consume the entire waveform. Wave III will thus decay asymptotically as an N wave (amplitude proportional to $1/\sqrt{x}$) and thus not nearly so rapidly as Wave II. Finally, Wave IV, which is just Wave III inverted, also has a doublet in the center, but the order of its negative and position phases is such that it becomes a single cycle of a sawtooth. Thus instead of dominating the distortion, as do the transients in Waves II and III, it dies rather quickly. Its decay is undoubtedly responsible for the rather strong attenuation of Wave IV over the 100 ft travel path.

SUMMARY AND ACKNOWLEDGMENTS

The earlier study of propagation of finite-amplitude noise[1,2] has been reviewed. The extension of those results, which are for plane waves, to spherical and other nonplanar waves has been described. The effect of shifting frequency and/or amplitude of a noise has been discussed. An argument has been given that the spectrum of an intense noise will, at great distances, have a high frequency rolloff of 6 dB/octave. Phase effects have been discussed; some evidence has been presented to support the proposition that phase is not important in nonlinear propagation provided the noise is truly random.

The support of AFOSR in carrying out this research is gratefully acknowledged. Discussions with R. L. Rolleigh, T. G. Flemons, and H. O. Berktay on a number of points have been quite helpful.

REFERENCES

1. F. M. Pestorius and D. T. Blackstock, "Propagation of Finite-Amplitude Noise," Proceedings, Interagency Symposium on University Research in Transportation Noise, Stanford University, Stanford, California, 28-30 March 1973, Vol. II, pp. 466-477.

2. F. M. Pestorius, "Propagation of Plane Acoustic Noise of Finite Amplitude," Ph.D. Dissertation, University of Texas at Austin, Austin, Texas (August 1973), also available as Technical Report ARL-TR-73-23, Applied Research Laboratories, University of Texas at Austin, Austin, Texas (August 1973).

3. D. F. Pernet and R. C. Payne, "Nonlinear Propagation of Signals in Air," J. Sound Vib. 17, 383-396 (1971). See also "Propagation of Finite Amplitude Sound Waves in Tubes," AERO Report AC 43, National Physical Laboratory, Teddington, England (1969).

4. F. M. Pestorius and D. W. Williams, "Upper Limit on the Use of Weak-Shock Theory," to appear in J. Acoust. Soc. Am. 55 (1974).

5. See, for example, D. T. Blackstock, "Nonlinear Acoustics (theoretical)," in Amer. Inst. Phys. Handbook, D. E. Gray, ed. (McGraw-Hill Book Co.,

Inc., New York, 1972), Chap. 3n, pp. 3-183 to 3-205.

6. J. C. Lockwood, T. G. Muir, and D. T. Blackstock, "Directive Harmonic Generation in the Radiation Field of a Circular Piston," J. Acoust. Soc. Am. 53, 1148-1153 (1973).

7. J. M. Burgers, "Statistical Problems Connected with Asymptotic Solutions of the One-Dimensional Nonlinear Diffusion Equation," in Statistical Models of Turbulence, M. Rosenblatt and C. Van Atta, eds. (Springer, Berlin, 1972), pp. 41-60.

8. F. M. Pestorius and D. T. Blackstock, "Propagation of Finite-Amplitude Noise," in Proceedings, Symposium on Finite-Amplitude Wave Effects in Fluids, Copenhagen, Denmark, 20-22 August 1973, L. Bjørnø, ed. (IPC Science and Technology Press Ltd, Guildford, England, 1974).

9. See, for example, D. T. Blackstock, "Connection between the Fay and Fubini Solutions for Plane Sound Waves of Finite Amplitude," J. Acoust. Soc. Am. 39, 1010-1026 (1966).

10. See, for example, B. D. Mugridge and C. L. Morfey, "Sources of Noise in Axial Flow Fans," J. Acoust. Soc. Am. 51, 1411-1426 (1972).

ALPHABETICAL LISTING OF AUTHORS

Ahuja, K. K. 162
Allen, G. 601
Arndt, R. E. A. 142
Arnold, L. 533
Arnold, W. R. 888
Aupperle, F. A. 768
Ayoub, A. 238

Barra, V. 179
Bassiouni, M. R. 162
Beckemeyer, R. J. 859
Bell, W. A. 843
Bhutiani, P. K. 162
Blackstock, D. T. 448
Borsky, P. N. 673
Bruce, E. P. 281

Camelier, I. A. 249
Chiu, H. H. 733
Cho, T. C. 714
Cho, Y. C. 816
Chu, W. T. 50,59
Chung, J. Y. 562
Clark, L. R. 432
Cole, J. E., III 874
Cook, E. L. 859
Crocker, M. J. 562
Culick, F. E. C. 683

Daniel, B. R. 843
Dickinson, P. J. 588
Donavan, P. R. 491,505
Dosanjh, D. S. 162
Dunnill, W. A. 186

Eberhardt, A. C. 520
Eversman, W. 859

Farassat, F. 363
Fletcher, J. L. 617,634
Foss, J. F. 264

George, A. R. 328
George, W. K. 142
Goodman, M. J. 664
Gunn, W. J. 617,634

Hamilton, J. F. 562
Hammersley, R. J. 36
Handley, J. C. 708
Hassan, H. A. 697
Henderson, R. E. . . 299
Henry, J. J. 555
Hillery, H. B. . . . 573
Ho, C. 756
Holmes, D. G. 475
Homicz, G. F. 328
Huerre, P. 924

Ingard, U. 816

Janardan, B. A. . . 843
Johnston, G. W. . . 748
Johnston, J. P. . . 784
Jones, B. G. 7,20,36

Kaiser, J. E. 818
Kaplan, R. E. 50,59
Karamcheti, K. . . . 238,249,386,
924
Kelsall, T. 2
Kentzer, C. P. . . . 128
Kim, Y. N. 328
Kisner, L. 797
Kitaplioglu, C. . . . 328
Kovasznay, L. S. G. 756
Kulkarny, V. A. . . . 402
Kumar, R. N. 683

Lakshminarayana, B. 346
Lambert, R. F. . . . 768
Large, J. B. 588,601
Laufer, J. 50,59
Lawther, J. M. . . . 555
Leshner, M. D. . . . 723
LeVere, T. E. 648
Lumsdaine, E. 371,432
Lyon, R. H. 475,491,505

Marble, F. E. 584
Maus, J. R. 186
McLaughlin, D. K. . . 113
McShane, W. R. . . . 550
Morrison, G. L. . . . 113
Mungur, P. 888
Muthukrishnan, M. . . 708
Meecham, W. C. . . . 938
Nayfeh, A. H. 818,829

Pan, Y. S. 204
Panunzio, S. 179
Patrick. W. P. 816
Patterson, G. T. 186
Pearson, R. G. 664
Pestorius, F. M. 448
Pien, W. S. 328
Pignataro, L. J. 550
Planchon, H. P., Jr. . . . 20
Plett, E. G. 723

Raj, R. 346
Rannie, W. D. 916
Reddy, N. N. 219
Reethof, G. 90
Reiter, W. F. 520
Reynolds, W. C. 579
Ribner, H. S. 748
Richarz, W. G. 748
Roberts, D. W. 784
Regan, D. R. 938
Sanai, M. 416
Sarris, I. I. 874
Schlinker, R. H. 59
Schmidt, W. E. 784
Sears, W. R. 328
Seiner, J. M. 90
Shashaani, R. 797
Shivashankara, B. N. . . . 708,714
Siddon, T. E. 74
Silver, M. L. 462
Singhal, V. K. 816
Slutsky, S. 179,533,550
Strahle, W. C. 708,714
Sturtevant, B. 402
Succi, G. P. 816
Sullivan, J. 797
Summerfield, M. 723,733

Tam, C. K. 107
Telionis, D. P. 818
Thompson, D. E. 313
Toong, T. Y. 416
Troutt, T. R. 113
Tsai, M. S. 829

Vaidya, P. G. 797
Venema, T. 462

Walker, J. G. 601
Weber, D. P. 7
Whitesides, J. L., Jr. . . 219,888
Williams, S. W. 448

Yee, P. M. 186
Yu, J. C. 219,888
Yu, Y. H. 386

Zinn, B. T. 843
Zukoski, E. E. . . . 902